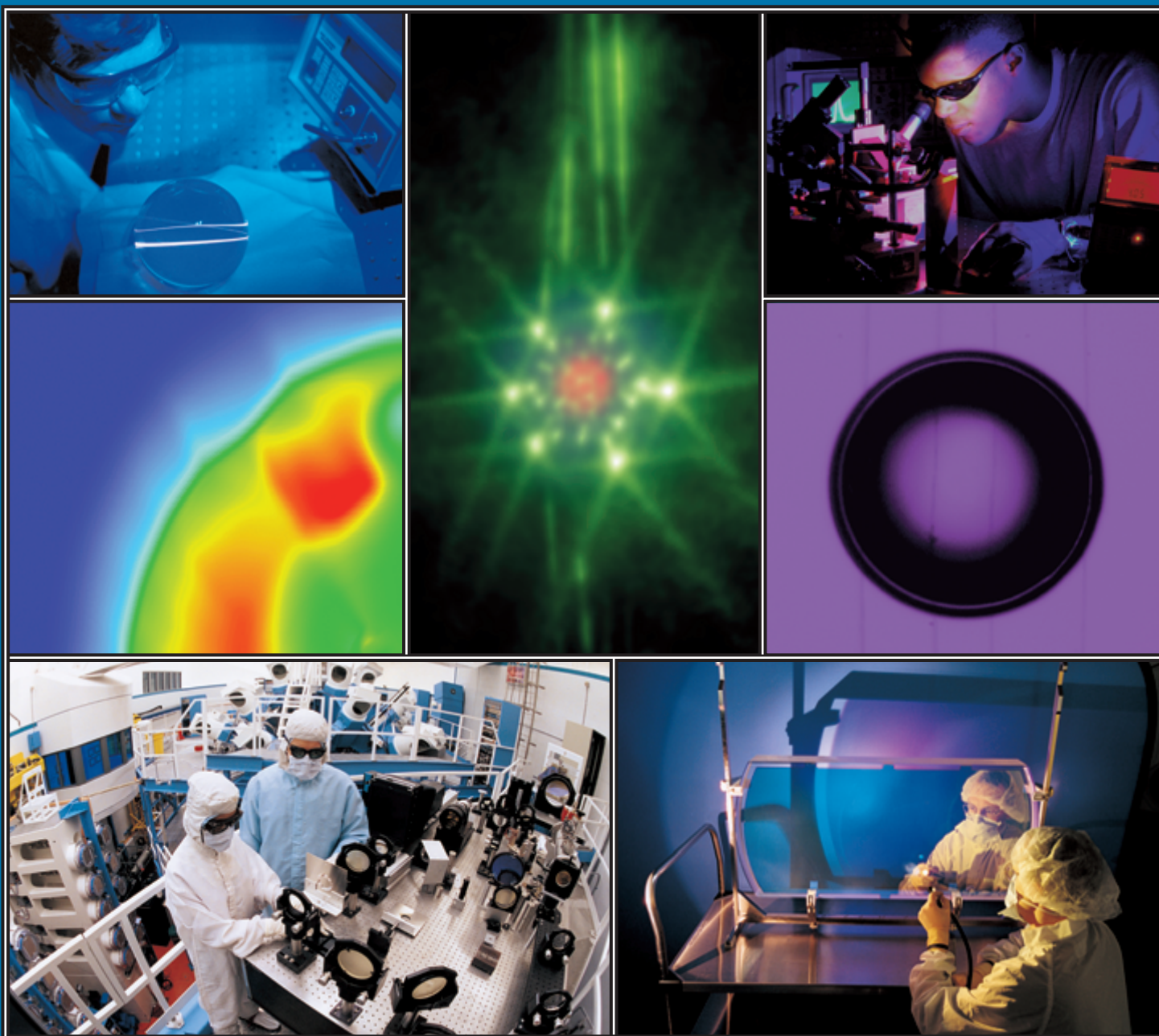


LLE 2001 Annual Report

October 2000 – September 2001



Cover Photos

Upper Left: Senior Research Engineer Terrance Kessler inspects a precision glass sphere. The sphere, produced by LLE's Optical Fabrication Shop and the Center for Optics Manufacturing at the University of Rochester, is part of the vacuum OTIS (OMEGA Transport Instrumentation System) diagnostic used in the OMEGA laser facility. Precise beam transport measurements are routinely made with this sphere, located at the center of the OMEGA target chamber. Continuous-wave UV laser light is transported through the UV optical portion of each beamline, focused onto the surface of the sphere, and retroreflected back through the beamline to a charge-coupled-device (CCD)-based power ratiometer. The OTIS diagnostic is capable of 0.1% relative laser beam transport measurements.

Center Left: A mass density contour plot at peak neutron production of a two-dimensional (2-D) *DRACO* calculation of a recent cryogenic 1-ns square implosion experiment performed on the OMEGA laser. The target's inner ice surface was perturbed with modes $\ell = 2$ to $\ell = 30$ (even modes only) taken from the cryogenic characterization station prior to shooting. The predicted 2-D yield was 57% of the clean 1-D calculation.

Lower Left: Summer high school student intern Uyen Tran (in white), now a senior at the Wilson Magnet High School of Rochester, and her LLE research supervisor, Dr. Sean Regan, are shown aligning the apparatus used to record the far-field laser beam pattern of one of the OMEGA beams. Ms. Tran's summer project was to investigate the OMEGA far-field energy distribution with an annular aperture placed in the near field of the beam.

Center: Time-integrated photograph of an imploding OMEGA cryogenic target. Simulations based on ray-tracing calculations show that the 60 OMEGA beams are both reflected from the front of the target and refracted from behind the target into the camera lens. In this way all 60 laser spots are visible in this photograph.

Upper Right: Graduate student Carlo Williams positions an optoelectronic switch embedded in a coplanar strip line for a high-speed characterization experiment using an electro-optic sampling system. The system is capable of measuring subpicosecond transients.

Center Right: Shadowgram of a layered cryogenic target with a 919- μm outer diameter, a 3.9- μm CH thickness, and an 80- μm nominal fuel thickness. The bright band is a caustic generated by the ice/gas interface. Detailed analysis of this band produces a measure of the uniformity of the ice layer. This measurement can be carried out with a spatial resolution of 1 to 2 μm .

Lower Right: A mirror coated by the Optical Manufacturing Group (OMAN) is being inspected by Senior Technical Associate Gary Mitchell. This mirror was one of the Z-Beamlet optics coated by OMAN for the Sandia National Laboratory. The mirror is 440 mm \times 940 mm \times 118 mm thick and weighs 114 kg. Specifications for this optic were reflectance $R_p > 99\%$ at 527 nm and $R_s < 20\%$ at 1053 nm at 61° incidence. This is the largest optic coated by LLE with uniformity requirements maintained across the aperture.

This report was prepared as an account of work conducted by the Laboratory for Laser Energetics and sponsored by New York State Energy Research and Development Authority, the University of Rochester, the U.S. Department of Energy, and other agencies. Neither the above named sponsors, nor any of their employees, makes any warranty, expressed or implied, or assumes any legal liability or responsibility for the accuracy, completeness, or usefulness of any information, apparatus, product, or process disclosed, or represents that its use would not infringe privately owned rights. Reference herein to any specific commercial product, process, or service by trade name, mark, manufacturer, or otherwise, does not necessarily constitute or imply its endorsement, recommendation, or favoring by the United States Government or any agency thereof or any other sponsor. Results reported in the LLE Review should not be taken as necessarily final results as they represent active research. The views and opinions of authors expressed herein do not necessarily state or reflect those of any of the above sponsoring entities.

The work described in this volume includes current research at the Laboratory for Laser Energetics, which is supported by New York State Energy Research and Development Authority, the University of Rochester, the U.S. Department of Energy Office of Inertial Confinement Fusion under Cooperative Agreement No. DE-FC03-92SF19460, and other agencies.

For questions or comments, contact Laboratory for Laser Energetics, 250 East River Road, Rochester, NY 14623-1299, (716) 275-5286. Worldwide-Web Home Page: <http://www.lle.rochester.edu/>

Prepared for
U.S. Department of Energy
San Francisco Operations Office
DOE/SF/19460-332

Distribution Category UC712
October 2000–September 2001

Printed in the United States of America
Available from
National Technical Information Services
U.S. Department of Commerce
5285 Port Royal Road
Springfield, VA 22161

Price codes: Printed Copy A11
Microfiche A01

University of Rochester
Laboratory for Laser Energetics

DOE/SF/19460-405
January 2002

LLE 2001 Annual Report

October 2000 – September 2001



**Inertial Fusion Program and
National Laser Users' Facility Program**

Contents

Executive Summary	iii
Theory of the Hot-Spot Dynamics and Deceleration-Phase Instability of Imploding ICF Capsules	1
The Effect of Shock Heating on the Stability of Laser-Driven Targets	11
Spherical Cavity Expansion in Material with Densification	15
Design and Performance of a Selectable-Rate Streak-Camera Deflection Ramp Generator	21
Unique High-Bandwidth, UV Fiber Delivery System for OMEGA Diagnostics Applications	29
Fabrication and Properties of an Ultrafast NbN Hot-Electron Single-Photon Detector	34
Preliminary Design of NIF 2-D SSD	39
Characterization of Direct-Drive-Implosion Core Conditions on OMEGA with Time-Resolved Ar <i>K</i> -Shell Spectroscopy	47
Study of Direct-Drive, DT-Gas-Filled-Plastic-Capsule Implosions Using Nuclear Diagnostics on OMEGA	54
A Consistent Measurement-Based Picture of Core-Mix in Direct-Drive Implosions on OMEGA	68
High-Resolution Neutron Imaging of Laser-Imploded DT Targets	74
The Smoothing Performance of Ultrafast Pickets on the NIF	79
Tests of EXAFS on OMEGA: Feasibility for Shock-Heating Measurements	92
Microhardness and Indentation Fracture of Potassium Dihydrogen Phosphate (KDP)	101
A Self-Calibrating, Multichannel Streak Camera for Inertial Confinement Fusion Applications	109
Evolution of Shell Nonuniformities Near Peak Compression of a Spherical Implosion	122
Multibeam Stimulated Brillouin Scattering from Hot Solid-Target Plasmas	128
Hot-Electron Effect in Superconductors and Its Applications for Radiation Sensors	134
Scaling Law for Marginal Ignition	153

Wide-Dynamic-Range “Neutron Bang Time” Detector on OMEGA	171
Functional Damage Thresholds of Hafnia/Silica Coating Designs for the NIF Laser	177
High-Gain Direct-Drive Target Designs for the National Ignition Facility	183
Ultrafast Optoelectronic Interface for Digital Superconducting Electronics	188
Optimizing the Fabrication of Polyimide Shells	196
LLE’s Summer High School Research Program	206
FY01 Laser Facility Report	208
National Laser Users’ Facility News	210
Publications and Conference Presentations	231

Executive Summary

The fiscal year ending September 2001 (FY01) was the fourth year of the cooperative agreement (DE-FC03-92SF19460) five-year renewal with the U.S. Department of Energy (DOE). This report summarizes progress and research at the Laboratory for Laser Energetics (LLE), operation of the National Laser Users' Facility (NLUF), and programs involving education of high school, undergraduate, and graduate students during the year.

Inertial Confinement Fusion Research

LLE is the principal laboratory investigating the direct-drive approach to inertial fusion for an ignition and gain demonstration on the National Ignition Facility (NIF) currently under construction at the Lawrence Livermore National Laboratory (LLNL). This requires precision laser diagnostics and controls, a cryogenic target handling system, sophisticated experimental diagnostics, robust theoretical and computational modeling, and the development of new laser and optical technologies.

The minimum drive energy needed to achieve ignition in inertial confinement fusion implosions is an important consideration to determine how much margin there will be on the NIF. Beginning on p. 153, we present a new model that consistently incorporates two competitive scaling approaches. The model includes a discussion of hot-spot dynamics, two approaches to model shell dynamics, derivations of ignition scaling, and verification of the initial assumptions of the model. Agreement with other published results from scaling laws derived from numerical simulations is also presented. In related work (p. 1), a model for the deceleration phase of an imploding inertial fusion capsule shows that the ablative flow off the inner shell surface plays a critical role in reducing the growth rate and suppressing short-wavelength modes in the deceleration-phase Raleigh–Taylor instability. This increased stability means that with proper care in drive symmetry and the use of techniques

to reduce laser imprinting, the results of the model calculations (one-dimensional) may be achievable in the laboratory.

Experimental results this year include measurements to assess the effects of shock heating on the stability of direct-drive inertial fusion capsules. Pulses that rise rapidly to 10^{14} W/cm² produce shock-induced temperatures near 25 eV, whereas more slowly rising pulses show less heating (p. 11). We see a correlation between greater hydrodynamic stability for square-pulse drive (which has more shock heating) compared to the ramp-pulse drive that exhibits less shock heating and reduced stability.

Additional understanding of moderate-convergence-ratio (~10 to 20) direct-drive implosions was achieved using a consistent measurement-based static model of the stagnated core and fuel–pusher mix. The model (p. 68) assumes that the imploded core is comprised of a clean fuel region and a mix region where the shell material is mixed into the fuel. Excellent agreement with a suite of neutron and particle diagnostics is obtained through the use of this model. Results indicate that approximately 1 μ m of shell material is mixed into the fuel during the thermonuclear burn in the experiments. It suggests that the fuel areal density is distributed equally between the clean core and fuel–shell mix region. In related experimental work for the same moderate radial convergence for DT-gas-filled polymer capsules, nuclear diagnostics (p. 54) employed a comprehensive array of knock-on deuteron, triton, and proton spectra in addition to traditional neutron measurements to compare the performance of capsules irradiated with full beam smoothing on OMEGA [1-THz, 2-D smoothing by spectral dispersion (SSD) and polarization smoothing (PS)] versus implosions of similar targets carried out with reduced beam smoothing (0.35-THz, 2-D SSD without PS). With full beam smoothing, the implosions show neutron yields, fuel areal densities, and shell areal densities approximately 80%, 60%,

and 35% higher, respectively, than those with the reduced level of beam smoothing. Modeling and shot data showing the evolution of shell modulations near the point of peak compression in spherical direct-drive implosions for two different levels of beam smoothing show that modulations in the shell areal density decrease during compression and increase during decompression.

Our collaborative research [led by scientists from the Commissariat à l'Énergie Atomique (CEA) of France and scientists from Los Alamos National Laboratory (LANL)] on high-resolution neutron imaging of capsules using penumbral images with a biconical aperture demonstrated the highest spatial resolution yet achieved on ICF implosions (45 to 60 μm) using the CEA-designed diagnostic on direct-drive implosions carried out on the OMEGA facility (p. 74). Modifications that are expected to improve the resolution to 13 μm for OMEGA implosions have recently been carried out on this diagnostic.

Characterization of direct-drive implosion core conditions using time-resolved Ar *K*-shell spectroscopy in collaborative work with research scientists from the University of Wisconsin and the University of Florida using polymer shells filled with Ar-doped deuterium gas driven with up to 24-kJ, 1-ns square laser pulses smoothed with 1-THz, 2-D SSD and PS allowed us to infer the emissivity-averaged core electron temperature and density from the time-dependent Ar *K*-shell spectral line shapes (p. 47). We infer electron densities in excess of $2.5 \times 10^{24} \text{ cm}^{-3}$ and electron temperatures $\sim 2.5 \text{ keV}$. This represents the highest combination of electron temperature and density measured for these types of implosions in laser-driven inertial fusion experiments.

A test of the feasibility of using extended x-ray absorption fine structure (EXAFS) to characterize the properties of solid materials shocked at moderately high pressures (up to a few Mbar) shows very-high-contrast EXAFS modulations when a thick, undriven Ti foil is backlit by the x-ray radiation from an imploded CH shell (p. 92). This research is part of LLE's participation in the Department of Energy's Stewardship Science Program (SSP).

We report on the first multibeam laser-plasma interaction experiments with a critical density surface present at all times (p. 128). The plasma conditions are tailored to resemble future direct-drive laser fusion implosions on the NIF. The results show strong evidence of electromagnetic (EM) wave seeding of stimulated Brillouin scattering (SBS) backscatter as well as

evidence of strongly driven, common, symmetrically located ion waves. The expected SBS scattering levels for NIF direct-drive ignition experiments are well below 1%. This gives increased confidence that good direct-drive target performance will be achieved on the NIF.

FY01 has seen significant progress in the development of new diagnostic capabilities for laser fusion. A selectable-streak-rate streak-camera deflection ramp generator produces streak-camera deflection voltage ramps with a 50- Ω composite MOSFET/avalanche transistor step generator and a relay-selectable low-pass filter network (p. 21). The design allows the remote selection of four different sweep rates and provides a 50- Ω interface to the streak camera's deflection plates. In other diagnostic development work, we highlight a low-cost, wide-dynamic-range, neutron bang time (NBT) detector (p. 171). The instrument complements the capabilities of the streak-camera-based neutron temporal diagnostic, which is also installed on OMEGA. It measures the neutron bang time of D₂- and DT-filled ICF implosion capsules at neutron yields between 10^7 and 10^{11} with an absolute timing accuracy of better than 100 ps. This level of accuracy allows the modeling of the implosions to be effectively guided using hydrocode calculations.

The self-calibrating, multichannel streak camera used on OMEGA is described beginning on p. 109. The article describes the system and focuses on the hardware and software calibration techniques that maximize the camera's utility. The system can diagnose each of the beams on every target shot and can measure beam energies with 8% accuracy and timing at 7 ps rms. Beam-to-beam power variations of less than 5% can be detected.

Laser and Optical Materials Research

We report on a new model for material behavior under compression (p. 15). The model was motivated by the fact that fused silica densifies permanently under sufficiently large compressive stresses. It is observed that the appearance of shear will facilitate densification. The model is based on a new constitutive law used to study spherical cavity expansion in material with densification.

We have developed a UV fiber-optic beam delivery system (p. 29) for OMEGA. The new fiber-optic system uses 15-m-long fibers with attenuation less than 220 dB/km at a wavelength of 351 nm to deliver optical pulses to the multibeam, streak-camera-based pulse characterization system. The modal

dispersion of the fibers is low enough to allow an overall bandwidth of the streak camera's diagnostic system to be less than or equal to 30 GHz.

Preliminary design work for the NIF's 2-D SSD beam-smoothing system is presented beginning on p. 39. Broad-bandwidth-beam-smoothing techniques are critical to high-performance, direct-drive implosions on the NIF. As a partner in the ICF program, LLE has the lead role in defining direct-drive requirements for the NIF and preparing a preliminary 2-D SSD system design. A prototype NIF 2-D SSD preamplifier module (PAM) will be built and tested at LLE. The article describes the base-line system design for the NIF's direct-drive beam-smoothing system, which will be capable of 1-THz bandwidth in the ultraviolet, $50 \times 100\text{-}\mu\text{rad}$ divergence, and 2×1 color cycles.

Ultrafast picket-fence pulses have been proposed by LLNL as a means to maximize the frequency-conversion efficiency and minimize beam-power imbalance on the NIF. We report on the results (p. 79) of the beam-smoothing performance of ultrafast picket-fence pulses for direct-drive targets on the NIF. The beam smoothing achieved with ultrafast picket-fence pulses is equivalent to the smoothing attained with the NIF base-line 2-D SSD design if the applied bandwidth and divergence used for the picket-fence-configuration SSD is close to that of the base-line-design SSD system. Furthermore, the diffraction-limited far-field pattern produced by chirped picket-fence pulses can reduce the pinhole loading, potentially leading to a larger permissible beam divergence for the NIF with 2-D SSD.

Potassium dihydrogen phosphate (KDP) is an important electro-optic tetragonal crystal used widely in high-power laser systems. We report (p. 101) on studies of the microhardness and indentation fracture of KDP, together with an approximate model for analyzing crack-load microindentation data in tetragonal crystals. The model uses the minimum elastic modulus of the material.

Current substrate cleaning and handling methods used in the application of high-reflectance optical coatings are so effective that is necessary to test large parts in order to achieve statistically meaningful assessments. This has led LLE's Optical Manufacturing Group to use equipment designed by LLNL to condition coatings on large NIF optics to test new coating designs. The equipment facilitates testing of full-sized NIF substrates by automatically scanning the optic relative to

an optical system that simultaneously subjects a small area to representative laser pulses and detects any resulting damage. Repeated scans at increasing fluence were used to quantify the performance of three candidate coating designs (p. 177).

Devices that could lead to revolutionary progress in areas ranging from multicast free-space satellite communications through quantum computing and quantum cryptography to semiconductor integrated circuit testing led us to fabricate and investigate the properties of a simple-to-manufacture and simple-to-operate NbN hot-electron photodetector with a picosecond response time, high intrinsic quantum efficiency, negligible dark counts, and the capability to detect single photons from the ultraviolet to the infrared wavelength range (p. 34).

We survey the main aspects of nonequilibrium hot-electron phenomena in superconducting films beginning on p. 134. Various theoretical models developed to describe the hot-electron effect are presented. The article describes a number of radiation-sensing devices that have been fabricated and tested and demonstrate significantly improved performance over conventional implementations.

Laser Facility Report

OMEGA operations during FY01 (p. 208) yielded a total of 1283 target shots (up from 1153 last year), including 311 shots for LLNL, 124 for LANL, 10 for Sandia National Laboratory (SNL), 11 for the French Commissariat à l'Énergie Atomique (CEA), and 125 for the National Laser Users' Facility (NLUF). The report summarizes highlights and other achievements during the year. All investigators have benefited from the improvements that have increased the reliability and repeatability of the OMEGA system.

National Laser Users' Facility and External Users of OMEGA

During FY01, external use of OMEGA increased by over 5% over the prior fiscal year, accounting for nearly 47% of the total target shots. Eight NLUF experiments were carried out in FY01 and are summarized beginning on p. 210. Target experiments conducted during the year for the national laboratories, nuclear weapons effects testing (NWET), and the CEA programs are summarized beginning on p. 217. LLNL carried out experiments on laser-plasma interactions; investigations of the potential of "cocktail" hohlraums to increase the energy coupling to NIF targets; high-convergence HEP-5 implosions; NIF-relevant hohlraum symmetry; planar Rayleigh-Taylor

experiments; development of ignition diagnostics; tests of a new laser-driven, high-pressure source (IDrive); high-Z and low-Z equation-of-state measurements; direct-drive Richtmyer–Meshkov instability; supersonic jets; nonideal backlit implosions; slit closure measurements; and gas-filled x-ray sources for NWET applications. Along with LLNL scientists, SNL performed shock-timing and ablator burnthrough measurements.

The LANL campaigns examined double-shell capsule designs, the development of x-ray backlighting sources, several classified experiments, direct-drive cylindrical implosions, and the development of NIF diagnostics. CEA carried out work on neutron imaging and gamma-ray measurements.

Education at LLE

As the only major university participant in the National ICF Program, education continues to be an important mission for the Laboratory. Graduate students are using the world's most powerful ultraviolet laser for fusion research on OMEGA, making significant contributions to LLE's research activities. Twenty-three faculty from five departments collaborate with LLE's scientists and engineers. Presently 60 graduate students are pursuing Ph.D. degrees at the Laboratory. The research includes theoretical and experimental plasma physics, high-energy-density plasma physics, x-rays and atomic physics, nuclear fusion, ultrafast optoelectronics, high-power-laser development and applications, nonlinear optics, optical materials and optical fabrications technology, and target fabrication. Technological developments from ongoing Ph.D. research will continue to play an important role on OMEGA.

One hundred fifty-one University of Rochester students have earned Ph.D. degrees at LLE since its founding. An additional 81 graduate students and 23 postdoctoral positions from other universities were funded by NLUF grants. The most recent University of Rochester Ph.D. graduates and their thesis titles are

Roman Adam	<i>Fabrication and Characterization of Ultrafast Superconducting Optoelectronic Devices</i>
Luis de Araujo	<i>Quantum Control of Atoms and Molecules</i>

Guy Delmarter	<i>Hydrodynamic Models of Outflows from Young and Evolved Stars</i>
---------------	---

Galina Grom	<i>Nanocrystalline Silicon/Silicon Oxide Superlattices: Fabrication, Characterization, and Applications in Nano-Flash Memories</i>
-------------	--

Viktor Lobatchev	<i>Hydrodynamics of Inertial Fusion Implosions: Feedout and Deceleration-Phase Instability</i>
------------------	--

Herman Lopez	<i>Porous Silicon Nanocomposites for Optoelectronic and Telecommunication Applications</i>
--------------	--

Eduard Startsev	<i>Ponderomotive Particle Acceleration in a Plasma</i>
-----------------	--

Carlo Williams	<i>Ultrafast Photodetectors Based on the Hot-Electron Effect in Superconductors</i>
----------------	---

Hong Ye	<i>Hot Carrier Dynamics in GaN</i>
---------	------------------------------------

York Young	<i>Cold Collisions of Laser-Cooled Na and Rb Atoms</i>
------------	--

Approximately 40 University of Rochester undergraduate students participated in work or research projects at LLE this past year. Student projects include operational maintenance of the OMEGA laser system; work in laser development, materials, and optical-thin-film coating laboratories; programming; image processing; and diagnostic development. This is a unique opportunity for students, many of whom will go on to pursue a higher degree in the area in which they gained experience at the Laboratory.

In addition, LLE directly funds research programs within the MIT Plasma Science and Fusion Center, the State University of New York (SUNY) at Geneseo, and the University of Wisconsin. These programs involve additional graduate and undergraduate students in the LLE ICF Program. The joint work with SUNY Geneseo, for example, currently involves approximately 15 undergraduates.

For the past 11 years LLE has run a Summer High School Student Research Program (p. 206) in which this year 13 high school juniors spent eight weeks performing individual research projects. Each student is individually supervised by a staff scientist or an engineer. At the conclusion of the program, the students make final oral and written presentations on their work. The reports are published as an LLE report.

In 2001, LLE presented its fifth William D. Ryan Inspirational Teacher Award to Mr. David Dussault, a mathematics and computer science teacher at Livonia High School. Alumni

of our Summer High School Student Research Program were asked to nominate teachers who had a major role in sparking their interest in science, mathematics, and/or technology. This award, which includes a \$1000 cash prize, was presented at the Summer High School Student Research Symposium. Mr. Dussault was nominated by Mr. Michael Harvey, a 1999 participant in the program.

Robert L. McCrory
Director

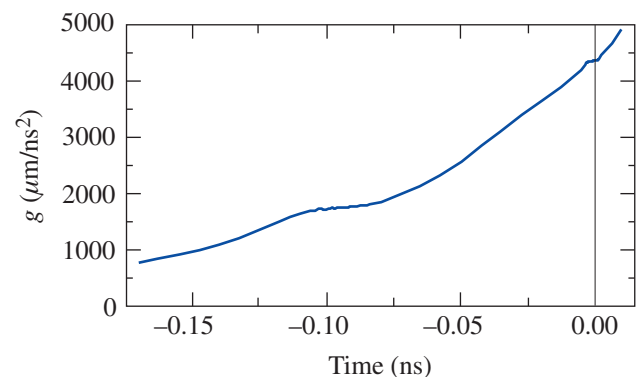
Theory of the Hot-Spot Dynamics and Deceleration-Phase Instability of Imploding ICF Capsules

Introduction

In inertial confinement fusion¹ (ICF), a spherical shell of cryogenic deuterium and tritium (DT) filled with DT gas is accelerated by direct laser irradiation (direct drive) or x-rays produced by a high-Z enclosure (indirect drive). In direct-drive ICF, the laser pulse starts from a constant, low-intensity foot designed to drive a uniform shock through the shell. After the shock breaks out on the shell's inner surface, the latter expands forward, launching a shock in the gas and a rarefaction wave in the shell. As the rarefaction wave travels across the shell, the shell's outer surface moves at approximately constant velocity. When the rarefaction wave reaches the shell's outer surface, the latter starts accelerating and the so-called *acceleration phase* begins. At about the shock breakout time, the laser power begins to rise, first slowly and then more rapidly to keep the shell close to the shock front traveling inside the gas. A second shock originating within the shell is launched during the initial pulse rise and merges with the first shock before reaching the center of the capsule. The acceleration phase ends when the laser is turned off and the shell starts traveling at approximately constant velocity. Standard direct-drive pulse designs make use of such a sequence of two shocks merging into one, whereas the latest pulse designs of indirect-drive ICF make use of a sequence of four shocks² coalescing into one before reaching the center.

In both direct- and indirect-drive ICF, the single shock resulting from the multiple-shock coalescence travels in the gas in the form of a *strong* shock; i.e., $\Delta P/P_b \gg 1$, where ΔP is the pressure jump across the shock and P_b is the gas pressure before the shock. Such a shock is reflected off the center of the capsule (return shock) and subsequently off the incoming inner shell surface, which in turn is impulsively decelerated. The shock reflected off the shell travels toward the center, where it is reflected again and subsequently reflected a second time from the shell. At each reflection off the shell, the latter is impulsively decelerated and the shock gets weaker until the pressure jump across the shock front is smaller than the pressure before the shock ($\Delta P/P_b < 1$). The time interval corresponding to the multiple shock reflections is referred to as

the *impulsive deceleration phase*. Typically, the reflected shock becomes *weak* after the first or second reflection off the shell. At this point the material enclosed by the inner shell surface develops a fairly uniform pressure profile and is referred to as the *hot spot*. After the return shock reflects off the shell, the hot spot is formed, and its pressure is large enough that the shell velocity is lower than the hot-spot sound speed, i.e., the flow is subsonic. When the hot spot is formed, the shell is decelerated in a continuous (not impulsive) manner while acting like a piston on the hot spot. Such a continuous slowing down of the shell up to the stagnation point occurs over a period of a few hundred picoseconds and is referred to as the *continuous deceleration phase*. Figure 85.1 shows the time evolution of the deceleration g of a shell designed for direct-drive ignition³ on the National Ignition Facility (NIF). The time $t = 0$ ns represents the stagnation point, and the continuous deceleration starts at about 200 ps before stagnation. The NIF capsule is a 345- μm -thick shell of DT ice with an inner radius of 1350 μm . The shell is filled with DT gas at a temperature of 18 K and a density of 2×10^{-4} g/cm³. During the deceleration phase, the hot-spot pressure, density, and temperature increase until reaching the ignition conditions. If the shell is sufficiently dense, the ignited hot spot will trigger a propagating burn wave



TC5421

Figure 85.1
Time evolution of the inner-shell-surface deceleration for a direct-drive NIF capsule. Time $t = 0$ is the stagnation time.

in the shell and a significant fraction of the shell mass will undergo thermonuclear burn if the shell's areal density exceeds a few g/cm^2 .

It is well known that the outer shell surface is unstable to the Rayleigh–Taylor (RT) instability during the acceleration phase; however, because of mass ablation, the instability growth rates are significantly reduced^{4–10} with respect to their classical values. The theory of the RT instability in an accelerated planar foil has been carried out in Refs. 6–9, where the growth rate's dependence on the ablation velocity V_a , density-gradient scale length $L_m = \min[\rho(\rho')^{-1}]$, front acceleration g , and power index for thermal conduction ν (here the thermal conductivity is approximated by $\kappa \approx \kappa_0 T^\nu$) is calculated by analytically solving the conservation equations. In Refs. 6–9, the stability of long ($kL_m < 1$) and short ($kL_m > 1$) wavelength modes is investigated for large and small Froude numbers (Fr), where $Fr = V_a^2/gL_0$ and $L_0 = L_m \nu^\nu / (\nu + 1)^{\nu+1}$. It is found that short-wavelength modes are completely suppressed when $Fr > 1$ and the unstable spectrum exhibits a cutoff at long wavelengths, i.e., $k_{\text{cutoff}} L_m < 1$. Instead, when $Fr < 1$, the cutoff occurs at short wavelengths ($k_{\text{cutoff}} L_m \sim 1/Fr^{1/3}$), and both long- and short-wavelength modes (up to the cutoff) are unstable. The stability analysis in Refs. 8 and 9 has been carried out separately for large and small Froude numbers as well as long and short wavelengths. In Ref. 10 the different growth-rate solutions have been combined into a single formula that asymptotically matches those solutions in the different parameter ranges.

Despite the significant growth-rate reduction induced by mass ablation and finite-density-gradient scale-length effects, the amplification of surface perturbations can be substantial, so the thickness of ICF shells must be chosen to prevent the shell from breaking up when the RT bubble amplitude equals the shell thickness.

Even when the shell integrity is preserved during the acceleration phase, the hot-spot ignition can be quenched¹¹ by the deceleration-phase RT instability. The latter is the instability of the inner shell surface that occurs when the shell is decelerated by the high pressure building up inside the hot spot. The deceleration-phase RT causes the cold shell material to penetrate and cool the hot spot, preventing it from achieving ignition conditions. Furthermore, if the inner-surface perturbation becomes nonlinear, a fraction of the shell's kinetic energy is used to feed the lateral shell motion induced by the instability, reducing the compression of the hot spot. Typical seeds for the deceleration-phase RT are the surface nonuniformities that

feed through the shell from the outer surface during the acceleration-phase instability.

It is known that the deceleration-phase RT is classical¹² and all modes are unstable. The finite-density-gradient scale length¹³ reduces the instability growth rates, which can be approximated by the classical fitting formula¹

$$\gamma_{\text{dec}} \approx \sqrt{\frac{kg}{1+kL}}, \quad (1)$$

where L is the shell's density-gradient scale length and k is the perturbation wave number approximately equal to l/R with R being the hot-spot radius and l the mode number. Observe that Eq. (1) indicates that all modes are unstable, with the fastest-growing modes having short wavelengths ($kL \gg 1$) and growth rates $\gamma_{\text{dec}}(kL \gg 1) = \sqrt{g/L}$. As described in Ref. 13, the finite-density-gradient scale length is produced by the thermal conduction inside the hot spot. It is shown in this article that mass ablation from the shell's inner surface significantly reduces the deceleration RT growth rates, leading to much lower growth rates than predicted by Eq. (1) and to a cutoff in the unstable spectrum. Mass ablation is caused by the heat flux leaving the hot spot and depositing on the shell's inner surface. We have calculated the ablation velocity and the shell's density-gradient scale length during the deceleration phase. Then, using the RT theory of Ref. 10, we have calculated the growth rates and compared them with the results of numerical simulations. For the direct-drive NIF-like capsule under consideration,³ the cutoff mode number for the deceleration-phase RT is approximately $l_{\text{cutoff}} \approx 90$.

The remainder of this article is divided into two major sections that describe the hot-spot dynamics and the linear stability. The hot-spot model is valid from the beginning of the continuous deceleration phase (after the shock reflection off the shell) until the onset of the ignition process. The evolution of the hot-spot radius, mass, temperature, and density is calculated in terms of initial conditions and hot-spot pressure. The second section is devoted to the hydrodynamic stability analysis of the shell during the continuous deceleration phase. The growth rate of the RT instability is derived, including finite-density-gradient scale length and ablation velocity.

Hot-Spot Dynamics

The hot spot is a low-density plasma heated by the shock and by the PdV work of the cold, dense surrounding shell. Its mass is made of the ionized DT gas and the plasma ablated off

the inner shell surface. The hot-spot dynamics is governed by the mass, momentum, and energy conservation equations. The energy equation must include the electronic thermal conduction and alpha-particle energy deposition. Bremsstrahlung radiation energy losses are neglected in this model because they add great complexity to the mathematical solution and their contribution is typically smaller than the mechanical work and/or the fusion power. The magnitude of the radiation losses is larger than the fusion power for temperatures below 4.4 keV, when the PdV work rate is typically greater than both radiation and fusion power. Thus at such low temperatures both radiation losses and alpha power are negligible with respect to the compression work rate. The PdV work rate decreases near the shell's stagnation point, where higher temperatures are reached within the hot spot. If such temperatures are well above 4.4 keV, the alpha-particle power is greater than the radiation losses and the bremsstrahlung term can again be neglected in the energy equation. The model described in this section may not apply to capsules that do not ignite or with small ignition margins (small mechanical work rate and low final temperatures) as their evolution can be significantly affected by radiation losses.

This model is expected to predict the main characteristics of the deceleration phase up to the onset of ignition. The actual ignition process in the hot spot is not accurately modeled because the alpha-particle energy is assumed to be locally deposited within the hot spot. Instead, the alpha-particle mean free path is typically of the same order of magnitude as the hot-spot radius, and a fraction of the alpha particles leaves the hot spot and is deposited on the shell's inner surface. Those alpha particles trigger the propagation of a burn wave in the cold, dense shell, which burns until it disassembles. The thermonuclear burn wave propagation is not described by our model and requires a diffusion (or kinetic) treatment of the alpha-particle population. Detailed analysis of the burn wave propagation and the effects of the RT instability on the capsule gain can be found in Ref. 11.

Even though the local deposition approximation used here is strictly valid only when all the alpha particles are absorbed within the hot spot, we artificially include the effect of alpha-particle diffusion by adding a multiplicative factor $\theta \leq 1$ to the alpha power term. When $\theta < 1$, one should also include the alpha power deposited at the inner shell surface due to the $1-\theta$ fraction of leaking alpha particles. Such a contribution is not included in the derivation of the hot-spot profiles, ablation velocity, and density-gradient scale length because an analytic solution of the conservation equations could not be found.

Thus, an additional limitation of this model is that the fraction of alpha particles leaving the hot spot is small compared to the fraction absorbed.

In conclusion, the model described below is suitable to describe the deceleration phase up to the onset of ignition, but it does not include the relevant physics pertaining to the ignition process or the burn wave propagation. We speculate that most of the RT instability growth occurs before ignition takes place when our model captures the essential physics of the hot-spot dynamics.

1. General Equations

The model is based on the Lagrangian form of the equations of motion as the boundary of the hot spot moves before and after stagnation. The Lagrangian equations of motion in spherical geometry can be written in the following form:

$$\frac{1}{\rho} = \frac{1}{3} \frac{\partial r^3}{\partial m}, \quad (2)$$

$$\frac{\partial U}{\partial t} + r^2 \frac{\partial P}{\partial m} = 0, \quad (3)$$

$$c_v \rho^{\Gamma-1} \frac{\partial}{\partial t} \frac{T}{\rho^{\Gamma-1}} = \frac{\partial}{\partial m} \kappa(T) r^4 \rho \frac{\partial T}{\partial m} + \frac{\rho}{4m_i^2} \theta E_\alpha \langle \sigma \mathbf{v} \rangle, \quad (4)$$

where $c_v = 3/2 A$ is the specific heat at constant volume, $A = m_i / (1 + Z)$, m_i and Z are the ion mass and atomic number, respectively ($Z = 1$ for DT), Γ is the ratio of specific heats or adiabatic index ($\Gamma = 5/3$ for a monoatomic gas), $\kappa(T) = \kappa_0 T^\nu$ is the Spitzer thermal conductivity, $\nu = 5/2$, $E_\alpha = 3.5$ MeV, θ is the absorbed alpha-particle fraction, and $\langle \sigma \mathbf{v} \rangle$ is the fusion reaction rate. The independent variable m is proportional to the mass within the radius r :

$$m = \int_0^r \rho(x, t) x^2 dx. \quad (5)$$

Equation (4) has been derived by using the standard ideal gas equation of state $P = \rho T / A$ and by neglecting bremsstrahlung losses. To solve the conservation equations, we adopt the subsonic flow ordering, which represents a good approximation after the shock transient. We let $t \sim R / C_s$ (or $t \sim R / U$), $r \sim R$, and $U \sim \epsilon C_s$, where $\epsilon \ll 1$ represents the flow Mach number. We find the solution of Eqs. (2)–(4) by a formal

expansion in powers of ϵ . By inspection, Eq. (3) reduces to $\partial_m P = O(\epsilon P/m)$, yielding

$$P \approx P_{\text{hs}}(t) \quad (6)$$

and reproducing the well-known flat pressure approximation.

The density in the energy equation can be eliminated by using the equation of state, and the fusion rate can be approximated with a quadratic term $\langle \sigma v \rangle = S_\alpha T^2$. Such an approximation is valid as long as $5 < T < 25$ keV, which is a temperature range relevant to ICF ignition experiments. After a straightforward manipulation, the energy equation can be rewritten in the following form:

$$\begin{aligned} c_v \frac{P_{\text{hs}}(t)^{\Gamma-1}}{T^{\Gamma-1}} \frac{\partial}{\partial t} \frac{T^\Gamma}{P_{\text{hs}}(t)^{\Gamma-1}} \\ = A \kappa_0 P_{\text{hs}}(t) \frac{\partial}{\partial m} r^4 T^{\nu-1} \frac{\partial T}{\partial m} + \frac{\theta E_\alpha S_\alpha A}{M_i^2} P_{\text{hs}}(t) T. \end{aligned} \quad (7)$$

Equation (7) can be further simplified by defining the variables $\Pi \equiv T/P_{\text{hs}}^{1-1/\Gamma}$ and

$$\tau = \frac{3^{4/3}}{A^{1/3}} \frac{\kappa_0}{\Gamma c_v} \int_0^t P_{\text{hs}}(t')^\beta dt' + \tau_0, \quad \beta = \frac{3(\Gamma-1)\nu-1}{3\Gamma}, \quad (8)$$

where τ_0 is a constant to be determined by the initial conditions. Using Eq. (2) to determine the relation between the volume within the radius r and Π , one finds

$$r^3 = \frac{3}{A P_{\text{hs}}(t)^{1/\Gamma}} \Phi, \quad \Phi \equiv \int_0^m \Pi(m', \tau) dm', \quad (9)$$

and the energy equation can be rewritten in the following simple form:

$$\frac{\partial \Pi}{\partial \tau} = \frac{\partial}{\partial m} \Pi^{\nu-1} \Phi^{4/3} \frac{\partial \Pi}{\partial m} + \Delta_\alpha \Pi P_{\text{hs}}(t)^\delta, \quad (10)$$

where

$$\delta = \frac{3\nu+1+3\Gamma(1-\nu)}{3\Gamma}, \quad \Delta_\alpha = \left(\frac{A}{3}\right)^{4/3} \frac{\theta E_\alpha S_\alpha}{4\kappa_0 m_i^2}. \quad (11)$$

The next step is to integrate Eq. (10) between 0 and m and to eliminate Π , leading to the following equation for Φ :

$$\frac{\partial \Phi}{\partial \tau} = \Phi^{4/3} \left(\frac{\partial \Phi}{\partial m}\right)^{\nu-1} \frac{\partial^2 \Phi}{\partial m^2} + \Delta_\alpha \Phi P_{\text{hs}}(t)^\delta. \quad (12)$$

Observe that the α particle term on the right-hand side of Eq. (12) can be combined with the left-hand side by defining the new dependent (Ψ) and independent (η) variables:

$$\Psi = \Phi \exp\left[-D_\alpha \int_{t_0}^t P_{\text{hs}}(t') dt'\right], \quad (13)$$

$$\begin{aligned} \eta = \eta_0 + \frac{3^{4/3} \kappa_0}{A^{1/3} \Gamma c_v} \int_{t_0}^t dt' P_{\text{hs}}(t')^\beta \\ \exp\left[\left(\nu + \frac{1}{3}\right) D_\alpha \int_{t_0}^{t'} P_{\text{hs}}(t'') dt''\right], \end{aligned} \quad (14)$$

where $t = t_0$ represents the beginning of the continuous deceleration phase,

$$D_\alpha = \frac{\Gamma-1}{4\Gamma} \frac{\theta E_\alpha S_\alpha}{(1+Z)^2}, \quad (15)$$

and η_0 is a new constant. After a short calculation, Eq. (12) can be rewritten in the following simple form:

$$\frac{\partial \Psi}{\partial \eta} = \Psi^{4/3} \left(\frac{\partial \Psi}{\partial m}\right)^{\nu-1} \frac{\partial^2 \Psi}{\partial m^2}. \quad (16)$$

A self-similar solution of Eq. (13) can be found by setting

$$\Psi = \left(\frac{a^{-3(\nu+1)}}{\eta^3 [1-\Omega(\nu+1)]}\right)^{\frac{1}{3\nu+1}} F(\xi), \quad \xi = \frac{am}{\eta\Omega}, \quad (17)$$

where ξ and $F(\xi)$ are dimensionless and a is a constant with the dimensions of η^Ω/m to be determined using the initial conditions. Substituting Eq. (17) into Eq. (16) yields the following ordinary differential equation for $F(\xi)$:

$$\frac{3[1-\Omega(\nu+1)]}{3\nu+1}F + \Omega\xi \frac{dF}{d\xi} + F^{4/3} \left(\frac{dF}{d\xi} \right)^{\nu-1} \frac{d^2F}{d\xi^2} = 0. \quad (18)$$

At the hot spot/shell interface, the temperature is considerably less than the central hot-spot temperature. Since the temperature is proportional to $dF/d\xi$, one can neglect corrections of the order of $T_{\text{shell}}/T(r=0)$ and look for solutions of Eq. (18), satisfying $dF/d\xi = 0$ at the hot-spot radius. The function F is proportional to the internal energy inside the hot spot and therefore positive by definition. Thus, the solution of Eq. (18) satisfying the boundary conditions can be found only when $\Omega = 1/(\nu+1)$, leading to the simplified hot-spot equation

$$\frac{1}{\nu+1}\xi + F^{4/3} \left(\frac{dF}{d\xi} \right)^{\nu-2} \frac{d^2F}{d\xi^2} = 0. \quad (19)$$

The numerical solution of such an equation requires the derivative at $\xi=0$, $F'(0)$. It can be easily shown, however, that all the physical quantities are independent of the choice of $F'(0)$; thus, without loss of generality, we set $F'(0) = 1$. The solution of Eq. (19) for $\nu = 5/2$, $F(0) = 0$, and $F'(0) = 1$ is shown in Fig. 85.2. Observe that $dF/d\xi$ (and therefore T) vanishes at $\xi_0 = 1.23$ and $F(\xi_0) = 0.70$. Defining the hot spot as the region

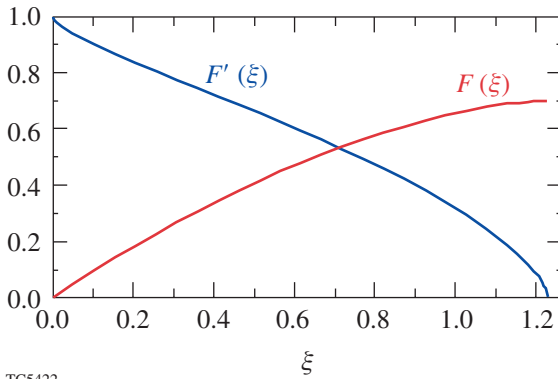


Figure 85.2
Functions $F(\xi)$ (proportional to the internal energy) and $F'(\xi)$ (proportional to the temperature) obtained from the numerical solution of Eq. (19) with $\nu = 5/2$, $F(0) = 0$, and $F'(0) = 1$. The hot spot is defined to be the region with $\xi \leq 1.23$.

with $\xi \leq \xi_0$ leads to the following expression of the hot-spot mass:

$$M_{\text{hs}} = 4\pi m_{\text{hs}} = 4\pi\xi_0\eta^{1/(\nu+1)}/a. \quad (20)$$

The constants a and η_0 can be determined from the initial conditions applied to Eqs. (20), (17), and (9), leading to

$$a = \left[\frac{3F(\xi_0)}{AR_{\text{hs}}(0)^3 P_{\text{hs}}(0)^{1/\Gamma}} \right]^{\frac{3\nu+1}{3(\nu+1)}}, \quad \eta_0 = \left[\frac{aM_{\text{hs}}(0)}{4\pi\xi_0} \right]^{\nu+1}, \quad (21)$$

where $R_{\text{hs}}(0)$, $P_{\text{hs}}(0)$, and $M_{\text{hs}}(0)$ are the initial hot-spot radius, pressure, and mass, respectively. A short calculation using Eqs. (9), (13), (17), and (20) and the equation of state yields the relevant hot-spot parameters [mass, areal density (ρR), density, and temperature] as functions of the hot-spot pressure and radius:

$$M_{\text{hs}}(t) = \left\{ M_{\text{hs}}(0)^{\nu+1} + \chi_0 \kappa_0 A^{\nu+1} \right.$$

$$\left. \int_{t_0}^t P_{\text{hs}}(t')^\beta \left[R_{\text{hs}}(t')^3 P_{\text{hs}}(t')^{1/\Gamma} \right]^{\nu+1/3} dt' \right\}^{\frac{1}{\nu+1}}, \quad (22)$$

$$\rho R \equiv \int_0^{R_{\text{hs}}} \rho dr = \mu_0 \frac{M_{\text{hs}}(t)}{4\pi R_{\text{hs}}(t)^2}, \quad (23)$$

$$\rho_{\text{hs}}(m, t) = \frac{3M_{\text{hs}}(t)}{4\pi R_{\text{hs}}(t)^3} \frac{F(\xi_0)}{\xi_0 F'(\xi)}, \quad (24)$$

$$T_{\text{hs}}(m, t) = \frac{AP_{\text{hs}}(t)}{\rho_{\text{hs}}(m, t)},$$

where

$$\chi_0 \equiv \frac{\Gamma-1}{\Gamma} \frac{3^{1-\nu} (4\pi\xi_0)^{\nu+1}}{F(\xi_0)^{\nu+1/3}}, \quad (25)$$

$$\mu_0 = \frac{F(\xi_0)^{2/3}}{\xi_0} \int_0^{\xi_0} \frac{d\xi}{F(\xi)^{2/3}}.$$

For $\nu = 5/2$ and $\Gamma = 5/3$, we find $\mu_0 = 2.27$ and $\chi_0 = 3052.8$. Observe that the hot-spot mass increases with time at a rate that depends on the thermal conductivity coefficient. The mass increase is due to the ablation off the shell's inner surface. The hot-spot radius and pressure are related through Eq. (9), which can be rewritten by using the initial conditions, leading to

$$\frac{R_{\text{hs}}(t)^3}{R_{\text{hs}}(0)^3} = \left[\frac{P_{\text{hs}}(0)}{P_{\text{hs}}(t)} \right]^{1/\Gamma} \exp \left[D_\alpha \int_{t_0}^t P_{\text{hs}}(t) \right]. \quad (26)$$

In the absence of alpha-particle heating ($D_\alpha = 0$), Eq. (26) yields $P_{\text{hs}} R_{\text{hs}}^{3\Gamma} = \text{constant}$, indicating that the hot spot behaves like a closed system that is adiabatically heated ($PV^\Gamma = \text{constant}$, where V is the volume). This result is somewhat surprising because the hot spot is not a closed system since its mass increases with time. From the energetic point of view, however, the hot spot is indeed insulated as the heat conduction losses are recycled into the hot spot via the ablated shell material. This can be shown by writing the total (internal + kinetic) energy equation in the conservative form:

$$\begin{aligned} \frac{\partial}{\partial t} \left(\frac{P}{\Gamma-1} + \rho \frac{U^2}{2} \right) + \nabla \cdot \left[\mathbf{v} \left(\frac{\Gamma P}{\Gamma-1} + \rho \frac{U^2}{2} \right) \right] \\ = \nabla \cdot \kappa(T) \nabla T + \frac{\rho^2}{4M_i^2} \theta E_\alpha \langle \sigma \mathbf{v} \rangle. \end{aligned} \quad (27)$$

Using the subsonic flow assumption, we neglect the hot-spot kinetic energy with respect to the internal energy. Then, after approximating the fusion cross section with the quadratic form $\langle \sigma \mathbf{v} \rangle \approx S_\alpha T^2$, Eq. (27) is integrated over the hot-spot volume enclosed by the inner shell surface. At the inner surface, the shell material is cold and the thermal conduction can be neglected. A straightforward calculation leads to the following form of the energy equation:

$$\begin{aligned} \frac{d}{dt} (P_{\text{hs}} R_{\text{hs}}^3) + 3R_{\text{hs}}^2 P_{\text{hs}} \left[\Gamma U(R_{\text{hs}}, t) - \frac{dR_{\text{hs}}}{dt} \right] \\ = \Gamma D_\alpha P_{\text{hs}}^2 R_{\text{hs}}^3, \end{aligned} \quad (28)$$

where $U(R_{\text{hs}}, t)$ is the flow velocity at the shell's inner surface. The flow velocity results from the combination of the inner

surface motion and the ablative flow:

$$U(R_{\text{hs}}, t) = \dot{R}_{\text{hs}} - V_a, \quad (29)$$

where V_a is the ablation velocity and \dot{R}_{hs} scales with the implosion velocity. Since $V_a \ll \dot{R}_{\text{hs}}$, the ablation velocity can be neglected, and Eq. (28) yields the exact solution shown in Eq. (26). Thus, Eqs. (26) and (28) are equivalent forms of the energy equation. Notice that the heat conduction losses do not enter into the global energy balance of the hot spot. This is because the heat flux leaving the hot spot is deposited onto the shell's inner surface. A fraction of this energy is transformed into internal energy of the shell material ablating into the hot spot. The remaining fraction produces the PdV work done by the ablated plasma entering the hot spot against the hot-spot pressure. In other words, the energy leaving the hot spot in the form of heat conduction losses goes back into the hot spot in the form of internal energy and compression work of the ablated plasma. Therefore, conduction losses are not real energy losses and do not affect the global energy balance of the hot spot as shown by Eq. (28). It is important to emphasize that the hot-spot energy is proportional to its pressure and the conduction losses affect the hot-spot temperature but not its pressure. This conclusion implies that greater heat conduction losses would lower the temperature and raise the density (through larger ablation at the shell's inner surface), leaving the pressure ($P \sim \rho T$) unaltered.

Equation (26) relates hot-spot radius and pressure. All the hydrodynamic quantities shown in Eqs. (22)–(24) can therefore be expressed as functions of the pressure only, using Eq. (26). It follows that a fully self-consistent implosion model requires additional equations relating $P_{\text{hs}}(t)$ to the shell's properties. The coupling between the hot spot and the shell will be discussed in a forthcoming LLE Review. Here, we consider P_{hs} as a given function of time and use the hot-spot analysis developed in this section to determine the ablation velocity and density-gradient scale length.

2. Ablation Velocity and Density-Gradient Scale Length

An important result of the analysis carried out in the previous section concerns the hot-spot mass. Equation (22) shows that the hot-spot mass increases with time. Its rate of increase depends on the magnitude of the heat conduction coefficient κ_0 [here, $\kappa(T) = \kappa_0 T^\nu$] and the hot-spot pressure. The ablation velocity at the shell's inner surface follows by noticing that the mass ablation rate off the shell, \dot{M}_a , must equal the rate of change of the hot-spot mass \dot{M}_{hs} . Given the

hot-spot radius R_{hs} and the shell's peak density ρ_{shell} , the ablation rate is $\dot{M}_a = 4\pi R_{\text{hs}}^2 \rho_{\text{shell}} V_a$, where V_a is the ablation velocity. Thus setting $\dot{M}_a = \dot{M}_{\text{hs}}$ yields the ablation velocity

$$V_a = \frac{\dot{M}_{\text{hs}}}{4\pi R_{\text{hs}}^2 \rho_{\text{shell}}}, \quad (30)$$

where \dot{M}_{hs} can be determined from Eq. (22). Then, using the m -derivative of Φ to relate T and η , the ablation velocity can be written in terms of standard hot-spot and shell parameters

$$V_a = \frac{3(\Gamma-1)}{(\nu+1)\Gamma} \frac{\xi_0}{F'(0)^\nu F(\xi_0)^{1/3}} \frac{A\kappa_0 T_{\text{hs}}(0,t)^\nu}{\rho_{\text{shell}}(t) R_{\text{hs}}(t)}, \quad (31)$$

where both the central hot-spot temperature and radius depend only on the hot-spot pressure. Using $F'(0) = 1$ and $\nu = 5/2$ to solve Eq. (18) leads to $\xi_0 = 1.23$, $F(\xi_0) = 0.7$. The ablation velocity can then be calculated using standard ICF units, leading to the following simple form:

$$V_a (\mu\text{m/ns}) = 6 \times 10^3 \frac{(T_{\text{keV}}^{\text{hs}})^{5/2}}{R_{\mu\text{m}}^{\text{hs}} \rho_{\text{g/cm}^3}^{\text{shell}} \Lambda^{\text{hs}}}, \quad (32)$$

where R^{hs} , T^{hs} , and Λ^{hs} are the hot-spot radius in μm , central temperature g in keV, and Coulomb logarithm, and ρ^{shell} is the shell's peak density in g/cm^3 . Figure 85.3 shows the temporal evolution of the ablation velocity for a direct-drive NIF cap-

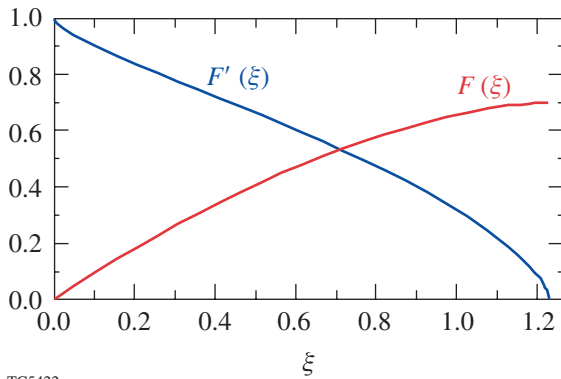


Figure 85.3

Evolution of the ablation velocity at the shell's inner surface of a NIF-like capsule as predicted by Eq. (32) (dashed) and the result of numerical simulations (solid).

sule obtained from Eq. (32) and the result of numerical simulations using $\Lambda^{\text{hs}} = 5$.

In addition to the ablative stabilization, the RT growth rates are reduced by the well-known finite-density-gradient effects. Since the ablative flow at the inner shell surface is subsonic, the minimum density-gradient scale length can be calculated using the well-known isobaric model¹⁴ characterized by the following approximate form of the energy equation:

$$\nabla \cdot \left[\mathbf{v} \frac{\Gamma P_{\text{hs}}(t)}{\Gamma-1} - \kappa \nabla T \right] = 0. \quad (33)$$

Integrating Eq. (33) and using the continuity of the mass flow ($\rho U = \text{constant}$) leads to the following ordinary differential equation for the density profile near the shell's inner surface:

$$\frac{1}{\hat{\rho}} \frac{\partial \hat{\rho}}{\partial r} = \hat{\rho}^\nu \frac{(1-\hat{\rho})}{L_0}, \quad (34)$$

where $\hat{\rho} = \rho/\rho_{\text{shell}}$ is the density normalized to the peak density in the shell (ρ_{shell}) and

$$L_0 = \frac{\Gamma-1}{\Gamma} \frac{A\kappa(T_{\text{shell}})}{\rho_{\text{shell}} V_a}. \quad (35)$$

Here $T_{\text{shell}} = AP_{\text{hs}}(t)/\rho_{\text{shell}}$ represents the temperature calculated at the peak of the density. Equation (35) is valid only near the shell's inner surface within a distance of the order of the length L_0 . The minimum value of the density-gradient scale length (L_m) can be determined by setting to zero the radial derivative of Eq. (34). A straightforward manipulation yields

$$L_m = L_0 \frac{(\nu+1)^{\nu+1}}{\nu^\nu}. \quad (36)$$

Using $\nu = 5/2$ in Eq. (36) and substituting Eq. (32) into Eq. (35) leads to the following simple expression of the density-gradient scale length:

$$L_m = 6.8 R_{\text{hs}} [AP_{\text{hs}}(t)/\rho_{\text{shell}} T_{\text{hs}}(0,t)]^{5/2}, \quad (37)$$

where $P_{\text{hs}}(t)$ is the hot-spot pressure. Figure 85.4 shows the temporal evolution of L_m calculated from Eq. (37) and from the

numerical simulations of a NIF direct-drive capsule. Observe that the density-gradient scale length is quite smaller than the hot-spot radius, implying that its stabilizing effects will impact only short-wavelength modes (large l -mode numbers).

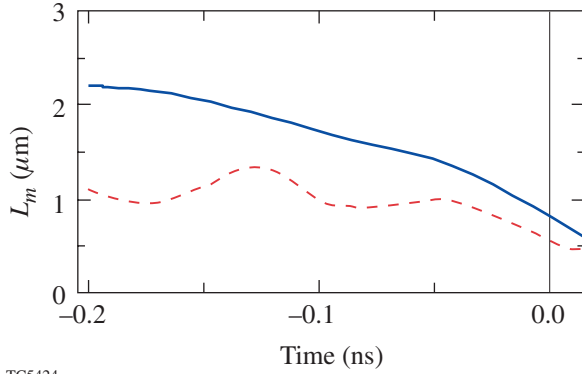


Figure 85.4 Evolution of the density-gradient scale length at the shell's inner surface of a NIF-like capsule as predicted by Eq. (37) (dashed) and the result of numerical simulations (solid).

In the next section, the theory developed in the **General Equations** section is used to calculate the hydrodynamic profiles inside the hot spot and to show how the profiles are affected by the ablation process.

3. Hot-Spot Profiles

The density, temperature, and velocity profiles inside the hot spot can be determined easily from the theory developed in the **Hot-Spot Dynamics** section. The theory is based on the solution of the gas dynamic equations in a Lagrangian form with m, t as independent variables. All the spatial profiles are described by the function $F(\xi)$, where $\xi = am/\eta^{2/7}$ for $\nu = 5/2$. Instead of the variable ξ , a more convenient expression of the profiles should make use of the spatial coordinate $\hat{r} \equiv r/R_{\text{hs}}(t)$. The relation between \hat{r} and ξ can be found by rewriting Eq. (9) using Eqs. (26), (17), and (21). A simple manipulation yields the following relation:

$$\hat{r}^3 = \frac{F(\xi)}{F(\xi_0)}. \quad (38)$$

All the spatial hot-spot profiles for $\nu = 5/2$ can be found by inverting Eq. (38) and finding ξ in terms of \hat{r} ; however, since $F(\xi)$ is not analytical, the inversion must be carried out numerically, leading to the following approximation for ξ and $F'(\xi)$:

$$\xi \approx \xi_0 \left\{ 1 - [1 - \hat{r}^3]^{3/5} \right\}, \quad (39)$$

$$F'(\xi) \approx \frac{(1 - \hat{r}^2)^{2/5}}{1 - 0.15 \hat{r}^2}. \quad (40)$$

The hot-spot temperature profile follows immediately from Eq. (24) and Eq. (40) leading to

$$T_{\text{hs}}(r, t) \approx T_{\text{hs}}(0, t) \frac{(1 - \hat{r}^2)^{2/5}}{1 - 0.15 \hat{r}^2}. \quad (41)$$

When compared with the commonly used profile¹ $T_c = T_0(1 - \hat{r}^2)^{2/7}$, Eq. (41) is in very good agreement except near the boundary of the hot spot $\hat{r} \approx 1$. The different behavior near the hot-spot boundary is relevant to the calculation of the heat flux leaving the hot spot, which is proportional to $[T^{5/2} d_r T]_{\hat{r}=1}$. The common profile with the power $2/7$ yields a finite heat flux while the profile given by Eq. (41) yields zero flux. Since the hot-spot boundary represents the cold shell's inner surface, the heat flux cannot propagate through the shell because the heat conductivity is negligible throughout the shell material. The correct temperature profiles must therefore produce a vanishing heat flux at the hot-spot boundary as indicated by Eq. (41). As mentioned in the **General Equations** section, the heat flux is absorbed on the shell's inner surface by the material that ablates into the hot spot.

The hot-spot density profile follows from Eq. (41) and the isobaric assumption, leading to

$$\rho_{\text{hs}}(r, t) \approx \rho_{\text{hs}}(0, t) \frac{1 - 0.15 \hat{r}^2}{(1 - \hat{r}^2)^{2/5} + \epsilon}, \quad (42)$$

where the *ad hoc* term $\epsilon \equiv 0.85 \rho_{\text{hs}}(0, t) / \rho_{\text{shell}} \ll 1$ has been included to remove the singularity at $\hat{r} = 1$, which arises from the zero shell temperature approximation used to solve the hot-spot equation [Eq. (16)].

The velocity profile can be determined from the Lagrangian equation $u = \partial_r r$ and Eq. (9). Using the definition of the ablation velocity given in Eq. (30), the hot-spot velocity profile has the form

$$u(r,t) = \hat{r} \dot{R}_{\text{hs}} - \frac{\xi(\hat{r})}{\xi_0} \frac{\rho_{\text{shell}}}{\rho_{\text{hs}}(r,t)} \frac{V_a}{\hat{r}^2}, \quad (43)$$

where $\xi(\hat{r})$ and $\rho_{\text{hs}}(r,t)$ are given in Eqs. (38) and (43), respectively. During the deceleration phase, the velocity is negative (i.e., directed in the negative r -direction) and the velocity profile has a minimum (i.e., a maximum for the absolute value of u) due to the blowoff of the material ablated off the shell [the second term in Eq. (43)]. The minimum occurs at the radial position

$$\hat{r}_{\text{min}} \approx \frac{1 + 0.6 \hat{V}_b}{1 + 0.72 \hat{V}_b}, \quad (44)$$

where $\hat{V}_b = \rho_{\text{shell}} V_a / \rho_{\text{hs}}(0,t) |\dot{R}_{\text{hs}}|$. Near stagnation, $\hat{V}_b \gg 1$, $\hat{r}_{\text{min}} \approx 0.8$, and the velocity at the point of minimum is approximately

$$u(\hat{r}_{\text{min}}, t) \approx 0.8 \dot{R}_{\text{hs}} - 0.6 V_a \frac{\rho_{\text{shell}}}{\rho_{\text{hs}}(\hat{r}_{\text{min}}, t)}, \quad (45)$$

where $\rho_{\text{hs}}(\hat{r}_{\text{min}}, t) \approx 1.46 \rho_{\text{hs}}(0, t)$ is the density at the location of minimum velocity. Observe that Eq. (45) is a useful tool for calculating the ablation velocity near stagnation from the numerical simulations because the velocity $u_{\text{min}} = u(\hat{r}_{\text{min}}, t)$, and the densities $\rho_{\text{hs}}(\hat{r}_{\text{min}}, t)$ and ρ_{shell} can be easily determined from the codes' output, while \dot{R}_{hs} is small and can be neglected.

Growth Rates of the Deceleration RT Instability

During the continuous deceleration phase after the interaction of the shell with the return shock, the shell's inner surface is unstable to the RT instability and any small perturbation in the hydrodynamic quantities would grow rapidly. The general formula derived in Ref. 10 yields the growth rate of the ablative RT as a function of the ablation velocity V_a , the shell deceleration g , the power index for thermal conduction $\nu = 5/2$, and the mode wave number $k \approx l/R_{\text{hs}}$ for $l \gg 1$. Since all such quantities are functions of time, the exponential growth of the linear perturbation occurs for sufficiently large l 's only when the typical growth time is shorter than the characteristic time scale of the one-dimensional evolution. In order to verify the theoretical results, we have carried out several 2-D single-mode simulations.

The 1-D code *LILAC*'s¹⁵ output for the NIF-like capsule at 9.3 ns, characterizing the beginning of the coasting phase, was later used as input for a high-resolution Eulerian hydrocode.¹⁶ The latter solves the single fluid mass, momentum, and energy equations, including Spitzer conduction, local alpha deposition, and bremsstrahlung on a very fine grid. The high resolution is needed to correctly simulate the growth of short-wavelength modes on the shell's inner surface. Aside from the bremsstrahlung losses, the code solves the same single fluid model on which the theory is based, providing a robust check of the theoretical results. The RT evolution is investigated by introducing a small-amplitude, 2-D perturbation of the hydrodynamic variables at about 200 ps before stagnation when the continuous deceleration phase begins.

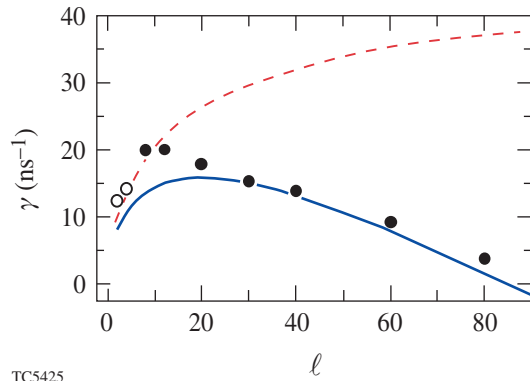
For a direct-drive NIF-like capsule the deceleration phase occurs over an interval of approximately 200 ps. During that time (see Fig. 85.1) the deceleration varies from a few hundreds $\mu\text{m}/\text{ns}^2$ to about 4000 $\mu\text{m}/\text{ns}^2$, the ablation velocity increases from ~ 13 to ~ 25 $\mu\text{m}/\text{ns}$, the density-gradient scale length varies between 1 to 2 μm , and the hot-spot radius reduces from 100 μm to about 55 μm . The RT growth becomes significant during the last 100 ps before stagnation when the acceleration is large, and the hot-spot radius decreases from 75 to 55 μm . The growth rate of large l modes can be determined using the planar results of Ref. 10 derived for the acceleration-phase RT. For a NIF-like capsule during the continuous deceleration phase in the 100-ps interval before stagnation $\langle g \rangle \approx 3100$ $\mu\text{m}/\text{ns}^2$, $\langle V_a \rangle \approx 18$ $\mu\text{m}/\text{ns}$, $\langle L_m \rangle \approx 1.5$ μm , and $\langle R_{\text{hs}} \rangle \approx 65$ μm , leading to a Froude number $Fr \approx 0.5$, where $Fr = V_a^2 / g L_0$ and $L_0 = 0.12 L_m$. Using Eq. (23) and Fig. 6 of Ref. 7, we determine the appropriate growth-rate formula:

$$\gamma = 0.9 \sqrt{\frac{k \langle g \rangle}{1 + k \langle L_m \rangle}} - 1.4 k \langle V_a \rangle, \quad (46)$$

where $k \approx l/R_{\text{hs}}$ for large l 's.

Figure 85.5 compares the unstable spectrum calculated using Eq. (46) with $R_{\text{hs}} = 65$ μm , the classical RT spectrum without ablation [Eq. (1) with $L = L_m$], and the results of numerical simulations. Except for $l = 2, 4$ (open circles), the numerical growth rates are calculated in the 100-ps time interval before stagnation. The simulations of modes $l = 2, 4$ (open circles) show a clear exponential growth only after the shell stagnation time, and their numerical growth rate is calcu-

lated during the 50-ps interval after stagnation. It is important to observe that the planar theory agrees well with the numerical results only for $l \geq 20$. Low l modes seem to grow faster (almost classically) than predicted by Eq. (46), indicating that convergence effects may reduce the ablative stabilization at low l . Furthermore, Fig. 85.5 shows that the finite ablation velocity off the shell's inner surface induces a cutoff in the RT unstable spectrum, suppressing short-wavelength modes with $l > 90$.



TC5425

Figure 85.5

Growth rate versus mode number for the deceleration-phase RT of a NIF-like capsule as predicted by this work [Eq. (46) (solid)], by the classical fitting formula [Eq. (1)] with $L = L_m$ (dashed), and by the results of numerical simulations (open circles). The classical formula overestimates the growth rate of the instability for $l \approx 10$.

Conclusion

In conclusion, an analytic model of the hot-spot dynamics has been developed, and all hot-spot profiles and hydrodynamic quantities relevant to the deceleration-phase instability have been determined. We have shown that the ablative flow off the shell's inner surface plays a crucial role in reducing the growth rate and suppressing short-wavelength modes in the deceleration-phase RT instability. The ablation velocity and the density-gradient scale length have been calculated in terms of standard hot-spot parameters. Using the theory of Ref. 10, the growth rate formula has been determined. Detailed numerical simulations have confirmed the theoretical results and have shown RT suppression at short wavelengths. Calculations of the unstable spectrum of a direct-drive NIF-like capsule³ during the deceleration phase have indicated that the instability is suppressed for mode numbers $l > 90$.

ACKNOWLEDGMENT

This work was supported by the U.S. Department of Energy Office of Inertial Confinement Fusion under Cooperative Agreement No. DE-FC03-92SF19460, the University of Rochester, and the New York State Energy Research and Development Authority. The support of DOE does not constitute an endorsement by DOE of the views expressed in this article.

REFERENCES

1. J. D. Lindl, *Inertial Confinement Fusion: The Quest for Ignition and Energy Gain Using Indirect Drive* (Springer-Verlag, New York, 1998).
2. T. R. Dittrich *et al.*, Phys. Plasmas **6**, 2164 (1999).
3. Laboratory for Laser Energetics LLE Review **79**, 121, NTIS document No. DOE/SF/19460-317 (1999). Copies may be obtained from the National Technical Information Service, Springfield, VA 22161.
4. S. E. Bodner, Phys. Rev. Lett. **33**, 761 (1974).
5. H. Takabe *et al.*, Phys. Fluids **28**, 3676 (1985).
6. J. Sanz, Phys. Rev. Lett. **73**, 2700 (1994).
7. R. Betti, V. N. Goncharov, R. L. McCrory, P. Sorotokin, and C. P. Verdon, Phys. Plasmas **3**, 2122 (1996).
8. V. N. Goncharov, R. Betti, R. L. McCrory, P. Sorotokin, and C. P. Verdon, Phys. Plasmas **3**, 1402 (1996).
9. V. N. Goncharov, R. Betti, R. L. McCrory, and C. P. Verdon, Phys. Plasmas **3**, 4665 (1996).
10. R. Betti, V. N. Goncharov, R. L. McCrory, and C. P. Verdon, Phys. Plasmas **5**, 1446 (1998).
11. R. Kishony, "Ignition Criterion in Inertial Confinement Fusion Using Self-Similar Solutions, and the Effect of Perturbations on Ignition," Ph.D. thesis, Tel Aviv University, 1999.
12. F. Hattori, H. Takabe, and K. Mima, Phys. Fluids **29**, 1719 (1986).
13. M. Murakami, M. Shimoide, and K. Nishihara, Phys. Plasmas **2**, 3466 (1995).
14. H. J. Kull, Phys. Fluids B **1**, 170 (1989).
15. J. Delettrez and E. B. Goldman, Laboratory for Laser Energetics Report No. 36, University of Rochester (1976); also NTIS document No. DOE/SF/19460-118. Copies may be obtained from the National Technical Information Service, Springfield, VA 22161.
16. V. A. Lobatchev, "Hydrodynamics of Inertial Fusion Capsules: Feedout and Deceleration Phase Instability," Ph.D. thesis, University of Rochester, 2000.

The Effect of Shock Heating on the Stability of Laser-Driven Targets

Introduction

Hydrodynamic instability is a key issue for inertial confinement fusion (ICF).^{1–3} The effects of the Rayleigh–Taylor (RT) instability can be reduced by shocks that heat the target shell, causing a slight decompression; this increases the ablation velocity and reduces the RT growth rate.^{4,5} ICF target designs use shock heating to determine the implosion isentrope to establish a balance between performance and stability. This article presents the first experimental demonstration of a correlation between increased hydrodynamic stability and higher shock temperatures produced early in the interaction. This correlation is attributed to increased ablative stabilization resulting from target decompression caused by shock heating.

Experimental Implementation

Pulse shapes with different rise times were used to irradiate planar CH targets that had embedded Al layers whose temperatures were probed using time-resolved x-ray absorption spectroscopy. The $1s-2p$ Al absorption lines provided information about the ionization state of the Al, which, in turn, was used to infer both the shock-induced temperature and the heat-front propagation into the targets. The experiments indicate that steeply rising drive pulses produce shocks that heat the embedded Al layer to ~ 25 eV, while the slowly rising pulses produce shock heating below ~ 15 eV—our detection threshold. The heat front driven by the rapidly rising pulses showed the

expected behavior, whereas the slowly rising pulses experienced mixing⁶ caused by the RT instability that is seeded by laser imprinting.⁷ Mix was not observed in the rapid-rise pulses because increased shock heating produces higher ablative stabilization.

In these experiments, 20- μm -thick CH targets were irradiated by six UV OMEGA⁸ beams having 0.2-THz smoothing by spectral dispersion (SSD).⁹ A 0.5- μm -thick layer of Al was embedded at either 5 or 10 μm below the irradiated surface. The laser pulses were either (1) a steeply rising (~ 200 -ps rise time), nearly square shaped pulse with 1-ns duration and on-target intensity of $\sim 4 \times 10^{14}$ W/cm² or (2) a “ramp” pulse that rose linearly to 3×10^{14} W/cm² in 3 ns. One-dimensional calculations indicate that these pulses produce shock pressures of ~ 35 Mb and ~ 15 Mb, respectively. The targets were probed with x rays from a microdot of Sm that were dispersed by a streaked x-ray spectrometer.

Observations

Figure 85.6(a) shows the time-resolved absorption spectrum from a 20- μm -thick CH target (with the Al layer 10 μm deep) irradiated with the square pulse. Along the spectral direction, the $1s-2p$ absorption lines (dark bands) due to ionization states from F-like Al to Li-like Al are identified. The detailed structure of these transition arrays is not re-

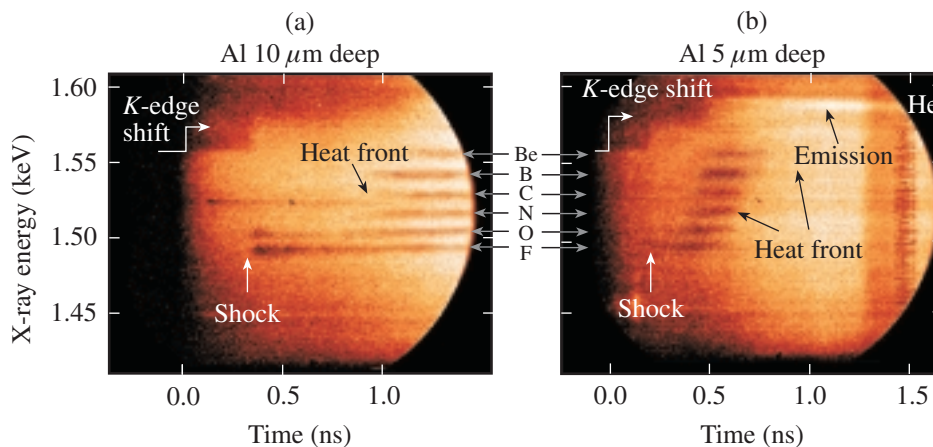


Figure 85.6

(a) Time-resolved absorption spectrum (dark horizontal bands) from an Al layer embedded 10 μm deep in a 20- μm -CH target irradiated by a square pulse. The F- and O-like absorption lines appear at ~ 325 ps due to shock heating. Later (~ 800 ps), higher ionization states occur when the heat front reaches the Al. (b) Absorption spectrum with the Al layer 5 μm deep. The F- and O-like absorption lines appear at ~ 200 ps and the heat front arrives at ~ 400 ps. He-like Al emission is observed when the heat front reaches the Al.

S18244, S18243
E10346

solved, but their mean energies and widths are consistent with predictions¹⁰ and other observations.¹¹ The data in Fig. 85.6(a) indicate that both F-like and O-like lines appear at ~325 ps, and then later at ~800 ps, higher ionization states appear in progression.

Time is referenced to the start of the drive pulse that is preceded 300 ps by the backlighter. This allows observation of the *K*-shell absorption edge (at ~1.56 keV) in *cold* Al. At approximately the same time that the F-like and O-like lines appear, the *K* edge shifts to higher energy. This results primarily from the change in ionization of the Al ions. Later, as higher ionization states (N-like and above) appear, the *K* edge shifts to higher energy.

The abrupt onset of the F-like and O-like absorption lines is caused by shock heating of the Al layer; the higher ionization states (that appear later at a time ~800 ps) result from the incipient heating by the laser-driven heat front. These dynamics are confirmed by data from a target with the Al layer closer to the surface. Figure 85.6(b) is the spectrum from an experiment with the Al layer 5 μm deep. Here the onset of the F-like and O-like Al absorption lines is not clear, but one can readily see the abrupt change in the *K*-edge energy occurring at ~200 ps, consistent with the shock speed inferred from Fig. 85.6(a). Here the heat front also arrives earlier (~400 ps), but, in this case, the heating is sufficient to not only create absorption in higher ionization states but also produce He-like emission. The He-like emission occurs because the heat front has penetrated the 5 μm CH, and has then heated and ablated the Al. The absorption lines are short lived because the temperature rises sufficiently to “burn through” these states, thereby reducing the population in the lower tail of the charge-state distribution.

The dependence of shock heating on the temporal profile of the drive was measured by irradiating similar targets with the ramp pulse. Figure 85.7 shows an extended temporal record of absorption spectra from a target having the Al layer 5 μm deep and irradiated by the ramp pulse. The backlighter produces bright, broadband emission that ceases at ~2 ns. Coincidentally at that time He-like Al emission begins, which indicates that portions of the Al are heated to over 500 eV. Preceding this emission, no Al absorption lines (1.48 to 1.56 keV) are observed. Similar experiments on targets with the Al 10 μm deep also showed no absorption lines on these shots; the He-like emission occurred ~400 ps later than that shown in Fig. 85.7. These results are significant for two reasons: (1) They indicate the absence of significant shock heating before emission

begins. (Note, however, that the *K* edge at 1.56 keV becomes diffuse at about 600 ps, suggesting some low-level shock heating.) (2) The lack of absorption lines preceding the He-like emission suggests that Al is instantaneously heated from <15 eV to >500 eV, contrary to expected behavior. Heat fronts in both directly driven¹² and indirectly driven targets¹¹ normally exhibit a succession of Al absorption lines that appear before the emission lines, as in Fig. 85.6(b).

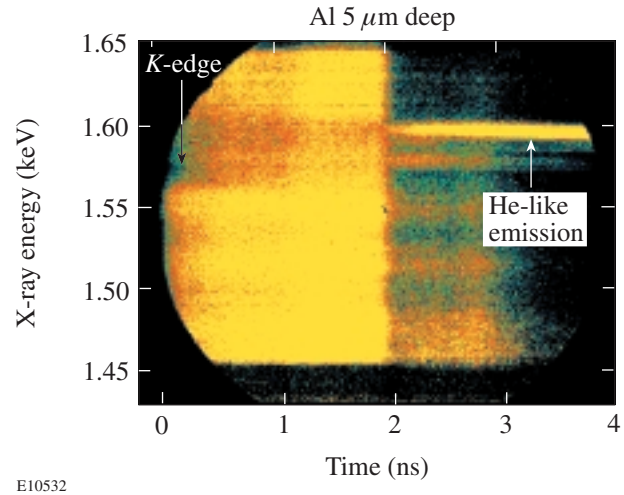


Figure 85.7

Absorption spectra from a target with the Al layer 5 μm deep and irradiated by a ramp pulse. No Al absorption lines are observed preceding the Al He-like emission lines that begin at ~1.9 ns.

In summary, the slowly rising ramp pulse produces less shock heating (no absorption lines) than the square pulse, and targets driven by the ramp pulse show no Al absorption lines even in the presence of He-like emission. The latter observation will be attributed to the effects of RT instability, while the former will confirm the correlation of ablative stabilization with shock heating.

Analysis and Discussion

The relative populations of Al charge states and the resulting absorption spectra were calculated for steady-state conditions at various temperatures.¹³ This allowed the Al temperature to be inferred as a function of time. Figure 85.8 shows the Al temperature measured (points) and predicted (curves) by 1-D simulations (*LILAC*¹⁴). Figure 85.8(a) compares calculations and measurements for square-pulse irradiation of targets with the Al layer 5 μm deep (solid line and circles) and 10 μm deep (dashed line and triangles). Both the shock heating of the Al to ~25 eV and the heat-front penetration (≥ 40 eV) are correctly predicted by the 1-D simulations, indicating stable

target behavior. The minor discrepancy in timing of the heat-front arrival times is likely the result of 2-D effects (see below). The lower limit for this measurement technique is the onset of F-like absorption lines that occurs at about 15 eV. The error bars indicate a ± 100 -ps timing uncertainty in the camera and a ± 10 -eV precision of the temperature measurement.

Similar temperature profiles for the ramp pulse are shown in Fig. 85.8(b) [5 μm deep (solid/circles); 10 μm deep (dashed/triangles)]. Since there were no absorption lines in the data, only the onset times for Al emission (defined as 500 eV) are shown. The predicted temperatures are below the ~ 15 -eV experimental detection threshold until about 1.7 ns, when the heat front arrives at the Al, which reaches ~ 500 eV at 1.9 ns for the 5- μm case. The 10- μm case is not predicted to be heated above ~ 40 eV, yet the experiment reaches 500 eV at ~ 2.3 ns. The temperature rise predicted (by a 1-D code) for the ramp pulse is similar to that for the square pulse [Fig. 85.8(a)], indicating that the lack of absorption lines is not due to a steep temperature rise.

To explain the observation that the heat front reaches the 10- μm -deep Al layer and the He-like emission occurs with no preceding Al absorption lines, the existence of a mixing region is postulated. The emission lines could result from Al that is prematurely mixed into the ablation region.⁶ Using the model discussed in Ref. 15, the thickness of that mix layer was calculated and then added to the depth predicted by 1-D simulations. The mix layer is produced by the RT instability that amplifies imprinted perturbations,⁷ producing considerable two-dimensional effects. The model uses the measured spectrum of irradiation nonuniformities to calculate the imprinted perturbations, and then calculates their growth¹⁶ and

saturation.¹⁷ The curves in Fig. 85.9 show the calculated location of the ablation surface (the point of steepest density gradient) in uncompressed CH thickness for the square and ramp pulses. The heavy lines are the predictions of 1-D calculations, and the shaded regions are the calculated mix layers centered on those predictions. The data represent the times when the Al layer (buried at the plotted depth) begins to produce He-like emission. Once ablated, this material must traverse the conduction zone before it is heated in the corona. The square-pulse data are not significantly affected by the RT instability and are therefore reasonably predicted by 1-D simulations. In contrast, the ramp pulse has a mix layer that affects the apparent penetration at both 5- and 10- μm depths in the original target. [The temporal offset (~ 250 ps) between the data and simulations corresponds to the time for the Al to travel from the ablation surface to the 500-eV isotherm.¹⁸] This explains both the unexpected emission from the Al [10- μm result in Fig. 85.8(b)] and the lack of preceding absorption lines for the 5- and 10- μm cases. Specifically, the RT spikes can “leach” Al from the embedded layer out into the corona (where it emits), whereas the Al in the bubbles has not been heated significantly and therefore has no absorption signature. The relative size of the bubbles and spikes is such that the bubbles dominate the spectroscopic radiography (no absorption line), while the bright (but smaller-sized) spikes are detected in emission but not resolved in absorption.

Simulations indicate that targets driven by either the square or ramp pulse have traveled $\sim 50 \mu\text{m}$ when the heat front has penetrated 5 μm of CH. Thus, in the absence of any stabilizing mechanisms, both pulses should experience similar RT growth. Targets irradiated by these two pulse shapes behave differently because the square pulse produces a shock that heats the target

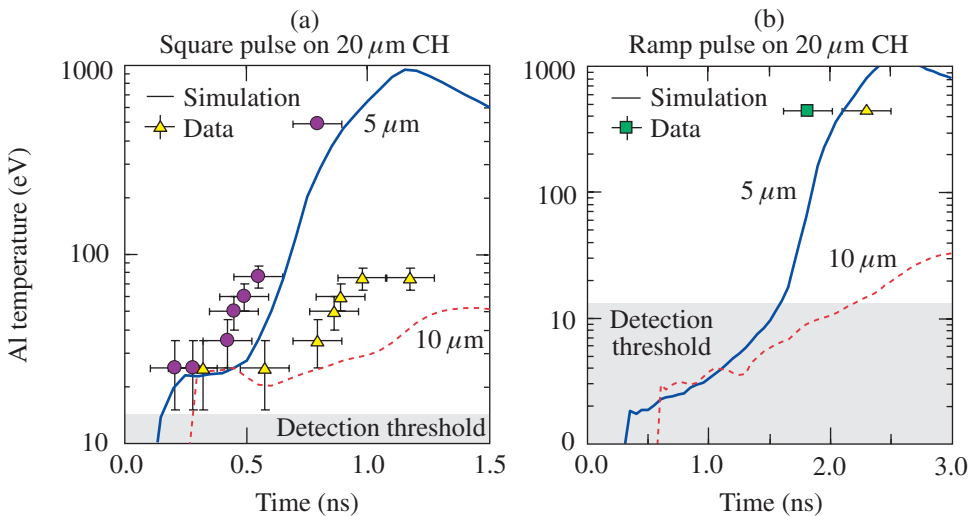
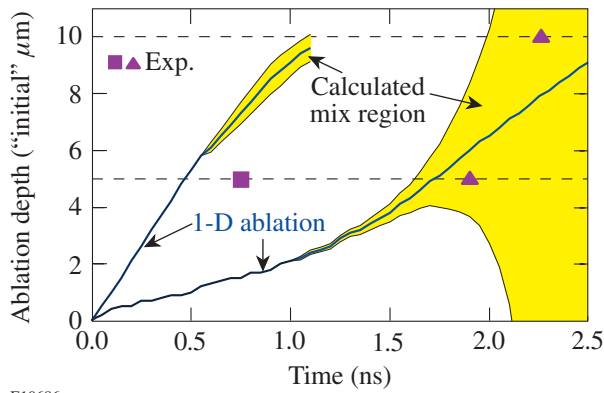


Figure 85.8 Comparison of the temperatures of the embedded Al layer as predicted by the 1-D code *LILAC* (curves) for various experiments and experimental data (points). (a) Square pulse driving the 5- μm case (solid/circles) and the 10- μm case (dashed/triangles). (b) Ramp pulse driving the 5- μm case (solid/circles) and the 10- μm case (dashed/triangles). Ramp-pulse data were present only for emission lines.

E10476, E10477



E10686

Figure 85.9

The ablation depths in uncompressed CH thickness. The heavy lines are the 1-D simulations, and the shaded regions are the calculated thickness of RT mixing. The measured penetration times are plotted at the embedded layer depths for the experiments.

to ~ 25 eV, causing it to decompress, thereby increasing the ablation velocity. This lowers the RT growth rate compared to that of the ramp pulse, which experiences less shock heating (<15 eV) and therefore little ablative stabilization. The simulations (which correctly model the observed shock temperatures) confirm that the square pulse produces ablation velocities that are as much as five times larger than those for the ramp pulse.

It has been shown that for the square-pulse drive, 1-D simulations accurately predict the observed shock heating (~ 25 eV) produced by an ~ 35 -Mb shock and the heat-front penetration depth. In contrast, the ramp pulses produce ~ 15 -Mb shocks that do not appreciably heat the target (<15 eV). The targets exhibit apparent anomalous heat-front penetration that results from two-dimensional effects caused by the RT instability.¹⁵ Simulations of these experiments indicate that the shock heating produced by rapidly rising pulses causes the target to decompress, creating higher ablation velocities that reduce the RT growth rates. In contrast, the slowly rising pulse causes considerably less shock heating, producing less ablative stabilization, and therefore experiences significant effects due to the RT instability. This confirms the expected effect of shock heating and ablative stabilization on the stability of directly driven ICF targets.

ACKNOWLEDGMENT

This work was supported by the U.S. Department of Energy Office of Inertial Confinement Fusion under Cooperative Agreement No. DE-FC03-92SF19460, the University of Rochester, and the New York State Energy Research and Development Authority. The support of DOE does not constitute an endorsement by DOE of the views expressed in this article.

REFERENCES

1. J. D. Lindl, *Phys. Plasmas* **2**, 3933 (1995).
2. S. E. Bodner, D. G. Colombant, J. H. Gardner, R. H. Lehmborg, S. P. Obenschain, L. Phillips, A. J. Schmitt, J. D. Sethian, R. L. McCrory, W. Seka, C. P. Verdon, J. P. Knauer, B. B. Afeyan, and H. T. Powell, *Phys. Plasmas* **5**, 1901 (1998).
3. J. D. Kilkenny, S. G. Glendinning, S. W. Haan, B. A. Hammel, J. D. Lindl, D. Munro, B. A. Remington, S. V. Weber, J. P. Knauer, and C. P. Verdon, *Phys. Plasmas* **1**, 1379 (1994).
4. H. Takabe, L. Montierth, and R. L. Morse, *Phys. Fluids* **26**, 2299 (1983).
5. R. Betti, V. N. Goncharov, R. L. McCrory, P. Sorotokin, and C. P. Verdon, *Phys. Plasmas* **3**, 2122 (1996).
6. D. K. Bradley, J. A. Delettrez, and C. P. Verdon, *Phys. Rev. Lett.* **68**, 2774 (1992).
7. T. R. Boehly, V. N. Goncharov, O. Gotchev, J. P. Knauer, D. D. Meyerhofer, D. Oron, S. P. Regan, Y. Srebro, W. Seka, D. Shvarts, S. Skupsky, and V. A. Smalyuk, "The Effect of Plasma Formation Rate and Beam Smoothing on Laser Imprinting," submitted to *Physical Review Letters*.
8. T. R. Boehly, D. L. Brown, R. S. Craxton, R. L. Keck, J. P. Knauer, J. H. Kelly, T. J. Kessler, S. A. Kumpan, S. J. Loucks, S. A. Letzring, F. J. Marshall, R. L. McCrory, S. F. B. Morse, W. Seka, J. M. Soures, and C. P. Verdon, *Opt. Commun.* **133**, 495 (1997).
9. S. Skupsky and R. S. Craxton, *Phys. Plasmas* **6**, 2157 (1999).
10. C. Chenais-Popovics *et al.*, *Phys. Rev. A* **42**, 4788 (1990).
11. T. S. Perry *et al.*, *J. Quant. Spectrosc. Radiat. Transf.* **51**, 273 (1994).
12. D. Hoarty *et al.*, *Phys. Rev. Lett.* **82**, 3070 (1999).
13. D. Hoarty *et al.*, *Phys. Rev. Lett.* **78**, 3322 (1997).
14. M. C. Richardson, P. W. McKenty, F. J. Marshall, C. P. Verdon, J. M. Soures, R. L. McCrory, O. Barnouin, R. S. Craxton, J. Delettrez, R. L. Hutchison, P. A. Jaanimagi, R. Keck, T. Kessler, H. Kim, S. A. Letzring, D. M. Roback, W. Seka, S. Skupsky, B. Yaakobi, S. M. Lane, and S. Prussin, in *Laser Interaction and Related Plasma Phenomena*, edited by H. Hora and G. H. Miley (Plenum Publishing, New York, 1986), Vol. 7, pp. 421–448.
15. J. Delettrez, D. K. Bradley, and C. P. Verdon, *Phys. Plasmas* **1**, 2342 (1994).
16. R. Betti, V. N. Goncharov, R. L. McCrory, and C. P. Verdon, *Phys. Plasmas* **5**, 1446 (1998).
17. S. W. Haan, *Phys. Rev. A* **39**, 5812 (1989).
18. J. A. Delettrez, S. P. Regan, P. B. Radha, and R. P. J. Town, *Bull. Am. Phys. Soc.* **45**, 224 (2000).

Spherical Cavity Expansion in Material with Densification

Introduction

Fused silica (SiO_2) exhibits some unique features when it is ground or polished. It also densifies permanently under large compressive stresses at room temperature;¹⁻³ up to 15% permanent densification has been observed.^{2,3} The experimental data for densification from different works, however, are obviously inconsistent,⁴ which may result from different levels of shear stresses present in the experiments. The molecular dynamics simulation by Tse *et al.*⁵ proved this suggestion by showing that the densification is caused by extensive bending of atomic bonds, even under pure hydrostatic pressure. Based on these observations, a new constitutive law was suggested by Lambropoulos *et al.*⁶ for this kind of material.⁷

To understand the material behavior under compression, the cavity expansion problem is solved analytically. Both associated and non-associated flow theories have been studied. A densification parameter has been introduced in the proposed material model. The material is assumed to be perfectly plastic; however, the introduction of densification produces an effect similar to hardening.

Constitutive Model

The traditional shear flow theory cannot describe the plastic behavior of fused silica because the permanent densification is so large that its effects cannot be neglected. Experiments and observations on fused silica have suggested that the shear will facilitate the densification.^{4,5,7} Lambropoulos *et al.*⁶ suggested a new material model to describe this kind of material. The yield surface is defined by the effective stress

$$\sigma_e = -\alpha\sigma_m + (1-\alpha)\tau_e, \quad (1)$$

where

$$\sigma_m = \frac{1}{3}\sigma_{kk} = \frac{1}{3}(\sigma_{11} + \sigma_{22} + \sigma_{33}),$$

$$\tau_e = \sqrt{\frac{1}{2}s_{ij}s_{ij}}, \quad s_{ij} = \sigma_{ij} - \sigma_m\delta_{ij},$$

and α is the densification parameter, which ranges from 0 to 1. Here the summation convention is used. δ_{ij} is the Kronecker delta. For pure hydrostatic compression, where $\sigma_{11} = \sigma_{22} = \sigma_{33} = -p$, the mean hydrostatic stress $\sigma_m = -p$ and effective shear $\tau_e = 0$. For pure shear, $\sigma_m = 0$ and $\tau_e = |\tau|$. For uniaxial tension, $\sigma_m = \sigma/3$ and $\tau_e = \sigma/\sqrt{3}$. Notice that τ_e is always positive.

The material yields when $\sigma_e > Y$. The normal of yield surface can be expressed as

$$\mu_{ij} = \frac{\partial f}{\partial \sigma_{ij}} = -\frac{\alpha}{3}\delta_{ij} + \frac{(1-\alpha)}{2}\frac{s_{ij}}{\tau_e}. \quad (2)$$

When the inner product $\mu_{ij}d\sigma_{ij} > 0$, the small change of stress $d\sigma_{ij}$ causes further deformation loading. When $\mu_{ij}d\sigma_{ij} < 0$, it is unloading. Permanent strains ε_{ij}^p evolve as

$$d\varepsilon_{ij}^p = \begin{cases} 0, & \text{if } \mu_{ij}d\sigma_{ij} \leq 0 \\ \neq 0, & \text{if } \mu_{ij}d\sigma_{ij} > 0 \end{cases}. \quad (3)$$

With continued loading, we assume that the permanent strains are not affected by the rate of loading; thus, the flow rule gives

$$d\varepsilon_{ij}^p = d\lambda \frac{\partial g}{\partial \sigma_{ij}}, \quad g(\sigma_{ij}) = -\alpha'\sigma_m + (1-\alpha')\tau_e, \quad (4)$$

where $g(\sigma_{ij})$ is the flow potential. Generally the material constant α' in Eq. (4) is different from α in Eq. (1), which is called the non-associated flow theory. For special case $\alpha = \alpha'$, called the associated flow theory, the permanent strain increment is normal to the yield surface in stress space.

By using the principle of plastic work equivalence $\sigma_{ij}d\varepsilon_{ij}^p = c\sigma_e d\bar{\varepsilon}^p$, where c is a numerical factor, the plastic strain increment can be solved as

$$d\varepsilon_{ij}^p = \frac{d\bar{\varepsilon}^p}{C} \left(-\frac{\alpha'}{3} \delta_{ij} + \frac{1-\alpha'}{2} \frac{s_{ij}}{\tau_e} \right), \quad (5)$$

where

$$C = \sqrt{\frac{2}{9} \alpha'^2 + \frac{1}{3} (1-\alpha')^2}.$$

For a standard elastic theory (Hooke's law), the elastic strain increment is

$$d\varepsilon_{ij}^e = \frac{1}{2G} ds_{ij} + \frac{(1-2\nu)}{E} \delta_{ij} d\sigma_m, \quad (6)$$

where G is shear modulus, defined as $G = E/2(1+\nu)$. Then the total strain increment is given by

$$d\varepsilon_{ij} = d\varepsilon_{ij}^e + d\varepsilon_{ij}^p. \quad (7)$$

The incremental stress-strain relation, written in tensor format, is

$$d\sigma_{ij} = D_{ijkl} d\varepsilon_{kl}, \quad (8)$$

where the fourth-order tensor D_{ijkl} is the material's incremental constitutive law matrix.

Cavity Expansion

A spherical cavity embedded in an infinite medium with an initial radius a_0 is subjected to inner pressure P . With the increase of P , the cavity wall expands. When the pressure is larger than the initial yield pressure P_c , a plastic zone forms outside the cavity wall. Due to the symmetry, a spherical polar Lagrangian system (r, θ, φ) at the center of the cavity has been used. The material deforms only along the radius, and the displacement is a function of the radius only. There are only three nonzero stresses $(\sigma_r, \sigma_\theta, \sigma_\varphi)$ and strains $(\varepsilon_r, \varepsilon_\theta, \varepsilon_\varphi)$. By symmetry, we also have $\sigma_\theta = \sigma_\varphi$ and $\varepsilon_\theta = \varepsilon_\varphi$. Then the equilibrium equations reduce to

$$r \frac{d\sigma_r}{dr} + 2(\sigma_r - \sigma_\theta) = 0. \quad (9)$$

From elastic solution and yield function, the initial yield pressure is

$$P_c = \frac{2\sqrt{3}}{3(1-\alpha)} Y. \quad (10)$$

Equation (10) is plotted in Fig. 85.10. With the increase of α , the material yields at higher inner pressure.

It can be proved that $\sigma_\theta > \sigma_r$ at any point, so the effective stress can be simplified to

$$\sigma_e = -\frac{\alpha}{3} (\sigma_r + 2\sigma_\theta) + \frac{1-\alpha}{\sqrt{3}} (\sigma_\theta - \sigma_r). \quad (11)$$

With the help of the yield function, the relation of stresses in a plastic zone is solved by

$$\sigma_\theta = \frac{3Y + [\sqrt{3} - \alpha(\sqrt{3} - 1)]}{\sqrt{3} - \alpha(2 + \sqrt{3})} \sigma_r. \quad (12)$$

Substituting Eq. (12) into the equilibrium Eq. (9), the stresses in the plastic zone are

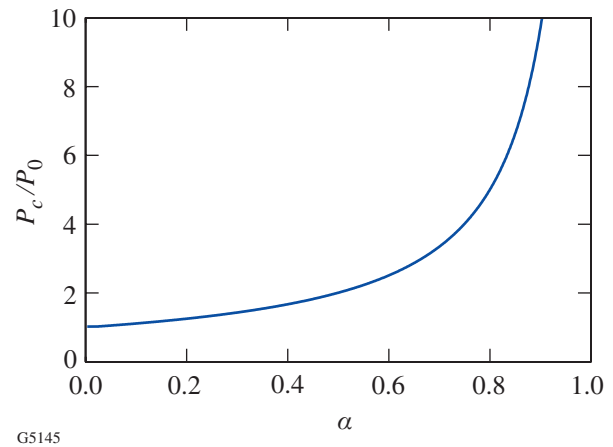


Figure 85.10

Initial yield pressure versus densification parameter. P_0 is the initial yield pressure without densification.

$$\sigma_r = -\frac{Y}{\alpha} + Cr \frac{6\alpha}{\sqrt{3} - (2 + \sqrt{3})\alpha}, \tag{13}$$

$$\sigma_{\theta,\varphi} = -\frac{Y}{\alpha} + C \frac{\sqrt{3} - (\sqrt{3} - 1)\alpha}{\sqrt{3} - (2 + \sqrt{3})\alpha} r \frac{6\alpha}{\sqrt{3} - (2 + \sqrt{3})\alpha},$$

where C can be solved from the boundary condition at the cavity wall ($r = a$). At the plastic-elastic boundary ($r = b$), traction continuity gives

$$\left(\frac{b}{a}\right)^{\frac{6\alpha}{(2+\sqrt{3})\alpha-\sqrt{3}}} = \frac{\sqrt{3}(1-\alpha)\left(1-\alpha\frac{P}{Y}\right)}{\sqrt{3}-(2+\sqrt{3})\alpha}. \tag{14}$$

It can be easily verified that $b \geq a$ if and only if $P > P_c$.

For the cavity problem, the flow potential [Eq. (4)] is

$$g = -\alpha' \frac{\sigma_r + \sigma_\theta + \sigma_\varphi}{3} + \frac{1-\alpha'}{2\sqrt{3}} (\sigma_\theta - \sigma_r) + \frac{1-\alpha'}{2\sqrt{3}} (\sigma_\varphi - \sigma_r). \tag{15}$$

By the flow theory $d\varepsilon_{ij}^p = d\lambda \partial g / \partial \sigma_{ij}$, we have

$$\begin{aligned} d\varepsilon_r^p &= d\lambda \left(-\frac{\alpha'}{3} - \frac{1-\alpha'}{\sqrt{3}} \right), \\ d\varepsilon_\theta^p &= d\lambda \left(-\frac{\alpha'}{3} + \frac{1-\alpha'}{2\sqrt{3}} \right), \\ d\varepsilon_\varphi^p &= d\lambda \left(-\frac{\alpha'}{3} + \frac{1-\alpha'}{2\sqrt{3}} \right). \end{aligned} \tag{16}$$

From the elastic theory, the elastic strain rate is

$$d\varepsilon_r^e = \frac{1}{E} (d\sigma_r - 2\nu d\sigma_\theta), \tag{17}$$

$$d\varepsilon_\theta^e = d\varepsilon_\varphi^e = \frac{1}{E} [-\nu d\sigma_r + (1-\nu) d\sigma_\theta].$$

The total strain rate contains both elastic and plastic parts: $d\varepsilon_{ij} = d\varepsilon_{ij}^e + d\varepsilon_{ij}^p$. By eliminating the $d\lambda$, we have

$$A' d\varepsilon_r + 2d\varepsilon_\theta = \frac{1}{E} \{ (A' - 2\nu) d\sigma_r + 2[1 - (1 + A')\nu] d\sigma_\theta \}, \tag{18}$$

$$A' = \frac{\sqrt{3} - (2 + \sqrt{3})\alpha'}{\sqrt{3} - (\sqrt{3} - 1)\alpha'}.$$

Hill has solved this problem for the shear flow theory.⁸ Following his method, the displacement increment can be written as

$$du(r, b) = \frac{\partial u}{\partial b} db + \frac{\partial u}{\partial r} dr = \left(\frac{\partial u}{\partial b} + \nu \frac{\partial u}{\partial r} \right) db, \tag{19}$$

where ν is defined as the “velocity” of the particle. Defined in terms of the total displacement u and plastic-elastic boundary b ,

$$\nu = \frac{\frac{\partial u}{\partial b}}{1 - \frac{\partial u}{\partial r}}. \tag{20}$$

Written in terms of ν and db , the nonzero stress and strain increments are

$$\begin{aligned} d\varepsilon_r &= \frac{\partial}{\partial r} (du) = \frac{\partial \nu}{\partial r} db, \\ d\varepsilon_\theta &= \frac{du}{r} = \frac{\nu db}{r}, \\ d\sigma_r &= \left(\frac{\partial \sigma_r}{\partial b} + \nu \frac{\partial \sigma_r}{\partial r} \right) db, \end{aligned} \tag{21}$$

$$d\sigma_\theta = \left(\frac{\partial \sigma_\theta}{\partial b} + \nu \frac{\partial \sigma_\theta}{\partial r} \right) db.$$

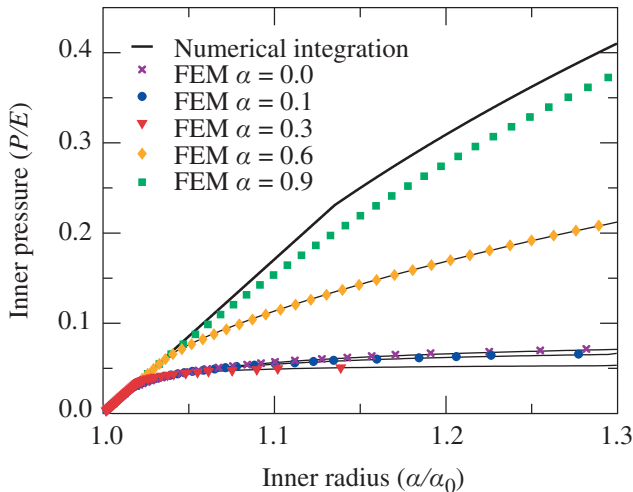
Substituting Eqs. (21) and (13) into (18), we have

$$\begin{aligned}
 A' \frac{\partial v}{\partial r} + \frac{2v}{r} &= \frac{Y}{E} \frac{2\sqrt{3}}{1-\alpha} \left(\frac{b}{r}\right)^{\frac{6\alpha}{(2+\sqrt{3})\alpha-\sqrt{3}}} \left(\frac{v}{r} - \frac{1}{b}\right) \\
 &\times \left[\left(A' + \frac{2}{A}\right) - \left(2 + 2\frac{A'}{A} + \frac{2}{A}\right)v \right], \\
 A &= \frac{\sqrt{3} - (2 + \sqrt{3})\alpha}{\sqrt{3} - (\sqrt{3} - 1)\alpha}.
 \end{aligned} \tag{22}$$

This is a first-order partial differential equation for v . By integrating Eq. (22) from the cavity wall ($r = a$) to the plastic–elastic boundary ($r = b$), the problem is solved. Equation (22) is coupled (via a , b) and subject to numerical integration. The fourth-order Runge–Kutta method is used to solve this equation. For verification, the problem is also solved by using the finite-element package Abaqus (Hibbitt, Karlsson, & Sorensen, Inc.). The large deformation theory is used in the finite-element simulation.

Associated Flow Theory

For the associated flow theory, $\alpha = \alpha'$ and $A = A'$. The flow potential coincides with the yield surface. Perfect plastic deformation is also assumed. Pressure–expansion curves are shown in Fig. 85.11 from both the finite-element and numerical integration results. It is interesting that with the increase of α the material becomes “softer” for small α and “harder” for large α . It is also noticed that for small α , there is a pressure



G5146

Figure 85.11
Cavity pressure–expansion curves for different α 's.

limit for cavity expansion, as expected for perfect-plastic material deformed with shear flow only. When the inner pressure is close to this limit, the cavity expands spontaneously. For large α , we do not see this pressure limit. The difference between finite-element and numerical integration results is due to the use of the finite deformation theory in the finite-element simulation.

The densification parameter α also affects the distribution of stresses at maximum load. The stresses at maximum load ($1.45 P_c$) are plotted in Figs. 85.12(a) and 85.12(b). For small α , the hoop stress is compressive; for large α , the hoop stress is tensile. We know that fracture under load is controlled by these stresses. For small α , if there is fracture under load, it happens under the surface; for large α , it will happen at the surface.

The residual stresses after $1.45 P_c$ loading are plotted in Figs. 85.12(c) and 85.12(d) for $\alpha = 0.3$ and 0.6 . The densification parameter also affects the residual stresses. For small α , the surface layer is under compression; for large α , it is under tension. The layer with large residual stresses is thicker for small α . It needs to be mentioned that the initial yield pressure P_c will increase with α , so we expect, under the same load, even smaller residual stresses for large α . It is observed that fused silica has smaller residual stresses after grinding.⁹ Figure 85.12(e) also compares the hoop stress under the same load for $\alpha = 0.1, 0.3$, and 0.6 . At this load, only elastic deformation occurs for $\alpha = 0.6$.

Non-associated Flow Theory

For the non-associated flow theory, the material behavior is controlled by both yield function [Eq. (1)] and plastic potential [Eq. (4)]; now α is not equal to α' . Thus we have three material parameters (α , α' , Y) to describe the plastic deformation. The reasonable combinations of α and α' should be investigated. It is not possible to have $\alpha = 1$ and $\alpha' = 0$, which means that the material yields with pressure but can be permanently deformed only with shear.

The integration of Eq. (22) has been carried out numerically for different combinations of α and α' . The results for $\alpha = 0.3$ and $\alpha = 0.6$ are shown in Fig. 85.13. When $\alpha = 0.3$, it is physically impossible for $\alpha' = 0.6$ and 0.9 , which means that the cavity cannot decrease in size with an increase in inner pressure. For the same reason, α' cannot be 0.1 or 0.3 for $\alpha = 0.6$. From the analysis, we found the number separating these two regions to be around 0.46 . These findings have been summarized in Fig. 85.14. For small α , α' must be small and vice versa.

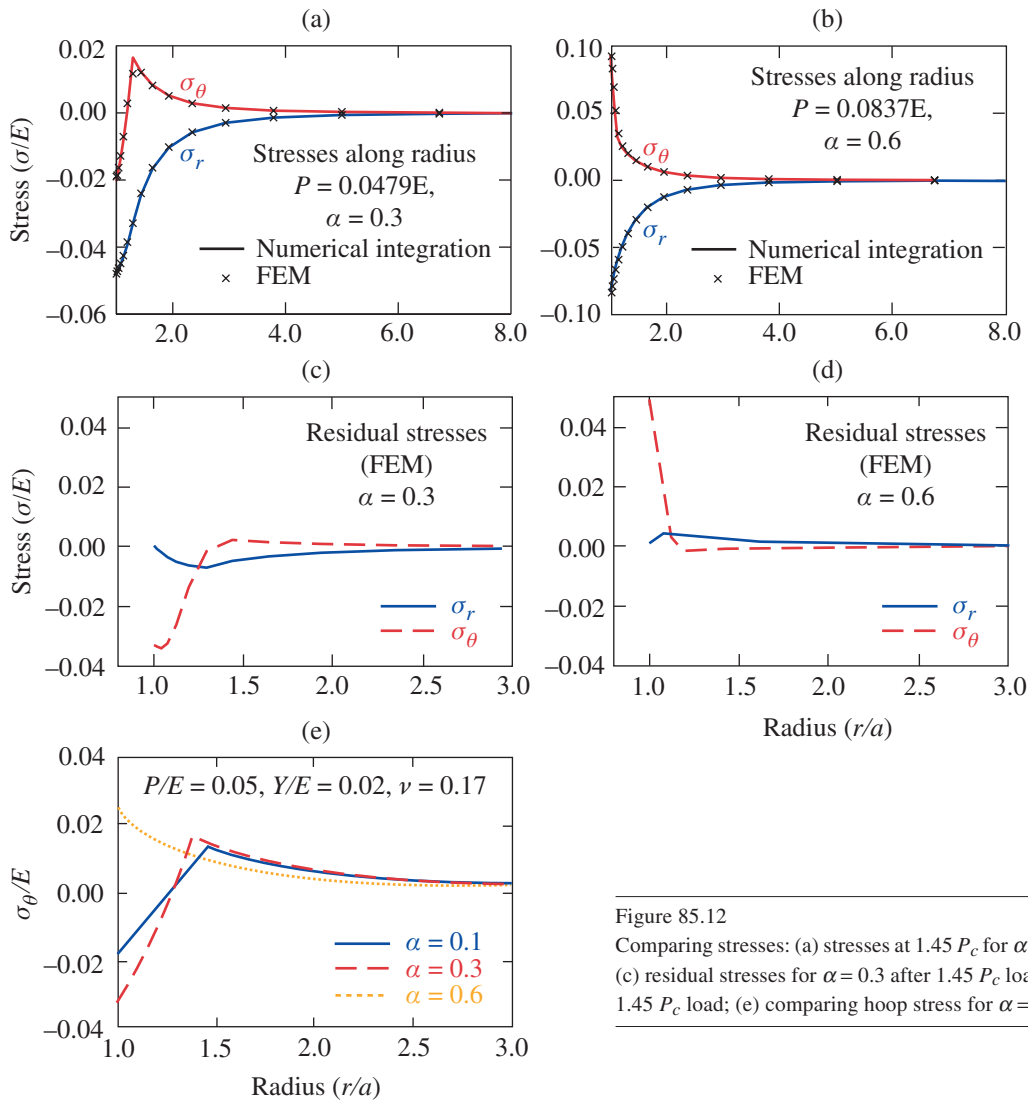


Figure 85.12
 Comparing stresses: (a) stresses at $1.45 P_c$ for $\alpha = 0.3$; (b) stresses at $1.45 P_c$ for $\alpha = 0.6$;
 (c) residual stresses for $\alpha = 0.3$ after $1.45 P_c$ load; (d) residual stresses for $\alpha = 0.6$ after
 $1.45 P_c$ load; (e) comparing hoop stress for $\alpha = 0.1, 0.3$, and 0.6 .

G5147

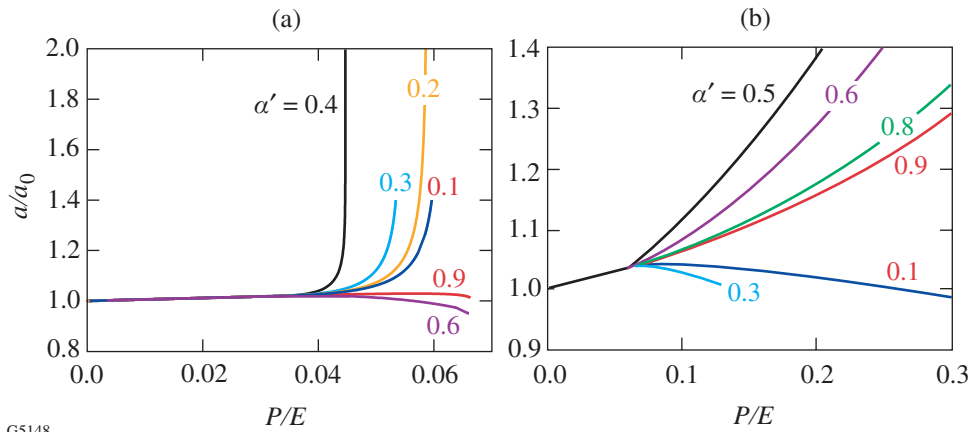


Figure 85.13
 Pressure-expansion curves for non-associated flow theory: (a) $Y/E = 0.02$,
 $\alpha = 0.3$; (b) $Y/E = 0.02$, $\alpha = 0.6$.

G5148

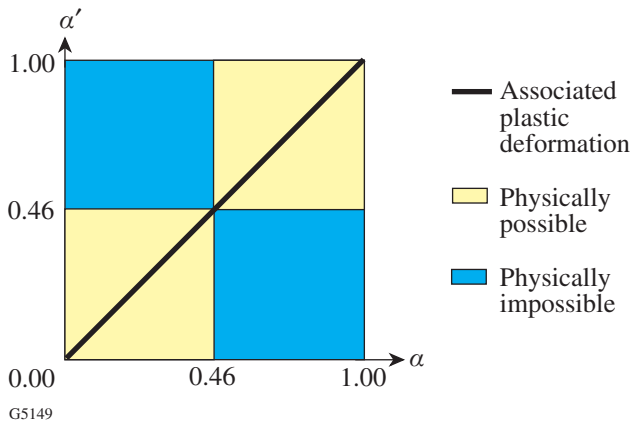


Figure 85.14
Material possibility map.

Figure 85.13(a) shows the pressure expansion curves for small α and α' . As observed in the associated theory, there is a pressure limit for spontaneous growth. For small α , with the increase of α' , the limit pressure decreases, which means that the material becomes “softer.” The spontaneous growth pressure is not observed for large α and α' [see Fig. 85.13(b)]. We also noticed that, for large α , the material becomes “harder” with the increase of α' .

Conclusion

The cavity problem has been studied by using a new material model. Both associated and non-associated flow theories have been examined. For the associated case, $\alpha = \alpha'$ and plastic potential is coincident with yield surface. We have two material parameters (α, Y) to describe plastic deformation with densification. The initial yield pressure increases with α . When α is small (small densification), there is a small softening with the increase of α . The cavity can grow spontaneously when the inner pressure reaches a limit. When α is large (large densification), there is a remarkable strengthening with the

increase of α . The spontaneous cavity growth is not observed. The densification affects stress distributions at loading. When the densification parameter α is small, the hoop stress under load is compressive, similar to the material flowing without densification. When α is large, the hoop stress under load is tensile. The residual stresses are also affected by densification. For small densification, the surface residual stress is compressive; it is tensile for large densification.

For the non-associated case, the plastic behavior is described by three material parameters: α, α', Y . By investigating the non-associated case, we found that there are physically impossible combinations for α and α' . It is necessary to keep both α and α' small (<0.46) or large (>0.46). The increase of α' causes softening for small α and hardening for large α .

REFERENCES

1. P. W. Bridgman and I. Simon, *J. Appl. Phys.* **24**, 405 (1953).
2. R. Roy and H. M. Cohen, *Nature* **190**, 789 (1961).
3. E. B. Christiansen, S. S. Kistler, and W. B. Gogarty, *J. Am. Ceram. Soc.* **45**, 172 (1962).
4. J. D. Mackenzie, *J. Am. Ceram. Soc.* **46**, 461 (1963).
5. J. S. Tse, D. D. Klug, and Y. Le Page, *Phys. Rev. B* **46**, 5933 (1992).
6. J. C. Lambropoulos, S. Xu, and T. Fang, *J. Am. Ceram. Soc.* **79**, 1441 (1996).
7. A. B. Shorey, K. Xin, K.-H. Chen, and J. C. Lambropoulos, in *Inorganic Optical Materials*, edited by A. J. Marker III (SPIE, Bellingham, WA, 1998), Vol. 3424, pp. 72–81.
8. R. Hill, *The Mathematical Theory of Plasticity* (Clarendon Press, Oxford, 1950).
9. J. C. Lambropoulos, S. Xu, T. Fang, and D. Golini, *Appl. Opt.* **35**, 5704 (1996).

Design and Performance of a Selectable-Rate Streak-Camera Deflection Ramp Generator

Introduction

Electro-optic streak cameras have been used at LLE for many years to resolve high-bandwidth, low-repetition-rate, pulsed laser phenomena. Until now the sweep rate was governed by a fixed-rate voltage ramp generator used to drive the sweep deflection plates.

Altering the time base required physically changing the ramp generator. In this article a new method of generating the sweep deflection ramps is presented that permits changing the sweep rate by computer control without replacing the ramp generator. A logic level signal can now be used to change sweep rates without the need for invasive component changes. This new development permits fast and easy sweep rate changes for streak cameras in any location throughout the laboratory, especially in low accessibility locations such as clean rooms and high-power-laser environments.

As a result of this work, a 50- Ω matched-impedance voltage ramp generator was developed. The matched-impedance design of the generator allows the deflection signals to propagate on standard 50- Ω coaxial cable without distortion of the ramp waveform regardless of cable length. The ramp generator's location and interconnect length to the deflection plates are less restricted than with the previous design. In situations where access to the streak camera's tube deflection electrodes is limited by space or environmental constraints, this feature can be a great asset.

The first production circuit has been installed in an infrared-sensitive streak camera, and tests have been performed to measure sweep rate and linearity. The infrared camera contains a Phillips P510 streak tube¹ coupled to a 512 \times 512-pixel CCD. The circuit is designed with four selectable sweep ramp rates, which produce voltage ramps of ± 1000 V in 2, 6, 10, and 20 ns. Measured results agree well with design modeling.

Background

The LLE streak camera used for this work contains two deflection plates that are differentially driven by two equal

but opposite-polarity voltage ramp signals. Throughout this discussion only one of the ramp generators will be described. It is assumed that the other ramp generator uses the same technology and produces the same result with the opposite-polarity voltage.

The original streak-camera ramp generator designs at LLE were based on a resistor, inductor, capacitor (RLC) resonator.² The resonator, when driven by a voltage-step waveform, produced a damped sinusoidal response. The voltage step was produced by switching a fast avalanche transistor stack. Proper selection of the resonant frequency (the frequency where the capacitive reactance equals the inductive reactance) and the resistive damping factor produced a voltage ramp with the desired sweep slope. Closed-form expressions and computer simulations were developed to determine the required values of the resonator components for a specified sweep ramp. The basic circuit configuration is illustrated in Fig. 85.15.

The RLC ramp generator had several shortcomings: In the RLC circuit the values of the rate-determining reactances are small enough that parasitic reactances, such as those introduced by electromechanical relay contacts and deflection-plate feed lines, can greatly affect the sweep ramp characteristics. For this reason a selectable-rate ramp generator could not be

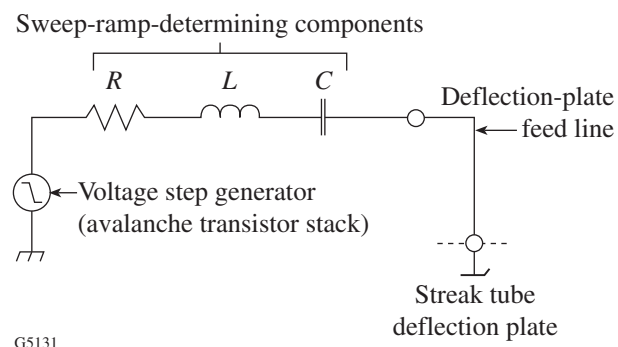


Figure 85.15
Original RLC resonator streak-camera ramp generator design.

designed using the RLC circuit configuration. To change ramp rates, removal and replacement of the RLC ramp generator module was required. For many this limitation was both time consuming and inconvenient.

Another disadvantage of the RLC resonator approach was that the feed line between the ramp generator and the deflection plate connection forms part of the RLC resonant circuit. A feed line that is too long or physically positioned improperly will distort the ramp shape significantly. As a result the ramp generator had to be mounted as close as physically possible to the streak tube deflection plate connections. In streak cameras where space around the tube deflection plate connections is limited, this complicates the overall design of the instrument.

The limitations of the RLC base ramp were overcome by a new sweep ramp generator design. The new design is a matched low-impedance ramp generator. With the low-impedance design, small shunt impedance parasitics, such as relay capacitance and feed line parasitics, have a negligible effect on the sweep ramp shape. Matching the impedance of the generator to the load removes the problems associated with the feed lines. Theoretically, the input impedance of an ideal transmission line terminated in its characteristic impedance is equal to the characteristic impedance regardless of line length. Thus the matched impedance ramp generator will produce the same waveform regardless of the interconnection length between the generator and the deflection plates as long as the generator, cable, and termination are of matched impedance.

The step generator needed for the matched-impedance ramp generator must be able to withstand higher switching

current than the step generator for the RLC resonator. An avalanche transistor stack alone will not withstand the step current for a long enough duration when driving a 50-Ω load.³ The step current duration must be long enough to maintain the step voltage at a specific potential following the active portion of the sweep to avoid retrace problems prior to camera shutter closure. In addition a matched generator and load will divide the switching potential, one half across the step generator internal impedance with the other half developed across the load. For a matched generator a higher voltage step is required to produce the same ramp voltage as developed by the RLC resonator approach.

Multi-rate Network

The block diagram of the selectable-rate streak-camera deflection ramp generator is illustrated in Fig. 85.16. The first production ramp generator module is shown in Fig. 85.17. The basic parts of the generator are the matched-impedance (50 Ω) voltage step generator and the filter network that determines the sweep rate.

Details of the low-pass-filter network are illustrated in Fig. 85.18. There are four individual electromechanical relay-selectable, low-pass filters. A remote-control logic interface within the filter network controls the relays. Each filter limits the high-frequency spectral components produced by the step generator, which in turn produces an output sweep ramp at a slower rate. Selection of the low-pass-filter cutoff frequency f_c determines the produced slope of the ramp. Each filter consists of a three-section inductor/capacitor (LC) passive low-pass circuit. With four filters the generator is capable of four different sweep rates. A fifth filter is included in series with the

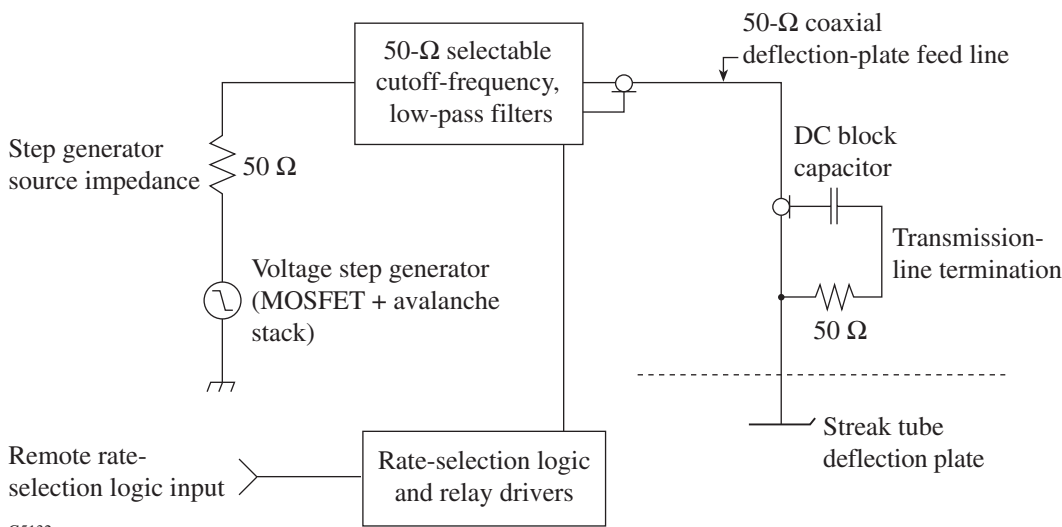


Figure 85.16
Block diagram of a new selectable-rate streak-camera deflection ramp generator.

selectable filters to limit high-frequency-signal leakage through the four selectable low-pass filters. The cutoff frequency of the fifth filter is set higher than the other filters so their passband performance is not affected.

Each 50-Ω matched-impedance low-pass filter is based on the coefficients that produce a Butterworth characteristic.⁴ A Butterworth low-pass filter produces monotonically increasing attenuation with increasing frequency. Closed-form equations are well known relating the component values to the one-half-power, or 3-dB, cutoff frequency f_c . Equations (1) through (3) provide the formulas required to calculate the component values for the three-section 50-Ω filters:

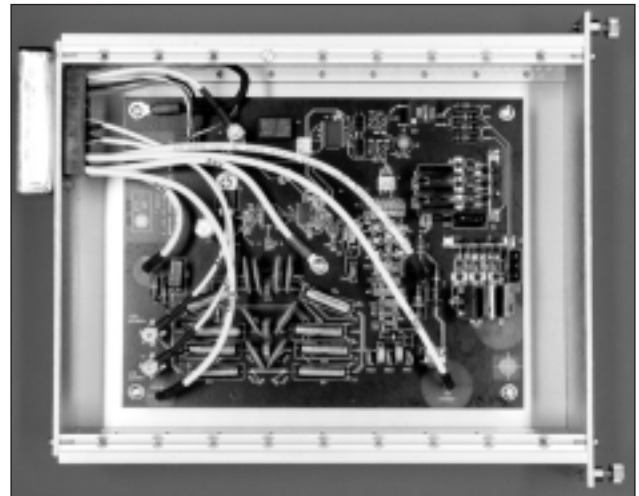
$$\omega_c = 2\pi f_c \tag{1}$$

(low-pass cutoff radian frequency, rad/s)

$$L = 2Z/\omega_c \text{ (henrys),} \tag{2}$$

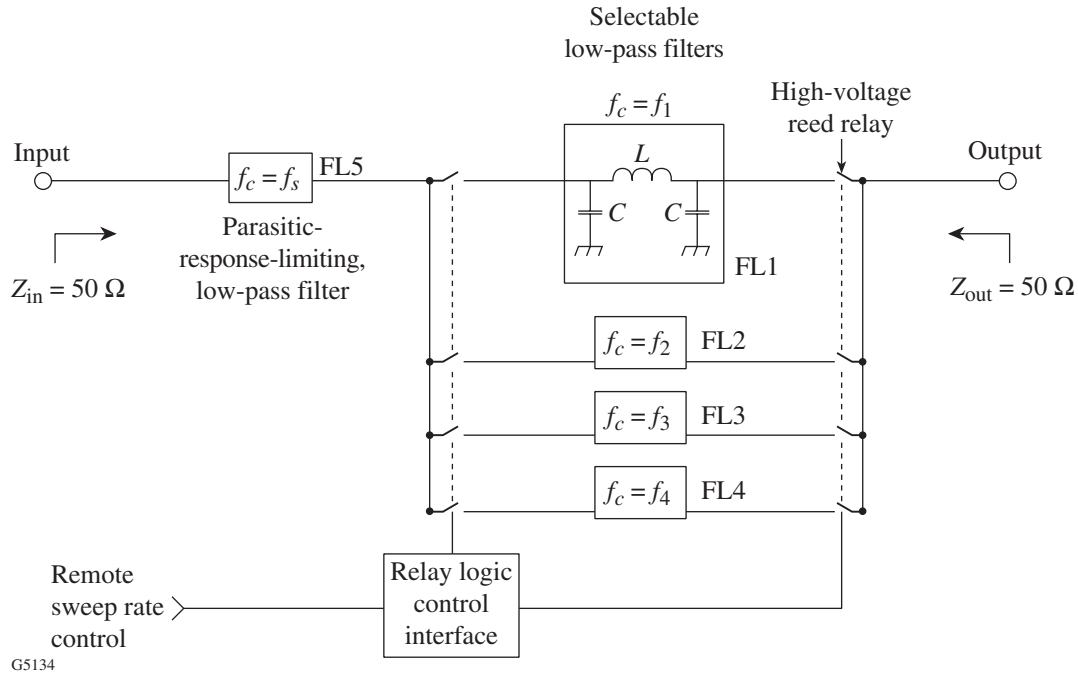
$$C = 1/(\omega_c Z) \text{ (farads),} \tag{3}$$

where $Z = 50 \Omega$ is the impedance of the filter.



G5133

Figure 85.17 Photograph of the selectable-rate streak-camera deflection ramp generator module. The top side of the board (shown) contains the negative-slope ramp generator, rate-selection logic, and relay drivers. The opposite side of the board (not shown) contains the positive-slope ramp generator.



G5134

Figure 85.18 Block diagram of the 50-Ω selectable cutoff low-pass filters that determine the sweep ramp rate.

A SPICE⁵ computer circuit simulation that includes the low-pass filters was developed for the ramp generator. A simplified schematic of the circuit model is shown in Fig. 85.19. Filters with low-pass cutoff frequencies from 1 to 155 MHz were evaluated using the circuit model to determine their effect on the ramp slope. Two parameters are used to relate the effect of the low-pass filter to the ramp slope. The first parameter t_r is the time required for the voltage ramp to change by 1000 V over its most linear portion. This is the region of the ramp generator's output waveform that produces the sweep deflection over the active region of the streak tube's output window. The second parameter K_f is the product of t_r with the low-pass cutoff frequency f_c . This product is the ratio of the ramp time to the period of the low-pass cutoff frequency. Knowing K_f , the low-pass cutoff frequency can be calculated for a specific active ramp duration t_r using

$$f_c = K_f / t_r \tag{4}$$

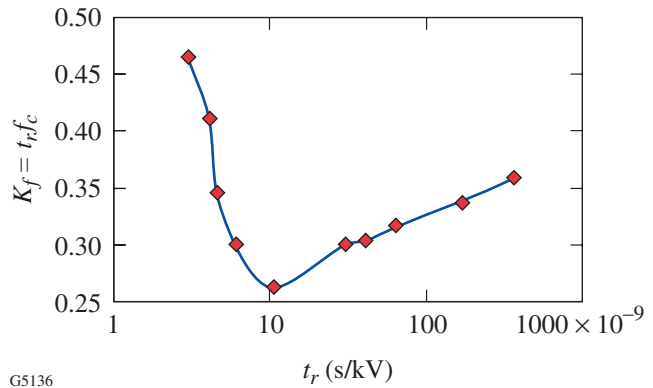
Figure 85.20 illustrates the relation between the active sweep ramp time t_r and the constant K_f as determined through computer modeling. Rearranging and substituting terms from Eq. (4) in Eqs. (2) and (3) leads to the following equations that are needed to determine the values of the low-pass filter components from the value of t_r and K_f :

$$L = (2Zt_r) / (2\pi K_f) \text{ (henries),} \tag{5}$$

$$C = t_r / (2\pi K_f Z) \text{ (farads),} \tag{6}$$

where t_r = active ramp duration in seconds.

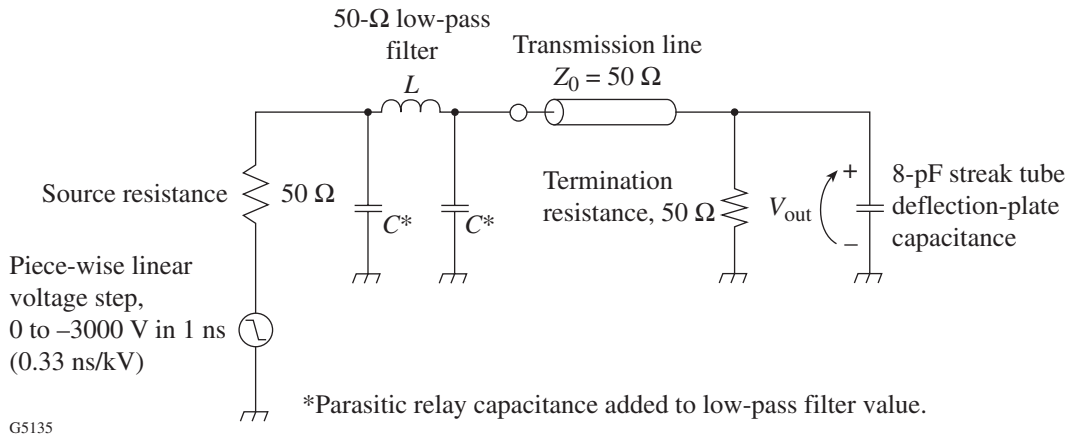
In an ideal step generator the step transition occurs instantaneously. For any practical step generator the step transition is of finite duration. In the SPICE circuit simulation the transition rate for the step generator was chosen to be 0.33 ns/kV. Typically an avalanche transistor stack can produce this ramp rate; however, as stated previously, the avalanche stack cannot



G5136

Figure 85.20

Plot of frequency product constant K_f as a function of sweep time t_r . Results produced by SPICE circuit simulation of the selectable-rate ramp generator.



G5135

Figure 85.19

Simplified schematic of the SPICE circuit simulation model used to determine a correlation between low-pass-filter cutoff frequency and sweep ramp rate. Actual circuit model contains detailed relay, step generator, and component parasitic models.

withstand the 30-A switching current for a duration of several microseconds as required for a matched 50-Ω step generator.³ High-voltage MOSFET's (metal-oxide silicon field effect transistors) can support a 50-Ω step generator switching current and voltage but cannot provide a transition rate of 0.33 ns/kV. Typical MOSFET switching speeds are of the order of 3.3 ns/kV. Combining the two switch technologies in parallel provides both the speed and durability required for the 50-Ω step generator by utilizing the speed of the avalanche transistor switch and the current-handling capabilities of the MOSFET switch. The avalanche transistor switch is triggered first, followed by the MOSFET switch after a short delay. This step generator is illustrated in Fig. 85.21.

The avalanche transistor stack follows a design using a tapered transmission line–matching technique developed at Lawrence Livermore National Laboratory.⁶ This technique uses the internal self-inductance of the avalanche transistors combined with added collector-to-ground capacitance chosen to effectively create a transmission line that tapers from a low impedance of several ohms at the bottom to 50 Ω at the top of the stack. An avalanche stack designed in this manner produces a faster switching rate into 50 Ω than a conventionally designed stack where impedance matching is not included. The tapered transmission line stack is capable of driving a 50-Ω load for

short periods (50 ns) with a typical rise time of 0.33 ns/kV. To limit the switching current duration in the avalanche stack, a capacitance of 220 pF is connected in series with the 50-Ω load. Well before the avalanche transistors are stressed, the series capacitor discharges and reduces the avalanche stack current.

The MOSFET switch is designed to have a switching rate of 3.3 ns/kV with an output matched to 50 Ω through the use of a series resistor. The MOSFET stack has a lower on-state resistance than 50 Ω, and the series resistor raises it up to the desired level. This switch is connected in parallel with the avalanche transistor stack. The MOSFET switch is triggered immediately after the avalanche transistor stack and is fully on before the avalanche stack series current-limiting capacitor is discharged. Thus the avalanche transistor stack provides the leading edge of the voltage step, and the MOSFET stack provides the step-holding time to prevent streak camera retrace and avalanche stack degradation. The source impedance of the composite switch is 50 Ω except for the time interval between the MOSFET switch turn-on and when the avalanche transistor stack series capacitor is fully discharged. This does not produce a measurable effect on the output since any mismatch reflection is terminated at the deflection plate termination and not re-reflected. The composite switch waveform is illustrated in Fig. 85.22.

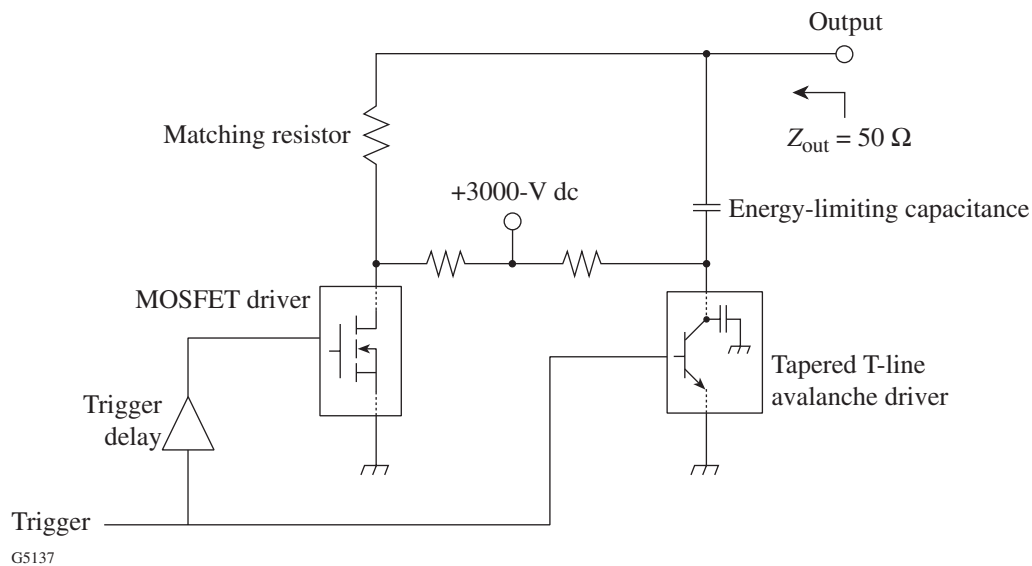


Figure 85.21 Block diagram of the 3000-V composite avalanche transistor stack and MOSFET step generator. The MOSFET driver contains three series-connected, simultaneously triggered 1200-V MOSFET's. The avalanche transistor stack is a ten-level transistor stack designed using the tapered transmission line technique developed at Lawrence Livermore National Laboratory.⁶

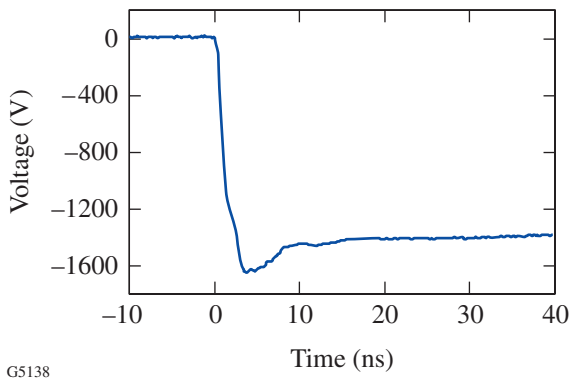


Figure 85.22 Measured output waveform produced by the composite avalanche transistor and MOSFET step generator. Fall time of step is 1 ns/kV.

The composite switch and selectable filter network form the selectable-rate ramp generator. A positive- and negative-voltage pair of these generators are needed to produce a complete differential deflection-plate generator. A 50-Ω transmission line is used to connect the ramp generator to the deflection plates. A matched 50-Ω termination is connected at the deflection-plate end of the transmission line.

Measured Electrical Performance

The electrical performance of the selectable-rate ramp generator is summarized in Figs. 85.23 and 85.24 and Table 85.I. In Fig. 85.23 all four sweep waveforms are superimposed. In Table 85.I the design parameters are listed with the measured results for each of the four sweep rates. The measured data for Fig. 85.23 and Table 85.I were recorded using a high-bandwidth oscilloscope⁷ and a high-voltage, high-bandwidth probe⁸ connected to the deflection plate of the streak tube. In Fig. 85.24 the measured and desired sweep rates for the four different selectable speeds are compared.

The differences between the desired and measured sweep rates indicate that more refinement of the filter factor K_f must be performed to get a closer correlation between the calculated and measured sweep rates. With an accurate K_f factor any reasonable sweep rate can be defined, and the appropriate low-pass filter can be designed using Eqs. (5) and (6). Errors in K_f are generated by incomplete modeling of the actual circuit parasitics in the SPICE computer simulation model for the ramp generator and by non-ideal characteristics of the composite voltage step generator. Since the measured sweep rates may be faster or slower than the desired rates, it should be possible to determine K_f to a high degree of accuracy with more-accurate computer circuit simulations.

Measurements of the sweep-speed nonlinearity indicate that the deflection rate slope is not uniform across the active sweep. Figure 85.25 illustrates the nonuniformity in the ramp slope for a sweep rate of 4.4 ps/pixel. The sweep rate is generally slow on the edges of the sweep and fast in the center. The measured sweep waveform has a sinusoidal characteristic instead of being a linear ramp. This nonlinearity is produced by the limited summation of sinusoids as theoretically generated by a step response propagated through a low-pass filter. The nonlinearity is reproducible with respect to the sweep waveform timing and should be removable when processing the streak image data. Increasing the ramp generator voltage swing

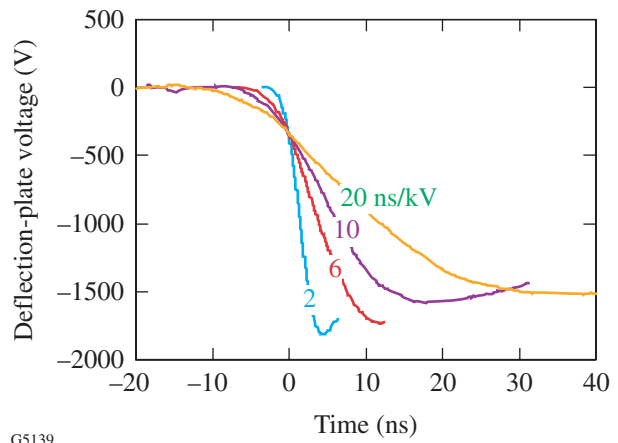


Figure 85.23 Measured output waveforms from the selectable-rate deflection ramp generator. The sweep waveforms for the four different ramp rates are superimposed.

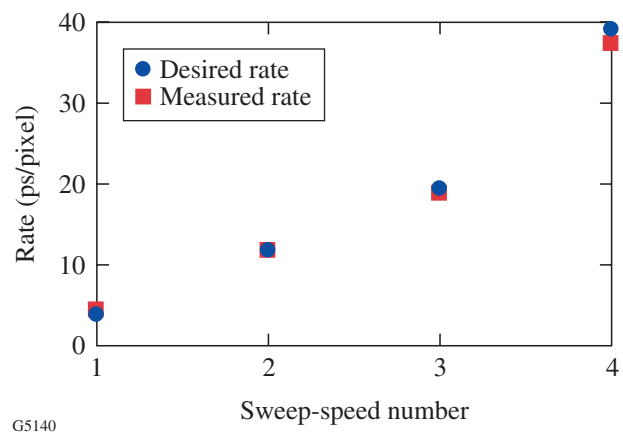


Figure 85.24 Comparison of desired and measured sweep rates.

would reduce the nonlinearity. This would place the active portion of the ramp generator output in an area of the waveform where the slope is more constant. The improved linearity must be traded off with increased complexity of the step generator and low-pass filter networks to accommodate the increased voltages and currents.

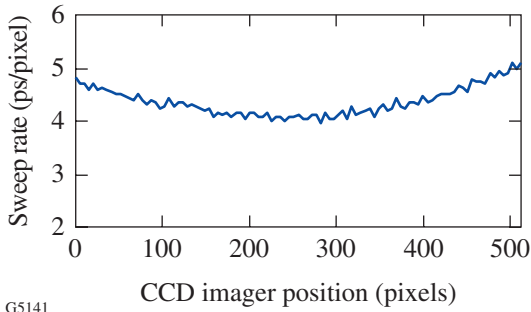


Figure 85.25 Measured sweep rate versus position on the CCD for a 4.4 ps/pixel sweep rate.

Optical Characterization of the Ramp Generator

A selectable-rate ramp generator was installed in a streak camera and characterized at a designed ramp rate of 17 ps/pixel using a 4.5-ns optical comb pulse.⁹ The measurement setup (Fig. 85.26) shows the streak camera input illuminated with the comb pulse and the streak camera’s deflection plate ramp generator triggered from a timing system synchronized with the comb pulse. Since the duration of the comb pulse is less than the sweep time of the ramp generator, the time delay between the ramp generator trigger and the arrival of the comb pulse at the streak camera was varied in order to scan the comb pulse over the full sweep duration. A series of streaks were recorded while changing this delay. The streak camera’s sweep speed was characterized by using the constant time interval between each pair of adjacent peaks within the comb pulse to determine the average sweep dwell time at the center CCD pixel location (Fig. 85.27). By analyzing the acquired streaks of the comb pulse the streak camera’s sweep speed as a function of deflection position, in this case CCD pixel position, was determined and compared to the measurement made by the

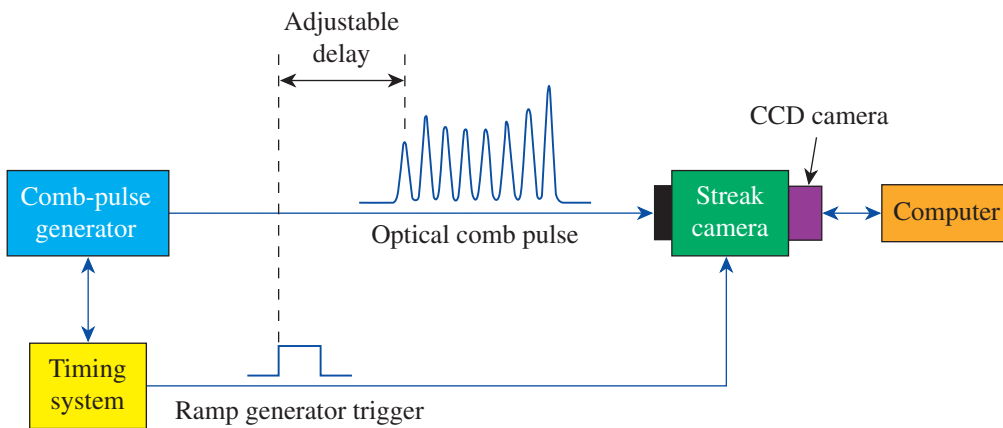


Figure 85.26 The streak camera is illuminated with a 4.5-ns-duration comb pulse, and the deflection-plate ramp generator is triggered from a timing system with an adjustable delay relative to the comb pulse.

Table 85.I: Measured and simulated result comparison for the ramp generator.

Full-Width Sweep Time t_r (ns)	Desired Rate (ps/pixel)	Filter Factor K_f	Theoretical Filter f_c (MHz)	Actual Filter f_c (MHz)	Measured Average Rate (ps/pixel)	Measured Rate Deviations from Average (ps/pixel)	
						min	max
2	3.9	0.47	235.0	155.0	4.4	-0.5	0.3
6	11.7	0.30	50.7	50.8	11.6	-1.7	1.1
10	19.5	0.26	26.0	29.3	18.9	-3.6	3.1
20	39.1	0.29	14.5	15.6	37.5	-8.8	7.3

electrical technique discussed earlier (Fig. 85.28). The spacing between the peaks of the comb pulse limits how close to the beginning and end of a streak the sweep speed can be reliably characterized because two adjacent peaks are required to determine the sweep speed at the point midway between them. We have found that for different ramp-rate selections, the electrical characterization of the ramp generator agrees well enough with the optical characterization to allow the initial setup to be done electrically and then perform the final optical characterization using the comb pulse. This will expedite the building and testing of new ramp generators while maintaining the availability of the streak cameras for use with experiments on OMEGA.

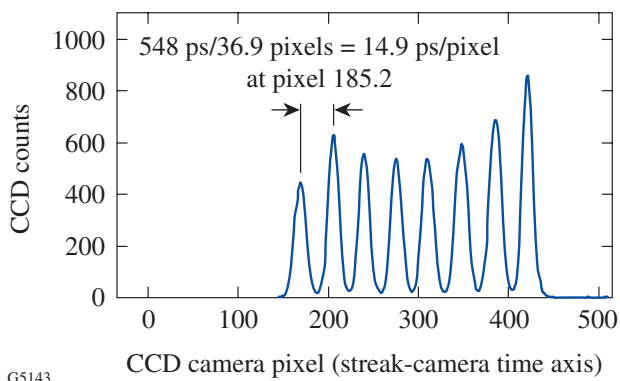


Figure 85.27

The constant time interval between each pair of adjacent peaks within the comb pulse is used to determine the sweep dwell time at the CCD pixel location midway between the peaks.

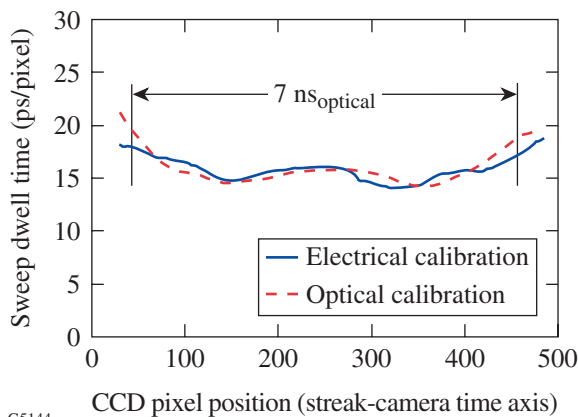


Figure 85.28

The optical and electrical measurements of the ramp generator agree well enough to allow the initial setup to be done electrically and then to perform the final optical characterization using the comb pulse.

Conclusion

A new method of generating streak-camera deflection ramps utilizing a 50- Ω composite MOSFET/avalanche transistor step generator and a relay-selectable low-pass-filter network was presented. This new design allows remote selection of four different sweep rates and provides a 50- Ω interface to the streak tube deflection plates. The 50- Ω interface relieves the requirement of mounting the ramp generator in close proximity to the deflection plates since the deflection signal can propagate along any length of standard 50- Ω coaxial cable.

There is good agreement between the modeled and measured sweep rates. The observed differences can be reduced by incorporating a more detailed computer-aided simulation model that accounts for all non-ideal component behavior. The nonlinearity in the ramp rate is reproducible and can be corrected in the data analysis.

ACKNOWLEDGMENT

This work was supported by the U.S. Department of Energy Office of Inertial Confinement Fusion under Cooperative Agreement No. DE-FC03-92SF19460, the University of Rochester, and the New York State Energy Research and Development Authority. The support of DOE does not constitute an endorsement by DOE of the views expressed in this article.

REFERENCES

1. P510PSU streak tube, Philips Photonics, Slatersville, RI 02876.
2. Laboratory for Laser Energetics LLE Review **73**, 6, NTIS document No. DOE/SF/19460-212 (1997). Copies may be obtained from the National Technical Information Service, Springfield, VA 22161.
3. Zetex, Inc., Commack, NY 11725.
4. E. C. Jordan, *Reference Data for Engineers: Radio, Electronics, Computer, and Communications*, 7th ed. (H. W. Sams, Indianapolis, IN, 1985), pp. 9-14, 9-19.
5. SPICE 3F2, developed by the Department of Electrical Engineering and Computer Sciences, University of California, Berkeley, CA 94720.
6. E. S. Fulkerson and R. Booth, Lawrence Livermore National Laboratory, Livermore, CA, UCRL-JC-116309 (1994).
7. Oscilloscope Model No. TDS684, Tektronix Corporation, Beaverton, OR 97077.
8. Oscilloscope Probe Model No. P5100, Tektronix, Inc., Wilsonville, OR 97070.
9. Laboratory for Laser Energetics LLE Review **72**, 184, NTIS document No. DOE/SF/19460-199 (1997). Copies may be obtained from the National Technical Information Service, Springfield, VA 22161.

Unique High-Bandwidth, UV Fiber Delivery System for OMEGA Diagnostics Applications

Introduction

The OMEGA laser at the Laboratory for Laser Energetics was built for direct-drive inertial confinement fusion (ICF) experiments.¹ Sixty symmetrically disposed laser beams are used to compress ICF capsules that typically contain deuterium–tritium (DT) or deuterium. The laser beams heat and compress the target, causing the fuel to undergo thermonuclear fusion. Special temporally shaped pulses, which typically have a 1- to 3-ns duration, must be generated to optimize the target compression. To avoid hydrodynamic instabilities during the target compression the target illumination must be highly uniform.² This requires good power balance of all 60 OMEGA beams. The characteristic time of the hydrodynamic instability seed is under 100 ps, which means that the laser drive must be uniform on a 100-ps time scale. This defines the time scale over which power balance must be achieved.³

To measure the UV pulse shape and OMEGA power imbalance (see Fig. 85.29), we developed a ten-channel streak camera based on a commercial P510 streak tube.⁴ Six such cameras are used to measure the pulse shape in the 60 OMEGA beams.

Motivation

High fusion neutron yield produced during OMEGA target shots causes excessive noise in the streak camera’s charge-coupled devices (CCD’s), significantly reducing the camera’s dynamic range. The neutron-induced noise could be reduced by placing the cameras behind the Target Bay’s shield wall. This required the development of a longer fiber optic system to deliver light from the sampling point to the streak camera input.

The most important parameters of the optical fiber to be used in this delivery system are high transmission at the OMEGA working wavelength (351 nm) and low modal dispersion. We require ~15-m-long fibers, so we set our attenuation requirement to ≤ 220 dB/km at 351 nm. The modal dispersion must be low enough to allow an overall bandwidth of the streak camera diagnostic to be ≥ 30 GHz.

To assure pulse-shape fidelity of the frequency-modulated and wavelength-dispersed laser pulse,⁵ a speckle pattern is launched into the fibers, which is matched to the multimode

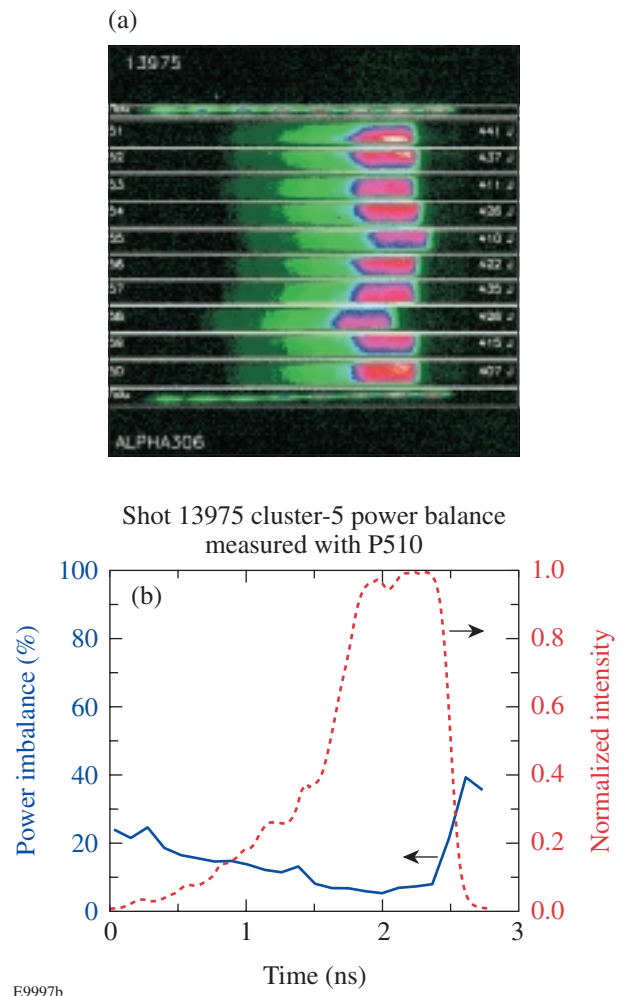


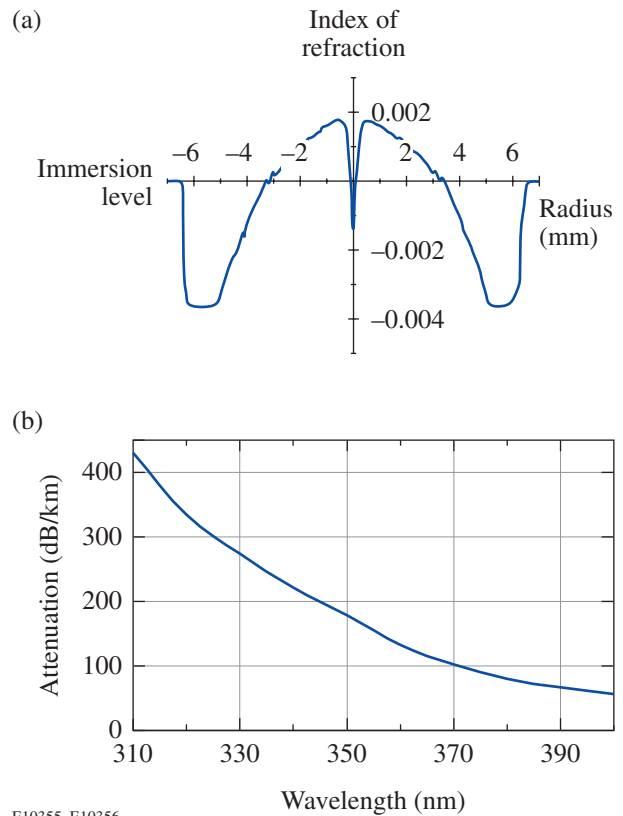
Figure 85.29 P510 streak cameras provide pulse-shape and power-imbalance measurements for all 60 beams of OMEGA. (a) Streak camera recording of all ten beams in one OMEGA cluster. (b) P510 streak camera average pulse shape for all ten beams of cluster 5 on shot 13975 (dashed line) and beam-to-beam power imbalance (solid line) determined from the streak records.

pattern of the fiber. The statistics are further improved by launching into a bundle of seven fibers (Fig. 85.30). To increase the fiber bundle's light-launching efficiency, the ratio of the cladding diameter to the core diameter (clad/core ratio) should be close to 1.

Assembling fiber bundles requires high precision in matching individual fiber lengths. Unequal fiber lengths will reduce the bandwidth of the optical fiber delivery system.

Optical Fiber Manufacturing

Optical fibers were made using the modified chemical vapor deposition (MCVD) method.⁶ The 13-mm-diam preforms used consisted of a P₂O₅ doped silica core and a pure silica glass cladding; initial clad/core ratio was 2. Before fiber drawing, the preforms were etched in hydrofluoric acid (HF) to achieve a clad/core ratio of 1.25. The MCVD method ensured the required graded index profile and low dispersion at the working wavelength. Figure 85.31(a) shows the preform's index-of-refraction profile. The central dip in this profile is due to vaporization of P₂O₅ while the preform collapses under high temperature during the preform manufacturing process. While this dip cannot be removed completely, it can be minimized. The presence of the dip did not affect fiber performance. The optical fibers were drawn from preforms and covered in line with an epoxyacrylate coating using a pressurized die. The fibers have a core diameter of 100 μm, a cladding diameter of 125 μm, and a coating diameter of 250 μm. The typical fiber attenuation dispersion curve in Fig. 85.31(b) demonstrates that the optical fiber satisfies the <220-dB/km attenuation requirement at OMEGA's working wavelength.



E10355, E10356

Figure 85.31 (a) Index-of-refraction profile for the fiber preform and (b) the fiber attenuation dispersion curve.

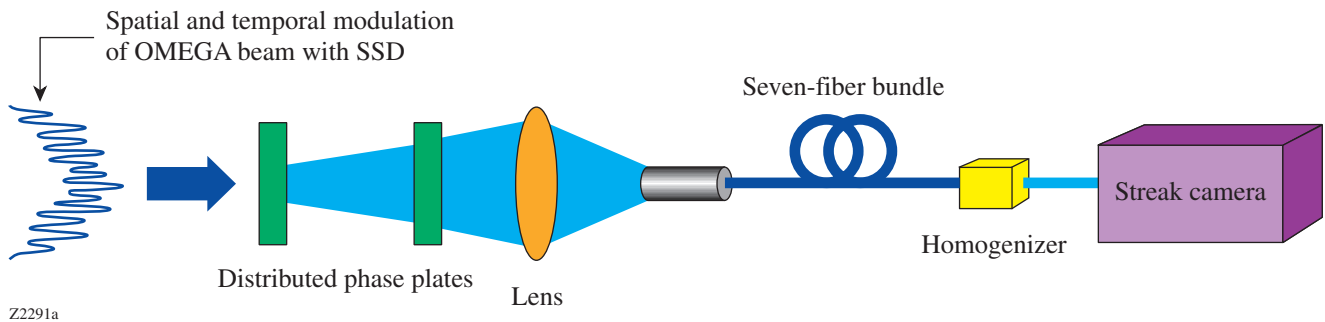


Figure 85.30 Schematic of optical UV fiber delivery system that was designed to sample the OMEGA laser beam and bring the light to the streak camera.

Laser System with Pulse Compression for Fiber Testing

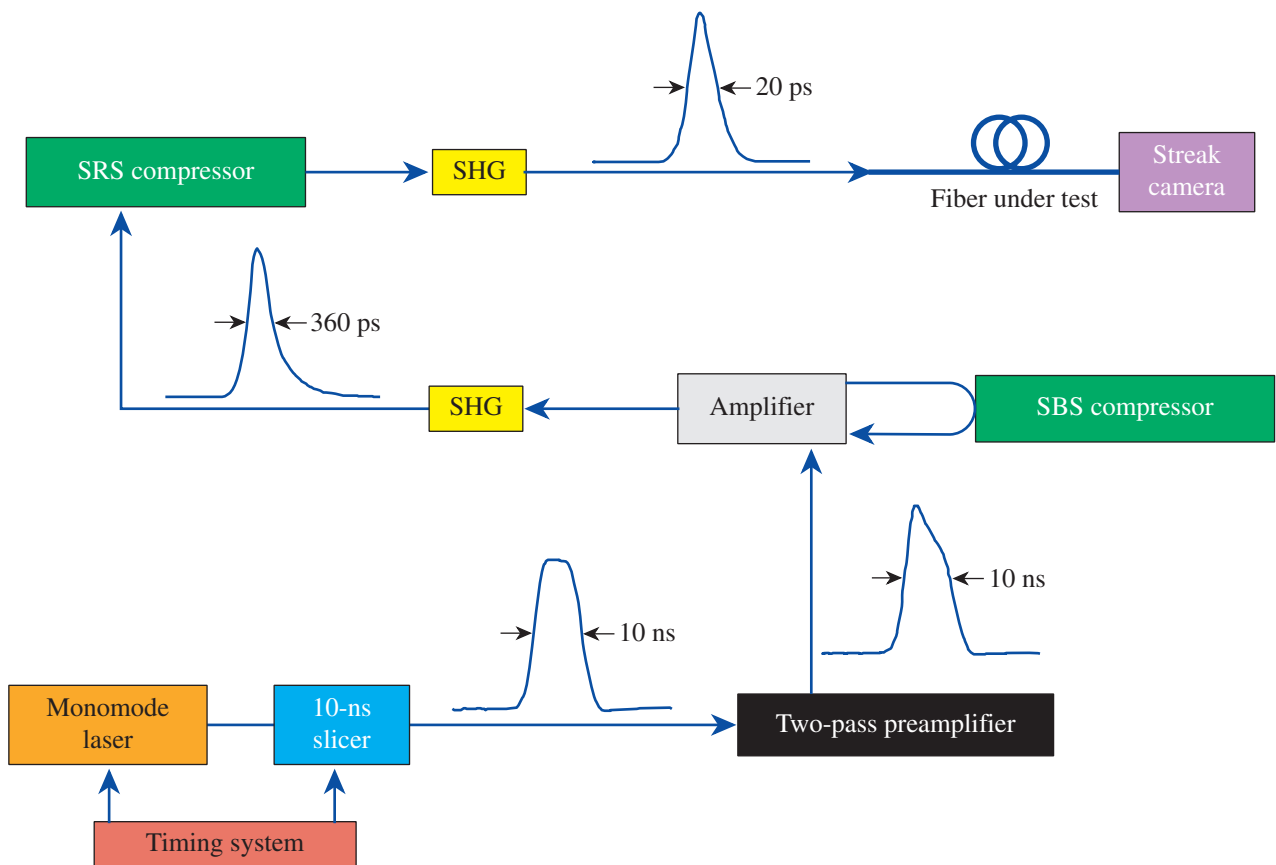
To test the optical fiber and fiber bundle bandwidth, a laser system similar to that described in Ref. 7 was used; it produced 20-ps synchronizable laser pulses at 337-nm wavelength at a ≤ 10 -Hz repetition rate. A block diagram of the laser system is shown in Fig.85.32. Starting with the Q-switched Nd:YLF monomode laser, a 10-ns square pulse with ~ 10 - μ J energy was sliced out. After amplification, this pulse was directed to a stimulated Brillouin scattering (SBS) cell filled with CCl₄. By choosing the right focusing geometry and input energy, the incoming 10-ns pulse was compressed to ~ 360 ps with more than 50% energy efficiency. After second-harmonic conversion the 527-nm pulse was further compressed to ~ 20 ps using a pressurized-hydrogen, stimulated Raman scattering (SRS) cell (frequency shift is 4156 cm⁻¹). The energy of the SRS 674-nm pulse was >2 mJ; another second-harmonic conversion resulted in a ~ 20 -ps, 337-nm, >0.5 -mJ externally synchronizable pulse. The timing jitter of this pulse was

measured to be ~ 150 -ps rms. The SBS pulse compression mechanism is the source of this timing jitter. The focused-laser-beam Rayleigh range inside the SBS cell defines the jitter of the compressed pulse because the compression process may start at any point within the Rayleigh range.

A streak camera was used to measure the single-fiber modal dispersion. Single-shot measurements were made, recording the pulse width after its propagation through a 40-m piece of optical fiber compared to propagation through air. The optical-fiber modal dispersion was calculated using the following relationship:

$$\Delta t = \sqrt{(t_{out})^2 - (t_{in})^2} / L_{fiber}$$

where Δt is the modal dispersion, t_{in} is the fiber input-pulse width, t_{out} is the fiber output-pulse width, and L_{fiber} is the



E10359, E10360

Figure 85.32 Schematic diagram of the SBS-SRS pulse-compression laser system that produces 500 \times compressed pulse in UV. The system can be externally synchronized.

length of the fiber under test. The modal dispersion was measured to be 0.3 to 0.7 ps/m, depending on the fiber preform. Hence, the single optical fiber bandwidth limited by the fiber modal dispersion is >33 GHz, which satisfies OMEGA requirements. A summary of the optical fiber parameters is shown in Table 85.II.

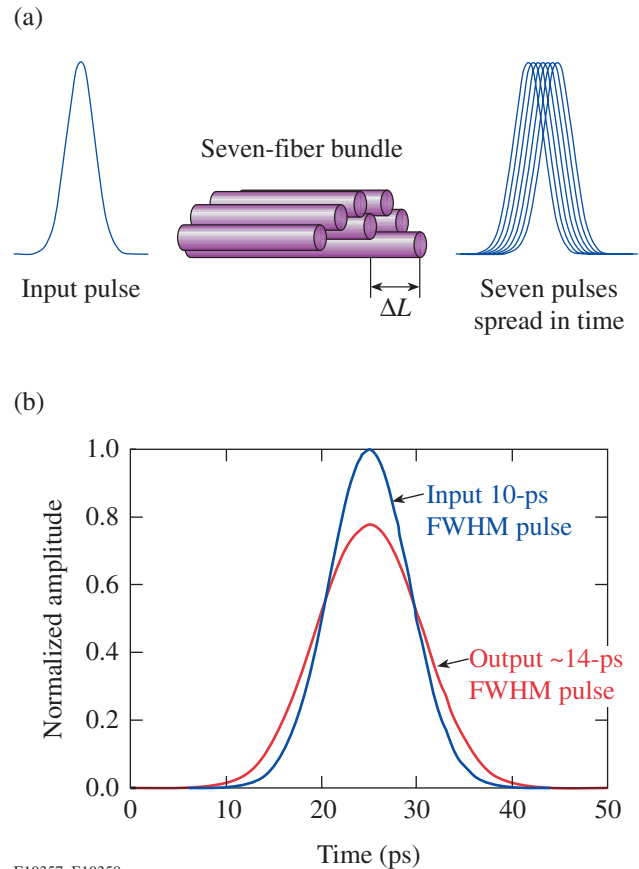
Table 85.II: Technical characteristics of the optical fiber.

Core diameter	100 μm
Cladding diameter	125 μm
Coating diameter	250 μm
Core/cladding concentricity	2.5 to 3 μm
Cladding/coating concentricity	<10 μm
Core noncircularity	4% to 5%
Cladding noncircularity	1.8% to 2%
Minimum working bend radius	100 mm
Numerical aperture	0.13
Attenuation @ 351 nm	170 to 220 dB/km
Modal dispersion	0.3 to 0.7 ps/m

Fiber Bundle Manufacturing and Testing

The seven-fiber-bundle assembly requires a close matching of the individual fiber lengths. Fiber-length differences will cause a spread in time of the output pulse [see Fig. 85.33(a)], which will degrade the fiber delivery system's bandwidth. Figure 85.33(b) shows the simulated broadening of a 10-ps input pulse in a 15-m seven-fiber bundle with ± 1 -mm fiber-length differences. In this case, unequal fiber lengths limit the fiber delivery system's bandwidth to ~ 35 GHz, which is still acceptable for OMEGA applications. The goal was to maintain fiber-length differences within a ± 1 -mm range for seven 15-m individual fibers. A process was developed that achieved this level in fiber-length accuracy. The process started with a stainless steel tube that accepts seven fibers in a hexagonal close-pack pattern. Fibers were aligned flush with the edge of the tube using a glass slide. Using a microscope, the seven-fiber pattern was rotationally aligned to a key of FC/PC fiber connector to minimize coupling losses when the two fiber bundles were connected. Next, the seven fibers were formed into a fiber ribbon. The fiber ribbon was tensioned, and the fibers were cut flush with the edge of another stainless steel tube installed in the far end. Finally a fiber jacket was placed over the fiber bundle, and the fiber connectors were polished.

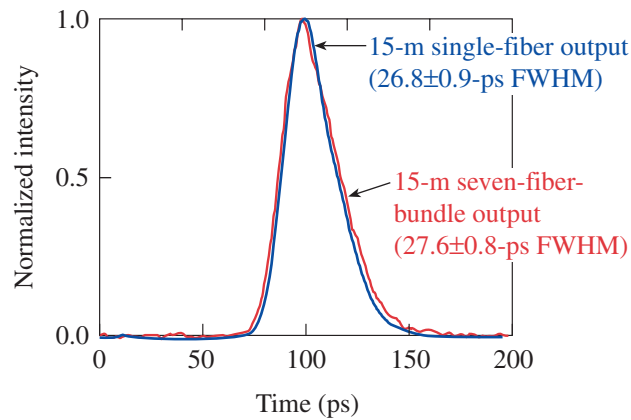
Forty fiber bundles were assembled by this method. To characterize the fiber-bundle bandwidth, a pulse propagated through a single 15-m fiber was compared with a pulse propagated through the seven-fiber bundles. Figure 85.34 shows minor spreading of the pulse in the fiber bundles caused by unequal fiber length, demonstrating that the fiber-bundle bandwidth exceeds 50 GHz.



E10357, E10358

Figure 85.33

(a) A fiber bundle broadens the output pulse because of fiber-length differences that limit the bandwidth of a fiber delivery system. (b) Simulated broadening of a 10-ps pulse in a 15-m fiber bundle when $\Delta L = \pm 1$ mm.



E10362

Figure 85.34

Streak camera recording of a pulse propagated through a single fiber is compared with that propagated through a seven-fiber bundle. The seven-fiber-bundle assembly procedure does not limit the bandwidth of the fiber-delivery system.

Conclusion

A special optical fiber for OMEGA laser pulse shape and power imbalance diagnostics was developed and tested. Modal dispersion of less than 1 ps/m was measured for this fiber. A fiber-bundle-assembly procedure was implemented that provides better than ± 1 -mm fiber length matching over a 15-m fiber length. The fiber delivery system based on these bundles has more than 30-GHz bandwidth and high transmission at 0.35- μm wavelength.

ACKNOWLEDGMENT

The high-bandwidth, UV-transmitting, graded-index optical fiber for this fiber delivery system was developed by the Vavilov State Optical Institute, St. Petersburg, Russia, for use in laser diagnostics on the NIF laser. Funding was provided by Lawrence Livermore National Laboratory. This work was supported by the U.S. Department of Energy Office of Inertial Confinement Fusion under Cooperative Agreement No. DE-FC03-92SF19460, the University of Rochester, and the New York State Energy Research and Development Authority. The support of DOE does not constitute an endorsement by DOE of the views expressed in this article.

REFERENCES

1. T. R. Boehly, R. S. Craxton, T. H. Hinterman, P. A. Jaanimagi, J. H. Kelly, T. J. Kessler, R. L. Kremens, S. A. Kumpan, S. A. Letzring, R. L. McCrory, S. F. B. Morse, W. Seka, S. Skupsky, J. M. Soures, and C. P. Verdon, *Fusion Technol.* **26**, 722 (1994).
2. J. M. Soures, R. L. McCrory, C. P. Verdon, A. Babushkin, R. E. Bahr, T. R. Boehly, R. Boni, D. K. Bradley, D. L. Brown, R. S. Craxton, J. A. Delettrez, W. R. Donaldson, R. Epstein, P. A. Jaanimagi, S. D. Jacobs, K. Kearney, R. L. Keck, J. H. Kelly, T. J. Kessler, R. L. Kremens, J. P. Knauer, S. A. Kumpan, S. A. Letzring, D. J. Lonobile, S. J. Loucks, L. D. Lund, F. J. Marshall, P. W. McKenty, D. D. Meyerhofer, S. F. B. Morse, A. Okishev, S. Papernov, G. Pien, W. Seka, R. Short, M. J. Shoup III, M. Skeldon, S. Skupsky, A. W. Schmid, D. J. Smith, S. Swales, M. Wittman, and B. Yaakobi, *Phys. Plasmas* **3**, 2108 (1996).
3. W. R. Donaldson, R. Boni, R. L. Keck, and P. A. Jaanimagi, in *Optical Pulse and Beam Propagation*, edited by Y. B. Band (SPIE, Bellingham, WA, 1999), Vol. 3609, pp. 121–127.
4. P510PSU streak tube, Philips Photonics, Slatersville, RI 02876.
5. S. Skupsky, R. W. Short, T. Kessler, R. S. Craxton, S. Letzring, and J. M. Soures, *J. Appl. Phys.* **66**, 3456 (1989).
6. S. R. Nagel, J. B. MacChesney, and K. L. Walker, *IEEE J. Quantum Electron.* **QE-18**, 459 (1982).
7. R. R. Buzyalis *et al.*, *Sov. J. Quantum Electron.* **17**, 1444 (1987).

Fabrication and Properties of an Ultrafast NbN Hot-Electron Single-Photon Detector

Introduction

Currently, visible photon counting is commonplace for advanced optical imaging and spectroscopy. Several types of devices, including photomultiplier tubes,¹ quantum semiconductor avalanche photodiodes,² and superconducting tunnel junctions,³ have been successfully implemented. In general, such detectors work by a cascade mechanism: an incident single photon is absorbed, releasing an electron, which then instigates a multiplication process, leading to a measurable electron current pulse. Unfortunately, vacuum photomultipliers are slow and bulky and have an extremely low quantum efficiency for longer-wavelength photons. The major drawback of the most popular and most successful silicon photodiodes is that the wavelength sensitivity is limited to below 1 μm , restricted by the Si bandgap. In addition, the single-photon avalanche photodiodes exhibit low detection rates due to complicated Geiger-mode readout schemes.

The current most-pressing need is to develop practical infrared single-photon detectors, operational at either 1.3 μm or 1.55 μm , for novel quantum communication and quantum computation systems. The problem is that infrared photons carry significantly less energy than those of visible light, so in this case it is difficult to engineer an efficient electron cascade mechanism. Avalanche photodiodes based on narrow-gap semiconducting materials exhibit unacceptably large dark counts, while recently proposed single-electron transistors⁴ are slow and require millikelvin temperatures and tesla-level magnetic fields.

In this article, we present a simple-to-manufacture and easy-to-operate, NbN hot-electron photodetector (HEP) with picosecond response time, high intrinsic quantum efficiency, negligible dark counts, and the capability to detect single photons from the ultraviolet to the infrared wavelength range. Our photodetector is the conversion of a well-known, unselective, superconducting hot-electron bolometer⁵ into an optical and infrared wavebands quantum detector.⁶ The detector consists of an ultrathin, submicron-width NbN stripe, maintained at 4.2 K and current-biased close to the critical

value. The detection mechanism is based on supercurrent-assisted, temporary formation of a resistive barrier across the stripe due to photon-induced hot-spot generation. Practical implementation of this device should lead to revolutionary progress in areas ranging from ultrafast free-space satellite communication⁷ through quantum computation⁸ and quantum cryptography⁹ to semiconductor integrated circuit testing.¹⁰

Device Fabrication

NbN films were sputtered onto sapphire substrates by reactive magnetron sputtering in an argon–nitrogen gas mixture. Using an optimized sputtering technique, the NbN samples exhibited a superconducting transition temperature of $T_c = 10.5$ K for 60-Å-thick films and 11 K for 100-Å-thick films, respectively. The superconducting transition width was equal to $\Delta T_c = 0.3$ K. A more detailed description of the NbN film deposition can be found in Ref. 11.

The fabrication process of the HEP's included several deposition and patterning manufacturing stages, resulting in the devices shown in Figs. 85.35 and 85.36. After the NbN film sputtering, TiAu alignment marks for future lithography steps and interior 5- $\mu\text{m} \times 16\text{-}\mu\text{m}$ Ti/Au contacts were formed using *e*-beam lithography and *e*-beam evaporation. Exterior contact pads for wire bonding of the entire structure were fabricated by a vacuum evaporation of 2000 Å of Au. The final, desired geometry of the NbN microbridge was achieved by ion milling the NbN film through a 200-Å-thick Ti mask placed inside the gap between the inner Ti/Au contacts. For a straight bridge (Fig. 85.35) this mask was a single 0.2- μm -wide stripe, while in the case shown in Fig. 85.36, it was a 0.2- μm -wide meander-type line covering the 4- $\mu\text{m} \times 4\text{-}\mu\text{m}$ area. After ion milling of the NbN detector, the remaining Ti layer was chemically removed.

After fabrication, each device was carefully inspected using both the AFM (Fig. 85.35) and SEM (Fig. 85.36) microscopes for bridge uniformity. In addition, the only samples selected were those in which room-temperature resistance was almost equal to the value calculated according to the structure dimen-

sions and measured sheet resistance of the unpatterned NbN film. This procedure assured homogeneity and high quality of the superconductor microbridge, with minimal, if any, variations along its width.

Experimental Setup

The experimental setup and device connections inside an optical liquid-helium cryostat are shown schematically in

Fig. 85.37. The NbN HEP was mounted on a cold plate and maintained at $T = 4.2$ K. Two cold glass filters were used to prevent the room-temperature thermal radiation from falling onto the device. The device was mounted on a rigid coplanar transmission line and connected with a cold bias-tee through a stainless steel, semirigid coaxial cable. The ac output of the bias-tee was connected to a cryogenic low-noise amplifier. Outside the dewar, the signal passed through a second power

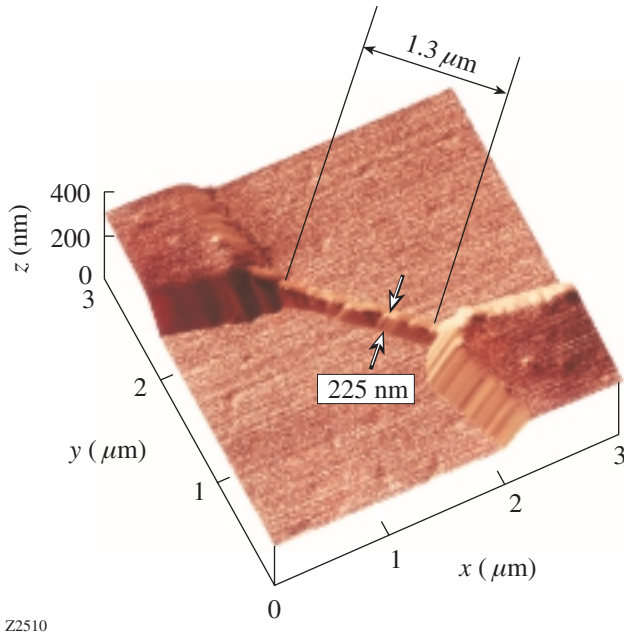


Figure 85.35
AFM image of a 1.3- $\mu\text{m} \times 0.23\text{-}\mu\text{m}$ simple bridge device.

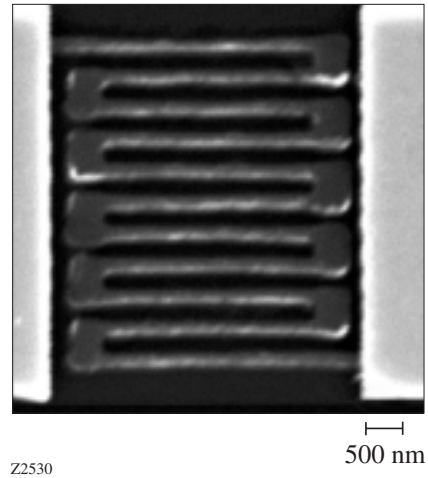


Figure 85.36
SEM photograph of a meander-type photodetector structure.

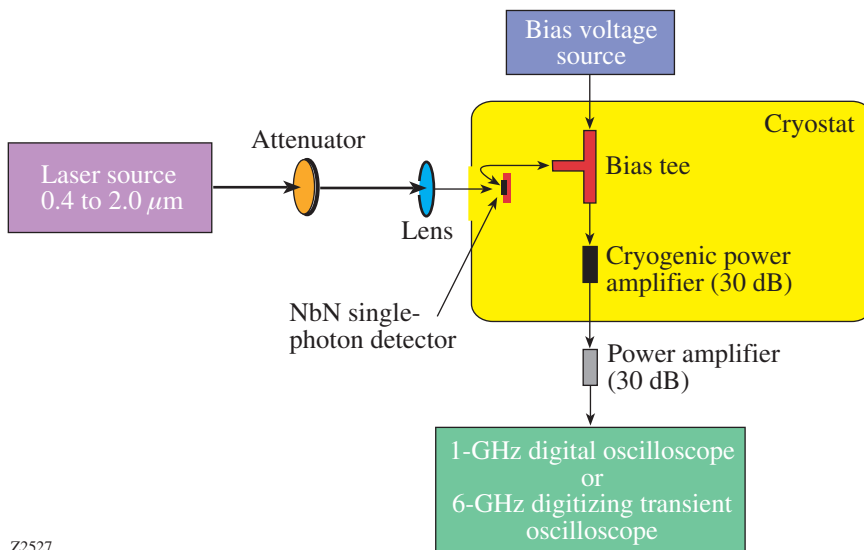
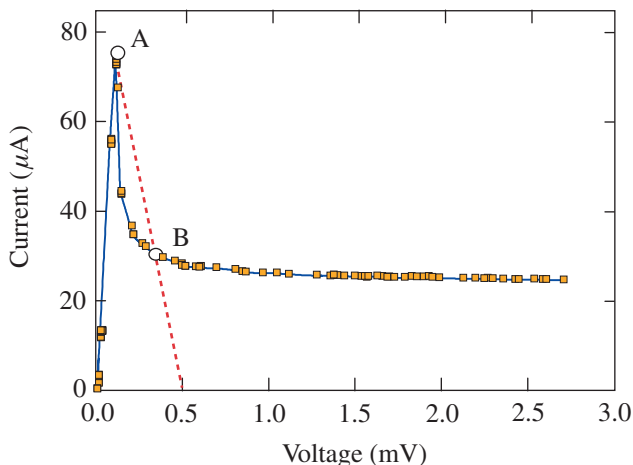


Figure 85.37
Experimental setup.

amplifier, connected to a single-shot oscilloscope and pulse counter (not shown). The oscilloscope was either externally triggered by laser pulses or self-triggered. The experiments were performed using 20-ps-wide, ~ 3 -pJ-energy, $0.85\text{-}\mu\text{m}$ -wavelength pulses generated by a GaAs laser with a repetition rate ranging from 1 Hz to 100 kHz, or 100-fs-wide optical pulses from a mode-locked Ti:sapphire laser. In this latter case, the wavelength could be varied quasi-continuously from $0.5\ \mu\text{m}$ to $2.1\ \mu\text{m}$, while the repetition rate was either 76 MHz or 1 kHz. The intensity of the laser pulses was attenuated using banks of neutral-density filters. The diameter of the beam incident on the device was always at least $200\ \mu\text{m}$, assuring stable (no “beam walking”) and uniform illumination throughout the experimental session.

Experimental Results

An experimental I - V curve for meander-type HEP, measured by a two-point method, is presented in Fig. 85.38. The curve is typical for a long superconducting microbridge and shows that depending on the biasing condition (either purely current-bias or voltage-bias), the device switches from the superconducting, zero-resistance state to the switched, resistive state. This particular device exhibits $I_c = 80\ \mu\text{A}$ and the switched-state resistance $R = 46\ \text{k}\Omega$. The dashed line between points A and B in Fig. 85.38 represents the switching condition when the device is connected to a $50\text{-}\Omega$ microwave transmission line. For a HEP biased close but below I_c (point A in Fig. 85.38), the photon absorption leads to a temporary switch along the dashed line to the metastable resistive point B. As a result, a voltage pulse is observed whose amplitude



Z2529

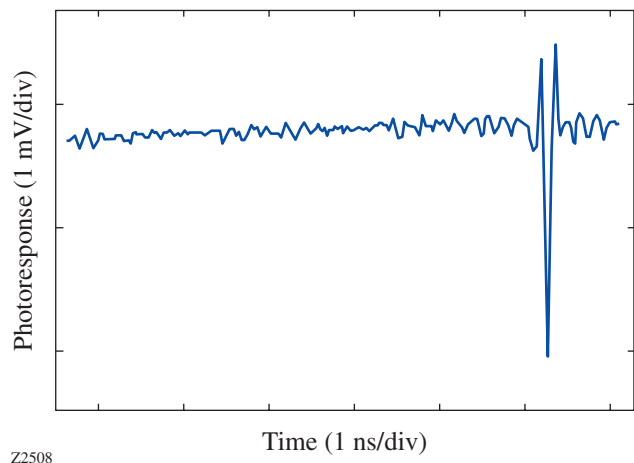
Figure 85.38
 I - V curve of a meander-type device measured at $T = 4.2\ \text{K}$.

corresponds to the voltage value of point B, while the duration depends on the dynamics of formation and destruction of the resistive state induced by the photon absorption (see the **Discussion** section).

The time-resolved HEP response to a $0.85\text{-}\mu\text{m}$ -wavelength, 20-ps-wide optical pulse, captured using a single-shot, 6-GHz-bandwidth digitizing oscilloscope, is shown in Fig. 85.39. The width of the photoresponse is equal to $\sim 150\ \text{ps}$ and, based on our earlier electro-optic time-domain measurements,¹² is limited by the upper cutoff frequency of our amplifier chain. The signal-to-noise ratio is $\sim 30\ \text{dB}$. Qualitatively, the same response pulses, with the same ~ 150 -ps pulse widths and essentially the same amplitudes, were obtained at all the studied photon energies, independently of the incident optical pulse width, or the laser repetition rate. In addition, the response amplitude did not depend on the laser beam intensity.

Device Operation

Figure 85.39 shows the quantum nature of the HEP detector, but it does not show indisputably that it is indeed a single-photon counter. To demonstrate the latter, the statistical dependence of the number of recorded photoresponse pulses on the number of input quanta per pulse per unit area was measured. We progressively attenuated the intensity of laser pulses, using calibrated neutral density filters, and observed the decreasing number of response pulses. The experimental data allowed us to calculate the probability of recording a detector output for a given photon flux input, which is shown in Fig. 85.40 for two different device types. Curves *a* and *b* correspond to a simple,



Z2508

Figure 85.39
Time-resolved, single-photon-type event recorded by a single-shot digitizing oscilloscope.

1- μm -long microbridge, biased at the current value $I_b = 0.92 I_c$ and $I_b = 0.8 I_c$, respectively. Curves *c* and *d* are taken for a meander-type device, under the same conditions as curves *a* and *b*, respectively.

Note that while for high photon fluxes both HEP's are saturated, showing 100% efficiency in photon counting, the significant decrease in the number of photons m per pulse results in lower probability of recording a photon. Based on simple statistics, one can expect that for very weak photon fluxes, the probability of detecting one photon should be proportional to m , while the probability of simultaneously detecting two photons depends on m^2 , the three-photon counting should obey the m^3 law, and so on. Indeed, we observe the linear decrease of response pulse probability versus number of quanta per unit area for curves *a* and *c*. At the same time, curve *b* follows a clear m^2 dependence, indicating a two-photon detection. Thus, the 0.92 ratio of I_{bias}/I_c is required for the single-photon operation. In general, photon detection probability versus I_{bias} was an exponentially decreasing function, indicating that the I_{bias} redistribution from the uniform state to the sidewalk-restricted flow, rather than the hot-spot formation, is the dominant factor of the device response.

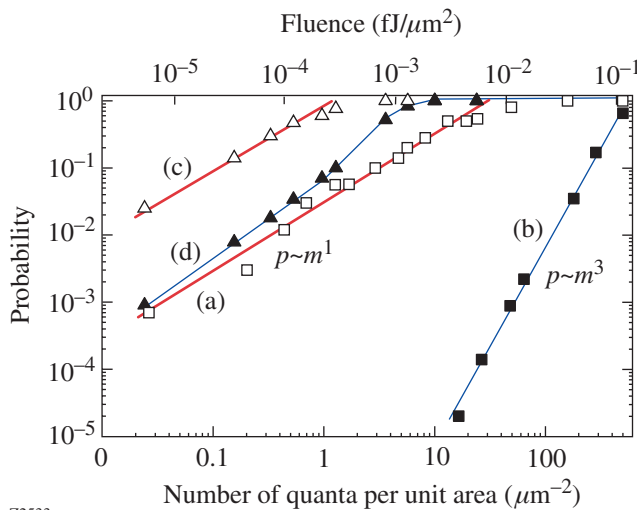
The other characteristic parameter of a single-photon detector is its quantum efficiency, defined as the ratio of the number of response pulses to the number of incident photons per area

for the device in the linear regime (Fig. 85.40, curves *a* and *c*). The quantum efficiency for the microbridge (curve *a*) may be estimated as 20%. The meander-type HEP's have been designed to increase both the active area of the device and its total quantum efficiency. As was expected, the absolute quantum efficiency for the meander device is significantly higher than that for the 1- μm device, but the detector's active area was increased by the factor of 80, while the quantum efficiency increased only 20 times. Thus, the intrinsic quantum efficiency for the meander HEP is equal to approximately 5%. The reason for the observed decrease in the meander device's performance might be associated with the limited uniformity of the device width over the very long length of the meander stripe. We also note that in the case of the lower bias current (Fig. 85.40, curve *b*), the meander device exhibits a nonlinear probability dependence on the photon flux.

Discussion and Conclusions

The physical mechanism of operation of the NbN HEP optical single-photon counter is based on supercurrent-assisted, temporary formation of a resistive barrier across the stripe due to photon-induced hot-spot generation and is presented in Ref. 13. A single optical photon is absorbed by an ultrathin, very narrow stripe of a NbN superconductor, maintained at a temperature well below T_c , and biased with I_{bias} close to the device I_c . The photon absorption generates a very high number of excited, hot electrons, leading to local suppression of superconductivity and hot-spot formation. The resistive hot spot pushes the supercurrent out of the center of the stripe, causing it to exceed the critical value for the remaining superconducting part, and leading to the formation of a resistive barrier across the entire width of the device. For the current-biased sample, this resistance results in a large, easily measurable voltage signal. The subsequent hot-electron out-diffusion and cooling lead to hot-spot healing and the collapse of the resistive barrier. The superconductivity is restored in approximately 30 ps,¹² and the detector is ready to register another photon.

The main difference between our detection mechanism and the earlier proposed hot-spot mechanism¹⁴ is that our response is due to a collaborative effect of the bias current and the radiation quantum, leading to a large voltage output signal. To a certain extent the magnitude of the voltage pulse does not depend on the quantum energy, although the pulse shape does, providing the basis for the spectral sensitivity of the device. The rate of photon counting, which can be defined as the inverse of the total photon response time, is also a direct function of the operating parameters and can be as fast as tens



Z2533

Figure 85.40
Dependence of the detector response probability on the number of incident photons per pulse per unit area. Curves *a* and *b*: microbridge-type device; curves *c* and *d*: meander-type device; Δ, \square : $I_b = 0.92 I_c$; $\blacktriangle, \blacksquare$: $I_b = 0.8 I_c$.

of gigahertz. Finally, as we have demonstrated, depending on the device's operating parameters, our HEP can act as a single-photon, two-photon, or even three-photon quantum counter.

Our device should be able to find immediate applications, primarily in the area of ultrafast near-infrared photon counting, where there are currently no competing technologies. The 1.3- μm - to 1.55- μm -wavelength range is important for optical communication. Already-identified applications of our superconducting HEP's range from sensing ultraweak electroluminescence from submicron complementary metal-oxide-semiconductor VLSI circuits to quantum cryptography and quantum computation.

ACKNOWLEDGMENT

We wish to thank Kenneth Wilsher and Steven Kasapi for helpful discussions.

REFERENCES

1. Photomultiplier tubes, Hamamatsu Photonics K.K., <http://www.hamamatsu.com> (2000).
2. F. Zappa *et al.*, *Opt. Eng.* **35**, 938 (1996).
3. A. Peacock *et al.*, *Nature* **381**, 135 (1996); R. J. Schoelkopf *et al.*, *IEEE Trans. Appl. Supercond.* **9**, 293 (1999).
4. S. Komiyama *et al.*, *Nature* **403**, 405 (2000).
5. G. N. Gol'tsman, *Infrared Phys. Technol.* **40**, 199 (1999).
6. K. S. Il'in *et al.*, *Appl. Phys. Lett.* **73**, 3938 (1998).
7. G. G. Ortiz, J. V. Sandusky, and A. Biswas, in *Free-Space Laser Communication Technologies XII*, edited by G. S. Mercherle (SPIE, Bellingham, WA, 2000), Vol. 3932, pp. 127–138.
8. E. Knill, R. Laflamme, and G. Milburn, "Efficient Linear Optics Quantum Computation," (<http://arXiv.org/abs/quant-ph/0006088>) (2000).
9. G. Gilbert and M. Hamrick, "Practical Quantum Cryptography: A Comprehensive Analysis (Part One)," *MITRE Technical Report*, Report No. MTR 00W0000052 (<http://xxx.lanl.gov/abs/quant-ph/0009027>) (2000); to appear in *Physics Reports*.
10. J. C. Tsang and J. A. Kash, *Appl. Phys. Lett.* **70**, 889 (1997).
11. S. Cherednichenko *et al.*, in *Proceedings of the Eighth International Symposium on Space Terahertz Technology* (Harvard University, Cambridge, MA, 1997), pp. 245–252.
12. K. S. Il'in, M. Lindgren, M. Currie, A. D. Semenov, G. N. Gol'tsman, R. Sobolewski, S. I. Cherednichenko, and E. M. Gershenzon, *Appl. Phys. Lett.* **76**, 2752 (2000).
13. G. N. Gol'tsman, O. Okunev, G. Chulkova, A. Lipatov, A. Semenov, K. Smirnov, B. Voronov, A. Dzardanov, C. Williams, and R. Sobolewski, "Picosecond Superconducting Single-Photon Optical Detector," submitted to *Applied Physics Letters*.
14. A. M. Kadin and M. W. Johnson, *Appl. Phys. Lett.* **69**, 3938 (1996).

Preliminary Design of NIF 2-D SSD

Introduction

Direct-drive operation of the National Ignition Facility (NIF) will require broadband beam smoothing to successfully implode a direct-drive inertial confinement fusion (ICF) capsule and achieve high gain.¹ The base-line system parameters for NIF beam smoothing with two-dimensional smoothing by spectral dispersion (2-D SSD) are 1-THz total bandwidth in the ultraviolet, $50 \times 100\text{-}\mu\text{rad}$ laser divergence, and 2×1 color cycle.

Broadband-beam-smoothing techniques critical to high-performance direct-drive implosions have been demonstrated successfully on OMEGA.² Two different configurations of a 2-D SSD system have been employed to improve irradiation uniformity. One mode producing a 1-THz bandwidth in the ultraviolet with approximately one color cycle in each SSD dimension dramatically improved direct-drive target performance, while another mode operating at only 0.35-THz bandwidth but with three color cycles in one direction also exhibited substantial benefits.³ Both broadband 2-D SSD systems depended on a high-frequency, bulk phase modulator to realize these beam-smoothing improvements.⁴

As a partner in the National Inertial Confinement Fusion (ICF) Program, LLE has taken a lead role in defining direct-drive requirements for NIF and preparing a preliminary 2-D SSD system design to meet the beam-smoothing requirements. A prototype NIF 2-D SSD preamplifier module (PAM) will be built and tested in the Laser Development Laboratory at LLE to demonstrate satisfactory performance before transferring it to LLNL, where it will be integrated into the Preamplifier Module Laboratory. This article provides a summary of this design, including discussions of NIF features that constrain the design and direct-drive requirements.

NIF Features Influencing the 2-D SSD Design

Two aspects of NIF's direct-drive operation dictate a different 2-D SSD system architecture than was demonstrated on OMEGA:

- the longer pulses required to drive ignition-scale targets, which increases the threat of pinhole closure in the laser system's spatial filters, and
- the extremely compact space limitations of the 48 independent PAM's.

1. Pinhole Closure

Pinhole closure occurs when plasma created at the edge of a spatial-filter pinhole expands into the region of the pinhole where the laser pulse is transmitted, as shown in Fig. 85.41(a). Pinhole closure is particularly troublesome for 2-D SSD operation since the large divergence of a beam smoothed with this technique fills a large fraction of the pinhole. Plasma interactions with the beam reduce the total 2-D SSD bandwidth propagated to the target and can even distort the beam profile or retroreflect the beam, which can cause laser damage. OMEGA pulse lengths are limited to less than 3.8 ns by these pinhole closure concerns.

Pulse lengths of the order of 10 ns are required for direct-drive NIF ignition capsules.⁵ This is long enough to cause significant pinhole closure, particularly for the large, $100 \times 50\text{-}\mu\text{rad}$ divergence required for high-gain, direct-drive target performance. Fortunately, it is anticipated that this large 2-D SSD divergence will be required only during the "foot" portion of the drive, when laser imprinting occurs. One solution to this problem is dynamically reducing the laser divergence after sufficient smoothing is applied, but before pinhole closure interferes with the beam. Detailed laser imprint experiments on OMEGA and early laser experiments on the NIF using a subset of beams outfitted with 2-D SSD will be required to establish the dynamic profile of this approach. Additional experiments will be performed to establish the lower limit of SSD bandwidth required late in the drive pulse to mitigate adverse laser-plasma interactions.

Since laser divergence is directly related to the product of grating dispersion and SSD bandwidth, dynamic SSD band-

width reduction can be implemented to achieve the desired reduction. Two different approaches are available to realize dynamic bandwidth reduction. First, the microwave signal applied to a phase modulator producing the SSD bandwidth can be reduced or turned off. This approach, shown in Fig. 85.42(a), requires fast microwave switches and an electro-optic modulator with sufficient bandwidth. Highly resonant

phase modulator designs like the bulk modulators used in OMEGA are unsuitable for this application, but traveling-wave integrated optic devices are commercially available.⁶ Fast microwave devices with switching times of approximately 2 ns, which may be satisfactory for this application, are also available.⁷

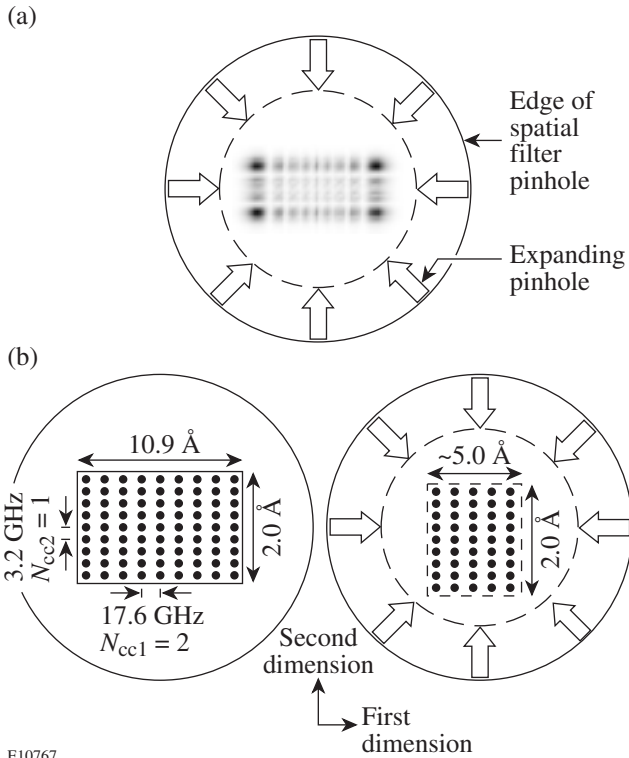


Figure 85.41

(a) Laser energy deposited at the edge of a spatial-filter pinhole creates a plasma that expands into the center of the pinhole. Pinhole closure is particularly troublesome with 2-D SSD beams since a large fraction of the pinhole is filled and the far-field energy distribution for phase-modulated 2-D SSD beams is corner-peaked. Interactions of the pinhole plasma with the SSD sidebands also convert phase modulation into amplitude modulation. (b) Dynamic bandwidth reduction can minimize the impact of pinhole closure by reducing the beam divergence before the pinhole closure affects the beam. A schematic representation of dynamic bandwidth reduction shows how full beam smoothing will be achieved during the foot of the pulse with reduced bandwidth later in the pulse.

E10767

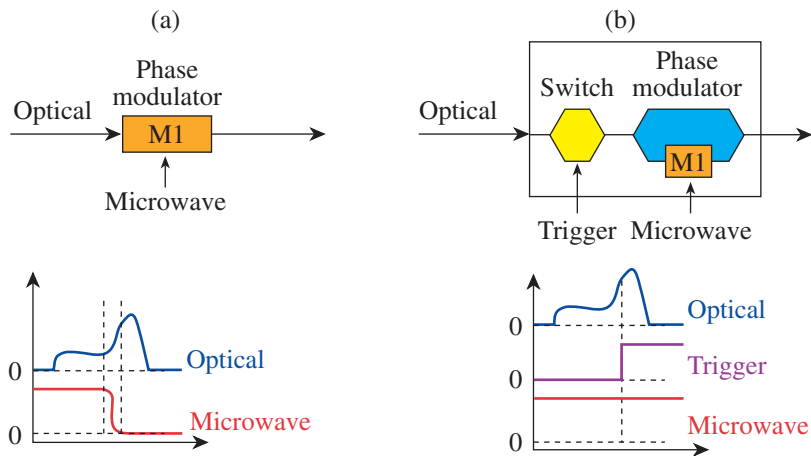


Figure 85.42

Dynamic bandwidth reduction can be implemented either electrically or optically. (a) Switching the microwave power delivered to an integrated-optic phase modulator poses the simplest approach since fast microwave switches are available, but switching times are limited to approximately a nanosecond. (b) Optical methods might also be applied to dynamically reduce SSD bandwidth during the pulse. One approach would direct the initial portion of the pulse through a phase modulator and then bypass the modulator during the latter portion.

E10768

An alternate approach to realizing dynamic bandwidth reduction for direct-drive NIF involves “optically splicing” two pulses with different SSD bandwidths, as shown in Fig. 85.42(b). This scheme produces the drive pulse in two separate sections that are combined to form the desired pulse shape and SSD bandwidth profile.

“Optical pulse splicing” offers a potential for extremely fast bandwidth reductions limited only by optical switching times of the order of ~ 40 ps, plus a straightforward approach for doubling the pulse-shaping contrast. Two separate front-end laser systems would be required in the Master Oscillator Room (MOR) to realize these improvements; some development would also be required. This approach is compatible with implementing ultrafast picket-fence pulses in the foot of the drive pulse, which is currently being evaluated to improve frequency-conversion efficiency and power balance.⁸

Microwave switching was selected for the base-line dynamic bandwidth reduction system since it utilizes existing technology. Preliminary design of this system has started and will be demonstrated in the NIF 2-D SSD PAM test-bed. Either approach is consistent with the all-fiber-optic front-end architecture currently implemented on the NIF.

2. Preamplifier Module (PAM) Space Constraints

A significant constraint on the NIF 2-D SSD design is the tight space limit imposed by the PAM design. A modular 2-D SSD design will be pursued so that 2-D SSD beam smoothing can be retrofitted into the first NIF PAM’s built for indirect drive that will not include this feature. The PAM design integrates a high-gain, Nd:glass regenerative amplifier, beam shaping, and a four-pass amplifier on a single optical breadboard assembly that composes a line replaceable unit (LRU). In comparison, these same functions are realized in OMEGA on two large optical tables. A 2-D SSD module must fit within the PAM LRU envelope for NIF, whereas for OMEGA this functionality occupies another 4-ft \times 14-ft optical table that is larger than the entire PAM assembly, shown in Fig. 85.43(a).

One side of the PAM includes the regenerative amplifier and beam-shaping module (BSM), as shown in Fig. 85.43(b). A shaped pulse launched into free space from an optical fiber is mode matched to the regenerative amplifier. This Q -switched cavity amplifies the pulse to approximately 20 mJ. After cavity dumping the pulse, two isolation Pockels cells provide high prepulse contrast. The beam-shaping module expands the pulse and reshapes the Gaussian beam into the square profile required to compensate the NIF gain with a serrated aperture

and transmission masks. The BSM output pulse is approximately 2 mJ and is directed to the four-pass amplifier on the other side of the PAM assembly.

The four-pass amplifier side of the PAM, depicted in Fig. 85.43(c), produces up to a 17-J output pulse required to inject four separate NIF main amplifiers. A location is provided inside the four-pass amplifier for the 1-D SSD grating required for indirect drive. This side of the PAM is extremely compact.

NIF’s 2-D SSD Preliminary Design

Figure 85.44 schematically highlights portions of the NIF architecture relevant to 2-D SSD. The seed pulse for all 192 NIF beams originates in the Master Oscillator Room (MOR) from a continuous-wave, single-frequency, fiber laser that is subsequently sliced into pulses and amplified. Frequency modulation is applied to the pulse by an integrated-optic phase modulator (M1). This device is actually three separate phase modulators integrated into a single package. One modulator applies a small amount of bandwidth (~ 0.5 Å) at a modulation frequency of ~ 3 GHz, which is required to suppress transverse stimulated Brillouin scattering (SBS) in the large NIF optics. The remaining two modulators are used to apply SSD bandwidth for beam smoothing. After bandwidth is applied in M1, the seed pulse is split and amplified into 48 channels, which supply each of the PAM’s. All pulses with FM bandwidth are transported by polarizing (PZ) fiber to minimize FM-to-AM conversion caused by polarization mixing at fiber connectors. An arbitrary waveform generator (AWG) shapes the input pulse and provides fine timing for each PAM.

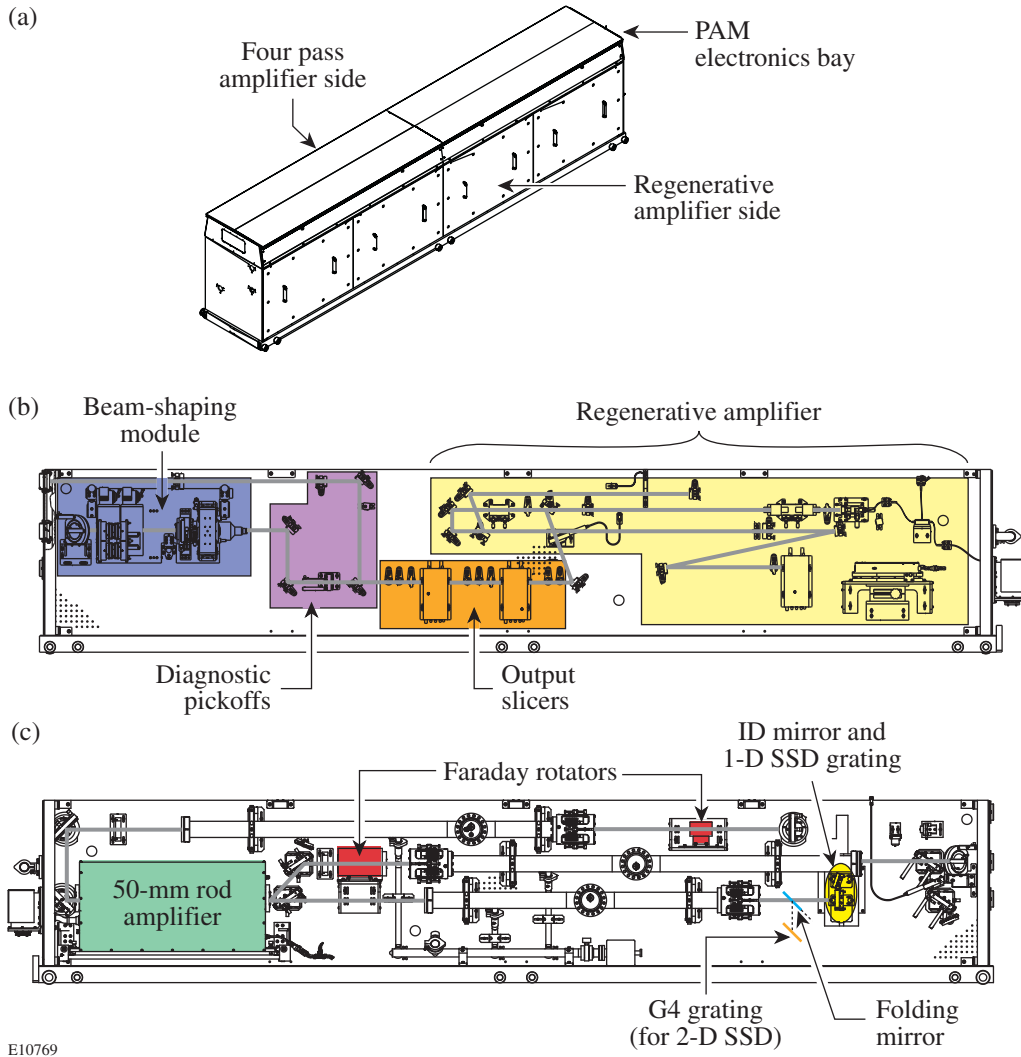
In addition to the amplification and beam shaping in the PAM, a 2-D SSD module will be added that can be bypassed during non-direct-drive NIF operation to avoid the additional system complexity and insertion loss when it is not required. Most of the 2-D SSD module will be located on the regenerative amplifier side of the PAM, including

- a “rolled” reflection grating (G2/G3),
- a bulk phase modulator (M2),
- spatial filters and telescopes required to control beam size and image relay the beam from the serrated aperture (RP₀) into the four-pass amplifier, and
- Faraday isolation stages used to double pass both the G2/G3 grating and bulk modulator.

It is significant to note that a precompensation grating (G1) for the first SSD direction is not possible with this design since the integrated-optic phase modulator (M1) is a single transverse mode device. As a result, the pulse shape is distorted by the G2/G3 grating, which is a reflection grating operated at the Littrow angle. This grating also precompensates the pulse before the second dimension of SSD bandwidth is applied by the bulk modulator (M2) and dispersed by the G4 grating. Both

the first SSD dimension dispersion (G2) and second SSD dimension precompensation (G3) grating functions are accomplished with a single grating by “rolling” the grating about its input (Littrow) axis, as shown in Fig. 85.45.

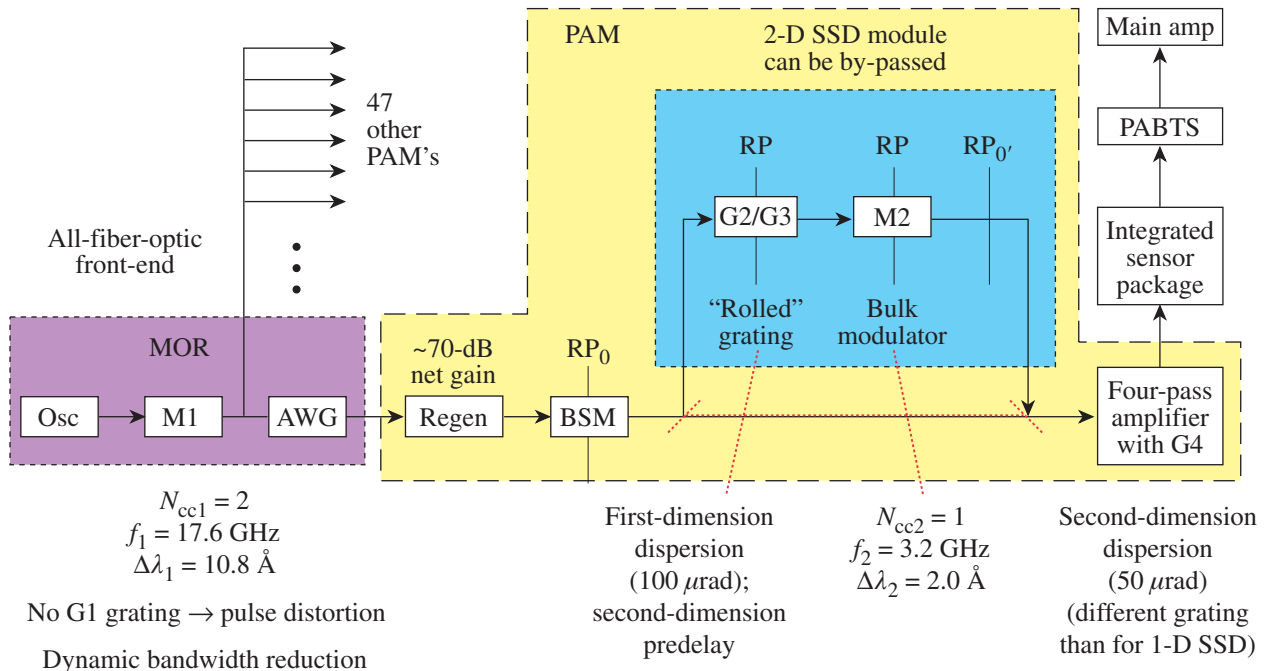
The NIF 2-D SSD bulk modulator will be based on an existing OMEGA design.⁹ The M2 bandwidth is dispersed in an orthogonal direction by a second 2-D SSD grating (G4)



E10769

Figure 85.43

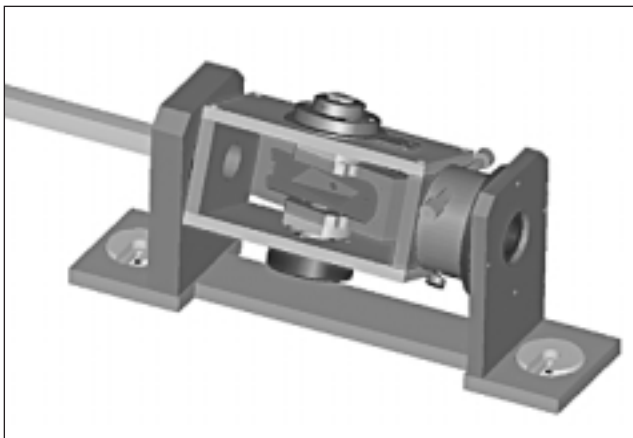
The NIF preamplifier module (PAM) poses severe space constraints on implementing 2-D SSD beam smoothing. (a) The PAM is a self-contained “line replaceable unit” that includes a regenerative amplifier (regen) and beam-shaping module (BSM) on one side of a vertically mounted optical breadboard and a four-pass amplifier on the other side. (b) The regen and BSM are highly engineered systems that ideally would require no changes when implementing a 2-D SSD module in the PAM. (c) The four-pass amplifier side is extremely compact but will require only the addition of another grating to disperse the bandwidth produced by the bulk phase modulator.



E10770

Figure 85.44

NIF architecture is significantly different from OMEGA. An all-fiber-optic front-end generates and distributes shaped pulses to 48 PAM's. The first 2-D SSD modulator (M1) is an integrated-optic phase modulator located in the Master Oscillator Room (MOR), but separate bulk modulators are required in each PAM. The BSM magnifies and spatially shapes the regen output pulse. The 2-D SSD module must be located after the BSM, where the pulse energy is lower, to avoid damaging the bulk modulator and to maximize the beam size.



E10771

Figure 85.45

A “rolled” reflection grating performs two separate 2-D SSD grating functions by taking advantage of the vector nature of grating dispersion. It disperses the bandwidth produced by the integrated-optic modulator, and it precompensates the distortion introduced by the grating that disperses the bandwidth produced by the bulk modulator. These grating functions are identified using the same OMEGA convention as G2/G3 and G4, respectively.

located in the four-pass amplifier, as shown in Fig. 85.43(c). The G4 grating required for 2-D SSD is different from the 1-D SSD grating currently implemented for indirect-drive operation. All SSD gratings are located at image-relay planes of the serrated aperture (RP_0) in the BSM, which is image relayed throughout the laser system. After the PAM, the alignment, energy, and pulse shape of the PAM output beam are diagnosed by the integrated sensor package (ISP) and transported to the NIF's main amplifiers by the preamplifier beam transport system (PABTS).

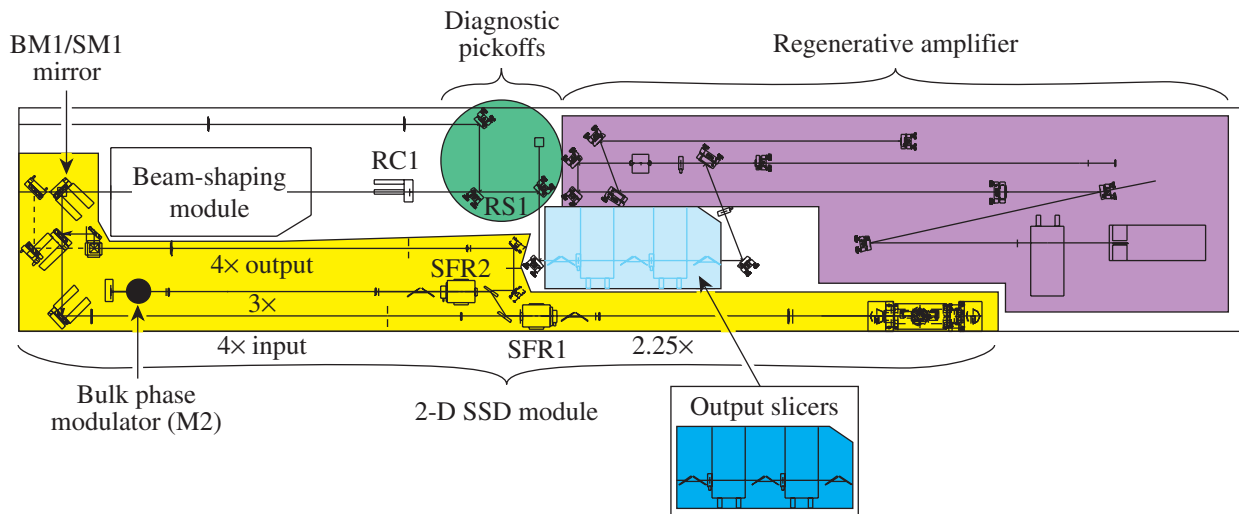
Description of the NIF PAM Operation with a 2-D SSD Module

Figure 85.46 represents the base-line layout of the regenerative amplifier side of the PAM in which a 2-D SSD module can be realized. A key aspect of this design is that the regenerative amplifier and beam-shaping module are unchanged, and only minor changes to the existing isolation stage and diagnostic pickoffs are required to provide adequate space for the 2-D SSD module. The isolation Pockels cells are reoriented and more compactly arranged to free up space for the G2/G3 grating telescope at the bottom of the PAM, as well as in the main section of the 2-D SSD module located adjacent to the BSM. Additionally, the centering glass (RC1), diagnostic wedge (RS1), and folding mirror assemblies are reconfigured to further increase the space envelope available for the 2-D SSD module.

The output direction from the BSM will be remotely selectable by a new BM1/SM1 mirror stage. A single mirror is used to select whether the beam proceeds directly to the four-pass amplifier (BM1) for non-direct-drive operation or is diverted into the 2-D SSD module (SM1) for direct-drive operation. Figure 85.47 shows both of these configurations. This scheme provides a 2-D SSD bypass that will not affect 1-D SSD performance for indirect-drive operations, plus it does not require relocating the BSM. Operation of the 2-D SSD module is described below.

The 30-mm-square beam produced by the BSM is down-collimated by a 4× input spatial filter to a 7.5-mm-square beam (~10.6-mm diagonal) to fit through a 15-mm-clear-aperture Faraday rotator (SFR1). The spatial-filter pinhole removes high-spatial-frequency components introduced by the serrated aperture and beam-shaping masks in the BSM before the beam is imaged into the bulk phase modulator. The pinhole assembly will include the ability to remotely select its position to either “IN” or “OUT” to facilitate alignment operations. The first Faraday isolation stage extracts the pulse from the double-pass grating section of the 2-D SSD module.

The 2.25× grating telescope magnifies the beam to the correct size to achieve two SSD color cycles for the integrated-optic modulator (M1) operating at 17.6 GHz, plus to pre-compensate a single color cycle for the bulk modulator (M2)



E10772

Figure 85.46

The regen side of the PAM will require minor modifications to accommodate a 2-D SSD module, but the regen and BSM will not need to be changed. The 2-D SSD module includes an input spatial filter, two Faraday isolation stages for the double-pass grating and modulator legs that include image relays, and an output spatial filter. A rotating mirror assembly (shown in Fig. 85.47) selects either indirect-drive or direct-drive PAM operation.

operating at 3.2 GHz. This image relay is sandwiched between two quarter-wave plates and preceded by polarizers to provide first-order ghost suppression in the double-pass section. Ultra-low-reflectivity antireflection (AR) coatings ($R \leq 0.05\%$) are also specified for the lenses to minimize ghost reflections since first-order ghosts will produce undesirable prepulses.

The G2/G3 reflection grating disperses the M1 bandwidth in each of two orthogonal components. The component normal to the plane of the PAM breadboard corresponds to the $100\text{-}\mu\text{rad}$ SSD divergence direction, while the in-the-plane component is matched but opposite to the dispersion produced by the G4 grating that produces the $50\text{-}\mu\text{rad}$ SSD divergence.

After the pulse is extracted from the double-pass grating section, it is injected into the double-pass bulk modulator section by a reflection off the input polarizer, in the second Faraday isolation stage. A $3\times$ bulk modulator telescope demagnifies the beam to a 3-mm-square beam that fits the $5\text{-mm} \times 6\text{-mm}$ aperture bulk modulator. Like the grating telescope, first-order ghost suppression is achieved with quarter-wave plates, double polarizers, and ultra-low-reflectivity AR-coated lenses.

The bulk modulator (M2) employs a LiNbO_3 crystal with 1° -wedged, AR-coated input surface. A retroreflecting mirror positioned behind M2 serves to double pass the modulator crystal. The return path length is carefully set to phase match the microwave and optical fields in the modulator during the second pass.

The beam height within most of the 2-D SSD module is 105 mm. An image rotation periscope lowers the 2-D SSD beam height to 45 mm. This beam height is required to reinject the beam back into the path toward the four-pass amplifier. The beam is reinjected using a mirror located between the SM1 mirror and the breadboard hole, as shown in Fig. 85.47. The image rotation periscope also rotates the beam 90° to compensate for an additional 90° rotation introduced when the beam is passed through the PAM breadboard into the four-pass amplifier.

Both the BSM and the 2-D SSD module output beams are delivered through leaky mirrors to the ISP for alignment operations and can be individually selected by shutters (not shown).

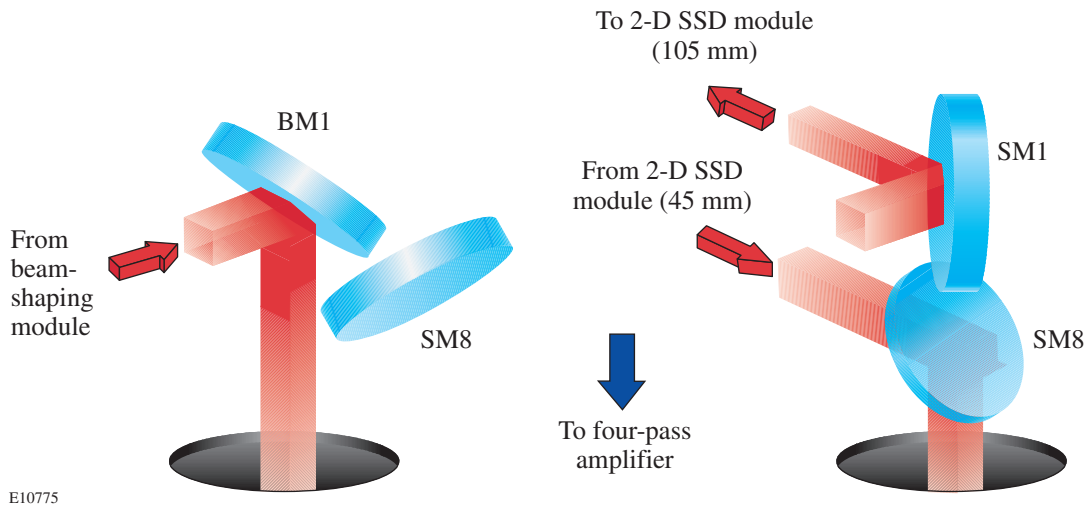


Figure 85.47

PAM operation in either the indirect-drive (2-D SSD bypassed) or direct-drive modes will be remotely selectable. A single mirror assembly rotating around the beam-shaping module's output axis will be used to reflect the beam either directly to the four-pass amplifier side of the PAM or into the 2-D SSD module. This mirror is designated BM1/SM1 and functions as a remotely operable centering mirror to support alignment in either mode. A second mirror in this rotating assembly (SM8) swings under the BM1/SM1 mirror to reflect the 2-D SSD module output beam that is returned at a 45-mm beam height. Remotely operable mirror SM7, shown in Fig. 85.46, provides the centering function during 2-D SSD operation since mirror SM8 must be stationary.

Conclusion

Direct-drive NIF operation will require a two-color-cycle, 1-THz 2-D SSD system to achieve beam smoothing required for ignition with high gain. A preliminary 2-D SSD design has been outlined in this article that is compatible with the NIF architecture and the existing PAM design. Detailed design is underway, and a prototype 2-D SSD module will be demonstrated at LLE before transferring it to LLNL for integration testing.

ACKNOWLEDGMENT

This work was supported by the U.S. Department of Energy Office of Inertial Confinement Fusion under Cooperative Agreement No. DE-FC03-92SF19460, the University of Rochester, and the New York State Energy Research and Development Authority. The support of DOE does not constitute an endorsement by DOE of the views expressed in this article.

REFERENCES

1. Laboratory for Laser Energetics LLE Review **84**, 181, NTIS document No. DOE/SF/19460-371 (2000). Copies may be obtained from the National Technical Information Service, Springfield, VA 22161.
2. Laboratory for Laser Energetics LLE Review **80**, 197, NTIS document No. DOE/SF/19460-321 (1999). Copies may be obtained from the National Technical Information Service, Springfield, VA 22161.
3. D. D. Meyerhofer, J. A. Delettrez, R. Epstein, V. Yu. Glebov, R. L. Keck, R. L. McCrory, P. W. McKenty, F. J. Marshall, P. B. Radha, S. P. Regan, W. Seka, S. Skupsky, V. A. Smalyuk, J. M. Soures, C. Stoeckl, R. P. J. Town, B. Yaakobi, R. D. Petrasso, J. A. Frenje, D. G. Hicks, F. H. Séguin, C. K. Li, S. Haan, S. P. Hatchett, N. Izumi, R. Lerche, T. C. Sangster, and T. W. Phillips, "Core Density and Temperature Conditions and Fuel-Pusher Mix in Direct-Drive ICF Implosions," to be published in *Physics of Plasmas*; T. R. Boehly, V. N. Goncharov, O. Gotchev, J. P. Knauer, D. D. Meyerhofer, D. Oron, S. P. Regan, Y. Srebro, W. Seka, D. Shvarts, S. Skupsky, and V. A. Smalyuk, "Optical and Plasma Smoothing of Laser Imprinting in Targets Driven by Lasers with SSD Bandwidths up to 1 THz," *ibid.*; Laboratory for Laser Energetics LLE Review **84**, 173, NTIS document No. DOE/SF/19460-371 (2000). Copies may be obtained from the National Technical Information Service, Springfield, VA 22161.
4. Laboratory for Laser Energetics LLE Review **78**, 53, NTIS document No. DOE/SF/19460-295 (1999). Copies may be obtained from the National Technical Information Service, Springfield, VA 22161.
5. C. P. Verdon, *Bull. Am. Phys. Soc.* **38**, 2010 (1993); Laboratory for Laser Energetics LLE Review **79**, 121, NTIS document No. DOE/SF/19460-317 (1999). Copies may be obtained from the National Technical Information Service, Springfield, VA 22161.
6. Alenia Marconi Systems, 00131 Roma, Italy (<http://www.crisel-instruments.it/alenia/html/index01.htm>) (2000).
7. MITEQ, Inc., Hauppauge, NY 11788 (<http://www.miteq.com>) (1999); M/A-COM, Inc., Lowell, MA 01853 (<http://www.macom.com>) (2000).
8. J. E. Rothenberg, *Appl. Opt.* **39**, 6931 (2000); J. A. Marozas and J. D. Zuegel, *Bull. Am. Phys. Soc.* **45**, 327 (2000).
9. Laboratory for Laser Energetics LLE Review **68**, 192, NTIS document No. DOE/SF/19460-139 (1996). Copies may be obtained from the National Technical Information Service, Springfield, VA 22161.

Characterization of Direct-Drive-Implosion Core Conditions on OMEGA with Time-Resolved Ar *K*-Shell Spectroscopy

Introduction

In the direct-drive approach to inertial confinement fusion (ICF), capsules are directly irradiated by a large number of symmetrically arranged laser beams.^{1,2} Time-resolved Ar *K*-shell spectroscopy has been established as a reliable technique to diagnose the compressed core of direct-drive implosions,^{3–10} as well as indirect-drive implosions.^{6,11–16} This technique has been used on the 60-beam OMEGA laser system¹⁷ to characterize the core conditions of direct-drive implosions. Plastic shells with an Ar-doped deuterium fill gas were driven with a 23-kJ, 1-ns square laser pulse smoothed with phase plates,¹⁸ 1-THz smoothing by spectral dispersion (SSD),^{19–21} and polarization smoothing (PS) using birefringent wedges.²² Laser beam smoothing reduces the effects of the ablative Rayleigh–Taylor hydrodynamic instability by reducing the initial imprint levels.²³ The targets in this experiment are predicted to have a convergence ratio of ~ 15 . Measured convergence ratios of 14 have been reported for similar capsules on OMEGA.²⁴ The emissivity-averaged core electron temperature and density were inferred from the measured time-dependent Ar *K*-shell spectral line shapes.

Two properties of the Ar *K*-shell spectrum emitted from hot, dense plasmas ($n_e > 10^{23} \text{ cm}^{-3}$; $T_e > 1 \text{ keV}$) are exploited to infer a unique combination of emissivity-averaged core electron temperature and density: (1) The line shapes depend strongly on density and are relatively insensitive to variations in electron temperature. (2) The relative intensities of the Ar *K*-shell lines and their associated *L*-shell satellites are sensitive to variations in electron temperature and density.⁸ The Stark-broadened line profiles for the Ar He β ($1s3l-1s^2$), He γ ($1s4l-1s^2$), He δ ($1s5l-1s^2$), and Ly β ($3l-1s$) resonant transitions and associated satellites were calculated using a second-order quantum mechanical relaxation theory.⁸ These line profiles were combined using relative intensities derived from a detailed non-LTE kinetics code corrected for the effects of radiative transfer using an escape-factor approximation. The Stark-broadened line profiles were corrected for the effects of opacity using a slab opacity model.

In this article we present time-resolved Ar *K*-shell spectroscopic measurements of a direct-drive implosion on OMEGA. The following sections (1) describe experimental setup, including the photometric calibration of the spectroscopic diagnostics; (2) describe the atomic physics model and the line-fitting procedure; (3) compare the modeled spectra with the measured data; and (4) give the inferred temporal evolution of the electron temperature and density. Conclusions are presented in the last section.

Experimental Setup

The layout of the experimental setup on OMEGA and a schematic of the target are shown in Fig. 86.1. The 20- μm -thick, 954- μm -diam plastic shell with an Ar-doped deuterium fill gas was driven with a 24-kJ, 1-ns square laser pulse, and the Ar *K*-shell emission was recorded with time-resolved and time-integrated flat crystal spectrometers. The total fill pressure was 15 atm with an atomic Ar percentage of 0.18 resulting in a partial pressure of Ar of $\sim 0.05 \text{ atm}$. The impact of the Ar dopant on the capsule performance reduces the primary neu-

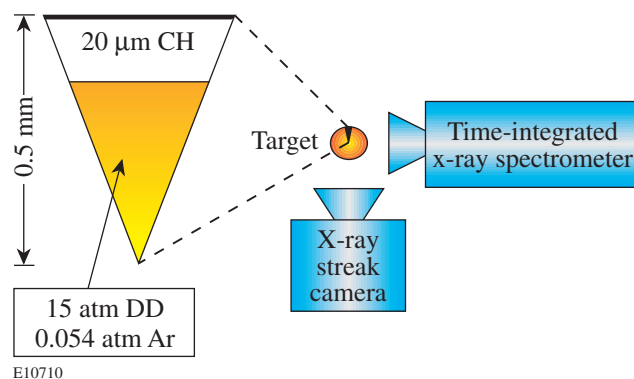


Figure 86.1

The layout of the experimental setup on OMEGA and a schematic of the target. The plastic shell with an Ar-doped deuterium fill gas was driven with a 23-kJ, 1-ns square laser pulse. The total fill pressure was 15 atm with an atomic Ar percentage of 0.18 resulting in a partial pressure of Ar of $\sim 0.05 \text{ atm}$. Streaked and high-resolution, time-integrated x-ray spectra of Ar *K*-shell emission were recorded with flat crystal spectrometers.

tron yield to ~75% of an undoped target.²⁴ The on-target beam uniformity has been significantly improved on OMEGA: single-beam irradiation nonuniformity has been reduced with 1-THz SSD and PS, and the beam-to-beam rms power imbalance is 5% or less for square laser pulses.²⁴

The time-dependent Ar *K*-shell spectral line shapes were monitored using time-resolved x-ray spectroscopy. Two x-ray streak cameras were fielded for this experiment: one had an ~2-ns temporal window and was used to measure the spectral line shapes with 25-ps temporal resolution; the other had an ~4-ns temporal window and was used to measure the absolute timing of the Ar *K*-shell emission with an accuracy of 50 ps.

The spectrum recorded with the faster streak camera is shown in Fig. 86.2 with temporal streak distortions removed. This spectral range includes the following Ar *K*-shell resonance lines: Ar Ly_α (2*l*-1*s*), He_β (1*s*3*l*-1*s*²), He_γ (1*s*4*l*-1*s*²), Ly_β (3*l*-1*s*), He_δ (1*s*5*l*-1*s*²), He_ε (1*s*6*l*-1*s*²), Ly_γ (4*l*-1*s*), Ly_δ (5*l*-1*s*), and Ly_ε (6*l*-1*s*). The prominent ones have been identified in Fig. 86.2. The x-ray streak camera,²⁵ which utilized a flat RbAP (rubidium acid phthalate) crystal to disperse the spectrum onto an Au photocathode, was timed (see Fig. 86.2) to capture the coronal plasma emission at the end of the laser pulse just after 1 ns through the peak x-ray emission at 2 ns. The slower streak camera recorded the same spectral range with a similar spectrometer; however, as shown in Fig. 86.3, it was timed to record the entire evolution of the x-ray emission from the start of the coronal plasma emission when the laser strikes the target to the peak x-ray production at

peak compression. Temporal streak distortions have also been removed from the time-resolved spectra in Fig. 86.3. The time axis of the slower streak camera was established with the temporally modulated ultraviolet fiducial laser pulse (see Fig. 86.3). The exponential rise of the coronal plasma emission was extrapolated back to the beginning of the laser pulse.

The absolute timing of the peak x-ray emission in Fig. 86.2 was taken from Fig. 86.3. The average sweep speed of the faster streak camera was measured to be 48 ps/mm on a subsequent shot during the experimental campaign using a temporally modulated ultraviolet fiducial laser pulse. As seen in Fig. 86.2, the onset of the Ar *K*-shell line emission occurs during the shock heating beginning at ~1.6 ns, and as the implosion proceeds, the amount of Stark-broadening increases. The dispersion of the streaked spectrum was determined using the relatively narrow spectral features observed just after the onset of the Ar *K*-shell emission lines at *t* = 1.77 ns (see Fig. 86.4). The modeled spectrum also shown in Fig. 86.4 is discussed in the next section. A portion of the streak camera's x-ray photocathode was blocked, providing a wavelength fiducial (see Fig. 86.2) to establish the orientation of the streak axis. The spectra were recorded on Kodak T-max 3200 film. The film was digitized using a PDS (Perkin-Elmer Photometric Data Systems) microdensitometer and corrected for film sensitivity.

The streaked spectra were corrected for variations in x-ray spectral sensitivity and streak camera flat-fielding effects using the photometrically calibrated spectra of a time-integrated

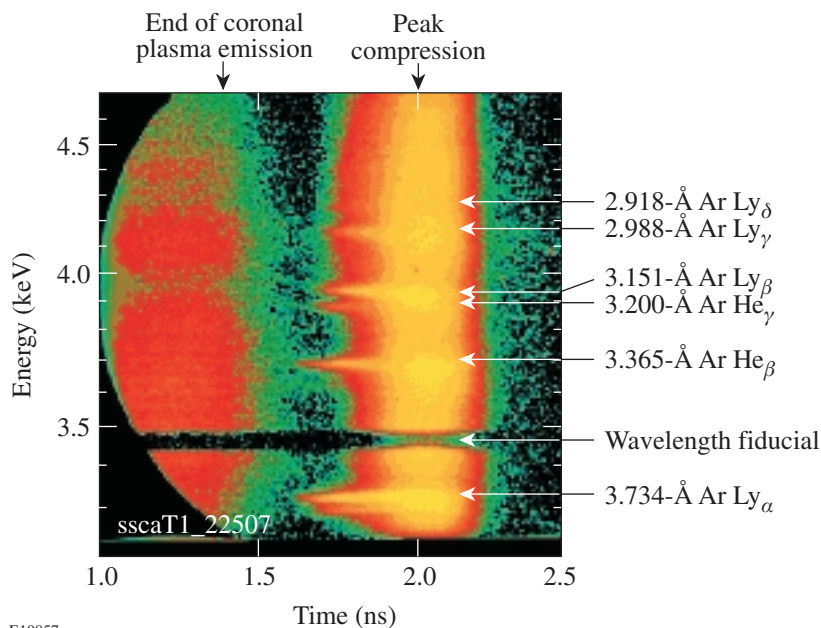


Figure 86.2

The time-resolved Ar *K*-shell spectral measurement with an ~2-ns temporal window for shot number 22507. Temporal streak distortions have been removed, and the orientation of the streak axis is determined with the wavelength fiducial. The onset of the Ar *K*-shell line emission occurs during the shock heating beginning at ~1.6 ns, and the Stark-broadening increases as the implosion proceeds. The dispersion of the streaked spectrum was determined using the relatively narrow spectral features observed just after the onset of the Ar *K*-shell emission lines.

spectrometer. The time-integrated instrument utilized an ADP (ammonium dihydrogen phosphate) crystal to disperse the spectrum onto Kodak DEF (direct exposure) film. This instrument was calibrated using a combination of measured and published crystal reflectivities,²⁶ and the film was digitized with the PDS microdensitometer and corrected for film sensitivity. The bremsstrahlung emission from an undoped capsule, which was measured with the time-integrated spectrometer and found to be characteristic of an electron temperature equal to 0.68 keV, was used to calibrate the time-resolved spectra. The streaked spectrum was integrated in time and compared

with the bremsstrahlung emission. The ratio of these two quantities is the photometric calibration of the streaked spectrum. The calibration, which is applied to each time-resolved spectra, is shown in Fig. 86.5.

Atomic Physics Modeling

Time-resolved Ar *K*-shell spectroscopy is a technique that allows the emissivity-averaged electron temperature and density to be inferred. The Stark-broadened Ar *K*-shell spectral line shapes are calculated with the Multi-Electron Radiator Lineshape (MERL) code²⁷ in the manner described in Ref. 8.

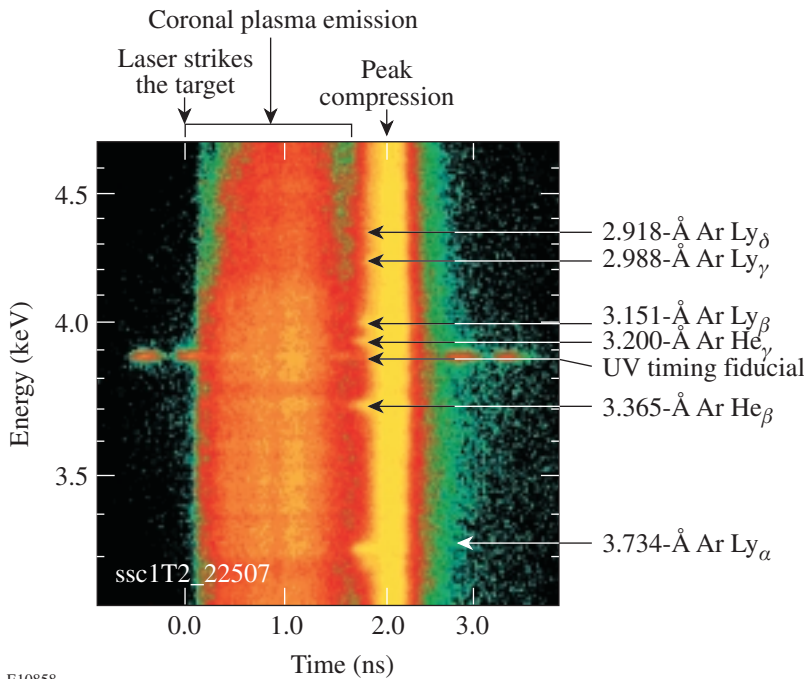


Figure 86.3
The time-resolved Ar *K*-shell spectral measurement with an ~4-ns temporal window for shot number 22507 with temporal streak distortions removed. The entire evolution of the x-ray emission from the start of the coronal plasma emission when the laser strikes the target to the peak x-ray production at peak compression is recorded. The time axis was established with the temporally modulated ultraviolet fiducial laser pulse, and the exponential rise of the coronal plasma emission was extrapolated back to the beginning of the laser pulse.

E10858

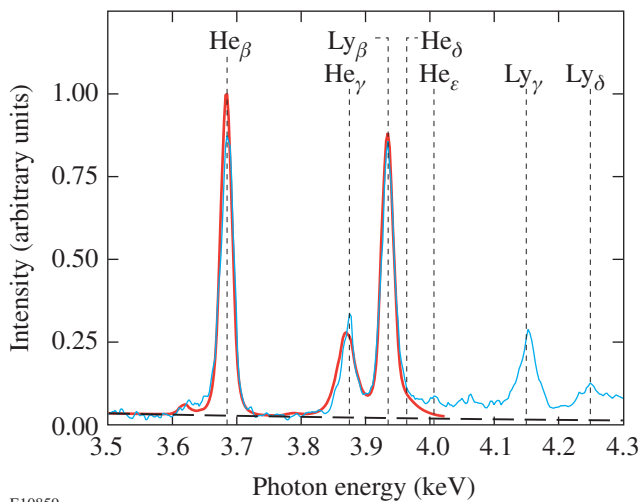
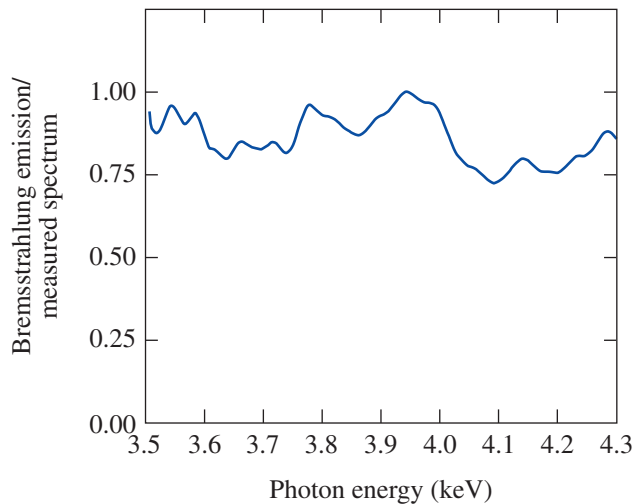


Figure 86.4
The measured spectrum (blue curve) observed just after the onset of the Ar *K*-shell emission lines at $t = 1.77$ ns is used to establish the photon-energy scale. The inferred electron density and temperature from the modeled spectrum for the 3.5- to 4.0-keV range (red curve) are $0.3 (\pm 0.03) \times 10^{24} \text{ cm}^{-3}$ and $1.3 (\pm 0.07) \text{ keV}$. The background bremsstrahlung emission spectrum is represented by the dashed curve. The vertical dotted lines represent the unshifted line centers of the Ar *K*-shell resonance lines. At present only the 3.5- to 4.0-keV range is analyzed; however, work is in progress for the spectrum above 4.0 keV, which is more challenging to model due to the presence of the He-like and H-like bound-free edges.

E10859



E10860

Figure 86.5

The photometric calibration of the streaked spectra to correct for variations in x-ray spectral sensitivity and streak camera flat-fielding effects is determined by recording continuum emission from an implosion with no Ar-dopant simultaneously on the time-resolved and time-integrated instruments. The measured time-integrated spectrum was modeled with a bremsstrahlung emission spectrum characteristic of an electron temperature equal to 0.68 keV. The time-resolved measurement was integrated in time and compared with the modeled spectrum. The ratio of the modeled emission to the measurement is the photometric calibration of the streaked measurement.

MERL utilizes the adjustable parameter exponential approximation (APEX)²⁸ for ion microfield calculation, the theory of Boercker, Iglesias, and Dufty (BID)²⁹ for the ion dynamics, and a quantum mechanical relaxation approximation for electron broadening.⁸

Ar *K*-shell spectra were calculated for many combinations of electron temperatures and densities. Collisional-radiative-equilibrium population distributions including 1380 levels (1 fully stripped, 25 H-like, 372 He-like, 918 Li-like, 28 Be-like, 15 B-like, 11 C-like, and 10 N-like) are solved using the CRETIN code.³⁰ The effects on the populations due to radiative transfer of the optically thick Ly_{α} and $He_{\alpha}(1s2l-1s^2)$ emissions are approximated using Mancini's escape factors.³¹ The Stark-broadened Ar *K*-shell resonance lines and satellites are calculated with MERL,²⁷ and opacity broadening is calculated assuming uniform core conditions.

The best fit to the measured spectra in the 3.5- to 4.0-keV range is determined using a least squares fitting routine. A look-up table is generated for 4000 combinations of electron temperature and densities in the range of interest. For each time-resolved measurement, the bremsstrahlung emission in

the 3.5- to 4.0-keV range is fitted in the measured spectra and added to the modeled Ar *K*-shell spectra. Modeled spectra are convolved with the spectral resolution of the streaked measurement, which was determined using the narrow spectral features that are observed when the Ar *K*-shell lines initially light up. The fitting routine searches the look-up table for the best fit for each time-resolved spectrum. At present only the 3.5- to 4.0-keV range is analyzed; however, work is in progress for the spectrum above 4.0 keV, which is more challenging to model due to the presence of the He-like and H-like bound-free edges.

Experimental Results and Analysis

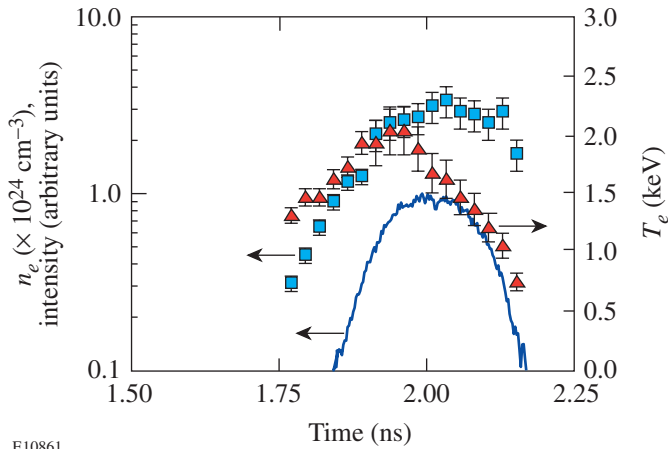
Significant changes in the Stark-broadened line widths and the relative ratios of the Ar *K*-shell emissions occur during the course of the implosion, making this diagnostic sensitive to the core electron temperature and density. A time history of emissivity-averaged core electron temperature (triangles) and density (squares) inferred from the time-resolved Ar *K*-shell spectroscopy is shown in Fig. 86.6. The measured x-ray continuum in the 3.50- to 3.55-keV range (blue line) is also shown for reference. An examination of Fig. 86.6 reveals the electron temperature peaks first, then the electron density peaks around the time of peak x-ray production. The electron temperature inferred from fitting the bremsstrahlung emission in the 3.5- to 4.0-keV spectral range slowly decreases with time from ~ 0.8 keV at $t = 1.77$ ns to ~ 0.5 keV at 2.15 ns.

As pointed out earlier in the **Experimental Setup** section, the Ar *K*-shell emission lines at early times are used to establish the photon energy scale (see Fig. 86.4). The narrow spectral features that are measured (blue curve) in the 3.5- to 4.0-keV range are modeled (red curve) with the spectral line shapes characteristic of core conditions with electron density and temperature of $0.3 (\pm 0.03) \times 10^{24} \text{ cm}^{-3}$ and 1.3 (± 0.07) keV. The error analysis of the inferred electron temperature and density is given below. The level of continuum emission is also shown in Fig. 86.4 (dashed line), and the vertical dotted lines represent the unshifted line centers of the Ar *K*-shell resonance lines. Selected spectra from the hot, dense plasma are examined below.

The spectrum recorded at 1.89 ns is shown in Fig. 86.7 along with the modeled spectrum. The inferred electron density and temperature are $1.25 (\pm 0.13) \times 10^{24} \text{ cm}^{-3}$ and 1.9 (± 0.1) keV. Line shifts to lower photon energies¹⁰ can be readily observed in the He_{β} , Ly_{β} , and Ly_{γ} by comparing the measured profiles with the position of the unshifted lines. The atomic physics model shows good agreement with the mea-

sured line shifts, which are observed throughout the high-density portion of the implosion. Compared with Fig. 86.4, the He_β is now weaker than the Ly_β , and the level of continuum emission has increased.

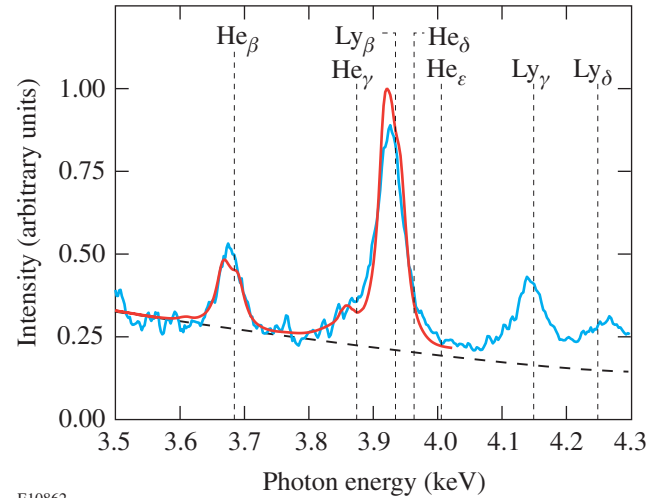
Simulations of the implosion with the 1-D hydrodynamic code *LILAC* indicate that the peak neutron production occurs at the same time as the peak emissivity-averaged electron temperature. Therefore, peak neutron production is assumed to be simultaneous with the peaking of the electron temperature at $t = 1.93$. The spectrum recorded at this time is shown in Fig. 86.8. The electron temperature and density at the time of peak neutron production are determined to be $2.0 (\pm 0.2)$ keV and $2.5 (\pm 0.5) \times 10^{24} \text{ cm}^{-3}$. This represents the highest combination of electron temperature and density measured with Ar-doped deuterium gas fill capsules in laser-driven fusion. As the implosion proceeds to peak compression, which occurs at $t = 2.01$ ns, the inferred electron density continues to increase to $3.1 (\pm 0.6) \times 10^{24} \text{ cm}^{-3}$, while the electron temperature decreases to $1.7 (\pm 0.17)$ keV. The spectrum measured at peak compression is shown in Fig. 86.9. As can be seen in Figs. 86.8 and 86.9, the background bremsstrahlung emission is comparable with the Ly_β intensity and is stronger than the He_β



E10861

Figure 86.6

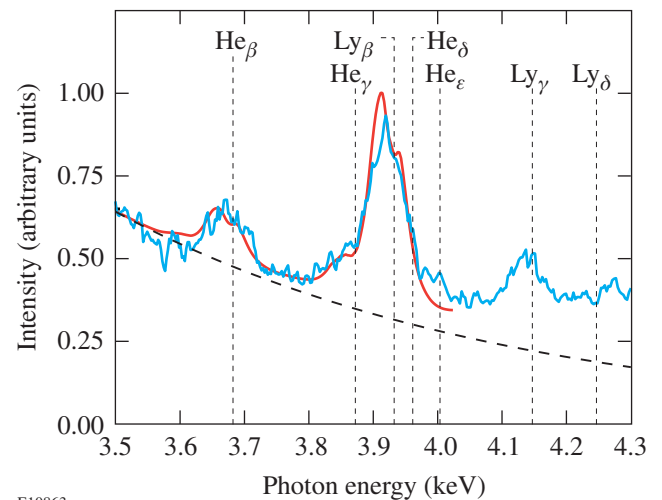
The time history of the emissivity-averaged core electron temperature (triangles) and density (squares) inferred from the time-resolved Ar *K*-shell spectroscopy for shot number 22507 reveals that the electron temperature peaks first, then the electron density peaks around the time the x-ray continuum in the 3.50- to 3.55-keV range (blue line) peaks. As the imploding shell decelerates, the emissivity-averaged electron temperature and density increase to $2.0 (\pm 0.2)$ keV and $2.5 (\pm 0.5) \times 10^{24} \text{ cm}^{-3}$ at peak neutron production ($t = 1.93$ ns), which is assumed to be simultaneous with the peaking of the electron temperature. This is followed by a further increase in the electron density to $3.1 (\pm 0.6) \times 10^{24} \text{ cm}^{-3}$ and a decrease in the electron temperature to $1.7 (\pm 0.17)$ keV at peak compression ($t = 2.01$ ns).



E10862

Figure 86.7

The measured spectrum (blue curve) observed at $t = 1.89$ ns and the modeled spectrum (red curve) in the 3.5- to 4.0-keV range are presented. The inferred electron density and temperature are $1.25 (\pm 0.13) \times 10^{24} \text{ cm}^{-3}$ and $1.9 (\pm 0.1)$ keV. The background bremsstrahlung emission spectrum is represented by the dashed curve, and the unshifted line centers of the Ar *K*-shell resonance lines are represented by the vertical dotted lines. Line shifts are observed in the He_β , Ly_β , and Ly_γ lines, and an increase in the linewidths is observed.



E10863

Figure 86.8

The measured spectrum (blue curve) observed at $t = 1.93$ ns and the modeled spectrum (red curve) in the 3.5- to 4.0-keV range are presented. The background bremsstrahlung emission spectrum is represented by the dashed curve, and the unshifted line centers of the Ar *K*-shell resonance lines are represented by vertical dotted lines. The inferred electron temperature and density are $2.0 (\pm 0.2)$ keV and $2.5 (\pm 0.5) \times 10^{24} \text{ cm}^{-3}$. The peak neutron production is estimated to occur at this time with the peaking of the electron temperature.

intensity. Finally, as the compressed core disassembles, the electron temperature and density rapidly decrease. The spectrum recorded at $t = 2.15$ ns is shown in Fig. 86.10. The inferred electron density and temperature are $1.7 (\pm 0.3) \times 10^{24} \text{ cm}^{-3}$ and $0.75 (\pm 0.08) \text{ keV}$. The dominant feature of the spectrum is the He_β and its Li-like satellites around 3.55 to 3.75 keV.

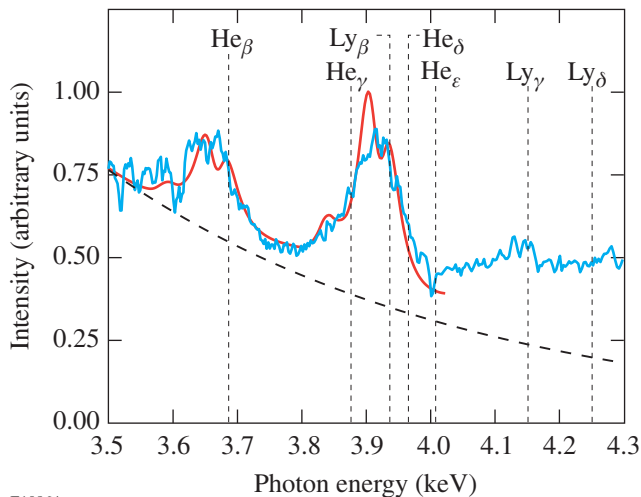
Many factors affect the accuracy of the electron temperature and density measurements. In this experiment strong signals of the spectral lines of interest were recorded throughout the implosion; therefore, the most influential factors affecting the accuracy are the determination of the background bremsstrahlung emission spectrum and the accuracy of the atomic physics model. As shown in the time-resolved spectra, the Stark-broadened spectral lines have a significant continuum emission background, which must be accounted for in the spectral line fitting procedure. Although the spectral fits examined here show good agreement with the measured line shapes and with the background levels between the spectral lines, there is some discrepancy between the measured and modeled line shapes at the peaks of the lines. The accuracy in the electron density is estimated to be $\pm 10\%$, and the accuracy in the electron temperature is estimated to be $\pm 5\%$ for the range of electron densities below $2 \times 10^{24} \text{ cm}^{-3}$. Above this density

the accuracy in the electron density is estimated to be $\pm 20\%$, and the accuracy in the electron temperature is estimated to be $\pm 10\%$. The precision of the least squares spectral line fitting routine is well within the accuracy error.

Work is in progress to compare time-resolved Ar K -shell spectroscopy measurements with the time-resolved neutron burn history to establish the timing between the peak neutron burn and peak x-ray production. Comparisons will be made between fuel- ρR measurements, gated x-ray images of the core, and the emissivity-averaged core electron density measurement to estimate the amount of mix in the core of shell material with the fuel. In addition, lower dopant levels of Ar were studied to minimize the impact of the enhanced radiative losses on the target performance, while maintaining detectable signals of the Ar K -shell emission. These results will be presented in a separate publication for a range of targets with predicted convergence ratios from 13 to 37.

Conclusion

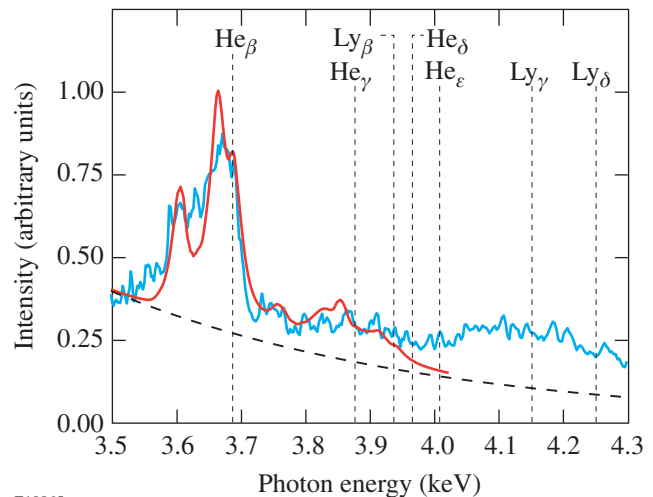
Time-resolved Ar K -shell spectroscopy has been used to diagnose the core conditions of direct-drive implosions on the 60-beam OMEGA laser system. Plastic shells with an Ar-doped deuterium fill gas were driven with a 23-kJ, 1-ns square laser pulse with a predicted convergence ratio of ~ 15 , and laser



E10864

Figure 86.9

The measured spectrum (blue curve) observed at $t = 2.01$ ns and the modeled spectrum (red curve) in the 3.5- to 4.0-keV range are presented. The background bremsstrahlung emission spectrum is represented by the dashed curve, and the unshifted line centers of the Ar K -shell resonance lines are represented by the vertical dotted lines. Peak compression occurs at this time, and the inferred electron temperature and density are $1.7 (\pm 0.17) \text{ keV}$ and $3.1 (\pm 0.6) \times 10^{24} \text{ cm}^{-3}$.



E10865

Figure 86.10

The measured spectrum (blue curve) observed at $t = 2.15$ ns and the modeled spectrum (red curve) in the 3.5- to 4.0-keV range are presented. The background bremsstrahlung emission spectrum is represented by the dashed curve, and the unshifted line centers of the Ar K -shell resonance lines are represented by the vertical dotted lines. The compressed core is disassembling, and the inferred electron temperature and density rapidly decrease to $0.75 (\pm 0.08) \text{ keV}$ and $1.7 (\pm 0.3) \times 10^{24} \text{ cm}^{-3}$.

beams were smoothed with 1-THz SSD and polarization smoothing using birefringent wedges. The measured time-dependent, Stark-broadened, Ar *K*-shell spectral line shapes were compared with modeled spectra to infer the emissivity-averaged core electron temperature and density. As the imploding shell decelerates, the emissivity-averaged electron temperature and density increase to 2.0 (± 0.2) keV and 2.5 (± 0.5) $\times 10^{24}$ cm $^{-3}$ at peak neutron production, which is assumed to occur at the time of the peak emissivity-averaged electron temperature. This is followed by a further increase in the electron density to 3.1 (± 0.6) $\times 10^{24}$ cm $^{-3}$ and a decrease in the electron temperature to 1.7 (± 0.17) keV at peak compression.

ACKNOWLEDGMENT

This work was supported by the U. S. Department of Energy Office of Inertial Confinement Fusion under Cooperative Agreement No. DE-FC03-92SF19460, the University of Rochester, and the New York State Energy Research and Development Authority. The support of DOE does not constitute an endorsement by DOE of the views expressed in this article.

REFERENCES

1. C. P. Verdon, *Bull. Am. Phys. Soc.* **38**, 2010 (1993).
2. S. E. Bodner, D. G. Colombant, J. H. Gardner, R. H. Lehmborg, S. P. Obenshain, L. Phillips, A. J. Schmitt, J. D. Sethian, R. L. McCrory, W. Seka, C. P. Verdon, J. P. Knauer, B. B. Afeyan, and H. T. Powell, *Phys. Plasmas* **5**, 1901 (1998).
3. B. Yaakobi, S. Skupsky, R. L. McCrory, C. F. Hooper, H. Deckman, P. Bourke, and J. M. Soures, *Phys. Rev. Lett.* **44**, 1072 (1980).
4. A. Hauer *et al.*, *Phys. Rev. A* **28**, 963 (1983).
5. C. F. Hooper, Jr., D. P. Kilcrease, R. C. Mancini, L. A. Woltz, D. K. Bradley, P. A. Jaanimagi, and M. C. Richardson, *Phys. Rev. Lett.* **63**, 267 (1989).
6. H. R. Griem, *Phys. Fluids B* **4**, 2346 (1992).
7. C. F. Hooper, Jr., R. C. Mancini, D. A. Haynes, Jr., and D. T. Garber, in *Elementary Processes in Dense Plasmas*, edited by S. Ichimaru and S. Ogata (Addison-Wesley, Reading, MA, 1995), pp. 403–414.
8. D. A. Haynes, Jr., D. T. Garber, C. F. Hooper, Jr., R. C. Mancini, Y. T. Lee, D. K. Bradley, J. Delettrez, R. Epstein, and P. A. Jaanimagi, *Phys. Rev. E* **53**, 1042 (1996).
9. D. K. Bradley, J. A. Delettrez, R. Epstein, R. P. J. Town, C. P. Verdon, B. Yaakobi, S. Regan, F. J. Marshall, T. R. Boehly, J. P. Knauer, D. D. Meyerhofer, V. A. Smalyuk, W. Seka, D. A. Haynes, Jr., M. Gunderson, G. Junkel, C. F. Hooper, Jr., P. M. Bell, T. J. Ognibene, and R. A. Lerche, *Phys. Plasmas* **5**, 1870 (1998).
10. G. C. Junkel *et al.*, *Phys. Rev. E* **62**, 5584 (2000).
11. B. A. Hammel *et al.*, *Phys. Rev. Lett.* **70**, 1263 (1993).
12. C. J. Keane *et al.*, *Phys. Fluids B* **5**, 3328 (1993).
13. B. A. Hammel *et al.*, *J. Quant. Spectrosc. Radiat. Transf.* **51**, 113 (1994).
14. H. Nishimura *et al.*, *Phys. Plasmas* **2**, 2063 (1995).
15. N. C. Woolsey *et al.*, *Phys. Rev. E* **56**, 2314 (1997).
16. N. C. Woolsey *et al.*, *Phys. Rev. E* **57**, 4650 (1998).
17. T. R. Boehly, D. L. Brown, R. S. Craxton, R. L. Keck, J. P. Knauer, J. H. Kelly, T. J. Kessler, S. A. Kumpan, S. J. Loucks, S. A. Letzring, F. J. Marshall, R. L. McCrory, S. F. B. Morse, W. Seka, J. M. Soures, and C. P. Verdon, *Opt. Commun.* **133**, 495 (1997).
18. T. J. Kessler, Y. Lin, J. J. Armstrong, and B. Velazquez, in *Laser Coherence Control: Technology and Applications*, edited by H. T. Powell and T. J. Kessler (SPIE, Bellingham, WA, 1993), Vol. 1870, pp. 95–104; Y. Lin, T. J. Kessler, and G. N. Lawrence, *Opt. Lett.* **21**, 1703 (1996).
19. S. Skupsky, R. W. Short, T. Kessler, R. S. Craxton, S. Letzring, and J. M. Soures, *J. Appl. Phys.* **66**, 3456 (1989).
20. S. Skupsky and R. S. Craxton, *Phys. Plasmas* **6**, 2157 (1999).
21. S. P. Regan, J. A. Marozas, J. H. Kelly, T. R. Boehly, W. R. Donaldson, P. A. Jaanimagi, R. L. Keck, T. J. Kessler, D. D. Meyerhofer, W. Seka, S. Skupsky, and V. A. Smalyuk, *J. Opt. Soc. Am. B* **17**, 1483 (2000).
22. T. R. Boehly, V. A. Smalyuk, D. D. Meyerhofer, J. P. Knauer, D. K. Bradley, R. S. Craxton, M. J. Guardalben, S. Skupsky, and T. J. Kessler, *J. Appl. Phys.* **85**, 3444 (1999).
23. T. R. Boehly, V. N. Goncharov, O. Gotchev, J. P. Knauer, D. D. Meyerhofer, D. Oron, S. P. Regan, Y. Srebro, W. Seka, D. Shvarts, S. Skupsky, and V. A. Smalyuk, *Phys. Plasmas* **8**, 2331 (2001).
24. D. D. Meyerhofer, J. A. Delettrez, R. Epstein, V. Yu. Glebov, V. N. Goncharov, R. L. Keck, R. L. McCrory, P. W. McKenty, F. J. Marshall, P. B. Radha, S. P. Regan, S. Roberts, W. Seka, S. Skupsky, V. A. Smalyuk, C. Sorce, C. Stoeckl, J. M. Soures, R. P. J. Town, B. Yaakobi, J. D. Zuegel, J. Frenje, C. K. Li, R. D. Petrasso, D. G. Hicks, F. H. Séguin, K. Fletcher, S. Padalino, M. R. Freeman, N. Izumi, R. Lerche, T. W. Phillips, and T. C. Sangster, *Phys. Plasmas* **8**, 2251 (2001).
25. D. H. Kalantar *et al.*, in *22nd International Congress on High-Speed Photography and Photonics*, edited by D. L. Paisley and A. M. Frank (SPIE, Bellingham, WA, 1997), Vol. 2869, pp. 680–685.
26. B. L. Henke, E. M. Gullikson, and J. C. Davis, *At. Data Nucl. Data Tables* **54**, 181 (1993).
27. R. C. Mancini *et al.*, *Comput. Phys. Commun.* **63**, 314 (1991).
28. C. A. Iglesias, J. L. Lebowitz, and D. MacGowan, *Phys. Rev. A* **28**, 1667 (1983).
29. D. B. Boercker, C. A. Iglesias, and J. W. Dufty, *Phys. Rev. A* **36**, 2254 (1987).
30. H. A. Scott and R. W. Mayle, *Appl. Phys. B* **B58**, 35 (1994).
31. R. C. Mancini, R. F. Joyce, and C. F. Hooper, Jr., *J. Phys. B: At. Mol. Phys.* **20**, 2975 (1987).

Study of Direct-Drive, DT-Gas-Filled-Plastic-Capsule Implosions Using Nuclear Diagnostics on OMEGA

Introduction

High-gain inertial confinement fusion (ICF) requires uniform compression of a spherical capsule to a state of high density and temperature;^{1–3} current research is aimed at finding ways to achieve this goal. This article describes how a range of traditional and new nuclear diagnostics are used to study the compression performance of deuterium-tritium (DT)-filled target capsules imploded by direct laser drive on LLE’s 60-beam OMEGA laser system.⁴ The sensitivity of the implosion performance to the uniformity of laser power deposition is studied by measuring the fuel and shell areal densities (ρR) and the shell electron temperature (T_e). These parameters are studied using the first comprehensive set of separate spectral measurements of deuterons, tritons, and protons (“knock-ons”) elastically scattered from the fuel and shell by 14.1-MeV DT fusion neutrons.

To achieve fusion ignition, a DT-filled target needs sufficient compression to form two different regions: a small mass with low density but high temperature in the center (the “hot spot,” with $T_i \sim 10$ keV) and a large mass of high-density, low-temperature fuel surrounding this hot spot. The 3.5-MeV DT alphas generated in the central hot spot (with $\rho R \sim 0.3$ g/cm²) are stopped in the fuel, thereby propagating a thermonuclear burn. Two approaches to achieving this objective are indirect- and direct-drive implosions. For the indirect-drive approach, where laser beams irradiate the inner wall of a high-Z radiation case (hohlraum), laser energy is first converted to soft x rays, which subsequently compress the capsule. For the direct-drive approach, the laser beams directly irradiate and compress the target. The National Ignition Facility (NIF), which has both indirect- and direct-drive capabilities and is under construction at Lawrence Livermore National Laboratory, is designed to achieve this ignition objective. Experiments on OMEGA are currently investigating many aspects of the implosion physics relevant to future NIF experiments with scaled experimental conditions. For example, the OMEGA cryogenic program will study energy-scaled implosions based on NIF ignition target designs.⁵

OMEGA is a Nd-doped glass laser facility that can deliver 60 beams of frequency-tripled UV light (351 nm) with up to 30 kJ in 1 to 3 ns with a variety of pulse shapes; both direct and indirect drive are possible.⁴ Early direct-drive experiments on OMEGA have achieved high temperatures ($T_i \sim 15$ keV) and high fusion yields (for example, DT neutron yield $\sim 10^{14}$ and DD neutron yield $\sim 10^{12}$).⁶ In particular, a series of implosions of room-temperature capsules with gas fill (0 to 30 atm of either D₂ or D³He) and plastic shells (CH, 10 to 35 μ m thick) have recently been conducted with a variety of laser pulse shapes, irradiation uniformities, etc.^{7–11} These implosions generate typical fuel areal densities (ρR_{fuel}) of ~ 5 to 15 mg/cm² and shell areal densities (ρR_{shell}) > 50 mg/cm². Part of their importance lies in their relevance to OMEGA cryogenic-target implosions and the insights they provide into implosion physics of direct-drive ICF.

The OMEGA experiments included in this article involved room-temperature capsules with DT-gas fill and CH shells. The nominal parameters were 20- μ m shell thickness and 15-atm fill pressure. These types of capsules have total masses similar to those of OMEGA cryogenic targets and are expected to have comparable stability properties under similar experimental conditions.^{5,7} An OMEGA cryogenic capsule consists of three parts: a central part with low-pressure (triple-point vapor pressure) D₂ or DT gas (0.2 atm at ~ 19 K), a main fuel layer (~ 90 μ m of D₂ or DT ice), and a 1- to 3- μ m CH overcoat. The CH shell of a room-temperature target simulates the fuel part (DT ice) of a cryogenic target, and the fill gas simulates the hot-spot-forming central DT gas in a cryogenic target.⁵ The hydrodynamics are expected to differ in detail, in part due to the difference in the equation of state, ablation rate, and implosion velocity. Nevertheless, many aspects of high-energy-density physics and the target performances of cryogenic targets can be studied with these surrogate targets under current experimental conditions, including the effects of irradiation uniformity. The experiments also provide useful data for the development of advanced diagnostics (such as high-resolution, charged-particle spectroscopy¹²) and for benchmarking computer simulations.¹³

A primary emphasis in this study was the dependence of capsule performance on laser irradiation uniformity; the next section provides motivation by describing the importance of irradiation uniformity to the physics of capsule implosion performance. Subsequent sections (1) describe the experiments under study here, utilizing DT-filled capsules with CH shells and different laser-smoothing techniques; (2) discuss the measurement of knock-on spectra and the relationships between these measurements and the characteristics of imploded capsules; and (3) discuss the performance of imploded core and shell under different conditions, showing that 15-atm-DT capsules with appropriate laser smoothing achieved a moderate convergence ratio ($Cr \sim 12$ to 15); ρR_{fuel} and ρR_{shell} were determined to be ~ 15 mg/cm² and ~ 60 mg/cm², respectively.

Laser Drive Characteristics and Capsule Performance

Successful direct-drive implosions require control of Rayleigh–Taylor (RT) instability because direct-drive targets are susceptible to this instability during both acceleration and deceleration phases.^{5,7} This control requires shell integrity throughout the whole acceleration phase, which can be accomplished by a spherical target being irradiated uniformly. The instability is seeded by laser illumination nonuniformity and also by target imperfections (roughness on the outer ablative surface and/or the inner fuel–shell interface).⁷ During the acceleration phase, this instability can occur at the ablation surface and propagate to the fuel–shell interface, adding roughness to the inner shell surface and also feeding back out to the ablation surface; in the worst case, this could lead to shell breakup. During the deceleration phase, the distortions at the fuel–shell interface grow and result in the mixing of fuel and shell materials, which degrades target performance.

For the shots studied here, two approaches were used to control instabilities and improve target performance. The first was the choice of laser pulse shape. A high-shock-strength (high adiabat), 1-ns square laser pulse was used to maximize the ablation rate and reduce RT growth. Though a gradually rising pulse (low adiabat) produces, in principle, a larger target compression than a sharply rising pulse, because of lower fuel and shell isentropes,^{1,2} a low-shock-strength pulse generates a lower ablation rate and smaller in-flight shell thickness, leading to more instability for direct-drive implosions. This has been demonstrated in earlier experiments, where better target performance was obtained with a 1-ns square pulse than with other pulse types for room-temperature targets.^{8,9} Simulations have predicted that another advantage to using the 1-ns square pulse to implode room-temperature capsules with 20- μm -CH shells is that the target hydrodynamic and stability properties

are similar to those that result from using a shaped pulse with cryogenic targets (for example, the OMEGA $\alpha = 3$ design⁷).

The second approach is improved laser-irradiation uniformity. In discussing deviations from illumination uniformity, we distinguish two sources: Beam-to-beam energy imbalance causes low-order mode perturbations (mode number $\ell < 10$), while nonuniformities within individual beams generate higher-order perturbations ($\ell > 10$). To achieve a level of 1% or less for on-target irradiation nonuniformity, different beam energies must be matched to within an rms deviation of 5%.^{5,7} In the series of implosions studied here, an energy balance within 3% to 25% rms was achieved; however, after taking into account the effect of the laser-beam overlap on the target surface (as shown in Fig. 86.11), low-mode rms uniformity was between 1% and 9%, with an average $\leq 5\%$.

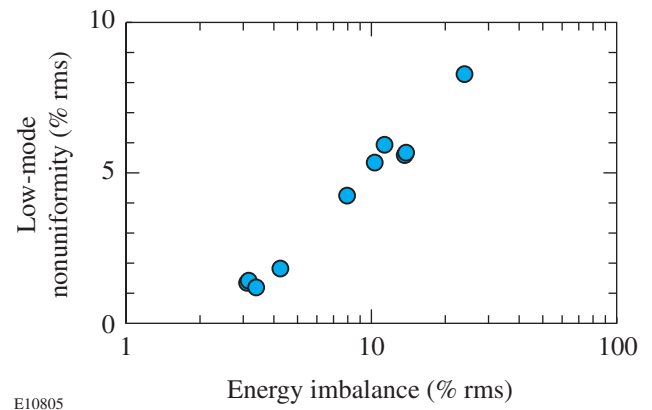


Figure 86.11

The low-mode rms irradiation nonuniformity plotted as a function of the beam energy imbalance. In general, a better energy balance results in better low-mode rms irradiation uniformity.

Single-beam uniformity is improved by two-dimensional smoothing by spectral dispersion (2-D SSD) combined with other smoothing techniques such as distributed phase plates (DPP's) and distributed polarization smoothing (PS).⁷ The two smoothing conditions used in this study were 0.35-THz-bandwidth, 3-color-cycle 2-D SSD and 1.0-THz-bandwidth, single-color-cycle 2-D SSD with PS. Theoretical simulations and recent experiments have demonstrated that PS improves irradiation uniformity by a factor of $\sim \sqrt{2}$ for higher-order perturbations ($\ell > 10$). The combination of PS with high-bandwidth 2-D SSD is expected to result in on-target nonuniformity $< 1\%$ after 300 ps.^{5,7,14}

Experiments

The OMEGA experiments reported here used 60 beams of frequency-tripled (351-nm) UV light to directly drive the targets. Targets were room-temperature capsules with DT gas enclosed in a CH shell. The actual DT-gas pressure was in the range of 11 to 15 atm. The CH-shell thickness was 19 to 20 μm , and the capsule diameters were 920 to 960 μm . Laser energy ranged from 20 to 23 kJ, with a typical intensity of $\sim 1 \times 10^{15}$ W/cm², and the laser-beam spot size on target was ~ 1 mm. The laser pulse was approximately square with a 1-ns duration, with rise and decay times of ~ 150 ps. Good pulse-shape repeatability was obtained, and the beam-to-beam laser energy balance was typically $\sim 5\%$ rms. Two laser configurations were used. In the first, individual beams were smoothed using 3-color-cycle 2-D SSD along two axes with a bandwidth of 0.35 THz. In the second, beams were smoothed by single-color-cycle 2-D SSD, with a 1.0-THz bandwidth, and PS using a birefringent wedge.

The primary DT neutron yields were measured using Cu activation.¹⁵ For this series of experiments, primary DT neutron yields of 10^{12} to 10^{13} were obtained, with an estimated measurement error of $\sim 10\%$. Ion temperatures T_i were measured using neutron time-of-flight (NTOF) Doppler widths.^{16–18} Typical values were 3.5 to 5 keV, with a measurement error of ~ 0.5 keV. Fusion burn history was obtained with the neutron temporal detector (NTD),¹⁹ and the typical fusion burn durations here were 140 to 190 ps with bang times occurring at several hundred picoseconds after the end of the laser pulse.

To obtain the areal densities for compressed fuel and shell (a fundamental measure of the implosion dynamics and quality), and to address other issues (such as the measurement of shell T_e , electrostatic potential due to capsule charging, etc.), spectra of emerging charged particles were measured with two magnet-based charged-particle spectrometers (CPS-1 and CPS-2)^{20,21} and several “wedge-range-filter (WRF)” spectrometers.^{11,22} The charged particles [knock-on deuterons (KOD), tritons (KOT), and protons (KOP)] are elastically scattered from the fuel and shell by 14.1-MeV DT neutrons.^{23,24} This is currently the only technique for studying the fuel and shell areal densities of DT capsule implosions on OMEGA. Other possible methods include neutron activation²⁵ and measurement of secondary^{26,27} and tertiary products (neutrons and protons^{27–29}), but these methods are currently impractical because of certain technical limitations.

CPS-1 and CPS-2 are nearly identical, and each uses a 7.6-kG permanent magnet^{20,21} constructed of a neodymium-iron-boron alloy with a steel yoke. Incoming particles are collimated by a slit whose width can be varied between 1 and 10 mm (giving an acceptance of 10^{-6} to 10^{-5} of the total yield), as appropriate for expected flux levels. The magnet separates particles into different trajectories according to the ratio of momentum to charge. Pieces of CR-39, used as particle detectors, are positioned throughout the dispersed beam normal to the particle flux. Both the energy and the species of the particle generating a track in CR-39 can be determined through the combined knowledge of its trajectory (determined by its position on the CR-39) and the track diameter. Particles with the same gyro radius, such as 8-MeV tritons and 12-MeV deuterons, are easily distinguished since their very different stopping powers generate measurably different track sizes in the CR-39 (the larger the stopping power, the larger the track). This configuration allows coverage over the proton energy range from 0.1 MeV to 40 MeV. The energy calibration uncertainty varies with particle energy, being about 30 keV at 2 MeV and about 100 keV at 15 MeV. The two spectrometers are 101° apart, thereby enabling studies of implosion symmetry. CPS-2 (CPS-1) is placed inside (outside) the 165-cm-radius OMEGA chamber at 100 cm (235 cm) from the target.

The WRF spectrometers, which are described in detail elsewhere,^{11,22} provide proton spectra by analyzing the distributions of proton-track diameters in a piece of CR-39 that is covered during exposure by an aluminum ranging filter with continuously varying thickness. The current energy calibration is accurate to about 0.15 MeV at 15 MeV. These spectrometers are simple and compact, allowing them to be used at multiple positions during a shot for symmetry studies and placed close to the target for good statistics when proton yields are low (down to about 5×10^5).

To analyze the measurements made during these experiments, the implosions were modeled with the one-dimensional hydrodynamic calculation code *LILAC*.³⁰ Several important physical models were used in the calculation, such as the tabulated equation of state (*SESAME*), flux-limited electron transport (with a flux limiter of $f=0.06$), local thermodynamic equilibrium (LTE), opacities for multigroup radiation transport, and inverse-bremsstrahlung-absorption energy deposition through a ray-trace algorithm in the underdense plasma. No effect of fuel-shell mix was included.

Knock-on Particles and Their Spectra

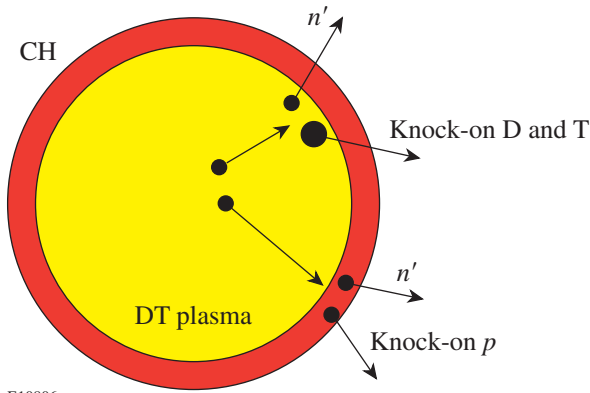
Knock-on particles are generated in a two-step process. A 14.1-MeV neutron is first generated from a DT fusion reaction. These neutrons usually escape the capsule without interacting. A small fraction of them (of the order of $\sim 0.1\%$), however, elastically scatter off either fuel D or T or CH-shell p , as described in Eqs. (1)–(4) and depicted schematically in Fig. 86.12. Information about the compressed fuel is carried out by these knock-on D and T; information about the compressed shell is carried out by knock-on p and is also contained in the energy downshifts of knock-on D and T spectra:

$$D + T \rightarrow \alpha(3.5 \text{ MeV}) + n(14.1 \text{ MeV}), \quad (1)$$

$$n(14.1 \text{ MeV}) + T \rightarrow n' + T(\leq 10.6 \text{ MeV}), \quad (2)$$

$$n(14.1 \text{ MeV}) + D \rightarrow n' + D(\leq 12.5 \text{ MeV}), \quad (3)$$

$$n(14.1 \text{ MeV}) + p \rightarrow n' + p(\leq 14.1 \text{ MeV}). \quad (4)$$



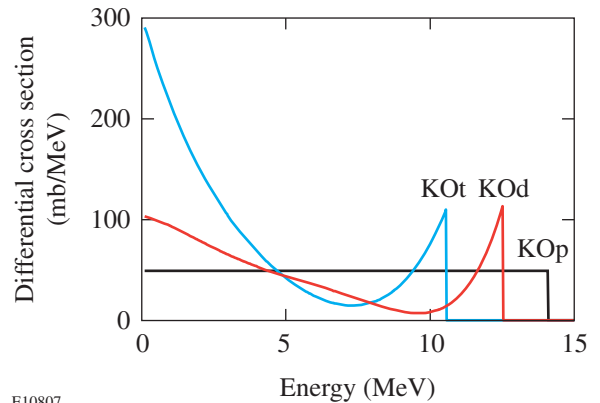
E10806

Figure 86.12

A schematic illustration of the knock-on processes in an imploded capsule. The central fuel part typically has an initial radius of 450 to 475 μm and a DT-gas fill of 15 atm. The initial shell layer is constructed of CH with a thickness of 19.5 to 20 μm . Primary 14.1-MeV DT neutrons, generated in the fuel, elastically scatter deuterons (KOd) and tritons (KOt) out of the fuel and protons (KOp) out of the shell. Consequently, information from the compressed core is carried out by these knock-on deuterons and tritons, and information from the compressed shell is carried out by knock-on protons. The energy downshifts of knock-on D and T spectra also contain information about the shell.

Figure 86.13 illustrates the differential cross sections of knock-on processes. When the collisions are head-on, the characteristic end-point energy for T (D) [p] is 10.6 MeV (12.5 MeV) [14.1 MeV]. The well-defined, high-energy peak for a knock-on deuteron (triton) spectrum represents about 15.7% (13.5%) of the total cross section and corresponds to an energy region of 9.6 to 12.5 MeV (7.3 to 10.6 MeV). For a model-independent determination of ρR_{fuel} , the knock-on diagnostic usually uses only these high-energy peaks. For knock-on protons, the cross section is virtually flat from 0 to 14.1 MeV because the neutron and proton masses are nearly identical. Because of a possible time-dependent distortion occurring in the low-energy region, however, only the flat region is used here. Two important parameters for this diagnostic are the number of knock-on particles and the downshifts of the knock-on spectra. The knock-on numbers provide information about the ρR of the layer (core or shell) in which they are produced, and the energy loss of these particles provides additional information about the ρR traversed.

It has been shown that, for a hot-spot model of the compressed fuel (where all primary neutrons are produced in an infinitesimal, high-temperature region at the center of a uniform-density DT plasma), ρR_{fuel} is related to the knock-on



E10807

Figure 86.13

Differential cross sections for elastic scattering of 14.1-MeV neutrons on deuterons, tritons, and protons, where the energy is the scattered ion energy. When these collisions are head-on, the characteristic end-point (maximum) energy for T (D) [p] is 10.6 MeV (12.5 MeV) [14.1 MeV]. The high-energy peak for knock-on deuterons (tritons) contains about 15.7% (13.5%) of the total cross section, which corresponds to an energy region of 9.6 to 12.5 MeV (7.3 to 10.6 MeV). [For deuterons and tritons, the integral under the high-energy peak gives an effective cross section that is used in Eq. (5)]. For knock-on protons, the cross section is flat from 0 to 14.1 MeV, and an integral over a 1-MeV interval gives an effective cross section that is used in Fig. 86.14.

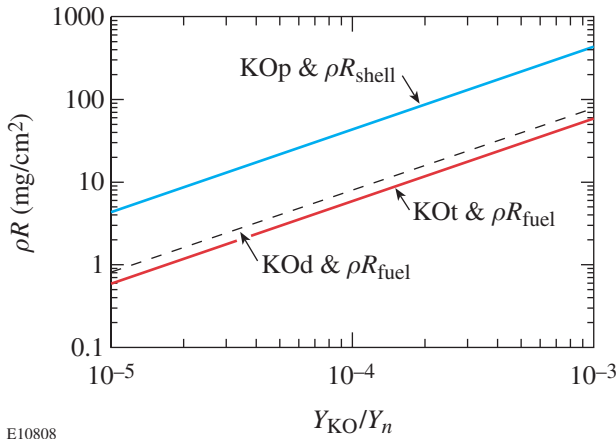
yield by the equation^{23,24}

$$\rho R_{\text{fuel}} = \frac{(2\gamma + 3)m_p}{(\gamma\sigma_d^{\text{eff}} + \sigma_t^{\text{eff}})} \frac{Y_{\text{KOd}} + Y_{\text{KOt}}}{Y_n}, \quad (5)$$

where Y_n is the measured primary neutron yield, Y_{KOd} and Y_{KOt} are deuteron and triton knock-on yields under the high-energy peak of their spectra (see Fig. 86.13); σ_t^{eff} (σ_d^{eff}) is the effective cross-section of knock-on triton (deuteron) as defined in Fig. 86.13; m_p is the proton mass; and $\gamma = n_d/n_t$. Similarly, the yield of knock-on protons, which are exclusively generated in the CH shell, can be shown to be related to ρR_{shell} by the equation

$$\rho R_{\text{shell}} = \frac{(\gamma + 12)m_p}{\gamma\sigma_p^{\text{eff}}} \frac{Y_{\text{KO}p}}{Y_n}, \quad (6)$$

where $Y_{\text{KO}p}$ is the measured knock-on- p yield in a 1-MeV range (see Fig. 86.13); σ_p^{eff} is an effective cross section for knock-on protons; and $\gamma = n_H/n_C$ (where n_H and n_C are the number densities of the hydrogen and carbon atoms, respectively, in the shell). Under some circumstances, it is useful to modify Eq. (5) for use with the “uniform” model, in which primary neutrons are generated throughout the volume containing deuterons and tritons, by multiplying the right-hand side by a factor of 1.33. Figure 86.14 displays inferred values



E10808

Figure 86.14

Areal density versus the ratio of knock-on particle yield to primary neutron yield. For knock-on D and T, a hot-spot model is assumed and the yields under the high-energy peaks are used (as described in Fig. 86.13’s caption). For knock-on p , a hot-spot model is assumed and the yield per MeV in the flat region is used.

of ρR as a function of the measured ratios of knock-on yield to primary neutron yield. The model-independent use of Eq. (5) breaks down when the total areal density exceeds about 100 mg/cm² because the knock-on spectra become sufficiently distorted by slowing-down effects that measurements can become ambiguous; the accurate determination of ρR_{fuel} will then have to rely on the guidance of model-dependent simulations.

The potential importance of knock-on particle measurements was realized some years ago, and measurements with both limited spectral resolution and a small number of knock-on particles (around 30) were subsequently obtained.^{23,24} Those measurements relied on range-filter data in the form of “coincident” (front-side and back-side) tracks generated in a CR-39 nuclear track detector or in nuclear emulsions. This early work relied on detailed assumptions about the spectra of knock-on particles, which were estimated in indirect ways from other diagnostic data (for example, from the downshifted D³He protons).²³ In contrast, charged-particle spectroscopy, as described here, measures the whole spectrum directly for each particle. With hundreds to thousands of knock-on particles being simultaneously detected from an individual implosion, comprehensive and high-resolution knock-on spectra are readily obtained.

Figure 86.15 shows sample spectra obtained by CPS-2 for shot 20231. For this shot, the capsule was filled with 12.3 atm of DT gas and had a 19.1- μm -thick CH shell. The laser energy was 22.1 kJ, and the primary neutron yield was $7.1(\pm 0.7) \times 10^{12}$. The bandwidth of the 2-D SSD was 0.35 THz, and no polarization smoothing (PS) was applied. The beam-to-beam energy balance was 13.7% rms, and the on-target, low-mode rms uniformity was 5.6% because of beam overlap on the target surface. An ion temperature of $T_i \cong 4.0(\pm 0.5)$ keV was obtained. The fusion burn occurred at $1810(\pm 50)$ ps and lasted for $180(\pm 25)$ ps. Figure 86.15(a) provides the knock-on T spectrum with a yield of about 5.7×10^8 tritons under the high-energy peak (between 3 to 10 MeV). The whole spectrum is downshifted by ~ 4 MeV (as described in the figure caption). Figure 86.15(b) shows the knock-on D spectrum with a yield of about 4.8×10^8 deuterons under the high-energy peak (between 3.5 to 12 MeV). An energy loss of about ~ 3 MeV, relative to the birth spectrum, is measured. Figure 86.15(c) displays the knock-on p spectrum, with a yield of about $5.7 \times 10^8/\text{MeV}$ protons in the flat region between 8 to 12 MeV. The end point of this spectrum is about 14 MeV because protons scattered from the outer part of the shell lose no energy. We note that CPS yield measurements represent an integral over

the fusion burn duration, so an inferred ρR value represents an average over the burn. In addition, the fact that the source of neutrons is distributed over a finite volume of fuel means that inferred ρR values represent spatial averages.

The measured knock-on spectra for shot 20698 are shown in Fig. 86.16. The capsule was filled with 15 atm of DT gas and had a 20- μm CH shell. The laser energy was 23.8 kJ, and the primary neutron yield was $1.4(\pm 0.1) \times 10^{13}$. In contrast to shot 20231, polarization smoothing was applied for this shot and the 2-D SSD bandwidth was increased to 1.0 THz. The beam-

to-beam energy balance (3.1% rms) and the on-target low-mode rms uniformity (1.3% rms) were thus improved. An ion temperature of $T_i \cong 4.1(\pm 0.5)$ keV was obtained. The fusion burn occurred at $1750(\pm 50)$ ps and lasted for $170(\pm 25)$ ps. Figure 86.16(a) shows the knock-on T spectrum, with a yield of about 1.2×10^9 tritons under the high-energy peak (between 2.5 to 10 MeV). The whole spectrum is downshifted by 4.8 MeV. Figure 86.16(b) shows the knock-on D spectrum, with a yield of about 1.7×10^9 deuterons under the high-energy peak (between 3.5 to 12 MeV). An energy loss of about 4.1 MeV is measured. Figure 86.16(c) shows the knock-on p

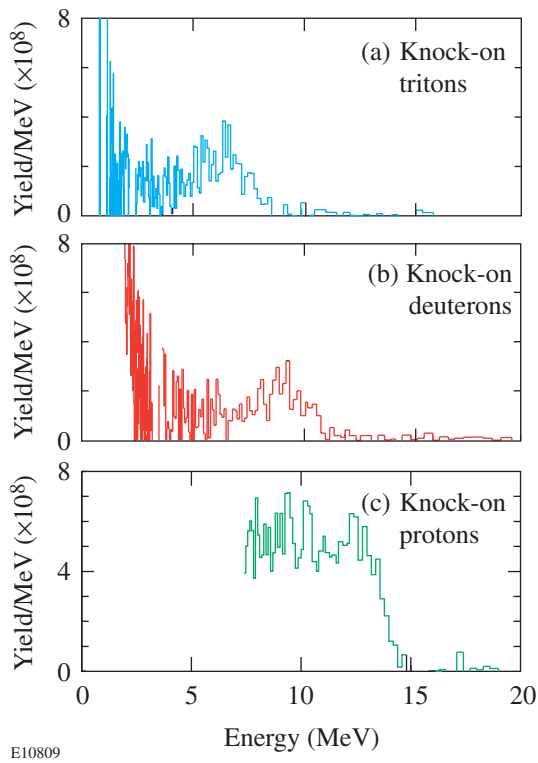


Figure 86.15
Knock-on spectra measured by CPS-2 for shot 20231. The capsule was filled with 12.3 atm of DT gas and had a 19.1- μm -thick CH shell. The laser energy was 22.1 kJ, and the primary neutron yield was 7.1×10^{12} . The bandwidth of 2-D SSD was 0.35 THz, and no PS was applied. (a) The knock-on T spectrum with a yield of about 5.7×10^8 tritons under the high-energy peak (between 3 to 10 MeV). The whole spectrum is downshifted by ~ 4 MeV (determined by the energy at which the yield/MeV reaches half of its peak value on the high-energy end of the spectrum). (b) The knock-on D spectrum with a yield of about 4.8×10^8 deuterons under the high-energy peak (between 3.5 to 12 MeV). An energy loss of about ~ 3 MeV is measured. (c) The knock-on p spectrum with a yield/MeV of about $5.7 \times 10^8/\text{MeV}$ protons in the flat region between 8 to 12 MeV. The end point of this spectrum is about 14 MeV, reflecting the fact that particles scattered from the outer part of the shell have no energy loss.

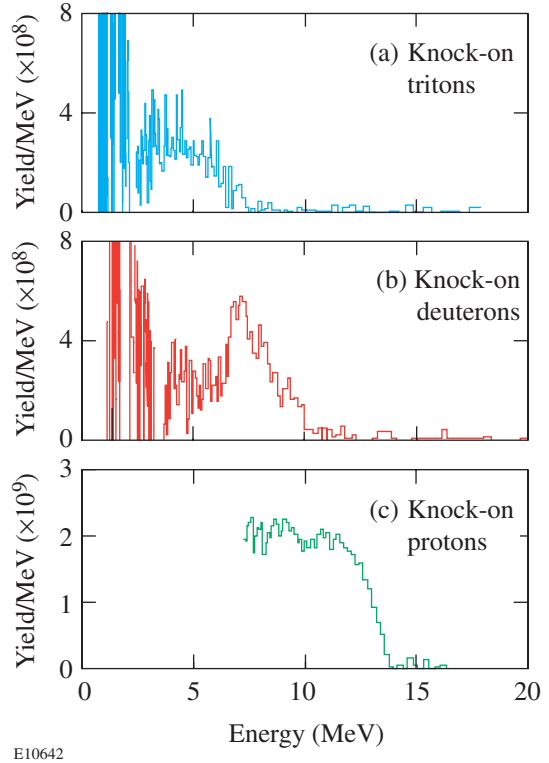


Figure 86.16
Knock-on spectra for shot 20698, measured by CPS-2. The capsule is filled with 15 atm of DT gas and has a 20- μm CH shell. For this shot, the laser energy was 23.8 kJ, and the primary neutron yield was 1.4×10^{13} . The 2-D SSD bandwidth was 1.0 THz, and polarization smoothing was applied. (a) The knock-on T spectrum, with a yield of about 1.2×10^9 tritons under the high-energy peak (between 2.5 to 10 MeV). The whole spectrum is downshifted by 4.8 MeV. (b) The knock-on D spectrum, with a yield of about 1.7×10^9 deuterons under the high-energy peak (between 3.5 to 12 MeV). An energy loss of about 4.1 MeV is measured. (c) The knock-on p spectrum, with a yield of about $2.0 \times 10^9/\text{MeV}$ protons in the flat region between 8 to 12 MeV. As in Fig. 86.15, the end point of this spectrum is about 14 MeV, reflecting the fact that particles scattered from the outer part of the shell have no energy loss.

spectrum, with a yield of about $2.0 \times 10^9/\text{MeV}$ in the flat region between 8 to 12 MeV. The end point of this spectrum is about 14 MeV, as for shot 20231. Relative to shot 20231, the primary neutron yield in shot 20698 is higher by a factor of ≈ 1.95 , and the knock-on particle yields are higher by factors of ≈ 3.48 (deuteron) and ≈ 3.45 (proton). In addition, because of increased compression, the energy loss of the knock-on particles from the fuel is greater by 15% to 30%.

Results and Discussions

1. Core Performance of Moderate-Convergence Capsule Implosions

In this section we examine the effects of illumination uniformity on core performance for moderate-convergence capsule implosions, as characterized by measurements of primary neutrons and knock-on charged particles. We start with the primary neutron yield, which provides one direct overall measure of core performance because of its strong dependence on ion temperature and density. Next we look at the yields of knock-on deuterons (Y_{KOd}) and tritons (Y_{KOt}), which provide a measure of ρR_{fuel} , and thus the amount of compression (which is quantified by the convergence ratio Cr, defined as a ratio of the initial fuel radius to the final compressed fuel radius). After showing that the data demonstrate an improvement in performance with improved laser smoothing, we examine comparisons of the data with numerical simulations. These comparisons suggest that the poorer performance observed with less smoothing is due to intrinsically 2-D or 3-D effects such as instabilities and mix.

Primary neutron yields between 3×10^{12} and 1.4×10^{13} were obtained, and, in general, better energy balance resulted in higher primary neutron yield. The highest yield was obtained for the shot with a low-mode rms nonuniformity of $\sim 1.3\%$ (energy balance to within 3.1%). Once on-target, low-mode nonuniformity due to beam imbalance has been decreased to the 5% rms range, single-beam nonuniformity becomes more important for capsule performance through its effects on high-order-mode perturbations. This is illustrated in Fig. 86.17(a), which indicates that beam smoothing with 1-THz, 2-D SSD + PS results in a primary yield ($Y_n \sim 1.1 \times 10^{13}$) about 80% higher than that obtained with 0.35-THz, 2-D SSD and no PS ($Y_n \sim 6.2 \times 10^{12}$). Since the ion temperature is found to be relatively insensitive to rms uniformity improvement, as shown in Fig. 86.17(b), higher Y_n must result from a higher ion density due to improved fuel compression.

While determining the ρR_{fuel} from knock-on yields, efforts to match the experimental primary yields by assuming differ-

ent temperature profiles led to a preference of the uniform model over the hot-spot model because highly peaked temperature profiles led to yields that were too low, so the ρR_{fuel} versus yield relationships shown in Fig. 86.14 must be modified. The corresponding inferred convergence ratio is

$$\text{Cr} = \sqrt{\rho R_{\text{fuel}} / \rho R_{\text{fuel}0}},$$

where $\rho R_{\text{fuel}0}$ is the fuel ρR before compression. As shown in Fig. 86.18, the data led to average values of $\rho R_{\text{fuel}} \sim 9.3 \text{ mg/cm}^2$ (Cr ~ 12) for the shots using 0.35-THz, 2-D SSD and $\rho R_{\text{fuel}} \sim 15 \text{ mg/cm}^2$ (Cr ~ 15) for 1-THz, 2-D SSD + PS. Increasing the smoothing rate increased ρR_{fuel} by $\sim 60\%$ and Cr by $\sim 25\%$.

One-dimensional (1-D) simulations were carried out for the studied shots. Figure 86.19 shows an example of how a measured knock-on deuteron spectrum compares with a prediction for shot 20698. Relative to the data, the simulation has a similar spectral shape, a similar energy downshift, and a similar, if somewhat higher, yield. Figures 86.20 to 86.23 provide an overview of data-to-simulation comparisons. Since the effects of beam smoothing are intrinsically 2-D or 3-D, the 1-D code predicts no difference due to smoothing; this can be seen in Figs. 86.20 and 86.21, which show that nearly all the shots are predicted to have the same values of ρR_{fuel} , Cr, and T_i , with small differences due only to the small differences in capsule parameters and total laser energy. On the other hand,

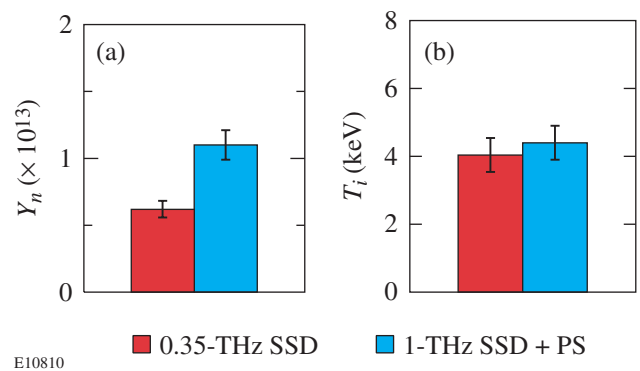


Figure 86.17

(a) Average primary yields achieved for two different single-beam smoothing conditions. The yield increases by about 80% when uniformity is improved using 1-THz, 2-D SSD + PS. (b) The yield-averaged ion temperature is insensitive to the improvement in uniformity. Consequently, the significant increase of primary yields cannot be attributed to the ion temperatures and is instead probably a consequence of an increase in ion density due to better fuel compression. The error bars display statistical uncertainties.

the measured values of ρR_{fuel} (or Cr) improve significantly for increased laser smoothing and approach the predicted values with 1-THz, 2-D SSD + PS. Other parameters also increase when smoothing is improved, including Y_n and Y_{KOd} , whose ratios to predicted values (YOC and $Y_{\text{KOd}}/Y_{1\text{-D}}$, respectively) are shown in Fig. 86.22. Plotting the ratio of measured to predicted values of Y_{KOd}/Y_n against measured Cr, in Fig. 86.23, shows that it approaches unity for full beam smoothing. This suggests that the improvement of single-beam irradiation uniformity results in increased compression through the reduction of 2-D phenomena such as instabilities and mix.

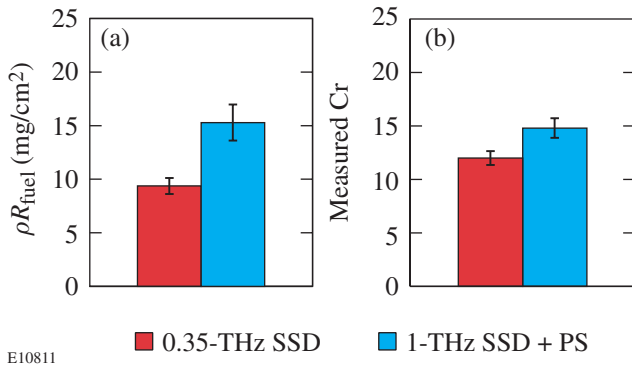


Figure 86.18 (a) Average fuel areal densities measured in experiments using 0.35-THz, 2-D SSD ($\rho R_{\text{fuel}} \sim 9.3$ mg/cm²) and 1-THz, 2-D SSD + PS ($\rho R_{\text{fuel}} \sim 15$ mg/cm²). A significant increase of the ρR_{fuel} (~60%) is obtained using 1.0-THz, 2-D SSD + PS. (b) Experimentally measured convergence ratios. Cr ~ 12 for shots using 0.35-THz, 2-D SSD, and Cr ~ 15 for shots using 1-THz, 2-D SSD + PS. The error bars display statistical uncertainties.

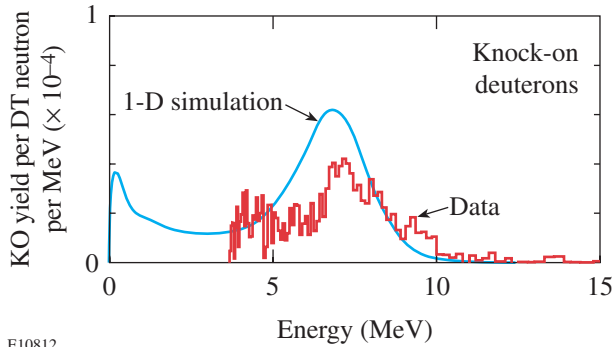


Figure 86.19 A comparison of the experimentally measured knock-on deuteron spectrum and the 1-D LILAC-predicted spectrum for shot 20698.

The credibility of this hypothesis is increased by more elaborate simulations that incorporate effects of Rayleigh–Taylor, Richtmyer–Meshkov, and Bell–Plesset instabilities, and 3-D Haan saturation^{5,7} in the postprocessing of 1-D calculation results. It was shown that using 0.35-THz, 2-D SSD without PS can result in a mix width that exceeds the in-flight shell thickness.^{5,7} The shell integrity is thus reduced, and the capsule compression is degraded. In contrast, the calculations show that with full beam smoothing (on-target beam nonuniformity less than 1% after 300 ps), the mix width is significantly smaller than the in-flight shell thickness.

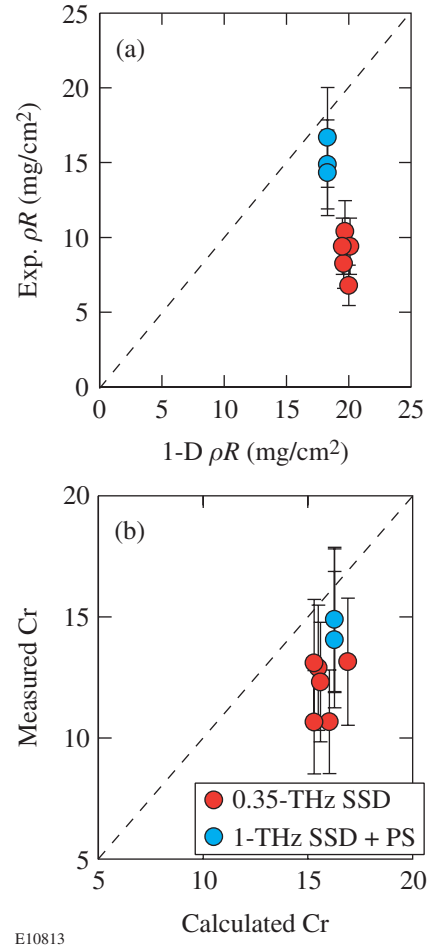
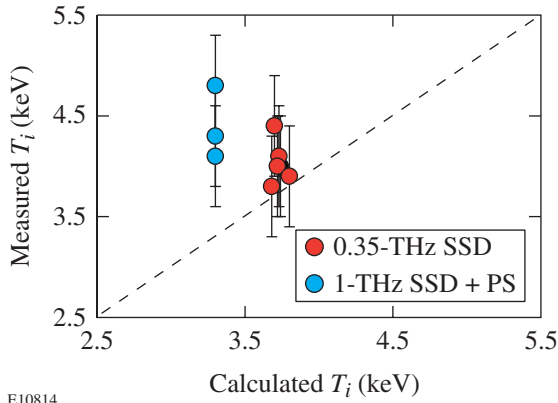
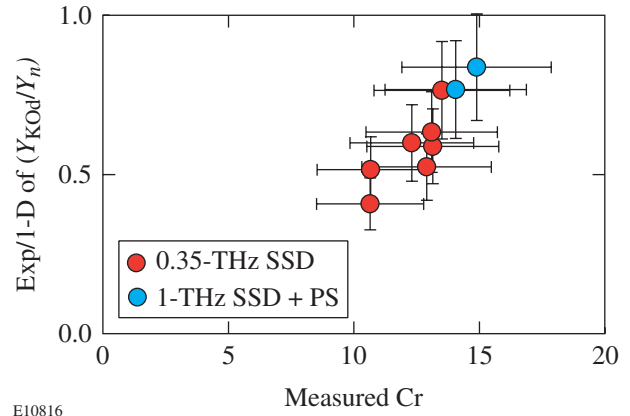


Figure 86.20 (a) Measured ρR_{fuel} versus 1-D simulation prediction. For the shots with 0.35-THz, 2-D SSD, the average measured ρR_{fuel} is about 60% of the prediction. For the shots with 1-THz, 2-D SSD + PS, an average of ~80% of the predicted ρR_{fuel} is measured. This comparison suggests that the improvement in irradiation uniformity makes implosions more 1-D-like. (b) The measured convergence ratio plotted against the calculation. The experimental data are slightly but consistently lower than those of 1-D predictions. The error bars display experimental uncertainties (~10% for neutrons, ~20% for charged particles).



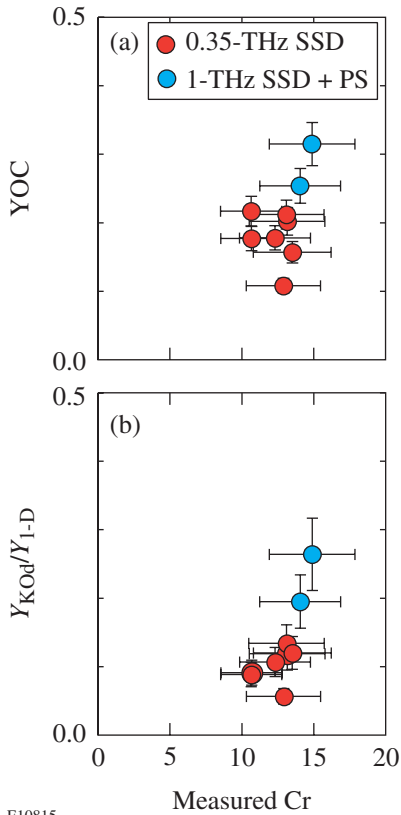
E10814

Figure 86.21
A comparison of measured ion temperatures to the 1-D LILAC predictions, showing that measured values are consistently higher than predictions. The error bars display experimental uncertainty (± 0.5 keV).



E10816

Figure 86.23
The ratio of the experimentally measured value of Y_{KOd}/Y_n to the 1-D prediction for different measured Cr. About ~60% is obtained for the shots using 0.35-THz, 2-D SSD, and ~80% is obtained for the shots using 1-THz, 2-D SSD + PS. This ratio approaches unity, while YOC is considerably smaller ($\leq 30\%$). The error bars indicate experimental uncertainties (~10% for neutrons, ~20% for charged particles).



E10815

Figure 86.22
(a) The ratio of measured primary neutron yield to clean 1-D prediction (YOC) plotted against the measured convergence ratio. An average of ~18% is obtained for the shots using 0.35-THz, 2-D SSD, while an average of ~30% is obtained for the shots using 1-THz, 2-D SSD + PS. (b) The ratio of measured KO deuteron yield to 1-D prediction (Y_{KOd}/Y_{1-D}) has an average of ~10% for the shots using 0.35-THz, 2-D SSD and of ~24% for the shots using 1-THz, 2-D SSD + PS. The error bars indicate experimental uncertainties (~10% for neutrons, ~20% for charged particles).

2. Shell Performance of Moderate-Convergence Capsule Implosions

The shell performance discussed in this section is based on measurements of ρR_{shell} and shell electron temperature T_e . The ρR_{shell} can be determined directly from the yield of knock-on protons (this is a temperature-independent method). Once ρR_{shell} is known and ρR_{fuel} has been determined as described in the previous section, the shell T_e can be estimated from the energy downshift of the deuteron and/or triton spectrum (slowing down of these particles is sensitive to T_e). Alternatively, if the shell T_e is already known from other measurements, then the deuteron and/or triton downshifts can be used in an independent estimation of ρR_{shell} .

Knock-on protons are generated only in the CH shell, and typical proton spectra are shown in Figs. 86.15(c) and 86.16(c). Values of ρR_{shell} can be calculated from the proton yields with Fig. 86.14. As displayed in Fig. 86.24, an average ρR_{shell} of ~45 mg/cm² is obtained for shots using 0.35-THz, 2-D SSD without PS, while an average ρR_{shell} of ~60 mg/cm² is obtained for 1-THz, 2-D SSD + PS. A 35% increase of the ρR_{shell} is thus obtained due to the improvement of single-beam uniformity. Figure 86.25 displays a 1-D calculated knock-on proton spectrum overlaid on an experimentally measured proton spectrum for shot 20698. The agreement between these two spectra suggests that, with full beam smoothing, shell performance of a moderate-convergence implosion is close to the 1-D prediction.

The directly determined value of ρR_{fuel} (described in the previous section), together with the measured energy loss of the deuteron and/or triton knock-ons, can also be used to determine shell T_e (if ρR_{shell} has been determined as described in the previous paragraph) or to study ρR_{shell} (if the shell T_e is known). As deuteron and/or triton knock-ons from the fuel travel through fuel and shell, they lose an amount of energy directly proportional to the areal density of the materials they pass through (assuming there is no particle acceleration, as discussed below in Subsection 4). Because these particles are not so energetic, their stopping power is not characterized as “cold plasma stopping,” where there is no temperature dependence, but “warm plasma stopping,” where there is a temperature dependence. The energy loss can be calculated from the stopping power in a fully ionized plasma:^{31,32}

$$\frac{dE}{dx} = - \left(\frac{Z^2 \omega_p e}{v_t} \right)^2 \times \left[G(x^{t/f}) \ell n \Lambda + \theta(x^{t/f}) \ell n \left(1.123 \sqrt{x^{t/f}} \right) \right], \quad (7)$$

where $\theta(x^{t/f})$ is a step function and equals 0 (1) when $x^{t/f} < 1$ (> 1); $\omega_p = (4\pi n_e e^2 / m_e)^{1/2}$ is the electron plasma frequency; Z is the charge of the incident charged particle; v_t (v_f) is the velocity of a test (field) charged particle; $x^{t/f} = v_t^2 / v_f^2$; and $\ell n \Lambda$ is the Coulomb logarithm. $G(x^{t/f})$ is defined as

$$G(x^{t/f}) = \mu(x^{t/f}) - \frac{m_f}{m_t} \left\{ \frac{d\mu(x^{t/f})}{dx^{t/f}} - \frac{1}{\ell n \Lambda} \left[\mu(x^{t/f}) + \frac{d\mu(x^{t/f})}{dx^{t/f}} \right] \right\}, \quad (8)$$

where

$$\mu(x^{t/f}) = 2 \int_0^{x^{t/f}} e^{-\xi} \sqrt{\xi} d\xi / \sqrt{\pi}$$

is the Maxwell integral and m_t (m_f) is the mass of the test (field) particle. Since the effects of large-angle scattering are negligible for charged particles traveling in plasmas of interest,³² the areal density through which a charged particle travels with an energy loss ($\Delta E \approx E_0 - E$) can be approximately determined as

$$\rho R = \int_E^{E_0} \rho \left(\frac{dE}{dx} \right)^{-1} dx. \quad (9)$$

Because of the relatively high temperature and low density of the fuel plasma, the energy loss is dominated by the lower-temperature but higher-density shell plasma. The total areal density is defined as $\rho R_{\text{total}} = \rho R_{\text{fuel}} + \rho R_{\text{shell}}$.

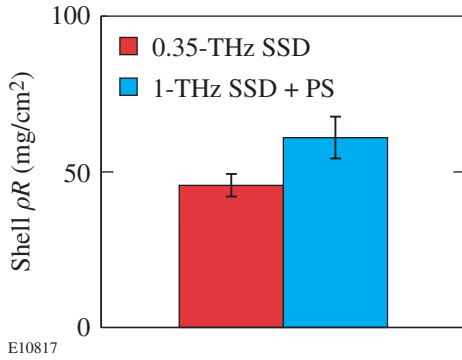


Figure 86.24
An average measured ρR_{shell} of ~ 45 mg/cm² is obtained for the shots using 0.35-THz, 2-D SSD, and a ρR_{shell} of ~ 60 mg/cm² is obtained for the shots using 1-THz, 2-D SSD + PS. The error bars display statistical uncertainties.

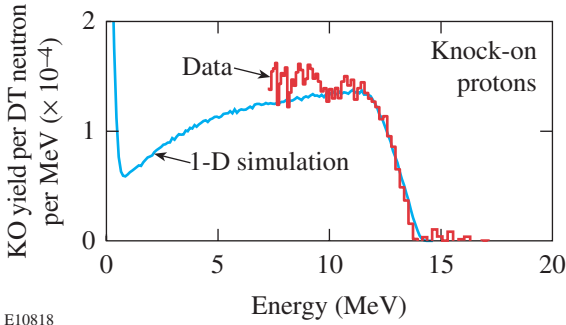


Figure 86.25
A comparison of the measured knock-on proton spectrum (red line) to the 1-D *LILAC* prediction (blue line) for shot 20698. The agreement between these two spectra suggests the compressed shell has nearly 1-D performance. (The fact that the predicted spectrum is not flat, and decays in the region between 0 to 8 MeV, is due to the fact that low-energy protons generated during the stagnation phase of the implosion may experience a large ρR_{shell} and be ranged out.)

The downshifts of the spectra shown in Figs. 86.16(a) and 86.16(b) (for shot 20698) are about 5 MeV for tritons and 4 MeV for deuterons. To be consistent with the temperature-independent, knock-on-derived values of $\rho R_{\text{fuel}} \sim 14 \text{ mg/cm}^2$ and $\rho R_{\text{shell}} \sim 64 \text{ mg/cm}^2$ calculated as described above for this shot, the value of shell T_e must be about 0.6 keV. A summary of calculated shell T_e values for different shots is given in Fig. 86.26. Shell T_e appears insensitive to single-beam irradiation uniformity, to first order, although some subtle issues such as time and spatial dependence of the knock-on spectra are involved in this determination. This topic is a subject for future study.

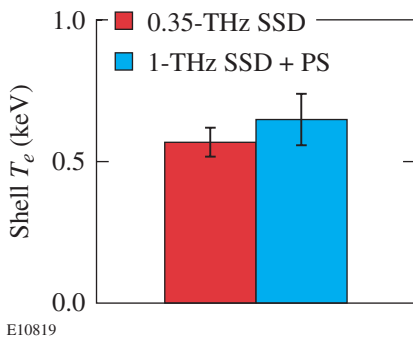


Figure 86.26 Average electron temperatures inferred from the knock-on spectra. Values of $\sim 0.58 \text{ keV}$ and $\sim 0.65 \text{ keV}$ are obtained for the shots using 0.35-THz, 2-D SSD and 1 THz, 2-D SSD + PS, respectively. The error bars display statistical uncertainties.

3. Similarity to D_2 -Filled-Capsule Implosions

With similar experimental conditions, implosions of DT- and D_2 -gas-filled plastic capsules are “hydrodynamically” equivalent. While some subtle differences, such as the mass, fusion cross section, equation of the state, etc., still exist, the basic capsule performance is expected to be similar. Recent work¹¹ has resulted in the study of fuel and shell parameters for D_2 shots on OMEGA by measuring spectra of secondary $D^3\text{He}$ protons. Those numbers are very similar to the knock-on-inferred numbers for related DT shots, as shown in Table 86.I. In general, the inferred and estimated ρR_{fuel} and ρR_{shell} along with ρR_{total} are very similar for both DT- and D_2 -capsule implosions under similar experimental conditions. While the corresponding values of YOC are similar, DT implosions result in higher ion temperatures than D_2 implosions. The improvement of the single-beam irradiation uniformity enhances the target performance of both DT and D_2 implosions: ρR_{fuel} (ρR_{shell}) increases $\sim 60\%$ ($\sim 35\%$) for DT implosions and $\sim 65\%$ ($\sim 40\%$) for D_2 implosions; Y_n increases $\sim 80\%$ for both DT and D_2 implosions; YOC increases $\sim 60\%$ for DT and $\sim 80\%$ for D_2 implosions. Ion temperatures are not so sensitive to the uniformity improvement ($\leq 10\%$).

4. Capsule Charging and Particle Acceleration

Time-dependent capsule charging is an essential issue in a spherical implosion. This charging may result in a strong electric field surrounding the capsule and an acceleration of emitted charged particles. Since the measurement of areal densities of imploded capsules through charged-particle spectroscopy relies on accurate determination of particle-energy downshift due to slowing in the capsule, any particle acceleration could introduce serious errors.

Table 86.I: Comparison of DT- and D_2 -gas-filled-plastic-shell implosions (the D_2 numbers are from Ref. 11).

Capsules	Single-beam smoothing	T_i (keV)	Y_n	YOC	Y_{Kod}/Y_{1-D}	Y_{2p}/Y_{1-D}	ρR_{fuel} (mg/cm ²)	ρR_{shell} (mg/cm ²)	ρR_{total} (mg/cm ²)
DT (15) CH(20)	0.3-THz, 2-D SSD	4.1±0.5	(6.2±1.4)×10 ¹²	0.18	0.10	—	9.3±1.9	46.8±7.6	~56*
	1-THz, 2-D SSD + PS	4.4±0.5	(1.1±0.3)×10 ¹³	0.30	0.24	—	15.3±2.1	61.4±6.9	~76*
D_2 (15) CH(20)	0.3-THz, 2-D SSD	3.4±0.5	(8.8±0.8)×10 ¹⁰	0.18	—	0.13	10.0±2.0	~43**	52
	1-THz, 2-D SSD + PS	3.7±0.5	(1.6±0.5)×10 ¹⁰	0.33	—	0.21	14.0±7.4	~57**	72
*Estimated based on measured ρR_{fuel} and ρR_{shell} .									
**Estimated based on measured ρR_{fuel} and ρR_{total} .									

Many previous experiments have demonstrated the existence of capsule charging and particle acceleration, even (unexpectedly) on OMEGA with laser intensities of $\sim 10^{15}$ W/cm² and 351-nm wavelength (where energy upshifts of ~ 1 MeV have been observed for charged-fusion products and ablator protons^{10,33,34}). The hot electrons generated by laser-plasma instabilities in the corona are thought to cause this capsule charging. Earlier experiments also suggest that the charge is time dependent.

For estimating the effects of the electric fields on charged-fusion products, it has previously been assumed that such effects are important only when the bang time occurs while the laser is on (for example, for a thin-glass-shell capsule driven by 1-ns square pulse).^{35,36} Such effects are assumed unimportant when the bang time occurs several hundreds of picoseconds after the laser turns off, when the electric field has largely decayed away (for example, a thick-plastic-shell capsule driven by a 1-ns square pulse^{10,33}). For the latter case, possible energy upshifts, if any, have been assumed to be completely negligible. Although widely used when determining the spectral downshifts of charged particles,^{10,33} these assumptions have never been directly proven by experiments because the effects of particle acceleration and slowing down are always mixed in an implosion for charged-fusion products.

The knock-on proton data described in this article provide direct proof of this assumption for thick-plastic-shell capsules driven by 1-ns square laser pulses. Any acceleration would cause the upper end points of the knock-on proton spectra to be up-shifted relative to the 14-MeV end point of the birth spectrum. In Figs. 86.15(c) and 86.16(c), the end points of the knock-on proton spectra are precisely (within statistical errors) at 14 MeV, which indicates that the protons are subject to no accelerations. Figure 86.27 shows the measured end points of these and other knock-on proton spectra for a number of shots, plotted against the bang time (a typical 1-ns square pulse on OMEGA is also displayed for reference). The laser pulse has completely ended at ~ 1400 ps, while the bang time occurs several hundreds of picoseconds later. No energy upshifts are observed.

5. Relevance to OMEGA Cryogenic-Capsule Implosions

Plans exist to implode on OMEGA cryogenic DT capsules that typically have low-pressure DT-gas fill in the center surrounded by about 90 μm of DT ice with $\sim 2 \mu\text{m}$ of CH as an ablator. These implosions are predicted to generate DT primary yields $>10^{13}$, with an ion temperature between 1 to 4 keV and areal densities up to ~ 300 mg/cm². Nuclear diagnos-

tics will play an important role in the OMEGA cryogenic program. Figure 86.28 shows the energy of knock-on deuterons plotted against their range (ρR) in a DT plasma (an electron temperature of 2 keV and an ion density of 5×10^{24} are assumed, although the density effects on these calculations are weak^{31,32}). For a typical areal density of 200 to 300 mg/cm², a knock-on deuteron will lose about 6 to 9 MeV as it traverses the capsule, and the remaining energy of 3 to 6 MeV is readily detectable using CPS.¹²

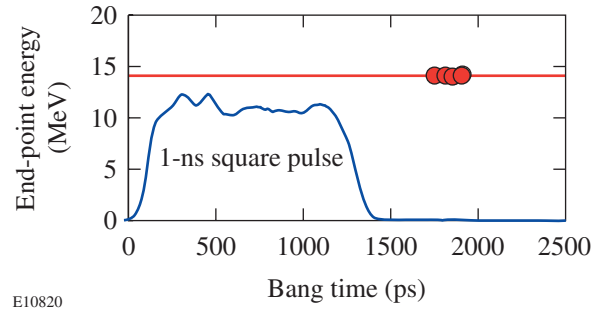


Figure 86.27 The measured upper-energy end points of the knock-on proton spectra for a number of shots in this study are plotted against the bang time (a typical 1-ns square pulse with an arbitrary unit for laser intensity on OMEGA is also displayed for reference). As seen, the laser pulse has completely ended at ~ 1400 ps, while the bang times occur at 1750 to 1950 ps. The energies match the maximum scattered-proton energy, indicating that there are no energy upshifts.

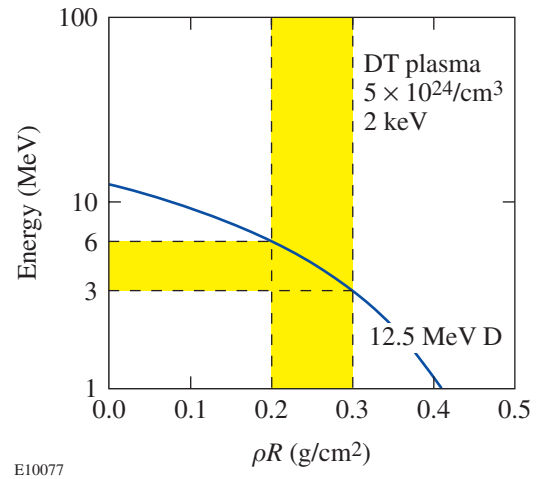


Figure 86.28 The energy of knock-on deuterons versus their range (ρR) in a DT plasma. In this calculation, an electron temperature of 2 keV and an ion density of 5×10^{24} have been assumed. For a typical predicted areal density of 200 to 300 mg/cm² for a cryogenic-capsule implosion, a knock-on deuteron will lose about 6 to 9 MeV of energy, and the residual energy (3 to 6 MeV) left after leaving the target is readily detectable using charged-particle spectrometry.

Summary and Conclusions

Direct-drive implosions of DT-gas-filled plastic capsules were studied using nuclear diagnostics on OMEGA. In addition to the traditional neutron measurements, comprehensive and high-resolution spectra of knock-on deuterons, tritons, and protons were obtained for the first time in ICF experiments and used to characterize target performance.

Target performance is improved, for moderate-convergence implosions ($Cr \sim 10$ to 20), with the reduction of on-target irradiation nonuniformity that results from an improvement in beam-to-beam laser energy balance and an enhancement of single-beam uniformity. With the use of a 1-THz bandwidth of smoothing by spectral dispersion and polarization smoothing, $Y_n \sim 1.1 \times 10^{13}$, $YOC \sim 0.3$, $\rho R_{\text{fuel}} \sim 15 \text{ mg/cm}^2$, and $\rho R_{\text{shell}} \sim 60 \text{ mg/cm}^2$, which are, respectively, approximately 80%, 60%, 60%, and 35% higher than those determined when using a 0.35-THz bandwidth of smoothing by spectral dispersion. Polarization smoothing of individual laser beams is believed to play an important role.

With full beam smoothing, these implosions have some performance parameters close to one-dimensional-code predictions (e.g., a measured ratio of Y_{KOD}/Y_n achieves $\sim 80\%$ of 1-D predictions). Data suggest that high irradiation uniformity results in reduced Rayleigh–Taylor growth and improved shell integrity. In addition, a brief comparison demonstrates the hydrodynamic “equivalence” of DT-filled capsules and D_2 -filled capsules for moderate-convergence implosions.

ACKNOWLEDGMENT

We express our appreciation to the OMEGA Laser and Experimental Operations and Target Fabrication crews for their excellent work and continuous support. This work has been supported in part by LLE (subcontract P0410025G) and LLNL (subcontract B313975), and by the U.S. Department of Energy Office of Inertial Confinement Fusion under Cooperative Agreement NO. DE-FC03-92SF19460, the University of Rochester, and New York State Energy Research and Development Authority. The support of DOE does not constitute an endorsement by DOE of the views expressed in this work.

REFERENCES

1. J. D. Lindl, R. L. McCrory, and E. M. Campbell, *Phys. Today* **45**, 32 (1992).
2. J. D. Lindl, *Inertial Confinement Fusion: The Quest for Ignition and Energy Gain Using Indirect Drive* (Springer-Verlag, New York, 1998).
3. S. W. Haan *et al.*, *Phys. Plasmas* **2**, 2480 (1995).
4. T. R. Boehly, D. L. Brown, R. S. Craxton, R. L. Keck, J. P. Knauer, J. H. Kelly, T. J. Kessler, S. A. Kumpan, S. J. Loucks, S. A. Letzring, F. J. Marshall, R. L. McCrory, S. F. B. Morse, W. Seka, J. M. Soures, and C. P. Verdon, *Opt. Commun.* **133**, 495 (1997).
5. R. L. McCrory, R. E. Bahr, R. Betti, T. R. Boehly, T. J. B. Collins, R. S. Craxton, J. A. Delettrez, W. R. Donaldson, R. Epstein, J. Frenje, V. Yu. Glebov, V. N. Goncharov, O. V. Gotchev, R. Q. Gram, D. R. Harding, D. G. Hicks, P. A. Jaanimagi, R. L. Keck, J. Kelly, J. P. Knauer, C. K. Li, S. J. Loucks, L. D. Lund, F. J. Marshall, P. W. McKenty, D. D. Meyerhofer, S. F. B. Morse, R. D. Petrasso, P. B. Radha, S. P. Regan, S. Roberts, F. Séguin, W. Seka, S. Skupsky, V. A. Smalyuk, C. Sorce, J. M. Soures, C. Stoeckl, R. P. J. Town, M. D. Wittman, B. Yaakobi, and J. D. Zuegel, “OMEGA ICF Experiments and Preparation for Direct-Drive Ignition on NIF,” to be published in the *Proceedings of the 18th IAEA Fusion Energy Conference*.
6. J. M. Soures, R. L. McCrory, C. P. Verdon, A. Babushkin, R. E. Bahr, T. R. Boehly, R. Boni, D. K. Bradley, D. L. Brown, R. S. Craxton, J. A. Delettrez, W. R. Donaldson, R. Epstein, P. A. Jaanimagi, S. D. Jacobs, K. Kearney, R. L. Keck, J. H. Kelly, T. J. Kessler, R. L. Kremens, J. P. Knauer, S. A. Kumpan, S. A. Letzring, D. J. Lonobile, S. J. Loucks, L. D. Lund, F. J. Marshall, P. W. McKenty, D. D. Meyerhofer, S. F. B. Morse, A. Okishev, S. Papernov, G. Pien, W. Seka, R. Short, M. J. Shoup III, M. Skeldon, S. Skupsky, A. W. Schmid, D. J. Smith, S. Swales, M. Wittman, and B. Yaakobi, *Phys. Plasmas* **3**, 2108 (1996).
7. D. D. Meyerhofer, J. A. Delettrez, R. Epstein, V. Yu. Glebov, V. N. Goncharov, R. L. Keck, R. L. McCrory, P. W. McKenty, F. J. Marshall, P. B. Radha, S. P. Regan, S. Roberts, W. Seka, S. Skupsky, V. A. Smalyuk, C. Sorce, C. Stoeckl, J. M. Soures, R. P. J. Town, B. Yaakobi, J. D. Zuegel, J. Frenje, C. K. Li, R. D. Petrasso, D. G. Hicks, F. H. Séguin, K. Fletcher, S. Padalino, M. R. Freeman, N. Izumi, R. Lerche, T. W. Phillips, and T. C. Sangster, *Phys. Plasmas* **8**, 2251 (2001).
8. F. J. Marshall, J. A. Delettrez, V. Yu. Glebov, R. P. J. Town, B. Yaakobi, R. L. Kremens, and M. Cable, *Phys. Plasmas* **7**, 1006 (2000).
9. F. J. Marshall, J. A. Delettrez, R. Epstein, V. Yu. Glebov, D. R. Harding, P. W. McKenty, D. D. Meyerhofer, P. B. Radha, W. Seka, S. Skupsky, V. A. Smalyuk, J. M. Soures, C. Stoeckl, R. P. Town, B. Yaakobi, C. K. Li, F. H. Séguin, D. G. Hicks, and R. D. Petrasso, *Phys. Plasmas* **7**, 2108 (2000).
10. C. K. Li, D. G. Hicks, F. H. Séguin, J. A. Frenje, R. D. Petrasso, J. M. Soures, P. B. Radha, V. Yu. Glebov, C. Stoeckl, D. R. Harding, J. P. Knauer, R. L. Kremens, F. J. Marshall, D. D. Meyerhofer, S. Skupsky, S. Roberts, C. Sorce, T. C. Sangster, T. W. Phillips, M. D. Cable, and R. J. Leeper, *Phys. Plasmas* **7**, 2578 (2000).
11. F. H. Séguin, C. K. Li, D. G. Hicks, J. A. Frenje, K. M. Green, R. D. Petrasso, J. M. Soures, D. D. Meyerhofer, V. Yu. Glebov, C. Stoeckl, P. B. Radha, S. Roberts, C. Sorce, T. C. Sangster, M. D. Cable, S. Padalino, and K. Fletcher, “Using Secondary Proton Spectra to Study Imploded D_2 -Filled Capsules at the OMEGA Laser Facility,” submitted to *Physics of Plasmas*.

12. J. A. Frenje, K. M. Green, C. K. Li, F. H. Séguin, R. D. Petrasso, S. Roberts, V. Yu. Glebov, D. D. Meyerhofer, J. M. Soures, D. G. Hicks, T. W. Phillips, T. C. Sangster, K. Fletcher, L. Baumgart, H. Olliver, S. Padalino, S. Thompson, and B. White, "Diagnostic Measurements of Charged Particles from DD, D³He, and DT Implosions at the OMEGA Laser Facility Using CR-39 Particle Detectors," to be submitted to Review of Scientific Instruments.
13. P. B. Radha, S. Skupsky, R. D. Petrasso, and J. M. Soures, *Phys. Plasmas* **7**, 1531 (2000).
14. S. Skupsky and R. S. Craxton, *Phys. Plasmas* **6**, 2157 (1999).
15. V. Yu. Glebov, D. D. Meyerhofer, and C. Stoeckl, *Bull. Am. Phys. Soc.* **45**, 144 (2000).
16. M. A. Russotto and R. L. Kremens, *Rev. Sci. Instrum.* **61**, 3125 (1990).
17. J. D. Kilkenny, M. D. Cable, C. A. Clower, B. A. Hammer, V. P. Karpenko, R. L. Kauffman, H. N. Kornblum, B. J. MacGowan, W. Olson, T. J. Orzechowski, D. W. Phillion, G. L. Tietbohl, J. E. Trebes, B. Chrien, B. Failor, A. Hauer, R. Hockaday, J. Oertel, R. Watt, C. Ruiz, G. Cooper, D. Hebron, L. Leeper, J. Porter, and J. Knauer, *Rev. Sci. Instrum.* **66**, 288 (1995).
18. R. J. Leeper, G. A. Chandler, G. W. Cooper, M. S. Derzon, D. L. Fehl, D. L. Hebron, A. R. Moats, D. D. Noack, J. L. Porter, L. E. Ruggles, J. A. Torres, M. D. Cable, P. M. Bell, C. A. Clower, B. A. Hammel, D. H. Kalantar, V. P. Karpenko, R. L. Kauffman, J. D. Kilkenny, F. D. Lee, R. A. Lerche, B. J. MacGowan, M. J. Moran, M. B. Nelson, W. Olson, T. J. Orzechowski, T. W. Phillips, D. Ress, G. L. Tietbohl, J. E. Trebes, R. J. Bartlett, R. Berggren, S. E. Caldwell, R. E. Chrien, B. H. Failor, J. C. Fernandez, A. Hauer, G. Idzorek, R. G. Hockaday, T. J. Murphy, J. Oertel, R. Watt, M. Wilke, D. K. Bradley, J. Knauer, R. D. Petrasso, and C. K. Li, *Rev. Sci. Instrum.* **68**, 868 (1997).
19. R. A. Lerche, D. W. Phillion, and G. L. Tietbohl, *Rev. Sci. Instrum.* **66**, 933 (1995).
20. D. G. Hicks, C. K. Li, R. D. Petrasso, F. H. Séguin, B. E. Burke, J. P. Knauer, S. Cremer, R. L. Kremens, M. D. Cable, and T. W. Phillips, *Rev. Sci. Instrum.* **68**, 589 (1997).
21. D. G. Hicks, "Charged Particle Spectroscopy: A New Window on Inertial Confinement Fusion," Ph.D. thesis, Massachusetts Institute of Technology, 1999.
22. F. H. Séguin *et al.*, "A Proton Spectrometer Based on a Wedge-Shaped Range Filter and CR39 Nuclear Track Detectors," to be submitted to Review of Scientific Instruments.
23. S. Skupsky and S. Kacenjar, *J. Appl. Phys.* **52**, 2608 (1981).
24. S. Kacenjar, S. Skupsky, A. Entenberg, L. Goldman, and M. Richardson, *Phys. Rev. Lett.* **49**, 463 (1982).
25. E. M. Campbell *et al.*, *J. Appl. Phys.* **51**, 6062 (1980).
26. M. D. Cable and S. P. Hatchett, *J. Appl. Phys.* **62**, 2233 (1987).
27. H. Azechi, M. D. Cable, and R. O. Stapf, *Laser Part. Beams* **9**, 119 (1991).
28. R. D. Petrasso, C. K. Li, M. D. Cable, S. M. Pollaine, S. W. Haan, T. P. Bernat, J. D. Kilkenny, S. Cremer, J. P. Knauer, C. P. Verdon, and R. L. Kremens, *Phys. Rev. Lett.* **77**, 2718 (1996).
29. S. Cremer, C. P. Verdon, and R. D. Petrasso, *Phys. Plasmas* **5**, 4009 (1998).
30. E. Goldman, Laboratory for Laser Energetics Report No. 16, University of Rochester (1973).
31. C. K. Li and R. D. Petrasso, *Phys. Rev. Lett.* **70**, 3059 (1993).
32. C. K. Li and R. D. Petrasso, *Phys. Plasmas* **2**, 2460 (1995).
33. D. G. Hicks, C. K. Li, F. H. Séguin, A. K. Ram, J. A. Frenje, R. D. Petrasso, J. M. Soures, V. Yu. Glebov, D. D. Meyerhofer, S. Roberts, C. Sorce, C. Stockl, T. C. Sangster, and T. W. Phillips, *Phys. Plasmas* **7**, 5106 (2000).
34. D. G. Hicks, C. K. Li, F. H. Séguin, J. D. Schnittman, A. K. Ram, J. A. Frenje, R. D. Petrasso, J. M. Soures, D. D. Meyerhofer, S. Roberts, C. Sorce, C. Stoeckl, T. C. Sangster, and T. W. Phillips, *Phys. Plasmas* **8**, 606 (2001).
35. Y. Gazit, J. Delettrez, T. C. Bristow, A. Entenberg, and J. Soures, *Phys. Rev. Lett.* **43**, 1943 (1979).
36. J. Delettrez, A. Entenberg, Y. Gazit, D. Shvarts, J. Virmont, T. Bristow, J. M. Soures, and A. Bennish, *Nucl. Fusion* **23**, 1135 (1983).

A Consistent Measurement-Based Picture of Core-Mix in Direct-Drive Implosions on OMEGA

Introduction

The central goal of direct-drive implosions on the OMEGA laser¹ is to validate the performance of the high-gain, direct-drive ignition designs² planned for use on the National Ignition Facility. Inferring the density, temperature, and fuel–shell mix of ignition-relevant capsule implosions is important in validating models of implosions. To this end, diagnostic information from sets of implosions that differ in their hydrodynamic properties has been obtained in direct-drive spherical-capsule implosions on OMEGA. In this article, we report on an analysis of the experimental charged-particle and neutron data that provide consistent information on densities and temperatures of one set of similar experiments.

In direct-drive implosions, a spherical target is illuminated uniformly with a laser. Any degradation in target performance is believed to occur primarily through the Rayleigh–Taylor instability,³ which is seeded by either target imperfections or laser nonuniformity. This instability, occurring at the ablation surface during the acceleration phase of the implosion, can then feed through to the fuel–shell interface and add to any pre-existing roughness on the inner surface. During the deceleration phase, these distortions at the fuel–shell interface grow, resulting in a mixing of the fuel and shell material. Neutron and charged-particle diagnostics carry direct information about this phase of the implosion, when fuel densities and temperatures are high enough for their production.

Several complementary approaches can be used to analyze the implosion observables. One route is to infer, from individual diagnostics, parameters such as the fuel areal density, which is a measure of compression. Comparisons of inferred quantities with those from simulations indicate the closeness of the actual implosions to the simulations. The problem with this technique is usually that simple models used to infer key quantities from individual diagnostics (such as “ice-block” models) may not apply to the actual implosion. Further, this technique ignores complementary information from other diagnostics that may be critical to devising the correct model. Another possible technique is to directly simulate the experi-

ment and post-process the simulation for the relevant diagnostic. Again, the comparison is very model dependent, and further light on any disagreement between simulations and experiment is difficult to obtain through this route. The third method, described in this article, is to use all observables from a set of hydrodynamically similar implosions and infer a picture that is consistent across all diagnostics. This picture would correspond to a neutron-weighted, “1-D” description of temperature and density profiles in the core and mix region of the imploding target. The advantage of such a scheme is that it provides a picture using all available information and allows for more detailed comparisons between simulation and experiment through a sensitivity analysis of the model parameters.

In this article, we describe a consistent picture, inferred from different diagnostics, of conditions in the fuel core and mix region for 20- μm -thick-plastic-shell implosions. These targets are of interest because their stability during the acceleration phase is calculated to be similar to those predicted for OMEGA cryogenic implosions,⁴ which, in turn, are energy-scaled surrogates⁵ for direct-drive ignition targets.² Studies on these targets should then be applicable to both OMEGA cryogenic and NIF ignition targets. Experiments with plastic targets also offer a larger array of diagnostic techniques, allowing for more information on target behavior.

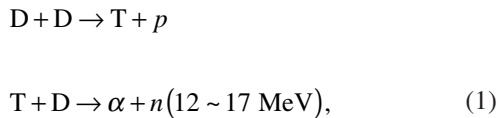
The following sections (1) describe the targets modeled and the diagnostics used to probe these targets, (2) present evidence for mixing and the mix model, and (3) present our conclusions.

Targets and Diagnostics

The experiments chosen for this analysis had nominally identical laser pulse shapes, smoothing conditions, target-shell thickness, and gas pressure. The makeup of the fill gas or details of the shell layers were then varied so that complementary diagnostics could be applied to hydrodynamically similar implosions. Since implosions on OMEGA show excellent reproducibility,⁴ variation between different shots is relatively small, allowing for such an analysis. We consider targets with 20- μm -thick plastic shells (pure CH or with CD layers) with

different gas fills (D_2 , DT, 3He) at 15 atm (see Fig. 86.29 for a description of targets and corresponding observables). These targets were irradiated with a 1-ns square laser pulse with 23-kJ energy and used full-beam smoothing (2-D smoothing by spectral dispersion with 1-THz bandwidth and polarization smoothing using birefringent wedges).

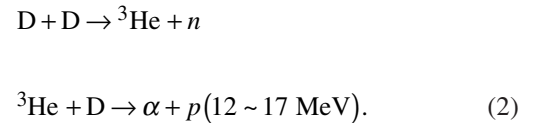
For the D_2 -filled targets, the neutron diagnostics involved measurements of primary neutron yields from the DD reactions and neutron-averaged ion temperatures, measured using neutron time-of-flight detectors.⁴ In addition, secondary neutron yields,⁶ which are produced by the following sequence of reactions,



are also measured using current-mode detectors.⁷ Tritons in the primary DD reaction produced at energies of about 1 MeV cause secondary reactions with the fuel deuterons as they move through the target. The ratio of the secondary neutron yields to the primary DD neutron yields depends on the fuel areal

density. Secondary neutron yields can also depend sensitively, however, on the temperatures in the target, through the slowing down of the triton and the energy-dependent cross section of the reaction. With the cross section increasing significantly with decreasing energy of the triton (the cross section increases by nearly a factor of 5 between the triton birth energy and about 0.1 MeV), this diagnostic is particularly sensitive to the effects of mix; the shell material mixed in with the fuel could contribute to the greater slowing down of the triton and consequently an increased secondary neutron yield.

Secondary protons,⁸ in an analogous reaction to that of the secondary neutrons, are produced in D_2 -filled targets. Here, the second main branch of the DD reaction produces primary 3He particles, which in turn fuse with the background deuterons as they traverse the fuel region:



Again, this reaction is dependent on the areal density of the fuel and the slowing down of the primary 3He particles. In this case, however, the cross section of the reaction decreases significantly with increasing slowing down of the 3He particle. Therefore, when slowing down is significant, the areal density local to the primary 3He production essentially determines the secondary proton yield. Measurements of secondary proton spectra are carried out using a magnet-based charged-particle spectrometer (CPS) as well as “wedge-range-filter”-based spectrometers using CR-39 track detectors.⁸

The number of elastically scattered deuterons and tritons (“knock-ons”) is directly proportional to the fuel areal density for DT-filled targets.⁹ Since the elastic scattering of the 14-MeV DT neutrons off the background fuel ions produces these particles, these diagnostics are relatively insensitive to the location of the fuel and therefore mix. A forward-scattered peak in the particle spectrum characterizes this diagnostic. The number of knock-on particles in this forward-scattered peak is expected to be a constant fraction of the total produced and therefore provides a measure of the total fuel areal density. Detailed knock-on particle spectra have been measured using the CPS and used to infer areal density in DT-filled targets.¹⁰

In addition to the plastic shells mentioned above, direct information regarding the clean core of fuel and the mixing of the fuel and shell can be obtained from plastic-shell implosions

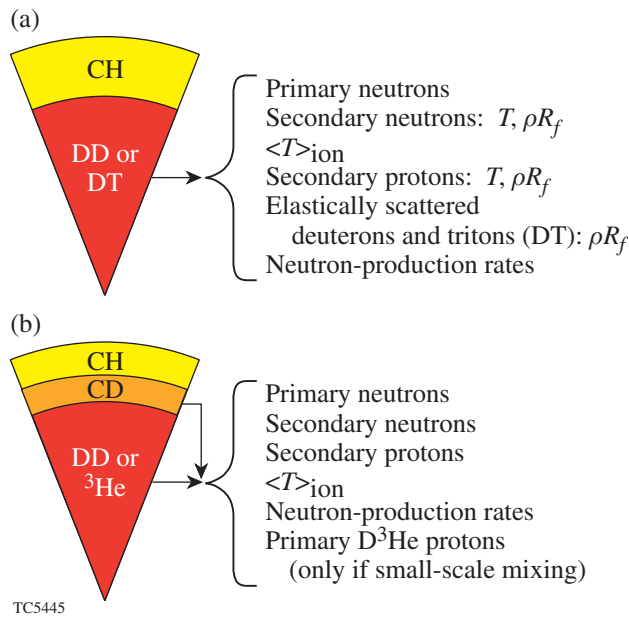


Figure 86.29 A large suite of diagnostics has been brought to bear on plastic shells with and without CD layers and with different gas fills. The different targets and the observables that are characteristic of the targets are shown.

with an embedded CD layer and with ^3He fill [Fig. 86.29(b)]. With a CD layer an observable signal of primary D^3He protons is produced when a significant number of deuterons from the CD layer come into contact with the ^3He in the fuel. Again, the proton yield is measured using the CPS. Preliminary experiments have used targets with the CD layer at both the fuel–shell interface and a distance of $1\ \mu\text{m}$ displaced from this interface.

Evidence of Mixing and the Mix Model

A comparison of particle yields with those from 1-D simulations using *LILAC*¹¹ suggests mixing of the fuel and shell. Figure 86.30 shows experimental observables and results from the corresponding 1-D simulations that contain no effects of mixing. The relatively model independent knock-ons indicate fuel areal densities of $15\ \text{mg}/\text{cm}^2$, nearly 93% of 1-D values. Figure 86.30 also indicates, however, that the neutron yields from the DD reaction are only about 33% of 1-D. One explanation for this reduction in the yield is the mixing of cold shell material into the hot fuel. The fuel consequently cools, quenching the yield. In the unmixed 1-D simulations, most of the neutron yield is produced at a radius that is about two-thirds the distance from the fuel–shell interface. Therefore, a small amount of mixing can considerably lower temperatures in this region and consequently quench the yield. Secondary neutron ratios that are higher in the experiment than in the simulations can also be explained using the same mixing scenario. In this case, the lower temperatures result in a larger slowing down of the intermediate tritons, and the resultant higher cross section

enhances the secondary neutron yield relative to unmixed 1-D simulations. Finally, direct evidence from experiment for small-scale mixing has been obtained from plastic shells with a $1\text{-}\mu\text{m}$ CD layer at the fuel–shell interface. With a ^3He fill, proton yields from the D^3He reaction are produced only if the ^3He is mixed with the deuterium from the CD layer. *LILAC* simulations with a ^3He gas fill, in principle, give zero yields for these protons. A conservative estimate of the proton yield can be obtained by assuming that the ^3He gas is isobarically diffused throughout the shell. The measured yields are nearly 50,000% higher than the simulation values, indicating the occurrence of small-scale mix.

The model used to describe the results presented above assumes a clean fuel region and a mixed region consisting of both fuel and shell material (Fig. 86.31). The mass of the fuel is fixed and corresponds to that of 15 atm of gas fill. Density and temperature are assumed to be constant in the clean fuel region and vary linearly in the mixed region. Further, the temperatures of the electrons and ions are assumed to be the same. This approximation can be justified since the equilibration time for electron and ion temperatures at these conditions is typically less than 5 ps. The model (Fig. 86.31) is described by six parameters (five free parameters since the mass of the fuel is known): the radius of the clean fuel region, the density of the clean region, the radius of the mixed region, the density of the shell material at the outer edge of the mix region, the temperature of the fuel in the clean region, and the temperature

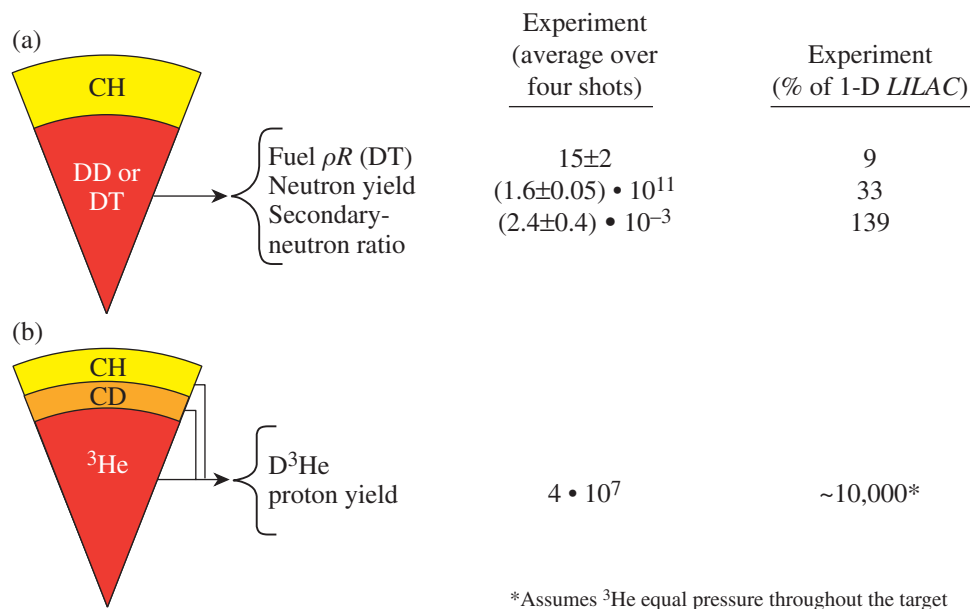


Figure 86.30
Evidence for mixing: primary yields and secondary ratios suggest mixing of the fuel and the shell. Despite a smaller inferred fuel areal density in the experiment, the secondary neutron yield ratio is higher than in 1-D simulations. Direct evidence for mixing comes from the enhanced D^3He proton yield relative to 1-D simulations for the ^3He -filled targets.

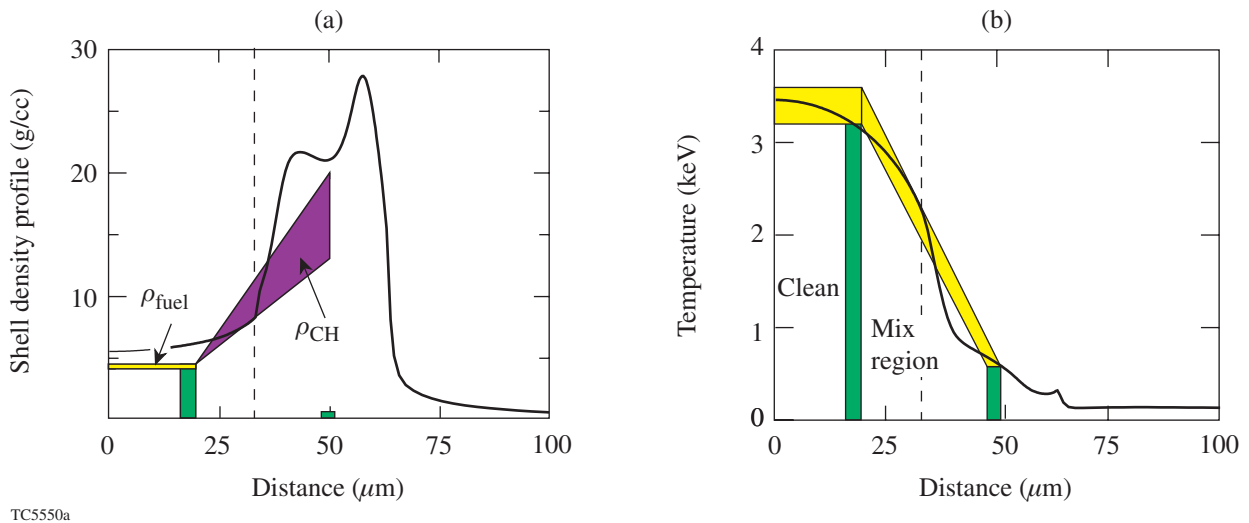
TC5446

of the shell material at the outer edge of the mixed region. Operationally, using the mass and a guess for the total and clean fuel areal density, one uniquely solves for the two radii and fuel density. A guess for the shell mass in the mixed region is made, which uniquely determines the shell-density profile. The guesses for the two fuel areal densities, the shell mass, and the temperatures are varied, and for each static model the yields for the secondary neutron and proton reactions, the neutron-production rates, and the neutron-averaged ion temperatures are calculated. This is repeated until good agreement with experimental data is obtained. The yields from the ^3He -filled targets are calculated using the optimal profiles and by replacing the DD or DT fuel with ^3He .

Particle yields are calculated using the Monte Carlo particle-tracking code *IRIS*. *IRIS* tracks particles in straight-line trajectories on a spherically symmetric mesh. Products of primary reactions are launched based on the location of the fuel and temperature and density distributions in the target. Secondary reactions are produced along primary trajectories, and secondary trajectories in turn are launched according to the differential cross section of the reaction. The energy loss of charged particles is continuous; the trajectory is divided into smaller sections, and at the end of each section the energy of the particle is updated, accounting for its energy loss over that

section. *IRIS* runs in the so-called “embarrassingly parallel” mode on an SGI Origin 2000 machine using MPI.¹² In this mode an identical copy of *IRIS* is placed on each processor, and, at the end of the simulation, yields and spectra are tallied.

The optimal profiles from this parameter variation are shown in Fig. 86.31. The profiles from the corresponding *LILAC* simulation at peak particle production are also overlaid on the figure. The narrow ranges on the figure indicate the tight constraints on the model parameters. For this set of parameters, which reproduces experimental data, the fuel areal density is distributed approximately equally between the clean and mixed regions. The shell mass in the mixing region [Fig. 86.31(a)] corresponds to a 0.5- to 1- μm -thick layer of the initial shell material mixing into the fuel region; the optimum fit occurs with about 1 μm of mixing. This shell areal density in the mixed region is about 20% of the compressed shell areal density inferred from other diagnostics such as the energy loss of the D^3He proton from the D^3He -filled targets.⁴ The density and temperature profiles compare very well with those from simulation, suggesting that these implosions are nearly 1-D in their compression; a small amount of mixing redistributes material near the fuel-shell interface without significantly altering the hydrodynamics of the implosion.



TC5550a

Figure 86.31

Core and fuel-shell mix density (a) and temperature (b) profiles inferred from the mix model. The range of the parameters, which is consistent with experimental observables, is shown by the width of the various parameter bands. The fuel-shell interface predicted by *LILAC* is shown as a dotted line in both. The dark solid lines represent the *LILAC*-predicted density and temperature profiles at peak neutron production.

The yields from the optimal profile are compared to experimental observables in Table 86.II. The model reproduces the experimental fuel areal densities, secondary neutron, proton ratio, and the neutron-averaged ion temperature. The time-dependent burn rate is also measured using the neutron temporal diagnostic (NTD)¹³ in the experiment. The burn rate in this static model is less than the maximum measured burn rate. A burn width for DD-filled targets can be calculated using the experimental DD yield and the burn rate in the static model for different fills. For instance, for the ³He fill in CD layer targets, this calculated burn width from DD targets is used to obtain yields from the static model. These yields are also in good agreement with the data.

Further evidence supporting this model has been obtained from recent implosion experiments on a 20- μm CH shell with a ³He gas fill and with a 1- μm CD layer offset from the fuel-shell interface by 1 μm . The D³He proton yields measured from this implosion are reduced significantly relative to the zero-offset CD layer implosion (preliminary proton yield $\sim 7 \times 10^5$ compared to 1×10^7 for the zero-offset case). The significantly lower number suggests that more than 90% of the mix-related yield is due to approximately 1 μm of the initial shell mixing into the fuel.

Pre-existing modes at the inner surface of the plastic shell and/or feedthrough of these modes have been considered earlier as possible sources of nonuniformities during the deceleration phase of ICF implosions.¹⁴ Multidimensional simulations, currently being pursued, are necessary to determine if feedthrough of the higher-order modes is significant for implosions on OMEGA and if the subsequent RT growth can account for the relatively small scales inferred from the experiments.

Conclusions

A large set of direct-drive implosions on OMEGA has been devoted to imploding hydrodynamically similar implosions with different gas fills and shell compositions. A complementary set of diagnostics has been obtained from such implosions, allowing for a more detailed analysis of the core and mix region of these targets. A static picture of 20- μm -thick-shell, direct-drive implosions on OMEGA has been presented. This model assumes a clean fuel region and a “mix” region where the shell material is mixed into the fuel. Excellent agreement with the suite of neutron and particle diagnostics is obtained through such a model. The model suggests that about 1 μm of the initial shell material is mixed into the fuel during nuclear-particle production and is responsible for the observed yield ratios. The model also suggests that the fuel areal density is distributed

Table 86.II: The model reproduces many experimental observables with 1 μm of shell material mixed into the fuel.

Fill	Shell	Parameter	Measurement	Model (% of expt)
DT	CH	Fuel ρR (mg/cm ²) (DT fill)	15 \pm 2	100
		T_{ion} (DT) (keV)	4.4 \pm 0.4 \pm 0.5 (sys)	86
D ₂	CH	Max: neutron burn rate (n/s)	(9 \pm 1) $\times 10^{20}$	110
		T_{ion} (D ₂) (keV)	3.7 \pm 0.2 \pm 0.5 (sys)	89
		Secondary neutron ratio (DD fill)	(2.4 \pm 0.4) $\times 10^{-3}$	100
		Secondary proton ratio (DD fill)	(1.8 \pm 0.3) $\times 10^{-3}$	78
³ He or D ₂	CD CH	Secondary neutron ratio (D ₂ fill)	(3.1 \pm 0.5) $\times 10^{-3}$	94
		D ³ He proton yield (³ He fill)	(1.3 \pm 0.2) $\times 10^7$	66
		D ₂ neutron yield (³ He fill)	(8.5 \pm 0.4) $\times 10^8$	97

equally between the clean core and the fuel–shell mix region. The density and temperature profiles of the core and the mix region obtained from this model compare very well with those from 1-D simulations without any mixing, suggesting that the mixing in these implosions does not significantly alter the 1-D, unmixed hydrodynamics of the implosion. This work will be extended to targets with different stability characteristics such as those with thicker shells, lower fill pressures, and different laser pulse shapes. Comparisons of this model with x-ray observables will also be performed in the future.

ACKNOWLEDGMENT

This work was supported by the U.S. Department of Energy Office of Inertial Confinement Fusion under Cooperative Agreement No. DE-FC03-92SF19460, the University of Rochester, and the New York State Energy Research and Development Authority. The support of DOE does not constitute an endorsement by DOE of the views expressed in this article.

REFERENCES

1. T. R. Boehly, D. L. Brown, R. S. Craxton, R. L. Keck, J. P. Knauer, J. H. Kelly, T. J. Kessler, S. A. Kumpan, S. J. Loucks, S. A. Letzring, F. J. Marshall, R. L. McCrory, S. F. B. Morse, W. Seka, J. M. Soures, and C. P. Verdon, *Opt. Commun.* **133**, 495 (1997).
2. P. W. McKenty, V. N. Goncharov, R. P. J. Town, S. Skupsky, R. Betti, and R. L. McCrory, *Phys. Plasmas* **8**, 2315 (2001).
3. Lord Rayleigh, *Proc. London Math Soc.* **XIV**, 170 (1883); G. Taylor, *Proc. R. Soc. London Ser. A* **201**, 192 (1950); R. Betti, V. N. Goncharov, R. L. McCrory, P. Sorotokin, and C. P. Verdon, *Phys. Plasmas* **3**, 2122 (1996) (and references therein).
4. D. D. Meyerhofer, J. A. Delettrez, R. Epstein, V. Yu. Glebov, V. N. Goncharov, R. L. Keck, R. L. McCrory, P. W. McKenty, F. J. Marshall, P. B. Radha, S. P. Regan, S. Roberts, W. Seka, S. Skupsky, V. A. Smalyuk, C. Sorce, C. Stoeckl, J. M. Soures, R. P. J. Town, B. Yaakobi, J. D. Zuegel, J. Frenje, C. K. Li, R. D. Petrasso, D. G. Hicks, F. H. Séguin, K. Fletcher, S. Padalino, M. R. Freeman, N. Izumi, R. Lerche, T. W. Phillips, and T. C. Sangster, *Phys. Plasmas* **8**, 2251 (2001); see also Laboratory for Laser Energetics LLE Review **84**, 191, NTIS document No. DOE/SF/19460-371 (2000). Copies may be obtained from the National Technical Information Service, Springfield, VA 22161.
5. Laboratory for Laser Energetics LLE Review **82**, 49, NTIS document No. DOE/SF/19460-344 (2000). Copies may be obtained from the National Technical Information Service, Springfield, VA 22161.
6. E. G. Gamalii *et al.*, *JETP Lett.* **21**, 70 (1975); T. E. Blue and D. B. Harris, *Nucl. Sci. Eng.* **77**, 463 (1981); T. E. Blue *et al.*, *J. Appl. Phys.* **54**, 615 (1983).
7. V. Yu. Glebov, D. D. Meyerhofer, C. Stoeckl, and J. D. Zuegel, *Rev. Sci. Instrum.* **72**, 824 (2001).
8. F. H. Séguin, C. K. Li, D. G. Hicks, J. A. Frenje, K. M. Green, R. D. Petrasso, J. M. Soures, D. D. Meyerhofer, V. Yu. Glebov, C. Stoeckl, P. B. Radha, S. Roberts, C. Sorce, T. C. Sangster, M. D. Cable, S. Padalino, and K. Fletcher, "Using Secondary Proton Spectra to Study Imploded D₂-Filled Capsules at the OMEGA Laser Facility," submitted to *Physics of Plasmas*.
9. S. Skupsky and S. Kacenjar, *J. Appl. Phys.* **52**, 2608 (1981); P. B. Radha, S. Skupsky, R. D. Petrasso, and J. M. Soures, *Phys. Plasmas* **7**, 1531 (2000).
10. C. K. Li, D. G. Hicks, F. H. Séguin, J. A. Frenje, K. Green, R. D. Petrasso, D. D. Meyerhofer, J. M. Soures, V. Yu. Glebov, P. B. Radha, S. Skupsky, C. Stoeckl, S. Roberts, and T. C. Sangster, "Study of Direct-Drive, DT-Gas-Filled-Plastic-Capsule Implosions Using Nuclear Diagnostics on OMEGA," submitted to *Physics of Plasmas*.
11. M. C. Richardson, P. W. McKenty, F. J. Marshall, C. P. Verdon, J. M. Soures, R. L. McCrory, O. Barnouin, R. S. Craxton, J. Delettrez, R. L. Hutchison, P. A. Jaanimagi, R. Keck, T. Kessler, H. Kim, S. A. Letzring, D. M. Roback, W. Seka, S. Skupsky, B. Yaakobi, S. M. Lane, and S. Prussin, in *Laser Interaction and Related Plasma Phenomena*, edited by H. Hora and G. H. Miley (Plenum Publishing, New York, 1986), Vol. 7, pp. 421–448.
12. MPI Version 1.2 Standard for IRIX—a communication language for parallel processing (Internet address: <http://www.mpi-forum.org>) (2001).
13. R. A. Lerche, D. W. Phillion, and G. L. Tietbohl, *Rev. Sci. Instrum.* **66**, 933 (1995).
14. J. Lindl, *Phys. Plasmas* **2**, 3933 (1995).

High-Resolution Neutron Imaging of Laser-Imploded DT Targets

Imaging the neutrons produced by implosions at the National Ignition Facility¹ or the Laser Mega Joule² will require spatial resolution as good as $5\ \mu\text{m}$ (Ref. 3) to identify failure mechanisms such as poor implosion symmetry or improper laser pulse shaping. An important step to achieving this goal is reported in this article. Neutron images were obtained from OMEGA implosions with both high resolution and narrow diameters that confirm the resolution and agree with calculations. Ress *et al.*⁴ obtained the first neutron images of ICF capsules with a geometric resolution of $80\ \mu\text{m}$ and a full width at half-maximum (FWHM) of $150\ \mu\text{m}$. Delage *et al.*⁵ reported geometrical resolution of $56\ \mu\text{m}$ and overall resolutions of 100 to $180\ \mu\text{m}$ with FWHM's of 150 to $250\ \mu\text{m}$. The measurements reported in this article [carried out on LLE's OMEGA laser by a team of scientists from Commissariat à l'Énergie Atomique (CEA), LLE, and LANL] achieved a geometrical resolution of $30\ \mu\text{m}$ and an overall resolution of $45\ \mu\text{m}$ with a FWHM of $62\ \mu\text{m}$.

Imaging neutrons at high resolution is a challenging task being carried out at several laboratories using pinhole⁶ or penumbral apertures. CEA's experimental system using the penumbral technique,⁷ as well as a new analytical approach for estimating the overall resolution, was successfully tested on OMEGA in a direct-drive experiment. The basis of the design is to use an aperture whose diameter is large compared to the size of the neutron source. The shape of the aperture is biconical and is optimized in order to amplify the penumbra of the source in the image plane. The aperture is larger than that for a pinhole, allowing easier fabrication and stronger signals, especially important when signal levels are low. An unfolding process is needed, however, to recover an image; this process includes low bandpass filtering, which affects the resolution. This article reviews the main mechanisms that limit the spatial resolution of a penumbral imaging system: the spatial resolution of the detector, the shape of the aperture, and the process of unfolding the image.

After propagating through the experimental chamber and target area and scattering from various experimental hardware

and structures, the 14-MeV neutrons arriving at the detector are spread in time and angle. Moreover, these neutrons create a large number of gamma rays in the 0- to 10-MeV range by (n, γ) reactions on the experimental hardware. The direct neutrons that form the image need to be discriminated from the scattered neutrons and the gamma rays. Bubble detectors⁸ can discriminate among gamma rays, low-energy neutrons, and 14-MeV neutrons. They offer potentially high spatial resolution, but their efficiency is still very low (1.4×10^{-5}) and they require a sophisticated readout system.

Plastic scintillators with response times of the order of 10 ns can discriminate particles by arrival time. The detector contains 8000 scintillating fibers, each with a length of 10 cm, a square section of $1.5\ \text{mm}^2$, and an e -fold decay time of 12 ns. The intrinsic detection efficiency ε is 27%. The sampling theorem limits the spatial resolution of the instrument to a geometrical resolution of $2\delta_{\text{pix}}/G$, where G is the magnification ratio of the system and δ_{pix} is the pixel size.

In a plastic scintillator, fast neutrons interact mainly by elastic scattering on hydrogen. The high-energy protons lose energy in the medium (calculated with the Birks model⁹) and produce light about the scattering point with a FWHM of $0.910\ \text{mm}$ (δ_{rec}).¹⁰ This limits the resolution of the system to δ_{rec}/G . This intrinsic limitation required a high magnification ratio to achieve a high-resolution design.

The image is relayed optically by a mirror and a lens from the detector onto a gated microchannel plate (MCP); the output image of the MCP is reduced by a fiber-optics taper and then recorded on a charge-coupled device (CCD) with a $19\text{-}\mu\text{m}$ pixel size. The CCD is shielded by a 25-cm-thick piece of plastic followed by 5 cm of lead. At 8 m from the source, the external dose of 12 mrad for a 10^{14} neutron yield is reduced to several mrad inside the shield (an upper acceptable limit for the CCD). The detector image size is reduced to 0.27 and 0.068 of its original dimension onto the MCP and the CCD, respectively. Each fiber of the detector is recorded on the average onto a 5-by-5 array of CCD pixels. The spatial resolution of the

MCP is $70 \mu\text{m}$ at FWHM, much smaller than the size of the detector pixel imaged onto the MCP ($405 \mu\text{m}$). We conclude that the spatial resolution of our recording system is negligible compared to the spatial resolution of the detector.

The point-spread function (PSF) of the aperture is the neutron intensity distribution in the image plane for an isotropic point source located in the middle of the field of view. For a given entrance hole diameter, this PSF depends only on the field of view and the distance from the source. Figure 86.32 shows dependence of the FWHM (δ_{bic}) of the PSF on the distance from the middle of the aperture to the target (L_0). Increasing the distance from the source to the aperture can improve the spatial resolution to less than $10 \mu\text{m}$. For these experiments, however, the magnification ratio decreases with L_0 because the distance between the source and the scintillator (L_i) is limited to 8 m. An optimal value for L_0 , including the resolution of the detector, is found to be 80 mm.

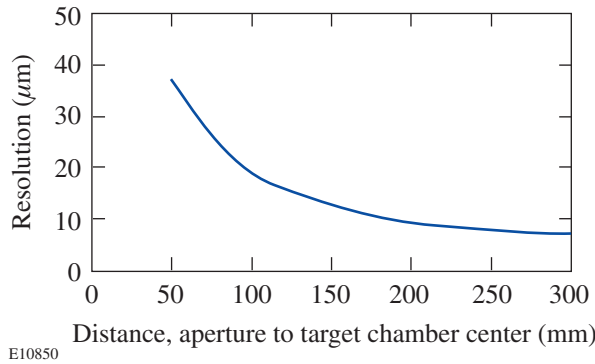


Figure 86.32

The spatial resolution limit (FWHM of the point-spread function) for the biconical aperture versus the distance (L_0) from its center to the source.

A hole was recently dug in the concrete floor of the OMEGA Target Bay to allow a 13-m line of sight. A new detector will be installed with $250\text{-}\mu\text{m}$ -diam capillaries filled with deuterated liquid scintillator. The new $250\text{-}\mu\text{m}$ pixel size and estimated δ_{rec} of $500 \mu\text{m}$ lead to a redesigned aperture placed at $L_0 = 160$ mm. These modifications should reduce the noise background by a factor of 100 and allow a $13\text{-}\mu\text{m}$ resolution.

Several methods exist to unfold penumbral images.¹¹ After testing these methods on synthetic penumbral images, the autocorrelation method¹² was found to give the best results with minimum mathematical complexity. Most penumbral unfolding processes assume that the aperture can be repre-

sented by a thin hole of radius R_d surrounded by a medium with a transmission τ to neutrons. With this assumption, the Fourier transform I of the image is the product of the Fourier transform S of the source and the aperture: $I(k) = S J_1(2\pi k R_d) / \pi k R_d$, where J_1 is the first-order Bessel function. The unfolding process consists of multiplying I by a function U , which has the following mathematical properties: inverse Fourier transform $[U J_1(2\pi k R_d) / \pi k R_d] = \delta$, the Dirac function, and a small amplitude oscillatory function at radius $2R_d$, which is outside the field of view. We find $U = 2J_1(2\pi k R_d) k^3 / \pi k R_d$. The multiplication of I by U gives the Fourier transform of the source image, avoiding any problems caused by dividing by zero.

In practice, the unfolded Fourier transform of the image contains both noise and the signal from the spatial distribution of the neutron source. The primary source of noise is the Poisson statistics of events in the detector. Reducing this noise requires a low band-pass filtration that limits overall design performance. A reliable criterion to find the frequency at which noise starts to dominate is to set the noise power spectrum equal to the power spectrum of the signal without noise.¹³

For Poisson noise, it can be shown that the power spectrum of the image with noise, P_{s+n} , is the sum of the power spectrum of the image without noise, P_s , and the spectrum N_s of the number of detected neutrons in the full field of the image.¹⁴ For an homogeneous neutron source of radius R_s and yield N , we have

$$N_s = \frac{\varepsilon N G^2}{4(L_i + L_0)^2} \left[(1 - \tau) R_d^2 + \tau (R_d + R_s)^2 \right],$$

$$P_s = \left[\frac{\varepsilon (1 - \tau) N R_d^2 G^2}{4(L_i + L_0)^2} \frac{J_1(2\pi k R_d)}{\pi k R_d} \frac{J_1(2\pi k R_s)}{\pi k R_s} \right]^2.$$

Using the first-order approximation of the Bessel function valid for $k R_{d,s}$ greater than about 1.2 (appropriate for penumbral imaging), the equation $P_s = N_s$ gives the cutoff frequency k_c :

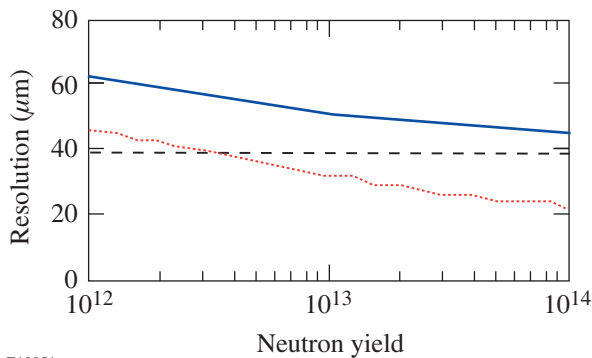
$$k_c = \frac{1}{\pi} \sqrt[6]{\frac{\varepsilon N G^2}{4\pi(L_i + L_0)} \frac{(1 - \tau)^2}{\left[(1 - \tau) R_d^2 + \tau (R_d + R_s)^2 \right]} \frac{R_d}{\pi R_s^3}}. \quad (1)$$

The spatial spectrum of the signal beyond the cutoff frequency is within one standard deviation of the noise. Recovering signal information beyond k_c requires sophisticated filtering.¹² In our design, $1/k_c$ is used as a preliminary estimation of the limit of spatial resolution due to the signal-to-noise ratio and the unfolding process.

Combining the effects of statistics on resolution, the shape of the aperture, the pixel size, and the recoil proton range leads to an estimation of the overall spatial resolution δ_s :

$$\delta_s = \sqrt{\frac{1}{k_c^2} + \delta_{\text{bic}}^2 + \left(\frac{2\delta_{\text{pix}}}{G}\right)^2 + \left(\frac{\delta_{\text{rec}}}{G}\right)^2}. \quad (2)$$

Figure 86.33 shows the variation of the overall spatial resolution for neutron yield between 10^{12} and 10^{14} and for a neutron source size of $50\text{-}\mu\text{m}$ diameter. For a high-yield shot, the spatial resolution is $45\text{ }\mu\text{m}$, dominated by the sampling limit ($30\text{ }\mu\text{m}$) and the PSF of the aperture ($24\text{ }\mu\text{m}$) (dotted curve of Fig. 86.33). The design is unable to resolve spatial variation of such a source because the resolution and the source size are comparable. A neutron source size of $100\text{-}\mu\text{m}$ diameter, however, can be differentiated from one of $50\text{ }\mu\text{m}$.



E10851

Figure 86.33 The instrument’s contributions to the spatial resolution versus the neutron yield; overall resolution (solid), spatial resolution limit due to the cutoff frequency k_c (dashed) for a $50\text{-}\mu\text{m}$ -diam neutron source, and spatial resolution limit (dotted).

Correct alignment is crucial to the experiment. A straight reference line is established between a $400\text{-}\mu\text{m}$ -diam, back-lighted sphere at target chamber center and an autocollimator near the detector. The penumbral aperture axis is made colinear to an accuracy of 0.1 mrad using an attached, prealigned half reflecting plate. The aperture is then centered on the back-

lighted sphere to an accuracy of $50\text{ }\mu\text{m}$. The alignment procedure takes at least 2 h for a trained experimentalist to complete.

Several operations are conducted on the raw penumbral image before it is unfolded. First, the average of the CCD backgrounds before and after the shot is subtracted. Then CCD pixels in which neutrons or gamma rays have interacted directly are detected by amplitude discrimination and replaced by the average value of the neighboring pixels. This eliminates CCD pixels that have values more than three times higher than the standard variation of the local average signal; however, CCD pixels where neutrons or gamma rays have created comparable or lower levels than the signal coming from the scintillator still remain. Several shots are also acquired without the aperture. The average of these images is used to correct the image for the spatial variation of the response of the detector and the recording system.

Figure 86.34 shows an unfolded image; Figs. 86.35 and 86.36 show the profiles obtained from the implosions (shots 21054 and 20290) of two glass microballoons filled with 20 atm of DT driven by 1-ns square laser pulses. The shells had thicknesses of $4.2\text{ }\mu\text{m}$ and $2.5\text{ }\mu\text{m}$, diameters of $890\text{ }\mu\text{m}$ and $920\text{ }\mu\text{m}$, and laser energies of 23.1 kJ and 31.1 kJ; they produced yields of 3.6 and 6×10^{13} neutrons, with measured ion temperatures of 10.3 and $\sim 9\text{ keV}$. The FWHM of the measured neutron source sizes is $62\text{ }\mu\text{m}$ (21054) and $78\text{ }\mu\text{m}$ (20290), respectively. The filter processing limits the minimum detail that can be resolved to $45\text{ }\mu\text{m}$ for shot 21054 and

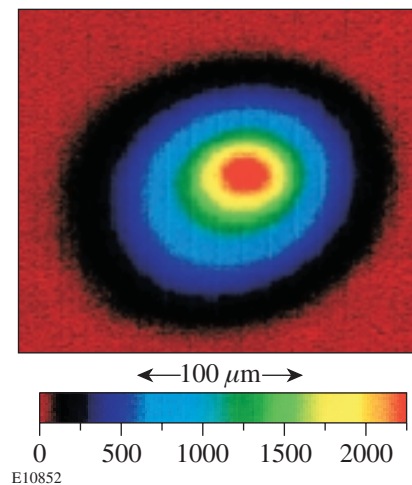
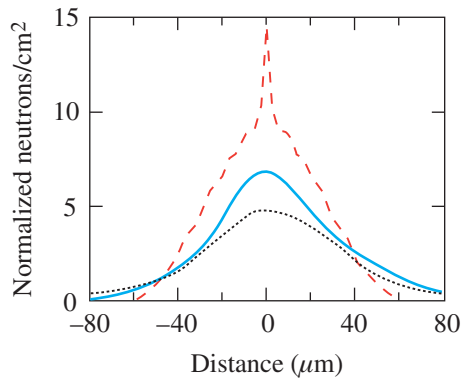


Figure 86.34 Unfolded image of shot 21054 showing a slight asymmetry.

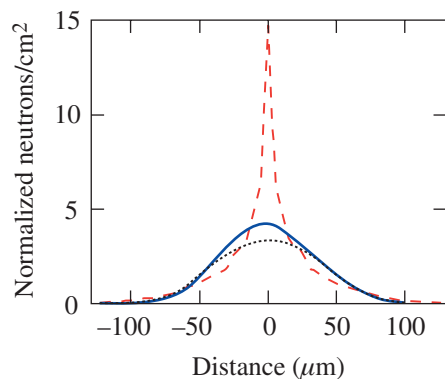
53 μm for shot 20290. These values are in agreement with the expected performance calculated with Eq. (2) (see Fig. 86.33). For comparable neutron yield, the diagnostic resolution performance is better when the source size is smaller, as predicted by Eq. (1).

One-dimensional calculations of these implosions with a radiation-hydrodynamic code¹⁵ were postprocessed using a neutron transport code to produce the calculated neutron image profiles shown in Figs. 86.35 and 86.36. These images were then processed to include the effects of noise by first calculat-



E10853

Figure 86.35
Horizontal lineout (solid) of a DT capsule with a 4.2- μm -thick glass shell (shot 21054) compared to calculated profiles without (dashed) and with (dotted) the effects of experimental noise.



E10854

Figure 86.36
Horizontal lineout (solid) of a DT capsule with a 2.5- μm -thick SiO_2 glass shell (shot 20290) compared to calculated profiles without (dashed) and with (dotted) the effects of experimental noise.

ing a simulated penumbral image, then adding Poisson noise at the level seen in the experiments, and finally deconvolving and smoothing using the same process as used for the data. The resulting profiles in both cases are within the experimental resolution of the observed profiles (all profiles are normalized in 2-D to the same integral). The implosion of the capsule with a 4.2- μm -thick wall had a calculated convergence ratio (initial fuel radius/final fuel radius) of 9, producing the smaller source. The implosion of the capsule with a 2- μm -thick wall was very similar to that of Ress *et al.*⁴ (capsule with a 2- μm wall, 1000- μm diameter, 25 atm DT, 20-kJ laser energy, 1-ns square pulse, convergence ratio of <3 , neutron yield of $\sim 10^{13}$, and a 9-keV ion temperature). Both capsules were calculated to produce an image with a strong central peak. We find that the inclusion of instrumental resolution, which Ress *et al.*⁴ did not address, explains the lack of an observed peak in our data. Our smaller observed FWHM of 78 μm compared to their 150 μm reflects the higher resolution of our imaging system as well as the better irradiation symmetry of OMEGA's 60 beams compared to Nova's 10 beams.

ACKNOWLEDGMENT

We would like to acknowledge the assistance of the OMEGA laser team in executing these experiments, and General Atomics and Los Alamos National Laboratory for fabricating and filling the DT capsules. These experiments were carried out in collaboration and participation of many people, including R. Fisher at General Atomics; S. Chiche, Ph. Millier, C. Ducrocq, C. Labbe, R. Debure, M. C. Monteil, B. Canaud, X. Fortin, and N. Dague at Bruyères le Châtel; S. J. Loucks, J. Mathers, G. Pien, J. Armstrong, and D. D. Meyerhofer at LLE; G. Morgan, F. Cverna, J. Faulkner, M. Wilke, T. Murphy, and C. Barnes at Los Alamos; R. A. Lerche, C. Sangster, and M. Cable at Lawrence Livermore National Laboratory. This work was funded by the Commissariat à l'Énergie Atomique, France, and the US Department of Energy.

REFERENCES

1. J. Paisner *et al.*, Laser Focus World **30**, 75 (1994).
2. P. A. Holstein *et al.*, Laser Part. Beams **17**, 403 (1999).
3. S. M. Pollaine *et al.*, Phys. Plasmas **8**, 2357 (2001).
4. D. Ress *et al.*, Science **241**, 956 (1988).
5. O. Delage *et al.*, Rev. Sci. Instrum. **66**, 1205 (1995).
6. G. L. Morgan *et al.*, Rev. Sci. Instrum. **72**, 865 (2001).
7. J. P. Garçonnet *et al.*, Laser Part. Beams **12**, 563 (1994); R. A. Lerche *et al.*, Laser Part. Beams **9**, 99 (1991).
8. R. K. Fisher *et al.*, Rev. Sci. Instrum. **72**, 796 (2001).

9. J. Birks and D. Fry, *Theory and Practice of Scintillation Counting*, International Series of Monographs in Electronics Instrumentation, Vol. 27 (Pergamon Press, New York, 1964).
10. G. Mosinski and B. Roy, CEA Bruyères le Châtel, Report No. 79/DR 83 (1983).
11. K. A. Nugent and B. Luther-Davies, *Opt. Commun.* **49**, 393 (1984).
12. A. Rouyer, "Unfolding Neutron Penumbral Images Using an Autocorrelation Technique," submitted to *Physical Review Letters*.
13. J. S. Beis, A. Celler, and J. S. Barney, *IEEE Trans. Nucl. Sci.* **42**, 2250 (1995).
14. J. W. Goodman and J. F. Belsher, in *Imaging Through the Atmosphere*, edited by J. C. Wyant (SPIE, Bellingham, WA, 1976), Vol. 75, pp. 141–154.
15. G. B. Zimmerman and W. L. Kruer, *Comments Plasma Phys. Control. Fusion* **2**, 51 (1975).

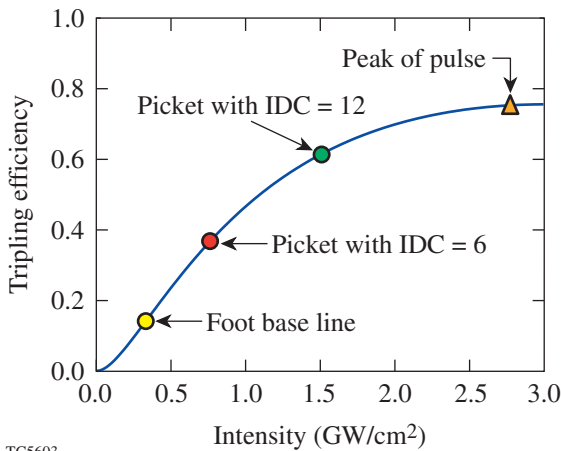
The Smoothing Performance of Ultrafast Pickets on the NIF

Introduction

In the direct-drive approach to inertial confinement fusion (ICF), the focal spots of a symmetrically arranged cluster of high-intensity, ultraviolet (UV) laser beams directly irradiate a capsule.^{1,2} The base-line design for a direct-drive ignition target on the National Ignition Facility (NIF) uses shock preheat to control the isentrope of the ablation surface and the fuel. Control of the isentrope α (where α is the ratio of the fuel pressure to the Fermi-degenerate pressure) is achieved by changing the laser pulse shape. The UV pulse shape corresponding to $\alpha=3$ is chosen for the base-line design. This shape can be logically divided into two regions: a low-intensity “foot” (of duration ~ 4.2 ns) followed by a high-intensity “drive” (duration ~ 5 ns). This pulse shape represents a compromise that provides a certain safety margin for the implosion by reducing the target’s sensitivity to laser nonuniformity by ensuring that the target will remain intact during the drive portion of the pulse; however, laser nonuniformity still re-

mains an important issue. The laser irradiation nonuniformity seeds the Rayleigh–Taylor hydrodynamic instability, which consequently degrades target performance.^{3,4}

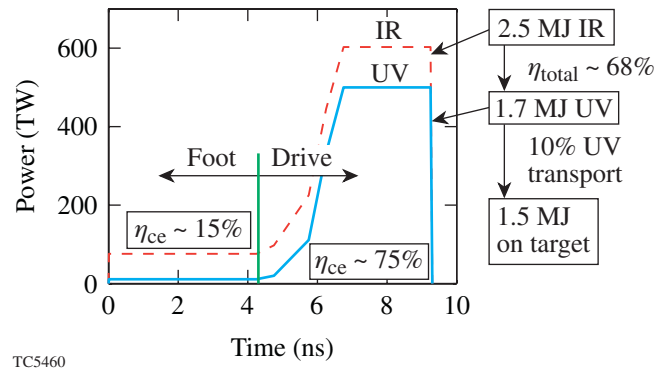
The energy efficiency of the KDP frequency-conversion crystals used in ICF lasers is a function of input intensity; efficiency increases as the third power of input intensity increases until saturation occurs (see Fig. 86.37). Consequently, the low-intensity foot portion of the pulse converts inefficiently and can represent a substantial overall reduction in the laser’s energy efficiency. As shown in Fig. 86.38, an $\alpha=3$, direct-drive pulse has a total infrared (IR) energy of 2.5 MJ and a total UV energy delivered to target of 1.5 MJ (including 10% UV transport losses). The frequency-conversion efficiency in the foot of the $\alpha=3$ pulse is $\sim 15\%$ and $\sim 75\%$ in the drive portion, yielding an overall efficiency of $\sim 68\%$. This issue is even more problematic for the indirect-drive approach, where the overall conversion efficiency is as low as



TC5603

Figure 86.37

The IR to UV frequency-conversion-efficiency curve for the NIF. The drive portions of an $\alpha=3$ ICF pulse converts at efficiencies around 75%, where the efficiency is in saturation. The foot portion of the ICF pulse converts at a low efficiency of 15%. In addition, the frequency-conversion efficiency exhibits a third-power dependence for low-IR input intensity. This exacerbates any beam-to-beam power imbalance during the foot portion of an $\alpha=3$ ICF pulse.



TC5460

Figure 86.38

The $\alpha=3$, direct-drive ICF pulse, which is logically divided into two regions: a low-intensity “foot” (about 4.2 ns) followed by a high-intensity “drive” (about 5 ns). The IR power as a function of time (dashed line) required to produce the desired UV power onto target (solid line). The total IR energy is 2.5 MJ, and the total UV energy delivered to target (accounting for 10% UV transport losses) is 1.5 MJ. The frequency-conversion efficiency is $\sim 15\%$ in the foot and $\sim 75\%$ in the drive, which yields an overall efficiency of $\sim 68\%$.

50% due to a much longer low-intensity foot.⁵ Beam-to-beam power imbalance is also exacerbated for the low-intensity foot because of the third-power dependence of conversion efficiency on intensity at low intensities; during the drive portion of the ICF pulse the conversion efficiency is in saturation at $\sim 75\%$ and does not contribute significantly to beam-to-beam power imbalance.

Ultrafast picket-fence pulses were proposed by Rothenberg⁵ as a way to maximize conversion efficiency and minimize beam-to-beam power imbalance. In this article, we consider the application of the ultrafast pickets only to the foot portion of the $\alpha = 3$ pulse. We assume that the pickets are temporally blended into the drive portion of the pulse. Ultrafast pickets consist of a train of laser pulses with an inverse duty cycle (IDC), which is defined as the ratio of the pulse-repetition period to the pulse width, chosen to maintain near-constant target illumination and a peak intensity that delivers the same average power to the target as when picket-fence modulation is absent. For example, if a pulse train of 20-ps pulses with $\text{IDC} = 6$ is applied to the foot, the peak intensity of each picket can be increased sixfold while maintaining the same average power on target. Increasing the peak intensity sixfold boosts the conversion efficiency of the foot from 15% to 39% and the overall efficiency from 68% to 73% (see Fig. 86.39). (For indirect drive the overall conversion efficiency can be increased from $\sim 50\%$ to $\sim 72\%$ by using ultrafast pickets.⁵) For a pulse train of 10-ps pulse with $\text{IDC} = 12$, the efficiency of the foot is increased to 51% with an overall efficiency of 74%. The benefit of this shorter pulse is the minimized affect on beam-to-beam power imbalance as seen in Fig. 86.37.

The goal of this investigation is to assess the impact and benefits of implementing ultrafast pickets for direct-drive capsules on the NIF. The smoothing performance (defined as the time-integrated laser nonuniformity as a function of time) is the metric used to compare the ultrafast-picket-fence scheme to that of base-line 2-D SSD on the NIF. Various beam-smoothing techniques to be employed on the NIF are similar to those employed on the OMEGA^{6,7} laser to improve on-target laser uniformity, which reduces laser imprint. These techniques include two-dimensional smoothing by spectral dispersion (2-D SSD),^{8–10} distributed phase plates (DPP's),^{11,12} polarization smoothing,^{6,13,14} and multiple-beam overlap.

The code *Waaikwa*'¹⁵ is used to calculate the time evolution of the far field and the single-beam time-integrated laser nonuniformity for the first 3 ns of the foot. *Waaikwa*' will be

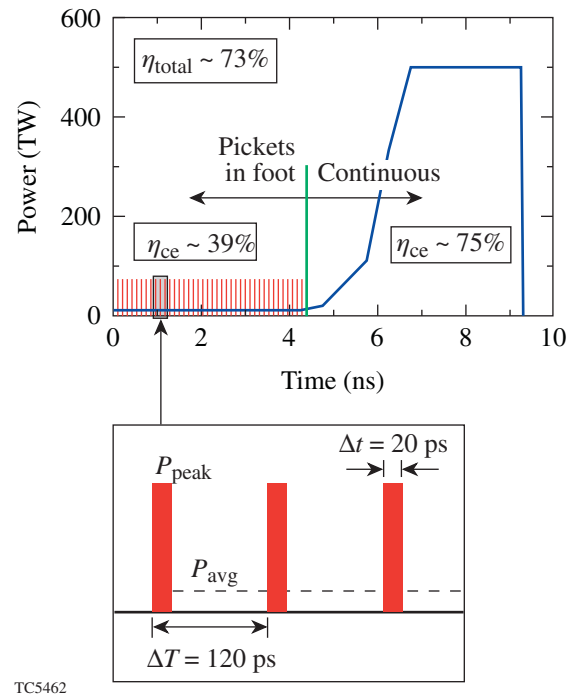


Figure 86.39

The UV power of an $\alpha = 3$, direct-drive pulse with ultrafast pickets applied during the foot. The frequency-conversion efficiency has been increased in the foot from 15% to $\sim 39\%$, which yields an overall efficiency of $\sim 73\%$.

used under a variety of near-field conditions that describe the base-line 2-D SSD system as well as various ultrafast-picket configurations. The calculated single-beam, time-dependent, laser nonuniformity will be used as the basis of comparison.

In the following sections we describe the base-line 2-D SSD system, the generation of an ultrafast picket pulse train, the far-field characteristics of ultrafast pickets, the smoothing performance, and conclusions.

Base-Line 2-D SSD

The 2-D SSD system on the NIF is similar to that on OMEGA with one exception: only one grating is used in the first SSD dimension on the NIF because it is implemented with a fiber-optic-based phase modulator. As a result, the beam suffers a residual time shear. OMEGA utilizes a bulk phase modulator in the first dimension so it can precompensate for this shear (compare Ref. 16). The second SSD dimension on the NIF has two gratings, like OMEGA. A schematic of the NIF's 2-D SSD design is shown in Fig. 86.40.

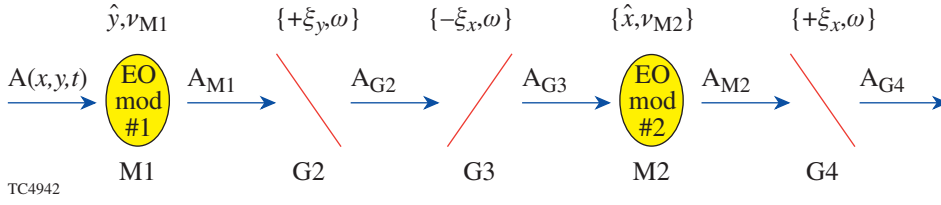


Figure 86.40

A schematic representation of the NIF's 2-D SSD system. Notice that the first dimension has only one grating, which causes a residual temporal shear across the beam.

The spatiotemporal evolution the complex-valued UV electric field of a 2-D SSD pulsed beam can be expressed as

$$E(x, y, t) \equiv E_0(x, y, t) e^{i\phi_{2\text{-D SSD}}(x, y, t)} e^{i\phi_{\text{DPP}}(x, y)}, \quad (1)$$

where $E_0(x, y, t)$ defines the electric field's pulse and beam shape, $\phi_{2\text{-D SSD}}$ is the 2-D SSD phase contribution, and $\phi_{\text{DPP}}(x, y)$ is the static DPP phase contribution. The mapping of the DPP phase contribution was designed to yield a far-field intensity distribution of an eighth-order super-Gaussian with a 95% enclosed energy contour of 3.40-mm diameter in the target plane. For these simulations, the fundamental spatial and temporal shapes of the pulsed beam are assumed to be separable prior to the 2-D SSD operation. The uncompensated grating operation distorts this fundamental shape and can be written as

$$E_0(x, y, t) \equiv G\{\text{beam}(x, y) \cdot \text{pulse}(t)\}, \quad (2)$$

where $\text{beam}(x, y)$ is the near-field beam shape, $\text{pulse}(t)$ is the temporal pulse shape, and $G\{\bullet\}$ represents an uncompensated grating operator, which is defined by

$$G\{f(x, y, t)\} \equiv f(x, y, \zeta), \quad (3)$$

where the spatially coupled time domain is given by $\zeta \equiv t - \xi_y y$ and ξ_y is the angular grating dispersion (see Ref. 16 for a detailed examination of the angular spectrum representation of the 2-D SSD operation). As a consequence of the assumed separability, the uncompensated grating operation couples the temporal pulse shape to the spatial dimension corresponding to the first SSD dimension while the spatial beam shape remains unaltered and is given by

$$E_0(x, y, t) \equiv \text{beam}(x, y) \cdot \text{pulse}(t - \xi_y y). \quad (4)$$

For the *Waasikwa*' simulations the fundamental beam shape at the final magnification is defined as a square-shaped 20th-order super-Gaussian:

$$\begin{aligned} \text{beam}(x, y) \equiv & \exp\left[-\ln(2)\left(\frac{|x|}{30.8 \text{ cm}}\right)^{20}\right] \\ & \times \exp\left[-\ln(2)\left(\frac{|y|}{30.8 \text{ cm}}\right)^{20}\right], \quad (5) \end{aligned}$$

which has an intensity full-width half-maximum (FWHM) width in each direction of $D_{\text{FWHM}} = 30.8 \text{ cm}$ and a 95% enclosed energy contour with a width in each direction of $D_{\text{NIF}} = 35.1 \text{ cm}$, and the fundamental pulse shape is given by a fourth-order super-Gaussian to a "flat-top":

$$\text{pulse}(t) \equiv \begin{cases} \exp\left[-\ln(2)\left(\frac{t-t_0}{19 \text{ ps}}\right)^4\right]; & 0 < t \leq t_{\text{peak}} \\ 1 & ; t > t_{\text{peak}} \end{cases}, \quad (6)$$

where the quantity t_0 is defined to yield a nominally, small initial value for the pulse, e.g., $\text{pulse}(0) = 0.001$, and the quantity t_{peak} defines the time when the pulse shape achieves a value of unity, i.e., $\text{pulse}(t_{\text{peak}}) = 1$. The foot pulse is defined in this manner to make a more accurate comparison of the early development of the nonuniformity with the ultrafast pickets defined later.

The spatially and temporally varying phase due to 2-D SSD is given by (see Ref. 16)

$$\begin{aligned} \phi_{2\text{-D SSD}}(x, y, t) \equiv & 3\delta_{\text{M1}} \sin[\omega_{\text{M1}}(t + \xi_y y)] \\ & + 3\delta_{\text{M2}} \sin[\omega_{\text{M2}}(t + \xi_x x)], \quad (7) \end{aligned}$$

where δ_{M1} is the first-dimension modulation depth, $\nu_{M1} \equiv \omega_{M1}/(2\pi)$ is the first-dimension microwave or radio frequency (RF) modulation frequency, ξ_y is the first-dimension angular grating dispersion, δ_{M2} is the second-dimension modulation depth, $\nu_{M2} \equiv \omega_{M2}/(2\pi)$ is the second-dimension RF modulation frequency, and ξ_x is the second-dimension angular grating dispersion. The factor of 3 in Eq. (7) indicates that the electric field has undergone frequency tripling from the IR to UV. The relevant NIF 2-D SSD base-line system parameters are assumed to be $\delta_{M1} = 16.7$, $\nu_{M1} = 8.76$ GHz, $\xi_y = 0.325$ ns/m, $\Delta\lambda_{M1} = 10.8$ Å, $\delta_{M2} = 8.37$, $\nu_{M2} = 3.23$ GHz, $\xi_x = 0.878$ ns/m, and $\Delta\lambda_{M2} = 2.0$ Å, assuming a nominal beam diameter of $D_{NIF} = 35.1$ cm.

The base-line 2-D SSD design for direct-drive NIF is defined in this article as having IR bandwidths of

$$\Delta\lambda_{M1} = 2\delta_{M1}\nu_{M1}\lambda_{IR}^2/c = 10.8 \text{ Å}$$

and

$$\Delta\lambda_{M2} = 2\delta_{M2}\nu_{M2}\lambda_{IR}^2/c = 2.0 \text{ Å}$$

in the first and second dimensions, respectively, where c is the vacuum speed of light and $\lambda_{IR} = 1053$ nm is the IR wavelength. Two different measures of combined UV bandwidth or widths of the temporal power spectrum are used here: the first measure is the root-sum-square and is defined by

$$\Delta\nu_{\text{rss}} = \sqrt{\Delta\nu_{M1}^2 + \Delta\nu_{M2}^2}, \quad (8)$$

where the UV bandwidths of each modulator are given separately by $\Delta\nu_{M1} \equiv 6\delta_{M1}\nu_{M1}$ and $\Delta\nu_{M2} \equiv 6\delta_{M2}\nu_{M2}$; and the second measure is known as the autocorrelation width¹⁷ and is defined by

$$\Delta\nu_{\text{eff}} = \frac{\left| \int \tilde{I}(\nu) d\nu \right|^2}{\int \tilde{I}(\nu)^2 d\nu}, \quad (9)$$

where the quantity $\tilde{I}(\nu) \equiv |\tilde{E}(\nu)|^2$ represents the smoothed envelope of the temporal power spectrum due to the 2-D SSD phase modulation ϕ_{2-D} SSD. The base-line 2-D SSD system yields $\Delta\nu_{\text{rss}} = 891$ THz and $\Delta\nu_{\text{eff}} = 979$ THz in the UV.

The bandwidth $\Delta\lambda_M$, laser divergence $\Delta\theta_M$ and the number of color cycles N_{cc} determine the required grating dispersion ξ , the temporal delay τ_D , modulator frequency ν_M , and modula-

tion depth δ_M for the given beam diameter D_{NIF} . Due to current pinhole requirements of the spatial filters, the imposed laser divergence is limited to $\Delta\theta_{M1} = 100$ μrad and $\Delta\theta_{M2} = 50$ μrad in the first and second dimensions, respectively. The number of color cycles across the beam is defined by $N_{\text{cc}} \equiv \tau_D\nu_M$, where τ_D is the time shear imposed by the dispersion gratings and ν_M is the modulator's frequency. It can be shown that the laser divergence $\Delta\theta_M$ is proportional to the applied SSD bandwidth $\Delta\lambda_M$ and is given by

$$\Delta\theta_M = \tau_D \Delta\lambda_M \frac{c}{\lambda_{IR} D_{NIF}}, \quad (10)$$

where c is the vacuum speed of light, $\lambda_{IR} = 1053$ nm is the IR vacuum wavelength, and $D_{NIF} = 35.1$ cm is the nominal beam diameter. Since the pinholes restrict the laser divergence $\Delta\theta_M$, and the base-line 2-D SSD design calls for $\Delta\lambda_{M1} = 10.8$ Å, applying Eq. (10) to the first dimension yields a time delay $\tau_{D1} = 114.15$ ps, which implies that the required modulator frequency for the first dimension, to achieve $N_{\text{cc}1} = 1$, is $\nu_{M1} = 8.76$ GHz. Similarly, applying Eq. (10) to the second dimension yields $\tau_{D2} = 309.60$ ps and $\nu_{M2} = 3.23$ GHz for $N_{\text{cc}2} = 1$. This base-line design will be designated as BL1 in this article. An alternative base-line 2-D SSD design, designated as BL2, is also proposed, which has $N_{\text{cc}1} = 2$, $\delta_{M1} = 8.33$, and $\nu_{M1} = 17.52$ GHz with all other parameters left the same. In addition, a base-line design the same as BL1 but without the temporal shear will be designated as BL1b. The relevant parameters are summarized in Table 86.III.

Ultrafast-Picket-Smoothing Scheme

The ultrafast-picket-smoothing scheme produces a sub-apertured near field that sweeps across the full-beam aperture when using a pulse-modulated laser whose pulse width is smaller than the residual time shear τ_{D1} due to the dispersing grating. The sweeping motion causes smoothing in the time-integrated far field because the speckle pattern changes as the sub-apertured near field moves across the randomly phased background of the DPP. Applying a time-varying phase or phase chirp to each picket enhances the efficiency of this smoothing mechanism. The phase chirp increases the inherent bandwidth of each pulse and asymptotically produces many independent speckle patterns (or far-field modes), similar to SSD, as long as the grating dispersion matches the pulse repetition rate. Unlike SSD, the phase chirp can be tailored to produce a uniform far-field distribution of modes that not only reduces the asymptotic nonuniformity but also alleviates pinhole loading in the laser amplification chain. The ultrafast-picket-smoothing scheme supplants only the first SSD

dimension. The efficient and asymptotic smoothing of the ultrafast pickets depends on a second and orthogonal SSD smoothing dimension in the same way that 2-D SSD does.

The ultrafast-picket-pulse train is defined to have an intensity FWHM pulse width of Δt_{FWHM} , a pulse repetition period of ΔT , and an inverse duty cycle given by $\text{IDC} \equiv \Delta T/\Delta t$, where Δt is the pulse width that contains 99% of the pulses's energy. The pulse train that will be discussed is a fourth-order super-Gaussian and can be written as

$$\text{picket}(t) \equiv \sum_{n=0}^N \exp \left[-\ln(2) \left(\frac{t-t_0-n\Delta T}{\Delta t_{\text{FWHM}}} \right)^4 \right], \quad (11)$$

s.t. $N\Delta T \leq 3$ ns. The pulse width as defined in Eq. (11) is $\Delta t = 28.1$ ps. The fundamental beam shape for the pickets is defined to be the same as the base-line 2-D SSD [i.e., Eq. (5)].

A pulsed laser beam followed by a phase modulator that is then dispersed by a grating describes any ultrafast-picket scheme schematically (see Fig. 86.41). This schematic graphically describes the mathematical functions of the resultant pulsed beam used in the *Waasikwa'* simulations. The phase modulator in Fig. 86.41 represents an optional phase chirp that can be applied to the pickets. If the phase chirp is locked to the pulse repetition rate of the pickets, the phase chirp of each picket, whose function is given by $\phi_{\text{chirp}}(t)$, is then appended to Eq. (11) in the form of $\exp[i\phi_{\text{chirp}}(t-t_0-n\Delta T)]$.

The grating G2, in Fig. 86.41, disperses the ultrafast pickets with a grating dispersion, ξ_y , which temporally shears the beam by an amount τ_{D1} . Consequently, the beam becomes sub-apertured and then sweeps across the whole near-field aperture as time progresses (see Fig. 86.42). The sub-apertured width

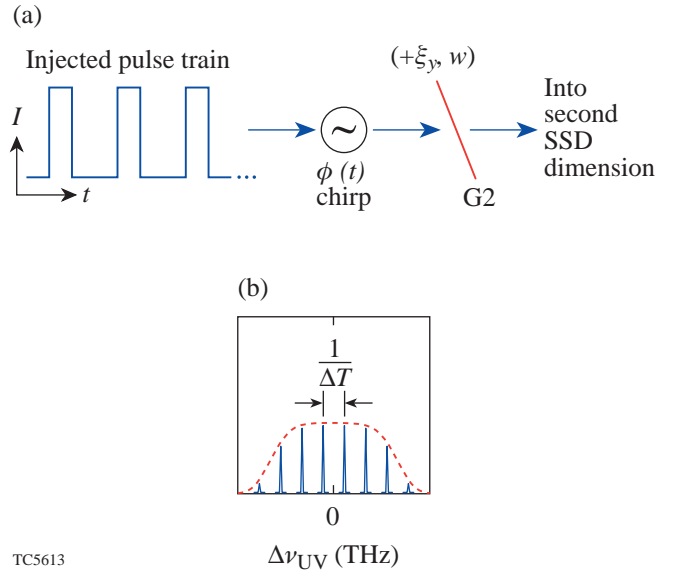


Figure 86.41 (a) Schematic describing a chirped UV pulsed beam in the *Waasikwa'* simulations. A pulse-modulated laser is chirped by the phase modulator M₁ with the phase given by $\phi_{\text{chirp}}(t)$ and then dispersed by the grating G2. This schematic does not describe the layout of an actual implementation; it is simply a graphical representation of the mathematical function of the resultant pulsed beam. (b) A plot representing the envelope of the temporal spectrum from a generic chirped-pulse train, which is identical to the temporal spectrum from a single chirped pulse. The series of delta functions represents the temporal-spectral modes from the chirped-pulse train that are spaced by $1/\Delta T$. The envelope modulates these modes.

W_a is equivalent to the ratio of the pulse width Δt to the grating dispersion ξ_y , which can then be related to other quantities,

$$W_a = \frac{\Delta t}{\xi_y} = \frac{\Delta T}{\xi_y \text{IDC}} = \frac{D_{\text{NIF}}}{\text{IDC} \cdot N'_{\text{cc}}}, \quad (12)$$

Table 86.III: Summary of the relevant parameters for the NIF 2-D SSD base-line models.

Sim Name	2-D SSD Base-Line Models													
	First Applied SSD Dimension						Second Applied SSD Dimension						Combined BW	
	δ_{M1}	ν_{M1} (GHz)	$\Delta\lambda_{M1}$ (Å) IR	$\Delta\nu_{M1}$ (GHz) UV	$\Delta\nu_{\text{eff}}$ (GHz) UV	$N_{\text{cc}1}$	δ_{M2}	ν_{M2} (GHz)	$\Delta\lambda_{M2}$ (Å) IR	$\Delta\nu_{M2}$ (GHz) UV	$\Delta\nu_{\text{eff}2}$ (GHz) UV	$N_{\text{cc}2}$	$\Delta\nu_{\text{rss}}$ (GHz)	$\Delta\nu_{\text{eff}}$ (GHz)
BL1	16.67	8.76	10.8	876	665	1	8.37	3.23	2.0	162	167	1	891	979
BL1b	16.67	8.76	10.8	876	665	1							891	979
BL2	8.333	17.52	10.8	876	656	2							891	979

where N'_{cc} is analogous to the number of color cycles in an SSD system and is defined as

$$N'_{cc} \equiv \frac{\tau_D}{\Delta T}. \tag{13}$$

When the quantity $N'_{cc} > 1$, multiple pickets will simultaneously illuminate the near field and will result in improved low-spatial-frequency smoothing and resonant features in the far-field power spectrum similar to an SSD system of multiple color cycles. The target will experience an intensity ripple when N'_{cc} is not an integer. Under these conditions, however, the IDC decreases, which degrades the benefit of improved frequency conversion and decreased power imbalance. When the quantity $N'_{cc} < 1$, the IDC increases (for a given grating dispersion) and will increase frequency conversion and reduce power imbalance. The target will experience an intensity ripple, however, due to the absence of any pickets over the duration of $\Delta T - \tau_D$ (unless the pickets can be timed to alter-

nately illuminate different beams in each quad to compensate). More importantly, the smoothing will become inefficient because the far-field modes will become statistically dependent, just as in the SSD case. When the quantity $N'_{cc} = 1$, the target will experience little ripple (in fact, if the pulse is rectangular, the target will experience no intensity ripple) and the smoothing will be efficient over all spatial wavelengths.

As originally conceived, the chirp would be applied by allowing the pickets to enter a phase-locked phase modulator such as the current fiber modulator. In this scenario the pulse period is phase-locked to the phase modulator such that the maximum instantaneous wavelength shift is applied to each picket (see Fig. 86.43). The pickets effectively “sample” the central portion of the bandwidth produced by the phase modulator. Notice in Fig. 86.43 how the “sampled” spectrum of the ultrafast pickets is nearly uniform and centrally distributed, unlike the distinctive Bessel mode pattern produced by the frequency-modulated (FM) spectrum of SSD.

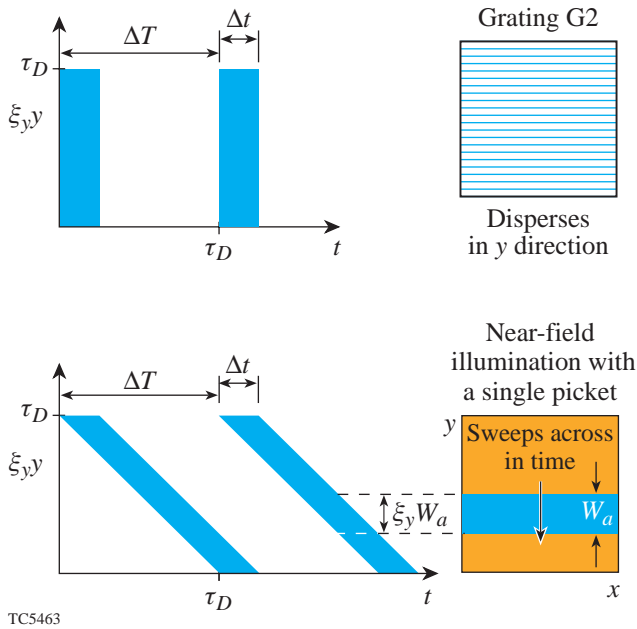


Figure 86.42 The two plots on the left-hand side represent beam cross sections before and after the grating G2, which temporally skews the beam. Consequently, the beam becomes sub-apertured and then sweeps across the whole near-field aperture as time progresses (see the plot on the lower right-hand side). If the pulse period Δt is chosen to equal the temporal shear τ_D from grating G2, the target will be continuously illuminated since as one picket exits the aperture, the next one will enter on the opposite side.

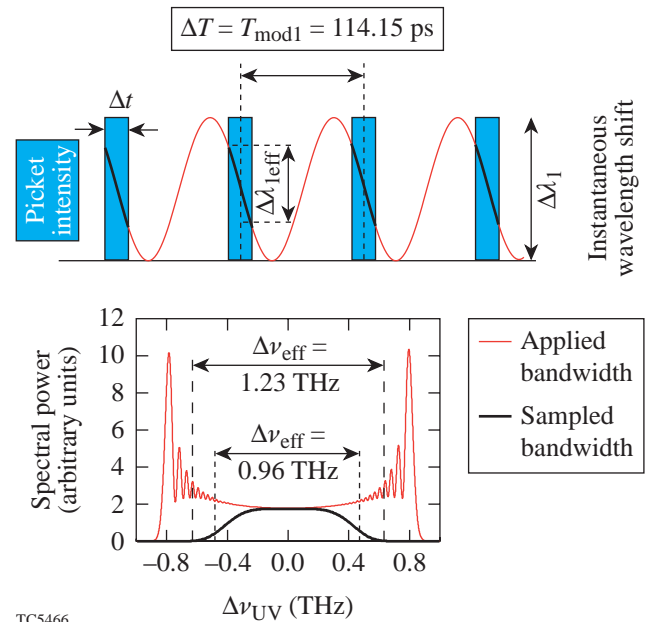


Figure 86.43 A chirp is applied to each picket using a phase-locked modulator. This diagram graphically illustrates how the modulator applies the maximum instantaneous wavelength shift to each picket. The pickets effectively “sample” the central portion of the bandwidth applied by the modulator.

1. Temporal Spectrum and Diffraction-Limited Far-Field Pattern of Ultrafast Pickets

The centrally distributed sampled spectrum directly translates into reduced pinhole loading. The applied temporal spectrum maps into the pattern of a diffraction-limited far field since the dispersed beam maps the applied temporal bandwidth into spatial bandwidth (see Ref. 16 for a detailed description). The time-integrated, diffraction-limited far-field patterns of the NIF 2-D SSD base-line and ultrafast pickets are illustrated in Fig. 86.44. The pattern from the NIF 2-D SSD base line

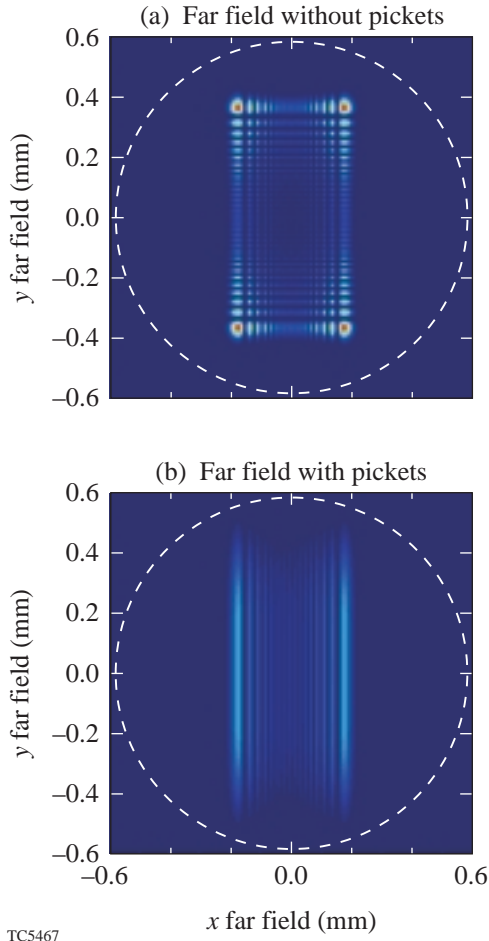


Figure 86.44

The time-integrated diffraction-limited far-field patterns for the NIF 2-D SSD (a) base-line and (b) ultrafast pickets. The images are plotted using the same gray scale to indicate relative fluence levels. The pattern from the NIF 2-D SSD base line shows high fluence levels near the four outer corners of the pattern. In contrast, the pattern from the ultrafast-picket design shows a much lower, uniform fluence level more evenly distributed about the center. Both images show the distinct Bessel pattern in the direction corresponding to the second SSD dimension.

[Fig. 86.44(a)] shows high fluence levels near the four outer corners of the pattern. In contrast, the pattern from the ultrafast-picket design [Fig. 86.44(b)] shows a much lower and uniform fluence level more evenly distributed about the center. Both images show the distinct Bessel mode pattern in the direction corresponding to the second SSD dimension.

The temporal spectral modes of the ultrafast picket fence are separated by the inverse of the pulse repetition period, e.g., $1/\Delta T$, and they conform to the envelope of the spectrum of a single pulse [see Fig. 86.41(b)]. These spectral modes become modes in the far field and lead to the number of independent speckle patterns in the asymptotic limit. The mode spacing in the far field in the direction corresponding to the grating G2 is calculated by $N'_{cc} f_{NIF} \lambda_{UV} / D_{NIF}$. The number of modes due to the ultrafast pickets can be calculated using

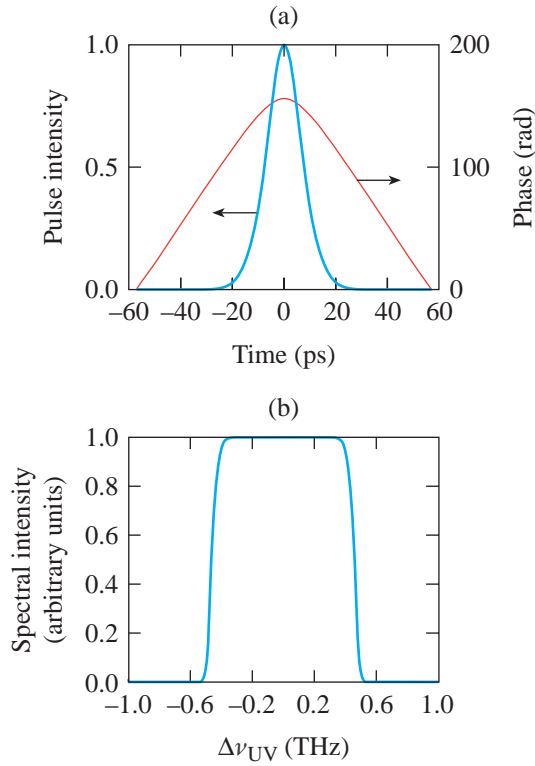
$$\text{Modes}' = \Delta v'_{UV} \cdot \Delta T = \frac{\Delta \theta'_{M1}}{\xi_y \lambda_{UV}} \Delta T = \frac{\Delta \theta'_{M1} D_{NIF}}{\lambda_{UV} N'_{cc}}. \quad (14)$$

The number of modes due to the SSD for either dimension can be calculated using

$$\text{Modes} = \frac{\Delta v_{UV}}{v_M} = \frac{\Delta \theta_M D_{NIF}}{\lambda_{UV} N_{cc}}, \quad (15)$$

where the laser divergence $\Delta \theta_M$ and number of color cycles N_{cc} corresponding to either SSD dimension is substituted into Eq. (15). The total number of modes in the far field is computed as the product of the number of modes from the first smoothing dimension (either SSD or ultrafast picket fence) and the number due to the second orthogonal SSD dimension. If the temporal spectrum of either the ultrafast pickets or SSD is nonuniform, the effective number of modes is reduced, similar to SSD.¹⁸ The reduction ratio is approximated as the ratio of the effective bandwidth calculated using Eq. (9) to the overall bandwidth of each smoothing direction separately. The ultrafast-picket-fence schemes proposed in this article have a very uniform distribution, which can decrease the asymptotic level reached by approximately 20% as compared to base-line 2-D SSD.

The temporal spectrum of the ultrafast pickets can be modified or tailored to reduce the pinhole loading due to the tails of the spectrum seen in Fig. 86.43. Through an iterative Fourier technique, similar to phase-retrieval techniques, a chirped pulse can be designed to produce the high-order super-Gaussian temporal spectrum as illustrated in Fig. 86.45.



TC5594

Figure 86.45

A chirped pulse (a) and its temporal spectrum (b). The spectrum was the design point of an iterative Fourier technique to find the required shape and phase of the pulse in (a). This spectrum can further reduce the pinhole loading by removing the energy located in the tails of the spectrum seen in Fig. 86.43.

2. Alternate Methods of Producing Chirped Ultrafast Pickets

Alternate methods are available for producing chirped ultrafast pickets that need not be phase locked. One method is to reflect a stretched and longer chirped pulse from a fiber-Bragg grating; this results in a train of chirped pulses of desired shape and chirp by properly engineering the fiber. This technique meshes well with the tailored chirped pulse seen in Fig. 86.45 since the pulse shape is approximately a $\text{sec } h^2$ and the chirp is nearly linear, both of which are easily obtained using current laser and fiber technologies.

Far-Field Simulation and Analysis

Waasikwa' calculates the planar far-field fluence using

$$F(x_{\text{ff}}, y_{\text{ff}}) \equiv \int_{\text{pulse duration}} I_{\text{ff}}(x_{\text{ff}}, y_{\text{ff}}, t) dt, \quad (16)$$

where $I_{\text{ff}}(x_{\text{ff}}, y_{\text{ff}}, t)$ represents the instantaneous far-field intensity. The evolution of the far-field intensity is calculated by taking the modulus squared of a 2-D spatial Fourier transform of the UV near field [comp. Ref. 19, pp. 83–89]:

$$I_{\text{ff}}(x_{\text{ff}}, y_{\text{ff}}, t) \equiv \left| \iint_{\nabla_{\text{space}}} E(x, y, t) \exp \left[-i \frac{2\pi}{\lambda_{\text{UV}} f_{\text{NIF}}} (x_{\text{ff}} x + y_{\text{ff}} y) \right] dx dy \right|^2, \quad (17)$$

where $E(x, y, t)$ represents the complex-valued UV electric field strength in the near field and (x, y) and $(x_{\text{ff}}, y_{\text{ff}})$ are the near- and far-field coordinate systems, respectively; $\lambda_{\text{UV}} = 351$ nm is the UV vacuum wavelength; and $f_{\text{NIF}} = 770$ cm is the assumed NIF focal length. The integrations are calculated as a running summation at every simulation time step dt . For these ~ 1 -THz-bandwidth pulsed beams, the time step is defined to be $dt = 0.75$ ps, which sufficiently over-samples the bandwidth based on the Nyquist criterion.

The 2-D power spectral density (2-D power spectrum or simply the 2-D PSD) is derived from the simulated far-field fluence by taking the modulus squared of the 2-D spatial Fourier transform:

$$\text{PSD}(k_{x_{\text{ff}}}, k_{y_{\text{ff}}}) \equiv \left| \iint_{\nabla_{\text{far field}}} F(x_{\text{ff}}, y_{\text{ff}}) \exp \left[-i (k_{x_{\text{ff}}} x_{\text{ff}} + k_{y_{\text{ff}}} y_{\text{ff}}) \right] dx_{\text{ff}} dy_{\text{ff}} \right|^2, \quad (18)$$

where $F(x_{\text{ff}}, y_{\text{ff}})$ represents the far-field fluence as defined by Eq. (16), $(x_{\text{ff}}, y_{\text{ff}})$ is the far-field coordinate system, and $(k_{x_{\text{ff}}}, k_{y_{\text{ff}}})$ is the far-field's spatial-frequency coordinate system. The azimuthal sum at each radial wave number of the 2-D power spectrum defines the 1-D power spectral density (1-D power spectrum or simply the 1-D PSD) and is given by

$$\text{psd}(k_{\text{ff}}) \equiv \oint \text{PSD}(k_{x_{\text{ff}}}, k_{y_{\text{ff}}}) k_{\text{ff}} d\theta, \quad (19)$$

where the transformation into polar coordinates is defined as $k_{\text{ff}} \equiv \sqrt{k_{x_{\text{ff}}}^2 + k_{y_{\text{ff}}}^2}$ and $\tan \theta \equiv k_{y_{\text{ff}}} / k_{x_{\text{ff}}}$. The single-beam

irradiation nonuniformity σ_{rms} is defined as the square root of the ratio of the speckle power (e.g., the high frequencies $k_{\text{ff}} \geq 5.88$ rad/mm at the NIF target plane or ℓ -modes $\ell \geq 10$) to the envelope power of the far-field spot (i.e., the low frequencies $k_{\text{ff}} < 5.88$ rad/mm). The wave number 5.88 rad/mm divides the envelope and speckle frequencies. A finite entrance pupil imposes a limitation on the spatial-frequency bandwidth of an optical system (compare the intensity-impulse response or point-spread function of a diffraction-limited system with a rectangular exit-pupil function in Ref. 19, pp. 110–113). On the NIF, the highest spatial frequency of the far field, regardless of the near-field beam profile, is limited by the finite square shape of the full aperture beam whose width is defined as $D_{\text{NIF}} = 35.1$ cm. Consequently, the 2-D PSD possesses a square-shaped absolute cutoff whose width along both the $k_{x\text{ff}}$ and $k_{y\text{ff}}$ axes corresponds to the f -number limited spatial frequency

$$k_{\text{cutff}} = \frac{2\pi D_{\text{NIF}}}{\lambda_{\text{UV}} f_{\text{NIF}}} = 0.816 \frac{\text{rad}}{\mu\text{m}}. \quad (20)$$

Due to the square-shaped cutoff of the 2-D PSD, the 1-D PSD has an absolute cutoff of

$$k'_{\text{cutff}} = \sqrt{2} \cdot k_{\text{cutff}}. \quad (21)$$

For the ultrafast picket fence schemes, the high aspect ratio (which is proportional to IDC) of the sub-apertured near field corresponds to an absolute cutoff $k'_{\text{cutff}} \cong k_{\text{cutff}}$.

Smoothing Performance Results

Waasikwa' far-field simulations calculated the single-beam nonuniformity as a function of time for a duration of 3 ns. Three NIF 2-D SSD base-line designs and four ultrafast picket designs were calculated using the parameters listed in Tables 86.III and 86.IV. The names listed under the ‘‘Sim Name’’ column in these tables will be used to designate each model.

The smoothing performances for Picket1, Picket2, and the BL1 designs are plotted in Fig. 86.46 for a 3-ns duration for all

Table 86.IV: Summary of the relevant parameters for the NIF ultrafast-picket-smoothing schemes. The second SSD dimension has the same parameters as in Table 86.III.

Sim Name	Pulse Type	First Smoothing Dimension										Combined BW
		Applied SSD				Ultrafast Pickets						
		δ_{M1}	ν_{M1} (GHz)	$\delta\lambda_{\text{M1}}$ (Å) IR	N_{cc1}	IDC	N'_{cc}	ΔT (ps)	Δt_{FWHM} (ps)	Δt (ps)	$\Delta\nu_{\text{eff}}$ (GHz) UV	
Picket1	Single SG4	31.02	8.76	20.1	1	4	1	114.15	19.0	28.1	970	994
Picket1b	Single SG4	31.02	8.76	20.1	1	4	1	114.15	19.0	28.1	970	994
Picket2	Double SG4	31.02	8.76	20.1	1	2	2	57.075	19.0	28.1	970	995
Chirped1	Single sech^2	n/a	n/a	n/a	n/a	2.5	1	114.15	19.0	45	947	993

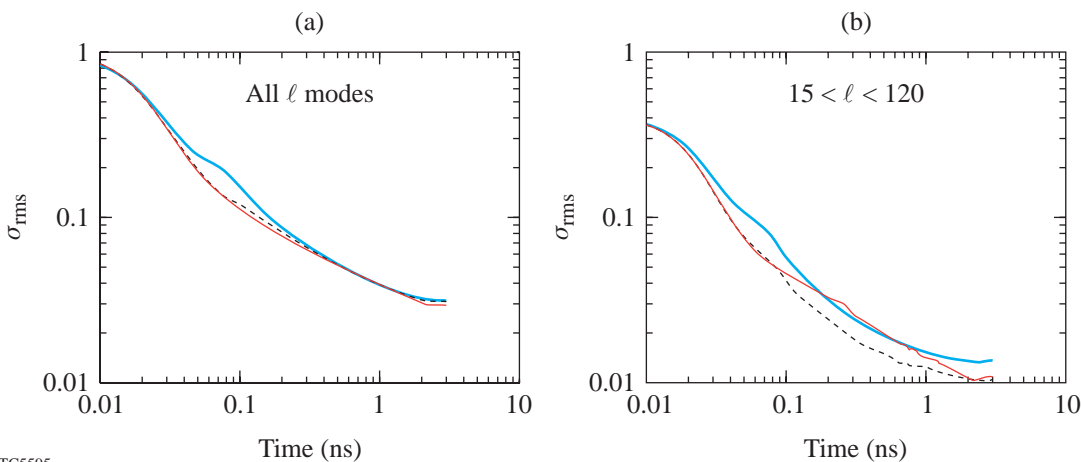


Figure 86.46 The nonuniformity plotted against time for (a) all ℓ modes and (b) the ℓ -mode range $15 < \ell < 120$. The red line is the NIF ultrafast Picket1, the dashed line is the NIF ultrafast Picket2, and the blue line is the NIF 2-D SSD base-line BL1.

TC5595

the ℓ modes and over the ℓ -mode range of $15 < \ell < 120$. The smoothing performance of both picket designs is initially better than and later is nearly equivalent to BL1 design. The Picket2 design produces better smoothing than the other two designs for the range $15 < \ell < 120$ because two pickets are simultaneously illuminated, which is analogous to a two-color-cycle 2-D SSD system. The smoothing performances for the tailored chirped pulse (designated as Chirped1), Picket1, and BL1 are plotted in Fig. 86.47 for a 3-ns duration for all the ℓ -modes and over the ℓ -mode range, $15 < \ell < 120$.

The smoothing performances for the BL1, Picket1, and Picket2 simulations are identical for the first 15 ps because they have the same pulse rise time and a similarly shaped sub-apertured near field (BL1 is sub-apertured during the time corresponding to the initial temporal shear and the shape matches the picket's shape for the first 15 ps). The smoothing performance for Chirped1 is initially not as good as Picket1 or Picket2 because it has a much longer rise time of approximately 25 ps. The smoothing performance for both picket types, however, is better than BL1 over the duration $20 \text{ ps} < t < 200 \text{ ps}$. This is due to the fact that the ultrafast picket designs are designed to smooth efficiently, i.e., full-smoothing, full-bandwidth for a sub-apertured near field; whereas the base-line designs do not achieve full-smoothing/full-bandwidth until the aperture is filled, i.e., after the initial temporal shear $\tau_{D1} = 114.15 \text{ ps}$. Therefore, the picketed designs effectively have $\sim 115 \text{ ps}$ of smoothing accomplished before the base-line designs achieve efficient smoothing. Over the ℓ -band

range $20 \leq \ell < 120$, Picket2 has better smoothing performance than Picket1 for $t > 80 \text{ ps}$ because by this time the second picket has appeared in Picket2 and remains for the rest of the simulation. The second picket reduces the nonuniformity in this ℓ -band range due to the aforementioned multiple-color-cycle effects. The overall smoothing performance for all the simulations are nearly equivalent, for the duration $t > 200 \text{ ps}$ and until the asymptotic levels are reached (approximately $t \sim 3 \text{ ns}$). The Picket #1 simulation has reduced asymptotic overall nonuniformity because of the uniform bandwidth distribution. The simulation Picket1 has a lower asymptotic nonuniformity relative to Picket2 because of $N'_{cc} = 2$. The asymptotic levels for both picket-type simulations, however, are nearly equivalent for the ℓ -band range $15 \leq \ell \leq 120$.

The instantaneous 1-D PSD, defined by Eq. (19), for the ultrafast-picket-fence schemes is approximately $4\times$ higher over the ℓ -band range $15 \leq \ell \leq 120$ as compared to BL1 (see Fig. 86.48). The ultrafast-picket-fence schemes produce a sub-apertured near field, which corresponds to a 2-D PSD whose extent (i.e., its cutoff wave number k_{cutff}) is reduced in the corresponding direction by a factor of $\sim \text{IDC}$ (for $N'_{cc} = 1$). By conservation of energy, the sub-apertured near field increases the spectral power in the picketed direction by a factor of $\sim \text{IDC}$. Consequently, the azimuthal sum (i.e., the 1-D PSD) reflects this additional power. Note also that there is still power up to $k_{\text{cutff}} = 0.816 \text{ rad}/\mu\text{m}$ because the second SSD dimension is still full aperture.

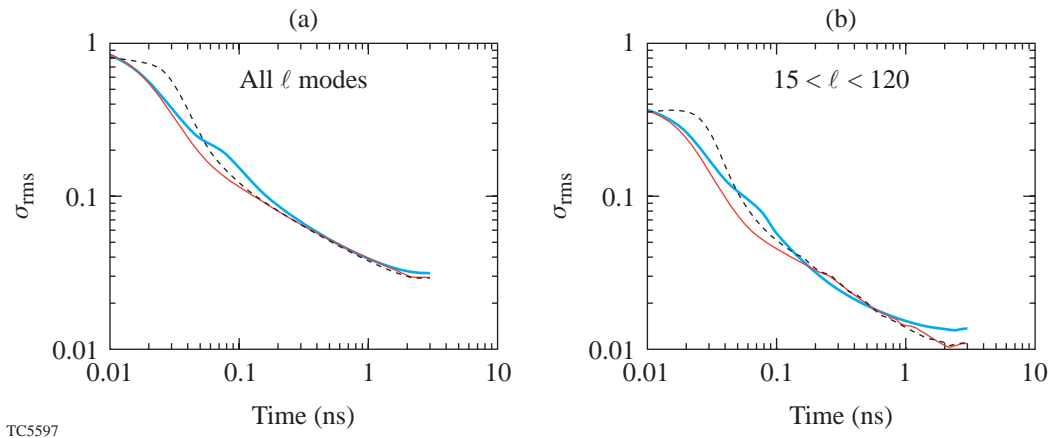


Figure 86.47

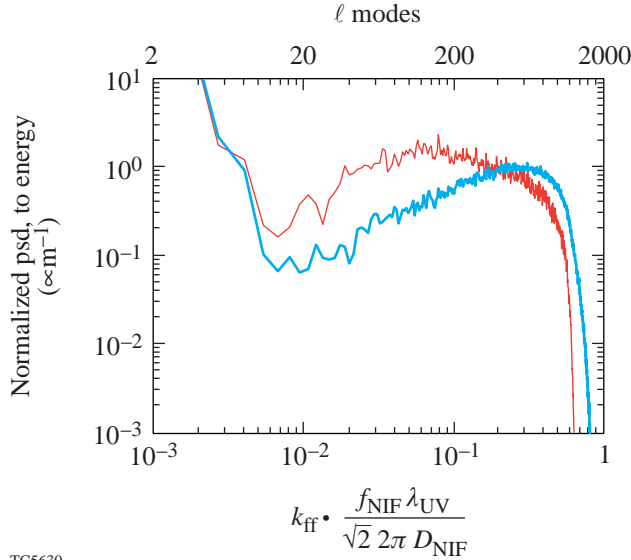
The nonuniformity plotted against time for (a) all ℓ modes and (b) the ℓ -mode range $15 < \ell < 120$. The red line is the NIF ultrafast Picket1, the dashed line is the NIF ultrafast chirped-picket Chirped1, and the blue line is the NIF 2-D SSD base-line BL1.

To relate the smoothing performance to effective bandwidth or inverse coherence time, the initial rise-time behavior must be eliminated because the simple model of the nonuniformity as a function of time and wave number does not account for this rise-time behavior⁷

$$\sigma^2(t, k_{\text{ff}}) = \sigma_0^2(k_{\text{ff}}) \frac{t_c}{t + t_c} + \sigma_{\text{asym}}^2(k_{\text{ff}}), \quad (22)$$

where $\sigma_0^2(k_{\text{ff}}) = \sigma^2(0, k_{\text{ff}})$ is the initial value of the nonuniformity and $\sigma_{\text{asym}}^2(k_{\text{ff}}) = \sigma^2(\infty, k_{\text{ff}})$ is the asymptotic level of the nonuniformity for the radial wave number k_{ff} . Advancing the pulse by this delay and delaying the time-integrated far field by the same time accomplish this task. Therefore, two additional simulations were run with a delay of an amount corresponding to the rise-time delay for each model. The base-line model BL1b is identical to BL1 except for the included delay of 130 ps. The ultrafast-picket-fence model Picket1b is identical to Picket1 except for the included delay of 30 ps.

The nonuniformity of Picket1b is nearly equivalent to BL1b over the ℓ -band range $15 \leq \ell \leq 120$ even though the instanta-



TC5630

Figure 86.48

The instantaneous far-field 1-D power spectra for models BL1 (blue line) and Picket1 (red line). The subapertured near field of the ultrafast picket scheme increases the power in modes $\ell < 400$ relative to the base-line 2-D SSD model. The increase is approximately equal to the IDC value for the ultrafast picket scheme over the majority of the affected ℓ modes.

neous power is $4\times$ higher in these modes (see Fig. 86.48). The reason for this behavior is simple: the effective bandwidth or inverse coherence time is approximated $4\times$ higher for Picket1b relative to BL1b. The sub-apertured near field of the Picket1b causes the bandwidth to be distributed over a reduced wave-number range and consequently smoothes these wavelengths faster. This effect is calculated two independent ways: (1) smoothing performance of a full simulation is fit to the model of Eq. (22) and (2) a phenomenological model is developed.

Calculating the effective bandwidth distribution for either the 2-D SSD system or the ultrafast-picket-fence scheme is essentially a 2-D problem. Two- and one-dimensional phenomenological models of the effective bandwidth are given here. In the first smoothing direction, the bandwidth is distributed as¹⁰

$$\Delta v_x(k_{x_{\text{ff}}}) = 2\Delta v_{M1} \sin\left(k_{x_{\text{ff}}} \frac{\kappa_1}{2} N_{\text{cc1}}\right), \quad (23)$$

where Δv_{M1} is the FM modulator bandwidth in the UV for the first SSD modulator or the chirped-pulse bandwidth and the parameter κ_1 is the one-half speckle width, ($\kappa_1 = \kappa_{\text{SSD1}} = f_{\text{NIF}}/\lambda_{\text{UV}}/D_{\text{NIF}}$ for the first SSD dimension or $\kappa_1 = \kappa_{\text{picket}} = \text{IDC} \cdot f_{\text{NIF}} \lambda_{\text{UV}}/D_{\text{NIF}}$ for the ultrafast picket fence). In the second smoothing direction, the bandwidth is distributed as

$$\Delta v_y(k_{y_{\text{ff}}}) = 2\Delta v_{M2} \sin\left(k_{y_{\text{ff}}} \frac{\kappa_2}{2} N_{\text{cc2}}\right), \quad (24)$$

where Δv_{M2} is the FM modulator bandwidth in the UV for the second SSD modulator and $\kappa_2 = \kappa_{\text{SSD1}}$ is the one-half speckle width for the second SSD dimension. For the 2-D problem, it is assumed that the orthogonal components of the wave vector $\mathbf{k}_{\text{ff}} \equiv k_{x_{\text{ff}}} \hat{x} + k_{y_{\text{ff}}} \hat{y}$ are affected independently so that the effective bandwidth is given by the quadrature sum

$$\Delta v'_{\text{eff}}(k_{x_{\text{ff}}}, k_{y_{\text{ff}}}) = \sqrt{|\Delta v_x(k_{x_{\text{ff}}})|^2 + |\Delta v_y(k_{y_{\text{ff}}})|^2}. \quad (25)$$

The smoothing of the 1-D PSD then corresponds to the weighted azimuthal average of the two-dimensional effective bandwidth function Eq. (25).

$$\Delta v_{\text{eff}}(k_{\text{ff}}) = \frac{\oint \Delta v'_{\text{eff}}(k_{x_{\text{ff}}}, k_{y_{\text{ff}}}) \text{PSD}_0(k_{x_{\text{ff}}}, k_{y_{\text{ff}}}) k_{\text{ff}} d\theta}{\oint \text{PSD}_0(k_{x_{\text{ff}}}, k_{y_{\text{ff}}}) k_{\text{ff}} d\theta}, \quad (26)$$

where the weighting function $\text{PSD}_0(k_{x\text{ff}}, k_{y\text{ff}})$ is the 2-D PSD of the aberration-free ideal near field of Eq. (4) at one instant of time for either the 2-D SSD base-line full-aperture designs or the sub-apertured ultrafast picket-fence designs.

The nonuniformity $\sigma^2(t, k_{\text{ff}})$ calculated from the simulations BL1b and Pickets1b is fit to the nonuniformity model of Eq. (22) using the coherence time as the one degree of freedom in order to estimate the effective bandwidth by $\Delta\tilde{v}_{\text{eff}}(k_{\text{ff}}) = 1/t_c$. The simulation data $\sigma^2(t, k_{\text{ff}})$ is averaged over ± 5 neighboring wave numbers before being fit to the model of Eq. (22). The estimated effective bandwidth by $\Delta\tilde{v}_{\text{eff}}(k_{\text{ff}})$ is compared to that calculated with the phenomenological effective bandwidth model given by Eq. (26) [see Fig. 86.49(a)]. The ratio of the effective bandwidths from the phenomenological model is plotted in Fig. 86.49(b). The fact that the effective bandwidth for the Picket1b is approximately 4x higher than the BL1b over the ℓ -band range $15 \leq \ell \leq 120$ explains why they have a similar smoothing performance over the l-band range in Fig. 86.46(b).

Conclusion

The underlying motivation of implementing the ultrafast pickets on the NIF is the ability to increase the frequency-conversion efficiency and to reduce the contribution to the beam-to-beam power imbalance in the foot portion of an ICF laser pulse.⁵ In this article, the smoothing performance of the ultrafast pickets was analyzed and shown to be equivalent to the NIF 2-D SSD base-line designs for direct-drive ICF as long as the applied bandwidths and divergences are close to the base-line designs. If no bandwidth is applied in the first dimension or if the IDC is too large, the early-time smoothing performance is not as effective. It was also discovered that the diffraction-limited far-field pattern produced by the chirped pickets can reduce pinhole loading, which might lead to an increase in the permitted laser divergence. Overall, a properly designed ultrafast picket system offers many system-wide benefits at the cost of a more complicated front end.

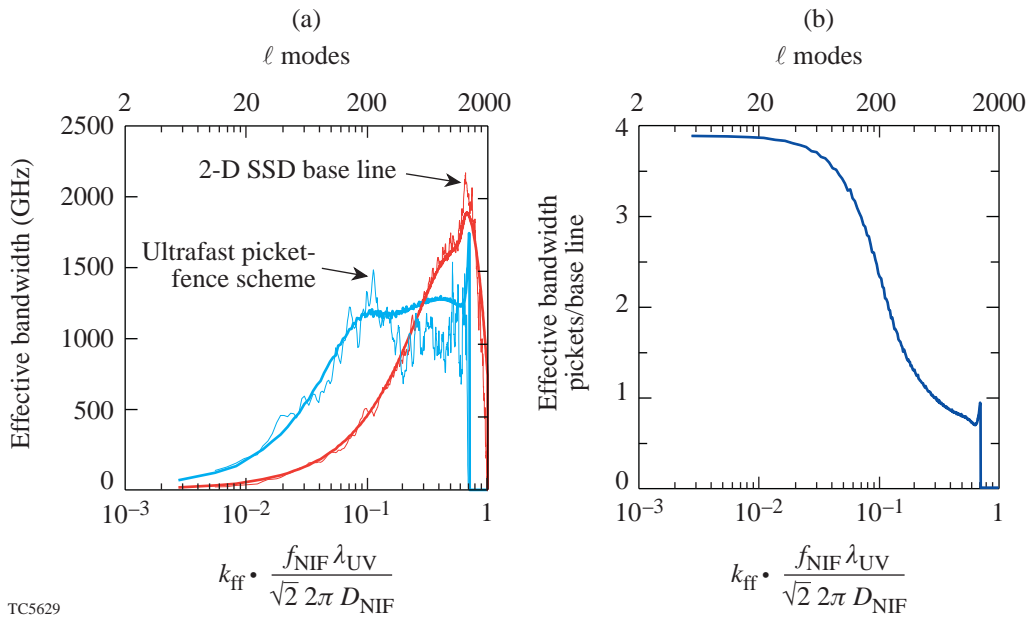


Figure 86.49

(a) The one-dimensional phenomenological model of the effective bandwidth $\Delta v_{\text{eff}}(k_{\text{ff}})$ and the estimated effective $\Delta\tilde{v}_{\text{eff}}(k_{\text{ff}})$ bandwidth are compared for both the BL1b and Picket1b *Waasikwa*' simulations. The bold traces represent the phenomenological model $\Delta v_{\text{eff}}(k_{\text{ff}})$, and the thin traces represent the simulation's effective bandwidth $\Delta\tilde{v}_{\text{eff}}(k_{\text{ff}})$. (b) The ratio of phenomenological models $\Delta v_{\text{eff}}(k_{\text{ff}})$ for Picket1b to BL1b is plotted, which shows the increased bandwidth in the lower ℓ -band range.

ACKNOWLEDGMENT

This work was partially supported by the U.S. Department of Energy Office of Inertial Confinement Fusion under Cooperative Agreement No. DE-FC03-92SF19460, the University of Rochester, and the New York State Energy Research and Development Authority. The support of DOE does not constitute an endorsement by DOE of the views expressed in this article.

REFERENCES

1. C. P. Verdon, *Bull. Am. Phys. Soc.* **38**, 2010 (1993).
2. S. E. Bodner, D. G. Colombant, J. H. Gardner, R. H. Lehmborg, S. P. Obenschain, L. Phillips, A. J. Schmitt, J. D. Sethian, R. L. McCrory, W. Seka, C. P. Verdon, J. P. Knauer, B. B. Afeyan, and H. T. Powell, *Phys. Plasmas* **5**, 1901 (1998).
3. D. K. Bradley, J. A. Delettrez, and C. P. Verdon, *Phys. Rev. Lett.* **68**, 2774 (1992); J. Delettrez, D. K. Bradley, and C. P. Verdon, *Phys. Plasmas* **1**, 2342 (1994); J. D. Kilkenny, S. G. Glendinning, S. W. Haan, B. A. Hammel, J. D. Lindl, D. Munro, B. A. Remington, S. V. Weber, J. P. Knauer, and C. P. Verdon, *Phys. Plasmas* **1**, 1379 (1994); R. Epstein, *J. Appl. Phys.* **82**, 2123 (1997); V. A. Smalyuk, T. R. Boehly, D. K. Bradley, V. N. Goncharov, J. A. Delettrez, J. P. Knauer, D. D. Meyerhofer, D. Oron, and D. Shvarts, *Phys. Rev. Lett.* **81**, 5342 (1998).
4. F. J. Marshall and G. R. Bennett, *Rev. Sci. Instrum.* **70**, 617 (1999); F. J. Marshall, J. A. Delettrez, V. Yu. Glebov, R. P. J. Town, B. Yaakobi, R. L. Kremens, and M. Cable, *Phys. Plasmas* **7**, 1006 (2000).
5. J. E. Rothenberg, *Appl. Opt.* **39**, 6931 (2000).
6. T. R. Boehly, D. L. Brown, R. S. Craxton, R. L. Keck, J. P. Knauer, J. H. Kelly, T. J. Kessler, S. A. Kumpan, S. J. Loucks, S. A. Letzring, F. J. Marshall, R. L. McCrory, S. F. B. Morse, W. Seka, J. M. Soures, and C. P. Verdon, *Opt. Commun.* **133**, 495 (1997).
7. S. P. Regan, J. A. Marozas, J. H. Kelly, T. R. Boehly, W. R. Donaldson, P. A. Jaanimagi, R. L. Keck, T. J. Kessler, D. D. Meyerhofer, W. Seka, S. Skupsky, and V. A. Smalyuk, *J. Opt. Soc. Am. B* **17**, 1483 (2000).
8. S. Skupsky, R. W. Short, T. Kessler, R. S. Craxton, S. Letzring, and J. M. Soures, *J. Appl. Phys.* **66**, 3456 (1989).
9. Laboratory for Laser Energetics LLE Review **69**, 1, NTIS document No. DOE/SF/19460-152 (1996) (copies may be obtained from the National Technical Information Service, Springfield, VA 22161); S. Skupsky and R. S. Craxton, *Phys. Plasmas* **6**, 2157 (1999).
10. J. E. Rothenberg, *J. Opt. Soc. Am. B* **14**, 1664 (1997).
11. T. J. Kessler, Y. Lin, J. J. Armstrong, and B. Velazquez, in *Laser Coherence Control: Technology and Applications*, edited by H. T. Powell and T. J. Kessler (SPIE, Bellingham, WA, 1993), Vol. 1870, pp. 95–104.
12. Y. Lin, T. J. Kessler, and G. N. Lawrence, *Opt. Lett.* **21**, 1703 (1996).
13. Y. Kato, unpublished notes from work at LLE, 1984; K. Tsubakimoto *et al.*, *Opt. Commun.* **91**, 9 (1992); K. Tsubakimoto *et al.*, *Opt. Commun.* **103**, 185 (1993).
14. Laboratory for Laser Energetics LLE Review **45**, 1, NTIS document No. DOE/DP40200-149 (1990) (copies may be obtained from the National Technical Information Service, Springfield, VA 22161); T. E. Gunderman, J.-C. Lee, T. J. Kessler, S. D. Jacobs, D. J. Smith, and S. Skupsky, in *Conference on Lasers and Electro-Optics*, Vol. 7, 1990 OSA Technical Digest Series (Optical Society of America, Washington, DC, 1990), p. 354.
15. J. A. Marozas, S. P. Regan, J. H. Kelly, D. D. Meyerhofer, W. Seka, and S. Skupsky, "Laser Beam Smoothing Caused by the Small-Spatial-Scale *B*-Integral," to be published in the *Journal of the Optical Society of America B*.
16. Laboratory for Laser Energetics LLE Review **78**, 62, NTIS document No. DOE/SF/19460-295 (1999). Copies may be obtained from the National Technical Information Service, Springfield, VA 22161.
17. R. N. Bracewell, *The Fourier Transform and Its Applications*, 2nd ed., rev., McGraw-Hill Series in Electrical Engineering. Circuits and Systems (McGraw-Hill, New York, 1986).
18. J. E. Rothenberg, in *Solid State Lasers for Application to Inertial Confinement Fusion*, edited by W. F. Krupke (SPIE, Bellingham, WA, 1995), Vol. 2633, pp. 634–644.
19. J. W. Goodman, *Introduction to Fourier Optics* (McGraw-Hill, New York, 1968).

Tests of EXAFS on OMEGA: Feasibility for Shock-Heating Measurements

Introduction

As part of its participation in the Stockpile Stewardship Program (SSP), LLE is studying the feasibility of using extended x-ray absorption fine structure (EXAFS)¹ to characterize the properties of solid materials shocked at moderately high pressures (up to a few megabars). In particular, there is an interest in examining material properties since they affect the growth of hydrodynamic instabilities. Thus, a shocked material that retains its strength (or shear) will be more resistant to such instabilities than a molten solid. EXAFS is sensitive to the short-range order in crystals (as opposed to diffraction, which depends on longer-range order). It can be seen in amorphous materials^{2,3} as well as liquids,⁴⁻⁶ but the reduction in short-range order due to melting is then evident in the EXAFS spectrum. EXAFS can measure the density and temperature of the shocked solid in addition to indicating melting. The main limitation in shock-heating studies is the reduction of the EXAFS modulation amplitude with increasing temperature. This problem is discussed in detail in this article. EXAFS can possibly indicate whether the shock compression of the solid is one- or three-dimensional: the distances to the nearest atomic neighbors (which is measured by EXAFS) are different in the two cases. Initial tests show very high contrast EXAFS modulations when a thick, undriven Ti foil is backlit by the x-ray radiation from an imploded CH shell. The high contrast achieved in these tests is due to three factors: (a) using an imploded target as a backlighter, (b) using a very thick Ti absorber, and (c) using a CID array for detection. In preparation for future shocked-Ti experiments, we scope out the range of shock strengths where significant EXAFS modulation can be expected. Briefly, although a higher temperature reduces the amplitude of EXAFS modulations, a higher density mitigates this reduction (by raising the Debye temperature). For varying shock strengths we determine the temperature and density of the Ti metal and then the expected EXAFS visibility. EXAFS has been previously seen in laser-produced plasma experiments,⁷ and at LLE it has been studied⁸ in imploded spherical targets (where the absorber was also Ti).

Experiment

The tests reported here were performed with undriven, 12.5- μm -thick Ti foils, positioned in front of an x-ray spectrometer. Such tests are useful for determining the ability of the diagnostic system to measure the high-quality EXAFS modulations required to analyze shock-heated materials. The last section of this article discusses the problem of EXAFS visibility in future shocked-Ti experiments. In the present experiment, the 60-beam OMEGA laser system with SSD-smoothed beams (1.5 \times 11- \AA bandwidth) was used to implode CH shells. We show data from two almost identical shots (21238 and 21239), where a 1-ns square pulse of energy \sim 22.8 kJ was used to implode 20- μm -thick CH shells of 937- μm outer diameter, filled with a mixture of hydrogen at 2.4 atm and deuterium at 0.6 atm.

Figure 86.50 shows the spectrum from shot 21238 obtained when the radiation emitted by the imploding CH shell is transmitted through the 12.5- μm -thick Ti foil and measured by a Ge(1,1,1) crystal and a CID array (see below). The EXAFS modulations above the Ti *K* edge are clearly seen. The high-contrast modulations are due to three factors employed in these tests:

- (a) Using the intense (and smooth) emission of an imploding CH target as a backlighter. The smoothness of the incident spectrum is important for measuring modulations in the absorption. In other applications, a high-*Z* planar target is typically used for backlighting because it generates a line spectrum. The compressed CH, on the other hand, produces a smooth continuum spectrum; the high radiation intensity ($\sim 10^{17}$ keV/keV at 5 keV) is due to the high density, not the high *Z*. Additional advantages of the imploded backlighter are the short emission time, \sim 120 ps (which may yield useful results even without time resolution), and the small dimension, leading to higher spectral resolution.

(b) Using a thick Ti foil, which results in a very high attenuation, $\sim \exp(-4)$, rather than the customary attenuation of $\sim \exp(-1)$. This increases the relative modulations in the measured signal: if the latter is written as $I \sim \exp(-\tau d)$, where τ is the opacity and d is the foil thickness, the relative modulation $|\Delta I/I| \sim d\Delta\tau$ is proportional to the foil thickness. The optimal thickness is the largest for which the signal is still above the noise level. The choice of 12.5- μm thickness is possible due to the high intensity of the flux from an imploded target. We show below that measuring an EXAFS spectrum through such a thick foil does not detract from our ability to study shocks launched into the foil. Specifically, the shock is quite uniform when its front has reached the back of the foil. This is important for an unambiguous interpretation of the absorption results. The choice of titanium (rather than a lower- Z foil) results from the fact that with a high attenuation the detected spectrum is dominated by the second-order crystal diffraction (for which the attenuation is much smaller). In Ti the second-order radiation (around ~ 10 keV) is too weak to affect the results.

(c) Using CID electronic detection rather than film. The CID array we used (from CID Technologies, Inc.) was an 812×604 array having square pixels with 38.5- μm center-to-center spacing, uncooled and with no conversion phosphor. The analog-to-digital converter with 16-bit resolution was fast enough to minimize the effect of dark current. The superior performance with respect to film is mainly due to the lower noise. CID arrays are more immune to radiation damage than CCD arrays; they have been extensively studied, implemented, and calibrated at LLE.⁹

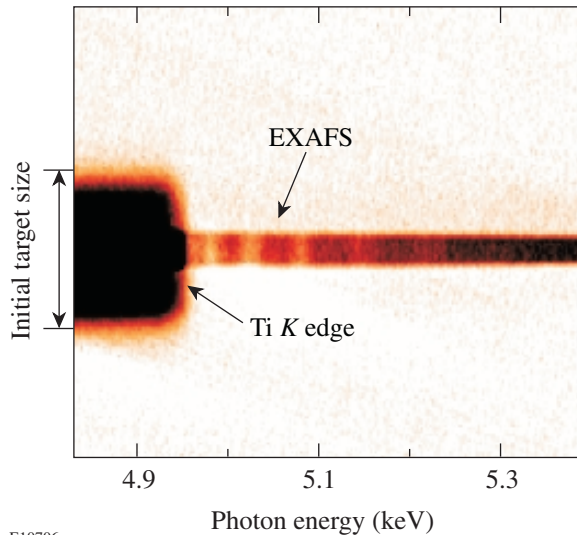
The spectrum in Fig. 86.50 is spatially resolved in the vertical direction. Above the K edge, because of the strong attenuation, only the more intense radiation from the compressed core can be seen. Below the K edge the intensity is high enough to be seen over the whole target volume (and to saturate the core image). The spectrum without the absorber (i.e., the incident spectrum) is measured in parallel by employing additional filtering.

Figure 86.51 is a lineout through the calibrated spectrum, and it shows that the depth of modulation is indeed high. The choice of Ti foil thickness is about optimal for the available x-ray flux, as seen from the fact that the minimum intensity is close to zero.

The theory of EXAFS¹ yields an expression for $\chi(k) = \mu(k)/\mu_0(k) - 1$, where $\mu(k)$ is the absorption coefficient (or opacity) and $\mu_0(k)$ is the absorption of the isolated atom (i.e., without the EXAFS oscillations). By passing a smooth curve through the EXAFS oscillations, $\mu_0(k)$ can be obtained (it is also known from published tables). The wave number k of the ejected photoelectron is given by $\hbar^2 k^2 / 2m = E - E_K$, where E is the absorbed photon energy and E_K is the energy of the K edge. Figure 86.52 shows the quantity $\chi(k)$ derived from Fig. 86.51. The period and magnitude of the oscillations agree well with what is obtained in synchrotron experiments on Ti,¹⁰ but the first peak is too high in comparison.

To assess the noise in the measured spectrum we compare successive spectra in adjacent rows of pixels (horizontal rows in Fig. 86.50). If S_i is the signal (or spectrum) of the i th row, the average signal S (such as was used in Fig. 86.51) is given by

$$S = \sum_{i=1}^m S_i / m, \quad (1)$$



E10706a

Figure 86.50
EXAFS modulation spectrum obtained on a CID array (shot 21238) when the x rays from an OMEGA-imploded CH target are absorbed by a 12.5- μm -thick Ti foil. Below the K edge the radiation from the entire target is strong enough to be seen; above the K edge only radiation from the compressed core is seen.

where we select m central rows within the spatial (vertical) profile to avoid edge effects. For the average noise N , using the same rows, we write

$$N = \sum_{i=1}^{m/2} (S_{2i-1} - S_{2i})/m. \quad (2)$$

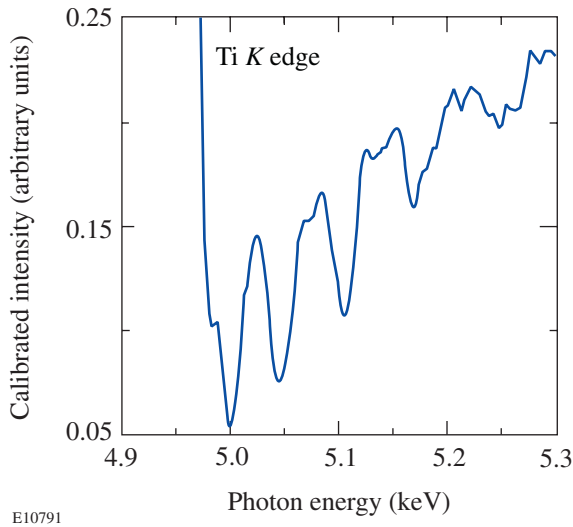


Figure 86.51
The calibrated EXAFS signal for shot 21238 in arbitrary units. The relative depth of modulation is seen to be very high.

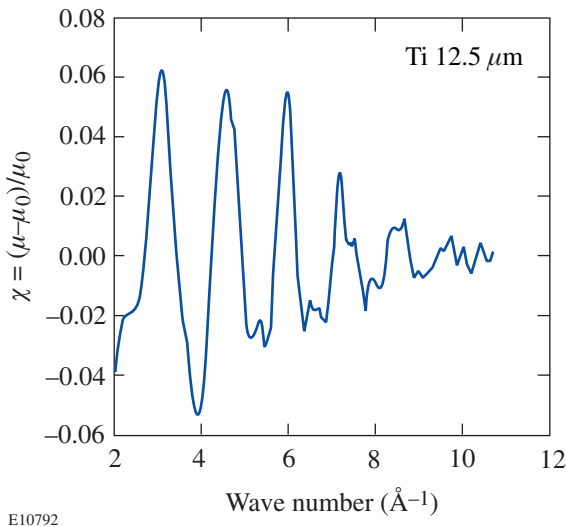


Figure 86.52
Measured relative modulation of the absorption in Ti derived from Fig. 86.51 as a function of the wave number of the ejected electron (following K -shell photoionization).

The random components of the measured signal add up in Eq. (2), whereas the net signal cancels out; thus, N is the appropriate noise quantity to be compared with S . Figure 86.53 compares the signal (above the K edge) and the noise in the same units (pixel values). The signal is taken to be the modulations in Fig. 86.51 around a smooth average curve [the subtraction in Eq. (2) cancels out both this smooth curve and the EXAFS modulation around it]. The noise is seen to be negligible relative to the signal up to $k \sim 10.5 \text{ \AA}^{-1}$, beyond which the data is ignored.

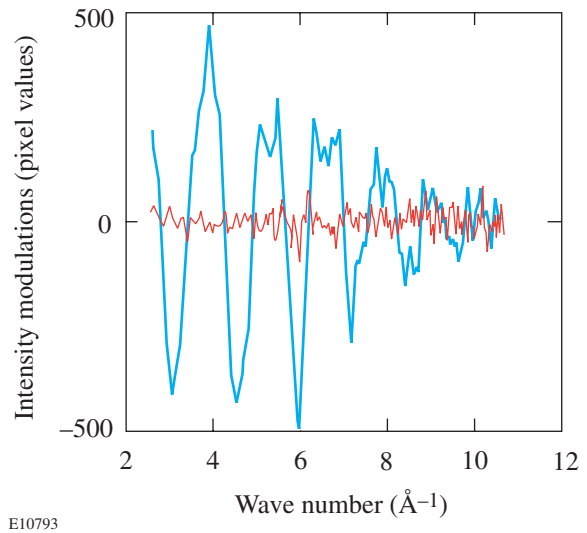


Figure 86.53
Comparison of the EXAFS signal and noise using the results of Fig. 86.50 and Eqs. (1) and (2). The signal is given by the modulations in Fig. 86.51 around a smooth average curve.

Theory of EXAFS

When photons of energy above the K edge (say, of Ti) are absorbed, a K -shell electron is ejected. In a solid material, the electron wave can be reflected from neighboring atoms and interfere with the outgoing electron wave. For different photon energies, the energy (and hence the wavelength) of the ejected electron will vary and so will the phase difference between the two waves. Thus, the interference translates into modulations in the cross section for photon absorption (i.e., the opacity). The period of the modulations is clearly related to the inverse of the interatomic distance and thus yields the density. The rate of decay of the modulations depends mostly on the temperature because at higher temperatures the ion-vibration amplitude increases, which causes a random phase shift of the reflected electron waves.

The basic theory yields the following expression for $\chi(k)$:

$$\chi(k) = \sum_j N_j F_j(k) \exp[-2\sigma^2 k^2 - 2R_j/\lambda(k)] \times \sin[2kR_j + \phi_j(k)]/kR_j^2, \quad (3)$$

where N_j is the number of atoms surrounding the absorbing atom at a distance R_j ($N_1 = 12$ in Ti). The sum over j relates to the various shells of atoms around the photo-absorbing atom, in increasing distances. The backscattering amplitude $F_j(k)$ and phase-shift factor $\phi_j(k)$ for titanium were taken from the detailed calculations by Teo and Lee;¹¹ the mean free path of the ejected electron in titanium, $\lambda(k)$, was taken from the calculations of Blanche *et al.*¹⁰ The vibration amplitude σ^2 (the Debye-Waller factor) and the interatomic distances R_j are treated as adjustable parameters in fitting the experimental EXAFS spectrum to Eq. (3). The distances R_j (in particular R_1) yield the density of the absorber. As discussed below, σ^2 depends on both the temperature and the density; once the density is determined from R_1 , the temperature can then be determined from σ^2 . Equation (3) shows that the oscillations decay with increasing k , even if σ^2 were negligibly small. For the temperatures of interest here, however, the decay is dominated by σ^2 . In addition, an adjustable shift Δ is introduced¹² in the K -edge energy because of solid-state effects at energies close to the edge. Equation (3) is based on some simplifying assumptions (such as plane rather than spherical electron waves and neglect of multiple scattering). More advanced theories^{13–15} include such effects, but such improvements are not essential here because the shock compression will change the interatomic distance appreciably; thus a highly precise determination of the R_j 's is not required.

We next fit the experimental EXAFS spectrum to Eq. (3). The customary procedure is to work with the function $k\chi(k)$ [or even $k^3\chi(k)$] rather than $\chi(k)$. By doing so we place less weight on the low- k part of the spectrum, where the theory is uncertain. Also, to simplify the fitting, we use only the first term ($j = 1$) in Eq. (3). The equivalent experimental spectrum is obtained in the following manner. First, the experimental spectrum is Fourier transformed to the R space. The amplitude of the Fourier transform of $\chi(k)$ gives the charge distribution around an absorbing Ti atom.¹ Simply put, a constructive interference occurs when the interatomic distance equals an integer multiple of half the electron wavelength. Figure 86.54 shows this distribution for the two consecutive laser shots analyzed in this article. The distribution is seen to be reproducible, and it agrees

well with the published data on Ti obtained with synchrotron radiation.^{10,15} The major peak is due to the nearest neighbors around the absorbing atom, whereas the minor peak is due to the next shell of neighboring atoms.

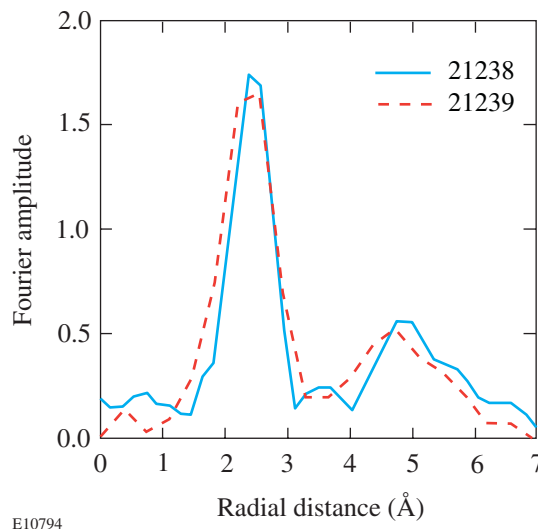


Figure 86.54

Amplitude of the Fourier transform of the EXAFS spectrum $\chi(k)$ for two consecutive laser shots. The transform corresponds to the charge distribution around the photon-absorbing Ti atom. The weaker peak is particularly sensitive to reduction in short-range order due to melting.

In addition to crystalline materials, EXAFS has been measured in amorphous materials^{2,3} as well as in liquids.^{4–6} As compared with crystals, the amplitude of modulations in the absorption coefficient is lower; in addition, in the R space, the farther-shell peaks are reduced more than the nearest-neighbor peak. This provides a method for detecting melting. Of particular importance in these studies is the demonstrated ability to observe the minor peak since it is more sensitive to melting or to any change in short-range order. The main peak in Fig. 86.54 is selected by multiplying the distribution by a super-Gaussian filter centered on that peak. Finally a transform back to the k space is performed. This procedure is sufficient for determining the temperature and density. The range of 2 to 10.5 \AA^{-1} was used to analyze $k\chi(k)$. Below 2 \AA^{-1} the curve is negligibly small; above $k \sim 10.5 \text{\AA}^{-1}$ the EXAFS spectrum is limited by noise.

Figure 86.55 shows the best fit, with $R_1 = 2.9 \text{\AA}$, $\sigma^2 = 0.0049 \text{\AA}^2$, and $\Delta = -13 \text{ eV}$. These values agree with the results found for Ti in synchrotron-radiation experiments.¹⁵ The experimental spectrum $k\chi(k)$ had to be multiplied by a factor ~ 1.8 to normalize it to the theoretical spectrum. This is consistent

with what is found in other EXAFS studies:¹⁶ Rehr *et al.*¹⁶ have shown that the relaxation of bound electrons that accompanies the ejection of *K*-shell electrons reduces the EXAFS amplitude from Eq. (3) by about a factor of 2. The quality of the fit can be improved if more-sophisticated versions of the theory are used. As explained above, however, this is not required in these studies.

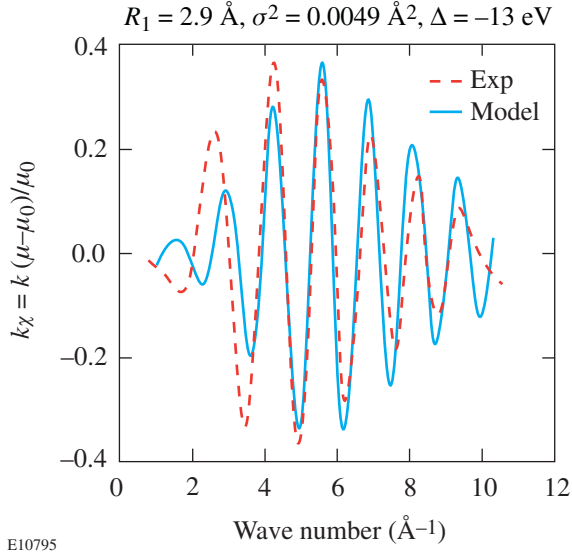


Figure 86.55

Fitting the model [Eq. (3)] to the observed EXAFS $k\chi(k)$ spectrum. Shown are the parameter values giving the best fit. The interatomic distance R_1 depends on the density, and the Debye–Waller factor σ^2 depends mostly on the temperature. Δ is an adjustable shift applied to the *K*-edge energy to account for solid-state effects.

EXAFS Visibility

1. Dependence of σ^2 on Temperature and Density

As seen from Eq. (3), when the temperature (and thus σ^2) increases, the EXAFS modulations decay faster with k and may become useless for diagnosing the target. To determine the useful temperature range for EXAFS observation we use the calculated dependence¹⁷ of σ^2 on temperature:

$$\sigma^2 = \frac{3\hbar^2}{Mk\Theta_D} \left[\left(\frac{1}{4} \right) + \left(\frac{T}{\Theta_D} \right)^2 \int_0^{\Theta_D/T} \frac{x dx}{e^x - 1} \right], \quad (4)$$

where M is the atomic mass. Equation (4) was derived using a Debye model of lattice oscillations in a cubic, perfect crystal. It assumes harmonic oscillations so its validity is restricted to low temperatures. It also assumes uncorrelated vibrations of the absorbing and neighboring atoms. This correlation gives

rise to an additional term¹⁷ in Eq. (4), which we have neglected. Studies of the correlation^{18,19} show that it reduces σ^2 by a about a factor ~ 1.6 around room temperatures; this correction factor was incorporated in subsequent calculations at all temperatures. Figure 86.56 shows the dependence of the corrected σ^2 on temperature for Ti at solid density. At room temperature the value of σ^2 ($\sim 0.005 \text{ \AA}^2$) agrees with the value found from the present experiment (Fig. 86.55), which also agrees with the results of synchrotron experiments on Ti.¹⁰

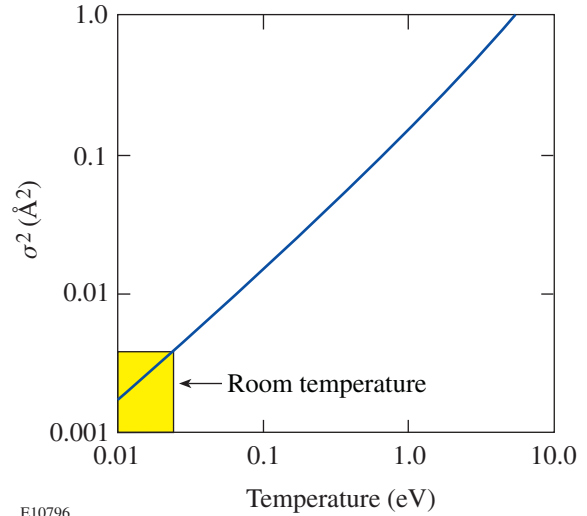


Figure 86.56

The dependence of the vibration amplitude σ^2 (corrected for correlation) on temperature for solid Ti density.

Although the increased temperature due to the shock increases σ^2 and reduces the EXAFS visibility, the increased density behind the shock *decreases* σ^2 because σ^2 depends on T/Θ_D and Θ_D increases with density. The latter can be understood by noting that Θ_D is related to k_D , the maximum wave number of phonon vibrations, which changes as R^{-1} ; thus, shock compression reduces R and increases Θ_D .

The density dependence of Θ_D can be determined from an empirical model²⁰ due to Cowan, in terms of the nuclear charge Z and the atomic weight A . The result is

$$k\Theta_D = [1.68/(Z + 22)] \left[\xi^{b+2} / (1 + \xi)^2 \right] \text{eV}, \quad (5)$$

where

$$b = 0.6 Z^{1/9}, \quad \xi = \rho / \rho_{\text{ref}}, \quad \rho_{\text{ref}} = (A/9Z^{0.3}) \text{g/cm}^3. \quad (6)$$

Figure 86.57 shows the dependence of the Debye temperature of Ti on the density; ρ_s is the solid density. At solid density Θ_D of Ti is 0.0366 eV;²¹ the model overestimates this value by about 15%, so we reduce the model-calculated Θ_D by that factor. Because σ^2 depends on both temperature and density, both parameters must be determined as a function of shock strength in order to assess the expected EXAFS visibility.

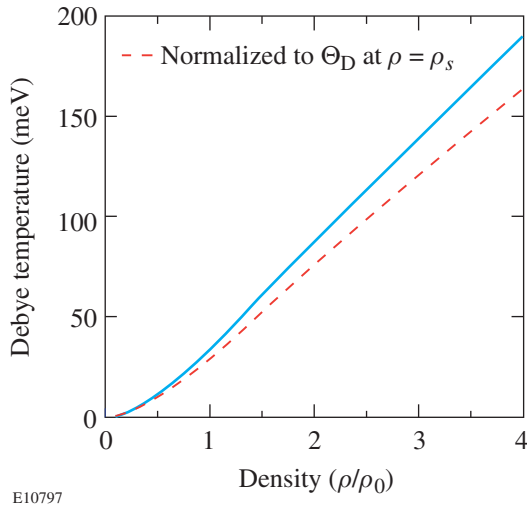


Figure 86.57
Calculated dependence of the Debye temperature of Ti on compression using Cowan's model.²⁰ The dashed curve is normalized to the known Θ_D of Ti at solid density ρ_s .

2. Dependence of Density and Temperature on Shock Strength

In future experiments the Ti foil will be embedded in a double CH layer and driven by a single laser beam, while still backlit by a spherically imploded target. The front CH layer will be thick enough to ensure that no burnthrough occurs before the shock traverses the Ti layer; the role of the rear-surface CH layer is to avoid extraneous effects due to unloading of the shock when arriving at the target–vacuum interface. The parameter space where high-amplitude EXAFS oscillations can be expected to be observed is now estimated. As seen above, both temperature and density achieved by shock compression of Ti as a function of laser irradiance must be determined by (a) using the experimentally known²² Hugoniot of Ti and (b) simulating the interaction with the 1-D code *LILAC*. In these simulations a 10- μm -thick Ti layer was assumed to be coated on each side by a 5- μm -thick CH layer and irradiated by a 1-ns square pulse of various powers. These simulations also determine the uniformity behind the shock over a thick Ti layer.

This requirement is essential for an unequivocal interpretation of the EXAFS results. The *LILAC* simulations (see examples in Fig. 86.58) show that when the shock arrives at the back surface of the Ti layer, the temperature and density within the layer are uniform to within $\pm 10\%$ and the Ti layer is unaffected by rarefaction.

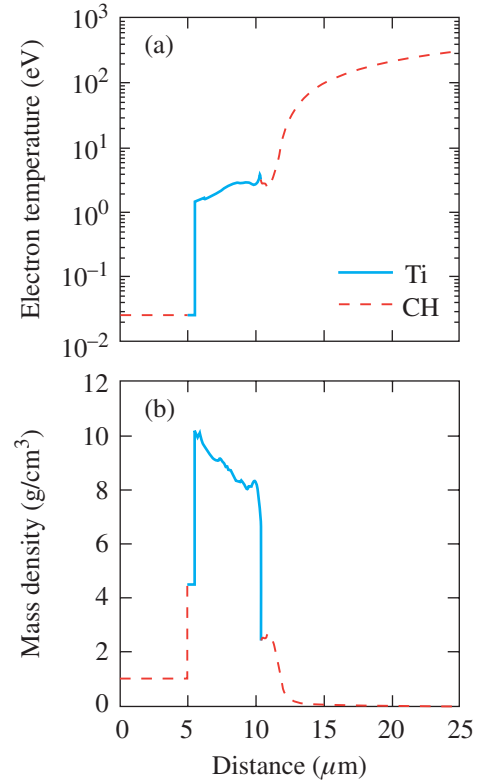


Figure 86.58
Example of *LILAC* simulations of a shock wave in a 10- μm -thick Ti layer sandwiched between two 5- μm -thick CH layers, produced by a 1-ns square pulse at 20 TW/cm². The density and temperature profiles are shown for the instant the shock arrives at the back surface of the Ti layer.

LILAC was run for a series of increasing values of laser intensity, and in each case the density and temperature (averaged over the Ti layer) were determined at the instant the shock arrived at the back surface of the Ti layer. The results are shown in Fig. 86.59 (for the density) and in Fig. 86.60 (for the temperature) as points marked by the value of laser intensity in TW/cm². In parallel to these simulations the density and temperature were determined from experimentally known data. In Fig. 86.59, the red curve shows the measured principal Hugoniot of Ti.²² Although the curves are shown over a wide pressure range, the main interest here is in their low-pressure portion; thus, the melting temperature of Ti at solid density is at 1941°K, or 0.167 eV.

Using the Hugoniot curve, we now determine the temperature in the shocked Ti layer. First, from the Rankine–Hugoniot relation

$$E - E_0 = (P/2) \left[(1/\rho_0) - (1/\rho) \right] \quad (7)$$

we determine the energy increase due to the shock. Here E , P , and ρ are the energy per unit mass, the pressure, and the density behind the shock front, and the subscripted quantities refer to the region in front of the shock front ($P_0 = 0$ was assumed). From the energy increase $E - E_0$ we calculate the temperature behind the shock front, using the quotidian equations of state for ions and electrons described in Ref. 20. For the ions, the energy per ion above Θ_D is given by

$$E_i = 3kT \left[1 + (u^2/20) - \dots \right], \quad u = \Theta_D(\rho)/T. \quad (8)$$

For temperatures much higher than Θ_D , as is the case here, this reduces to $E_i = 3kT$ (the Dulong–Petit law). For the electrons, a modified Fermi–Thomas (FT) equation of state is used.²³ The FT theory at low temperatures yields too high an electron pressure (\sim Mbars) because the bonding between adjacent atoms is neglected and must be corrected. In a convenient semi-empirical correction method devised by Barnes²⁴ an

expression for the bonding energy ΔE (negative for densities higher than solid) is added to the electron energy. ΔE (energy per cm^3) is given by

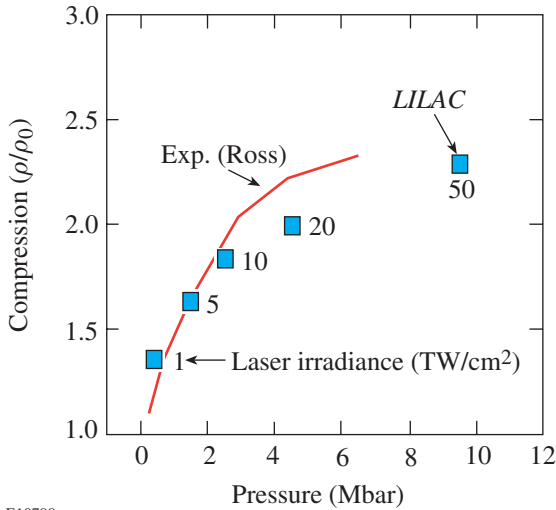
$$\Delta E = E_0 \left\{ 1 - \exp \left[b - b(\rho_s/\rho)^{1/3} \right] \right\}, \quad (9)$$

where ρ_s is the solid density and E_0 and b are adjustable parameters. To be consistent with thermodynamic relations, this change in energy must be accompanied with a change in pressure given by

$$\begin{aligned} \Delta p &= \rho^2 \frac{\delta \Delta E}{\delta \rho} \\ &= - \left(\frac{E_0 b \rho_s}{3} \right) \left(\frac{\rho}{\rho_s} \right)^{2/3} \exp \left[b - b \left(\frac{\rho_s}{\rho} \right)^{1/3} \right], \end{aligned} \quad (10)$$

and the revised bulk modulus becomes

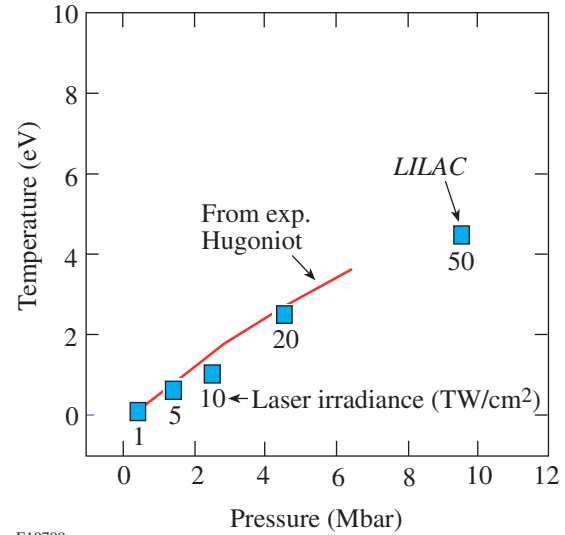
$$B = \rho (\delta p_e / \delta \rho)_{\rho_s} - (b + 2)(E_0 b \rho_s) / 9. \quad (11)$$



E10798

Figure 86.59

Experimentally determined²² principal Hugoniot in Ti (red curve). The points were obtained from *LILAC* code simulations of a shock created when a laser of the shown irradiance (in TW/cm^2) irradiated the buried-Ti target.



E10799

Figure 86.60

Temperature behind the shock as a function of the shock pressure in Ti (red curve) calculated from the known principal Hugoniot and the corrected Fermi–Thomas equation of state. The points were obtained from *LILAC* code simulations of a shock created when a laser of the shown irradiance (in TW/cm^2) irradiated the buried-Ti target.

Here we neglected the ion pressure p_i . Using these two relations for the energy and the pressure, E_0 and b are found from the following two conditions: (a) the corrected pressure $p + \Delta p$ (where p is the Fermi–Thomas pressure) at solid density and $T = 0$ should be 0, and (b) B should agree with the known bulk modulus at normal temperature and density (for Ti, B equals²⁵ 1.1×10^{12} dyn/cm²). We now add ΔE from Eq. (9), with E_0 and b thus determined, to the Fermi–Thomas energies²³ for Ti, using for the latter the fitting expressions worked out by Bell.²⁶ Using Eq. (7), the energy along the experimental Hugoniot (Fig. 86.59) can be calculated. We now equate these energy values with the revised Fermi–Thomas energies. Since these energies depend on density and temperature, using the known densities (Fig. 86.59), we can now search for the temperatures along the Hugoniot. The results are shown as a red curve in Fig. 86.60. Good agreement between the *LILAC* simulations and the experiment-based model is seen in Figs. 86.59 and 86.60, especially for the low-pressure range of relevance in this study.

3. EXAFS Visibility as a Function of Shock Strength

Finally, the vibration amplitude σ^2 can be determined as a function of shock strength from Figs. 86.59 and 86.60, using Eqs. (4) and (5). The results, over the range of pressures of the experimental Hugoniot, are shown in Fig. 86.61. Using Eq. (3) we can show that significant EXAFS modulations can be seen whenever $\sigma^2 \leq 0.1$, so Fig. 86.61 indicates that such modulations in forthcoming shock experiments are expected to show significant amplitude. It should be noted, however, that the density affects the EXAFS visibility directly, in addition to affecting it through σ^2 . Thus, at a higher density the modulation amplitude increases because of the appearance of the interatomic distance R in the denominator of Eq. (3). On the other hand, at a higher density the period of the EXAFS oscillations increases, and there are fewer oscillation periods within the range of k where their amplitude is significant. To demonstrate these effects, the EXAFS spectrum calculated from Eq. (3) was plotted in Fig. 86.62 for two conditions: (a) $\sigma^2 = 0.04 \text{ \AA}^2$ at solid density. From Fig. 86.56 this corresponds to $T \sim 0.25$ eV, just above the melting point. Significant EXAFS modulations are seen for this case. (b) $\sigma^2 = 0.1 \text{ \AA}^2$ at $2.5 \times$ solid density. This represents an extreme case where σ^2 is higher than what will be encountered in these experiments (see Fig. 86.61). The EXAFS spectrum in this case is only marginally useful, especially for determining the density; however, it can still provide a good indication of the temperature. Finally, in calculating the expected EXAFS spectrum we have not included the effect of noncrystallinity, which would modify Eq. (3). Experiments on EXAFS in molten metals [see, e.g.,

Ref. 6(b)] show that the modulation amplitude upon melting is reduced by about a factor of 1.5. Thus, the conclusions reached above should not change significantly when melting is included in the analysis.

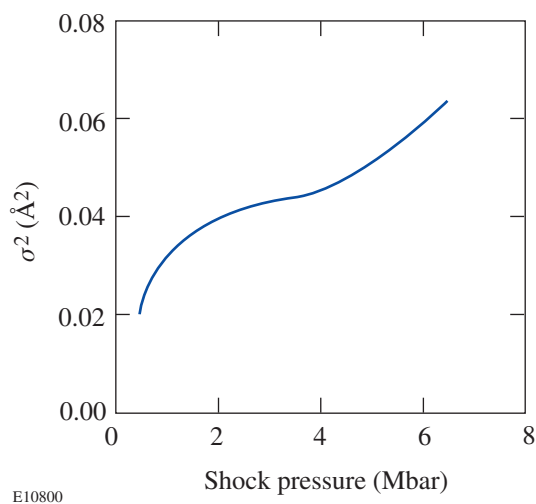


Figure 86.61
The vibration amplitude σ^2 as a function of shock strength, calculated from Figs. 86.59 and 86.60, using Eqs. (4) and (5).

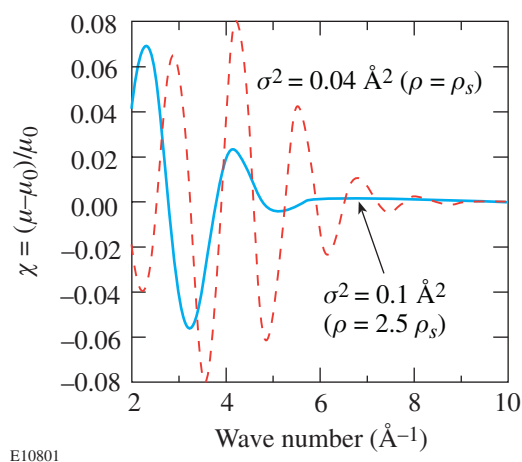


Figure 86.62
Demonstration of the effects of σ^2 and the density on the EXAFS spectrum in Ti. The density affects the spectrum both directly and through σ^2 .

ACKNOWLEDGMENT

This work was supported by the U.S. Department of Energy Office of Inertial Confinement Fusion under Cooperative Agreement No. DE-FC03-92SF19460, the University of Rochester, and the New York State Energy Research and Development Authority. The support of DOE does not constitute an endorsement by DOE of the views expressed in this article.

REFERENCES:

1. P. A. Lee *et al.*, *Rev. Mod. Phys.* **53**, 769 (1981).
2. M. C. Ridgway *et al.*, *Nucl. Instrum. Methods Phys. Res. B* **147**, 148 (1999).
3. D. E. Sayers, E. A. Stern, and F. W. Lytle, *Phys. Rev. Lett.* **27**, 1204 (1971).
4. Y. Katayama, O. Shimomura, and K. Tsuji, *J. Non-Cryst. Solids* **250–252**, 537 (1999).
5. K. Tamura *et al.*, *J. Non-Cryst. Solids* **150**, 351 (1992).
6. E. D. Crozier, in *EXAFS Spectroscopy: Techniques and Applications*, edited by B. K. Teo and D. C. Joy (Plenum Press, New York, 1981), Chap. 6, p. 89; E. D. Crozier and A. J. Seary, *Can. J. Phys.* **58**, 1388 (1980).
7. R. W. Eason *et al.*, *J. Phys. C, Solid State Phys.* **17**, 5067 (1984); B. A. Shiwai *et al.*, *Laser Part. Beams* **10**, 41 (1992).
8. B. Yaakobi, F. J. Marshall, D. K. Bradley, J. A. Delettrez, R. S. Craxton, and R. Epstein, *Phys. Plasmas* **4**, 3021 (1997).
9. F. J. Marshall, T. Ohki, D. McInnis, Z. Ninkov, and J. Carbone, *Rev. Sci. Instrum.* **72**, 713 (2001).
10. G. Blanche *et al.*, *Ultramicroscopy* **50**, 141 (1993).
11. B.-K. Teo and P. A. Lee, *J. Am. Chem. Soc.* **101**, 2815 (1979).
12. See Ref. 1, Sec. IV(B); Ref. 15, p. 6358.
13. P. A. Lee and J. B. Pendry, *Phys. Rev. B* **11**, 2795 (1975).
14. J. J. Rehr and R. C. Albers, *Rev. Mod. Phys.* **72**, 621 (2000).
15. A. Balzarotti, M. De Crescenzi, and L. Incoccia, *Phys. Rev. B* **25**, 6349 (1982).
16. J. J. Rehr *et al.*, *Phys. Rev. B* **17**, 560 (1978); see also Ref. 1, Sec. III(G).
17. G. Beni and P. M. Platzman, *Phys. Rev. B* **14**, 1514 (1976).
18. R. B. Gregor and F. W. Lytle, *Phys. Rev. B* **20**, 4902 (1979).
19. G. Dalba and P. Fornasini, *J. Synchrotron Radiat.* **4**, 243 (1997).
20. R. M. More *et al.*, *Phys. Fluids* **31**, 3059 (1988).
21. R. E. Bolz and G. L. Tuve, eds. *CRC Handbook of Tables for Applied Engineering Science*, 2nd ed. (CRC Press, Boca Raton, FL, 1973), Chap. 2.2, p. 231.
22. M. Ross, *Rep. Prog. Phys.* **48**, 1 (1985).
23. R. Latter, *Phys. Rev.* **99**, 1854 (1955).
24. J. F. Barnes, *Phys. Rev.* **153**, 269 (1967).
25. G. V. Samsonov, ed. *Handbook of the Physicochemical Properties of the Elements* (IFI/Plenum, New York, 1968), Chap. VI, p. 397.
26. A. R. Bell, Rutherford and Appleton Laboratories, Chilton, Didcot, Oxon, England, Report RL-80-091 (1980).

Microhardness and Indentation Fracture of Potassium Dihydrogen Phosphate (KDP)

Introduction

Potassium dihydrogen phosphate (KDP) is an important electro-optic tetragonal crystal. For example, it is used as a photonic material in the third-harmonic generation (THG) to reduce light wavelength from 1.054 μm to 351 nm. Microindentation has been used to measure the Vickers and Knoop hardness of KDP and the resulting cracking on (100) and (001) faces. Hardness anisotropy on the (001) face, or among the (100) and (001) faces, was found to be small (about 20%). An indentation size effect for both Vickers and Knoop hardness for indenting loads in the range of 25 to 200 g was observed. The large-load Vickers hardness was estimated as 1.4 ± 0.1 GPa. Anisotropy in the crack sizes on (100) and (001) faces was also observed. Cracks were longer on (100) faces, scaling like $c \sim P^{2/3}$; cracks on (001) faces were shorter, scaling like $c \sim P^{1/2}$. Assuming elastic and plastic isotropy, crack sizes were analyzed and fracture toughness K_c was extracted. An approximate model for analyzing crack-load microindentation data in tetragonal crystals is presented in this article. The model uses the minimum elastic modulus of the material. The effect of the isotropy assumption on the extracted fracture toughness is estimated at about 33%, with a 23% contribution from elastic anisotropy and 10% from the slip system plastic anisotropy. Strain-rate effects are identified as important aspects of KDP deformation, especially in laser damage applications.

One of the limiting factors in the use of KDP in THG is its susceptibility to laser damage, a process that couples light absorption with thermal and mechanical effects. (For a summary of the electro-optical properties, see Milek and Neuberger.¹)

KDP crystals are water soluble and brittle. Above its ferroelectric Curie temperature (123 K) the crystal structure of KDP is tetragonal, lacking a center of inversion. KDP is optically uniaxial with the optic axis along the tetragonal z axis or [001] direction. At room temperature the lattice constants are $a = 0.7453$ nm and $c = 0.6975$ nm, as cited in Ref. 1. The natural habit of crystals grown from solution is a tetragonal prism combined with a tetragonal bipyramid. The prism faces are (100) and (010) planes. The prism axis is [001].

KDP is relatively soft and brittle as compared to other optical materials, including glasses. In this article microhardness and indentation cracking fracture measurements of KDP indented on crystal planes (100) and (001) are summarized.

Kishan Rao and Sirdeshmukh² measured the Vickers microhardness of KDP at loads of 50 and 100 g, reporting a value of $H_v = 1.43$ GPa for indentation normal to {100} planes (what they called “ a -direction”) and 1.29 GPa for indentation normal to {001} planes (“ c -direction”). Their error was reported as $\pm 4\%$. Anbukumar *et al.*³ also measured the Vickers hardness of {100} planes of KDP. They reported hardness in the range of 1.77 to 1.57 GPa for loads in the range of 5 to 50 g and an indentation size effect (ISE) where the hardness decreased with increased load.

Shaskol'skaya *et al.*⁴ and Guin *et al.*⁵ reported measurements of both hardness and cracking in the Vickers measurements of KDP and $\text{KD}_{2x}\text{H}_{2-2x}\text{PO}_4$ (deuterated KDP, with $x = 0$ to 0.95). They used loads of 50 to 200 g and reported a hardness reduction from 1.44 GPa to 1.22 GPa as the extent of deuteration x increased from 0 to 0.95. Shaskol'skaya *et al.*⁴ also measured the length of cracks (tip-to-tip distance $2c$) due to Vickers indents. They observed that $(2c)/D$ varied from 3.87 to 3.61 as x increased from 0 to 0.95. They also reported a value of 51 MPa for the microstrength $P/(2c)^2$ of both KDP and 95% deuterated KDP.

Guin *et al.*⁵ reported measurements similar to those of Shaskol'skaya.⁴ They also identified two types of slip systems in KDP: the first system consisted of slip planes (110), (101), (112) and (123) with a common Burgers vector $\langle 111 \rangle/2$; the second slip system was identified as (010)[100].

More recently, Marion⁶ has reported measured values of fracture toughness in KDP crystals. Marion apparently used the direct crack method described by Anstis *et al.*,⁷ although the measured data were not described. Marion⁶ reported fracture toughness K_c of 0.2 MPa.m^{1/2}, as well as 0.09 MPa.m^{1/2} along the weakest direction (longest crack). No crystallo-

graphic orientation of the indented faces was reported, however, nor was the applicable elastic constant (modulus) given.

Given the importance of KDP in third-harmonic generation for 351-nm-wavelength laser systems, a systematic study of indentation hardness (Vickers and Knoop) and microindentation cracking in KDP is described below.

Measurements

Vickers indentation was used to measure the indentation size effect on H_V and also to extract the fracture toughness from the measured dependence of crack size on indenting load. Vickers hardness on (100), (010), and (001) planes of single-crystal KDP was measured at room temperature with a Tukon Microhardness Tester equipped with a video image-capture camera. Typical descent rate of the indenter is about 1 mm/min.

The KDP crystal was provided by a commercial vendor and had been grown from the solution. The crystal surfaces were polished by conventional means with nonaqueous slurries to optical standards. Although surface roughness was not directly measured, it was estimated to be approximately 3 to 5 nm (rms).

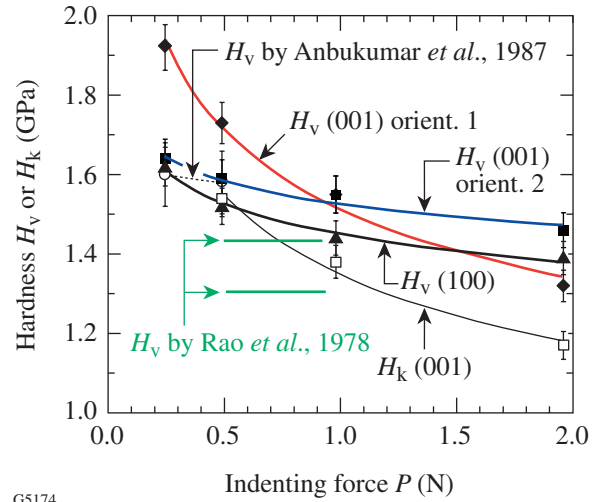
The indentation load was in the range of 2 to 200 g, and each load was applied for 15 s. Five indentations were performed at each load. The indentation diagonal D and crack size $2c$ (tip-to-tip distance) were measured with an optical microscope with a 50 \times objective lens. For the Vickers indentation of (100) and (010) planes, the indenter diagonals were along the principal directions of the type $\langle 100 \rangle$. No differences were observed in the indentation diagonal or crack size of (100) and (010) faces.

For the indentation of (001) planes, we selected two indenter orientations: in orientation (1), the indenter diagonals were parallel to [100] and [010]; in orientation (2), the indenter sides were along [100] and [010].

Figure 86.63 shows the measured hardness over the range of indenting loads used. Figure 86.64 shows the measured crack size for Vickers indentation of (100) and (001) faces. The crack-to-indent ratio $c/(D/2)$ varied from 2 to 4.5, depending on load and orientation.

Knoop indentation was used to measure the indentation size effect on Knoop hardness and also the hardness anisotropy of the (001) faces. For the indentation size effect (loads of 50 to

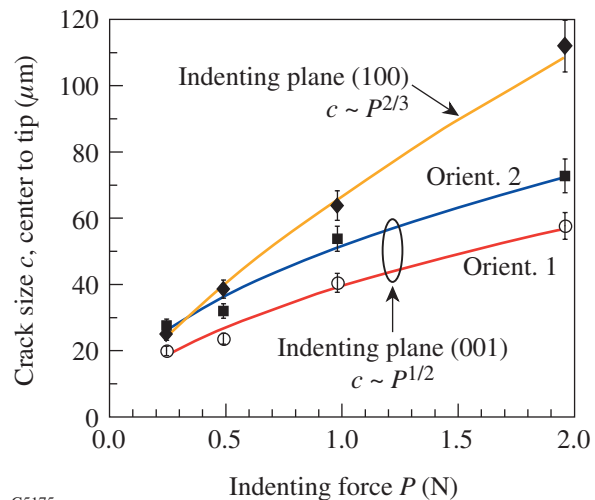
200 g), the indenter's long diagonal was along [010]. These results are included in Fig. 86.63.



G5174

Figure 86.63

Variation of measured hardness (Vickers and Knoop) with load for KDP at room temperature. Vickers indentation was done on faces (100) and on indenter orientations (1) and (2) on the (001) faces. Orientation (1) had the indent diagonals parallel to (100) and (010). Orientation (2) had the indent edges parallel to (100) and (010). Also shown are Vickers measurements by Anbukumar *et al.*³ and Rao *et al.*² Guin *et al.*⁵ reported Vickers hardness 1.45 GPa at 200 g.



G5175

Figure 86.64

Variation of indentation crack size c with indenting load. The tip-to-tip surface crack length is $2c$.

For the hardness anisotropy, we used a load of 50 g and measured the variation of H_k with orientation θ of the Knoop indenter with respect to the indented surface. Angle $\theta = 0^\circ$ corresponds to the indenter long diagonal along the [010] direction. The angle θ was changed in increments of 10° from $\theta = 0^\circ$ to 90° . The hardness anisotropy is shown in Fig. 86.65.

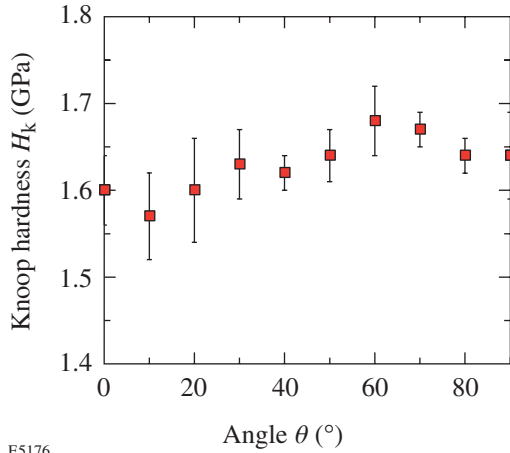


Figure 86.65
Dependence of Knoop hardness on angle θ of indent on the (001) plane. $\theta = 0$ corresponds to the Knoop diagonals being along (100) and (010).

Results

The measured Vickers hardness is seen to vary between 1.7 and 1.4 GPa over the indenting load range of 50 to 100 g. This hardness range is consistent with the measurements of Rao *et al.*² over the same load range. Our measurements are also consistent with those of Anbukumar *et al.*³ over the load range of 25 to 50 g, and with Guin *et al.*⁵ and Shaskol'skaya *et al.*⁴ who reported a hardness of 1.45 GPa at a load of 200 g.

The measured Vickers hardness brings up two questions: What is the relative hardness of (100) and (001) faces? What is the relative hardness of orientations (1) and (2) of the indenter on face (001)?

Our results show that for loads less than 150 g, (001) faces are harder than (100) faces by as much as 14% at lower loads. On (001) faces, orientation (1) is harder than orientation (2), by as much as 10%. At loads of about 200 g, however, both faces and both orientations have hardness in the range 1.4 ± 0.1 GPa; therefore, this value may be used as the load-independent, orientation-insensitive Vickers hardness of KDP.

Our results also show that the Knoop hardness on the (001) face is not strongly anisotropic. The variation of hardness with direction is seen to be less than 10%.

No analysis is available to convert measured micro-indentation crack sizes to fracture toughness in tetragonal crystals. The only available analysis is for isotropic materials, such as glasses or polycrystalline ceramics (see Ref. 8). Therefore, to convert our direct measurements of indentation crack size to a fracture toughness, we shall assume that KDP can be described by an equivalent isotropic Young's modulus $E = 38.7$ GPa. This value is the mean of the Reuss and Voigt averages for the Young's modulus, with the derivation presented in the Appendix. We have analyzed the microindentation crack measurements (indentation diagonal D , tip-to-tip crack size $2c$) using the model of Evans⁹ and Anstis *et al.*⁷ The comparative merits and applicability of various models to extract the fracture toughness by microindentation cracking in optical glasses and brittle ceramics have been discussed by Ponton and Rawlings^{10,11} and Lambropoulos *et al.*¹²

Evans⁹ used dimensional analysis and curve fitting over a range of $c/(D/2)$ from 1.5 to 7 and for many polycrystalline ceramic materials; thus, this model should be applicable to both short and long indentation cracks. According to the Evans model,⁹

$$K_c = H\sqrt{D/2} \left(\frac{E}{H}\right)^{0.4} 10^{f(x)}, \quad x = \log_{10}\left(\frac{c}{D/2}\right), \tag{1}$$

$$f(x) = -1.59 - 0.34x - 2.02x^2 + 11.23x^3 - 24.97x^4 + 16.23x^5,$$

where K_c is the fracture toughness, H is the hardness, D is the indentation diagonal, E is the Young's modulus, and c is the half-crack size. Lankford¹³ included Al_2O_3 , soda-lime silicate glass, and NaCl to the materials analyzed by Evans.⁹

Anstis *et al.*⁷ examined various glasses (glass-ceramic, soda-lime, aluminosilicate, lead alkali), polycrystal Al_2O_3 and sapphire, Si_3N_4 , SiC, Ca-PSZ ZrO_2 , Si, and SiC/Co and concluded that

$$K_c = (0.016 \pm 0.002) \left(\frac{E}{H}\right)^{1/2} \frac{P}{c^{3/2}}. \tag{2}$$

The Anstis model is based on the assumption that the observed surface cracks are surface traces of sufficiently large radial cracks, so that $c \sim P^{3/2}$. On the other hand, the Evans model is applicable for both shorter near-surface cracks, where $c \sim P$, and deeper radial cracks.

As an example of this approach, when the data by Shaskol'skaya *et al.*⁴ or Guin *et al.*⁵ are analyzed via the Evans model and with $E = 38.7$ GPa, they yield $K_c = 0.24 \pm 0.04$ MPa.m^{1/2} at the indentation load of 200 g. The Anstis model leads to $K_c = 0.17 \pm 0.03$ MPa.m^{1/2} over the same increase of indentation load. The Anstis model predictions are in agreement with the reported values of 0.09 to 0.20 MPa.m^{1/2} by Marion.⁶ Note, however, that the work of neither Shaskol'skaya *et al.*⁴ nor Guin *et al.*⁵ describes the orientation of the indented planes or the orientation of the indenter with respect to the indented plane.

The results of our data analysis using the Evans model are shown in Fig. 86.66, where we have used $E = 38.7$ GPa. We observe that the crack-to-indent aspect ratio $2c/D$ is in the range of 2 to 4.5, therefore within the range of applicability of the Evans model. It is seen that the computed fracture toughness K_c of indenting the (001) planes is higher than that when indenting the (100) planes. It is also observed that smaller crack sizes apparently produce higher fracture toughness. For $2c/D$ values of 3 or higher, however, it is seen that the fracture toughness becomes independent of the geometry of the indent producing the cracks. For completeness, Fig. 86.66 shows the (average) \pm (one standard deviation) of the computed fracture toughness for each of the two orientations (1) and (2) on faces (001), as well as that for face (100). The standard deviation was computed from the fracture toughness variation over all the indenting loads used. The results for the two orientations of face (001) overlap, while exceeding that for (100).

The comparisons of the models by Evans⁹ and Anstis *et al.*⁷ are shown in Fig. 86.67. Both results are based on using Young's modulus $E = 38.7$ GPa. We observe that the Evans model predicts fracture toughness that is a factor of 1.2 to 1.45 higher than the predictions of the Anstis model; however, both models give the same qualitative ranking of the data.

Discussion

The analysis above rests on two important assumptions. The first assumption is that the anisotropic KDP crystals can be analyzed for fracture toughness using an equivalent isotropic Young's modulus.

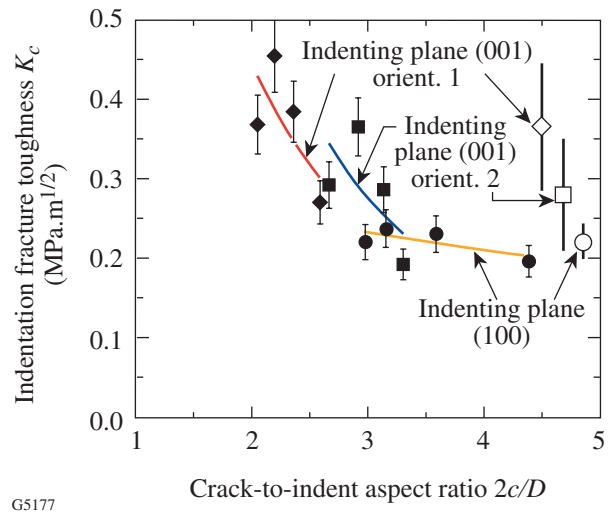


Figure 86.66

Dependence of fracture toughness computed via the Evans model⁹ on the crack-to-indent aspect ratio $2c/D$, using the average Young's modulus $E = 38.7$ GPa. Error bars on the data points reflect measurement uncertainty at each crack size. The thick vertical bars on the right show the (average) \pm (one standard deviation) for each indent orientation. The standard deviations shown on these bars reflect the variation of the fracture toughness over the whole range of indenting loads. To convert these values of fracture toughness to those with the minimum Young's modulus of $E = 20.4$ GPa, multiply these values by 0.774.

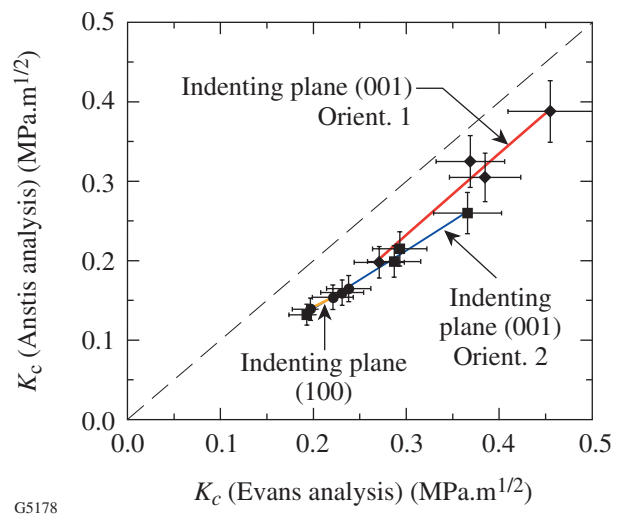


Figure 86.67

Comparison of prediction of fracture toughness by the Evans model⁹ and the Anstis *et al.*⁷ Results are for $E = 38.7$ GPa. The dashed straight line is a line of slope 1.

To estimate the effect of such an assumption, for example, on the predictions by the Evans model, we observe that that model uses the term $(E/H)^{0.4}$. As the unconstrained Young's modulus E varies from 20.4 to 65 GPa, we conclude that the minimum fracture toughness corresponds to the lowest Young's modulus of 20.4 GPa. This, in turn, leads to a change in K_c by $(20.4/38.7)^{0.4} = 0.774$. Therefore, the effect of elastic anisotropy is estimated to be about 23% on the computed fracture toughness. These results are summarized in Table 86.V. In our data, we give the uncertainty over all the indenting loads used. It is seen that the Anstis *et al.* model,⁷ when used in conjunction with the minimum Young's modulus of 20.4 GPa, yields fracture toughness in the range of 0.09 ± 0.02 to 0.22 ± 0.06 MPa.m^{1/2}, in agreement with the values 0.09 to 0.2 MPa.m^{1/2} cited by Marion.⁶

The other important assumption is that the material can be described as an elastic-plastic solid. With a melting point of $T_m = 525.6$ K, the room temperature at which the tests were conducted represents a homologous temperature of $293/525.6 = 0.57$. At such a relatively high temperature, and under the action of the high compressive stresses due to indentation, it is expected that KDP may deform by a variety of mechanisms, including dislocation glide on crystallographic slip systems, or power-law creep by dislocation climb/glide. At temperatures of about 110°C, KDP is known to exhibit macroscopic plasticity in a uniaxial compression.⁵ The room-temperature compressive yield stress does show anisotropy, being 140 MPa for compression along [100], 100 MPa along [110], and 130 MPa for compression along [001]. At 110°C, these values are

reduced by a factor of about 10;⁵ therefore, anisotropy under uniaxial conditions is about 20% of the uniaxial compressive yield stress. The anisotropic variation of Knoop hardness that we have measured on the (001) faces was seen to be within 10% of the average value. Likewise, the largest observed difference in Vickers hardness of (100) and (001) faces was no more than about 10%. Therefore, a total variation of 20% in hardness due to crystallographic anisotropy is expected, consistent with the anisotropy of the uniaxial compressive yield stress. On the other hand, as Eqs. (3) and (4) show, a 20% variation in hardness is expected to lead to a variation in the computed fracture toughness of about 10%.

Thus, the estimates of the effects of the Young's modulus anisotropy and hardness anisotropy, when combined, lead to a difference of about 33% in the fracture toughness as computed by an isotropic elastic-plastic model such as by Evans⁹ or Anstis *et al.*⁷

On the other hand, at a homologous temperature of 0.57 with respect to the melting point, power-law creep is a time-dependent process. Now, the strain rate depends on stress via a power law of exponent in the range of 3 to 8. In our experiments we have imposed a fixed strain rate, as determined by applying the indentation load for 15 s on the KDP faces. In typical laser-damage applications, the laser pulse duration over which damage accumulates is of the order of 10 ns, implying, therefore, that the applicable strain rates are much higher than those in indentation.

Table 86.V: Calculated fracture toughness K_c (Mpa.m^{1/2}) for KDP.

Indents on	Using average $E = 38.7$ GPa		Using minimum $E = 20.4$ GPa	
	Evans model ⁹	Anstis <i>et al.</i> model ⁷	Evans model ⁹	Anstis <i>et al.</i> model ⁷
(100) plane	0.22 ± 0.02	0.13 ± 0.03	0.17 ± 0.02	0.09 ± 0.02
(001) plane, indent orientation (1)	0.37 ± 0.08	0.30 ± 0.08	0.29 ± 0.06	0.22 ± 0.06
(001) plane, indent orientation (2)	0.28 ± 0.07	0.19 ± 0.06	0.22 ± 0.05	0.14 ± 0.04
Shaskol'skaya <i>et al.</i> ⁴	0.24 ± 0.04	0.17 ± 0.03	0.19 ± 0.03	0.12 ± 0.03
As cited in Marion ⁶	0.09–0.20 Using direct crack method of Anstis <i>et al.</i> ⁷ but with no information on E value used.			

Given the lack of data describing the dependence on stress and temperature of the deformation mechanisms of KDP, the strain-rate effects are more difficult to estimate. The development of deformation mechanism maps for KDP is thus an area identified for future research.

ACKNOWLEDGMENT

We wish to thank Prof. Stephen D. Jacobs and Mr. Douglas Smith, both of the Laboratory for Laser Energetics at the University of Rochester, for many discussions and suggestions and sample preparation.

Appendix A: Elastic Anisotropy of KDP

The elastic behavior of the single-crystal KDP is characterized by six elastic constants, which are shown in Table 86.VI.

Figure 86.68 shows the variation of the Young’s modulus of a rod of KDP with orientation of the rod. The figure shows the unconstrained Young’s modulus E_u (i.e., when the only stress is in the direction of the rod, without any transverse stresses):

$$\frac{1}{E_u} = \frac{S_{13}}{4} + \frac{S_{44}}{8} + S_{33} \cos^4 \theta - \frac{2S_{13} + S_{44}}{8} \cos 4\theta + \left[S_{11} + \frac{(-2S_{11} + 2S_{12} + S_{66})}{4} \sin^2 2\phi \right] \sin^4 \theta, \quad (A1)$$

where θ is the angle between the direction of the rod and the cubic axis [001] and ϕ is the angle between the projection of the

rod axis on the (001) plane and the [100] direction. The Young’s modulus E_u varies from about 20 GPa to about 65 GPa. When averaged over all rod directions (i.e., integrated over the surface of a unit-radius sphere with differential element of area $dA = \sin \theta d\theta d\phi$), we find $\langle E_u \rangle = 35.5$ GPa.

Likewise, the constrained Young’s modulus E_c (where no strains transverse to the rod are allowed) is

$$E_c = \frac{C_{13}}{4} + \frac{C_{44}}{2} + C_{33} \cos^4 \theta - \frac{C_{13} + 2C_{44}}{4} \cos 4\theta + \left[C_{11} + \frac{(-C_{11} + C_{12} + 2C_{66})}{2} \sin^2 2\phi \right] \sin^4 \theta; \quad (A2)$$

E_c varies from about 40 GPa to 70 GPa, as shown in Fig. 86.68. When averaged over all directions, the result is $\langle E_c \rangle = 51.4$ GPa. The results in Fig. 86.68 clearly show that KDP is quite anisotropic.

To get a better idea of the elastic anisotropy, we can also determine the Reuss and Voigt averages as described by Hirth and Lothe,¹⁶ who summarize the earlier results by Hill.¹⁷ The Voigt averages for the shear modulus G_V and Lamé constant λ_V are given by

$$G_V = (3C_{ijj} - C_{iij})/30, \quad \lambda_V = (-C_{iij} + 2C_{ijj})/15, \quad (A3)$$

Table 86.VI: Elastic constants of KDP at 20°C.

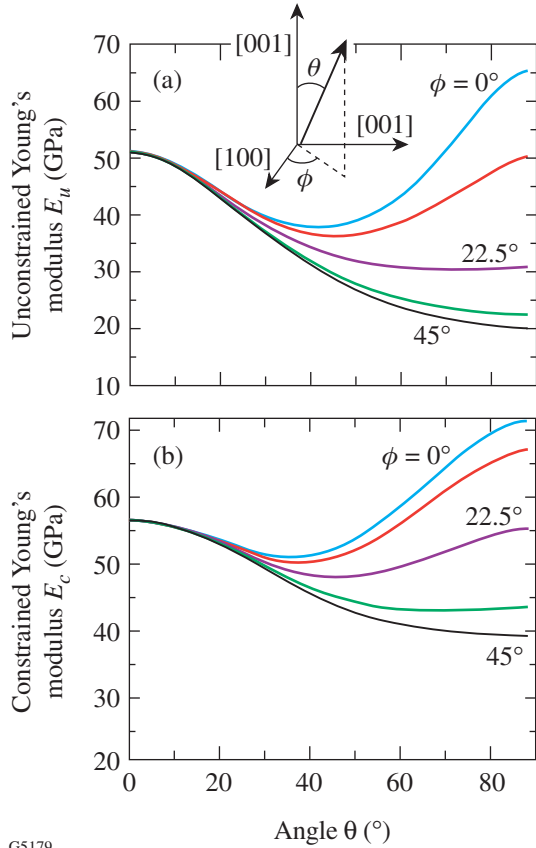
C_{11}	C_{33}	C_{12}	C_{13}	C_{44}	C_{66}
71.65	56.4	-6.27	14.94	12.48	6.21
Units of C_{ij} are GPa; data from Haussühl, ¹⁴ as cited in Milek and Neuberger. ¹ Stiffnesses C_{ij} relates stresses and engineering strains.					
S_{11}	S_{33}	S_{12}	S_{13}	S_{44}	S_{66}
1.51	1.95	0.18	-0.40	7.81	16.2
Units of S_{ij} are 1/(100 GPa); data from Hearmon, ¹⁵ as cited in Milek and Neuberger. ¹ Compliances S_{ij} relate engineering strains and stresses.					

where repeated indices are summed over the range $i, j = 1, 2, 3$. Here the constants C_{ijkl} relate the stress σ_{ij} and strain ϵ_{ij} tensors, $\sigma_{ij} = C_{ijkl} \epsilon_{kl}$. We thus find the average Young's modulus based on the Voigt scheme as $E_V = 44.3$ GPa. The corresponding Poisson ratio is $\nu_V = 0.23$.

The Reuss averages are given by

$$\frac{1}{E_R} = (2S_{ijj} + S_{ijj})/15, \quad \frac{1}{G_R} = (6S_{ijj} - 2S_{ijj})/15, \quad (A4)$$

where the constants S_{ijkl} relate the strain ϵ_{ij} and stress σ_{ij} tensors, $\epsilon_{ij} = S_{ijkl} \sigma_{kl}$. We find the Reuss average of the Young's modulus $E_R = 33.0$ GPa. The corresponding Poisson ratio is $\nu_R = 0.30$.



G5179

Figure 86.68
Variation of Young's modulus of KDP with crystallographic orientation. The Young's modulus is the ratio of stress to strain for a rod making angles θ, ϕ with the crystallographic axes and stretched in the direction of the rod. Unconstrained E_u corresponds to no transverse stresses acting on the rod. Constrained E_c is valid when the rod is not allowed to strain in the transverse directions.

REFERENCES

1. S. Anbukumar, S. Vasudevan, and P. Ramasamy, *Indian J. Phys. A* **61A**, 397 (1987).
2. G. R. Anstis *et al.*, *J. Am. Ceram. Soc.* **64**, 533 (1981).
3. R. F. Cook and G. M. Pharr, *J. Am. Ceram. Soc.* **73**, 787 (1990).
4. A. G. Evans, in *Fracture Mechanics Applied to Brittle Materials*, edited by S. W. Freiman (American Society for Testing and Materials, Philadelphia, 1979), Vol. ASTM STP 678, Part 2, pp. 112–135.
5. C. H. Guin *et al.*, *Krist. Tech.* **15**, 479 (1980).
6. R. F. S. Hearmon, *Br. J. Appl. Phys.* **3**, 120 (1952).
7. S. Haussühl, *Z. Kristallogr.* **120**, 401 (1964).
8. R. Hill, *Proc. Phys. Soc.* **65A**, 349 (1952).
9. J. P. Hirth and J. Lothe, *Theory of Dislocations*, 2nd ed. (Wiley, New York, 1982), Chap. 13, Sec. 13.2, pp. 424–428.
10. K. K. Rao and D. B. Sirdeshmukh, *Indian J. Pure Appl. Phys.* **16**, 860 (1978).
11. J. C. Lambropoulos, T. Fang, P. D. Funkenbusch, S. D. Jacobs, M. J. Cumbo, and D. Golini, *Appl. Opt.* **35**, 4448 (1996).
12. J. Lankford, *J. Mater. Sci. Lett.* **1**, 493 (1982).
13. J. E. Marion, *J. Appl. Phys.* **62**, 1595 (1987).
14. J. T. Milek and M. Neuberger, *Linear Electrooptic Modular Materials*, Handbook of Electronic Materials, Vol. 8 (IFI/Plenum, New York, 1972), pp. 177–222.
15. C. B. Ponton and R. D. Rawlings, *Mater. Sci. Technol.* **5**, 865 (1989).
16. *ibid.*, p. 961.
17. M. P. Shaskol'skaya, H.-K. Ch'ang, and M. D. Katrich, *Izv. Akad. Nauk SSSR Neorg. Mater.* **14**, 716 (1978).

A Self-Calibrating, Multichannel Streak Camera for Inertial Confinement Fusion Applications

Introduction

The OMEGA laser at LLE uses 60 symmetrically aimed laser beams to compress direct-drive inertial confinement fusion (ICF) targets.¹ The ICF targets are, typically, deuterium-tritium (DT)-filled microballoons. The laser beams heat and compress the target, causing the DT fuel to undergo nuclear fusion, which releases energy in the form of neutrons. The fuel must be highly compressed for this process to proceed efficiently.² The shape of the laser pulse, which typically has a length of 1 to 3 ns, can be adjusted to optimize the compression and produce a hot core of DT fuel;³ however, optimal compression will happen only if the driving force imparted by the laser beams to the spherical target is uniform. If one laser beam is more energetic than its neighbors, it can seed hydrodynamic instabilities that can prevent the formation of the highly compressed core.⁴ Because these hydrodynamic instabilities can be seeded in about 100 ps, it is necessary to ensure that the driving force imparted by the laser be uniform on the 100-ps time scale. This defines the period over which power balance must be achieved. To achieve the best target performance, the OMEGA laser must ultimately achieve 1% irradiation uniformity during each 100-ps time slice of the pulse. Achieving this goal is aided by the fact that several different beamlines illuminate any single point on the target. The averaging effect of the overlapping beams reduces the requirement for beam-to-beam power balance to 5%.⁵

Several factors affect power balance: In theory, if all of the optical components and all of the electrical power-conditioning units in each beamline are identical, every beamline should have the same energy and pulse shape. In practice, not all flash lamps are equal and not all optical components are equal, especially after being exposed to many shots at high optical fluences. The result is that when the laser is fired, the beams are currently energy balanced on target to 3% rms.

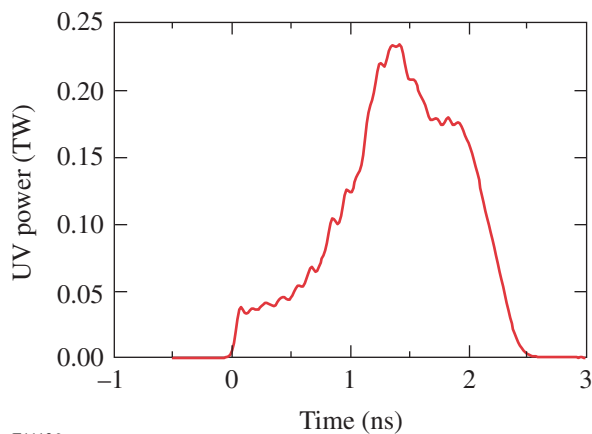
Equalizing the beam energies does not guarantee equal pulse shapes. The gains and losses of each beamline must be equal if the system is to be power balanced, which is not necessarily true for energy balance because the system is

nonlinear. For example, increasing the gain in an amplifier farther downstream can compensate for a poorly performing optic in a beamline. Although this would allow the system to be energy balanced, it will likely change the temporal shape of the optical pulse. Power balance requires that the pulse shape of all 60 beamlines be measured.

Another major factor affecting the pulse shape is the spatial-smoothing technique employed on OMEGA. Smoothing by spectral dispersion (SSD) is used to rapidly shift the speckle pattern produced at the focus of the laser.⁶ The rapid shifting of the speckle pattern produces a uniform, time-integrated illumination profile on the ICF target. SSD works by modulating the laser frequency across the spatial and temporal profiles of the beam. Each frequency propagates at a slightly different angle with respect to the optic axis of the laser. The speckle pattern produced at the target then shifts rapidly in time. Misalignment of the SSD system, however, can cause the frequency modulation (FM) of the laser pulse to be converted into amplitude modulation (AM) at SSD drive frequencies of 3 and 10 GHz as well as at the harmonics and sum and difference frequencies. The AM can damage optical components as well as adversely affect power balance.

All of these factors can be adjusted, but only if their impact is measured. Any system that is used to measure pulse shapes on OMEGA must meet several stringent requirements. The temporal bandwidth must be able to detect temporal features in the pulse shape with frequencies as high as 10 GHz. The bandwidth is high for two reasons: First, the recorded pulse shapes are fed into theoretical models of the implosion dynamics. Higher-bandwidth signals allow more-faithful models of the implosion dynamics. Second, the 10-GHz bandwidth allows us to see any FM-to-AM conversion, which could be specific to a single beamline. The recorded signal should span a range of pulse intensities of over 1000:1. Much of the interesting implosion physics happens during the initial “foot” portion of the pulse, which is at 27% of the peak for a typical shaped optical pulse (as shown in Fig. 87.1). The recorded intensity range should be sufficient to measure the pulse shape

with an accuracy of a few percent at the peak and within about 10% in the foot. The longest pulse that can be generated with the OMEGA laser is about 4.5 ns, with 1-ns to 2-ns pulses being the most typical. The instrument record length should be slightly longer to allow us to handle the case of deliberately delayed beams, so the total record length should be about 6 ns. The OMEGA laser operates at a wavelength of 351 nm; this defines the wavelength at which the streak cameras must operate. Since there are 60 beamlines in the OMEGA system, the acquisition system must support 60 simultaneous data-acquisition channels. This data must be recorded on all OMEGA system shots, which occur on a 1-h shot cycle, so reliable operation as well as the ability to recover from equipment failure on a 1-h shot cycle is essential.

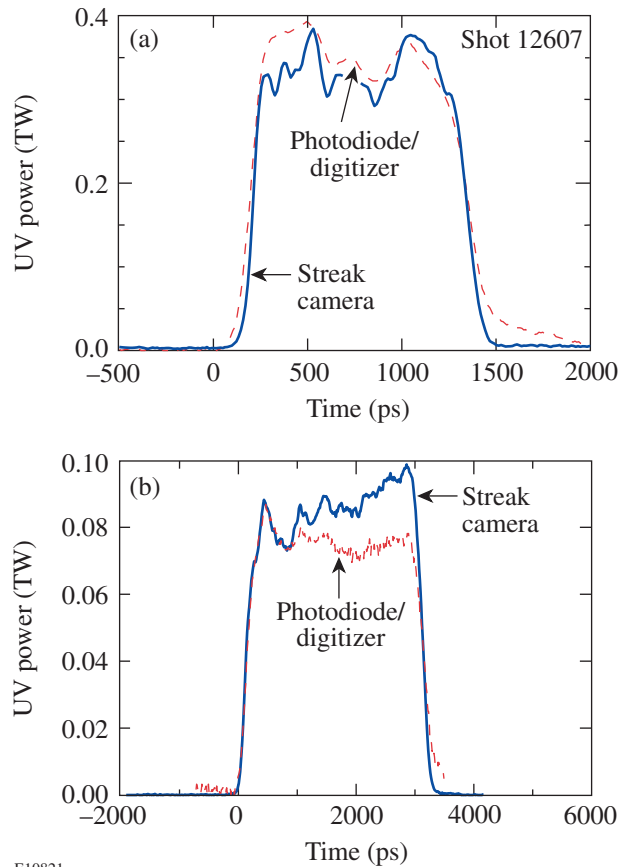


E11136

Figure 87.1

A typical shaped pulse used for ICF experiments has an initial, low-energy "foot," followed by the more-intense main part of the pulse.

Two possible alternatives were considered for a measurement system that would meet these requirements. The first alternative was to use photodiodes and transient digitizers. When the OMEGA laser was first activated, the UV pulse shape was measured with a Tektronics SCD5000 transient digitizer and a Hamamatsu photodiode. The temporal resolution of this system was about 4 GHz, which was insufficient to see the modulation due to SSD, as shown in Fig. 87.2. We have also found that photodiodes, which are optimized to measure high-bandwidth pulses, experience a droop in the signal when measuring long pulses. With a cost approaching \$70,000 per channel, this was an inappropriate option for a 60-beam laser. By way of comparison, the National Ignition Facility (NIF) at Lawrence Livermore National Laboratory is planning to monitor the 192 beams of the NIF with vacuum photodiodes and transient digitizers.⁷ The NIF will use temporal and power multiplexing to reduce the number of digitizers and detectors



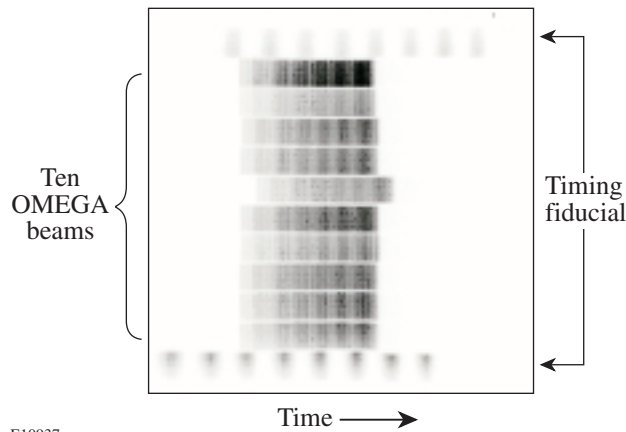
E10821

Figure 87.2

A comparison of a 4-GHz diode/digitizer to a 10-GHz streak camera. (a) The photodiode (dashed trace) was unable to reproduce the high-frequency structure measured with the streak camera (solid line). (b) One of the problems with the transient digitizer and diode measurement system (dashed trace) is a tendency for the signal to droop when measuring long pulses. This results in a distorted pulse shape as compared to the streak camera data (solid line).

to 48. The multiplexing scheme is designed to achieve a dynamic range of 5000:1 at 1 GHz with a cost per channel of \$6200. Such a system would not meet the requirements of the OMEGA laser system as stated above.

The second alternative, which is the one described in this article, uses six streak cameras to measure the UV pulses shapes in each of the 60 OMEGA beamlines. The photocathode of each streak camera is illuminated by a small portion of the light from ten OMEGA beamlines. A typical image is shown in Fig. 87.3. This system can measure all 60 beams of OMEGA with a bandwidth of 10 GHz and a per-beam dynamic range of over 10^3 :1. The cost per channel is about \$12,000, plus in-house labor.



E10937

Figure 87.3 The corrected image of the cluster 5 streak camera showing ten multiplexed beams and two fiducial traces. All of the beams are actually nominally co-timed. The apparent delays are due to differences in the fiber OPD to the cameras. The striations are due to FM-to-AM conversion of the 10-GHz SSD.

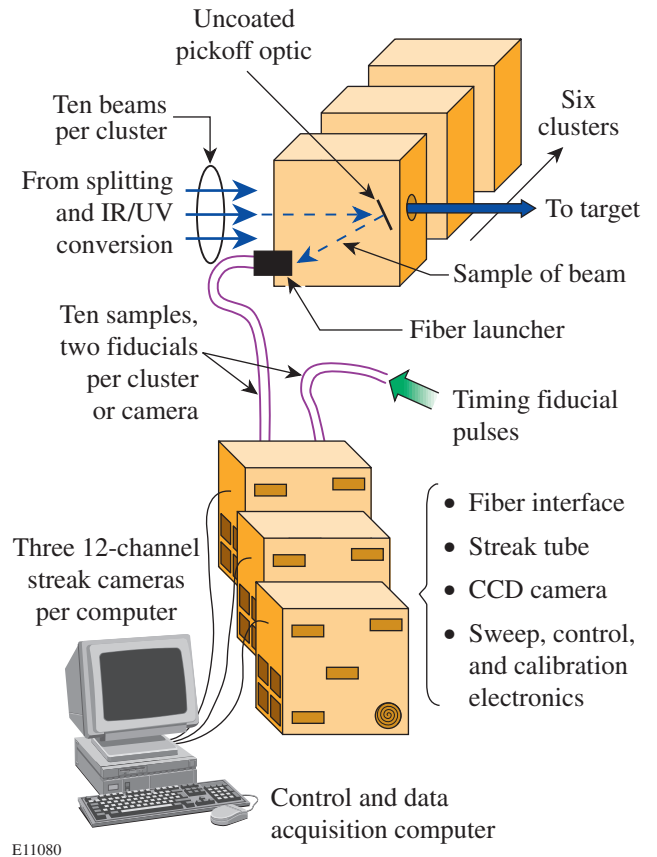
The System

Multichannel streak cameras are not new. A number of research groups have used them for a variety of measurements.⁸⁻¹⁰ What is unique about this system is the enhanced signal-to-noise ratio (SNR) of the recorded data and the suite of autocalibration modules. These allow accurate, photometrically calibrated measurements over a period of months. OMEGA's pulse-shape-measurement system is composed of six major subsystems: the fiber launcher assembly, the optical-fiber bundles, the fiber-bundle imaging optics, the streak tube, the tube electronics, and the charge-coupled-device (CCD) camera. Each of these subsystems (illustrated in Fig. 87.4) must be optimized to meet the specifications listed above. Figure 87.5 shows the layout of the streak camera.

Each OMEGA beamline can deliver about 550 J of 351-nm light to the target. An uncoated glass surface (4% reflection) is inserted into each beam for diagnostic purposes. After three additional 4% reflections, part of the diagnostic energy is delivered to the streak camera's fiber launchers. One consequence of SSD is that each beam is about 300 times diffraction limited with an instantaneous spatial profile that has 100% speckle modulation. It is impossible to couple this light into the UV gradient-index fibers available at the time the system was constructed. The time-varying speckle coupled with angular deviation of each frequency would result in coupling losses, which would manifest themselves as AM at the output of the fiber. To overcome this problem, a system of lenses and diffrusers was used to uniformly sample the spatial profile of the beam with a seven-fiber bundle. The light passes through a lens

with a 20-cm focal length, then immediately passes through a precision diffractive-optics diffuser, which spreads the light into a 2° cone angle. A second diffuser, with a 0.5° cone angle, is placed at the focus of the first lens. Finally, a 1-cm lens focuses the light into the fiber bundle. This arrangement produces a weakly modulated 2-mm-FWHM Gaussian profile at the fiber input plane at a wavelength of approximately 351 nm.

To accurately reproduce the waveform, the beam must be sampled at several points over the central portion of the 2-mm spot. The use of a 1-mm-diam-core, step index fiber would be incompatible with the required bandwidth of the system, so an alternative method was used. The 351-nm light must propagate through the 15 m of fiber from the launcher to the streak camera. The 15 m allows for equal optical path lengths from the pickoff to the camera, as well as transport through the radiation shield wall that surrounds the target chamber. To maintain the



E11080

Figure 87.4 The OMEGA pulse-shape-measurement system consists of six streak cameras, each measuring a single cluster. Optical fibers transport a small portion of the energy from each beamline to the streak cameras.

highest-possible bandwidth, a 100- μm -core UV fiber was chosen. This high-bandwidth, UV-transmitting, graded-index optical fiber was developed by the Vavilov State Optical Institute, St. Petersburg, Russia, for use in laser diagnostics on the National Ignition Facility.¹¹ This fiber has a dispersion of 1 ps/m at 351 nm, giving a maximum bandwidth of 11 GHz. Since one fiber is inadequate to sample the entire beam, a bundle of seven fibers is used with six fibers hexagonally packed around a seventh fiber. The fiber lengths are matched such that broadening due to optical path differences (OPD's) in the bundle is negligible. To verify that the OPD's were the same, the output of a single fiber, injected with a 20-ps pulse at 351 nm, was compared with the output of a fiber bundle injected with the same pulse. The measured pulse lengths were 28 and 29 ps, respectively. The impulse response of the input fiber is therefore 21 ps, assuming the broadening and pulse width add in quadrature.

When the light emerges from the fiber bundle, it is coupled into a homogenizer bar, which produces a uniform rectangular spot from the seven-fiber hexagonal bundle by multiple surface reflections. This maximizes the fill factor on the photocathode. Ten bars are arranged in a linear array as shown in Fig. 87.6. At either end of the array are two additional homogenizer bars, which are fed by a fiducial laser operating at 527 nm. The fiducial laser is co-timed with the UV pulse from the OMEGA laser and consists of eight pulses separated by 548 ps. The fiducial pulses enable cross-timing between the six

UV streak cameras and other diagnostics in the system. An off-axis Offner triplet is used to image the optical signals onto the linear photocathode, as shown in Fig. 87.7. The mirrors are metallic, thus reducing chromatic defocus. This particular arrangement was chosen so that a variety of illumination fixtures could be placed on a computer-controlled motorized stage and individually selected to be focused onto the photocathode. The other illumination fixtures are used for *in-situ* calibration of the streak camera, which will be described later.

The streak tube is a standard commercial tube—a Philips P510—with an S-20 photocathode at the input. The electron optic terminals were biased as follows: photocathode -15 kV, slot -12.5 kV, and focus -14.5 kV. These voltages were adjusted for each tube to produce the sharpest image in the time dimension of the photocathode at the CCD with the sweep voltages held at 0 V. Figure 87.8 shows that at best focus the FWHM of the photocathode image varies as a function of both position on the photocathode and signal intensity. A low signal near the center of the image induces a broadening that has an equivalent effective bandwidth of 13.5 GHz. At the other extreme, an intense signal near the edge of the photocathode induces a broadening equivalent to 10.5 GHz. The intense signal result represents the worst possible case. The signal level was near the CCD's full well capacity. The bandwidth was limited by both saturation of the CCD and diffusive scattering in the fiber-optic coupling of the light into the CCD. This signal level is ten times what is used in normal operation.

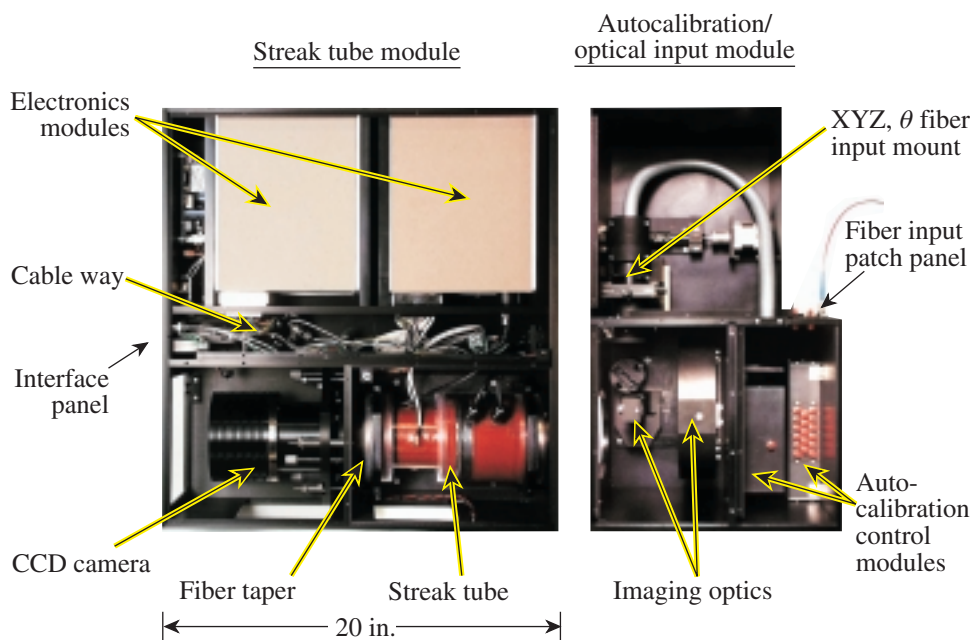
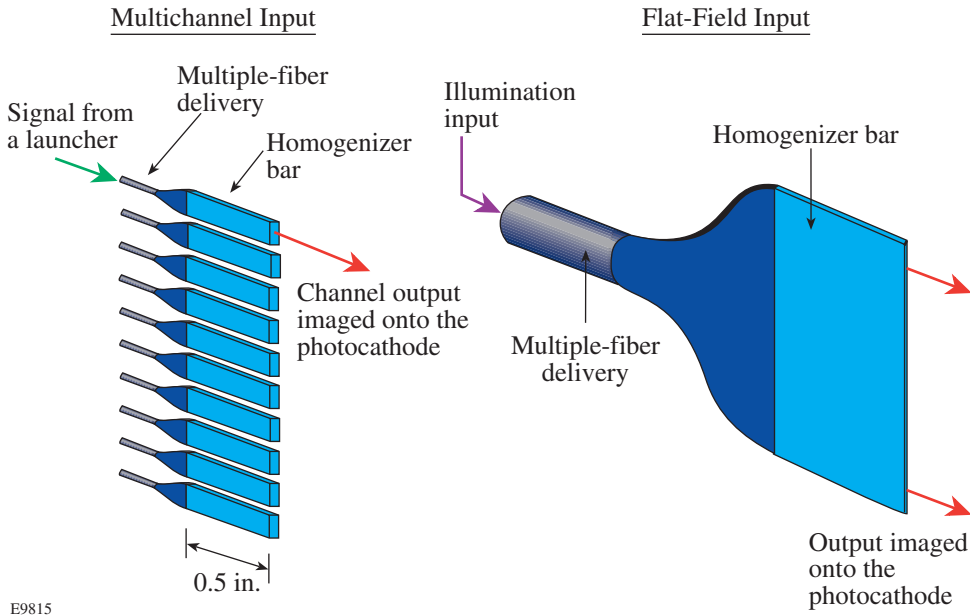
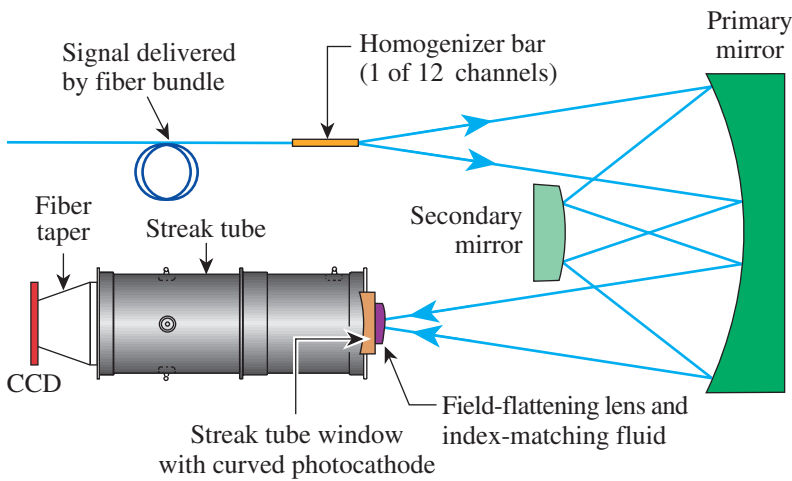


Figure 87.5
The layout of the self-calibrating, multi-channel streak camera employed on the OMEGA laser.



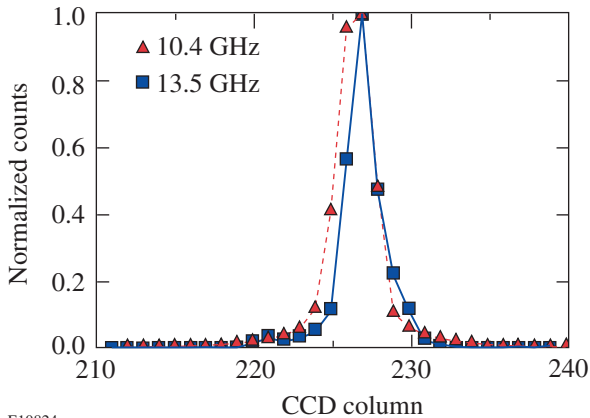
E9815

Figure 87.6
A mechanical translation stage allows several different illumination heads to be placed at the object plane of the Offner triplet. Layouts of two illumination heads are shown here. Multiple reflections from the edges of the glass homogenizer bars produce a uniform illumination source.



E9820a

Figure 87.7
The optical input to the streak camera uses an Offner triplet to image the fiber bundle onto the streak tube photocathode. The streak tube window is curved, and a field-flattening lens is attached to it with index-matching fluid.



E10824

Figure 87.8
In focus mode, the image of the photocathode is adjusted to give the sharpest line at the CCD. The width of the line varies with position and intensity. The solid line shows the best focus at the center on the streak tube axis at low intensity. The FWHM is 2.5 superpixels (binned 2×2) giving a bandwidth of 13.5 GHz. Off-axis and with an intense signal, the line width degrades to 3.4 pixels, corresponding to a bandwidth of 10.4 GHz.

The output fiber-optic faceplate of the tube has a P20 phosphor screen, which is reasonably well matched to the spectral sensitivity of the back-thinned CCD used to acquire the image. To match the image size at the P20 phosphor to the CCD camera, a 1.3:1 fiber-optic taper is used. Index-matching fluid is used at the mating surface between the fiber-optic taper and the streak tube to prevent the formation of Newton rings in the image recorded by the CCD camera. The CCD camera is a Roper Instruments Series 300 with a fiber-coupled 1024×1024 CCD array using a back-thinned SITE003AB chip. There are only passive optical components between the phosphor and the CCD; no image intensifiers are used in the system. The large format of the array allows us to keep the image compression ratio of the fiber taper small, which reduces transport losses. Typically the output of this camera is binned 2 by 2 to give a 512×512 image. This allows a rapid, low-noise readout of the array without compromising the data. At the best focus of the electron optics, the width of the photocathode image is about 2.5 superpixels wide; thus we gain no additional information by unbinning the pixels. For the remainder of this article these superpixels will be used as the standard CCD row and column unit.

The electronics for controlling the streak tubes were designed at LLE. Each camera has four interchangeable modules. The modules control the high-voltage bias, the sweep voltages, triggering, and external communications. The external communications module uses a RS-232 serial port to tell the onboard processor to read and set voltage levels, optical head positions, and sweep speeds. The high-voltage bias module sets a single high-voltage level that biases the cathode, slot, and focusing electrodes of the tube through a resistive divider. The electron optics of the tube are such that the focusing conditions are relatively insensitive to the absolute magnitude of these three voltages but very sensitive to their ratios. Thus, small variations in the power supply do not significantly affect the final image quality. In normal operation, the deflection plates of the tube are driven by a filter network, which, in turn, is driven by a MOSFET/avalanche transistor stack.¹² This arrangement produces a ramp that sweeps the electron beam across the phosphor screen in 6 ns and has a deviation from linearity of less than 12%. This is the standard operating sweep speed for these cameras; however, three additional sweeps of 2-ns, 20-ns, and 45-ns duration can be selected electronically. It is also possible to sweep the electron beam very slowly by ramping the voltage with a high-voltage digital-to-analog ramp. The slow ramp is used for the flat-field and geometric-distortion corrections, which are discussed in the next section.

Calibration

The six streak cameras that measure OMEGA's 60 beams are essential to acquiring data reliably on a 1-h shot cycle. If a camera should fail, the modular design of the electronics allows us to rapidly repair the camera before the next shot. Simply acquiring data, however, is not sufficient. The data must be well calibrated and give meaningful results. *In-situ* calibration fixtures facilitate rapid recalibration of the streak cameras. It is insufficient to calibrate the streak cameras only at installation time. To ensure valid measurements at the 1% level, the streak cameras are recalibrated weekly.

A unique feature of the streak camera is the ability to slowly and uniformly ramp the electron beam across the phosphor in about 1 s. The slow ramp was designed to facilitate the acquisition of flat-field images with a large signal-to-noise ratio at very low tube currents. The slow ramp is also used to acquire images that are used to correct geometric distortions.

Several sources of geometric distortion exist in the streak camera images. The system has a set of several optic or electron-optic axes defined by the fiber-bundle array, the photocathode-electron optics, and the CCD camera. Ideally all of these axes should be aligned, but variations in tube construction cause misalignment in the electron optics. The CCD is aligned such that the image of the photocathode in focus mode (no voltage on the sweep plates) is parallel to the column axis. When voltage is applied to the streak plates, the streaked image may not move parallel to the row axis of the CCD. Fringing fields at the edges of the sweep electrodes cause pincushion distortion in the image. Also, the electron optics produce a curved image that is recorded on a flat phosphor screen. These effects must be removed from the image.

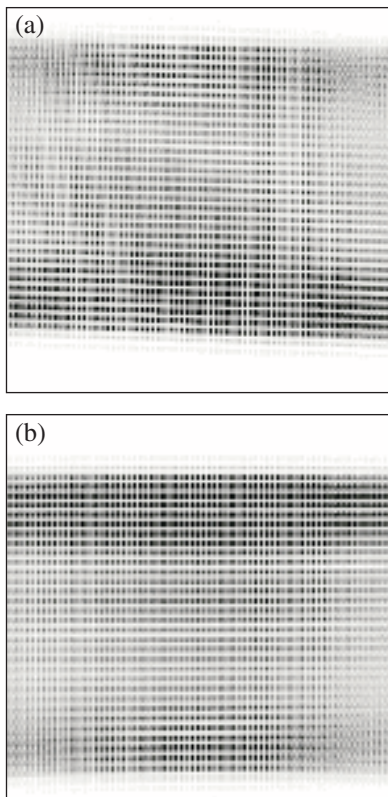
To correct these distortions, the motorized translation stage in the input optics assembly is set to the geometric distortion position. In this position, a fiber array, fed by a light-emitting diode (LED), is coupled to a homogenizer bar that uniformly illuminates the photocathode (see Fig. 87.6). A uniform wire mesh in front of the homogenizer modulates the light in the spatial direction. In this configuration, the slow ramp is used to sweep the electron beam. It takes about 1 s for the signal to sweep across the CCD. During this time, the current to the LED is modulated with a 30-Hz square wave. The resulting image consists of a uniform grid of bright rectangles (Fig. 87.9). The rectangles should be uniformly separated in space and time; however, the distortion mentioned above causes irregularities in the grid. A deconvolution algorithm is used to find the

position of each of the rectangles in the image. Next, an indexing routine assigns each rectangle its correct location in a uniform grid. The indexing of approximately 2000 points defines a mapping from the distorted to the undistorted image. Using standard image-processing techniques, the mapping can be described as an n th-order polynomial.¹³ This procedure does not use the Jacobian of the coordinate transformation to conserve the total CCD analog-to-digital units (ADU) count. Future software upgrades will include this feature; however, when a typical geometric distortion correction is applied, the total ADU count between the corrected and uncorrected image differs by less than 0.5%, which gives acceptable results for the current implementation. Polynomial fits up to the fourth order are calculated for each mapping. The undistorted images are cross-correlated with an ideal grid to determine which polynomial degree gives the best distortion correction. The undistorted

image consists of uniformly spaced rectangles in vertical columns and horizontal rows.

Once the geometric-distortion correction has been calculated, the streak camera can be flat fielded. A traditional flat field of a CCD is insufficient because we are mapping a line to a 2-D image. Each point on the photocathode maps to a trajectory on the CCD. The geometric-distortion correction maps the trajectory of a single point on the photocathode to a single row of pixels in the undistorted image. Variations of the photocathode efficiency and the homogenizer mean that different rows are essentially illuminated with different light sources. It is important to correct the geometric distortion before correcting the flat field to guarantee that the entire row derives from the same point on the photocathode. Each pixel in a row is subjected to variations in the phosphor screen, the fiber taper, and the sensitivity of each CCD element, so the first operation in calculating the flat-field image is to normalize each pixel with respect to all the other pixels in the row. Next, the sum of the pixels in each row is normalized to all the other rows. This procedure ignores regions of the image illuminated by the edges of the photocathode where the sensitivity of the system drops down to the noise level. The flat-field illuminator is similar to the geometric-distortion fixture, but the light source is continuous and the wire grid is removed. The slow-ramp module is used to sweep the electron beam across the phosphor. In this configuration, the illumination level can be adjusted so that only a few (<10) photoelectrons are in the tube at any time during the sweep. As a result, the electron current will not distort the electric field of the focusing optics, and the signal can be collected at a larger fraction of the CCD's full well capacity than is possible in pulse mode.

Aberrations in the electron optics cause some vignetting of the electron beam at the ends of the aperture. This causes a roll-off of about 20% to 30% in the sensitivity near the edges of the sweep, as shown by the lineout of a single row (see Fig. 87.10). The slight upturn at the very edge is due to scattered photoelectrons in the tube when the beam is outside the viewing area. This creates an uncalibrated region at the edges of the tube, so trigger timing should be set to keep the signal away from the edges of the image in normal operation. The high signal levels provided by the calibration source give excellent signal to noise in the flat-field image. Additionally, the signal to noise is enhanced by averaging 120 flat-field images. These flat-field images are acquired automatically in 10 min, so the volume of calibration data greatly exceeds the volume of signal data. The slow sweep is vulnerable to stray magnetic fields at



E10829

Figure 87.9

Calibration image produced by the geometric distortion source and the slow sweep. (a) The electron optics produce a skewed and distorted image at the CCD. (b) The modulation in the distorted image is removed by a transformation that maps the image to a regular grid.

the power line frequency, which causes a ripple at the 1% level. Since the sweeps are not synchronous with the power line frequency, the ripples are averaged to zero when the 120 flat fields are averaged. In normal operation these stray fields are not a problem because their oscillation period is 10^8 times greater than the duration of the sweep. When the camera is operated in the fast-sweep mode, these stray fields would manifest themselves as a small, uniform dc offset in the flat field. A planned upgrade to these cameras will include the addition of μ -metal shielding to the cameras to decrease the susceptibility to magnetic fields.

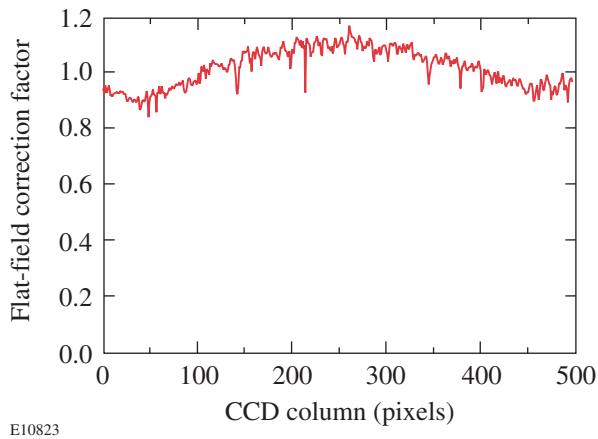


Figure 87.10

The flat-field correction factor is an image the same size as the CCD image. After geometric-distortion correction, each row in the image can be mapped to a single point on the photocathode. A lineout of one of the flat-field rows is shown. The roll-off toward the edges is due to the focusing optics obscuring part of the electron beam. The high-spatial-frequency structures are correlated with adjacent rows and are associated with dead spots in the hexagonal grid of the fiber-optic taper.

Next, the sweep speed must be calibrated. A square optical pulse is modulated with a 1.824-GHz sine wave to produce a train of eight pulses separated by 548 ps. The pulse train is injected into a fiber, and, using a 1:16 commercial fiber-optic splitter, it is divided into 12 fibers that feed a third calibration illuminator head on the streak camera. When this illuminator is placed at the object plane of the Offner triplet, the pulse train is fed to all 12 channels of the streak camera. Approximately 120 images are acquired with different trigger timing delays. The midpoint of each pulse pair in the image is assigned the derivative $\Delta\tau$ (ps)/ Δx (pixel), which gives about 700 independent measurements of the sweep speed for each channel distributed over the 512 pixel positions. The sweep speed cannot be calibrated at points within 274 ps of the edges. A best-fit interpolation is used to calculate dt/dx . This function is

integrated to determine time as a function of position in the CCD image. The constant of integration is chosen to assign a time of 60 ns to the center pixel. This prevents the uncalibrated region near the ends of the sweep from affecting beam-to-beam timing for all sweep speeds. The sweep speed is calculated independently for each channel. The geometric-distortion correction ensures that the sweep speed for each channel deviates from a linear fit by less than 20 ps over 5 ns, as shown in Fig. 87.11. The distortion correction should also guarantee that the sweep speeds of all the channels are identical; in practice this is not the case. Residual errors are due to uncorrected higher-order geometric distortions, resulting in slightly different sweep speeds for each channel. Finally, the sweep speed data is used to correct the recorded pixel values for the electron beam's dwell time (dt/dx) on the pixels by dividing the recorded CCD analog to digital units (ADU) by the relative dwell time on each pixel.

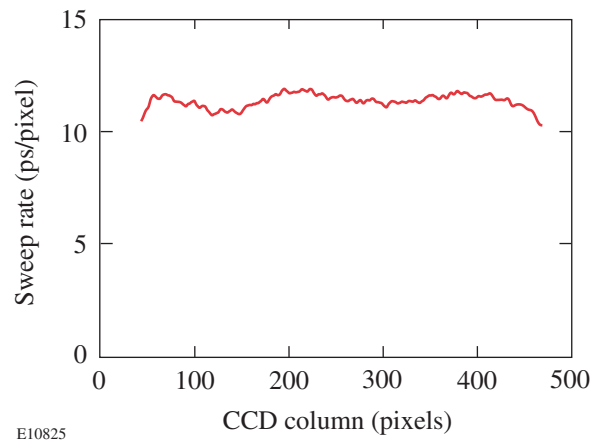


Figure 87.11

The sweep rate of a streak camera channel typically has about a 10% variation from perfect linearity. Roughly 40 channels at either end of the trace cannot be calibrated properly because of the spacing of the fiducial pulses used to calibrate the system. Most of this uncalibrated region lies in the dead zone of the flat-field image.

Operational Considerations

Once the streak cameras are calibrated, they are approved for operation during OMEGA system shots. The calibration procedures listed above are carried out with specific voltage levels applied to the various electrodes within the streak tube. If those voltages change, the calibration is no longer valid. To guarantee that the streak cameras remain in calibration, all of the voltages applied to the streak tube are recorded at the time of the laser shot. The image acquired on the shot is stored in Hierarchical Data Format (HDF). This format allows the image, voltage settings, and background frames to be saved in

the same platform-independent computer file. We have observed that the on-shot voltages do change with time. Typically they exhibit a slow drift, which appears to be associated with the aging of components. While a feedback loop partially compensates for this drift, weekly recalibrations are still required to keep the on-shot voltage values within 1% from the average values recorded during the calibration measurements. The acceptable range is arbitrarily set at 1.5 standard deviations of the variations recorded during the calibration measurements. If more than a week elapses since the last calibration, this condition may not hold and the software will report the voltages as being out of specification.

Two positions of the motorized illumination fixture can be used to acquire streak optical data. The first illuminates the entire photocathode with the light from a single optical-fiber bundle. The second is the standard configuration, which will be discussed exclusively in the remainder of this article. The standard configuration has ten OMEGA beamlines multiplexed onto each camera along with two fiducial pulse trains, as shown in Fig. 87.3. The fiducial laser pulses serve two purposes: First, they verify the integrity of the calibration. The fiducial laser signal consists of eight pulses evenly spaced in time. On each shot, we can measure the fiducial spacing and verify that time-axis calibration is within acceptable limits. On a typical shot, the average measured period of the fiducial pulses over all six streak cameras will be 550 ps with a standard deviation of about 8 ps. The average time displacement between two binned 2×2 superpixels is 12 ps. Thus, the timing of events with separations of the order of 0.5 ns can be determined with subpixel resolution. If, for some reason, the voltages on a streak camera go out of specification on a shot, the streak waveforms from that shot can be rescaled along the time axis by the ratio of the average fiducial period to the true fiducial period. This has been found to reduce timing errors on the distorted streak traces by 60%.

The second function of the fiducial pulse train is to determine the timing of the OMEGA beamlines. A separate instrument is used to guarantee that all beams are co-timed at target chamber center to within 10 ps. The instrument utilizes a cw mode-locked laser to check the path length of all the OMEGA beamlines and cannot operate when the main laser is fired. Data from a series of laser shots are acquired, and the timing of all the beams relative to the fiducial pulses is determined. Typically the rms timing difference between any one beam and the fiducial laser is about 15 ps averaged over 20 laser shots. Once this on-shot calibration has been completed, the streak cameras become the primary diagnostics for determining the

delay between beams and the fiducial. The OMEGA laser is often shot with some beamlines intentionally delayed. The streak cameras allow the fine adjustment of the delay. The fiducial pulse is also fed to many other target diagnostics such as x-ray streak cameras. By cross-timing with respect to the ultraviolet streak cameras, the absolute timing of any signal with respect to the laser pulse can be determined for consecutive system shots to about 10 ps rms. Over a period of several months, the jitter between the UV streak cameras and any instrument using a fiducial is less than 50 ps.

One of the primary uses of the streak cameras on OMEGA is monitoring power balance on the system, i.e., to ensure that all of the beams have the same instantaneous power.⁵ A separate diagnostic, using a calibrated pickoff, measures the energy in each beamline to $\pm 1\%$ precision.¹⁴ The integral under the power curve measured on the streak cameras is normalized to equal the measured energy of the beamline. A plot of the streak-integrated CCD ADU versus measured UV energy is a straight line over the usable operating range of the streak cameras as shown in Fig. 87.12. This shows that not only are the streak cameras photometrically calibrated, but the response is linear over the range of typical signal levels measured on the OMEGA system. If the images show signifi-

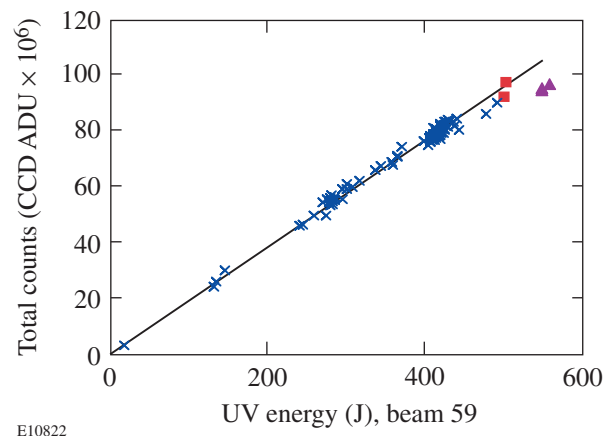


Figure 87.12 The responses of the streak cameras are photometrically calibrated. The total number of CCD counts associated with channel 59 is plotted against the measured UV energy in the beam in joules. The total number of counts is multiplied by the installed filtration. The response is linear up to 500 J UV (x's) over many different pulse shapes. The points above 500 J were 1-ns square pulses (triangles). The filtration on these shots was insufficient to prevent distortion of the streak camera image. The amount of distortion in the image depends on the number of active beams. The two points denoted by squares illustrate that the photometric calibration depends on the total streak tube current.

cant distortion, the linearity of the response breaks down, as indicated by the points designated with triangles. The ambiguity of the maximum-allowed signal level is illustrated by the two points labeled with squares at the 500-J level, which differ by about 10%. On both shots, the signal level in the channel exceeded the maximum-allowed counts. In one case, ten beams were active on the camera and the imaged was distorted. In the other case, only one beam was active for that shot and the image showed no distortion. The linearity of the sensitivity was also preserved in the latter case. Thus, it is possible for the local current density extracted from the photocathode to exceed the threshold for distortion as long as the average current density for distortion is not exceeded.

The measurable range of signal levels is determined by the optical filtration placed in front of the optical-fiber launchers. In addition to the fixed filters, two filters are on removable shuttles. These filters have attenuations of 1.75 and 5.75 and can be inserted separately or jointly, giving four possible intensity levels at the photocathode. The filtration level is chosen to get the maximum performance from the streak camera. The peak signal detected at the CCD camera is limited by the current in the electron tube. As the number of electrons in the tube increases, the image at the phosphor becomes distorted. Initially the distortion manifests itself as a spreading of the signal in both the space and time directions. As the distortion becomes more severe, the image starts to compress and bend. The maximum-acceptable level of distortion has been arbitrarily set in terms of the crosstalk between the channels in the spatial direction. When all beams on a given camera are active, the signal in the interstitial region between channels should not exceed 5% of the signal in the channel. This guarantees that the interchannel crosstalk is approximately 1% to 2% in the pixels adjacent to interchannel dead space and decays to zero in less than one-third of the channel width. Of course, this limit is flexible. If only one beam is present on a camera at a given signal level, the crosstalk distortion will be less than if all ten beams were present at the same level. The distortion is affected by both the local current density and total current in the tube. The 5% level was chosen to accept signals with 1% to 2% crosstalk between adjacent channels. At this level, the crosstalk is dominated by the decay characteristics of the streak tube phosphor and not the electron optics. Although most of the phosphorescence generated by the electron beam arrives at the CCD within a few hundred milliseconds, the phosphor will continue to emit light for as long as 10 s.⁹ To achieve the highest optical transfer efficiency, the coupling between the CCD and the phosphor is a fiber taper. This precludes putting a shutter between the phosphor and the

CCD. Thus, as the image in the CCD shifts from row to row, it acquires an exponentially decaying tail from the phosphor decay. The last channel to be read is most affected because it has been shifted through all residual images of the other channels. We have limited this effect by choosing long exposure times, which give the phosphor time to decay before the image starts to shift, but dark current in the CCD limits exposure times. The compromise of a 3-s exposure time generates a crosstalk of 1% to 2%.

Within these limitations the useful range of the streak camera has been quantified. Each of the 12 channels is defined by 512 individual measurements. The input optics are arranged such that each channel illuminates a 24-pixel-high column on the CCD with approximately uniform intensity; thus, each of the 6144 ($= 512 \times 12$) individual intensity measurements is the average of 24 individual pixel measurements. Therefore, an average, standard deviation and the signal-to-noise ratio can be calculated for each point in the waveform. Figure 87.13 shows the standard deviation plotted against the average signal for a single image on the cluster 2 camera on a log-log scale. The solid line is fit to the data at signal levels greater than the read noise of the CCD. It has a slope equal to 0.4996 ± 0.0574 , which implies that the noise equals the square root of the signal times a gain factor. Thus, we are measuring a quantity that follows Poisson statistics, i.e., the photoelectrons in the streak tube. The x axis has units of CCD ADU. The dashed line is what would be expected if the streak tube photoelectrons were

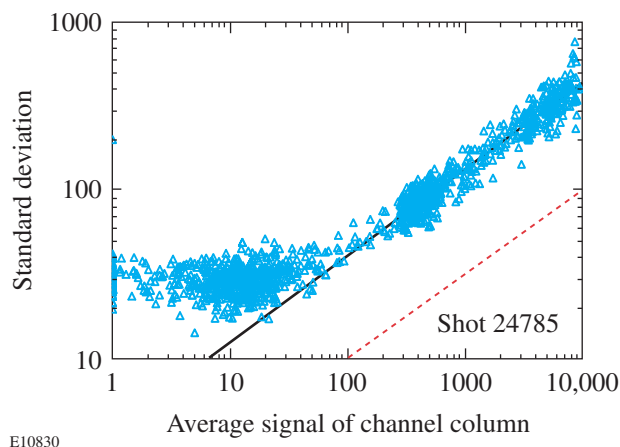


Figure 87.13

The standard deviation for 24×1 pixel regions on the cluster 2 streak camera. At signal levels above about 30 ADU, the signal obeys Poisson statistics. Below that level, the noise is dominated by a constant read noise in the CCD electronics. The solid line is a fit of the form $\ln(\text{std. dev}) = Ae^{[B \ln(\text{signal})]}$, where $B \sim 0.5$, implying Poisson statistics. This represents the expected standard deviation if gain is removed from the system.

measured directly. The ratio or horizontal shift between the two lines is the gain of the system from streak tube photoelectrons to CCD ADU. In this case the gain is 19.2 ADU/photoelectron. In operation the optical signal was adjusted using the filters mentioned above to produce the maximum tube current that would not introduce distortion at the peak of the optical pulse. Under these conditions, the peak tube current produced 9000 CCD ADU per pixel on the cluster 2 camera. Inserting this value into the fitted equation, we find the ratio of the signal to the standard deviation at the peak to be 36. Since 24 pixels are averaged, the signal-to-noise ratio, defined as the signal times the square root of the number of averaged points divided by the standard deviation, is about 100. The signal-to-noise ratio and the peak current varied somewhat from camera to camera. The averaging time for this measurement is 12 ps. The signal-to-noise ratio drops to 1 at a signal level of 6.2 ADU.

From Fig. 87.13 the dynamic range can be estimated. At the peak, the total signal is 9000 ADU, so the dynamic range is about $9000/6.2 = 1453$. The noise floor is the signal level where the $SNR = 1$ times the number of rows in a column divided by the gain, which gives a noise level of 7 photoelectrons. The noise is equivalent to about 0.3 photoelectrons per pixel. The power-balance specification for OMEGA, as well as for the NIF, requires a minimum acceptable bandwidth of 3 GHz, which corresponds to a resolution element of about 100 ps or about eight columns, so the dynamic range would increase to about 4.1×10^3 . Quoting a dynamic range, however, is misleading. It is more important to state how the dynamic range is defined in terms of the signal-to-noise ratio. The signal-to-noise ratio is not constant over the dynamic range, and it is possible to have a very large dynamic range with a very small signal-to-noise ratio at the peak. The lower end of the dynamic range is defined as the point where the signal-to-noise ratio is equal to 1 for 12-ps averaging. At the high end of the range, tube current is just below the distortion level and the signal-to-noise ratio varies from 90:1 to 110:1. Thus at the peak of the optical pulse, measurements can be made with about 1.0% accuracy. At intensities equal to 1% and 10% of peak, the respective signal-to-noise ratios are approximately 2.3% and 7.1%. If the pulse shape being measured has regions of temporally uniform intensity, it is possible to average over longer times and get better accuracy; however, this cannot be done in regions where the pulse shape is rapidly changing in time. At the peak of this pulse the average rms error was 1.0%, which is less than the 5% error budget allotted to each beam for establishing the 1% irradiation uniformity required by OMEGA. On the rising edge, the beam timing is usually determined by the 2% threshold level. Here the signal had a 30% rms error.

Dividing the error in the power by the derivative of the power with respect to time, the error in determining the 2% point was found to be less than one CCD superpixel. These measurements show that this streak camera-based optical power measurement system is meeting the power-balance requirements of the OMEGA laser system, and in its present configuration it exceeds the specifications for the proposed NIF power-balancing system.

It is instructive to look at a single beamline to gauge how well it can be characterized. Figure 87.14 shows a beamline with a nominal, 1-ns flattop pulse with SSD. The measured pulse shape showed that both 3- and 10-GHz modulations were present. This indicated that some of the SSD bandwidth was being clipped in the amplifiers or tripling crystals. This analy-

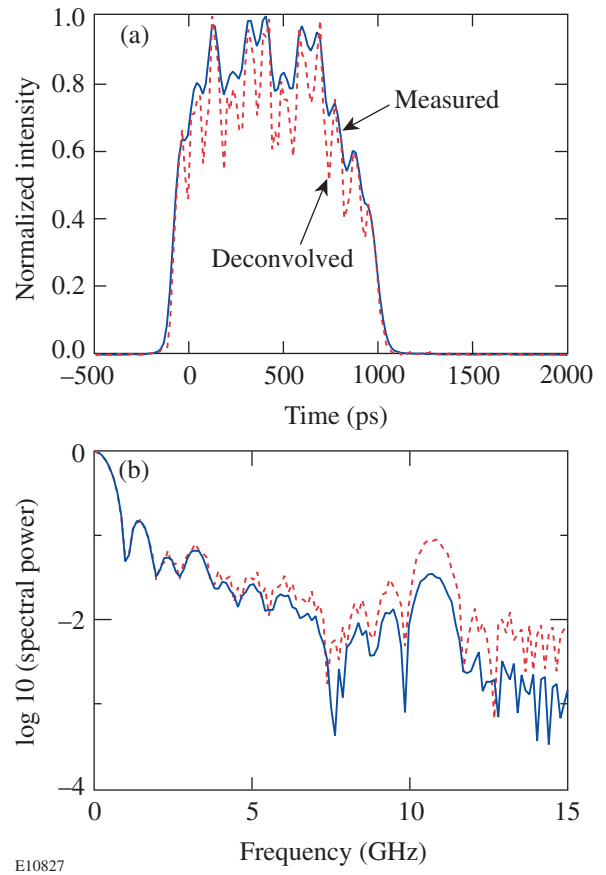


Figure 87.14 (a) The bandwidth limitation of the streak camera masks the true modulation on the pulse (solid curve). Using the measured response of the streak camera to the effects of focusing and the optical fibers, it is possible to deconvolve the bandwidth limitations (dashed curve). (b) Taking the FFT of the traces in (a), the modulation at 10 GHz is found to be three times greater in the deconvolved data than in the raw data.

sis did not take into account the bandwidth limitation of the optical-fiber bundle or the electron focusing optics discussed above. The impulse function of the camera was calculated by convolving the impulse response of the fiber bundle with the measured line spread of the focus image (see Fig. 87.8) mapped onto the sweep-speed time base. Deconvolving both of these responses from the measured signal indicated that the modulation at 10 GHz was three times higher than was being displayed.

Figure 87.15 illustrates how the streak cameras measure the power balance on the OMEGA system. The solid curve represents the normalized average pulse shape. All the beams recorded on the shot were mapped onto a uniform time base, temporally aligned, and averaged together pointwise for one of the standard OMEGA pulse shapes. The standard deviation was also calculated at each point and divided by the average, giving the dashed curve in Fig. 87.15, which is the percent of imbalance at any given time. Near the peak of the pulse, the power imbalance drops below 5%, which is the goal of the OMEGA system. The single-beam measurements indicate that the peak power of any given beamline is known with an accuracy of 1.0%. In the foot portion of the pulse, where the power is 15% to 20% of the peak, the imbalance in the system is about 10%. Here, depending on which camera is used, the single-beam measurements indicate that the power can be measured with 2% to 4% accuracy. Thus, at both the foot and the peak of this particular pulse shape, the single-beam mea-

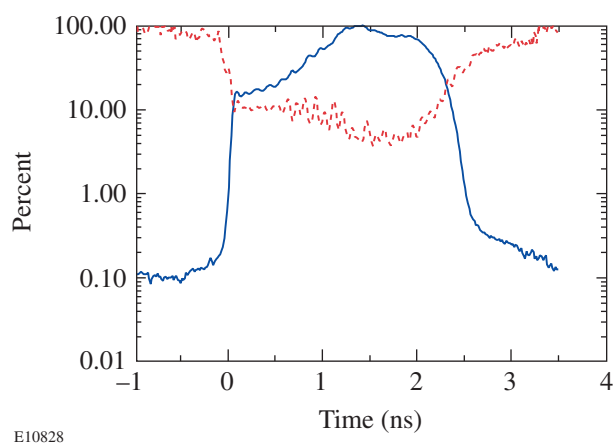


Figure 87.15

The solid curve is the average pulse shape for OMEGA shot 22708 normalized to 100% UV power at the peak averaged over 50 beams. The dashed curve is the measured standard deviation at each point across 50 beams.

surements have a smaller error than the measured beam-to-beam imbalance. As a result we have an instrument that can measure power balance on the OMEGA system and provide feedback to the engineering staff. This information can be used to modify the system, which will improve power balance. It should also be noted how well the average pulse shape of the system can be characterized. When the average shape falls to 0.1% of the peak, the average imbalance or percent error in the signal goes to 100%, implying that the SNR equals 1; thus the average pulse shape is well characterized over a 1000:1 range of powers.

Conclusion

The design and operation of a multiplexed streak camera system have been described. The unique feature of this system is its built-in self-calibration ability. The geometric distortions, flat field, and sweep speed of each channel can be measured and adjusted on a routine basis. By maintaining a strict regime of weekly calibrations, accurate power-balance measurements on the OMEGA laser can be obtained. Over 12-ps time intervals, a single beam can be measured with 1.0% accuracy; the beam-to-beam power imbalance has been measured at less than 5%. The timing of the beams can be measured to 7-ps rms. This set of high-precision instruments is proving very useful in establishing power balance on the 60-beam OMEGA laser.

ACKNOWLEDGMENT

This work was supported by the U.S. Department of Energy Office of Inertial Confinement Fusion under Cooperative Agreement No. DE-FC03-92SF19460, the University of Rochester, and the New York State Energy Research and Development Authority. The support of DOE does not constitute an endorsement by DOE of the views expressed in this article.

REFERENCES

1. T. R. Boehly, R. S. Craxton, T. H. Hinterman, P. A. Jaanimagi, J. H. Kelly, T. J. Kessler, R. L. Kremens, S. A. Kumpan, S. A. Letzring, R. L. McCrory, S. F. B. Morse, W. Seka, S. Skupsky, J. M. Soures, and C. P. Verdon, *Fusion Technol.* **26**, 722 (1994).
2. J. M. Soures, R. L. McCrory, C. P. Verdon, A. Babushkin, R. E. Bahr, T. R. Boehly, R. Boni, D. K. Bradley, D. L. Brown, R. S. Craxton, J. A. Delettrez, W. R. Donaldson, R. Epstein, P. A. Jaanimagi, S. D. Jacobs, K. Kearney, R. L. Keck, J. H. Kelly, T. J. Kessler, R. L. Kremens, J. P. Knauer, S. A. Kumpan, S. A. Letzring, D. J. Lonobile, S. J. Loucks, L. D. Lund, F. J. Marshall, P. W. McKenty, D. D. Meyerhofer, S. F. B. Morse, A. Okishev, S. Papernov, G. Pien, W. Seka, R. Short, M. J. Shoup III, M. Skeldon, S. Skupsky, A. W. Schmid, D. J. Smith, S. Swales, M. Wittman, and B. Yaakobi, *Phys. Plasmas* **3**, 2108 (1996).
3. A. Okishev, M. D. Skeldon, S. A. Letzring, W. R. Donaldson, A. Babushkin, and W. Seka, in *Superintense Laser Fields*, edited by A. A. Andreev and V. M. Gordienko (SPIE, Bellingham, WA, 1996), Vol. 2770, pp. 10–17.

4. D. K. Bradley, J. A. Delettrez, R. Epstein, R. P. J. Town, C. P. Verdon, B. Yaakobi, S. Regan, F. J. Marshall, T. R. Boehly, J. P. Knauer, D. D. Meyerhofer, V. A. Smalyuk, W. Seka, D. A. Haynes, Jr., M. Gunderson, G. Junkel, C. F. Hooper, Jr., P. M. Bell, T. J. Ognibene, and R. A. Lerche, *Phys. Plasmas* **5**, 1870 (1998).
5. W. R. Donaldson, R. Boni, R. L. Keck, and P. A. Jaanimagi, in *Optical Pulse and Beam Propagation*, edited by Y. B. Band (SPIE, Bellingham, WA, 1999), Vol. 3609, pp. 121–127.
6. S. P. Regan, J. A. Marozas, J. H. Kelly, T. R. Boehly, W. R. Donaldson, P. A. Jaanimagi, R. L. Keck, T. J. Kessler, D. D. Meyerhofer, W. Seka, S. Skupsky, and V. A. Smalyuk, *J. Opt. Soc. Am. B* **17**, 1483 (2000).
7. S. W. Thomas *et al.*, in *Solid State Lasers for Applications to Inertial Confinement Fusion: Second Annual International Conference*, edited by M. L. Andre (SPIE, Bellingham, WA, 1997), Vol. 3047, pp. 700–706.
8. J. Chang *et al.*, in *Digest of Technical Papers, Fifth IEEE Pulsed Power Conference*, edited by P. J. Turchi and M. F. Rose (IEEE, New York, 1985), pp. 1–4.
9. R. A. Lerche, D. S. Montgomery, and J. D. Wiedwald, in *Ultra-high- and High-Speed Photography, Videography, and Photonics '91*, edited by P. A. Jaanimagi (SPIE, Bellingham, WA, 1992), Vol. 1539, pp. 68–75.
10. G. A. Kyrala *et al.*, *Rev. Sci. Instrum.* **68**, 664 (1997).
11. A. V. Okishev, R. Boni, M. Millecchia, P. A. Jaanimagi, W. R. Donaldson, R. L. Keck, W. Seka, K. V. Dukelsky, M. A. Eronyan, V. S. Shevandin, G. A. Ermolaeva, G. Nikolaev, and V. B. Shilov, “Unique High-Bandwidth, UV Fiber Delivery System for the OMEGA Diagnostic Applications,” to be published in the *IEEE Journal on Selected Topics in Quantum Electronics*.
12. Laboratory for Laser Energetics LLE Review **73**, 6, NTIS document No. DOE/SF/19460-212 (1997). Copies may be obtained from the National Technical Information Service, Springfield, VA 22161.
13. E. L. Hall, *Computer Image Processing and Recognition*, Computer Science and Applied Mathematics (Academic Press, New York, 1979), pp. 186–188.
14. Laboratory for Laser Energetics LLE Review **63**, 110, NTIS document No. DOE/SF/19460-91 (1995). Copies may be obtained from the National Technical Information Service, Springfield, VA 22161.

Evolution of Shell Nonuniformities Near Peak Compression of a Spherical Implosion

Introduction

In inertial confinement fusion (ICF), a spherical target is imploded by either direct illumination of laser beams (direct drive)¹ or x rays produced in a high-Z enclosure (hohlraum).² Target perturbations can result from imperfections in the target itself or from drive nonuniformities. In direct-drive ICF, these include imprinted modulations from laser nonuniformities. These target perturbations can be amplified by hydrodynamic instabilities to disrupt the implosion and degrade target performance. The unstable growth of target perturbations has been extensively studied in planar geometry with preimposed modulations using indirect drive^{3,4} and both preimposed and imprinted modulations using direct drive.^{5–8} Experiments in cylindrical⁹ and spherical¹⁰ geometry have studied effects of convergence on the unstable growth. The modulation growth is typically measured by backlighting the driven target with x rays.¹¹ The backlighter x rays are attenuated while passing through the target, allowing measurements of the target-areal-density modulations.

Near peak compression in a spherical-target implosion, when the maximum density and temperature occur, the hot, compressed core and inner surface of the shell produce strong x-ray emission. These emissions can be used as a backlighter to probe the outer, colder shell.¹² The first shell-integrity measurements based on this method were time integrated over the duration of peak compression (~200 to 300 ps) of the implosion.^{12,13} They used shells with titanium-doped layers and imaging at photon energies above and below the titanium *K* edge. Core images at photon energies below the *K* edge (not absorbed by the shell) provide the spatial shape of the backlighter, while core images at photon energies above the *K* edge (highly absorbed by the shell's titanium) contain information about the structure of shell-areal-density modulations in the titanium-doped layer.

The experiment described in this article, based on the techniques developed in time-integrated experiments,^{12,13} is the first measurement of the evolution of shell nonuniformities near peak compression of a spherical-target implosion using

targets with titanium-doped layers. The growth of shell modulations in the deceleration phase is measured for the first time in ICF implosion experiments. The core emission, temperature, and shell-areal-density histories are also measured. Areal-density modulations in a titanium-doped layer have been determined from the intensity ratios of time-resolved, two-dimensional (2-D) core images taken above and below the titanium *K* edge. The average areal density has been measured using streak spectroscopy of titanium absorption of core radiation above the titanium *K* edge.

Experimental Configuration

Spherical targets with an initial diameter of about 920 μm filled with 15 atm of D_2 gas were imploded using direct-drive, 351-nm laser illumination on the 60-beam OMEGA laser system.¹⁴ The pulse shape was a 1-ns square with total on-target energy of about 23 kJ. The target shells had 1.9- μm -thick, titanium-doped (6% by atom) CH inner layers and ~18- μm -thick, pure-CH outer layers. The initial areal density of titanium in the shell was about 0.05 mg/cm^2 . All laser beams were smoothed with distributed phase plates (DPP's);¹⁵ 1-THz, 2-D smoothing by spectral dispersion (2-D SSD);¹⁶ and polarization smoothing (PS)¹⁷ using birefringent wedges. The average beam-to-beam energy imbalance was about 3.8%. The target emission was imaged on a four-strip framing camera^{18,19} by a 6- μm -diam pinhole array, protected by a 200- μm -thick beryllium filter. The upper two strips of the framing camera were filtered with a 75- μm -thick titanium filter, and the lower two strips by a 50- μm -thick iron filter to image core radiation at photon energies below (~4.8 keV) and above (~6.5 keV) the titanium *K* edge (4.966 keV), simultaneously.¹⁹ The two x-ray energy channels had spectral bandwidths ($\Delta E/E$) of about 20%. Each image taken with the framing camera had a temporal resolution of ~40 ps and a spatial resolution of about 6 μm . The framing camera output was captured on a charge-coupled-device (CCD) camera with a 9- μm pixel size²⁰ and a magnification of 12.

The spectral evolution of the core emission was captured on an x-ray streak camera²¹ with a temporal resolution of ~20 ps.

The streaked spectrum was calibrated by a time-integrated spectrum measured with an ammonium di-hydrogen phosphate (ADP) crystal. Figure 87.16 shows a spectral evolution of core emission as a function of photon energy near peak compression (~2.0 ns) for one of the three similar shots, integrated over the core size for times 1.77, 1.82, 1.92 ns [Fig. 87.16(a)], and 1.97, 2.02, 2.07 ns [Fig. 87.16(b)]. Core images for the same six times on the same shot captured with the framing camera are shown in Fig. 87.17, with the upper six images corresponding to photon energy channel below the titanium *K* edge, and the lower six images to the channel above the *K* edge. These images have each been normalized to their highest intensities.

The measured spectra shown in Fig. 87.16 contain information about (1) the evolution of He α , H α , and He β line emission of titanium ions mixed with the core fuel, (2) 1*s*-2*p* absorption lines (near ~4.6keV) of warm titanium with temperatures

$T \sim 500$ to 700 eV in the shell, (3) absorption above the *K* edge (at 4.966 keV) of cold titanium ($T < 500$ eV) in the shell,^{12,13} and (4) hot core continuum emission. The effective electron temperature in the emission region T_e and average cold titanium areal density have been calculated by fitting the function

$$I(E) = I_0 e^{\{-E/T_e - \mu_{Ti}(E) \cdot [\rho d]_{Ti}\}}$$

to the measured spectra (outside the absorption area of warm titanium near ~4.6 keV, and the shifting *K* edge), where E is the photon energy, $\mu_{Ti}(E)$ and $[\rho d]_{Ti}$ are the cold titanium mass absorption coefficient and average areal density, respectively, and I_0 is the constant. The effect of CH absorption was negligible compared to titanium absorption in these experiments because all time-resolved images below and above the *K* edge were always identical within experimental noise in shots with CH-only shells (containing no titanium) taken at similar drive conditions.

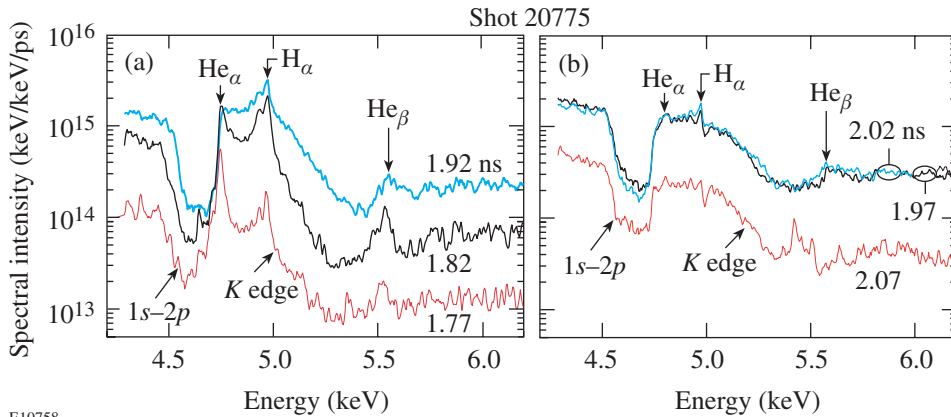


Figure 87.16 Evolution of core-emission spectral intensity as a function of photon energy for times 1.77, 1.82, 1.92, 1.97, 2.02, and 2.07 ns near peak compression of the spherical implosion.

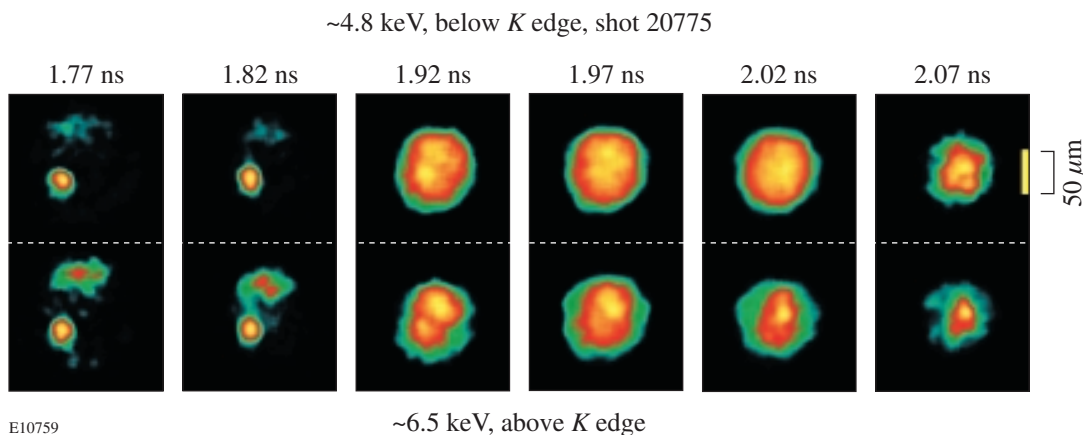


Figure 87.17 “Raw” core images near peak compression at energies below (~4.8 keV, upper row of images) and above (~6.5 keV, lower row of images) the titanium *K* edge for times 1.77, 1.82, 1.92, 1.97, 2.02, and 2.07 ns.

Figure 87.18 shows a temporal evolution of the electron temperature T_e of the core and the shell-emitting regions [circles connected by a thin solid line in Fig. 87.18(a)] and areal density of the cold titanium in the shell $[\rho d]_{Ti}$ [triangles connected by a thin solid line in Fig. 87.18(b)]. The measured areal density of titanium has been normalized to the initial titanium areal density of the undriven target and represents the amount of compression in the layer. The thick solid lines in Figs. 87.18(a) and 87.18(b) show the evolution of continuum emission intensity in arbitrary units at photon energies of 4.8 to 4.9 keV below the titanium K edge. These were calculated using core emission spectra measured with the streak camera. The diamonds in Figs. 87.18(a) and 87.18(b) show the intensity evolution (in arbitrary units) for the six images (Fig. 87.17) measured with the framing camera, also below the titanium K edge.

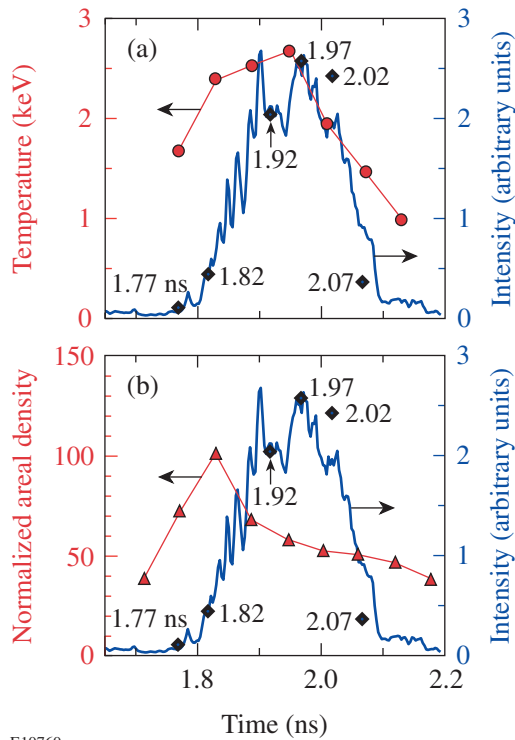


Figure 87.18

(a) Evolution of core continuum emission temperature (circles), core continuum emission intensity (at 4.8 to 4.9 keV, thick solid line), and emission intensity in images below the K edge (diamonds) for the same times as in Fig. 87.17. (b) Evolution of normalized areal density of titanium (triangles) together with core continuum emission intensity and emission intensity in images below the K edge from (a).

The modulations in the cold, or absorbing, part of the shell areal density $\delta[\rho d](\mathbf{r}, t)$ at time t (\mathbf{r} is the spatial coordinate) are proportional to the modulation in the logarithm of the ratio of intensities of the two images at photon energies above (highly absorbing by the shell) $I_{>K}(\mathbf{r}, t)$ and below (weakly absorbing by the shell) the titanium K edge, $I_{<K}(\mathbf{r}, t)$:

$$\delta[\rho d](\mathbf{r}) = \frac{\delta\{\ln[I_{<K}(\mathbf{r})/I_{>K}(\mathbf{r})]\}}{(\mu_{>K} - \mu_{<K})}, \quad (1)$$

where $\mu_{>K} = 0.37 \pm 0.02 \text{ cm}^2/\text{mg}$ and $\mu_{<K} = 0.11 \pm 0.02 \text{ cm}^2/\text{mg}$ are the spectrally weighed mass absorption coefficients of cold titanium at photon energies above and below the K edge, respectively.¹³ The absorption coefficients have been calculated for each time t using the measured x-ray spectra shown in Fig. 87.16 and filter functions of beryllium, titanium, and iron filters.¹³ Images $I_{<K}(\mathbf{r}, t)$ and $I_{>K}(\mathbf{r}, t)$ have been obtained from “raw” images (shown in Fig. 87.17) using the Wiener-filtering technique,^{13,19} which was based on the measured system resolution ($\sim 6 \mu\text{m}$)¹⁹ and the system noise (determined by the photon statistics of core x rays).¹⁹ All approximations and assumptions made in deriving Eq. (1) have been presented and discussed in detail in Refs. 12, 13, and 19.

Results and Discussion

Figure 87.19(a) shows the evolution of areal-density modulations calculated using core images at 1.92, 1.97, 2.02, and 2.07 ns, shown in Fig. 87.17 and Eq. (1), and normalized to their measured (with the streak camera) average areal densities, shown in Fig. 87.18(b). The images at early times 1.77 and 1.82 ns do not have sufficient backlighter area (first two images at ~ 4.8 -keV channel) to probe the nonuniformities in the cold shell. The spatial scale of modulations decreases from time 1.92 ns to time 2.02 ns (as evident from the motion of the red “circular” structure in corresponding images), and then shorter-scale modulations start to grow in the image at 2.07 ns. The image size at 2.07 ns is smaller than images at early times because the level of backlighter emission drops late in the implosion. The effect of titanium line emission on the spatial shape of images below the K edge was negligible because core images, routinely measured with a pinhole-array spectrometer,¹² always had the same spatial shapes at photon energies of titanium ($\text{He}\alpha$, $\text{H}\alpha$) lines and photon energies outside these lines below the K edge. The minimum level of modulations with $\sigma_{\text{rms}} = 18 \pm 8\%$ occurs near 2.0 ns. The modulation σ_{rms} decreases by about 20% from time 1.92 ns to time 2.02 ns,

when the maximum core emission intensity and temperature occur (see Fig. 87.18); then it grows by about 60% during decompression while emission intensity and temperature drop.

The shell modulation level at peak compression depends on the initial modulation level at the beginning of the implosion and the amount of unstable growth during implosion. In direct-drive ICF the initial target modulations come primarily from the imprinting^{5–8} of laser-beam nonuniformities. Beam-smoothing techniques such as DPP's,¹⁵ SSD,¹⁶ and PS¹⁷ are applied on OMEGA¹⁴ to minimize initial target modulations. To check the sensitivity of shell modulations at peak compression to the initial target modulations, two implosions with similar targets and drive conditions but with different levels of beam smoothing are compared: one shot was taken at best smoothing conditions, including 1-THz, 2-D SSD and PS; the other shot had 3-color-cycle, 0.35-THz, 2-D SSD and no PS. Figure 87.19(b) compares minimum levels of shell modulations near peak compression for these two shots. The level of shell modulation is significantly higher with less-uniform drive using 0.35-THz SSD and no PS ($\sigma_{\text{rms}} = 43 \pm 12\%$) than with 1-THz SSD and PS ($\sigma_{\text{rms}} = 18 \pm 9\%$). Implosions driven with more-uniform beams (1-THz SSD and PS) have primary neutron yields and fuel areal densities $\sim 70\%$ higher than with 0.35-THz SSD and no PS.²²

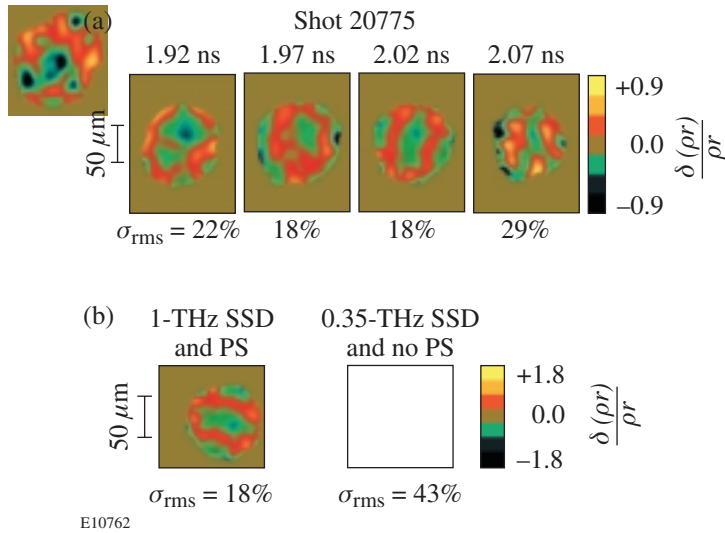


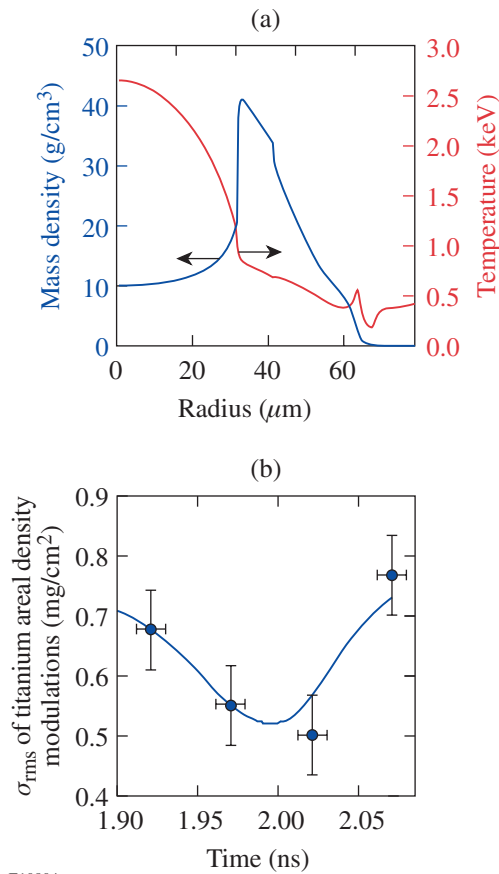
Figure 87.19

(a) Normalized areal-density modulations at 1.92, 1.97, 2.02, and 2.07 ns for shot 20775. (b) Normalized areal-density modulations for two shots: one with 1-THz SSD and PS from (a) at 2.02 ns; the other at peak compression with 3-color-cycle, 0.35-THz SSD and no PS.

A spherical-implosion postprocessor²³ to the one-dimensional (1-D) hydrocode *LILAC*²⁴ was applied to qualitatively explain the experimental data. This postprocessor uses a sharp-boundary model to study the perturbation evolution in the shell. During the acceleration phase of implosion, when the shell is driven by the laser beams, the shell nonuniformities grow due to the Rayleigh–Taylor (RT) instability.^{2–10} When the 1-ns laser drive is turned off, the shell slows down while converging inward to the target center, stops at stagnation, and then moves outward. Since the higher-density shell is slowed down by the lower-density D_2 gas, the inner surface of the shell is subject to the RT instability during the deceleration phase. The shell-areal-density modulation (the quantity measured in the experiment) can be written in the following form: $\delta(\rho d) \approx \pi\eta_f + \pi\eta_b$, where ρ is the average shell density, η_f and η_b are the amplitudes of the front- and back-surface distortions, and d is the shell thickness. During the shell acceleration, when the front surface is RT unstable, the first term $\rho\eta_f$ gives the dominant contribution to $\delta(\rho d)$. In addition, the front-surface perturbations feed through the shell ($\eta_b \sim \eta_f e^{-kd}$, where k is the modulation wave number), seeding the deceleration-phase RT instability on the inner surface. After the laser is turned off and the shell starts to decelerate, the ablation front becomes stable and perturbation η_f oscillates. One can estimate the period of such oscillations $T \sim 2\pi\sqrt{R/(\ell g)}$, where $R \approx 60 \mu\text{m}$ is the shell radius, ℓ is the mode number, and $g \approx 10^3 \mu\text{m/ns}$ is the deceleration. Substituting results of the 1-D *LILAC*²⁴ simulation to the above formula gives $T = 600$ ps for the dominant in the experiment mode $\ell = 6$ (which corresponds to a modulation wavelength of about $60 \mu\text{m}$). Therefore, during the time of measurement $\Delta t = 300$ ps, the front-surface modulation changes its sign. Thus, there are two competing effects: first, the reduction of front-surface modulations $\eta_f \sim \eta_0 \cos(2\pi t/T)$ due to phase change, and, second, an increase in back-surface modulations $\eta_b \sim \eta_0 \exp(\gamma t - kd)$ due to the RT growth, where γ is the instability growth rate. Initially, $\eta_f > \eta_b$, and the reduction in the front-surface amplitude leads to the reduction in the areal-mass modulation. Later, when η_b becomes dominant, growth in shell-areal-density modulation $\delta(\rho d)$ is caused by the exponential growth of the back-surface modulation. An additional reduction in cold $\delta(\rho d)$ could be due to the heating of the inner titanium-doped layer of the shell.

Figure 87.20(a) shows the profiles of target density and temperature in the deceleration phase of the implosion at peak compression (simulated by the 1-D code *LILAC*). The bulk of the shell is dense and relatively cold with an electron temperature less than 1 keV, while the core is hotter and less dense. The

solid line in Fig. 87.20(b) shows the evolution of shell-areal-density modulations calculated with the model for the dominant mode $\ell = 6$ based on the 1-D *LILAC* simulation. The modulations of total shell areal density $\delta(\rho d)$ decrease, while they are dominated by sinusoidally decreasing modulations at the outer surface. When exponentially growing modulations at the inner surface become higher than outer-surface modulations, the total shell-areal-density modulations grow. The circles in Fig. 87.20(b) show that σ_{rms} of measured shell-areal-density modulations [shown in Fig. 87.19(a)] follows the model prediction well. The results of the model were normalized to experimental point at $t = 1.97$ ns. The experimental points have been averaged using data from three shots taken at similar conditions. Since the measured spectrum of shell-areal-density modulations is located in the vicinity of the mode



E10804

Figure 87.20

(a) The simulated profiles of target density and temperature during the deceleration phase of the implosion. (b) The evolution of titanium areal-density modulations in the shell calculated by the model (solid line) and measured (circles).

$\ell = 6$ (similar to previous time-integrated measurements^{12,13}), the comparison of measured modulation σ_{rms} with the calculated amplitude of dominant spectral mode becomes qualitatively reasonable.

Figure 87.18 shows that average cold-shell areal density increases up to ~ 1.8 ns and then starts to decrease gradually while peak compression is measured to be near 2.0 ns. This indicates that some part of the inner shell mixes with the core fuel and/or heats up to ~ 2 keV when it stops absorbing core radiation at photon energies above the titanium *K* edge. Such an increase in shell temperature and the reduction of measured cold-shell areal density are expected in targets with titanium-doped layers because of the additional absorption of core radiation by titanium above the titanium *K* edge. As a result, the cold-shell average areal density and areal-density modulations may be reduced. This effect may be partially responsible for the decrease of measured areal-density modulations [shown in Fig. 87.20(b)] for times up to ~ 2.0 ns. The increase of measured areal-density modulation after 2.0 ns, however, should be due to the unstable RT growth in the deceleration phase of the implosion, as predicted by the model.

Conclusion

The evolution of shell modulations near peak compression of a spherical implosion has been presented. The minimum level of areal-density modulations, with $\sigma_{\text{rms}} = 18\%$, occurs at the peak of core emission with a laser drive that included 1-THz SSD and PS. In implosions using the less-uniform irradiation produced by 3-color-cycle, 0.35-THz SSD and no PS, the level of modulations was significantly higher, with $\sigma_{\text{rms}} = 43\%$. The level of measured shell-areal-density modulations decreases when it is dominated by the decreasing modulations at the stable outer surface, then increases when it is dominated by growing modulations at the unstable inner surface, as expected.

ACKNOWLEDGMENT

This work was supported by the U.S. Department of Energy Office of Inertial Confinement Fusion under Cooperative Agreement No. DE-FC03-92SF19460, the University of Rochester, and the New York State Energy Research and Development Authority. The support of DOE does not constitute an endorsement by DOE of the views expressed in this article.

REFERENCES

1. J. Nuckolls *et al.*, *Nature* **239**, 139 (1972).
2. J. D. Lindl, *Inertial Confinement Fusion: The Quest for Ignition and Energy Gain Using Indirect Drive* (Springer-Verlag, New York, 1998), Chap. 6, pp. 61–82.

3. S. G. Glendinning, S. N. Dixit, B. A. Hammel, D. H. Kalantar, M. H. Key, J. D. Kilkenny, J. P. Knauer, D. M. Pennington, B. A. Remington, R. J. Wallace, and S. V. Weber, *Phys. Rev. Lett.* **78**, 3318 (1997).
4. M. M. Marinak *et al.*, *Phys. Rev. Lett.* **80**, 4426 (1998).
5. C. J. Pawley *et al.*, *Phys. Plasmas* **6**, 565 (1999).
6. H. Azechi *et al.*, *Phys. Plasmas* **4**, 4079 (1997).
7. R. J. Taylor *et al.*, *Phys. Rev. Lett.* **76**, 1643 (1996).
8. D. H. Kalantar, M. H. Key, L. B. Da Silva, S. G. Glendinning, B. A. Remington, J. E. Rothenberg, F. Weber, S. V. Weber, E. Wolftrum, N. S. Kim, D. Neely, J. Zhang, J. S. Wark, A. Demir, J. Lin, R. Smith, G. J. Tallents, C. L. S. Lewis, A. MacPhee, J. Warwick, and J. P. Knauer, *Phys. Plasmas* **4**, 1985 (1997).
9. D. L. Tubbs, C. W. Barnes, J. B. Beck, N. M. Hoffman, J. A. Oertel, R. G. Watt, T. Boehly, D. Bradley, P. Jaanimagi, and J. Knauer, *Phys. Plasmas* **6**, 2095 (1999).
10. S. G. Glendinning *et al.*, *Phys. Plasmas* **7**, 2033 (2000).
11. S. G. Glendinning *et al.*, in *Applications of Laser Plasma Radiation II*, edited by M. C. Richardson and G. A. Kyrala (SPIE, Bellingham, WA, 1995), Vol. 2523, pp. 29–39.
12. B. Yaakobi, V. A. Smalyuk, J. A. Delettrez, F. J. Marshall, D. D. Meyerhofer, and W. Seka, *Phys. Plasmas* **7**, 3727 (2000).
13. V. A. Smalyuk, B. Yaakobi, J. A. Delettrez, F. J. Marshall, and D. D. Meyerhofer, *Phys. Plasmas* **8**, 2872 (2001).
14. T. R. Boehly, D. L. Brown, R. S. Craxton, R. L. Keck, J. P. Knauer, J. H. Kelly, T. J. Kessler, S. A. Kumpan, S. J. Loucks, S. A. Letzring, F. J. Marshall, R. L. McCrory, S. F. B. Morse, W. Seka, J. M. Soures, and C. P. Verdon, *Opt. Commun.* **133**, 495 (1997).
15. Y. Lin, T. J. Kessler, and G. N. Lawrence, *Opt. Lett.* **20**, 764 (1995).
16. S. P. Regan, J. A. Marozas, J. H. Kelly, T. R. Boehly, W. R. Donaldson, P. A. Jaanimagi, R. L. Keck, T. J. Kessler, D. D. Meyerhofer, W. Seka, S. Skupsky, and V. A. Smalyuk, *J. Opt. Soc. Am. B* **17**, 1483 (2000).
17. T. R. Boehly, V. A. Smalyuk, D. D. Meyerhofer, J. P. Knauer, D. K. Bradley, R. S. Craxton, M. J. Guardalben, S. Skupsky, and T. J. Kessler, *J. Appl. Phys.* **85**, 3444 (1999).
18. C. J. Pawley and A. V. Deniz, *Rev. Sci. Instrum.* **71**, 1286 (2000).
19. V. A. Smalyuk, T. R. Boehly, L. S. Iwan, T. J. Kessler, J. P. Knauer, F. J. Marshall, D. D. Meyerhofer, C. Stoeckl, B. Yaakobi, and D. K. Bradley, *Rev. Sci. Instrum.* **72**, 635 (2001).
20. R. E. Turner *et al.*, *Rev. Sci. Instrum.* **72**, 706 (2001).
21. D. H. Kalantar *et al.*, *Rev. Sci. Instrum.* **72**, 751 (2001).
22. D. D. Meyerhofer, J. A. Delettrez, R. Epstein, V. Yu. Glebov, V. N. Goncharov, R. L. Keck, R. L. McCrory, P. W. McKenty, F. J. Marshall, P. B. Radha, S. P. Regan, S. Roberts, W. Seka, S. Skupsky, V. A. Smalyuk, C. Sorce, C. Stoeckl, J. M. Soures, R. P. J. Town, B. Yaakobi, J. D. Zuegel, J. Frenje, C. K. Li, R. D. Petrasso, D. G. Hicks, F. H. Séguin, K. Fletcher, S. Padalino, M. R. Freeman, N. Izumi, R. Lerche, T. W. Phillips, and T. C. Sangster, *Phys. Plasmas* **8**, 2251 (2001).
23. V. N. Goncharov, P. McKenty, S. Skupsky, R. Betti, R. L. McCrory, and C. Cherfils-Clérouin, *Phys. Plasmas* **7**, 5118 (2000).
24. J. Delettrez and E. B. Goldman, Laboratory for Laser Energetics Report No. 36, University of Rochester (1976).

Multibeam Stimulated Brillouin Scattering from Hot Solid-Target Plasmas

Introduction

We report on the first multibeam laser–plasma interaction experiments with a critical density surface present at all times. Six interaction beams are incident on a preformed plasma, tailored to resemble future direct-drive-ignition laser fusion implosions. Stimulated Brillouin scattering (SBS) was observed using two full-aperture backscattering stations. The results show strong evidence of electromagnetic (EM) wave seeding of SBS backscatter and may also indicate strongly driven, common, symmetrically located ion waves. The latter could provide for efficient sidescattering that provides the EM seed for SBS backscattering. Quenching SBS before the peak of the interaction beam is seen in all the experiments. For NIF direct-drive ignition experiments the expected SBS levels are well below 1%.

The details of laser coupling to the hot coronal plasma of direct-drive inertial confinement fusion (ICF) targets are extremely important since the laser provides the drive energy for the implosion.¹ Measurement and understanding of power (or energy) loss due to SBS are essential. Over the past 30 years, many detailed reports^{2–12} of SBS experiments have been published; however, few, if any, have investigated conditions relevant to direct-drive ICF plasma implosions.⁴ In direct-drive implosions, many individual laser beams are overlapped on the target. This allows multibeam interactions that may change the SBS instability characteristics.^{13,14} In particular, SBS instability can grow from an EM wave seed provided by other beams reflected near the critical-density surface, or common (shared) ion waves can reduce the instability threshold. Previous multibeam SBS experiments^{3,15} have been performed in plasmas with peak densities significantly lower than critical density and are, thus, not directly applicable to direct-drive ICF conditions. Those experiments indicated a redistribution of the scattered light but no significant increase in the overall SBS losses.¹⁵

In future direct-drive-ignition experiments on the National Ignition Facility (NIF),¹⁶ the conditions most vulnerable to SBS will occur before the laser reaches its peak power¹ and

will correspond to plasmas with $T_e \geq 2$ keV and density and velocity scale lengths of ~ 0.5 mm. These will be irradiated with 351-nm laser light with laser-beam smoothing¹⁷ by spectral dispersion (SSD) at ~ 1 THz and polarization smoothing (PS). The corresponding single-beam irradiation intensities are $\leq 10^{14}$ W/cm² (four beamlets, or one quad, of the NIF¹⁶).

The full plasma and intensity evolution of a NIF direct-drive implosion cannot be simulated with present laser systems, but a good approximation to the conditions that are most susceptible to SBS can be achieved using OMEGA. Past single-beam interaction experiments on OMEGA have shown that SBS is unlikely to represent a significant energy loss during the high-intensity portion of the NIF pulse.⁴ The present multiple-beam SBS experiments are the first reported in the literature with a critical-density surface present at all times and plasma conditions close to those expected on the NIF. Six interaction beams are symmetrically arrayed around the target normal. These interaction beams are overlapped on a plasma produced from a thick CH target by heater beams that strike the target in advance of the interaction beams.

Experiments

The experiments were carried out on the OMEGA laser system¹⁸ using a subset of its 60 UV (351-nm) beams. The experimental arrangement is shown schematically in Fig. 87.21. The CH targets were 100 μm thick and 5 mm in diameter (semi-infinite) with their normal pointed toward the center of the six symmetrically arranged interaction beams (see Figs. 87.21 and 87.22). These targets were sequentially irradiated with nine primary beams, followed in 1-ns intervals by six secondary heater beams and six interaction beams. The six interaction beams are identified with their beam numbers inside the circles in Fig. 87.22 and are located at $\sim 23^\circ$ to the target normal. The primary and secondary beams are at $\sim 62^\circ$ and 48° to the target normal, respectively.

All of the beams were equipped with distributed phase plates¹⁹ (DPP's) and were operated with 2-D SSD (1 THz) and PS.¹⁷ The phase plates in the primary and secondary beams

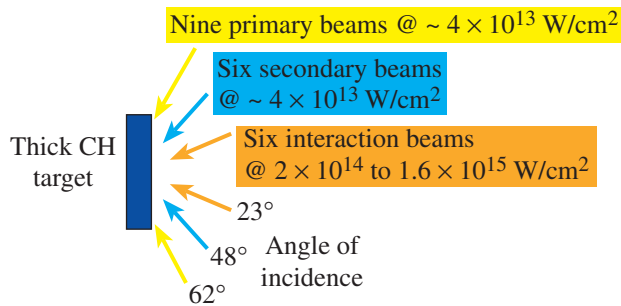
were standard OMEGA “SG3” phase plates (nominally Gaussian spots of 0.5-mm FWHM at best focus). These beams were defocused to produce a 2-mm-diam spot (~1-mm FWHM) with peak intensities (averaged over the speckle pattern) of $\sim 4 \times 10^{13}$ W/cm². Two alternative configurations were used on the six interaction beams: All were outfitted with either six standard phase plates with the target at best focus (nominal single-beam peak intensity of 2×10^{14} W/cm²) or three pairs of phase plates that produced smaller spots. In the latter case, the corresponding average single-beam peak intensities were 4, 8, and 16×10^{14} W/cm². The beam energy for all shots was ~365 J ($\pm 5\%$). The laser pulse shapes were a close approximation of those shown schematically in Fig. 87.21, i.e., a 0.5-ns linear rise followed by a 0.9-ns flattop.

Similar preformed plasmas have been diagnosed extensively using time-resolved x-ray spectroscopy, time-resolved stimulated Raman scattering (SRS) spectroscopy,⁴ and schlieren photography.^{5,20} Those experiments have been simulated with the two-dimensional hydrodynamic code *SAGE*.²¹ Because

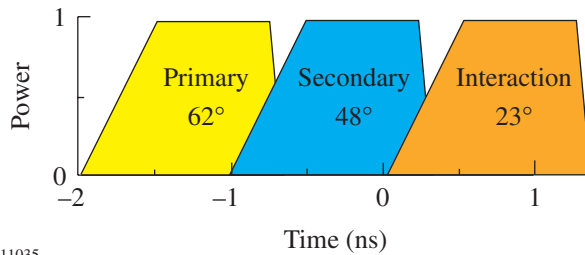
the *SAGE* simulations have generally closely replicated the measurements, we are confident that the *SAGE* predictions for the present experiments are equally valid: electron temperatures of ~2 to 3 keV with electron density and velocity scale lengths of ~1 mm.

Two full-aperture backscatter (FABS) stations were used to measure the SBS energies and the time-resolved SBS spectra. These stations collected the light propagated from the target in the direction opposite to the incoming high-energy beam path through the *f*/6 OMEGA focusing lens. This was accomplished using an uncoated, wedged, fused quartz optic ahead of the focusing lens. The arrangement allows the incoming high-energy beam to pass onward to the target while a full-aperture, reduced-energy sample of any outbound light is delivered to the FABS setup. Beams 25 and 30 (in Fig. 87.22) were instrumented in this manner. Within the FABS, the energies were measured with appropriately filtered and cross-calibrated calorimeters. The light for the time-resolved spectra was focused through an engineered diffuser (2° scattering angle)

(a) Beam geometry and intensity

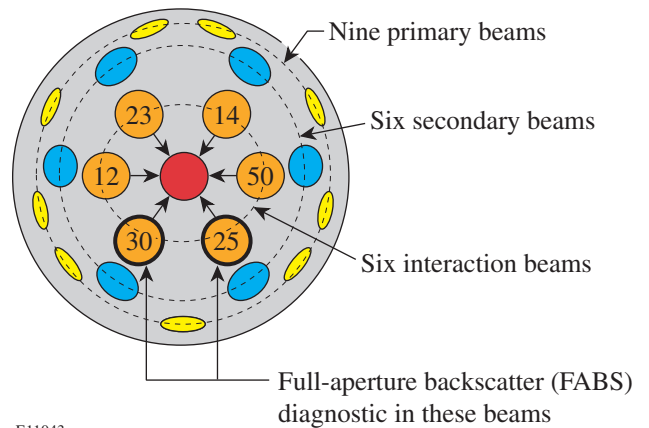


(b) Pulse shape and timing of beam groups



E11035

Beam number	25	30	12	23	14	50
I_{14} (10^{14} W/cm ²)	4	16	4	8	16	8



E11043

Figure 87.22

Schematic representation of the plasma-producing and interaction beams on the target chamber surface. The numbers inside the circles are the beam numbers for the interaction beams. Beams 25 and 30 are outfitted with full-aperture backscatter (FABS) stations. All beam energies are nominally 365 J. The intensities (in units of 10^{14} W/cm²) shown in the boxes below the beam numbers result from three different sets of phase plates. Standard OMEGA phase plates also permitted interaction intensities of 2×10^{14} W/cm² in any or all of the beams.

into 435- μm gradient-index fibers and sent to a 1-m grating spectrometer coupled to an S20 streak camera. The fibers from both FABS stations were time-multiplexed at the input to the spectrometer. The measured time resolution was 80 ps and the dynamic spectral resolution was $\sim 0.4 \text{ \AA}$.

Results

The multibeam, time-integrated SBS reflectivity is shown in Fig. 87.23 as a function of the interaction beam intensity. Data from both FABS stations are shown. The average peak intensities of the various interaction beams ranged from $2 \times 10^{14} \text{ W/cm}^2$ to $1.6 \times 10^{15} \text{ W/cm}^2$, depending on the phase plates used. The average peak intensity I_{05} is defined such that 95% of the laser energy has intensities at or below I_{05} . Thus, most shots yielded simultaneous multibeam backscatter data at two intensities. The squares in Fig. 87.23 represent through-the-lens reflectivities with all beams at nominal energy. The diamonds represent shots without interaction beams (e.g., without beam 25 for FABS25), while the circles represent shots without the beams opposing the interaction beams [beam 23 for FABS25, beam 14 for FABS30 (see Fig. 87.22)].

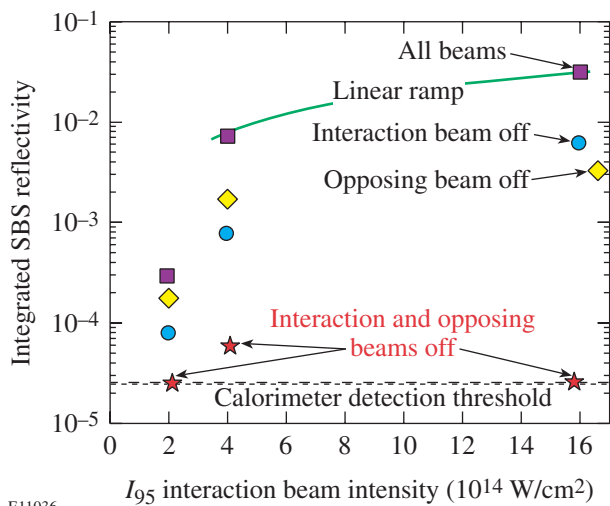


Figure 87.23

Multibeam, time-integrated SBS reflectivity measured by the calorimeters in two different locations (FABS25 and FABS30) for beam smoothing with 1-THz, 2-D SSD and PS. Squares represent measurements with all beams as indicated in Fig. 87.22, diamonds indicate shots without interaction beams (either beam 25 for FABS25 or beam 30 for FABS30), circles indicate shots without beams opposing the interaction beams (beam 23 for FABS25, beam 14 for FABS30). The stars indicate FABS energy measurements normalized to the mean beam energy with beams 25 and 23 (or 30 and 14) turned off. The linear ramp is shown to guide the eye and is indicative of saturation at intensities in excess of $\sim 3 \times 10^{14} \text{ W/cm}^2$. Each point plotted represents several actual shots with the shots clustered within the symbols shown.

The possible interplay and synergistic enhancement between specular reflection at the turning point, SBS side-scattering, and SBS backscattering are depicted in Fig. 87.24. Given the geometry of the interaction beams, the “opposing” beams (e.g., 23 and 14) are reflected at their respective turning points near the critical density ($n_e \sim 0.88 n_c$) and counter-propagate into beams 25 and 30. (Note: In this discussion, the term “opposing beam” means the beam on the opposite side of the circle of interaction beams. This is not the beam on the opposite side of the OMEGA target chamber that has a coincident optical axis, which was not used in these experiments.) These reflections can provide EM seed waves for SBS backscattering in beams 25 and 30. This is reminiscent of external EM-wave-seeding experiments by Baldis³ and Fernandez.⁶ In addition, the specular reflections can also provide EM seeds for SBS sidescattering in that direction.

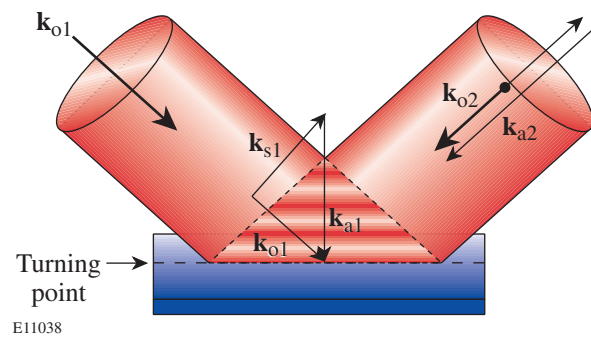


Figure 87.24

Schematic visualization of the interplay between SBS sidescattering and SBS backscattering on flat targets irradiated with symmetrically positioned interaction beams. The specular reflection at the turning point provides an EM seed for SBS sidescattering. That, in turn, provides an efficient EM seed for SBS backscattering of the “opposing” beam. These processes are most effective near the sonic point where the SBS wavelength shifts vanish.

The overall, multibeam reflectivities (squares in Fig. 87.23) saturate at a few percent for average irradiation intensities of 3 to $4 \times 10^{14} \text{ W/cm}^2$. Selectively turning off one of the interaction beams (beam 25 or 30—circles) or one of their opposing beams (beam 23 or 14—diamonds) leads to a significant drop in reflectivity. Furthermore, if both the interaction beam and its opposing beam are turned off, the residual reflectivities (stars) drop to the detection threshold for all but the point at $4 \times 10^{14} \text{ W/cm}^2$. For this point, the high-intensity beams 30 and 14 cause measurable sidescatter signal. For the other two intensities, the four remaining beams are too low in intensity to produce measurable SBS sidescattering into either

FABS25 or FABS30. Pure SBS backscattering for oblique incidence (circles) is observed if the beam opposing the interaction beam (e.g., beam 23) is turned off. In this case SBS grows from either noise or any existing seed (e.g., stars in Fig. 87.23).

The measured reflectivity in FABS25 is roughly twice that measured for pure backscattering when beam 25 is removed while the opposing beam 23 is left on. This signal (diamonds) represents SBS sidescattering of beam 23, which may be enhanced through ion-wave seeding by the symmetrically located ion waves produced by cooperative multibeam SBS side scattering from the other four interaction beams (see Fig. 87.24). In addition, this sidescatter SBS may also be EM-seeded by its own reflection at the turning point. As a result, the two processes cannot be separated by this measurement alone. As will be discussed later, both the sidescattering and backscattering power reflectivities peak before the maximum of the laser pulse and have essentially identical power histories.

When all beams are turned on (squares in Fig. 87.23), the signal is much stronger than a linear superposition of the backscatter and sidescatter signals. The backscatter signal by itself (circles) is negligible, while the sidescatter signal (diamonds) provides the main EM seed for backscattering when all beams are turned on.

Representative time-resolved power reflectivities are shown in Fig. 87.25 for two experimental conditions. The power reflectivities at other intensities as well as the sidescatter power reflectivities (corresponding to the diamonds in Fig. 87.23) show similar temporal behaviors: they peak well before the laser pulse reaches its maximum. This rules out a linear scattering (or reflection or refraction) process that would peak toward the end of the laser pulse due to the heating of the plasma by the interaction beams. These power reflectivities show that the SBS backscatter and sidescatter signals are quenched before the peak of the laser pulse, possibly due to filamentation. A similar suppression of SBS forward scattering due to filamentation has been observed recently in experiments by Fuchs *et al.*¹¹ and in simulations by Tikhonchuk.^{10,12}

The measured multibeam reflectivities in FABS25 (squares in Fig. 87.23) are principally EM-seeded backscattering of beam 25 with the seed provided by SBS sidescattering of the opposing beam 23. The ion waves involved in this process are the same as those involved in the cooperative multibeam SBS process of beams 14 and 30, 12 and 52 (see Fig. 87.22). To check whether these common ion waves indeed play a role in

the sidescattering of beam 23, the intensities of several of the four beams were varied; the resulting FABS25 reflectivities are shown in Fig. 87.26 as a function of overlapped intensity. The sidescatter reflectivity declined with decreasing overlapped intensity of the four beams while the energies and intensities in beams 25 and 23 were kept constant. Thus, the differences in measured FABS25 reflectivities are clearly associated with the four asymmetrically located interaction beams. These same beams provide only a negligible EM seed to the SBS backscatter signal in FABS25 (stars in Fig. 87.23), but they do heat the plasma. These observations are consistent with the existence of common, symmetrically located ion waves produced by these four beams; these ion waves contribute significantly to the sidescattering of beam 23 into beam 25. Since the SBS reflectivities in Fig. 86.26 are well into the saturated regime, we estimate that the ion-wave amplitudes decline roughly by the same factor as the reflectivities. Alternatively, the change in electron temperature with increasing overlapped irradiation intensity may increase the EM seed for sidescattering, and consequently, also the total seed provided for backscattering. In this case no common ion waves would be involved. Our present experiments cannot rule out this scenario.

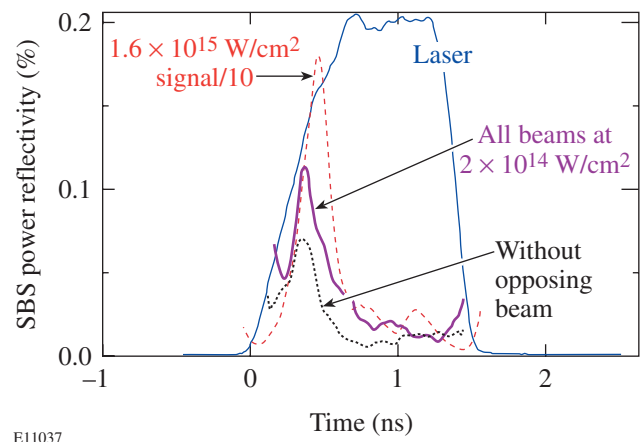
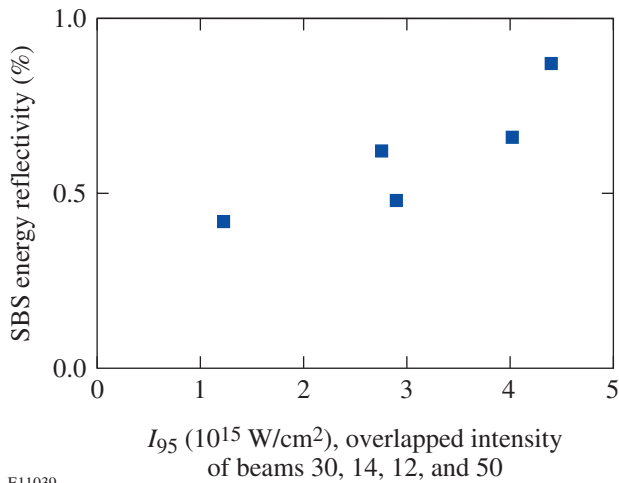


Figure 87.25 Measured multibeam SBS reflectivities for three different irradiation conditions along with a typical laser pulse shape. The dashed line is the backscatter signal in FABS30 for the irradiation conditions shown in Fig. 87.22. The dotted line and the thick solid line represent backscattering at low irradiation intensities with all interaction beams at $2 \times 10^{14} \text{ W/cm}^2$. For the dotted line the opposing beam 23 was turned off, resulting in pure backscattering of beam 25.



E11039

Figure 87.26

Backscatter reflectivities measured with FABS25 for the general irradiation conditions shown in Fig. 87.22 with some variations in beam energies of beams 30 and 14. The beam energies in beams 25 and 23 were kept constant. The increase in reflectivity with increasing overlapped intensity may be associated with a change in the common ion-acoustic-wave amplitudes generated by beams 30, 14, 12, and 50. Alternatively, the increase may be a consequence of decreased absorption as the plasma temperature increases with increasing overlapped intensity on target.

Conclusions

Multibeam interaction experiments were carried out in NIF-type, hot, long-scale-length plasmas on OMEGA using thick, planar CH targets. A symmetrical arrangement of six interaction beams with beam smoothing is consistent with strongly driven common ion waves located along the axis of symmetry of the six interaction beams. The present experiments, however, cannot rule out alternative interpretations that do not involve common ion waves. In either case, SBS sidescattering provides a large EM seed for SBS backscattering. These experiments have shown for the first time the synergistic enhancement of SBS sidescattering and backscattering. The fact that backscatter levels well below 1% are expected for typical NIF direct-drive irradiation conditions provides confidence in the expected direct-drive target performance on the NIF.²²

ACKNOWLEDGMENT

This work was supported by the U.S. Department of Energy Office of Inertial Confinement Fusion under Cooperative Agreement No. DE-FC03-92SF19460, the University of Rochester, and the New York State Energy Research and Development Authority. The support of DOE does not constitute an endorsement by DOE of the views expressed in this article.

REFERENCES

1. S. E. Bodner, D. G. Colombant, J. H. Gardner, R. H. Lehmborg, S. P. Obenschain, L. Phillips, A. J. Schmitt, J. D. Sethian, R. L. McCrory, W. Seka, C. P. Verdon, J. P. Knauer, B. B. Afeyan, and H. T. Powell, *Phys. Plasmas* **5**, 1901 (1998).
2. C. J. Walsh, D. M. Villeneuve, and H. A. Baldis, *Phys. Rev. Lett.* **53**, 1445 (1984).
3. D. M. Villeneuve, H. A. Baldis, and J. E. Bernard, *Phys. Rev. Lett.* **59**, 1585 (1987).
4. S. P. Regan, D. K. Bradley, A. V. Chirikikh, R. S. Craxton, D. D. Meyerhofer, W. Seka, R. W. Short, A. Simon, R. P. J. Town, B. Yaakobi, J. J. Carroll III, and R. P. Drake, *Phys. Plasmas* **6**, 2072 (1999).
5. W. Seka, R. E. Bahr, R. W. Short, A. Simon, R. S. Craxton, D. S. Montgomery, and A. E. Rubenchik, *Phys. Fluids B* **4**, 2232 (1992).
6. J. C. Fernández *et al.*, *Phys. Rev. Lett.* **81**, 2252 (1998).
7. J. C. Fernández *et al.*, *Phys. Plasmas* **4**, 1849 (1997).
8. J. A. Cobble *et al.*, *Phys. Plasmas* **7**, 323 (2000).
9. C. Labaune *et al.*, *Phys. Rev. Lett.* **85**, 1658 (2000).
10. V. T. Tikhonchuk *et al.*, *Phys. Plasmas* **8**, 1636 (2001).
11. J. Fuchs *et al.*, *Phys. Plasmas* **7**, 4659 (2000).
12. J. Myatt *et al.*, "Nonlinear Propagation of a Randomized Laser Beam Through an Expanding Plasma," to be published in *Physical Review Letters*.
13. D. F. DuBois, B. Bezzeridels, and H. A. Rose, *Phys. Fluids B* **4**, 241 (1992).
14. H. A. Rose and D. F. DuBois, *Phys. Fluids B* **4**, 252 (1992).
15. H. A. Baldis *et al.*, *Phys. Rev. Lett.* **77**, 2957 (1996).
16. J. D. Lindl, *Inertial Confinement Fusion: The Quest for Ignition and Energy Gain Using Indirect Drive* (Springer-Verlag, New York, 1998), Chap. 6, pp. 61–82.

17. S. Skupsky and R. S. Craxton, *Phys. Plasmas* **6**, 2157 (1999).
18. T. R. Boehly, R. S. Craxton, T. H. Hinterman, P. A. Jaanimagi, R. L. Keck, J. H. Kelly, T. J. Kessler, R. L. Kremens, S. A. Kumpan, S. A. Letzring, R. L. McCrory, S. F. B. Morse, W. Seka, S. Skupsky, J. M. Soures, and C. P. Verdon, in *Proceedings of the IAEA Technical Committee Meeting on Drivers for Inertial Confinement Fusion*, edited by J. Coutant (IAEA, Vienna, 1995), pp. 79–86.
19. T. J. Kessler, Y. Lin, L. S. Iwan, W. P. Castle, C. Kellogg, J. Barone, E. Kowaluk, A. W. Schmid, K. L. Marshall, D. J. Smith, A. L. Rigatti, J. Warner, and A. R. Staley, in *Second Annual International Conference on Solid State Lasers for Application to Inertial Confinement Fusion*, edited by M. L. André (SPIE, Bellingham, WA, 1997), Vol. 3047, pp. 272–281.
20. W. Seka, R. S. Craxton, R. E. Bahr, D. L. Brown, D. K. Bradley, P. A. Jaanimagi, B. Yaakobi, and R. Epstein, *Phys. Fluids B* **4**, 432 (1992).
21. R. S. Craxton and R. L. McCrory, *J. Appl. Phys.* **56**, 108 (1984).
22. P. W. McKenty, V. N. Goncharov, R. P. J. Town, S. Skupsky, R. Betti, and R. L. McCrory, *Phys. Plasmas* **8**, 2315 (2001).

Hot-Electron Effect in Superconductors and Its Applications for Radiation Sensors

Introduction

The term “hot electrons” was originally introduced to describe nonequilibrium electrons (or holes) in semiconductors (for a review see, e.g., Ref. 1). The term encompasses electron distributions that could be formally described by the Fermi function but with an effective elevated temperature. The concept is very fruitful for semiconductors, where the mobility of carriers can be shown to depend on their effective temperature. In metals, however, electrons do not exhibit any pronounced variation of the mobility with their energy. As a result, heating of electrons in a metal does not affect the resistance,² unless the change in the effective temperature is comparable with the Fermi temperature.

Schklovski³ was the first to discuss the idea of combining the steady-state electron heating with the strong dependence of the resistance on the effective electron temperature in a metal film undergoing the superconducting transition. In the steady-state regime, however, electron heating is always masked by the conventional bolometric effect; therefore, experimental results on the heating of electrons by the dc current were not very convincing. The regime of dynamic electron heating by external radiation was studied in a series of experimental and theoretical works.⁴⁻⁶ It was immediately realized that the very short relaxation time of electron excitations would make it feasible to design extremely fast radiation sensors with a sensitivity much better than that of conventional bolometers.

During the last decade, a new generation of hot-electron superconducting sensors has been developed. These include submillimeter and THz mixers, direct detectors, and photon counters for the broad spectral range from microwaves to optical radiation and x rays. Activity in the field of hot-electron superconducting sensors is growing rapidly. These sensors have already demonstrated performance that makes them devices-of-choice for many far-infrared (THz), infrared, and optical wavelength applications, such as plasma diagnostics, laser studies, ground-based and airborne heterodyne astronomy, and single-photon-detection and quantum communications. Parallel development of compact cryocoolers and THz radia-

tion sources opens hot-electron sensors for satellite astronomy and communication applications. This article reviews the physical background of the hot-electron phenomenon in superconducting films and discusses various technical realizations of hot-electron radiation sensors.

Physics of Hot Electrons

Thermal dynamics in a superconducting film on a dielectric substrate can be thought of in terms of four co-existing subsystems: Cooper pairs, quasiparticles (electrons from broken Cooper pairs), phonons in the film, and phonons in the substrate. Thermal equilibrium exists when all of these can be described by equilibrium distribution functions with the same temperature. If any distribution does not satisfy these conditions, the situation is considered nonequilibrium. General treatment of a nonequilibrium state requires solution of the integral kinetic equations for space- and time-dependent distribution functions. To avoid the above complexity, various simplifying assumptions are used to reduce the general problem to analytically solvable rate equations.

1. Hot-Electron Cooling and Diffusion

The hot-electron model is most relevant for nonequilibrium superconductors maintained at temperature T near the superconducting transition T_c , where quasiparticles and phonons can be described by thermal, normal-state distribution functions, each with its own effective temperature. The electron and phonon effective temperatures (T_e and T_p) are assumed to be established instantly and uniformly throughout the whole specimen. This assumption implies that a rapid thermalization mechanism exists inside each subsystem.

The main steps of the hot-electron phenomenon that lead to the global equilibrium are depicted in Fig. 87.27. Introducing characteristic times of the energy exchange between subsystems reduces the problem of the global equilibrium recovery to a pair of coupled heat-balance equations for T_e and T_p . The intrinsic thermalization time τ_T should be short compared to energy exchange times. This two-temperature (2-T) approach was used for the first time by Kaganov *et al.*² to describe

steady-state electron heating in metals. Below T_c , the electron specific heat exhibits an exponential temperature dependence that makes equations nonlinear for even small deviations from equilibrium. The description can, however, be simplified in the vicinity of T_c . At this temperature the superconducting energy gap is strongly suppressed, concentration of Cooper pairs is very small, and unpaired electrons exhibit no significant superconducting peculiarities: they are regarded as normal electrons having the ordinary Fermi distribution function. In the normal state, the specific heat of electrons has a much weaker temperature dependence, which can be neglected for small deviations of T_e from the equilibrium. With these assumptions, the equations describing the hot-electron effect in superconductors become linear and can be written as

$$\frac{dT_e}{dt} = -\frac{T_e - T_p}{\tau_{ep}} + \frac{1}{C_e} W(t), \quad (1a)$$

$$\frac{dT_p}{dt} = \frac{C_e}{C_p} \frac{T_e - T_p}{\tau_{ep}} - \frac{T_p - T_0}{\tau_{es}}, \quad (1b)$$

where $W(t)$ represents the external perturbation (i.e., the power per unit volume absorbed by the electron subsystem); τ_{ep} and τ_{es} are the electron energy relaxation time via electron–phonon interaction and the time of phonon escape into the substrate; C_e and C_p are the electron and phonon specific heats, respectively;

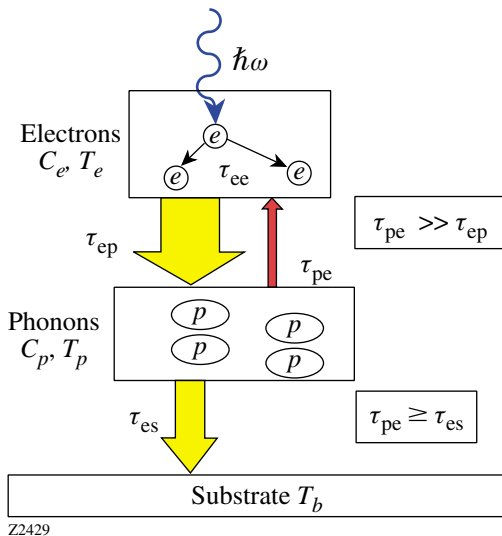


Figure 87.27
Thermalization scheme showing various channels of the energy transfer in a hot-electron device that relaxes toward global equilibrium.

and T_0 is the ambient (substrate) temperature. To derive the 2-T equations we used the condition of the energy-flow balance in equilibrium $\tau_{pe} = \tau_{ep}(C_p/C_e)$, where τ_{pe} is the phonon–electron energy relaxation time.

The first implementation of the electron-heating model to superconductors was made by Shklovski,³ who used a more general, nonlinear form of the heat-balance equations to describe hysteresis of the critical current in a thin lead film. An analytical solution of Eq. (1) was first obtained for sinusoidal perturbations by Perrin and Vanneste⁴ and for an optical pulse excitation by Semenov *et al.*⁵ In the latter case, thermalization of electrons was interpreted as an increase of T_e . The increase was assumed to occur during a time interval that depended on both the duration of the optical pulse and the intrinsic thermalization time τ_T . The model was used to describe the response of superconducting NbN and YBa₂Cu₃O_{7- δ} (YBCO) films in the resistive state to near-infrared and visible radiation.^{5,7} Figures 87.28 and 87.29 show a good agreement between experimental signals and the theoretical simulation.

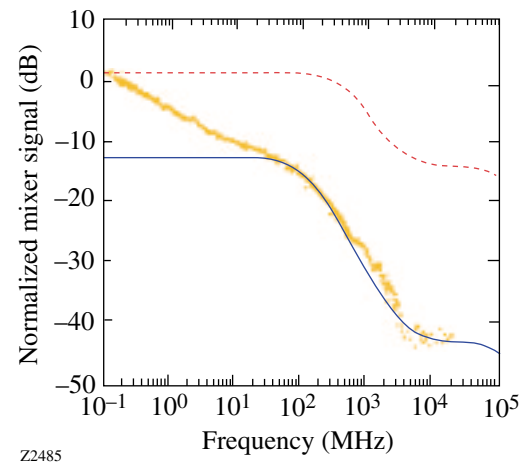


Figure 87.28
Response of a YBCO hot-electron photodetector (HEP) to optical radiation (dots) versus modulation frequency (Ref. 7). The solid line was calculated using Eqs. (1). The discrepancy at low frequencies is due to phonon diffusion in the substrate that was not accounted for in the model. The dashed line represents the thermal model.

Figure 87.30 presents the detailed thermalization diagrams for both YBCO [Fig. 87.30(a)] and NbN [Fig. 87.30(b)] thin films excited by 100-fs-wide optical pulses. The diagrams depict the process in the same manner as Fig. 87.27 but now include the actual values of the characteristic time constants for both materials. The values were obtained from the 2-T model via the fit of Eqs. (1) to the experimental photoresponse

data. The measurements were performed using the electro-optic sampling system, which allowed obtaining the intrinsic, time-resolved dynamics of the electron thermalization process in 3.5-nm-thick NbN⁸ and 100-nm-thick YBCO films.⁹ We note that, in general, the dynamic of the YBCO thermalization is roughly one order of magnitude faster than that of NbN. In both cases, the energy flow from electrons to phonons dominates the energy backflow due to reabsorption of nonequilibrium phonons by electrons; however, while the energy backflow in YBCO can be neglected because of the very large ratio $C_p/C_e = 38$, in NbN it constitutes a non-negligible 15% ($C_p/C_e = 6.5$) of direct electron-phonon energy relaxation. Consequently, in YBCO film excited on the femtosecond time scale, the nonthermal (hot-electron) and thermal, bolometric (phonon) processes are practically decoupled, with the former totally dominating the early stages of electron relaxation. On the other hand, the response of NbN devices is determined by the “average” electron cooling time τ_e , which is given by $\tau_{ep} + (1 + C_e/C_p)\tau_{es}$ ^{4,5} and corresponds to the time that elapses from the peak response until the magnitude of the response declines to $1/e$ of the maximum value. If the external perturbation is substantially longer than τ_{pe} (that is, >100 ps for YBCO films), the YBCO response is dominated by the bolometric process, as was shown by the bulk of the early photoresponse measurements.¹⁰ The very large difference in the τ_{es} values for YBCO and NbN is mainly due to the drastic difference in thickness of the tested films. Additionally, ultrathin NbN films are a better acoustical match to the substrate. This significantly reduces τ_{es} .

Electron heating in the limiting case of a very short phonon escape time, $\tau_{es} \ll \tau_{ep}, \tau_{pe}$, was first studied by Gershenson *et al.*⁶ for Nb films. Although for this material¹¹ $C_p/C_e \approx 0.25$ and, consequently, $\tau_{ep} > \tau_{pe}$, the effective escape of phonons to

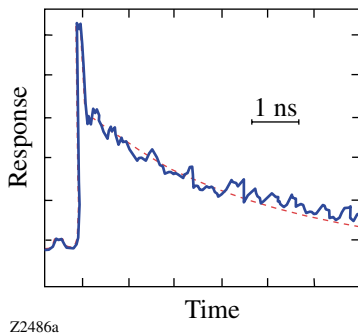


Figure 87.29 Response of a YBCO HEP to a femtosecond infrared pulse: experimental data (solid line) (Ref. 5) and simulations (dashed line) based on the 2-T model.

the substrate prevents energy backflow to electrons. As a result, τ_{ep} alone controls the response of ultrathin (<10 -nm) Nb films. Typical electron relaxation time in Nb is ≈ 1 ns at 4.2 K, which is over an order of magnitude larger than in NbN.

The 2-T model represented by Eqs. (1) is essentially the small-signal model. Deviations of the effective temperatures from equilibrium due to both the joule power dissipated by the bias current and absorbed radiation power are assumed small compared to their equilibrium values. The theory of operation of a hot-electron photodetector (HEP) was developed on the basis of this model by Gershenson *et al.*,¹² and a novel hot-electron mixer (HEM) was proposed.^{12,13}

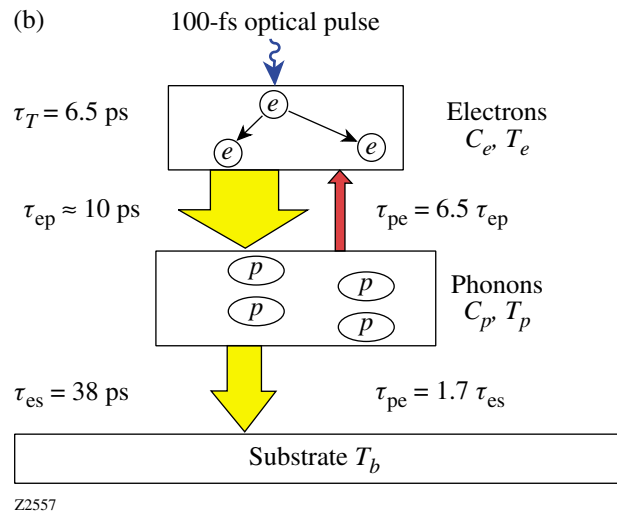
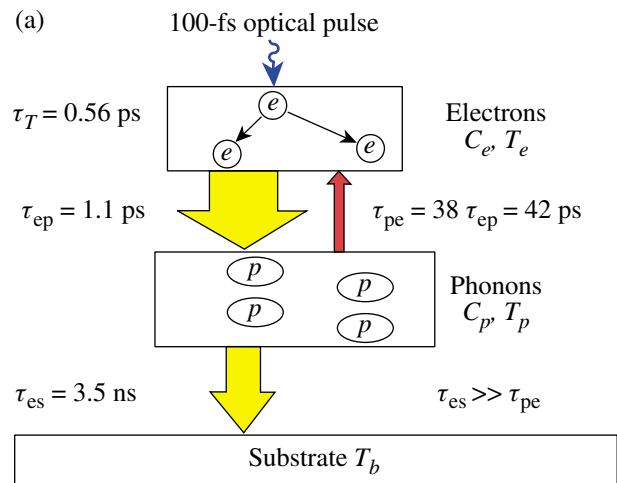


Figure 87.30 Hot-electron relaxation diagrams and characteristic times for (a) thin-film YBCO (Ref. 9) and (b) ultrathin NbN film (Ref. 8).

The 2-T approach neglects, however, diffusion of electrons and assumes that the effective temperatures remain uniform within the whole device. A different approach was proposed by Prober,¹⁴ who considered diffusion of hot electrons out of the active area, rather than the energy transfer to phonons, as the main mechanism of the electron cooling. If the device length L is short compared to the thermal diffusion length $L_{th} = (D\tau_e)^{1/2}$, where τ_e is the electron cooling time and D is the electron diffusivity, relaxation of T_e is controlled by the electron out-diffusion time $\tau_d = (L^2/\pi^2 D)$. In the limiting case $L \ll L_{th}$, T_e remains almost uniform through the device length. The device can then be described by Eq. (1a), in which τ_{ep} and T_p should be substituted for τ_d and T_0 , respectively. For longer devices, both the actual distribution of T_e along the device length and the phonon contribution to the electron relaxation should be taken into account.

2. Large-Signal Models

The common disadvantage of the small-signal model described above is that the optimal values of the bias current (for

HEP's) and power of the local oscillator (for the HEM theory) are not derived in the framework of the model, but rather taken from the experiment or independently estimated. To include the bias current and the local oscillator (LO) power in a consistent manner, one should specify the structure of the resistive state and account for the dependence of the electron-cooling rate on the deviation from the equilibrium. For large deviations from equilibrium, heat-balance equations become nonlinear.

The large-signal mixer theory was developed by Nebosis *et al.*¹⁵ for the uniform resistive state (which is, of course, a very crude approximation). The authors assumed a finite value of τ_{es} and introduced the superconducting critical current. Reasonable quantitative agreement (see Fig. 87.31) was found between the experimental data for NbN mixers and the theoretical results. Karasik *et al.*¹⁶ implemented a similar approach for modeling a bolometric mixer fabricated from a high-temperature superconducting material. Floet *et al.*¹⁷ considered the nonuniform resistive state of a hot-electron bolometer in the small-signal regime for $\tau_{es} = 0$, while Merkel *et al.*¹⁸ developed the large-signal nonlinear model for a finite, non-zero value of τ_{es} . Both models described the resistive state of the mixer at optimal operation conditions in terms of a normal hot spot, maintained by self-heating. The hot spot occupies only a portion of the device length, thus assuring a mixer resistance between zero and the normal-state value. In this approach, the LO power is assumed to be uniformly absorbed in the mixer, whereas the joule power dissipation due to the bias current appears in the hot-spot region only. Since the diffusion of electrons is introduced in the basic equations, this model naturally covers all intermediate cases between the extreme diffusion cooling ($L \ll L_{th}$) and phonon-cooling ($L \gg L_{th}$) regimes. Neglecting phonons ($\tau_{es} = 0$) and simulta-

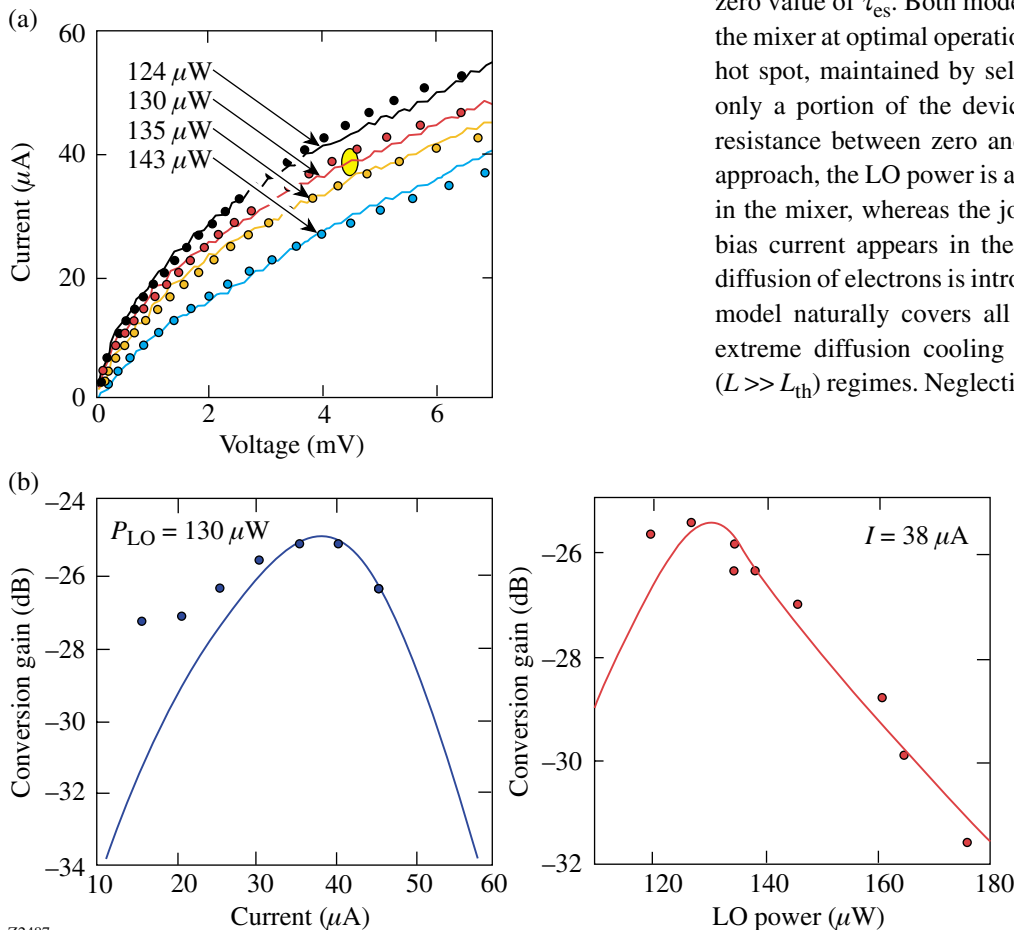


Figure 87.31
(a) Current–voltage characteristics for different LO power values. (b) Conversion gain curves for a NbN HEM compared with results of the uniform model (solid lines) (Ref. 15).

Z2487

neously assuming $\tau_T = 0$, one can reduce the problem to the following system of equations¹⁷ for T_e :

$$\begin{aligned} -K \frac{d^2 T_e}{dx^2} + \frac{C_e}{\tau_e} (T_e - T_0) &= j^2 \rho_n + P_{\text{RF}} \quad (\text{inside hot spot}), \\ -K \frac{d^2 T_e}{dx^2} + \frac{C_e}{\tau_e} (T_e - T_0) &= P_{\text{RF}} \quad (\text{outside hot spot}), \end{aligned} \quad (2)$$

where K is the thermal conductivity, j is the bias current density, ρ_n is the resistivity of the mixer in the normal state, and P_{RF} is the LO power absorbed per unit volume. This description allows for an analytical solution, which returns the bias current as a function of the hot-spot length, and, thus, a voltage drop across the device. Results of simulations¹⁷ are in good agreement with the experimental current–voltage (I – V) characteristics, especially for large P_{RF} values, which drive the mixer almost into the normal state. Surprisingly, results based on not only Eq. (2), but even on the more-accurate numerical model¹⁸ shown in Fig. 87.32, do not differ much from simulations based on the uniform 2-T model (Fig. 87.31). With the appropriate set of fitting parameters, both approaches describe fairly well the I – V characteristics of the HEM and predict reasonable values of the conversion efficiency and noise temperature.

A nonthermal regime of the diffusion-cooled HEM was described by Semenov and Gol'tsman.¹⁹ The authors considered a short device made from a clean material, in which τ_T is larger than τ_e . The device operated in the nonthermal regime

and had the advantage of a short response time (or, equivalently, a large bandwidth) in the heterodyne mode. On the other hand, incomplete thermalization hampered the responsivity and increased the relative contribution of the Johnson noise to the total electric noise of the device. Compared to HEM's operated in the thermal regime, the nonthermal mixer required more power from LO. At low temperatures, however, the nonthermal regime of operation provided almost quantum-limited sensitivity.

The electric noise of a hot-electron sensor is comprised of the same components as the noise of any conventional bolometer: shot noise, Johnson noise, thermal noise, and flicker noise. To our knowledge, there is no consistent theory for flicker noise, so its contribution may be determined only experimentally. Unless the sensitivity of the bolometer reaches the quantum limit, the noise due to fluctuations in the background radiation can be neglected. The typical length of hot-electron devices studied so far was much larger than the diffusion length associated with the electron–electron scattering. In this limiting case, the superposition of Johnson noise and shot noise reduces to the Nyquist form, i.e., the spectral density of the voltage noise is $S_V = 4 k_B T R$, where R is the resistance of the device. This noise has a “white” spectrum up to very high frequencies. The corresponding contribution to the system-noise temperature in the heterodyne regime increases rapidly when the conversion efficiency rolls off at intermediate frequencies (IF's) larger than $1/\tau_e$.

Thermal noise contributes to the total spectral density the amount $4 k_B T^2 I^2 \tau_e (\partial R / \partial T_e)^2 / (C_e v)$, where I is the bias current and v is the volume of the sensor. Since the conversion efficiency is proportional to $I^{-2} \tau_e^2 P_{\text{RF}} (\partial R / \partial T_e)^2 / (C_e v)^2$ and

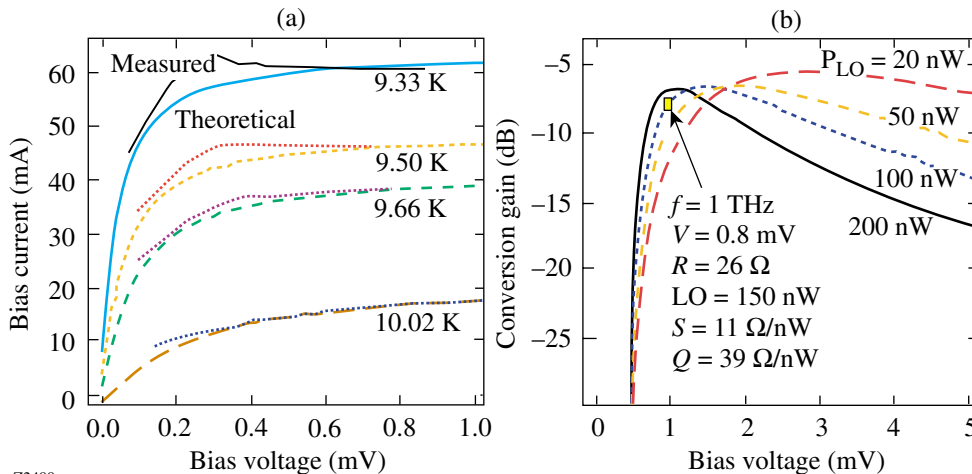


Figure 87.32

(a) Current–voltage characteristics and (b) conversion gain of a NbN HEM simulated in the framework of the hot-spot model (Ref. 18). Experimental characteristics are shown for comparison.

has the same roll-off frequency, the noise temperature of the mixer due to thermal fluctuations is given by $T_N \approx T_e^2 C_e v / (\alpha \tau_e P_{RF})$, where α is the optical coupling efficiency. The contribution to the noise temperature due to thermal fluctuations does not depend on the intermediate frequency; neither does the corresponding noise-equivalent power (NEP) in the direct-detection mode,

$$\text{NEP} \approx (T_e / \alpha) (k_B C_e v / \tau_e)^{1/2}.$$

On the contrary, the contribution due to the Nyquist term increases rapidly at IF's larger than $1/\tau_e$ and usually limits the IF noise bandwidth of the mixer.

Though the above simple treatment of the bolometer noise explains the main features, it does not provide an appropriate tool for computations. To obtain exact results, one should take into account the positive feedback via the load resistor and self-heating by the bias current. The former enhances the system output noise because the bolometer rectifies part of its own noise voltage drop across intrinsic resistance. The latter effect typically increases the IF bandwidth in the heterodyne regime and decreases the response time in the direct-detection mode. It is of little practical use, however, because operation in the vicinity of the thermal roll-off requires very precise stabilization of the ambient temperature. For a HEM with dc resistance R at the operation point and connected to the IF load with the impedance R_L , the dependence of the conversion efficiency $\eta(\omega)$ and single-sideband noise temperature $T_{SSB}(\omega)$ on the IF was derived in the framework of the uniform model¹⁵

$$\eta(\omega) = \frac{2\alpha}{I^2} \frac{R_L}{(R_L + R_\infty)^2} \frac{C^2 P_{RF}}{\left(C \frac{R - R_L}{R_L + R_\infty} + \xi \right)^2 + \varphi^2}, \quad (3)$$

$$T_{SSB}(\omega) = \frac{2T_e R_\infty I^2}{\alpha C^2 P_{RF}} (\xi^2 + \varphi^2) + \frac{2T_e^2 \tau_e}{C_e V \alpha P_{RF}}, \quad (4)$$

where

$$C = I^2 \tau_e \frac{\partial R / \partial T_e}{C_e V},$$

$$\xi(\omega) = \frac{1 + \omega^2 (\tau_1 \tau_3 + \tau_2 \tau_3 - \tau_1 \tau_2)}{1 + (\omega \tau_3)^2},$$

$$\varphi(\omega) = \frac{\omega (\tau_1 + \tau_2 - \tau_3) + \omega^3 \tau_1 \tau_2 \tau_3}{1 + (\omega \tau_3)^2},$$

$$\tau_{1,2}^{-1} = \frac{1}{2} \left(\frac{1}{\tau_{ep}} + \frac{C_e}{C_p \tau_{ep}} + \frac{1}{\tau_{es}} \right)$$

$$\times \left[1 \pm \sqrt{\frac{\frac{4}{\tau_{ep} \tau_{es}}}{\left(\frac{1}{\tau_{ep}} + \frac{C_e}{C_p \tau_{ep}} + \frac{1}{\tau_{es}} \right)^2}} \right],$$

and

$$\tau_3 = \frac{\tau_{ep} \tau_{es}}{\tau_e}.$$

In the above equations, R_∞ is the impedance of the bolometer at very high IF, and $\partial R / \partial T_e$ is the slope of the superconducting transition at the operation point on the scale of the electron temperature. The slope of the transition cannot be derived from first principles in the framework of the uniform model. Its temperature dependence should be calculated in a phenomenological manner (see, e.g., Ref. 15), or the value at the specific operation regime should be concluded from the experiment. Ekström *et al.*²⁰ showed that the magnitude of the parameter C in Eqs. (3) and (4) can be determined from the experimental dc I - V characteristic as

$$C = \frac{\frac{dV}{dI} - R}{\frac{dV}{dI} + R}, \quad (5)$$

where dV/dI is the differential resistance of the HEM at the operation point. The advantage of the hot-spot model¹⁸ is that it allows for numerical computation of the superconducting

transition slope for arbitrary values of the LO power, bias current, and ambient temperature.

3. Cooper-Pair, Kinetic–Inductive Photoresponse

Although the response of a superconductor that is kept well below T_c to external radiation cannot be adequately treated in the framework of the hot-electron approximation, we decided to include superconducting detectors operating at $T \ll T_c$ in our review. Rothwarf and Taylor²¹ were the first to successfully develop the phenomenological description for non-equilibrium Cooper-pair recombination and breaking processes (so-called the RT model). At low temperatures, when energies of nonequilibrium quasiparticles after thermalization are spread over a narrow interval above the superconducting energy gap 2Δ , the appropriate parameters to characterize this nonequilibrium state are the number Δn_q of excess quasiparticles and the number Δn_p of excess, so-called, 2Δ phonons. The 2Δ phonons are emitted in the Cooper-pair recombination process and, since they have the energy of at least 2Δ , they are responsible for secondary breaking of Cooper pairs. For small perturbations, concentrations of Δn_q and Δn_p are given by the following linearized RT rate equations:

$$\frac{d}{dt} \Delta n_q = -\frac{\Delta n_q}{\tau_R} + \frac{2\Delta n_p}{\tau_B}, \quad (6a)$$

$$\frac{d}{dt} \Delta n_p = -\frac{\Delta n_p}{\tau_B} - \frac{\Delta n_p}{\tau_{es}} + \frac{2\Delta n_q}{\tau_R}, \quad (6b)$$

where τ_R and τ_B are the quasiparticle recombination time and the time of breaking Cooper pairs by 2Δ phonons, respectively. We note that Eqs. (6) are mathematically analogous to the 2-T model [Eqs. (1)]. Like the 2-T model, the RT approach assumes that there is a quick, intrinsic thermalization mechanism inside both the quasiparticle and phonon subsystems.

When photons with energy typically much larger than 2Δ are absorbed by a superconducting film maintained at $T \ll T_c$, they produce a time-dependent population $\Delta n_q(t)$ of nonequilibrium quasiparticles, leading to a temporary decrease in the superconducting fraction of electrons, $f_{sc} = (n_0 - n_q)/n_0$, where $n_q = n_q(0) + \Delta n_q(t)$ is the instant concentration of the quasiparticles, $n_q(0)$ is their equilibrium concentration, and n_0 is the total concentration of electrons. Because the pairs are characterized by non-zero inertia, this process can be modeled as time-varying kinetic inductance:^{22,23}

$$L_{\text{kin}}(t) = \frac{L_{\text{kin}}(0)}{f_{sc}}, \quad (7)$$

where $L_{\text{kin}}(0) = \mu_0(\lambda_L)^2/d$ is the equilibrium value per unit area of the film, λ_L is the magnetic penetration depth, and d is the film thickness. The change in time of L_{kin} in a current-biased superconducting film leads to a measurable voltage signal across the film edges.

For the limiting case of very fast thermalization, i.e., when τ_T is small compared to both τ_R and τ_B , the kinetic-inductive response was described by Semenov *et al.*²⁴ as the product of the analytical solution of Eqs. (6) and a fitting factor exponentially growing in time. The latter parameter corresponded to the multiplication cascade of quasiparticles during thermalization. The kinetic-inductive model describes well the experimental results obtained with pulsed and modulated cw excitations, for both the low-temperature superconductor (LTS) films (Fig. 87.33 and Ref. 24) and the high-temperature superconductor (HTS) films (Fig. 87.34 and Refs. 9 and 25).

4. Single-Photon-Detection Mechanisms

So far this discussion has been limited to integrating detectors in which the energy of a large number of absorbed photons is distributed among an even larger number of elementary thermal excitations in the detector. That is, individual photons cannot be distinguished, and only the average radiation power absorbed by the detector is measured. In the particular case of a thermal detector, e.g., a bolometer or a hot-electron detector near T_c , this average absorbed radiation power corresponds to enhanced effective temperatures of phonons and electrons, respectively. In a quantum (photon) detector, a single photon creates excitations that are collected and counted before they relax and before another photon is absorbed. Thus, the detector registers each absorbed photon, while the number of collected excitations measures the energy of absorbed photons.

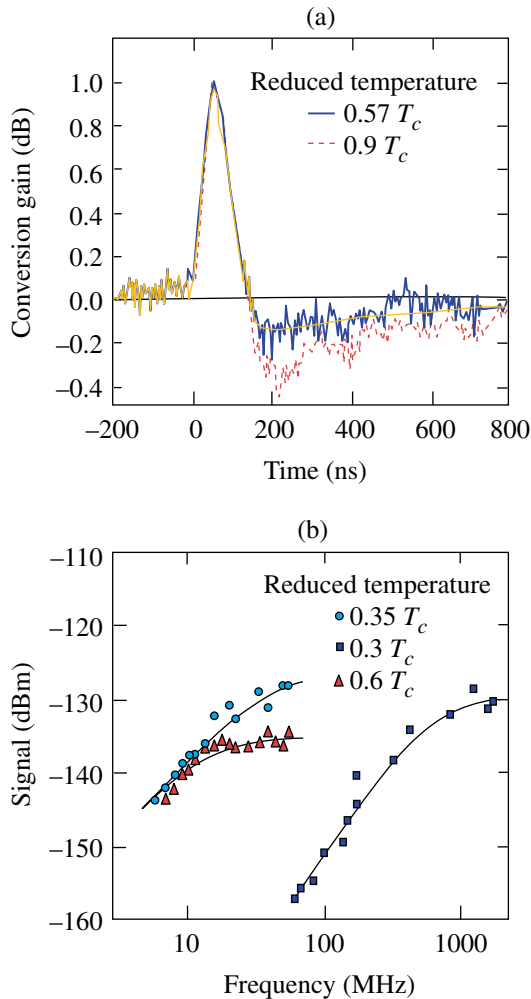
The hot-electron quantum detector was first proposed by Kadin and Johnson.²⁶ In this model, a photon absorbed somewhere in the film initiates a growing hot spot. The resistance inside the hot spot is larger than in the surrounding area. Even if the size of the hot spot is much smaller than the size of the film, the voltage drop across the current-biased film “feels” the presence of the hot spot. The disadvantage of this approach for practical devices stems from the fact that the film is operated near its T_c and can withstand only a very small current density without being driven into the normal state. Since the

detector response is proportional to the bias current, the small operating current requires a complicated, SQUID-based read-out scheme.²⁷

Semenov *et al.*²⁸ proposed a different quantum detection regime in a superconducting stripe that is operated well below T_c and carries a bias current only slightly smaller than the critical value at the operating temperature. Generation of a hot spot at the position where the photon has been absorbed creates a local region with suppressed superconductivity (normal region). The supercurrent is forced to flow around the normal

(resistive) spot, through those parts of the film that remain superconducting. If the diameter of the resistive spot is such that the current density in the superconducting portion of the film reaches the critical value, a resistive barrier is formed across the entire width of the stripe, giving rise to a voltage pulse with the magnitude proportional to the bias current.

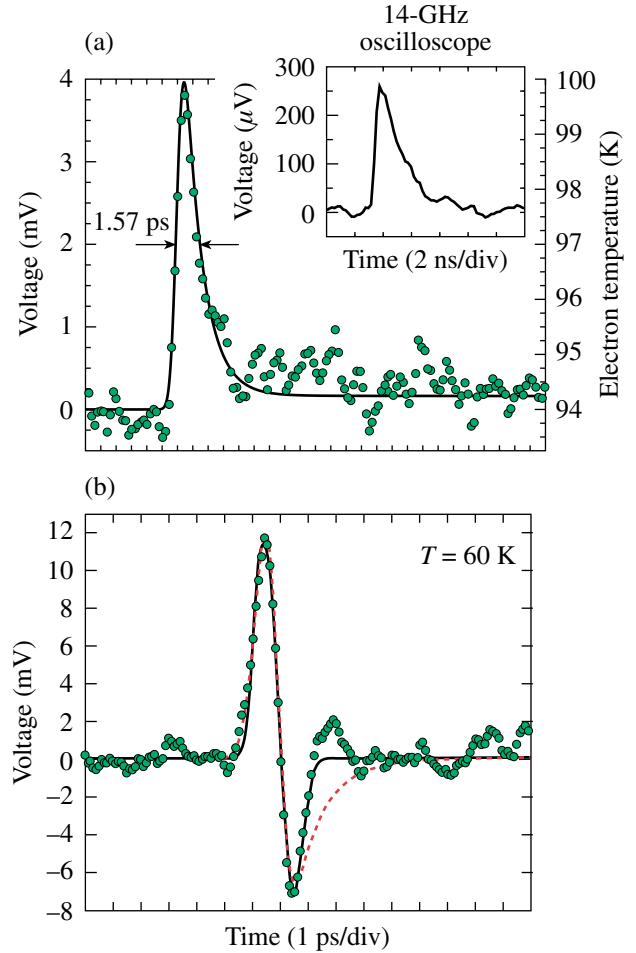
The physical difference of the quantum detection proposed in Ref. 28, as compared to Ref. 26, is that the resistive state and, thus, the response appear to be caused by the collaborative effect of the bias current and the hot-spot formation. In the hot



Z2494

Figure 87.33

(a) Conversion gain and (b) signal response of a NbN HEP to pulsed and modulated cw optical radiation in comparison with model simulations based on Eqs. (6) (Ref. 24).



Z2338

Figure 87.34

Experimental response (dots) of a YBCO HEP to 100-fs-wide optical pulses (Refs. 9 and 25). Simulated transients were obtained (a) with the uniform hot-electron model [Eqs. (1)] for the operation in the resistive state and (b) with the RT model [Eqs. (6)—solid line] and the 2-T model [Eqs. (1)—dashed line], for operation at low temperatures in the superconducting state. Inset in (a) shows a bolometric response.

spot, the nonequilibrium quasiparticle concentration increases due to hot-electron thermalization (multiplication) and decreases due to electron out-diffusion. The normal spot at the absorption site occurs when the concentration of nonequilibrium electrons exceeds the critical value corresponding to the local normal state. If the film thickness d is small compared to L_{th} , the concentration of nonequilibrium thermalized quasiparticles is given by

$$\frac{\partial}{\partial t} \Delta n_q = D \nabla^2 \Delta n_q + \frac{\Delta n_q}{\tau_e} + \frac{d}{dt} M(t), \quad (8)$$

where $M(t)$ is the multiplication factor and D is the normal-state electron diffusivity. The maximum value that $M(t)$ reaches during the avalanche multiplication process is called quantum yield or quantum gain; it is proportional to the energy of the absorbed quantum. Under assumptions that the $M(t)$ rate is much larger than the $1/\tau_e$ rate and that the photon is absorbed at $t = 0$ and $r = 0$, the solution for the time-dependent quasiparticle concentration profile takes the form

$$\Delta n_q(r, t) = \frac{M(t)}{4\pi D d} \frac{1}{t} e^{-t/\tau_e} e^{-r^2/4Dt}. \quad (9)$$

The diameter of the normal spot is determined from the condition $n_q(0) + \Delta n_q(r, t) > n_0$. The maximum diameter of the normal spot increases with the quantum energy. The model²⁸ predicts an almost-Gaussian response pulse with a magnitude that, up to a certain extent, does not depend on the photon energy. On the other hand, the pulse duration is a function of the maximum spot size, providing the basis for spectral sensitivity of the device. Finally, the single-quantum detection regime should have a cutoff wavelength that depends on operating conditions (bias current and temperature) and the detector size. Since such a detector counts individual photons, it should have ultimate background-limited sensitivity through the whole range of operation conditions.

Gol'tsman *et al.*²⁹ experimentally demonstrated the supercurrent-assisted, hot-spot-detection mechanism for single optical (790- μm -wavelength) photons. Figure 87.35 shows a collection of “snapshots” recorded by a 1-GHz-bandwidth oscilloscope for different energies per laser pulse, incident on the NbN quantum HEP. Each snapshot presents an 80-ns-long record of the response to six successive 100-fs-wide pulses and was randomly selected out of a real-time detector output data stream. Trace A in Fig. 87.35 corresponds to an average of 100

photons per pulse hitting the detector. In this case, the HEP responded to each optical pulse in the laser train. The same 100%-efficient response was observed (trace B) when there were approximately 50 photons per pulse. As the incident laser intensity was further decreased (with other experimental conditions unchanged), the quantum nature of the detector response emerged. Instead of the linear decrease of the signal amplitude with incident light intensity, which is characteristic of a classical integrating detector, the response amplitude of the single-photon HEP remained nominally the same. In addition, some of the response pulses were missing because of the limited quantum efficiency of the device as well as fluctuations in the number of photons incident on the detector. The quantum voltage response of the HEP is most apparent in the bottom two pairs of traces: C and D (five photons/pulse) and E and F (one photon/pulse). Each pair corresponds to two different randomly selected records obtained under exactly the same experimental conditions. Note that in each case the detector response is very different. Averaging over a long observation time, however, showed that both the average number of captured pulses and their magnitude remained constant if the pulse energy was unchanged. This unambiguously demonstrated the single-photon operation of the device.

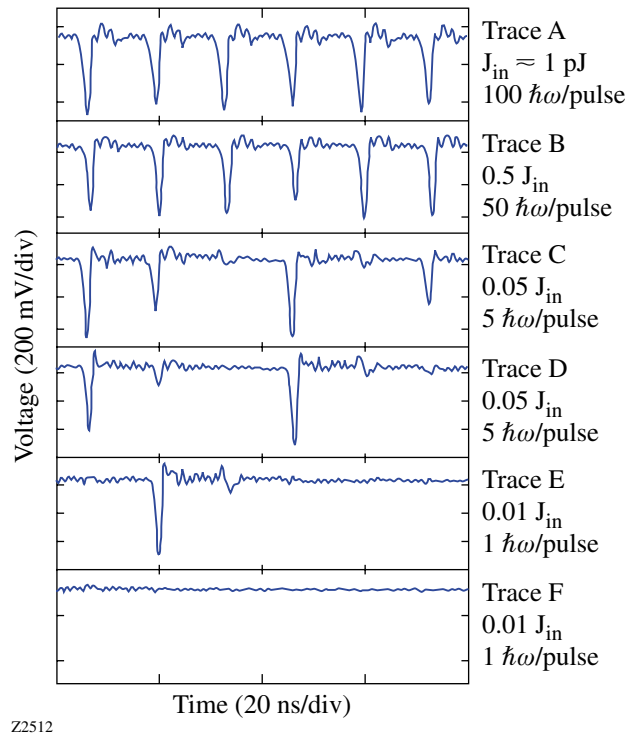


Figure 87.35

Response of a NbN quantum detector to trains of 100-fs optical pulses with a different number of photons per pulse (see text for details).

For a mean number of photons per pulse (m), the probability $P(n)$ of absorbing n photons from a given pulse is proportional to

$$P(n) \sim \frac{e^{-m} (m)^n}{n!}. \quad (10)$$

When the mean number of photons $m \ll 1$ (achieved, for example, by attenuating the radiation fluence to reduce the total number of photons incident on the detector to an average of much less than one photon per pulse),

$$P(n) \sim \frac{m^n}{n!}. \quad (11)$$

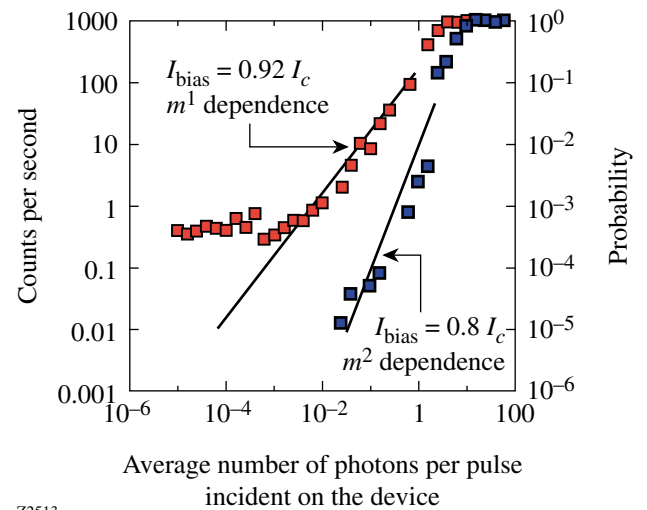
Consequently, for very weak photon fluxes, the probability of detecting one photon, two photons, three photons, etc., is

$$P(1) \sim m, \quad P(2) \sim \frac{m^2}{2}, \quad P(3) \sim \frac{m^3}{6}, \quad \text{etc.} \quad (12)$$

Figure 87.36 plots the probability of the detector producing an output voltage pulse as a function of the number of photons per pulse, incident on the device area for two different values of the bias current. The left vertical axis indicates the mean number of detector counts per second. The right vertical axis corresponds to the probability of detecting an optical pulse. Open squares correspond to the bias current $0.92 I_c$, where I_c is the critical current at the operation temperature. Saturation occurs at high incident photon fluxes. For smaller fluxes, as predicted by Eq. (11), the experimental data show the linear decrease of detection probability with the average number of incident photons over four orders of magnitude, clearly demonstrating the single-photon detection. At very low photon doses, experimental data points saturate at the level of 0.4-s^{-1} counts (probability 4×10^{-4}) since the experiment was performed in an optically unshielded environment. This level is regarded as the laboratory photon background. The solid squares in Fig. 87.36 correspond to the same device, operated under the same conditions as those for the solid-square data, but biased with $0.8 I_c$. Experimental data points now follow a quadratic dependence of detection probability [see Eq. (12)], showing the two-photon detection. As expected for a two-photon process, the quantum efficiency is significantly lower than for the single-photon detection. At the same time, photon background is no longer observed since the probability of two

uncorrelated, stray photons hitting the device within its response duration is negligibly small.

A nonequilibrium model of a single quantum x-ray detector with the readout via the superconducting tunneling junction was developed by Twerenbold.³⁰ Typically, a tunnel-junction detector consists of a relatively thick absorber film with an underlying thinner trapping layer, which forms one junction electrode. A photon captured in the absorber generates a high-energy photoelectron that relaxes via hot-electron multiplication into the energy gap of the absorber. Nonequilibrium quasiparticles excited during the cascade diffuse to the adjacent trapping layer, which has a smaller energy gap. There, quasiparticles scatter inelastically, reaching an energy level corresponding to the trapping-layer energy gap. The latter process is called “trapping” because it confines the charge to the region close to the tunnel barrier. The tunnel junction is externally biased in such a way that trapped quasiparticles can tunnel directly to the electrode characterized by the lower-energy gap. The same potential barrier prevents them from returning. They can, however, break Cooper pairs in the low-gap electrode and then form new pairs with unpaired electrons in their own electrode. Thus, the process returns unpaired electrons to the initial electrode, increasing the number of tunneling events per quasiparticle and providing intrinsic charge amplification. The time integral of the current transient



Z2513

Figure 87.36 Count rates and the corresponding counting probability for a NbN quantum detector as a function of the radiation intensity. Depending on bias current, the detector can count single-photon (red squares) or two-photon (blue squares) events (Ref. 29).

gives, with no free parameters, the charge that has been transferred through the tunnel junction. This latter value is proportional to the number of quasiparticles created in the cascade and, consequently, to the x-ray quantum energy.

The theoretical energy resolution of the tunnel junction detector is given by $2.4[h\nu\Delta(F+1+1/n)]^{1/2}$, where $h\nu$ is the quantum energy, n is the number of tunneling events per one quasiparticle, and F is the Fano factor that describes the statistical fluctuations of the charge-generation process. The Twerenbold model incorporates the two-dimensional diffusion equation for Δn_q and the general nonlinear form of the RT equations.

A more general approach, including time evolution of nonequilibrium distribution functions of quasiparticles and phonons, was developed by Nussbaumer *et al.*³¹ The authors solved the Chang-Scalapino equations numerically for the quasiparticle and phonon distribution functions in a spatially homogeneous situation and supplemented the solution by one-dimensional diffusion. The full theory includes the parameters that are important for the real detector, such as back tunneling and losses of quasiparticles at the edges of the device, resulting in good agreement between the calculated transient response signals and the experimentally measured pulse shapes.

Hot-Electron Detectors

A minor, but physically very important, difference exists between a superconducting HEP and a conventional superconducting bolometer when they are operated in the transition-edge regime. In the bolometer, thermal equilibrium between electrons and phonons is established instantly, whereas in the hot-electron detector these two systems are not in equilibrium. In this review, we restrict ourselves to publications where the nonequilibrium state between the electron and phonon subsystems was clearly observed. Basically, there are two ways to decouple electrons from phonons: nonequilibrium phonons should leave the detector at a time scale that is short compared to τ_{pe} , or the intensity of external radiation should vary faster than $1/\tau_{pe}$. Depending on the superconductor and experimental arrangement, a real hot-electron detector falls somewhere between these two extremes.

1. Transition-Edge Superconducting Detectors

Historically, the first HEP's were developed and studied in the early 1980s by Gershenson *et al.*,³² using ultrathin Nb films as the detector body. Niobium is characterized by relatively long τ_{pe} , typically a few hundred nanoseconds at liquid helium temperature, so that $\tau_{es} < \tau_{ep}$ for films thinner than

10 nm.¹¹ Therefore, detectors based on thin Nb films belong to the first limiting case in that their response time is approximately equal to τ_{ep} . The best performance that the Nb HEP's can achieve³³ is $NEP = 3 \times 10^{-13} \text{ W/Hz}^{1/2}$, detectivity $D^* = 4 \times 10^{11} \text{ cm s}^{1/2} \text{ J}^{-1}$, and a response time of 4.5 ns. Thus, these devices are less sensitive, although much faster, than semiconductor bolometers. When the detector area was adjusted properly, Nb HEP's demonstrated a constant value of sensitivity in the range from microwaves (150 GHz) to ultraviolet (10^{15} Hz). This is actually their greatest advantage when compared to semiconductor counterparts. A Nb-based HEP was implemented to study the emission of a cyclotron *p*-germanium laser.³⁴ The combination of large sensitivity and short response time made it possible to identify the Landau levels responsible for lasing.

In the late 1990s, the Gershenson group developed a HEP based on NbN superconducting films.³⁵ NbN has much shorter τ_{ep} and τ_{pe} than Nb; thus, even for 3-nm-thick films, NbN HEP's operate in the mixed regime (i.e., τ_{ep} and τ_{es} jointly determine the response time of the detector). Detectors made from ultrathin NbN films are much faster than Nb-based devices. The intrinsic $\tau_{ep} \approx 10$ ps, while the overall response time is about 30 ps near T_c .⁸ The best-demonstrated $NEP \approx 10^{-12} \text{ W/Hz}^{1/2}$ (Ref. 36). In spite of a rather-complicated electronic band structure,³⁷ the quantum yield in NbN reaches above 300 for near-infrared photons,³⁸ which corresponds to one-third of the upper theoretical limit. Detectors fabricated from NbN were used to study the emission of optically pumped

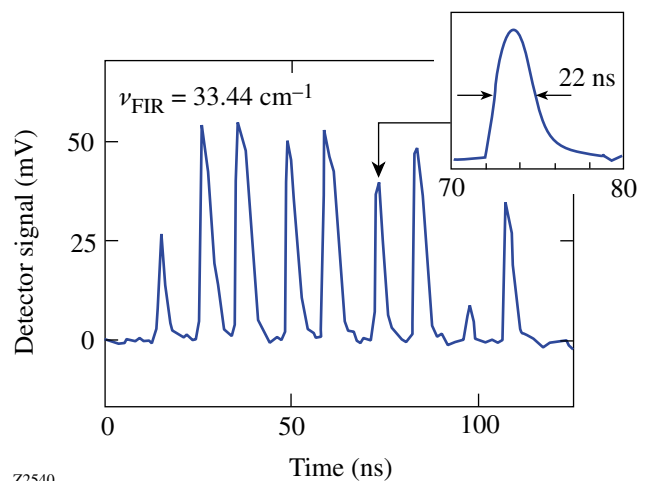
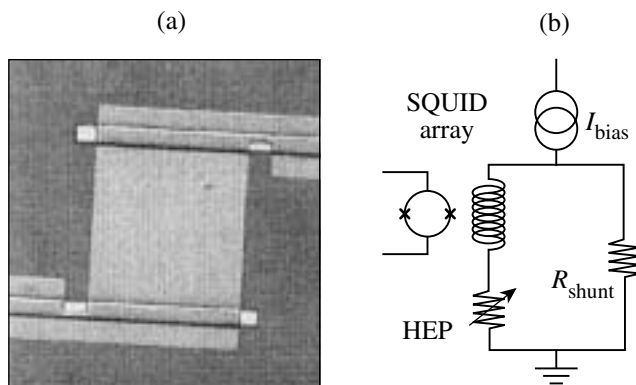


Figure 87.37

Pulses from a single-shot, optically pumped, far-infrared gas laser recorded with a NbN HEP (Ref. 39). The inset shows one of the pulses on an expanded time scale.

infrared gas lasers, in particular, pulsed lasers.³⁹ Figure 87.37 shows far-infrared laser pulses recorded with a NbN hot-electron detector. The unique combination of response time and sensitivity made it possible to detect and identify very weak emission lines.

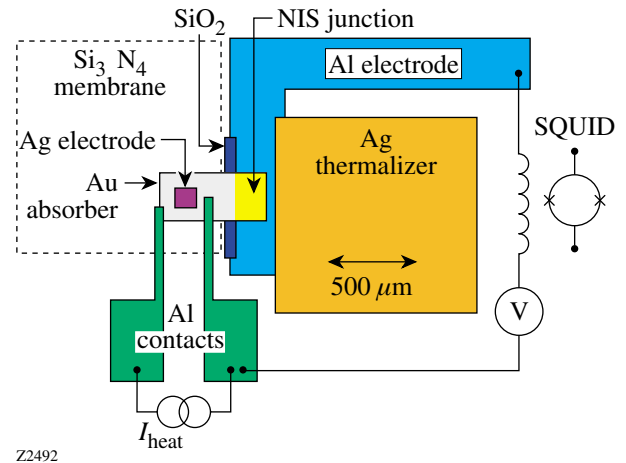
Miller *et al.*⁴⁰ have demonstrated a photon counter based on the transition-edge, hot-electron, direct detector. The device was a $20 \times 20\text{-}\mu\text{m}^2$ square of 40-nm-thick tungsten film (Fig. 87.38) having $T_c = 80\text{ mK}$ with a transition width of 1 mK. The device was operated at a bath temperature of 40 mK in a voltage-bias regime that maintained the sensor within the transition region via negative electrothermal feedback.⁴¹ This mode of operation was shown to increase the transition-edge sensor sensitivity and to decrease its time constant to $\tau_0/(1+\alpha/n)$. Here τ_0 is the intrinsic time constant of the sensor, n is the power of the temperature dependence of the thermal conductance between the film and substrate, and α is the dimensionless sharpness parameter of the superconducting transition.⁴¹ A photon absorbed in the sensor heats the electron system above its equilibrium temperature, leading to an increase of the sensor's resistance and, consequently, to the decrease of the bias current and dissipated joule power. The integral of the drop in current (read out by an array of dc SQUID's) gives the energy absorbed by the sensor with no free parameters. The detector described in Ref. 40 exhibited a time constant of about $60\ \mu\text{s}$ and was able to register 0.3-eV (4- μm -wavelength) single photons with an energy resolution of 0.15 eV. To test the detector, the authors observed the planetary nebula NGC 6572, using the 8-in. telescope. The energy resolution was somewhat lower than in the laboratory, although it was high enough to detect the strong emission lines.



Z2489

Figure 87.38
(a) Microphotograph of a transition-edge, hot-electron quantum detector and
(b) the corresponding equivalent circuit (Ref. 40).

A hot-electron microcalorimeter was developed by Nahum and Martinis.⁴² In this type of device, photon absorption gives rise to T_e in a metal absorber and is measured using the I - V characteristics of a normal-insulator-superconductor tunnel junction, in which part of the absorber forms the normal electrode. Figure 87.39 shows a schematic of the tested device. The current through the junction was measured with a low-noise dc SQUID. The absorber had an area of $100 \times 100\ \mu\text{m}^2$ and was deposited on a silicon nitride membrane. In this configuration, the phonons that escaped from the absorber were reflected back from the membrane and were further available for the energy exchange. Thus, the Si_3N_4 membrane prevented energy loss from the electron subsystem in the absorber. The microcalorimeter operated at 80 mK with a time constant of $15\ \mu\text{s}$ and demonstrated an energy resolution of 22 eV for 6-keV photons.



Z2492

Figure 87.39
Detailed schematic of the hot-electron microcalorimeter developed by Nahum and Martinis (Ref. 42) (see text for explanation).

In another version, Nahum and Martinis⁴³ proposed a microbolometer that consisted of a normal metal stripe connected to superconducting electrodes (Fig. 87.40). The device relied on Andreev reflections of low-energy, thermal quasiparticles at the edges of the stripe and on weak electron-phonon coupling at low temperatures. Both effects confined the energy delivered by the photons, providing a large rise of T_e . This was subsequently read out by the superconductor-insulator-normal metal junction, for which the metal strip formed the normal electrode. Projected responsivity and NEP of the device with the Cu absorber operated at 100 mK were about $10^9\ \text{V/W}$ and $3 \times 10^{-18}\ \text{W/Hz}^{1/2}$, respectively, which is at least a factor of 10 better than the performance of any currently available detectors. The time constant of the microcalorimeter is determined

by the rate of energy transfer from electrons to phonons that corresponds to τ_{ep} at the Fermi level. For the device under consideration in Ref. 43, the computed response time $\tau = 20 \mu\text{s}$. Since, for a bolometer, NEP scales as $\tau^{-1/2}$, the device performance can be further improved by increasing the response time up to a value only slightly less than that required by a specific application.

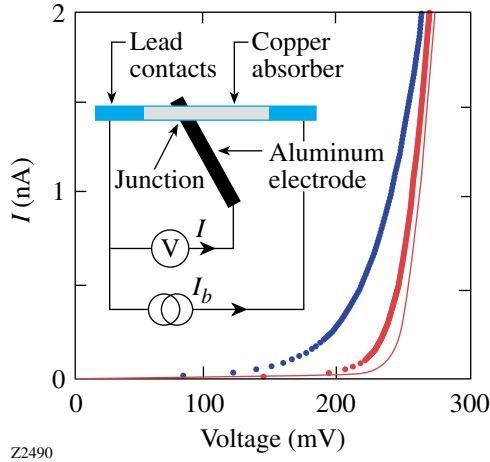


Figure 87.40

A hot-electron microbolometer using Andreev reflections of quasiparticles from superconducting contacts and the corresponding I - V characteristics (Ref. 43).

Finally, Karasik *et al.*⁴⁴ proposed the use of the dependence of the electron-phonon scattering time on the electron mean free path to control the intrinsic response time of a transition-edge detector. Increase of the intrinsic response time results in the decrease of the minimum detectable power, while at the same time, the device response time can be decreased to a reasonable value by exploiting the negative electrothermal feedback. According to estimates in Ref. 44, using this approach, a detector could be fabricated with $\text{NEP} = 10^{-20} \text{ W/Hz}^{1/2}$ and the millisecond τ at 100-mK bath temperature.

2. Superconducting Kinetic-Inductive Detectors

The detectors described in the preceding section produce a response when the device, or at least part of it, is in the resistive state. Kinetic-inductive integrating detectors represent their superconducting counterpart. The L_{kin} [see Eq. (7)] of a superconducting film makes it possible to monitor the concentration of Cooper pairs. In a constant current-biased superconducting film, after the destruction of a certain number of Cooper pairs, the remaining pairs accelerate to carry the same bias current. Because of non-zero inertia of pairs, or L_{kin} , acceleration requires an electric field. This intrinsically gener-

ated electric field is seen from the exterior as a voltage pulse developing across the film. Mathematically, this voltage transient is given by

$$V_{\text{kin}} = I \frac{dL_{\text{kin}}}{dt}. \quad (13)$$

Figure 87.34(b) presented earlier the V_{kin} transient, recorded for a YBCO microbridge excited by 100-fs optical pulses. The numerical fit was based on Eq. (13) and either Eqs. (1) or (6).

The main advantage of superconducting kinetic-inductive detectors is their low noise power. To realize this advantage, a SQUID readout should be used. Grossman *et al.*⁴⁵ described the design of a kinetic-inductive detector/mixer with an estimated $\text{NEP} = 2.5 \times 10^{-17} \text{ W/Hz}^{1/2}$ and a bandwidth of 5.5 MHz at 100 mK. Unfortunately, a laboratory prototype showed only $\text{NEP} = 4.4 \times 10^{-11} \text{ W/Hz}^{1/2}$ (Ref. 46). Sergeev and Reizer⁴⁷ performed thorough calculations for both s -wave and d -wave superconductors, including the appropriate quasi-particle distribution function and scattering times. They found NEP and D^* close to those reported in Ref. 45. Bluzer²³ proposed a balanced-bias scheme for a kinetic-inductive photodetector with directly coupled SQUID readout, intended to eliminate the losses inherent in inductively coupled readouts and increase the responsivity of the detector. Performance of the detector was simulated for a $0.1\text{-}\mu\text{m}$ -thick YBCO film at 9 K, resulting in $\text{NEP} = 2.5 \times 10^{-15} \text{ W/Hz}^{1/2}$ and $10\text{-}\mu\text{s}$ response time. It is believed that the use of a LTS material should result in a two- to three-orders-of-magnitude decrease in NEP.

3. Superconducting Quantum Detectors

A number of novel approaches proposed during the last decade have been aimed at the realization of detectors with ultimate quantum sensitivity. Kadin and Johnson²⁶ introduced the quantum detection regime in ultrathin resistive films. In the proposed mechanism, an absorbed photon induces a resistive hot spot, centered at the point where the photon hits the film. If the photon flux is sufficiently low, hot spots do not overlap until they disappear. Using material parameters of NbN, the authors estimated that a $0.1\text{-}\mu\text{m}^2$ size sample should respond to 1-eV photons with 1-mV-amplitude pulses and 10-GHz bandwidth. For technological reasons, practical detectors would require significantly larger areas and, consequently, much smaller responsivities, forcing the implementation of a sophisticated readout scheme such as an array of SQUID's.²⁷

A photon counter using the quantum detection regime in a current-carrying superconducting film²⁸ was recently demonstrated by Gol'tsman *et al.*²⁹ The counting element consisted of a 1.3- μm -long, 0.2- μm -wide microbridge, formed from a 6-nm-thick NbN film deposited on a sapphire substrate. The detector was operated at 4.2 K, with a bias current of approximately 90% of I_c . Voltage pulses generated by the bridge in response to absorbed photons were further amplified by a cooled, low-noise amplifier (see Fig. 87.35). The output pulses were time limited by electronics and had a duration of approximately 100 ps. The intrinsic dark count rate for the detector was measured to be below 0.001 s^{-1} (probability 10^{-6}), which corresponds to zero detected responses over 1000 s when the input was completely blocked. Table 87.I presents the basic parameters of the device operated at the 790-nm wavelength. Single-photon counting was observed in the photon-wavelength range from 0.4 μm to 2.4 μm .⁴⁸ We note that the device represents a unique combination of the picosecond response time and very high responsivity. These characteristics of NbN HEP's should lead to their practical implementation in areas ranging from free-space satellite communication,⁴⁹ through quantum communication and quantum cryptography,⁵⁰ to ultraweak luminescence observations and semiconductor integrated circuit testing.⁵¹ Another exciting application for this type of detector can be background-limited direct detector arrays⁵² for submillimeter astronomy.

Table 87.I: Experimental performance of a NbN photodetector at 790 nm.

Response time—intrinsic/measured	10 ps/100 ps
Quantum gain factor	340
A/W responsivity	220 A/W
V/W responsivity	$4 \times 10^4 \text{ V/W}$
Device quantum efficiency	~20%
Operating temperature	~4 K
Dark counts per second	<0.0001
Device noise temperature	~15 K

The most-advanced superconducting quantum detectors are tunnel-junction detectors, which are being developed for a wide range of applications from materials science and microanalysis to particle physics and astrophysics. Only a few recent publications are mentioned here because a full review of the activities in this field is beyond the scope of this article. Nb-based tunnel-junction detectors with Al trapping layers

have reached, for photon energies of about 70 eV, an energy resolution of 1.9 eV. This performance is limited by the statistics of quasiparticle multiplication.⁵³ A typical device had an area of $50 \times 50 \mu\text{m}^2$. The smallest-detectable, 0.3-eV (4.1- μm -wavelength) photon energy was achieved with Ta-based devices⁵⁴ since this material has an energy gap smaller than that of Nb. An energy resolution of 0.19 eV was demonstrated for 2.5-eV (0.5- μm -wavelength) photons, using Ta-based devices with an area of $20 \times 20 \mu\text{m}^2$ and 12- μs response time.

Hot-Electron Mixers

Historically, HEM's have been divided into two large categories: lattice- or phonon-cooled¹³ and diffusion-cooled¹⁴ devices. As presented earlier, the physics for these two types of HEM's is essentially the same. Both types can be described by Eqs. (2) using temperature-dependent parameters and proper boundary conditions. The analysis becomes easier, however, when the device is designed to be close to one of two extremes, namely, the lattice- or the diffusion-cooling regime. Typically, lattice-cooled mixers are made from thin films of NbN, whereas diffusion-cooled devices use Nb or Al.

1. Lattice-Cooled Mixers

Current state-of-the-art NbN technology is capable of routinely delivering 3.0-nm-thick devices that are $500 \times 500 \text{ nm}^2$ in size with T_c above 9 K. Near T_c , τ_{pe} is close to τ_{es} , which is about 40 ps for 3-nm-thick film [see Fig. 87.30(b)]. The τ_{ep} at 8 K is below 20 ps, which results, with the diffusivity of $0.5 \text{ cm}^2\text{s}^{-1}$, in a thermal healing length of about 30 nm. Since the device length is typically much larger, the mixer operates in the phonon-cooled regime. The mixer's intrinsic IF bandwidth is determined by the combination of τ_{ep} and τ_{es} time constants. In real devices, however, the measured bandwidth depends strongly on the bias regime. This makes it difficult to compare published data and reach meaningful conclusions. For HEM's on Si substrates, the best reported gain and noise bandwidths are 3.5 GHz⁵⁵ and 8 GHz,⁵⁶ respectively. Further increases in the bandwidth for lattice-cooled HEM's can be achieved by using a substrate material that is better thermally coupled to the superconducting film. One promising candidate is MgO. Recent measurements have shown⁵⁷ that MgO provides, for a 3.5-nm-thick bolometer, a 4.8-GHz gain bandwidth and 5.6-GHz noise bandwidth, respectively. Further progress in increasing the bandwidth may be achieved by decreasing the bolometer thickness. Recently a 9-GHz gain bandwidth was reported⁵⁸ for a 2.5-nm-thick device on MgO. Unfortunately, this direction is limited because NbN films thinner than 2.5 nm become inhomogeneous and lose their superconductivity.⁵⁹

A waveguide version of the receiver with the lattice-cooled NbN HEM has been installed and operated successfully in the frequency range of 0.6 to 0.8 THz⁶⁰ and 1.04 THz⁶¹ at the 10-m Sub-mm Telescope Facility on Mount Graham in Arizona. At this telescope, the measured noise temperature of the receiver was 560 K at 0.84 THz and 1600 K at 1.035 THz over a 1-GHz IF bandwidth centered at 1.8 GHz. The receiver was used to detect the CO molecular line emission in the Orion nebula (Fig. 87.41). It is worth noting that this was the first ground-based observation at a frequency above 1 THz. A quasi-optical version of the HEM receiver for the THz range is currently under preparation for test flights on a stratospheric airplane observatory.⁶² The mixer will be incorporated into a planar logarithmic spiral antenna (Fig. 87.42), which is integrated with an extended hyperhemispherical silicon lens.

Practical advantages of the lattice-cooled devices are their stability and the weak sensitivity of their noise temperature to operation parameters. Figure 87.43 shows that, indeed, the noise temperature of a NbN hot-electron mixer does not vary noticeably over a broad range of LO power and bias voltage.⁶³

2. Diffusion-Cooled Mixers

The bulk of diffusion-cooled mixers has been realized based on Nb films. At a 4.2-K bath temperature, the 10-nm-thick Nb film typically has τ_{ep} of about 1 ns and a diffusivity

of $2 \text{ cm}^2\text{s}^{-1}$,¹¹ which results in $L_{th} \approx 0.15 \mu\text{m}$. Therefore, Nb devices having a length of $0.1 \mu\text{m}$ or less operate in the diffusion-cooled regime. It has been shown experimentally⁶⁴ that the transition to diffusion cooling of electrons occurs at a

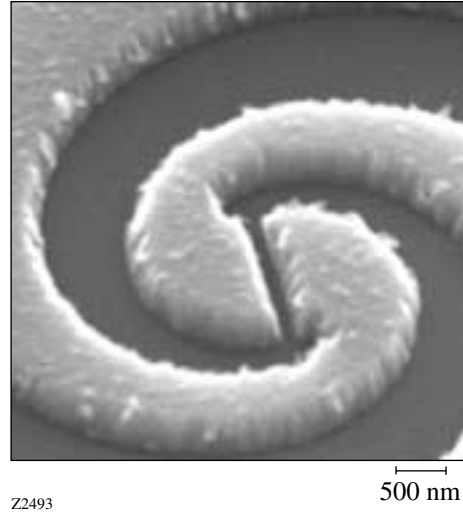


Figure 87.42

Central part of a planar logarithmic spiral antenna with the NbN hot-electron microbridge.

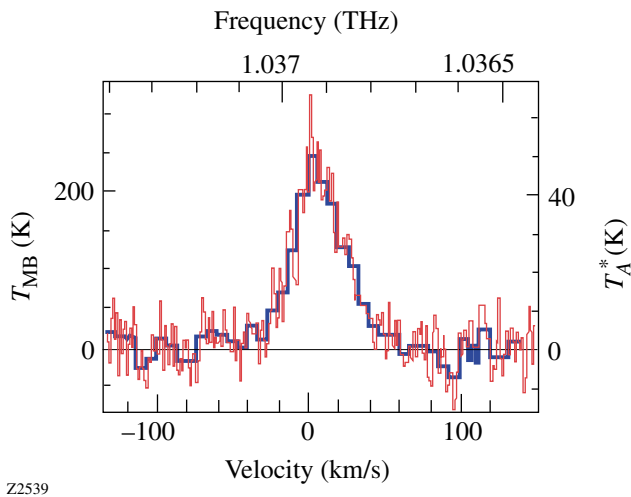


Figure 87.41

Terahertz CO line in the Orion IRc2 nebula recorded with a NbN hot-electron mixer at a ground-based telescope in Arizona (Ref. 61). The thick solid line shows a smoothed spectrum at a resolution of 25 MHz. The temperature scale of the spectrum is calibrated by taking into account the receiver noise temperature, the estimated atmospheric opacity, and the estimated efficiency of the telescope.

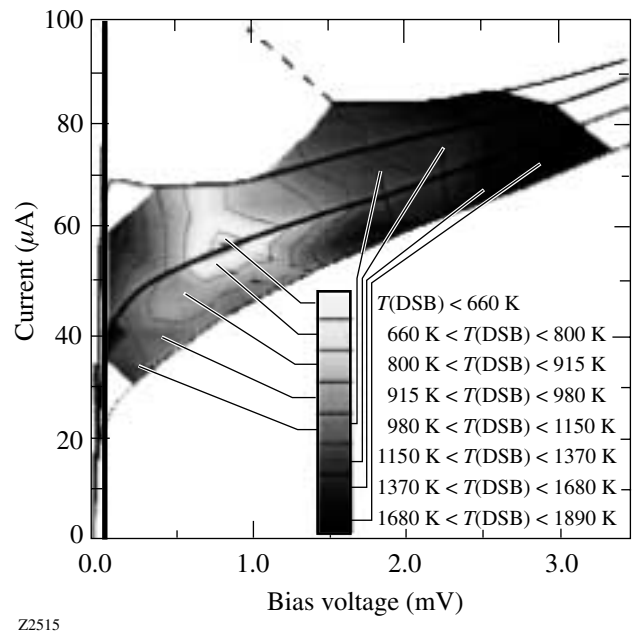


Figure 87.43

Double-sideband (DSB) noise temperature of a laboratory heterodyne receiver with NbN HEM at various bias regimes (Ref. 63).

device length $\approx 0.2 \mu\text{m}$. Expected gain bandwidth for a $0.1\text{-}\mu\text{m}$ -long device is about 7 GHz, if one assumes uniform electron heating through the length of the device. Laboratory tests at sub-THz frequencies confirmed theoretical expectations, and a 9-GHz gain bandwidth was measured for a $0.1\text{-}\mu\text{m}$ -long HEM.⁶⁵ No noise bandwidth data have been reported so far for diffusion-cooled mixers. Traditionally, quasi-optical, diffusion-cooled HEM's use a twin-slot or double-dipole planar antenna and a hemispherical lens to couple the LO and signal radiations to the mixer. The best reported noise temperatures for Nb diffusion-cooled mixers are presently almost twice as large as those of lattice-cooled devices.

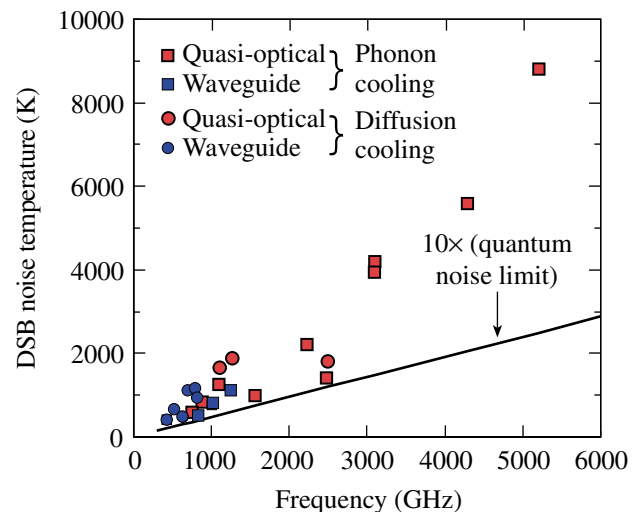
Another apparent difference between the two types of HEM's is the optimal bias regime, i.e., the regime resulting in the lowest noise temperature. For a lattice-cooled HEM, the optimal bias point is within the linear portion of the nonhysteretic I - V characteristics,⁶³ whereas optimal operation of diffusion-cooled devices corresponds to the nonlinear portion of a hysteretic I - V curve.⁶⁵ The difference stems from boundary conditions imposed on the normal domain. Movement of the domain walls caused by signal radiation is not influenced by the contacts⁶⁶ if they are located far enough from the domain borders. One can envision such a domain as a freestanding domain in a stable equilibrium state. In the opposite case, when domain walls are confined near the contacts, the temperature profile at the walls slopes more steeply and the wall movement is restricted by the contacts. This hampers the responsivity of the HEM. As a result, the length of a diffusion-cooled mixer is smaller than the thermal diffusion length L_{th} and corresponds to the length of the smallest freestanding domain. Therefore, in a diffusion-cooled HEM, the conversion loss and, consequently, the noise temperature are smaller when the domain is "overcooled" and is slightly shorter than the smallest freestanding domain. The actual domain length, as seen from the resistance in the normal state at the optimal operation point,⁶⁵ is about 0.6 of the mixer physical length, whereas for phonon-cooled HEM's,⁶³ the domain length is 0.2 of the device length. Since the total noise power at the HEM output is partly due to Nyquist noise, smaller responsivity should result in a somewhat larger noise temperature. Another disadvantage of the diffusion-cooled HEM is that its hysteretic regime may cause additional instability⁶⁷ when accessed by a practical receiver.

For both mixer types, it is common that optimal operation, aimed at the minimal noise temperature, does not provide the largest-possible IF bandwidth. Both the bandwidth and the noise temperature increase with the bias current. Thus, varying the bias regime allows a compromise between the desired

bandwidth and the noise temperature acceptable for a particular application.

A diffusion-cooled Al mixer has been recently proposed⁶⁸ as an alternative to Nb devices. Measurements at 30 GHz⁶⁹ showed that a diffusion-cooled Al mixer exhibits reasonably good performance, but these data are not conclusive for the desired THz operation since the quantum energy of 30-GHz photons remains smaller than the Al energy gap. Moreover, there are concerns¹⁹ that Al HEM's at THz frequencies would require a large LO power.

Table 87.II and Fig. 87.44 summarize the current state-of-the-art noise temperatures for both the lattice-cooled and diffusion-cooled HEM's. The rapid increase in noise temperature with frequency is inconsistent with the hot-electron model. The model suggests that the noise temperature, when corrected for optical losses, should not depend on frequency unless it approaches the quantum-limited value $h\nu/k_B$. A proper account of losses in coupling optics does not eliminate the above discrepancy; the noise temperature of the mixer alone increases with frequency, following closely the $10 h\nu/k_B$ law in the frequency range from 0.6 THz to 5.2 THz. It has been shown recently⁶⁴ that the nonuniform distribution of the high-frequency current across the device may account for this effect.



Z2339

Figure 87.44 Best double-sideband (DSB) noise temperatures for various types of superconducting hot-electron mixers as a function of signal frequency. The solid line is the hot-electron model prediction.

In Fig. 87.45, simulated frequency dependence of the conversion efficiency is compared with the noise temperature corrected for optical losses. Good agreement between the experimental and theoretical results up to 4 THz suggests that the increase in the noise temperature should be less pronounced for narrower HEM's.

Conclusions

Superconductor hot-electron radiation sensors, operated as either THz-frequency mixers or optical single-photon detectors, promise a revolutionary approach for diagnostics, radio astronomy, and quantum cryptography and communications. The unique performance of these devices in heterodyne as well as in the direct-detection regime results from a combination of the hot-electron phenomenon with the high sensitivity of a superconductor to nonequilibrium electronic states. To take full advantage of this combination, devices are routinely fabricated from ultrathin superconducting films and feature sub-micron lateral dimensions. They are also operated in the very-low-noise cryogenic environment.

HEM's proved their reliability and advantageous features during a two-year test on a ground-based telescope. In the frequency range from 1 THz to 5.2 THz, HEM's outperformed Schottky diodes, making them the device-of-choice for THz astronomy and communications.

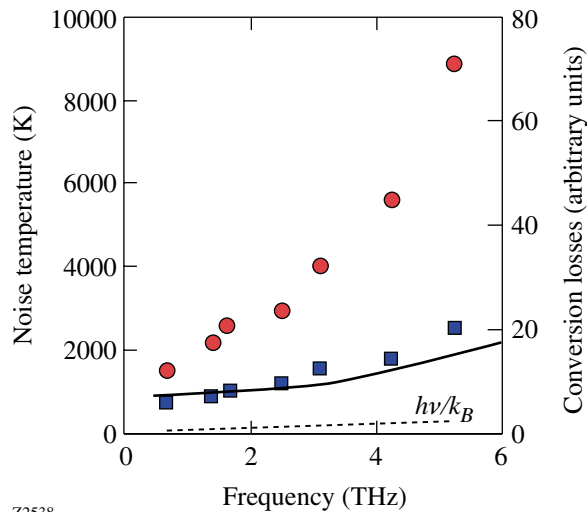
HEP's demonstrated excellent performance in the spectral range from far-infrared wavelengths to x rays when operated in either integrating or quantum regimes. Their future applications are expected in areas ranging from background-limited detector arrays for submillimeter astronomy and x-ray spectroscopy, through practical, high-speed quantum cryptography, to digital integrated-circuit diagnostics.

ACKNOWLEDGMENT

The authors thank S. Cherednichenko for helpful discussions and S. Svechnikov for systemizing published data. This research was made possible in part by Award No. RE-2227 of the U.S. Civilian Research and Development Foundation for the Independent States of the Former Soviet Union. G. N. Gol'tsman acknowledges support of the INTAS (#97-1453, #99-569). R. Sobolewski acknowledges support of the U.S. Office of Naval Research grant N00014-00-1-0237.

Table 87.II: Best double-sideband (DSB) noise temperatures reported in the literature for lattice-cooled and diffusion-cooled mixers.

Lattice-cooled mixers					
Quasi-optical layout			Waveguide layout		
Frequency (GHz)	DSB noise temperature (K)	Reference	Frequency (GHz)	DSB noise temperature (K)	Reference
620	500	70	430	410	73
750	600	65	636	483	73
910	850	65	840	490	61
1100	1250	65	1017	750	61
1560	1000	71	1030	800	61
1620	700	58	1260	1100	61
2240	2200	71			
2500	1100	58			
3100	4000	72			
4300	5600	72			
5200	8800	72			
Diffusion-cooled mixers					
Quasi-optical layout			Waveguide layout		
Frequency (GHz)	DSB noise temperature (K)	Reference	Frequency (GHz)	DSB noise temperature (K)	Reference
630	470	64	530	650	76
1100	1670	74	700	1100	17
1267	1880	75			
2500	1800	64			



Z2538

Figure 87.45

Frequency dependence of the noise temperature (circles) and conversion losses (squares) of a NbN HEM (Ref. 68). The solid line shows the calculated conversion losses that account for the skin effect in the device. The dashed line represents quantum-limited noise temperature $h\nu/k_B$. The scale of the right axis was adjusted to match calculated conversion losses and corrected noise temperature.

REFERENCES

1. E. M. Conwell, *High Field Transport in Semiconductors*, Solid State Physics Supplement 9 (Academic Press, New York, 1967).
2. M. L. Kaganov, I. M. Lifshitz, and L. V. Tanatarov, *Sov. Phys.-JETP* **4**, 173 (1957).
3. V. A. Schklovski, [*Sov. Phys.*] *FTT* **17**, 3076 (1975).
4. N. Perrin and C. Vanneste, *Phys. Rev B* **28**, 5150 (1983).
5. A. D. Semenov *et al.*, *Phys. Rev. B* **52**, 581 (1995).
6. E. M. Gershenzon *et al.*, *Sov. Phys.-JETP* **59**, 442 (1984).
7. M. Lindgren *et al.*, *Appl. Phys. Lett.* **65**, 3398 (1994).
8. K. S. Il'in, M. Lindgren, M. Currie, A. D. Semenov, G. N. Gol'tsman, R. Sobolewski, S. I. Cherednichenko, and E. M. Gershenzon, *Appl. Phys. Lett.* **76**, 2752 (2000).
9. M. Lindgren, M. Currie, C. Williams, T. Y. Hsiang, P. M. Fauchet, R. Sobolewski, S. H. Moffat, R. A. Hughes, J. S. Preston, and F. A. Hegmann, *Appl. Phys. Lett.* **74**, 853 (1999).
10. R. Sobolewski, in *Superconducting and Related Oxides: Physics and Nanoengineering III*, edited by D. Pavuna and I. Bozovic (SPIE, Bellingham, WA, 1998), Vol. 3481, pp. 480–491.
11. E. M. Gershenzon *et al.*, *Sov. Phys.-JETP* **70**, 505 (1990).
12. E. M. Gershenzon *et al.*, *Sov. Phys.-Tech. Phys.* **34**, 195 (1989).
13. E. M. Gershenzon *et al.*, *Supercond., Phys. Chem. Technol.* **3**, 1582 (1990); B. S. Karasik and A. I. Elantiev, *Appl. Phys. Lett.* **68**, 853 (1996).
14. D. E. Prober, *Appl. Phys. Lett.* **62**, 2119 (1993).
15. R. S. Nebosis *et al.*, in *Proceedings of the Seventh International Symposium on Space Terahertz Technology* (University of Virginia, Charlottesville, VA, 1996), pp. 601–613.
16. B. S. Karasik, W. R. McGrath, and M. C. Gaidis, *J. Appl. Phys.* **81**, 1581 (1997).
17. W. D. Floet *et al.*, in *Proceedings of the Tenth International Symposium on Space Terahertz Technology* (University of Virginia, Charlottesville, VA, 1999), pp. 228–236.
18. H. Merkel *et al.*, *IEEE Trans. Appl. Supercond.* **9**, 4201 (1999).
19. A. D. Semenov and G. N. Gol'tsman, *J. Appl. Phys.* **87**, 502 (2000).
20. H. Ekström *et al.*, *IEEE Trans. Microw. Theory Tech.* **43**, 938 (1995).
21. A. Rothwarf and B. N. Taylor, *Phys. Rev. Lett.* **19**, 27 (1967).
22. E. N. Grossman, D. G. McDonald, and J. E. Sauvageau, *IEEE Trans. Magn.* **27**, 2677 (1991).
23. N. Bluzer, *J. Appl. Phys.* **78**, 7340 (1995).
24. A. D. Semenov *et al.*, *IEEE Trans. Appl. Supercond.* **7**, 3083 (1997).
25. M. Lindgren, M. Currie, C. A. Williams, T. Y. Hsiang, P. M. Fauchet, R. Sobolewski, S. H. Moffat, R. A. Hughes, J. S. Preston, and F. A. Hegmann, *IEEE J. Sel. Top. Quantum Electron.* **2**, 668 (1996).
26. A. M. Kadin and M. W. Johnson, *Appl. Phys. Lett.* **69**, 3938 (1996).
27. D. Gupta and A. M. Kadin, *IEEE Trans. Appl. Supercond.* **9**, 4487 (1999).
28. A. D. Semenov, G. N. Gol'tsman, and A. A. Korneev, *Physica C* **351**, 349 (2001).
29. G. N. Gol'tsman, O. Okunev, G. Chulkova, A. Lipatov, A. Semenov, K. Smirnov, B. Voronov, A. Dzardanov, C. Williams, and R. Sobolewski, *Appl. Phys. Lett.* **79**, 705 (2001).
30. D. Twerenbold, *Phys. Rev. B* **34**, 7748 (1986).
31. Th. Nussbaumer *et al.*, *Phys. Rev. B* **61**, 9719 (2000).
32. E. M. Gershenzon *et al.*, *JETP Lett.* **34**, 268 (1981).
33. E. M. Gershenzon *et al.*, *Sov. Tech. Phys. Lett.* **15**, 118 (1989).
34. A. V. Bespalov *et al.*, *Solid State Commun.* **80**, 503 (1991).
35. B. M. Voronov *et al.*, *Supercond., Phys. Chem. Technol.* **5**, 960 (1992).
36. Yu. P. Gousev *et al.*, *J. Appl. Phys.* **75**, 3695 (1994).

37. S. V. Vonsovskii, I. U. A. Iziumov, and E. Z. Kurmaev, *Superconductivity of Transition Metals: Their Alloys and Compounds*, Springer Series in Solid-State Sciences (Springer-Verlag, Berlin, 1982).
38. K. S. Il'in, I. I. Milostnaya, A. A. Verevkin, G. N. Gol'tsman, E. M. Gershenson, and R. Sobolewski, *Appl. Phys. Lett.* **73**, 3938 (1998).
39. P. T. Lang *et al.*, *Appl. Phys. B* **B53**, 207 (1991); P. T. Lang *et al.*, *Opt. Lett.* **17**, 502 (1992).
40. A. J. Miller *et al.*, *IEEE Trans. Appl. Supercond.* **9**, 4205 (1999).
41. K. D. Irwin, *Appl. Phys. Lett.* **66**, 1998 (1995).
42. M. Nahum and J. M. Martinis, *Appl. Phys. Lett.* **66**, 3203 (1995); K. D. Irwin *et al.*, *Nucl. Instrum. Methods Phys. Res. A* **444**, 184 (2000).
43. M. Nahum and J. M. Martinis, *Appl. Phys. Lett.* **63**, 3075 (1993).
44. B. S. Karasik *et al.*, *Supercond. Sci. Technol.* **12**, 745 (1999).
45. E. N. Grossman, D. G. McDonald, and J. E. Sauvageau, *IEEE Trans. Magn.* **27**, 2677 (1991).
46. J. E. Sauvageau, D. G. McDonald, and E. N. Grossman, *IEEE Trans. Magn.* **27**, 2757 (1991).
47. A. V. Sergeev and M. Yu. Reizer, *Int. J. Mod. Phys. B* **10**, 635 (1996).
48. G. N. Gol'tsman, O. Okunev, G. Chulkova, A. Lipatov, A. Dzardanov, K. Smirnov, A. Semenov, B. Voronov, C. Williams, and R. Sobolewski, *IEEE Trans. Appl. Supercond.* **11**, 574 (2001).
49. G. G. Ortiz, J. V. Sandusky, and A. Biswas, in *Free-Space Laser Communication Technologies XII*, edited by G. S. Mercherle (SPIE, Bellingham, WA, 2000), Vol. 3932, pp. 127–138.
50. G. Gilbert and M. Hamrick, "Practical Quantum Cryptography: A Comprehensive Analysis (Part One)," to appear in *Phys. Rep.*; see also <http://xxx.lanl.gov/abs/quant-ph/0009027>.
51. J. C. Tsang and J. A. Kash, *Appl. Phys. Lett.* **70**, 889 (1997).
52. G. Gol'tsman *et al.*, "Background Limited Quantum Superconducting Detector for Submillimeter Wavelengths," to be published in the *Proceedings of the Twelfth International Symposium on Space Terahertz Technology*.
53. S. Friedrich *et al.*, *IEEE Trans. Appl. Supercond.* **9**, 3330 (1999).
54. P. Verhoeve *et al.*, *IEEE Trans. Appl. Supercond.* **7**, 3359 (1997).
55. S. Cherednichenko *et al.*, in *Proceedings of the Eighth International Symposium on Space Terahertz Technology* (Harvard University, Cambridge, MA, 1997), pp. 245–252.
56. H. Ekström *et al.*, *Appl. Phys. Lett.* **70**, 3296 (1997).
57. S. Cherednichenko *et al.*, in *Proceedings of the Eleventh International Symposium on Space Terahertz Technology* (Ann Arbor, MI, 2000), pp. 219–227.
58. M. Kroug *et al.*, *IEEE Trans. Appl. Supercond.* **11**, 962–965 (2001).
59. B. M. Voronov, Moscow State Pedagogical University, private communication (2000).
60. J. H. Kawamura *et al.*, *IEEE Trans. Appl. Supercond.* **9**, 3753 (1999); J. H. Kawamura *et al.*, *Publ. Astron. Soc. Pac.* **111**, 1088 (1999).
61. C.-Y. E. Tong *et al.*, in *Proceedings of the Eleventh International Symposium on Space Terahertz Technology*, (Ann Arbor, MI, 2000), pp. 49–59.
62. H.-W. Huebers *et al.*, in *Airborne Telescope Systems*, edited by R. K. Melugin and H.-P. Roeser (SPIE, Bellingham, WA, 2000), Vol. 4014, pp. 195–202.
63. P. Yagoubov *et al.*, *Appl. Phys. Lett.* **73**, 2814 (1998).
64. P. J. Burke *et al.*, *Appl. Phys. Lett.* **68**, 3344 (1996).
65. R. A. Wyss *et al.*, in *Proceedings of the Tenth International Symposium on Space Terahertz Technology* (University of Virginia, Charlottesville, VA, 1999), pp. 215–228.
66. A. D. Semenov and H.-W. Hubers, *IEEE Trans. Appl. Supercond.* **11**, 196 (2001).
67. A. D. Semenov *et al.*, *J. Appl. Phys.* **88**, 6758 (2000).
68. B. S. Karasik and W. R. McGrath, in *Proceedings of the Ninth International Symposium on Space Terahertz Technology* (1998), p. 73.
69. I. Siddiqi *et al.*, in *Proceedings of the Eleventh International Symposium on Space Terahertz Technology*, (Ann Arbor, MI, 2000), pp. 82–94.
70. P. Yagoubov *et al.*, *Supercond. Sci. Technol.* **12**, 989 (1999).
71. E. Gerecht *et al.*, in *Proceedings of the Tenth International Symposium on Space Terahertz Technology* (University of Virginia, Charlottesville, VA, 1999), pp. 200–207.
72. J. Schubert *et al.*, *Supercond. Sci. Technol.* **12**, 748 (1999).
73. J. Kawamura *et al.*, in *Proceedings of the Eighth International Symposium on Space Terahertz Technology* (Harvard University, Cambridge, MA, 1997), pp. 23–26.
74. A. Skalare *et al.*, in *Proceedings of the Ninth International Symposium on Space Terahertz Technology* (1998), pp. 115–120.
75. A. Skalare *et al.*, *IEEE Trans. Appl. Supercond.* **7**, 3568 (1997).
76. A. Skalare *et al.*, *Appl. Phys. Lett.* **68**, 1558 (1996).

Scaling Law for Marginal Ignition

Introduction

In recent years, a considerable effort¹⁻⁶ has been made to determine the minimum energy required for ignition in inertial confinement fusion (ICF) implosions. Though different conclusions have been reached by different authors, consensus is that the minimum energy required for ignition is a strong function of the shell implosion velocity as well as the shell adiabat. Various approaches to the study of ignition have led to scaling laws in which the shell kinetic energy required for ignition is given as a function of the implosion velocity, shell adiabat (in-flight and at stagnation), and other parameters such as the applied pressure at the end of the acceleration phase. Scientists from Lawrence Livermore National Laboratory (LLNL) have produced a scaling law^{1,5} for marginal ignition by fitting a large database of *LASNEX* simulations of implosions with gain approximately equal to unity. The first scaling law by Levedahl and Lindl (LL)¹ was obtained by fitting the shell kinetic energy with the in-flight shell adiabat and the shell implosion velocity. The LL scaling law yields

$$E_k \sim \frac{\beta_{if}^{1.7}}{V_{imp}^{5.5}}, \quad (1)$$

where E_k is the shell kinetic energy at the end of the acceleration phase, β_{if} is the in-flight shell adiabat, and V_{imp} is the shell implosion velocity. In the derivation of Eq. (1), the different hydrodynamic quantities have been rescaled by keeping the initial pressure constant. A similar result was also obtained by Piriz.² Later, Basko and Johner (BJ) derived a similar scaling law⁴ from a set of numerical simulations based on a self-similar rescaling of the hydrodynamic quantities. Their conclusion is that the minimum energy required for ignition scales as

$$E_k \sim \frac{\beta_{if}^3}{V_{imp}^{9.1}}. \quad (2)$$

At first glance, the BJ scaling appears quite different from the LL scaling; however, it must be emphasized that the hydrodynamic similarity used by Basko and Johner requires that the pressure scales as $P \sim V_{imp}^5 \beta_{if}^{-1.5}$ in contrast with the $P \sim \text{constant}$ assumption used in the derivation of the LL scaling. Relations (1) and (2) seem at odds with the standard static assembled scaling based on the isobaric model of Meyer-ter-Vehn,⁷

$$E_k \sim \frac{J_s^3 \beta_s^3}{V_{imp}^{10}}, \quad (3)$$

where β_s is the stagnation adiabat and $J_s \equiv \rho_s R_s T_s$ with ρ_s , R_s , and T_s representing the hot-spot density, radius, and temperature at stagnation.

It is important to emphasize that the shell adiabat used in Eq. (3) is calculated at stagnation and its value differs from the in-flight adiabat used in Eqs. (1) and (2). This point was not made by Basko and Johner, who did not distinguish between the in-flight and stagnation adiabats. It follows that a comparison between Eq. (3) and Eqs. (1) and (2) cannot be made unless a relation between the in-flight and stagnation adiabats is derived. Thus Eq. (3) and Eqs. (1) and (2) represent two different scalings that we denote as the ‘‘stagnation’’ scaling and ‘‘in-flight’’ scaling, respectively.

Another important point concerning the ignition condition is the following: If ignition is triggered at a fixed value of J_s (as commonly assumed), Eq. (3) yields a stagnation scaling

$$E_k \sim \frac{\beta_s^3}{V_{imp}^{10}}. \quad (4)$$

This result disagrees with the stagnation scaling recently found by Herrmann, Tabak, and Lindl (HTL)⁵ based on a numerical fit of *LASNEX* runs leading to

$$E_k \sim \frac{\beta_s^{2.66}}{V_{\text{imp}}^{7.2}}. \quad (5)$$

Basko and Johner⁴ pointed out that the condition $J_s = \text{constant}$ does not correctly represent the ignition conditions because it neglects the tamping effect of the shell. This is important because the shell's inertia determines the hot-spot disassembly time. Basko and Johner estimated analytically that, at ignition, J_s depends linearly on the implosion velocity $J_s \sim V_{\text{imp}}$, thus leading to the modified ignition scaling [from Eq. (3)]

$$E_k \sim \frac{\beta_s^3}{V_{\text{imp}}^7}. \quad (6)$$

Basko and Johner revised this scaling⁴ through a set of numerical simulations starting from the assembled state and derived what they define as the “dynamic assembled state scaling”

(7)

With the exception of minor differences in the exponents, all the stagnation scalings [Eqs. (5)–(7)] seem to agree and corroborate the argument that J_s is proportional to the implosion velocity or to some power (<1) of it.

Herrmann *et al.*⁵ revised the in-flight scaling of Levedahl and Lindl through a series of *LASNEX* simulations, allowing for changes in the shell pressure at the end of the acceleration phase, and concluded that the energy scaling in terms of the in-flight variables can be approximated by the following fit:

$$E_k \sim \frac{\beta_{\text{if}}^{1.8}}{V_{\text{imp}}^{5.8} P_a^{0.77}}, \quad (8)$$

where P_a is the applied pressure at the end of the acceleration phase (i.e., at the peak of the shell kinetic energy). It is important to notice that the in-flight HTL scaling [Eq. (8)] reproduces the in-flight BJ scaling [Eq. (2)] when the self-similar hydrodynamic scaling for the pressure $P \sim V_{\text{imp}}^5 / \beta_{\text{if}}^{3/2}$ is substituted into Eq. (8). Recently, Kemp, Meyer-ter-Vehn, and Atzeni (KMA)⁶ analytically reproduced a scaling law that resembles the in-flight HTL scaling [Eq. (8)]:

$$E_k \sim J_s^3 \frac{\beta_{\text{if}}^{1.8}}{V_0^6 P_0^{0.8}}. \quad (9)$$

Equation (9) was derived from a self-similar solution of an imploding shell where P_0 and V_0 are the peak pressure and velocity at the time of void closure. Even though it is unclear how to relate P_0 in Eq. (9) to P_a in the HTL scaling [Eq. (8)], the two scaling laws are strikingly similar if J_s is constant at the onset of ignition. However, if J_s scales linearly with the implosion velocity as suggested by Basko,³ the KMA scaling will produce a weak dependence on the implosion velocity and significantly deviate from the HTL scaling. Another important conclusion of the KMA self-similar solution is that the stagnation adiabat is related to its in-flight value through the shell Mach number:

$$\beta_s \sim \beta_{\text{if}} \sqrt{M_A} \sim \beta_{\text{if}}^{0.85} V_{\text{imp}}^{0.5} P_0^{-0.1}, \quad (10)$$

where M_A is the shell Mach number. A similar scaling between the adiabats was also derived in Ref. 5 through a fit of the *LASNEX* simulation database, yielding

$$\beta_s \sim \beta_{\text{if}}^{0.75} V_{\text{imp}}^{0.44} P_a^{-0.21}. \quad (11)$$

Observe that the HTL scaling [Eq. (8)] can also be approximately derived from the stagnation scaling [Eqs. (5)–(7)] by using Eq. (11) to relate the stagnation and in-flight adiabats.

Though many discrepancies have been resolved with regard to the different scalings, it is important to note that some differences persist. In particular, the analytic KMA scaling [Eq. (9)] reproduces the in-flight HTL scaling [Eq. (8)] only if J_s is independent of the implosion velocity. On the other hand, the stagnation scaling in Eq. (3) reproduces the stagnation HTL scaling [Eq. (5)] only if $J_s \sim V_{\text{imp}}$, as proposed by Basko and Johner. This leads to the paradox that the two analytic theories leading to Eqs. (3) and (6) and Eq. (9) match the numerical fits only when different ignition conditions are used ($J_s = \text{constant}$ or $J_s \sim V_{\text{imp}}$).

In this article, a new model is developed to determine the marginal ignition conditions and the minimum kinetic energy required for ignition. This model includes the propagation of the return shock through the shell and the change of the shell adiabat as well as the most-relevant ignition physics such as alpha-particle heating and heat-conduction losses. It repro-

duces BJ scaling and HTL scaling with respect to the stagnation adiabat, indicating that J_s is indeed proportional to the implosion velocity. Furthermore, the model yields a relation between the stagnation and in-flight adiabats that is in general agreement with the KMA scaling and the HTL scaling [Eqs. (10) and (11)].

The following sections of this article (1) describe hot-spot dynamics and shell dynamics; (2) derive the ignition scalings with respect to the stagnation adiabat; (3) relate the stagnation adiabat to the in-flight adiabat and derive the “in-flight” scaling; and (4) verify *a posteriori* all the assumptions concerning the hot-spot hydrodynamics.

Hot-Spot Dynamics

The hot spot is a low-density plasma heated by the shock and by the PdV work of the cold, dense surrounding shell. It is made of ionized DT gas and the plasma ablated off the inner shell surface. Its dynamics are determined by the compression of the shell, the energy conduction and radiation losses, and the alpha heating.

As the hot spot is formed after the shock reflection, its temperature is typically large enough that its sound speed is larger than the flow velocity. Therefore, it is a good approximation to neglect the hot-spot kinetic energy with respect to its internal energy throughout the assembly and ignition stages of the hot spot. Another consequence of the subsonic flow assumption is that the pressure is equilibrated and the pressure profile is flat within the hot spot, i.e., $P_{\text{hs}} \approx P_{\text{hs}}(t)$.

Bremsstrahlung radiation energy losses can also be neglected because their contribution is typically smaller than that of the mechanical work and/or the fusion power. The magnitude of the radiation losses is larger than the fusion power for temperatures below 4.4 keV, when the PdV work rate is typically greater than both radiation and fusion power. Thus, at such low temperatures, both radiation losses and alpha heating power are negligible with respect to the compression work rate. The PdV work rate decreases as the shell approaches the stagnation point, while higher temperatures are reached within the hot spot. If these temperatures are well above 4.4 keV, the alpha power is greater than the radiation losses and the bremsstrahlung term can again be neglected in the energy equation.

Another simplification is the assumption that the alpha particles are locally deposited. This approximation requires a condition on the hot-spot temperature and areal density that

can be satisfied for sufficiently large implosion velocities. Indeed, it will be shown *a posteriori* [Eq. (10)] that both bremsstrahlung radiation and alpha-particle diffusion can be neglected as long as the implosion velocity is larger than a critical value.

Based on previous assumptions, the energy conservation equation for the hot spot includes the PdV work of the shell, the conduction energy losses, the alpha-particle heating, and the change in internal energy:

$$\frac{3}{2} \frac{\partial}{\partial t} P + \nabla \cdot \left[\frac{5}{2} \mathbf{v} P \right] = \nabla \cdot \kappa(T) \nabla T + \frac{\rho^2}{4M_i^2} E_\alpha \langle \sigma v \rangle, \quad (12)$$

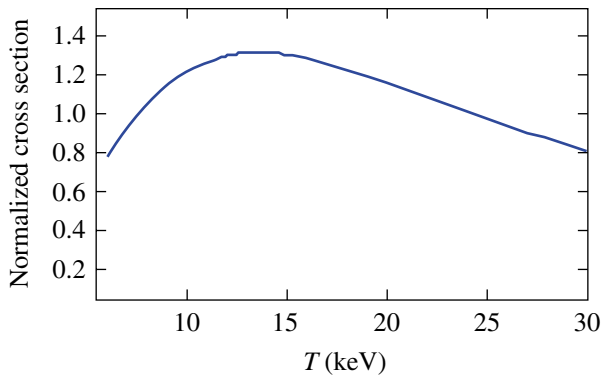
where ρ is the hot-spot density, M_i is the ion mass, $E_\alpha \approx 3.5$ MeV is the alpha-particle energy, $\kappa(T) = \kappa_0 T^{5/2}$ is Spitzer thermal conductivity, and $P \approx P_{\text{hs}}(t)$ for subsonic flows.

Following Ref. 8, we integrate Eq. (12) over the hot-spot volume enclosed by the inner shell surface and approximate the fusion cross section with the quadratic form $\langle \sigma v \rangle \approx S_\alpha T^2$ with $S_\alpha \approx 10^{-18} \text{ cm}^3 \text{ s}^{-1} \text{ keV}^{-2}$. Figure 87.46 shows that the error produced by the T^2 approximation of $\langle \sigma v \rangle$ is less than 30% for $6 < T < 25$ keV. At the inner surface, the shell material is cold and the thermal conduction can be neglected. This leads to the following form of the integrated energy equation:

$$\begin{aligned} \frac{d}{dt} (P_{\text{hs}} R_{\text{hs}}^3) + 3 R_{\text{hs}}^2 P_{\text{hs}} \left[\frac{5}{3} U(R_{\text{hs}}, t) - \frac{dR_{\text{hs}}}{dt} \right] \\ = \sum_\alpha P_{\text{hs}}^2 R_{\text{hs}}^3, \end{aligned} \quad (13)$$

where $U(R_{\text{hs}}, t)$ is the flow velocity at the shell inner surface and $\sum_\alpha \equiv E_\alpha S_\alpha / 24$. The flow velocity results from the combination of the inner surface motion and the ablative flow, $U(R_{\text{hs}}, t) = \dot{R}_{\text{hs}} - V_a$, where V_a is the ablation velocity and \dot{R}_{hs} scales with the implosion velocity. Since $V_a \ll \dot{R}_{\text{hs}}$, the ablation velocity⁸ can be neglected and Eq. (13) can be rewritten in the simplified form

$$\dot{P}_{\text{hs}} + 5 P_{\text{hs}} \frac{\dot{R}_{\text{hs}}}{R_{\text{hs}}} = \sum_\alpha P_{\text{hs}}^2. \quad (14)$$



TC5707

Figure 87.46

Plot of the normalized fusion cross section $\langle\sigma v\rangle/0.97 \times 10^{-18} T(\text{keV})^2$ between 6 and 30 keV. The maximum error is 27%. (The reference cross section is taken from Ref. 9.)

Note that the heat conduction losses do not enter into the global energy balance of the hot spot because the heat flux leaving the hot spot is deposited onto the inner shell surface. A fraction of this energy is transformed into internal energy of the shell material ablating into the hot spot. The remaining fraction produces the PdV work done by the ablated plasma entering the hot spot against the hot-spot pressure. In other words, the energy leaving the hot spot in the form of heat conduction losses goes back into the hot spot in the form of internal energy and compression work of the ablated plasma. Therefore, conduction losses do not affect the global energy balance of the hot spot and therefore do not represent net energy losses to the hot spot, as shown by Eq. (14). It is important to emphasize that the hot-spot energy is proportional to its pressure. The conduction losses do affect the hot-spot temperature but not its pressure. This conclusion implies that greater conduction losses would lower the temperature and raise the density (through larger ablation at the shell inner surface), leaving the pressure ($P \sim \rho T$) unaltered.

The next step is to couple the hot-spot-energy equation [Eq. (14)] with the shell dynamics through the shell momentum conservation and to determine the hot-spot radius as a function of the hot-spot pressure.

Shell Dynamics

In the initial stage of the deceleration phase, the hot spot is heated and compressed by the piston action of the shell. If a sufficiently large pressure is reached within the hot spot, a thermal instability is driven by the absorbed fusion power, leading to a rapid increase of the hot-spot energy. This instabil-

ity is referred to as “thermonuclear ignition.” In this section, we develop a simple model describing the shell motion and combine the shell and hot-spot equations in order to construct a self-consistent model of the deceleration phase and hot-spot ignition.

As mentioned in Ref. 8, the deceleration phase starts after the shock reflected from the center of the capsule interacts with the incoming shell. For simplicity, we assume that after the first shock reflects off the shell, all subsequent shocks are weak and do not produce large pressure jumps within the hot spot or the shell. For this reason, we refer to our model as the “one-shock model.” If multiple shocks are launched during the acceleration phase and do not merge into one before reaching the shell center but instead converge to the center at different times, the one-shock model may not be valid. After interacting with the shell, the return shock travels within the shell material and eventually reaches the shell’s outer surface.

Two shell configurations have been considered: the thin incompressible shell and the thick compressible shell. The thin shell model assumes that the shock reaches the outer shell surface immediately and that the whole shell acts like a rigid piston on the hot spot. This model is simple and provides useful physical insight into the ignition problem. However, it leads to a significant underestimation of the ignition energy requirements for two reasons: First, this model assumes that the entire shell kinetic energy is transformed into hot-spot internal energy at stagnation. Second, it does not include the shell decompression after the return shock has passed through the shell. ICF capsules are usually better described by the thick compressible shell model where the shock propagating through the shell divides it into two regions that provide compression work at different rates. At stagnation, the shock is still within the shell, and only the shocked part has released all its kinetic energy to the hot spot.

In Sec. 1, we determine the shell dynamics using the simple thin incompressible shell model. In Sec. 2, we derive the thick compressible shell model and determine all the relevant capsule properties, once the conditions at the beginning of the deceleration phase are known.

1. The Thin Incompressible Shell Model

To gain some physical insight into the shell dynamics, we consider the simple model of an incompressible shell of finite mass but infinitesimally small thickness.

The motion of the thin incompressible shell is governed by Newton's law balancing the shell inertia with the hot-spot pressure force:

$$M_{\text{sh}} \ddot{R}_{\text{hs}} = 4\pi R_{\text{hs}}^2 P_{\text{hs}}, \quad (15)$$

where M_{sh} is the shell mass. Here M_{sh} is constant and, according to the thin-shell approximation, the shell's center of mass coincides with the hot-spot radius. Note that the pressure applied to the shell's outer surface has been neglected since the laser is turned off during the deceleration phase. Equation (15) is combined with the hot-spot energy balance [Eq. (14)], which we rewrite in the following compact form:

$$\frac{d}{dt} [P_{\text{hs}} R_{\text{hs}}^5] = \Sigma_{\alpha} P_{\text{hs}}^2 R_{\text{hs}}^5. \quad (16)$$

Equations (15) and (16) constitute a closed system of coupled differential equations that can be easily solved to determine the hot-spot pressure and shell position.

2. The Thick Compressible Shell Model

The thin incompressible shell model provides a useful qualitative understanding of the deceleration phase and hot-spot ignition. If the shell is incompressible, however, its mass supplies a uniform PdV work rate to the hot spot, and the thin shell model leads to optimistic predictions about the onset of ignition. For a more accurate quantitative estimate of the ignition conditions, it is appropriate to use a compressible model, including the return shock propagation through the shell. After the interaction with the shell's inner surface, the return shock travels within the shell material and eventually reaches the shell's outer surface. We let $R_k(t)$ denote the shock position within the shell. The shell material with $r < R_k$ is shocked and compressed, while the material with $r > R_k$ is in a "free-fall" condition. A free-fall condition is the state of the shell in the absence of a hot spot. Since the shock wave reflected from the center carries the information regarding the high pressure within the hot spot, it is reasonable to assume that the unshocked material is not aware of the presence of the hot spot and moves at constant velocity toward the center.

The shocked part of the shell behaves as a thin shell and acts like a piston on the hot spot. The unshocked part is in the free-fall (ff) condition and provides compression work rate through the flow of momentum across the shock. This flow of momentum, however, is proportional to $[\rho_{\text{ff}}]_{R_k}$ and for a given

implosion velocity can be small if the unshocked shell density ρ_{ff} is small. In simple words, a thick compressible shell does not act as a uniform piston. The material near the hot-spot surface provides PdV work at a faster rate than the material on the opposite side of the shock. The PdV work would be grossly overestimated if we were to assume that the entire shell mass is uniformly compressing the hot spot, as in the thin incompressible shell model.

a. Free-fall conditions. Free-fall conditions describe the dynamics of the unshocked part of the shell. Here a distinction is made between the coasting phase and free-fall conditions. The coasting phase represents the time interval after the laser is turned off and before the return shock has interacted with the shell. The free-fall conditions apply to the unshocked part of the shell after the shock-shell interaction. In the absence of the return shock, the shell travels inward at approximately constant velocity while its thickness increases due to the expansion of the shell material into its surroundings. We consider the following simple form for the density profile of a free-falling shell:

$$\rho_{\text{ff}}(r, t) = \frac{3M_{\text{sh}}}{\pi r^2} \frac{[r - R_{\text{in}}(t)]^2 [R_{\text{out}}(t) - r]}{\Delta_{\text{ff}}^4}, \quad (17)$$

where M_{sh} is the shell mass, $\Delta_{\text{ff}} = R_{\text{out}}(t) - R_{\text{in}}(t)$ is the free-fall shell thickness, and $R_{\text{out}}, R_{\text{in}}$ are the trajectories of the outer and inner free-falling surfaces. The density profile described by Eq. (17) accurately reproduces the results of numerical simulations obtained using the code *LILAC*.

During the coasting and deceleration phase, the absence of an applied pressure causes the shell surfaces to expand at the speed of sound, suggesting that the shell thickness increases at the rate

$$\frac{d\Delta_{\text{ff}}}{dt} = \mu \langle C_{s(\text{ff})} \rangle, \quad (18)$$

where $\langle C_{s(\text{ff})} \rangle$ is the average unshocked-shell sound speed and μ is a proportionality constant. Typically the free-fall sound speed is much smaller than the shock velocity through the shell so there is no significant thickening of the shell during the deceleration phase as compared to the coasting phase. Furthermore, the shell sound speed during the free-fall phase is much lower than the implosion velocity. Therefore, changes in the

shell's internal energy do not significantly affect the free-falling shell's kinetic energy. It follows that the change in shell thickness, while significant during the coasting phase, can be neglected during the deceleration phase, and $\Delta_{\text{ff}} \approx \Delta_0 = \text{constant}$ from the shock-shell interaction time to the stagnation time. The inner and outer free-fall surface trajectories can therefore be approximated with linear functions of time:

$$R_{\text{in}} \approx R_0 - V_{\text{imp}} t, \quad R_{\text{out}} \approx R_0 + \Delta_0 - V_{\text{imp}} t, \quad (19)$$

where R_0 is the position of the inner shell surface at the beginning of the deceleration phase.

Since the free-fall profiles describe the conditions of the unshocked shell material, it is reasonable to assume that the free-fall conditions are isentropic. If, for simplicity, we use an ideal gas equation of state for the shell, the shell pressure evolves according to the simple adiabatic equation

$$P_{\text{ff}}(r, t) = \beta_{\text{ff}} \rho_{\text{ff}}(r, t)^{5/3}, \quad (20)$$

where P_{ff} and β_{ff} are the free-fall pressure and adiabat, respectively. Here, for simplicity, we assume that the free-fall adiabat is uniform and equal to its value (in flight) at the beginning of the deceleration phase $\beta_{\text{ff}} = \beta_{\text{if}}$.

b. Shocked-shell equations of motion. The shock front divides the shell into two parts, which have different dynamics. The shocked shell material encloses the hot spot and produces the true piston action of the shell. The shocked material is usually much denser than the unshocked material. The latter is described by the free-fall conditions mentioned earlier and contributes to the hot-spot compression work through the flow of momentum across the shock front. The contribution of the free-fall shell to the hot-spot compression is dominant during the initial stage of the deceleration phase, when the mass of the shocked shell is small. At later times, however, it is the shocked shell that provides most of the compression work.

As shown in Ref. 8, ablation off the shell's inner surface into the hot spot determines the hot-spot mass. This is typically a small fraction of the shell mass until a burn wave begins to propagate through the shell and the hot spot is filled with ablated material. This raises its density to a level comparable with the shell density. Thus, mass ablation off the shell into the hot spot significantly affects the shell dynamics only after the onset of the ignition process and during burn-wave propaga-

tion in the shell, stages that are not considered in this article. Here, we neglect the effect of mass ablation on the shell's dynamics and approximate the fluid velocity at the shell's inner surface (equal to the hot-spot radius) with the surface velocity:

$$U_{\text{ss}}(R_{\text{hs}}, t) = \dot{R}_{\text{hs}} - V_a \approx \dot{R}_{\text{hs}}, \quad (21)$$

where the subscript "ss" stands for *shocked shell* and "hs" for *hot spot*. Since the shocked material is dense, it is appropriate to approximate the shocked part of the shell as a thin shell. In the thin-shell approximation, the shocked shell's thickness is assumed to be much smaller than its radius. Here, the shocked shell extends from the hot-spot radius R_{hs} to the shock front R_k , and the fluid velocity within the shocked shell can be approximated by its Taylor expansion:

$$U_{\text{ss}}(r, t) = \dot{R}_{\text{hs}} + \left[\frac{\partial U}{\partial r} \right]_{R_{\text{hs}}} (r - R_{\text{hs}}). \quad (22)$$

Since the flow is isentropic within the shocked shell, it is straightforward to determine the spatial derivatives from the entropy conservation equation

$$\left[\partial_t (P^{3/5} r^2) + \partial_r (P^{3/5} r^2 U) \right] = 0,$$

leading to

$$\left[\frac{\partial U}{\partial r} \right]_{R_{\text{hs}}} = - \frac{1}{P_{\text{hs}}(t)^{3/5} R_{\text{hs}}(t)^2} \frac{d}{dt} \left\{ P_{\text{hs}}(t)^{3/5} R_{\text{hs}}(t)^2 \right\}. \quad (23)$$

Using the hot-spot-energy equation [Eq. (14)] to eliminate \dot{P}_{hs} in Eq. (23) and substituting (23) into (22) leads to the following simple form of the post-shock velocity:

$$U_{\text{ss}}(R_k, t) = \dot{R}_{\text{hs}} \frac{R_k}{R_{\text{hs}}} - \frac{3}{5} \sum_{\alpha} P_{\text{hs}}(R_k - R_{\text{hs}}). \quad (24)$$

Because of the mass flow through the shock front, the mass of the shocked part M_{ss} increases with time. The variation of the shocked shell's mass is determined by the mass flow through the shock front:

$$\dot{M}_{\text{ss}} = 4\pi R_k^2 \rho_{\text{ff}}(R_k, t) \left[\dot{R}_k + V_{\text{imp}} \right], \quad (25)$$

where $\rho_{\text{ff}}(R_k, t)$ is the unshocked density given by Eq. (17) calculated at the shock front. Here, the subscript “ff” (free fall) refers to the unshocked material.

The momentum balance of the shocked shell is obtained by integrating the momentum conservation equation from the hot-spot radius to the shock front, yielding

$$\frac{d}{dt} [M_{\text{ss}} \langle U_{\text{ss}} \rangle] + \dot{M}_{\text{ss}} V_{\text{imp}} = 4\pi R_{\text{hs}}^2 P_{\text{hs}}, \quad (26)$$

where $\langle U_{\text{ss}} \rangle = 0.5 [U_{\text{ss}}(R_{\text{hs}}, t) + U_{\text{ss}}(R_k, t)]$ is an average velocity of the shocked shell. In the derivation of Eq. (26), the shell’s free-fall pressure has been neglected with respect to the hot-spot pressure, and the velocity is assumed uniform and equal to the implosion velocity throughout the free-fall part of the shell. The average shocked-shell velocity can be rewritten using Eqs. (21) and (24), yielding

$$\langle U_{\text{ss}} \rangle = \dot{R}_{\text{hs}} \frac{R_{\text{hs}} + R_k}{2R_{\text{hs}}} - \frac{3}{5} \sum_{\alpha} P_{\text{hs}} \frac{R_k - R_{\text{hs}}}{2}. \quad (27)$$

The next step is to determine the shock position $R_k(t)$ using the Rankine–Hugoniot relations at the shock front. We assume that the return shock is strong and write the shock velocity as

$$\dot{R}_k \approx -V_{\text{imp}} + \sqrt{\frac{4P_{\text{ss}}(R_k, t)}{3\rho_{\text{ff}}(R_k, t)}}. \quad (28)$$

The quantity $P_{\text{ss}}(R_k, t)$ represents the pressure in the shocked shell calculated at the shock front. This pressure can be determined using another Hugoniot relation relating the velocities before ($-V_{\text{imp}}$) and after [$U_{\text{ss}}(R_k, t)$] the shock:

$$U_{\text{ss}}(R_k, t) \approx -V_{\text{imp}} + \sqrt{\frac{3P_{\text{ss}}(R_k, t)}{4\rho_{\text{ff}}(R_k, t)}}. \quad (29)$$

Thus, the post-shock pressure $P_{\text{ss}}(R_k, t)$ can be determined from Eq. (29) and substituted into Eq. (28), leading to the following equation for the shock position:

$$\dot{R}_k = \frac{V_{\text{imp}}}{3} + \frac{4}{3} U_{\text{ss}}(R_k, t), \quad (30)$$

where the post-shock velocity $U_{\text{ss}}(R_k, t)$ is given in Eq. (24). The last equation needed to close the system comes from the hot-spot energy balance [Eq. (14)] (derived earlier) relating the hot-spot pressure $P_{\text{hs}}(t)$ to the hot-spot radius $R_{\text{hs}}(t)$. Equations (14), (17), (24)–(27), and (30) represent a complete set of equations that describe the evolution of all the relevant hydrodynamic quantities during the deceleration phase and the onset of ignition. For convenience, the complete model is summarized in the following subsection.

c. Summary of the thick shell model. We summarize below all the relevant equations of the thick shell model, consisting of a set of four ordinary differential equations governing the evolution of the following hydrodynamic quantities:

1. The hot-spot pressure $P_{\text{hs}}(t)$, which obeys the following ordinary differential equation (ODE):

$$\dot{P}_{\text{hs}} + 5P_{\text{hs}} \frac{\dot{R}_{\text{hs}}}{R_{\text{hs}}} = \sum_{\alpha} P_{\text{hs}}^2. \quad (31)$$

2. The hot-spot radius $R_{\text{hs}}(t)$ equal to the shocked-shell inner-surface radius governed by Newton’s law:

$$M_{\text{ss}} \frac{d}{d\tau} \langle U_{\text{ss}} \rangle + \dot{M}_{\text{ss}} [\langle U_{\text{ss}} \rangle + V_{\text{imp}}] = 4\pi P_{\text{hs}} R_{\text{hs}}^2, \quad (32)$$

where $\langle U_{\text{ss}} \rangle$ is the average shocked-shell velocity,

$$\langle U_{\text{ss}} \rangle = \dot{R}_{\text{hs}} \frac{R_{\text{hs}} + R_k}{2R_{\text{hs}}} - \frac{3}{10} \sum_{\alpha} P_{\text{hs}} (R_k - R_{\text{hs}}), \quad (33)$$

and R_k is the shock position.

3. The shocked-shell mass $M_{\text{ss}}(t)$, which obeys mass conservation:

$$\dot{M}_{\text{ss}} = 4\pi R_k^2 \rho_{\text{ff}}(R_k, t) [\dot{R}_k + V_{\text{imp}}]. \quad (34)$$

4. The shock position within the shell $R_k(t)$ derived from Hugoniot relations:

$$\dot{R}_k = \frac{V_{\text{imp}}}{3} + \frac{4}{3} U_{\text{ss}}(R_k, t), \quad (35)$$

where $U_{ss}(R_k, t)$ is the post-shock velocity,

$$U_{ss}(R_k, t) = \dot{R}_{hs} \frac{R_k}{R_{hs}} - \frac{3}{5} \sum_{\alpha} P_{hs} (R_k - R_{hs}). \quad (36)$$

The unshocked shell material is described by the *free-fall* conditions:

$$\rho_{ff}(r, t) = \frac{3M_{sh}}{\pi r^2} \frac{[r - R_{in}(t)]^2 [R_{out}(t) - r]}{\Delta_0^4}, \quad (37)$$

where M_{sh} is the total shell mass, $\Delta_0 = R_{out}(t) - R_{in}(t)$ is the free-fall shell thickness (approximately constant), and $R_{in}(t) = R_0 - V_{imp}t$ is the inner-surface trajectory starting from the initial radius R_0 at the beginning of the deceleration phase.

A set of initial conditions at the beginning of the deceleration phase corresponding to the shell–shock interaction time must be provided to solve the system of equations:

1. the inner-surface, free-fall (or implosion) velocity $-V_{imp}$,
2. the inner shell radius R_0 ,
3. the shell thickness Δ_0 ,
4. the shell mass M_{sh} , and
5. the hot-spot pressure P_0 .

The solution of the four differential equations yields the time evolution of the shock position, hot-spot radius, and pressure. The last two quantities can be used to determine the evolution of all other relevant hydrodynamic quantities inside the hot spot, such as temperature, density, ablation velocity, density-gradient scale length, and areal density as described in Ref. 8.

Ignition Scaling Using the Thin Incompressible Shell Model

In this section, we first determine the ignition criterion in terms of the initial conditions at the beginning of the deceleration phase for the thin incompressible shell model. The ignition criterion has a very simple form and simple physical interpretation. Next, we derive a scaling law in terms of the shell's kinetic energy and an entropy function. The latter does not represent the shell adiabat since the shell is assumed incompressible. It will be shown in the section entitled **Ignition Scaling Using the Compressible Shell Model**, however, that this entropy function is directly proportional to the shell

adiabat at stagnation when the finite compressibility of the shell is included.

1. Ignition Criterion

The thin shell model can be simplified by eliminating P_{hs} between Eqs. (15) and (16) and by using the following dimensionless variables:

$$\hat{R}_{hs} \equiv R_{hs}/R_0, \quad \tau = V_{imp}t/R_0. \quad (38)$$

A straightforward manipulation of Eqs. (15) and (16) leads to the following single ordinary differential equation for the hot-spot radius:

$$\frac{d}{d\tau} \left(\hat{R}_{hs}^3 \frac{d^2 \hat{R}_{hs}}{d\tau^2} \right) = \frac{Y_{\alpha}}{\hat{\epsilon}_0} \hat{R}_{hs} \left(\frac{d^2 \hat{R}_{hs}}{d\tau^2} \right)^2, \quad (39)$$

where

$$Y_{\alpha} \equiv \frac{\sum_{\alpha} P_0 R_0}{V_{imp}} \hat{\epsilon}_0^2 = \frac{\tau_i^0}{\tau_{\alpha}^0} \hat{\epsilon}_0^{3/2}, \quad \hat{\epsilon}_0 = \frac{M_{sh} V_{imp}^2}{4\pi P_0 R_0^3}, \quad (40)$$

$$\tau_i^0 = \left[\frac{M_{sh}}{4\pi P_0 R_0} \right]^{1/2}, \quad \tau_{\alpha}^0 = \frac{1}{\sum_{\alpha} P_0}. \quad (41)$$

Here $\hat{\epsilon}_0$ represents the ratio between the initial shell kinetic energy and the initial hot-spot internal energy, which is much greater than unity in typical ICF implosions. (Small values of $\hat{\epsilon}_0$ require that the hot-spot radius at the beginning of the free-fall phase be very close to the stagnation hot-spot radius. This does not occur in typical ICF implosions.) The times τ_i^0 and τ_{α}^0 represent the inertial time of the shell and the alpha-particle heating time at the beginning of the deceleration phase. The shell trajectory is determined by solving Eq. (39) with the following initial conditions:

$$\hat{R}_{hs}(0) = 1, \quad \dot{\hat{R}}_{hs}(0) = -1, \quad \ddot{\hat{R}}_{hs}(0) = 1/\hat{\epsilon}_0, \quad (42)$$

where the “dot” indicates a derivative with respect to τ .

It is important to notice that as long as the alpha heating is smaller than the compression work, the right-hand side of Eq. (39) can be neglected and the shell trajectory is given by

$$\hat{R} = \sqrt{1 - 2\tau + \tau^2(1 + \hat{\epsilon}_0^{-1})}, \quad (43)$$

leading to the following values of the stagnation time, radius, acceleration, and pressure:

$$t_{\text{stag}} = \frac{R_0}{V_{\text{imp}}} \frac{\hat{\epsilon}_0}{1 + \hat{\epsilon}_0}, \quad R_{\text{stag}} = \frac{R_0}{\sqrt{1 + \hat{\epsilon}_0}}, \quad (44a)$$

$$g_{\text{stag}} = (1 + \hat{\epsilon}_0)^{3/2} \frac{R_0}{(\tau_i^0)^2}, \quad P_{\text{stag}} = P_0(1 + \hat{\epsilon}_0)^{5/2}. \quad (44b)$$

Equations (44) yield scaling relations for the stagnation values of the hydrodynamic quantities in terms of the shell and hot-spot properties at the beginning of the deceleration phase. Such relations are valid as long as the hot spot is not ignited. If the alpha heating becomes important, the right-hand side of Eq. (39) must be retained and the stagnation pressure and deceleration are significantly larger.

It is easy to show that, for a given $\hat{\epsilon}_0$, the solution of Eq. (39) develops an explosive instability when the parameter Y_α exceeds a critical value. Both parameters $\hat{\epsilon}_0$ and Y_α are functions of the shell and hot-spot properties at the beginning of the deceleration phase (M_{sh} , V_{imp} , R_0 , and P_0). A typical singular explosive solution (dashed line in Fig. 87.47) shows the shell ejected outward at an infinite velocity. Such solutions correspond to the thermal instability of the hot spot, which we denote as ‘‘ignition.’’ The singularity is due to the fact that the fusion reaction rate $\langle\sigma v\rangle$ is taken to be proportional to T^2 , and, therefore, it diverges to infinity with temperature. In reality, $\langle\sigma v\rangle$ is bounded at high temperatures and the shell ejection velocity is finite. Nevertheless, the occurrence of the singularity in the solution of Eq. (39) represents a simple and robust definition of ignition for the thin shell model. We therefore conclude that the hot spot is ignited when the solution of Eq. (39) is singular. The numerical solution of Eq. (39) indicates that singular solutions develop when the following approximate condition is satisfied:

$$Y_\alpha \left[1 + \left(\frac{3}{5} \right)^{1/3} \hat{\epsilon}_0^{-1} \right]^{3/2} > \sqrt{3}, \quad (45a)$$

which reduces to

$$Y_\alpha > \sqrt{3} \quad (45b)$$

in the limit $\hat{\epsilon}_0 \gg 1$. Equations (45) represent the ignition conditions in terms of the shell and hot-spot properties at the beginning of the deceleration phase. The physical interpretation of the ignition threshold is straightforward. We rewrite the hot-spot-energy equation [Eq. (14)] in the following intuitive form:

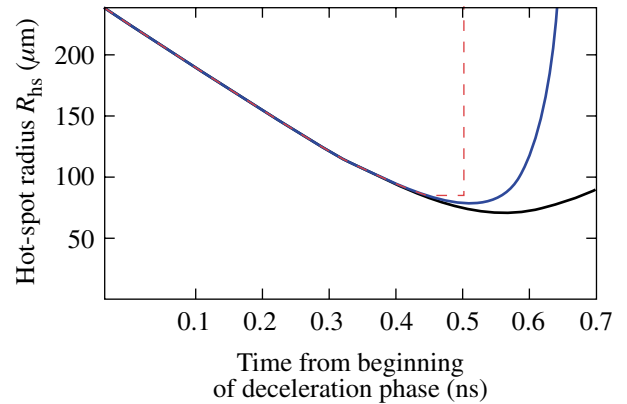
$$\frac{1}{E_{\text{hs}}} \frac{dE_{\text{hs}}}{dt} = \sum_\alpha P_{\text{hs}} - 2 \frac{\dot{R}_{\text{hs}}}{R_{\text{hs}}}, \quad (46)$$

where $E_{\text{hs}} = (4\pi/3)P_{\text{hs}}R_{\text{hs}}^3$ is the hot-spot energy. After stagnation, the second term on the right-hand side is negative ($\dot{R}_{\text{hs}} > 0$ after stagnation) and represents the inverse hot-spot decompression time ($\tau_{\text{decomp}} = R_{\text{hs}}/2\dot{R}_{\text{hs}}$) due to the outward motion of the shell pushed by the hot-spot pressure. This decompression time can be estimated by setting

$$\tau_{\text{decomp}} \sim 0.5 \sqrt{R_{\text{hs}}/\ddot{R}_{\text{hs}}}$$

and using Eq. (15), leading to

$$\tau_{\text{decomp}} = \frac{1}{2} \sqrt{\frac{M_{\text{sh}}}{4\pi P_{\text{hs}} R_{\text{hs}}}}. \quad (47)$$



TC5708

Figure 87.47

Thin incompressible shell model prediction for the evolution of the hot-spot radius for NIF-like capsules [obtained by solving Eq. (39)]. The dashed line represents an ignited solution with a singularity after stagnation. The solid lines represent two non-ignited solutions.

Note that the first term on the right-hand side of Eq. (46) represents the inverse alpha-particle heating time

$$\tau_\alpha = 1/\Sigma_\alpha P_{\text{hs}}.$$

Ignition occurs right after stagnation if the alpha heating time is shorter than the decompression time:

$$\tau_\alpha(\text{stag}) < \tau_{\text{decomp}}(\text{stag}). \quad (48)$$

If Eq. (48) is satisfied, a thermal instability (the ignition process) is triggered because the hot-spot pressure starts to increase and leads to a shorter alpha heating time $\tau_\alpha \sim 1/P_{\text{hs}}$. The decompression time is proportional to $1/\sqrt{P_{\text{hs}}}$ and decreases less than the alpha heating time. This leads to a further increase in pressure and a thermal explosive instability. To estimate the ignition threshold, we use the stagnation values (without alpha particles) given in Eqs. (44) to find $\tau_\alpha(\text{stag})$:

$$\tau_\alpha(\text{stag}) \approx \frac{1}{\Sigma_\alpha P_0 (1 + \hat{\epsilon}_0)^{5/2}} = \frac{\tau_\alpha^0}{(1 + \hat{\epsilon}_0)^{5/2}}. \quad (49)$$

Similarly, we find $\tau_{\text{decomp}}(\text{stag})$:

$$\tau_{\text{decomp}}(\text{stag}) \approx \frac{1}{2} \left(\frac{R_{\text{stag}}}{g_{\text{stag}}} \right)^{1/2} = \frac{\tau_i^0}{2(1 + \hat{\epsilon}_0)}, \quad (50)$$

where τ_i^0 [defined in Eq. (41)] represents the decompression time if the shell stagnates at time $t = 0$ [$\tau_{\text{decomp}}(0) = \tau_i^0$]. Substituting Eqs. (49) and (50) into (48) yields the approximate ignition condition

$$\frac{\tau_{\text{decomp}}(0)}{\tau_\alpha(0)} (1 + \hat{\epsilon}_0)^{3/2} = Y_\alpha (1 + \hat{\epsilon}_0^{-1})^{3/2} > 2, \quad (51)$$

where the identity $\tau_\alpha^0 \equiv \tau_\alpha(0)$ has been used and the term $(1 + \hat{\epsilon}_0)^{3/2}$ represents the amplification factor of the ratio τ_i^0/τ_α due to the hot-spot compression by the shell. Observe that condition (51) is similar to the numerical fit given in (45a) and yields approximately the same ignition threshold ($Y_\alpha > 2$) in the limit of $\hat{\epsilon}_0 \gg 1$.

2. Ignition Scaling

We consider the marginal ignition criterion given in Eq. (45b) in the relevant ICF limit $\hat{\epsilon}_0 \gg 1$ and rewrite Y_α [defined in Eq. (40)] in the following form:

$$Y_\alpha = \frac{\Sigma_\alpha}{(2\pi)^2} \frac{E_k^2}{P_0 R_0^5 V_{\text{imp}}}, \quad (52)$$

where $E_k = M_{\text{sh}} V_{\text{imp}}^2 / 2$ is the shell's kinetic energy. Using the thin-shell approximation, the shell mass can be written as

$$M_{\text{sh}} \approx 4\pi \rho_{\text{sh}}(0) R_0^3 / A_0, \quad (53)$$

where $\rho_{\text{sh}}(0)$ and $A_0 = R_0/\Delta_0$ are the shell density and aspect ratio at the beginning of the deceleration phase (here Δ_0 is the shell thickness). Equation (53) can also be cast in terms of shell kinetic energy by multiplying both sides by V_{imp}^2 and then using it to derive the initial hot-spot radius R_0 :

$$R_0 \approx \left(\frac{A_0 E_k}{2\pi \rho_{\text{sh}}(0) V_{\text{imp}}^2} \right)^{1/3}. \quad (54)$$

Substituting Eq. (54) into Eq. (52) and rewriting the ignition condition $Y_\alpha = \text{constant}$ in terms of the kinetic energy yields

$$E_k \approx \frac{2\pi Y_\alpha^3}{\Sigma_\alpha^3} \frac{\beta_0^3}{V_{\text{imp}}^7}, \quad (55)$$

where $Y_\alpha \approx \sqrt{3}$ for ignition and

$$\beta_0 \equiv \frac{P_0}{[\rho_{\text{sh}}(0)/A_0]^{5/3}} \quad (56)$$

has the dimensions of an adiabat. Note that the pressure P_0 is the hot-spot pressure at time $t = 0$ and not the shell pressure. Thus, at this stage, the parameter β_0 cannot be related to the shell adiabat as should be expected when approximating the shell with an incompressible layer. The scaling (56), though dimensionally similar to the HTL stagnation scaling [Eq. (5)], is still inconclusive and deserves further analysis as shown in the next section, where the effects of finite shell compressibility are retained.

Ignition Scaling Using the Compressible Shell Model

Since the right-hand side of Eq. (55) represents the minimum kinetic energy required for ignition, it is appropriate to determine A_0 in order to minimize the ignition requirements. The optimum A_0 can be determined by making use of the thick shell model described earlier [Eqs. (31)–(37)] and the following simple argument.

If the shell is too thin, the return shock reaches the outer shell surface before stagnation, causing the shell to rapidly expand outward, decompressing the hot spot and stopping the ignition process. If the shell is too thick, stagnation (and therefore ignition) is reached when the shock is still within the shell and the unshocked part of the shell is still free falling. In this scenario, ignition is triggered with a surplus of kinetic energy in the free-fall part of the shell. Ignition using the minimum kinetic energy occurs when the return shock is exactly at the shell's outer surface at the same time the shell reaches the stagnation point. We conclude that the optimum shell thickness is such that the shock reaches the outer shell surface at stagnation.

Because the shock position is the new information needed to optimize A_0 and minimize the shell's kinetic energy, the ignition condition needs to be determined using the compressible thick shell model. The next step is to rewrite the thick shell model in dimensionless form using the following definitions:

$$\hat{R}_{\text{hs}} = R_{\text{hs}}/R_0, \quad \hat{R}_k = R_k/R_0, \quad \hat{P}_{\text{hs}} = P_{\text{hs}}/P_0, \quad (57a)$$

$$\tau = V_{\text{imp}}t/R_0, \quad \hat{M} = M_{\text{ss}}/M_{\text{sh}}, \quad (57b)$$

where R_0 and P_0 are the shell's inner surface and hot-spot pressure at the beginning of the deceleration phase. A simple manipulation of Eqs. (31)–(37) using the definitions in (57) yields a closed set of four differential equations,

$$\begin{aligned} \frac{d}{d\tau} \left\{ \hat{M} \left[\hat{R}_{\text{hs}} \frac{\hat{R}_{\text{hs}} + \hat{R}_k}{2\hat{R}_{\text{hs}}} - \frac{3}{10} \frac{Y_\alpha}{\hat{\epsilon}_0^2} \hat{P}_{\text{hs}} (\hat{R}_k - \hat{R}_{\text{hs}}) + 1 \right] \right\} \\ = \frac{\hat{P}_{\text{hs}} \hat{R}_{\text{hs}}^2}{\hat{\epsilon}_0}, \end{aligned} \quad (58)$$

$$\dot{\hat{R}}_k = \frac{1}{3} + \frac{4}{3} \dot{\hat{R}}_{\text{hs}} \frac{\hat{R}_k}{\hat{R}_{\text{hs}}} - \frac{4}{5} \frac{Y_\alpha}{\hat{\epsilon}_0^2} \hat{P}_{\text{hs}} (\hat{R}_k - \hat{R}_{\text{hs}}), \quad (59)$$

$$\begin{aligned} \dot{\hat{M}} = 12A_0^4 (\hat{R}_k + \tau - 1)^2 \left| 1 + A_0^{-1} - \tau - \hat{R}_k \right| \\ \times (\hat{R}_k + 1) H(1 - \hat{M}), \end{aligned} \quad (60)$$

$$\dot{\hat{P}}_{\text{hs}} + 5\hat{P}_{\text{hs}} \frac{\dot{\hat{R}}_{\text{hs}}}{\hat{R}_{\text{hs}}} = \frac{Y_\alpha}{\hat{\epsilon}_0^2} \hat{P}_{\text{hs}}^2, \quad (61)$$

representing the evolution of the shocked shell's inner radius \hat{R}_{hs} , shock position \hat{R}_k , shocked shell mass \hat{M} , and hot-spot pressure \hat{P}_{hs} . The step function $H(1 - \hat{M})$ in Eq. (60) limits the magnitude of the shocked shell mass to the total shell mass. That is, when $M_{\text{ss}} = M_{\text{sh}}$ (i.e., $\hat{M} = 1$), the right-hand side of Eq. (60) vanishes and the shocked shell mass remains constant and equal to the total shell mass. Equations (58)–(61) can be solved using the following set of initial conditions:

$$\hat{R}_{\text{hs}}(0) = 1, \quad \dot{\hat{R}}_{\text{hs}}(0) = 0, \quad \hat{R}_k(0) = 1, \quad (62)$$

$$\hat{M}(0) = 0, \quad \hat{P}_{\text{hs}}(0) = 1.$$

The initial condition $\dot{\hat{R}}_{\text{hs}} = 0$ needs a clarification. Before the interaction with the return shock, the shell density vanishes on the inner surface. As a result of the interaction with the shock, the shell's inner surface is stopped, so the condition $\hat{R}_{\text{hs}} = 0$ is applicable right after the interaction with the shock. After this brief stop, the inner shell surface is set in motion by the imploding high-density shell material that is not stopped by the return shock.

Observe that Eqs. (58)–(61) depend on three dimensionless parameters Y_α , $\hat{\epsilon}_0$, and A_0 , which need to be determined to satisfy the following two conditions: (1) the hot spot must be ignited, and (2) the return shock must be on the outer surface at stagnation to assure that the kinetic energy is minimized. The first condition requires that the solution of Eqs. (58)–(61) be singular and the shell be ejected outward at infinite velocity after stagnation. The second requires that $\hat{M} = 1$ at stagnation, implying that the entire shell has been shocked.

We solve Eqs. (58)–(61) with the software program MATHEMATICA in the limit of $\hat{\epsilon}_0 \gg 1$, which is the correct limit for ICF implosions since the shell’s kinetic energy is much larger than the hot-spot internal energy at the beginning of the deceleration phase. We find that the singular solutions with $\hat{M} = 1$ at stagnation occur when

$$A_0 \approx 0.39 \sqrt{\hat{\epsilon}_0}, \quad Y_\alpha \approx 2.60. \quad (63)$$

Other results from the solution of Eqs. (58)–(61) are shown in Figs. 87.48–87.50. Figures 87.48 and 87.49 plot the evolution of the shocked shell mass and hot-spot pressure. Figure 87.50 shows the trajectories of the hot-spot radius and the shock front near stagnation. Analysis of the solution to the thick shell equations suggests that the stagnation scaling of the hot-spot pressure, hot-spot radius, and shock position are given by the following:

$$P_{\text{hs}}(\text{stag}) \approx 1.02 P_0 \hat{\epsilon}_0^{5/2}, \quad (64a)$$

$$R_{\text{hs}}(\text{stag}) \approx 1.23 R_0 / \sqrt{\hat{\epsilon}_0}, \quad (64b)$$

$$R_k(\text{stag}) \approx 1.40 R_0 / \sqrt{\hat{\epsilon}_0}. \quad (64c)$$

Observe that the relations for the stagnation values of P_{hs} and R_{hs} are similar (except for a numerical factor) to the ones obtained earlier [Eqs. (44)] with the thin shell model and

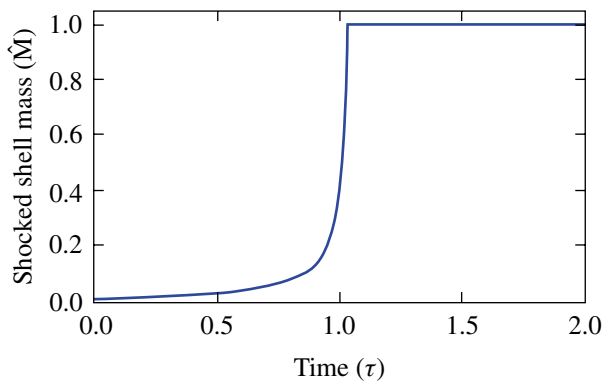


Figure 87.48
Thick compressible shell model results. Plot of the shocked shell mass versus time. Time $t = 0$ corresponds with the beginning of the deceleration phase. When $\hat{M} = 1$, the entire shell has been shocked.

$\hat{\epsilon}_0 \gg 1$. The ignition condition for Y_α in Eq. (63) is also similar to (but with a different numerical value) that derived with the thin shell model and leads to the same scaling for the minimum energy required for ignition:

$$E_k \approx \frac{2\pi Y_\alpha^3 \beta_0^3}{\Sigma_\alpha^3 V_{\text{imp}}^7}, \quad (65)$$

where β_0 is defined in Eq. (56). The new result here is that the shell’s aspect ratio A_0 at the beginning of the deceleration phase is related to the other shell properties through the first condition in Eq. (63). Furthermore, the position of the outer

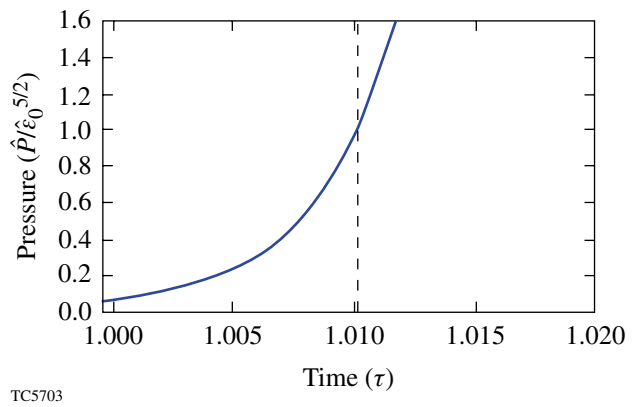


Figure 87.49
Thick compressible shell model results. Evolution of the hot-spot pressure, obtained from Eqs. (58)–(61). The vertical dashed line represents the shock breakout time (also stagnation time).

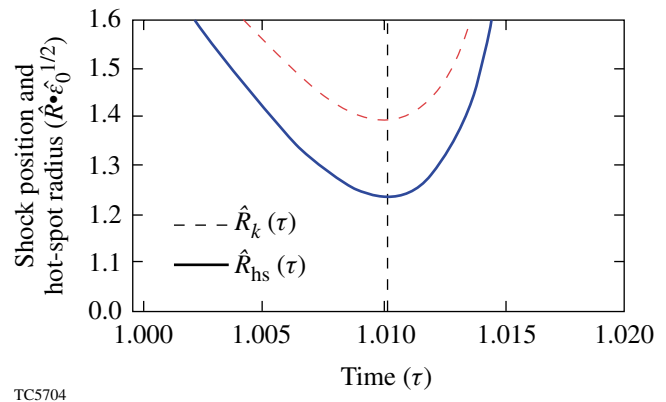


Figure 87.50
Thick compressible shell model results. Trajectories of the shock and the hot-spot radius, obtained from Eqs. (58)–(61). The vertical dashed line represents the shock breakout time (also stagnation time).

shell surface coincides with the shock position R_k and is determined in Eq. (64c). This latest result is essential to determine the ignition scaling in terms of the stagnation properties.

Setting the shell mass at the beginning of the deceleration phase equal to the stagnation mass,

$$4\pi \frac{R_0^3}{A_0} \rho_{sh}(0) \approx \frac{4\pi}{3} [R_k(\text{stag})^3 - R_{hs}(\text{stag})^3] \rho_{sh}(\text{stag}), \quad (66)$$

and substituting Eqs. (64) into Eq. (66) leads to the following relation between the shell densities:

$$\rho_{sh}(0) \approx 0.3 \rho_{sh}(\text{stag}) \frac{A_0}{\hat{\epsilon}_0^{3/2}}. \quad (67)$$

Then, using the definition of $\beta_0 \equiv A_0^{5/3} P_0 / \rho_{sh}(0)^{5/3}$ and Eqs. (64a) and (67), the following relation is easily derived:

$$\beta_0 \approx 7.52 \beta_s, \quad (68)$$

where $\beta_s \equiv P_{hs}(\text{stag}) / \rho_{sh}(\text{stag})^{5/3}$ represents the shell stagnation adiabat. Observe that the hot-spot pressure is used in the definition of the shell stagnation adiabat. While this is not an exact definition, it is sufficiently accurate because the stagnation pressure is continuous at the hot spot/shell interface.

The next step is to finalize the scaling law Eq. (65) using Eqs. (63) and (68) and the standard definition of the normalized stagnation adiabat

$$\alpha_s \equiv \frac{P(\text{Mbar})}{2.18 \rho_{sh}(\text{g/cm}^3)^{5/3}}. \quad (69)$$

A straightforward manipulation of Eq. (65) leads to the following formula for the minimum energy required for ignition:

$$E_k \approx 2.7 (\text{kJ}) \alpha_s^3 \left[\frac{3 \times 10^7}{V_{\text{imp}}(\text{cm/s})} \right]^7. \quad (70)$$

Equation (70) represents the marginal ignition scaling in terms of the stagnation adiabat. Observe that Eq. (70) is quite similar

in both the scaling relation as well as the numerical coefficient with the result of Ref. 5, which reads as

$$E_k \approx 2.1 (\text{kJ}) \alpha_s^{2.66} \left[\frac{3 \times 10^7}{V_{\text{imp}}(\text{cm/s})} \right]^{7.2}.$$

The next step is to relate the stagnation to the in-flight adiabat and determine the ‘‘in-flight’’ scaling for marginal ignition.

Ignition Scaling Using the In-Flight Adiabat

Comparisons of different ignition capsules are usually based on the magnitude of the in-flight adiabat, which can be easily controlled by tuning the initial foot of the laser pulse. In this section, the stagnation adiabat is related to the in-flight adiabat, and the ignition scaling law is expressed in terms of the in-flight hydrodynamic properties of the shell.

Starting from Eq. (63) ($A_0 = 0.39 \sqrt{\hat{\epsilon}_0}$) and the definition of $\hat{\epsilon}_0$ [Eq. (40)], we express the hot-spot pressure at the beginning of the deceleration phase $P_{hs}(0)$ in terms of the shell pressure at the same time $P_{sh}(0)$:

$$P_{hs}(0) \approx 0.25 P_{sh}(0) M_A(0)^2 / A_0^3, \quad (71)$$

where $M_A(0) = V_{\text{imp}} / C_s(0)$ is the shell’s Mach number at the beginning of the deceleration phase and $C_s(0)$ is the shell’s sound speed. Substituting Eq. (71) into Eq. (68) yields the following relation:

$$\beta_s \approx 0.034 \beta_{\text{if}} M_A(0)^2 / A_0^{4/3}, \quad (72)$$

where $\beta_{\text{if}} \equiv P_{sh}(0) / \rho_{sh}(0)^{5/3}$ is the shell’s in-flight adiabat. It is important to emphasize that time zero represents the beginning of the deceleration phase, which starts after the coasting phase.

The next step is to relate the shell’s Mach number and aspect ratio at the beginning of the deceleration phase to their values at the beginning of the coasting phase during which the laser is off and the ablation pressure vanishes. During the coasting phase, the shell travels at approximately constant velocity, while rarefaction waves propagate inside the shell from both the inner and outer surfaces since the shell pressure is much larger than the surrounding pressure. The expansion velocity induced by a rarefaction wave is

$$v_{\text{exp}} = 3C_s \left[1 - (\rho/\rho_{\text{max}})^{1/3} \right]$$

and depends on the location along the density profile. If we characterize the shell as the region enclosed by the two points where the density is equal to $1/e$ times the maximum density, then the expansion velocity of the inner and outer surfaces is $v_{\text{exp}} = 0.85 C_s$. Using these definitions, the shell thickness Δ_{sh} increases with time during the coasting phase, according to the following equation:

$$\frac{d\Delta_{\text{sh}}}{dt} = 1.7 C_s^c, \quad (73)$$

where C_s^c is the shell sound speed during the coasting phase. Equation (73) can be further simplified by using the following dimensionless variables:

$$\hat{\Delta}_{\text{sh}} = \Delta_{\text{sh}}/\Delta_c, \quad \hat{R}_{\text{sh}} = R_{\text{sh}}/R_c,$$

where R_{sh} is the shell radius and R_c, Δ_c are the shell radius and thickness at the beginning of the coasting phase. Assuming that the shell adiabat is constant during the coasting phase and using the thin-shell approximation $[M_{\text{sh}} = 4\pi\rho_{\text{sh}} R_{\text{sh}}^2 \Delta_{\text{sh}}]$, Eq. (73) can be rewritten as

$$\frac{d\hat{\Delta}_{\text{sh}}}{d\hat{R}_{\text{sh}}} = -1.7 \frac{A_c}{M_A^c} \frac{1}{\hat{R}_{\text{sh}}^{2/3} \hat{\Delta}_{\text{sh}}^{1/3}}, \quad (74)$$

where A_c and M_A^c are the shell's aspect ratio and Mach number at the beginning of the coasting phase. Equation (74) can be easily integrated to determine the evolution of the shell thickness during the coasting phase:

$$\Delta_{\text{sh}} = \Delta_c \left\{ 1 + 6.8 \frac{A_c}{M_A^c} \left[1 - \left(\frac{R_{\text{sh}}}{R_c} \right)^{1/3} \right] \right\}^{3/4}. \quad (75)$$

Assuming that the shell radius at the beginning of the deceleration phase is much smaller than the radius at the beginning of the coasting phase $[R_{\text{sh}}(0) \ll R_c]$, Eq. (75) yields the asymptotic value of the shell thickness at the beginning of the deceleration phase (i.e., time $t = 0$):

$$\Delta_{\text{sh}}(0) = \Delta_c \left(1 + 6.8 \frac{A_c}{M_A^c} \right)^{3/4}. \quad (76)$$

A relation between the aspect ratio A_c and Mach number M_A^c can be determined by matching the shell expansion rate at the beginning of the coasting phase with the one calculated at the end of the acceleration phase as explained below.

During the acceleration phase, the shell density can be obtained from the momentum conservation equation

$$\rho_{\text{sh}} g = \frac{\partial P}{\partial r}, \quad (77)$$

where $P = \beta_{\text{if}} \rho_{\text{sh}}^{5/3}$. A simple manipulation of Eq. (77) yields the density profile

$$\rho_{\text{sh}} = \rho_a \left(1 - \frac{R_a - r}{2\Delta_{\text{sh}}} \right)^{3/2}, \quad (78)$$

where R_a is the radius of the ablation surface, ρ_a is the density at the ablation surface, and

$$\Delta_{\text{sh}} = \frac{3C_s^2}{4g} \quad (79)$$

is the shell thickness from the ablation surface to the $1/e$ point. The shell's aspect ratio peaks at the beginning of the main pulse when its value is proportional to the square of the Mach number. It then decays during the main pulse and the following coasting phase when the shell radius decreases and the thickness increases. The thickness can be written in terms of the shell radius by using Eq. (79) and assuming that the ablation pressure P_a increases like $1/R$ as indicated by the result of several numerical simulations. Setting $g = 4\pi R^2 P_a / M_{\text{sh}}$ into Eq. (79) yields the shell thickness as a function of the radius:

$$\Delta_{\text{sh}} = \frac{5}{16\pi} \frac{\beta_{\text{if}}^{3/5} M_{\text{sh}}}{(P_a R_{\text{sh}})^{3/5}} \frac{1}{R_{\text{sh}}^{7/5}} \sim \frac{1}{R_{\text{sh}}^{7/5}}. \quad (80)$$

In deriving Eq. (80), the reduction of the shell mass due to the laser ablation has been neglected. This approximation may not be appropriate for indirect-drive capsules where a large portion of the shell material is ablated off during the implosion. The rate of the shell expansion during the acceleration phase follows from Eq. (80):

$$\dot{\Delta}_{\text{sh}} \approx -\frac{7}{5} \frac{\Delta_{\text{sh}}}{R_{\text{sh}}} \dot{R}_{\text{sh}}. \quad (81)$$

When the expansion velocity [Eq. (81)] reaches the sound speed, the shell pressure exceeds the applied ablation pressure. Typically, the laser is turned off at this point since the shell pressure is so large that the applied ablation pressure has little effect on the shell dynamics. From a mathematical standpoint, the acceleration phase turns into the coasting phase when the shell's expansion velocity calculated during acceleration phase [Eq. (81)] matches the expansion velocity calculated during the coasting phase [Eq. (73)]. The matching occurs when

$$\frac{7}{5} \frac{\Delta_{\text{sh}}}{R_{\text{sh}}} = 1.7 \frac{C_s^c}{-\dot{R}_{\text{sh}}}, \quad (82)$$

which leads to the following expression for the aspect ratio at the beginning of the coasting phase:

$$A_c = 0.82 M_A^c. \quad (83)$$

The next step is to rewrite the shell's Mach number at the beginning of the deceleration phase in terms of the hydrodynamic quantities at the beginning of the coasting phase. Using the thin-shell approximation, one finds

$$M_A(0) = M_A^c \left(\frac{R_0}{R_c} \right)^{2/3} \left(\frac{\Delta_0}{\Delta_c} \right)^{1/3}, \quad (84)$$

where $R_0 = R_{\text{sh}}(0)$ and $\Delta_0 = \Delta_{\text{sh}}(0)$. Substituting Eqs. (83), (84), and (76) into (72) leads to the following expression of the stagnation adiabat:

$$\beta_s = 0.74 \beta_{\text{if}} \left(M_A^c \right)^{2/3}, \quad (85)$$

which can be expressed in the convenient form

$$\alpha_s = 2.8 \alpha_{\text{if}}^{0.8} \left[\frac{V_{\text{imp}}(\text{cm/s})}{3 \times 10^7} \right]^{0.67} \left[\frac{100}{P(\text{Mbar})} \right]^{0.13}. \quad (86)$$

This relation is similar to the numerical fit of Herrmann *et al.*⁵ and to the self-similar scaling found by Kemp *et al.*:⁶

$$\alpha_s^{\text{HTL}} = 3.2 \alpha_{\text{if}}^{0.75} \left[\frac{V_{\text{imp}}(\text{cm/s})}{3 \times 10^7} \right]^{0.44} \left[\frac{100}{P(\text{Mbar})} \right]^{0.21}, \quad (87)$$

$$\alpha_s^{\text{KMA}} = 2.3 \alpha_{\text{if}}^{0.85} \left[\frac{V_{\text{imp}}(\text{cm/s})}{3 \times 10^7} \right]^{0.5} \left[\frac{100}{P(\text{Mbar})} \right]^{0.1}. \quad (88)$$

The final ignition energy scaling can be found by substituting Eq. (86) into Eq. (70), yielding

$$E_k = 59(\text{kJ}) \alpha_{\text{if}}^{2.4} \left[\frac{3 \times 10^7}{V_{\text{imp}}(\text{cm/s})} \right]^5 \left[\frac{100}{P(\text{Mbar})} \right]^{0.39}, \quad (89)$$

which is similar to Herrmann's numerical fit

$$E_k^{\text{HTL}} = 50.8(\text{kJ}) \alpha_{\text{if}}^{1.88} \left[\frac{3 \times 10^7}{V_{\text{imp}}(\text{cm/s})} \right]^{5.89} \left[\frac{100}{P(\text{Mbar})} \right]^{0.77}. \quad (90)$$

Observe that both Eq. (88) and (89) show a scaling relation resembling the one derived by Kemp *et al.* as long as the triple product $\rho_{\text{hs}} T_{\text{hs}} R_{\text{hs}}$ is a constant for marginal ignition. However, as shown in the following section, the model described in this article yields a triple product that is proportional to the implosion velocity. This is in agreement with Basko's analysis.

Assumptions About Hot-Spot Hydrodynamics

It is important to remember that Eq. (89) has been derived under three assumptions. The first relates the alpha-particle mean free path, which is assumed to be smaller than the hot-spot radius, implying that the alpha-particle energy is deposited locally. The second, that the behavior of the averaged fusion cross section is given by $\langle \sigma v \rangle \sim T^2$, is valid as long as

the volume average temperature \bar{T}_{hs} is above 6 keV. The third comes from neglecting the radiation losses with respect to the alpha heating. To verify these assumptions, we use the hot-spot solution derived in Ref. 8, where all the hot-spot hydrodynamic quantities are obtained as functions of the hot-spot radius and pressure.

We start with the first of Eq. (24) of Ref. 8, calculated at the hot-spot center $\xi = 0$. Observe that Eq. (24) is an integral equation because the hot-spot mass M_{hs} is a time integral. Equation (24) can be easily converted into a simple differential equation for the central hot-spot density ρ_{hs}^0 :

$$\dot{\rho}_{\text{hs}}^0 + 3\rho_{\text{hs}}^0 \frac{\dot{R}_{\text{hs}}}{R_{\text{hs}}} = 0.072 m_i^{7/2} \kappa_0 \frac{P_{\text{hs}}^{5/2}}{(\rho_{\text{hs}}^0)^{5/2} R_{\text{hs}}^2}, \quad (91)$$

where $\kappa_0 T^{5/2}$ represents Spitzer thermal conductivity. Equation (91) can be rewritten in a convenient dimensionless form by defining the following variables:

$$\hat{\rho} = \rho_{\text{hs}}^0 / \rho_*, \quad \hat{P} = P_{\text{hs}} / P_0, \quad (92)$$

$$\tau = t V_{\text{imp}} / R_0, \quad \hat{R}_{\text{hs}} = R_{\text{hs}} / R_0, \quad (93)$$

where P_0 , R_0 are the hot-spot pressure and radius at the beginning of the deceleration phase, and

$$\rho_* = 0.47 m_i \left(\kappa_0 \frac{P_0^{5/2} \hat{\epsilon}_0^{27/4}}{R_0 V_{\text{imp}}} \right)^{2/7}, \quad (94)$$

where $\hat{\epsilon}_0$ is defined in Eq. (40). The dimensionless form of the density evolution equation becomes

$$\frac{d\hat{\rho}}{d\tau} + \frac{3\hat{\rho}}{\hat{R}_{\text{hs}}} \frac{d\hat{R}_{\text{hs}}}{d\tau} = \left(\frac{\hat{P}}{\hat{\rho}} \right)^{5/2} \frac{1}{\hat{R}_{\text{hs}}^2} \frac{1}{\hat{\epsilon}_0^{27/4}}, \quad (95)$$

which can be numerically solved once the hot-spot radius and pressure have been determined by solving the set of Eqs. (58)–(61). The central hot-spot temperature follows from Eq. (24) of Ref. 8. A straightforward manipulation yields

$$T_{\text{hs}}(0, t) = 8.3 (\text{keV}) \left(\frac{Y_\alpha}{2.6} \right)^{2/7} \left(\frac{V_{\text{imp}} (\text{cm/s})}{3 \times 10^7} \right)^{4/7} \frac{\hat{P}}{\hat{\rho} \hat{\epsilon}_0^{5/2}}, \quad (96)$$

where Y_α is defined in Eq. (40). The hot-spot areal density can also be determined by using Eqs. (23) of Ref. 8 and the definition of $\hat{\rho}$, leading to the following expression:

$$\rho R = 0.18 (\text{g/cm}^2) \left(\frac{Y_\alpha}{2.6} \right)^{5/7} \left[\frac{V_{\text{imp}} (\text{cm/s})}{3 \times 10^7} \right]^{3/7} \hat{\rho} \hat{R}_{\text{hs}} \sqrt{\hat{\epsilon}_0}. \quad (97)$$

To determine the stagnation value of the areal density, Eq. (95) is numerically solved using the radius and pressure of the marginally igniting shells $\hat{\epsilon}_0 \rightarrow \infty$ discussed earlier [Eqs. (64)]. Since the hot-spot density at the beginning of the deceleration phase is negligible, we solve Eq. (95) with the initial condition $\hat{\rho}(0) \rightarrow 0$ leading to the stagnation value $\hat{\rho}_{\text{stag}} \approx 0.83$. Substituting the marginal ignition condition $Y_\alpha \approx 2.6$ and $\hat{R}_{\text{stag}} \approx 1.23 / \sqrt{\hat{\epsilon}_0}$ into Eqs. (96) and (97) yields the stagnation value of the hot-spot areal density and central temperature of marginally igniting capsules:

$$\rho R(\text{stag}) = 0.18 (\text{g/cm}^2) \left[\frac{V_{\text{imp}} (\text{cm/s})}{3 \times 10^7} \right]^{3/7}, \quad (98)$$

$$T_{\text{hs}}(r=0, \text{stag}) = 10 (\text{keV}) \left[\frac{V_{\text{imp}} (\text{cm/s})}{3 \times 10^7} \right]^{4/7}. \quad (99)$$

To estimate the fraction θ_α of absorbed alpha particles we follow the work of Basko and set $\theta_\alpha = \text{Min}[1, \theta_0]$, where $\theta_0 \approx 50 \int_0^{R_{\text{hs}}} (\rho / T_{\text{hs}}^{1.2}) dr$ with T_{hs} in keV and ρ in g/cm^2 . After a straightforward manipulation, we find that for marginally igniting capsules (i.e., $Y_\alpha \approx 2.6$),

$$\theta_\alpha \approx \text{Min} \left\{ 1, 1.4 \left[\frac{3 \times 10^7}{V_{\text{imp}} (\text{cm/s})} \right]^{9/35} \right\}, \quad (100)$$

indicating that the fraction of absorbed alpha particles is close to unity for implosion velocities typical of direct-drive ICF. If

we require that $\theta > 0.7$ for the theory to be applicable with a reasonably small error, then Eq. (100) provides a constraint on the implosion velocity, i.e., $V_{\text{imp}} < 4 \times 10^8$ (cm/s). The next step is to determine the volume average temperature to verify the assumption concerning the quadratic behavior of $\langle \sigma v \rangle$. Integrating Eq. (41) of Ref. 8 over the hot-spot volume yields $\bar{T}_{\text{hs}} \approx 0.7 T_{\text{hs}}(0, t)$. The average temperature of marginal igniting capsules is then found from Eq. (99), and the resulting condition $\bar{T}_{\text{hs}} > 6$ keV leads to another constraint on the implosion velocity, i.e., $V_{\text{imp}} > 2 \times 10^7$ (cm/s). In summary, both assumptions are simultaneously satisfied as long as the implosion velocity is in the range

$$2 \times 10^7 < V_{\text{imp}} \text{ (cm/s)} < 4 \times 10^8, \quad (101)$$

which is the typical range of directly driven capsules. Observe that the condition $\bar{T}_{\text{hs}} > 6$ keV also implies that the alpha heating is significantly larger than the radiation losses, indicating that the bremsstrahlung term can indeed be neglected in the energy equation.

Conclusions

A model for the deceleration phase and marginal ignition of imploding capsules is derived by solving a set of ordinary differential equations describing the hot-spot energy balance and the shell dynamics including the return shock propagation. The change of adiabat induced by the shock is also calculated, and the relation between the in-flight and stagnation adiabats is in general agreement with the numerical fit of *LASNEX* simulations⁵ and the self-similar solution of Ref. 6. The minimum kinetic energy required for ignition is also calculated from the same model. The marginal ignition scaling is determined in terms of the stagnation as well as the in-flight adiabat. Both scaling relations are in good agreement with the numerical fit of Ref. 5.

ACKNOWLEDGMENT

This work was supported by the U.S. Department of Energy Office of Inertial Confinement Fusion under Cooperative Agreement No. DE-FC03-92SF19460, the University of Rochester, and the New York State Energy Research and Development Authority. The support of DOE does not constitute an endorsement by DOE of the views expressed in this article.

REFERENCES

1. W. K. Levedahl and J. D. Lindl, *Nucl. Fusion* **37**, 165 (1997).
2. A. R. Piriz, *Fusion Eng. Des.* **32-33**, 561 (1996).
3. M. M. Basko, *Nucl. Fusion* **35**, 87 (1995).
4. M. M. Basko and J. Johner, *Nucl. Fusion* **38**, 1779 (1998).
5. M. C. Herrmann, M. Tabak, and J. D. Lindl, *Nucl. Fusion* **41**, 99 (2001).
6. A. Kemp, J. Meyer-ter-Vehn, and S. Atzeni, *Phys. Rev. Lett.* **86**, 3336 (2001).
7. J. Meyer-ter-Vehn, *Nucl. Fusion* **22**, 561 (1982).
8. Laboratory for Laser Energetics LLE Review **85**, 1, NTIS document No. DOE/SF/19460-378 (2001). Copies may be obtained from the National Technical Information Service, Springfield, VA 22161.
9. H.-S. Bosch and G. M. Hale, *Nucl. Fusion* **32**, 611 (1992).

Wide-Dynamic-Range “Neutron Bang Time” Detector on OMEGA

Introduction

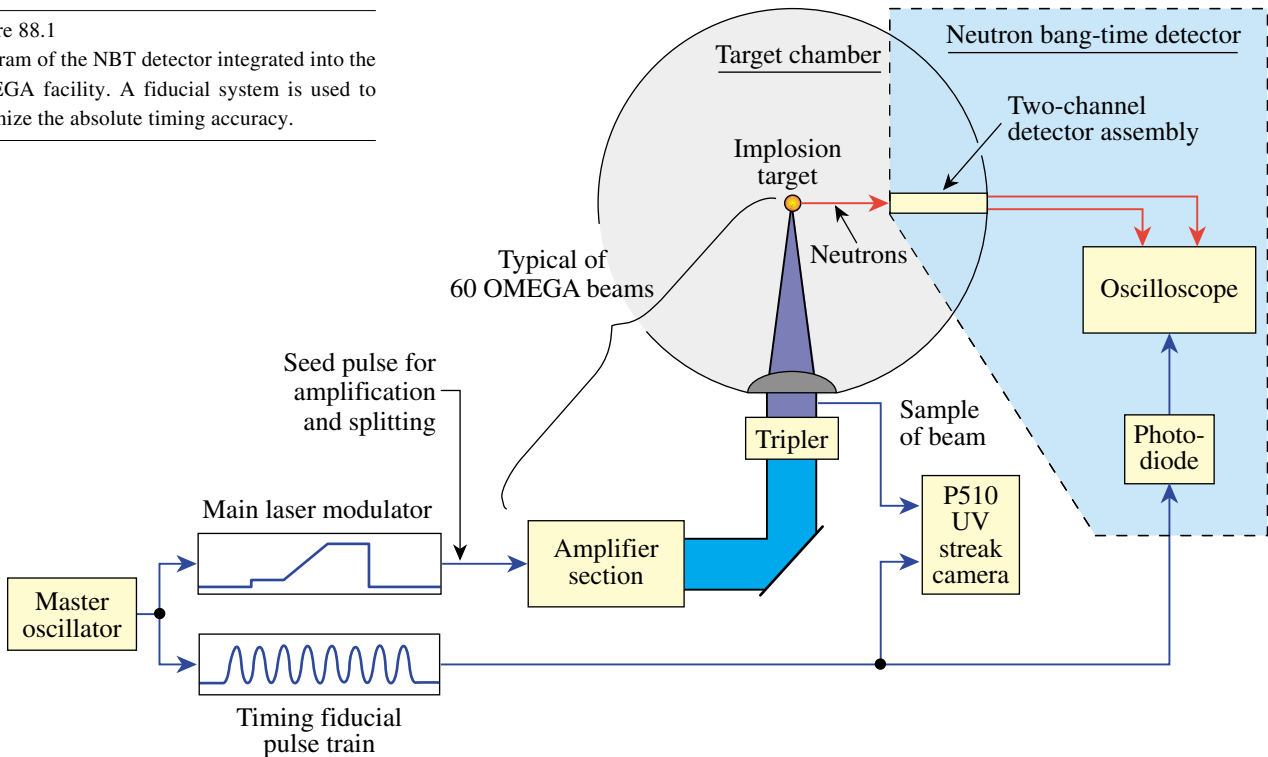
Measurements of the neutron emission from inertial confinement fusion¹ (ICF) implosions provide important information on the target performance, which can be compared directly with numerical models. Targets filled with deuterium (D₂) or a deuterium–tritium (DT) mixture are heated either by direct laser illumination or by soft x-ray radiation in a laser-heated hohlraum. In the resulting implosion, the target is compressed to conditions under which thermonuclear fusion occurs. Fuel atoms undergoing fusion release energetic charged particles, photons, and neutrons. The time of peak neutron emission—the “neutron bang time”—is very sensitive to the details of the energy absorption and the hydrodynamic response of the target. Several detectors that measure the neutron bang time^{2–4} have been described in the literature. These include a fast (<25 ps) streak camera–based neutron temporal diagnostic⁵

(NTD), which is also capable of resolving the details of the neutron burn history. The NTD is currently installed on LLE’s OMEGA laser. It needs a minimum neutron yield >10⁹ to measure the bang time and is incompatible with D₂ cryogenic target experiments due to mechanical constraints. These drawbacks, plus the complexity and cost of streak camera–based measurements, motivated the development of an alternative neutron bang time detector. This article describes a simple, low-cost, wide-dynamic-range, neutron bang time (NBT) detector that has been developed to complement the capabilities of the NTD.

Setup of the Detector System

The NBT is shown schematically in Fig. 88.1. It is composed of two detector channels to increase the dynamic range of the instrument, an optical fiducial system to cross-time the

Figure 88.1
Diagram of the NBT detector integrated into the OMEGA facility. A fiducial system is used to optimize the absolute timing accuracy.



E11451

diagnostic to the laser pulse, and a fast digitizing oscilloscope. As shown in Fig. 88.2(a), each channel of the NBT system consists of a fast, quenched plastic scintillator (Bicron BC-422Q⁶) coupled to a photomultiplier tube (PMT; Hamamatsu H5783⁷). The H5783 PMT uses an integrated high-voltage power supply that requires only a 15-V dc input. This voltage is supplied through the signal cable using two high-bandwidth bias tees⁸ to avoid ground loops and electromagnetic interference (EMI) noise pickup on the dc feed. The gain of the PMT is set by a voltage divider based on a reference voltage supplied by the H5783 to optimize the signal-to-noise ratio of the detection system. Both channels are packaged into a lead housing with copper foil wrapping to provide x-ray and EMI

shielding. The efficient x-ray shielding and EMI shielding makes it possible to use the NBT as a secondary neutron or hard x-ray detector in an energy range above 500 keV.⁹

As is shown in Fig. 88.2(b), the NBT detector assembly is positioned approximately 55 cm from the target chamber center (TCC) in a 3.8-cm-diam reentrant tube. Due to the small diameter of the reentrant tube, the second channel is located behind the first along the flight path of the neutrons produced in the target. This does not reduce the sensitivity of the back channel because of the long mean free path of the energetic neutrons in matter. To maximize the dynamic range of the system, different-sized scintillator volumes were selected for

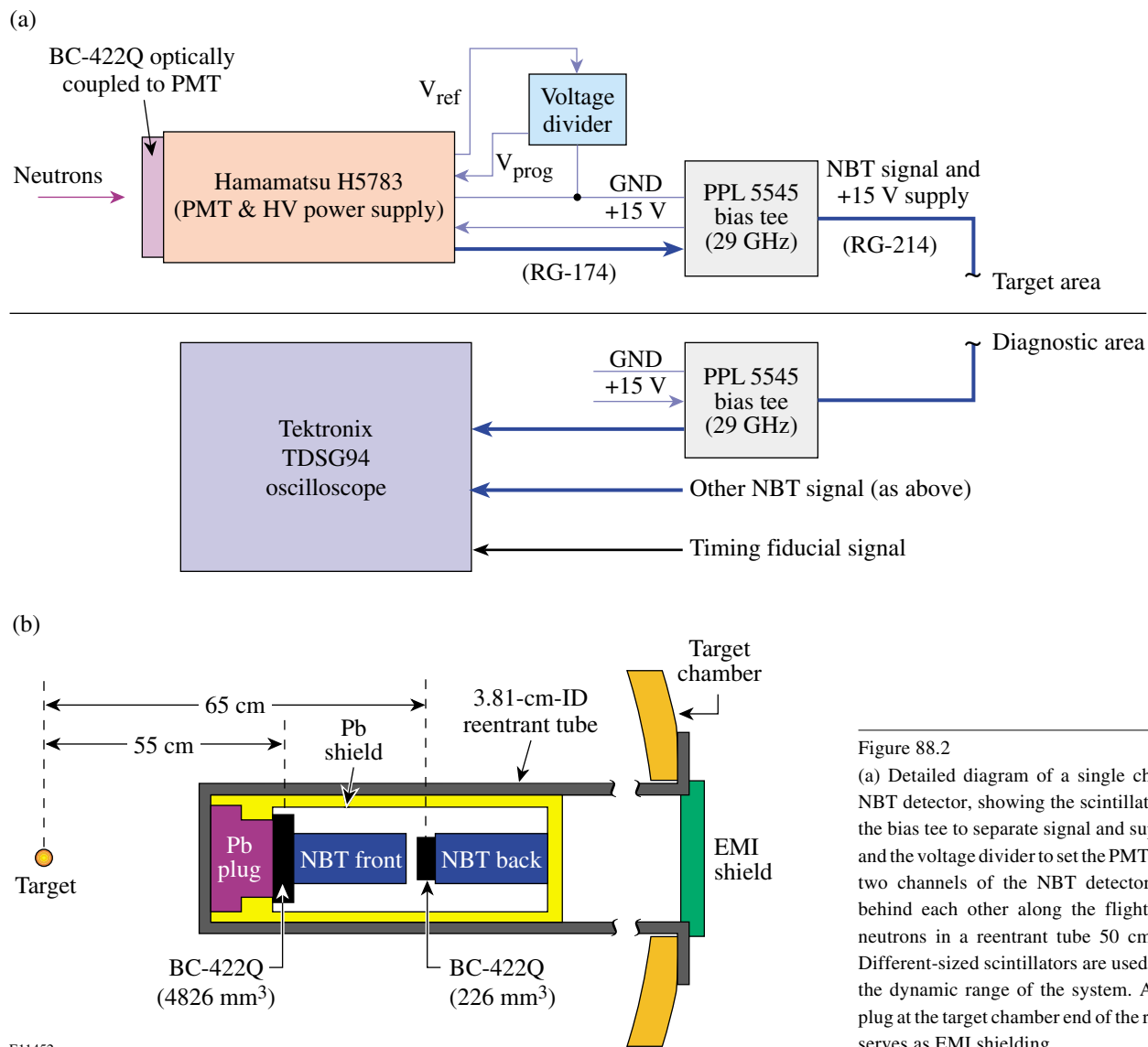


Figure 88.2
 (a) Detailed diagram of a single channel of the NBT detector, showing the scintillator, the PMT, the bias tee to separate signal and supply voltage, and the voltage divider to set the PMT gain. (b) The two channels of the NBT detector are located behind each other along the flight path of the neutrons in a reentrant tube 50 cm from TCC. Different-sized scintillators are used to maximize the dynamic range of the system. An aluminum plug at the target chamber end of the reentrant tube serves as EMI shielding.

E11452

each NBT channel, 4820 mm³ for the front channel and 230 mm³ for the back channel. The signals from the two NBT channels are recorded on separate channels using a four-channel Tektronix TDS694,¹⁰ 3-GHz digital oscilloscope at a sampling rate of 10 GS/s.

Absolute timing of the neutron bang time to better than 100 ps is accomplished using the OMEGA optical fiducial system. The fiducial pulse train consists of eight peaks spaced 548 ps apart and is synchronized to the shaped OMEGA laser pulse with a jitter of less than 20 ps. The optical fiducial is amplified separately from the main laser pulse and delivered to numerous system diagnostics. The fiducial pulse train is recorded on a separate channel of the NBT oscilloscope using a fast photodiode and also on the P510 ultraviolet streak camera,¹¹ which measures the laser pulse shape. The common optical fiducial serves as a reference for both the neutron signal and the laser pulse, enabling very accurate timing of the NBT signals.

Characterization of the NBT Components

The impulse response of the PMT was measured using a 100-fs laser pulse at 400-nm wavelength recorded on a 1-GHz sampling scope and found to be $\tau_{\text{rise}}^{\text{PMT}} = 940$ ps. Using the well-known relation

$$\tau_{\text{rise}}^{\text{PMT}} = \sqrt{\tau_{\text{rise}}^2 + \tau_{\text{scope}}^2}$$

with $\tau_{\text{scope}} = 350$ ps¹⁰ describing the rise time of the scope, the rise time of the PMT is found to be $\tau_{\text{rise}}^{\text{PMT}} = 650$ ps, in excellent agreement with the value given by the manufacturer.⁷

A low-jitter timing reference signal is critical to accurate measurement of the neutron bang time because the electrical oscilloscope trigger signal has a jitter relative to the laser pulse in excess of 100 ps. The simple solution of routing an optical fiducial fiber into the NBT detector and optically adding the fiducial pulse train to the scintillator signal does not provide a high-quality fiducial signal at the oscilloscope because the rise time of the PMT is slower than the fiducial peak spacing of 548 ps. Recording the optical fiducial pulse train using a high-bandwidth photodiode on a dedicated oscilloscope channel provides a high-quality fiducial signal where every fiducial peak is clearly resolved. The use of a separate channel for the fiducial does not degrade the timing accuracy significantly because the jitter between two channels of the TDS694 is reported by the manufacturer to be less than 10 ps. Sub-pixel resolution of the fiducial timing is accomplished by fitting a

pulse train of eight Gaussian pulses spaced at the well-characterized period of $d_t = 548$ ps:

$$\text{fidu}(t) = \sum_{i=0}^7 a_i \exp\left\{-\left[t - (t_0 + i \times dt)\right]^2 / 2\sigma\right\}$$

to the recorded signal. Here a_i is the amplitude of each fiducial peak, t_0 is the time of the first fiducial pulse, and σ is the width of an individual fiducial pulse. An example of the fiducial signal together with the fitted Gaussian pulse train is presented in Fig. 88.3 showing very good agreement between signal and fit.

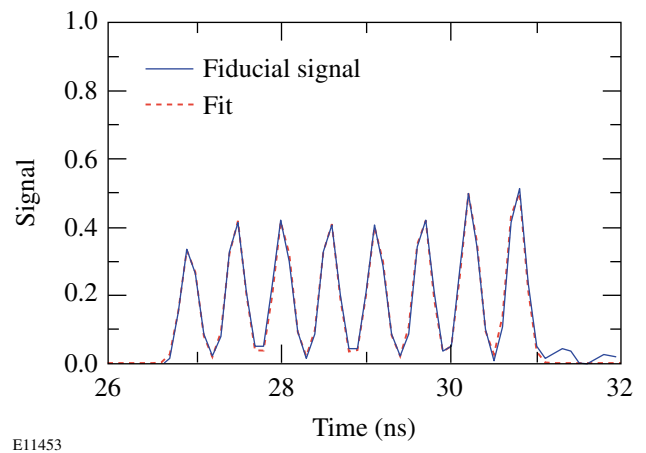


Figure 88.3 Optical fiducial and corresponding fit as recorded on the TDS694 oscilloscope. The high bandwidth of the oscilloscope makes it possible to see each individual fiducial pulse and to get a high-quality fit to obtain sub-pixel time resolution.

Because the output voltage of the PMT is limited to 5 to 10 V, EMI noise pickup effectively limits the dynamic range of each NBT detector channel. Several different shielding layers are used to limit the EMI noise to an acceptable level. The PMT is electrically isolated from the target chamber using the signal cable as its ground connection to the oscilloscope. The use of bias tees avoids ground loops in the dc power feed for the integrated PMT/high-voltage power supply. The lead housing was covered with a layer of Cu foil and grounded to the target chamber. The feedthrough holes for the signal cables were made as small as possible to limit high-frequency EMI penetration of the NBT housing. Finally, to improve the shielding, the reentrant tube was covered with an aluminum plug with only two small openings for the two signal cables. This

combined EMI shielding reduces the pickup noise from several 100 mV down to less than 10 mV for the front channel and less than 40 mV for the back channel.

The recorded neutron signal is broadened by several different mechanisms. Because the neutrons are produced at a high temperature, thermal broadening leads to a Gaussian shape of the arrival times. The plastic scintillator has a very short rise time followed by a relatively slow exponential decay.⁶ Scattering processes in the housing and lead shielding also create a tail in the neutron signal that has an effect similar to the scintillator decay. The effect of the finite neutron transit time through the scintillator¹² is less important for determining the bang time than it is for measuring the neutron-averaged ion temperature and can be approximated by a Gaussian for simplicity. The electronic part of the instrument response, which can be described also by a Gaussian, results from the finite bandwidth of the photomultiplier tube, the cable, and the oscilloscope.

Overall, the measured signal $m(t)$ can be approximated by a convolution of a Gaussian $g(t)$ and an exponential decay $d(t)$, as described in detail in Ref. 12:

$$g(t) = \frac{A}{\sqrt{2\sigma}} \exp\left[-\frac{(t-t_1)}{2\sigma}\right],$$

$$d(t) = \frac{1}{\tau} \exp\left(\frac{-t}{\tau}\right),$$

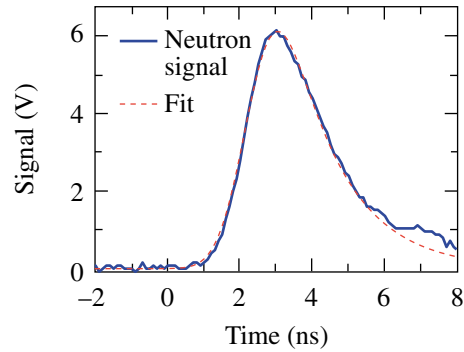
$$m(t) = g(t) \otimes d(t),$$

$$m(t) = \frac{A}{2\tau} \exp\left[-\frac{(t-t_1)}{\tau}\right] \times \exp\left(\frac{\sigma^2}{2}\right) \left\{ 1 + \operatorname{erf}\left[\frac{(t-t_1) - \sigma^2/\tau}{\sqrt{2\sigma^2}}\right] \right\}.$$

This function is fitted to the measured signal to improve the accuracy of the bang-time determination, especially in situations of low signal-to-noise ratio (see Fig. 88.4). Because the decay time of the scintillator and the neutron scattering effects are identical for every shot, a best-fit decay time can be determined once and used to analyze all of the data. The value used for this setup is $\tau = 1.5$ ns for both the front and the back

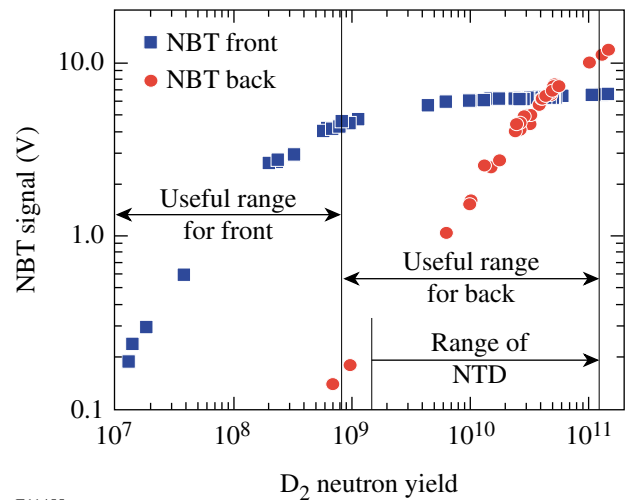
channels. The signal amplitude A , arrival time t , and signal width σ change from shot to shot and are fitted for every measurement to optimize timing accuracy.

Figure 88.5 shows the dynamic range in D_2 neutron yield for the current two-channel NBT setup. To show more clearly the limits of the linear PMT response, the NBT signal is shown in amplitude rather than collected charge (which would be more appropriate for a neutron-yield detector). In collected



E11454

Figure 88.4
Neutron signal and corresponding fit on one channel of the NBT detector.



E11455

Figure 88.5
Demonstrated dynamic range of the two-channel NBT detector setup. The detection threshold for the front channel is set by the yield that results in a single neutron hit. The threshold for the back channel is determined by the EMI noise pickup.

charge, the PMT’s show an even larger dynamic range that eventually distorts the temporal pulse shape. This makes it very difficult to determine the pulse arrival time and introduces large errors. The dynamic range for DT neutrons is very similar to the D₂ neutron dynamic range because, while the higher neutron energy results in a higher average signal per interacting neutron, the effect is mostly offset by the lower interaction cross section.

The front channel is relatively immune to EMI noise because even a single neutron hit results in a signal of the order of 100 mV due to the high PMT gain in the front channel. The EMI pickup noise affects mostly the back channel. A useful dynamic range from about 1 × 10⁷ to 1 × 10¹¹ can be realized in the present two-channel configuration.

Temporal Calibration and Bang Time Accuracy

The front NBT channel can be temporally calibrated using the hard x-ray emission from a Au target irradiated with a short (100 ps) laser pulse at best focus. To obtain a measurable signal for this calibration, the lead shield in front of the detector is replaced by a lead shield with a small hole. Previous experiments using the NTD have shown that the x-ray pulse closely follows the temporal shape of the laser irradiation.⁵ Figure 88.6 shows an x-ray-induced signal recorded by the front-channel NBT, a curve fit to this signal using the expression described in the previous section, and the shape of the 100-ps laser pulse as recorded on the OMEGA UV streak camera system.¹¹ The effects of the limited bandwidth and the noise on the recorded signal are clearly seen, but the accuracy of

determining the signal peak is improved considerably by the fitting procedure. The discrepancy that is apparent between the signal and the fit at the end of the pulse is attributed to the use of the expression that was derived for neutrons. Scattered x rays do not change speed as neutrons do, so the tail-off that is characteristic of the neutron signal is not present on the x-ray signal. This effect contributes approximately σ_{calib} = 50 ps uncertainty to the calibration.

The x-ray calibration can be easily carried over to the neutron measurements using the propagation delay difference from the TCC to the scintillator between x rays and neutrons:

$$\Delta t_n = L_{\text{scint}} \left(\frac{1}{v_n} - \frac{1}{c} \right),$$

where v_n^{D₂} = 2.16 cm/ns and v_n^{DT} = 5.12 cm/ns are the neutron velocities and L_{scint} = 55 cm (the distance between TCC and the scintillator). A measurement uncertainty in the scintillator distance of the order of 1 mm is estimated. This corresponds to a calibration error of σ_{dist}^{D₂} = 50 ps for D₂ and σ_{dist}^{DT} = 20 ps for DT neutrons. The scintillator distance can be measured *in situ* using the arrival-time difference between DT and D₂ neutrons for implosions of nominally identical bang time and was found to agree within the measurement error of the geometric measurement.

The back channel cannot be calibrated using this x-ray technique because the PMT and bias tee of the front channel effectively shield the back-channel detector from the hard x rays produced by the timing target. This channel can be cross calibrated to either the front channel in the common range of sensitivity or to the NTD. The very high accuracy of the NTD (<20 ps) provides a good measure of the bang time uncertainty of the NBT system. Figure 88.7 shows the cross-calibration of the back channel of NBT and NTD using many targets shots with D₂-filled plastic capsules. A very good correlation between the NTD and back-channel NBT data is observed, with a spread of σ_{back} = 50 ps. A correlation of similar quality is found between the front and back channels of the NBT detector in the common range of sensitivity. Given the 650-ps rise time of the PMT, this is a very good agreement.

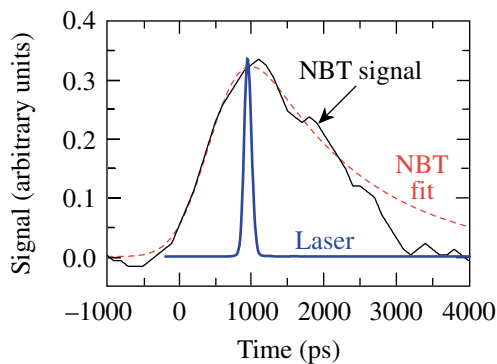
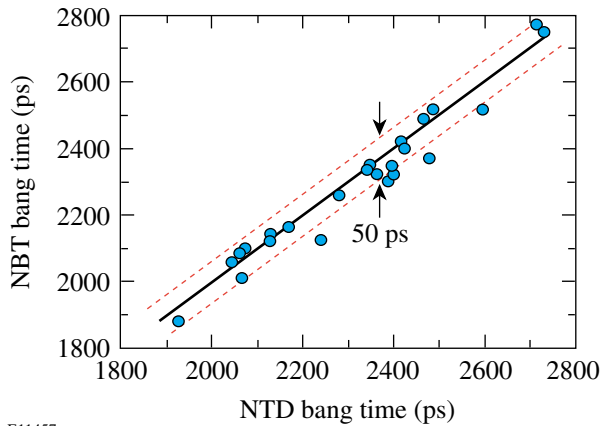


Figure 88.6 Front-channel NBT signal and corresponding fit for a hard x-ray emission produced by a 100-ps laser pulse irradiating a gold target at best focus. The 100-ps laser pulse is shown for comparison.

Because both NBT channels are analyzed by the same method, it is safe to assume that the bang time uncertainty from fitting the front-channel NBT data is the same as the measured back-channel spread: σ_{fit} = 50 ps. Adding the contributions from the x-ray calibration, σ_{calib}, σ_{dist}, and the uncertainty of



E11457

Figure 88.7

Cross-calibration between the back NBT channel and NTD. A very good correlation between NTD and NBT is observed with a rms difference of only 50 ps.

the bang time determination σ_{fit} in quadrature results in an overall absolute neutron bang time accuracy of $\sigma_{\text{front}} \leq 100$ ps for the x-ray-calibrated front NBT channel.

Summary and Conclusions

A simple, low-cost, two-channel neutron bang time detector having a wide dynamic range has been developed for OMEGA to complement the capabilities of the streak camera-based NTD. This instrument is able to measure the neutron bang time of D_2 - and DT-filled capsules at a neutron yield between 10^7 and 10^{11} with an absolute timing accuracy of better than 100 ps, using hard x rays to calibrate the system. A high-stability fiducial system and a high-bandwidth, fast digitizing oscilloscope are both essential to achieve this precision. Neutron bang time uncertainty as low as 50 ps has been demonstrated using cross-calibrations to a higher-precision instrument such as the NTD. This level of accuracy allows the modeling of the implosions to be effectively guided using hydrocode calculations.

ACKNOWLEDGMENT

This work was supported by the U.S. Department of Energy Office of Inertial Confinement Fusion under Cooperative Agreement No. DE-FC03-92SF19460 and the University of Rochester. The support of DOE does not constitute an endorsement by DOE of the views expressed in this article.

REFERENCES

1. J. Nuckolls *et al.*, *Nature* **239**, 139 (1972).
2. N. Miyanaga *et al.*, *Rev. Sci. Instrum.* **61**, 3592 (1990).
3. T. J. Murphy and R. A. Lerche, *ICF Quarterly Report* **3**, 35, Lawrence Livermore National Laboratory, Livermore, CA, UCRL-LR-105821-93-1 (1992).
4. R. A. Lerche, D. W. Phillion, and G. L. Tietbohl, in *Ultra-high- and High-Speed Photography, Videography, and Photonics '93*, edited by P. W. Roehrenbeck (SPIE, Bellingham, WA, 1993), Vol. 2002, pp. 153–161.
5. R. A. Lerche, D. W. Phillion, and G. L. Tietbohl, *Rev. Sci. Instrum.* **66**, 933 (1995).
6. Bicon Newbury, Newbury, OH 44065-9577.
7. Hamamatsu Photonics K.K. (<http://www.hamamatsu.com>).
8. Picosecond Pulse Labs, Boulder, CO 80301.
9. V. Yu. Glebov, D. D. Meyerhofer, C. Stoeckl, and J. D. Zuegel, *Rev. Sci. Instrum.* **72**, 824 (2001).
10. Tektronix Corporation, Beaverton, OR 97077.
11. Laboratory for Laser Energetics LLE Review **87**, 109, NTIS document No. DOE/SF/19460-397 (2001). Copies may be obtained from the National Technical Information Service, Springfield, VA 22161.
12. T. J. Murphy, R. E. Chrien, and K. A. Klare, *Rev. Sci. Instrum.* **68**, 610 (1997).

Functional Damage Thresholds of Hafnia/Silica Coating Designs for the NIF Laser

Introduction

LLE's Optical Manufacturing Group (OMAN) has been tasked with coating several types of optics for use on the National Ignition Facility (NIF) laser system. Until recently, the standard quality assurance technique for coating large optics has been to process a smaller "witness" optic along with the large optic. Tests and inspections performed on the witness optic were used to certify the quality of the larger optic. This approach reduces costs and avoids damage to the production part. (The NIF optics used in this effort were 412 mm square. The corresponding witness optic would be 51 mm in diameter.)

One of the process factors that affects the durability of an optic is the cleanliness of the substrate prior to deposition of the thin-film, high-reflective coating. A particle on the substrate surface that is coated over creates a nodule that is much more likely to fail than any other portion of the coating. Current substrate cleaning and handling methods are so effective, however, that the number of particles per unit area present prior to coating is very small. As a result, the small-surface-area witness substrates have become statistically less likely to represent the damage properties of full-sized parts. For this reason, OMAN has been conducting a damage-testing experiment on its mirror coatings using full-sized NIF substrates. A large-area conditioning (LAC) station designed by LLNL was used for this testing.

The LAC station facilitates testing of full-sized samples by automatically scanning the test optic relative to an optical system that simultaneously irradiates a small area and detects any resulting damage. Repeated scans at increasing fluence were used to quantify the performance of candidate coating designs.

Three candidate high-reflector, thin-film coating designs using hafnia and silica were developed for the LM7E mirrors on the NIF laser. Mirrors were prepared with each candidate and damage tested to provide data that NIF planners could use,

[†]This definition came from a presentation by C. Stolz at LLE regarding NIF definitions of damage.

along with spectrophotometric results, to determine which coating design would work best for the NIF laser.

Objectives and Scope

Coating durability is the main issue investigated in this experiment. The coatings must be durable enough to survive the maximum fluence of the NIF's main beam (fluence being beam pulse energy per square centimeter). The reflectance/transmittance properties at other wavelengths are a secondary issue because the NIF plans to use alignment lasers that will operate on a different wavelength than that of the main beam. The selection of that wavelength can be based on the coating designs of the various optics in the system. Because variations in the coating designs may have positive or negative impact on damage thresholds, the optic's spectral performance and damage threshold are linked. The objective of this experiment is to find the best combination of coating durability and overall spectral performance for the NIF laser.

LLNL's definition of damage is "Functional Damage Threshold (FDT) is the minimum fluence at which a damaged optic degrades the performance of the NIF laser."[†] This represents a departure from traditional damage testing. Using this criterion meant that our first objective was to create some form of damage, and our second objective was to find the practical limit at which the optic could continue to function with that damage present. When the FDT is found, the resulting damage is termed "failure damage." Once failure damage has occurred, that damage site is likely to grow at fluences lower than the FDT. Figure 88.8(a) shows a damage site that has not reached its FDT; Fig. 88.8(b) shows a damage site that has reached its FDT.

If testing is continued on a failure damage site at the FDT fluence, that site will grow very rapidly. However, if the fluence is decreased from the FDT, the rate at which the site grows will decrease correspondingly. The growth threshold fluence (GTF) is the lowest fluence at which a site will continue to grow after it has sustained failure damage. Below the GTF, the size of the failure damage site will remain stable.

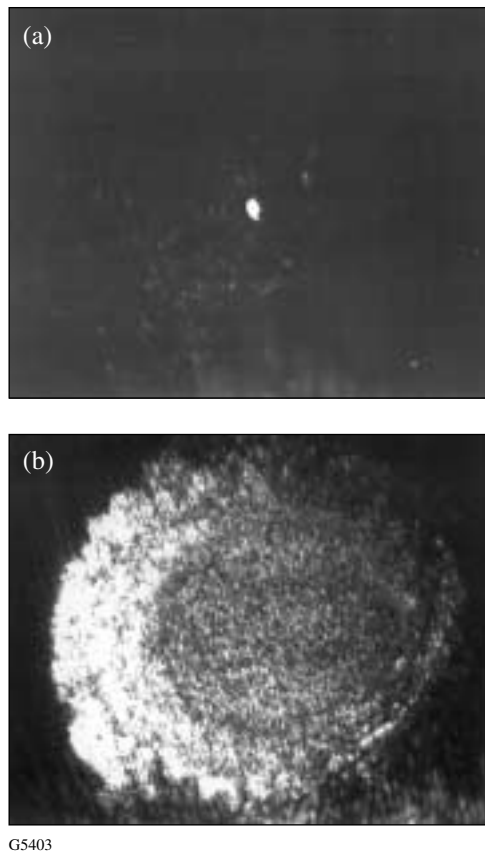


Figure 88.8

(a) A stable damage site ~ 0.13 mm in diameter. (b) The same site, after reaching its FDT. During a single miniscan it grew to ~ 2.3 mm in diameter.

At the GTF, growth occurs at the lowest rate that can be positively detected. The GTF is always lower than the FDT.

During the course of the experiment, it was observed that the rate at which a damaged site grows after reaching the FDT is a function of the fluence used. At the GTF, the damage site is growing slowly enough that its size can be accurately measured. At fluences above the GTF, this becomes more difficult since the damage size quickly grows larger than available equipment can accurately measure. In order to obtain data for large numbers of shots, growth-rate testing was done at the GTF.

In summary, if the FDT, GTF, and the growth rate at the GTF are known, the fluence range over which the optic can perform without being damaged is also known. In addition, should that optic experience failure damage, the resulting operating limits can be estimated. These data can be used along with spectrophotometric results as criteria to select a coating design that is most suitable for the NIF optics.

Coatings

Three coating design options were tested on BK-7 substrates against a requirement of $R_{s_{1054\text{ nm}}} > 99.5\%$ at 42.2° incidence. The NIF will be aligned with a UV laser, with a wavelength between 351 nm and 405 nm. (In this section, $R_{s_{\text{wavelength}}}$ stands for the reflectance in *s*-polarization at the wavelength in the subscript.) The different LLE coating designs try to maximize reflection about 351, 374, or 405 nm while maintaining the 1054-nm specification. They were named the Type-I, -II and -III coatings, respectively.

Types I and II used 22 alternating layers of HfO_2 and SiO_2 to form a first-order stopband reflector at 1054 nm. The refractive indices at 1054 nm are 1.993 for hafnia and 1.456 for silica. This resulted in physical thicknesses of 140.4 nm and 203.9 nm for the Type-I, high- and low-index quarter waves, respectively.

The Type-I and Type-II designs differed in that the stopband of Type II was shifted to 1078 nm, enabling the third-order reflectance $R_{s_{374\text{ nm}}}$ to be $>94\%$. In this design, the reflectance at 1054 nm is still above the specification but a slightly higher E-field is allowed to stand at the substrate/coating interface. Optimally a coating has E-field peaks occurring within a given layer of coating material instead of at an interface since the interface is structurally the weaker of the two. The spectral characteristics of the two types of coatings are shown in Fig. 88.9.

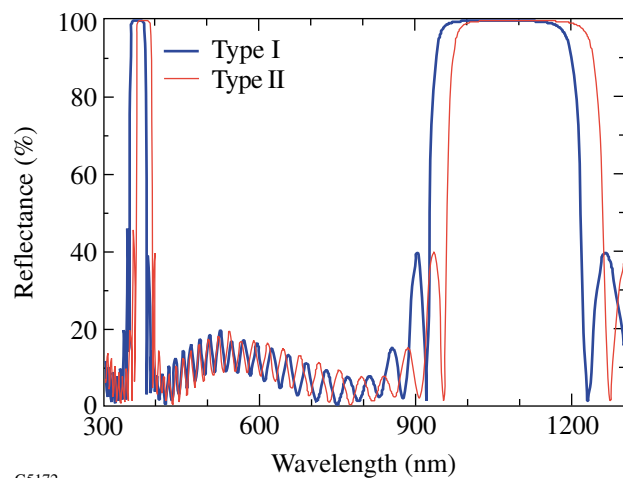
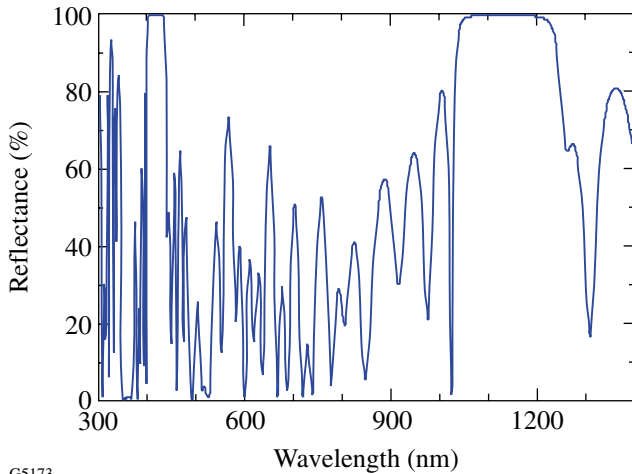


Figure 88.9

Reflectance versus wavelength for Type-I and -II coatings. The Type-II design at 42° incidence has a third-order stopband at 374 nm versus 351 nm for Type I.

The Type-III design is a computer-optimized, 32-layer design, with all layers of non-quarter-wave thickness. This was necessary to obtain $R_{s_{351\text{ nm}}} < 7\%$ and $R_{s_{405\text{ nm}}} > 94\%$ while maintaining $R_{s_{1054\text{ nm}}} > 99.5\%$. Figure 88.10 shows the spectral characteristics of the Type-III design.



G5173

Figure 88.10 Reflectance versus wavelength for Type-III coating. The Type-III design is a non-quarter-wave design achieving high reflectance at 1054 nm and 405 nm while transmitting 351 nm at 42° incidence.

The coatings were deposited using electron-beam sources placed 120 cm below the planetary substrate plane. Hafnia layers were deposited at 0.16 nm/s by the evaporation of pure hafnium metal using a 7.5-kV electron-beam gun. This provided a consistent spit-free vapor in a 1×10^{-4} -Torr oxygen environment. Silica layers were deposited at 0.44 nm/s in 5×10^{-5} Torr of oxygen using an electron-beam gun at 6.0 kV. Achieving the correct oxygen pressure during silica deposition is important in balancing stresses for the two materials in their operating environment, which is air controlled to 40% relative humidity.

Experiment

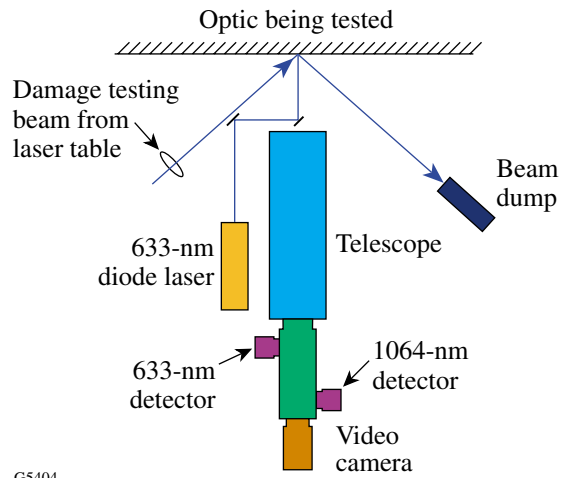
The experiment was conducted using the LLNL-designed LAC station. The LAC station is capable of automating the entire damage testing and damage site detection process with a minimum of operator input. It consists of a precision x-y translation stage (shown in Fig. 88.11) that supports and positions the optic being processed, a fixed optical system for optic monitoring, a laser table that delivers the damage-testing beam and monitors beam characteristics, and a computer controller that operates the system and logs data sets.



G5184

Figure 88.11 The LAC station monitors an optic’s surface quality at the same time it is being damage tested. The translation stage shown here can handle a variety of NIF optics, such as a NIF polarizer, which is 810 × 420 mm. Pictured on the stage is an LM2 substrate, approximately 420 × 420 mm.

The optical system that monitors the test optic is mounted in a fixed position in front of the translation stage (see Fig. 88.12). It is aligned so that the point at which its optical path intersects the front surface of the optic is the same point at which the damage-testing beam strikes the optic and is reflected away into a beam dump. This system uses a 633-nm diode laser to monitor scatter. A small reflector, mounted to the front of the telescope, reflects the diode’s beam toward the



G5404

Figure 88.12 Optic monitoring system.

optic. If there is no scatter, i.e., the optic surface is undamaged, the diode beam will reflect back into this small reflector. If there is scatter, light will miss the reflector and be collected by the telescope. A 633-nm detector mounted to the back of the telescope collects the scatter data and relays it to the computer, which produces a scatter map of the optic.

In addition to the 633-nm detector, there is also a 1064-nm detector. Should the damage-testing beam strike the optic's surface and cause damage, 1064-nm light will scatter instead of reflecting into the beam dump. This scattered light is collected by the telescope and seen by the 1064-nm detector, which relays that data to the computer, which, in turn, produces what is called a "plasma map." A video camera completes the system; its output is sent to a video monitor and to the computer controller. The computer uses this input to capture digital still images when requested by the operator.

The laser table (shown in Fig. 88.13) includes the damage-testing laser (characteristics discussed below), a camera, and a power meter. The camera monitors the beam's cross section, while energy levels are measured via the power meter head. Both sets of data are relayed to the LAC computer program, which calculates the geometric characteristics of the beam based on the camera data and then combines it with the measured energy levels to determine the instantaneous and average fluence of the beam. All of these results are logged by the program.

An OMAN addition to the LAC system was a digital video recorder. The signal was taken from the line connecting the video monitor to the computer. The recorder was used to document the actual damage as it occurred when a miniscan was performed (miniscans are defined below).

The experiment was conducted using the LAC in a class-1000 clean-room environment at LLE as follows: Damage tests were performed by raster-scanning a Q-switched Spectra Physics Quanta-Ray Pro Nd:YAG laser emitting 1064-nm light with a 30-Hz repetition rate and a 10-ns pulse length. Beam characteristics (energy/shot and beam cross section) were sent directly from the data acquisition hardware to the LAC program. The program automated all pertinent calculations and controlled the substrate position with respect to the laser beam. The program scales the fluences it reports to a 3-ns pulse length, using the following experimentally derived scaling equation:

$$F_x = F_y(x/y)^{0.35}, \tag{1}$$

where x and y are the two pulse lengths of interest and F_x or F_y is the fluence at that pulse length.

During the procedure described below, the clear aperture of the optic was divided into two halves: one half was reserved for s -polarization testing, the other for p -polarization. Damage testing was performed on one half of the optic at a time.

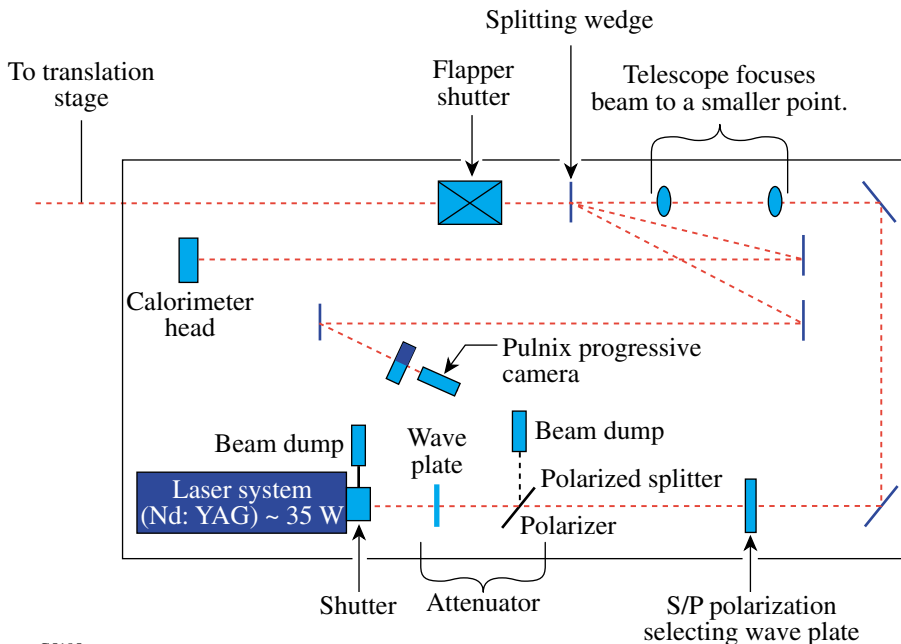


Figure 88.13
Schematic of the LAC laser table layout. The length of the beam path between the splitting wedge and camera is equal to that between the splitting wedge and testing plane.

G5185

A full scan was performed first on the half of the aperture being tested. The fluences (scaled to a 3-ns pulse) used for these scans were 15, 18, 22, 25, 30, and 35 J/cm². After each full scan was completed (approximately 6 h), the scatter map of the optic's surface was examined for possible defect sites. The optic was also examined by eye for possible defect sites.

Once a defect site (or potential defect site) was found, it was made the center of a "miniscan." A miniscan is a 10-mm-wide by 5-mm-tall raster scan, with the candidate defect site at the center. A scatter site was said to be "stable" at a given fluence if no growth occurred after three sets of five miniscans (15 miniscans total) were done on the site. If the site was determined to be stable, another full scan was done at the next-highest fluence. The miniscan process was then repeated at that fluence. This fullscan/miniscan process was repeated until the damage site became unstable.

Once a scatter site was found to be unstable (damage growth occurred prior to the 15th miniscan), the fluence causing the damage growth was recorded as the FDT and determination of the GTF was started.

The procedure used to determine the GTF is the same as that used to determine the FDT, with two exceptions: (1) no full scan is performed, and (2) the first miniscan fluence is 12 J/cm² instead of 15 J/cm² (the scaled-to-3-ns-fluence steps are 12, 15, 18, 22, and 25 J/cm²). The same criteria that determined the FDT also apply to the GTF (three sets of five miniscans). If the damage site was found to be stable at 12 J/cm², the fluence was increased and the procedure repeated.

Data Gathering

Multiple damage sites were examined on each of the Type-I, -II, and -III optics. A photothermal printer was used to produce images of identified damage sites prior to and after each full scan and group of miniscans. These images were then measured with a circle template and scaled to the appropriate dimensions. It should be noted that one constraint of this method is that only the lateral size of defects, not changes in depth, can be measured; therefore, throughout this experiment, damage growth refers only to a change in dimension tangent to the surface of the optic.

The fluence at which a scan, or group of scans, was performed was also recorded, as well as how many of those scans were performed. These three parameters—lateral defect size, scan fluence, number of scans—were then used for analysis.

Data Analysis

The average growth rate can be determined if an extended number of shots are taken at the GTF. Two sites were tested in excess of 50 raster scans at the GTF. A definite trend in the growth of the damage size could be seen when it was plotted as a function of the number of raster scans. A trend line was fit to the data points, the slope of which is the change in size as a function of raster scans, or the average growth rate.

Figure 88.14 is a plot of the data collected at the GTF at two sites. As is evident, the growth rates of these two sites are nearly identical (roughly 14.0 and 14.4 μm/miniscan) through the course of approximately 120 miniscans.

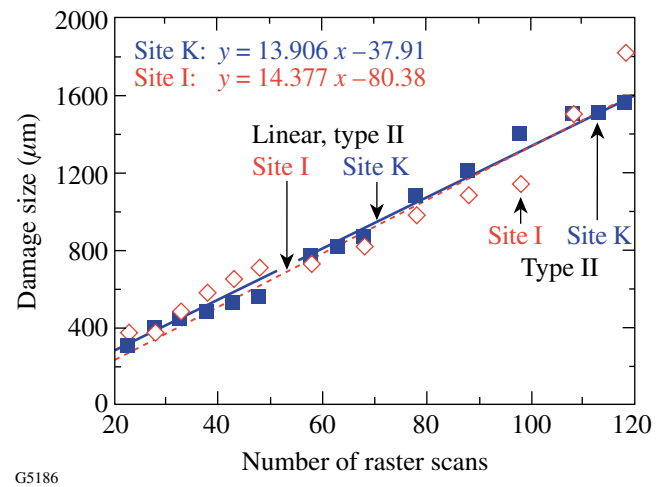


Figure 88.14
Plot of damage size versus number of raster scans at a fluence of 22.5 J/cm² for 10-ns pulses.

Results and Conclusion

The results for the Type-I, -II, and -III coated LM7E's are listed in Table 88.I. Each fluence listed is the lowest for its particular category and is scaled from the 3-ns-pulse-length number reported by the LAC program to its 10-ns counterpart. The FDT numbers represent the lowest damage thresholds found on a particular coating design/polarization. For each coating design/polarization combination, a minimum of ten damage sites were investigated.

The following conclusions can be drawn:

1. The damage thresholds of the Type-I coatings were greater than those of the Type-II or -III coatings.
2. The GTF was the same for all three coating designs.

Due in part to the results of this experiment, the NIF project has decided to go with a slightly modified version of the Type-II coating. This “Type-IV” coating differs from the Type II in that the top and bottom three layers of the coating stack are modified. This was done for two reasons. The first is to improve performance over the Type-II design. The second has to do with an additional requirement (not addressed by this experiment) regarding backscattered stimulated Brillouin scattering (SBS) and 400- to 700-nm stimulated Raman scattering (SRS) light from the target chamber. Spectral measurements performed by LLNL show the Type-IV design more effectively suppresses SBS and SRS than the Type-II design.

ACKNOWLEDGMENT

This work was supported by the U.S. Department of Energy Office of Inertial Confinement Fusion under Cooperative Agreement No. DE-FC03-92SF19460, the University of Rochester, and Lawrence Livermore National Laboratories under subcontract B399901. The support of DOE does not constitute an endorsement by DOE of the views expressed in this article.

Table 88.I: FDT’s and GTF’s for the three LM7E mirror designs.

(All 10 ns in J/cm ²)	<i>p</i> -pol FDT	<i>s</i> -pol FDT	<i>p</i> -pol GTF	<i>s</i> -pol GTF
Type I	37	42	22	22
Type II	37	33	22	22
Type III	33	33	22	22
The precision of the listed fluences is ±3 J/cm ² .				

High-Gain Direct-Drive Target Designs for the National Ignition Facility

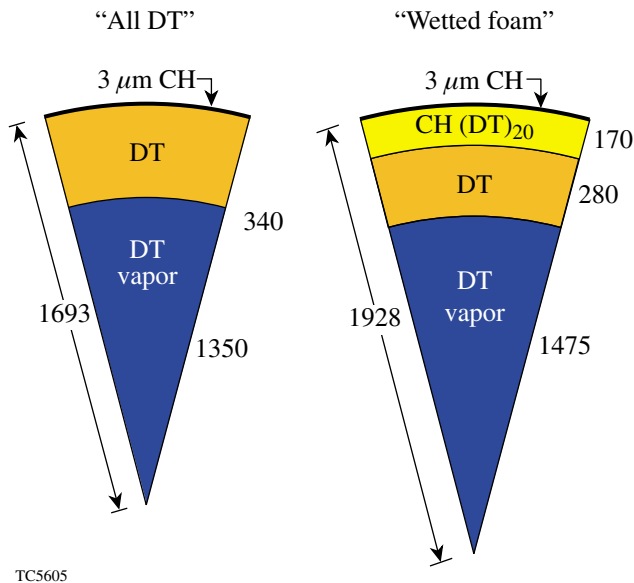
Introduction

Direct drive¹ offers the potential of higher target gain for the National Ignition Facility (NIF)² than indirect drive.³ Direct-drive targets have been designed that reach a gain of 45 in one-dimensional (1-D) simulations using primarily a pure cryogenic DT shell driven on an isentrope where the pressure is three times the Fermi-degenerate pressure ($\alpha=3$). The sensitivity of this design to laser and target-surface nonuniformities has been studied with two-dimensional (2-D) simulations.⁴ At the levels of nonuniformity expected for the NIF, the neutron yield was calculated to be about 70% of the 1-D value, producing a target gain of 30. A second class of targets has the potential of achieving even higher gain. In these designs, the outer portion of the cryogenic DT shell is replaced with a region of low-density CH foam. Liquid DT is “wicked” into the voids of the foam.⁵ The advantage of these “wettered-foam” designs over the “all-DT” target is that the presence of higher-Z material (C) in the laser deposition region results in increased laser absorp-

tion. For the NIF designs, the laser absorption increases by ~40% (going from 60% absorption in DT to 85% in the wetted foam). For a scaled-down version of the wetted-foam target, which can be examined on LLE’s OMEGA laser, the laser absorption is increased by almost a factor of 2, effectively doubling the amount of energy available to drive the target. With the increased laser energy, the capsules can contain an increased amount of fuel. The wetted-foam targets are thicker, providing increased stability, and the additional fuel provides higher neutron yield.

Results–NIF

A comparison between one possible wetted-foam design for the NIF and the base-line “all-DT” design is shown in Fig. 88.15, with the targets drawn approximately to scale. (In Fig. 88.15 and the other figures, distances are labeled in microns and IFAR is the in-flight aspect ratio.) The main result is that the wetted-foam design achieves a 1-D target gain that



1.5-MJ Designs		
	All DT	Wetted foam
Gain	45	120
Absorption (%)	60	85
ρR (g/cm ²)	1.3	1.7
Adiabat (α)	3	2
Peak IFAR	60	50
Margin	44	32

Figure 88.15

Comparison between the wetted-foam and all-DT direct-drive target designs for the NIF. The wetted-foam design has ~40% higher laser absorption and more than twice the target gain.

is almost three times higher than the gain for the all-DT target. Most of this large increase in target gain is directly related to the increase in target size. The foam target is about 30% thicker, its outer diameter is about 20% larger, and it contains about 80% more fuel. Since the foam target is thicker, it can be driven on a lower adiabat ($\alpha = 2$) than the all-DT target ($\alpha = 3$), without compromising shell integrity during the acceleration phase of the implosion. This, combined with the larger fuel mass, results in a 30% increase in the peak areal density ρR (where ρ is the density and R is the radius) achieved by the fuel (1.85 versus 1.3 g/cm²). The fraction of fuel burned (or *fractional burnup*) by thermonuclear reactions is roughly proportional to the peak ρR (in this range). The 80% increase in fuel mass combined with a 30% increase in fractional burnup of the fuel increases the target gain by a factor of 2.5 and accounts for most of the increased gain shown in Fig. 88.15.

A preliminary stability analysis of the wetted-foam design shows that this target is more stable than the all-DT target during the acceleration phase of the implosion. Figure 88.16 shows the result of applying a stability postprocessor⁶ to the 1-D simulations for these targets. The shell thickness and the size of the mixed region resulting from hydrodynamic instabilities are plotted as functions of time. Both simulations use the same “seeds” for the Rayleigh–Taylor instability caused by laser-beam nonuniformity and target-surface roughness. In these simulations the foam is treated as a homogeneous material. The shell size is four times larger than the mix region for the foam target and three times larger for the all-DT target. This improved margin for stability of the foam design is mainly the result of the increased thickness of the target shell.

A similar stability analysis for the deceleration phase of the implosion showed that the fractional distortion of the hot spot was significantly larger for the foam target than for the all-

DT target. This was the result of a lower implosion velocity for the foam target than for the all-DT target: 3×10^7 cm/s versus 4×10^7 cm/s. Because of the lower implosion velocity, the target decelerates for a longer time before the ignition temperature is reached. Lower temperatures during deceleration also reduce the ablative stabilization of the Rayleigh–Taylor growth.⁷ These two factors—increased deceleration time before ignition and increased growth rates—result in increased distortion of the hot spot even though the initial seed for deceleration growth is somewhat smaller for the foam design. These stability estimates will be verified with multidimensional simulations.

To achieve greater stability during the deceleration phase, a second foam design with a higher implosion velocity has been developed. This design (target #1 in Fig. 88.17) is smaller, has a thinner shell, and is less massive than the higher-gain wetted-foam design (target #2 in Fig. 88.17) in order to achieve the higher velocity. The foam density was increased from 30 mg/cm³ to 140 mg/cm³ to maintain high laser absorption for the smaller target. Because the target is thinner, the adiabat had to be increased from $\alpha = 2.0$ to $\alpha = 2.5$ to maintain sufficient stability during the acceleration phase of the implosion. The penalty paid for the increased stability was a reduction in target gain due to the higher adiabat and smaller amount of fuel. Nonetheless, the 1-D target gain for this foam design is still almost a factor of 2 higher than for the all-DT gain: 80 versus 45. A stability analysis for both the acceleration and deceleration portions of the implosion shows distortion comparable to that of the all-DT design, which was calculated to achieve 70% of the 1-D yield.

Results—OMEGA

The high-velocity, wetted-foam design was scaled down to 35 kJ to examine what experiments could be performed using

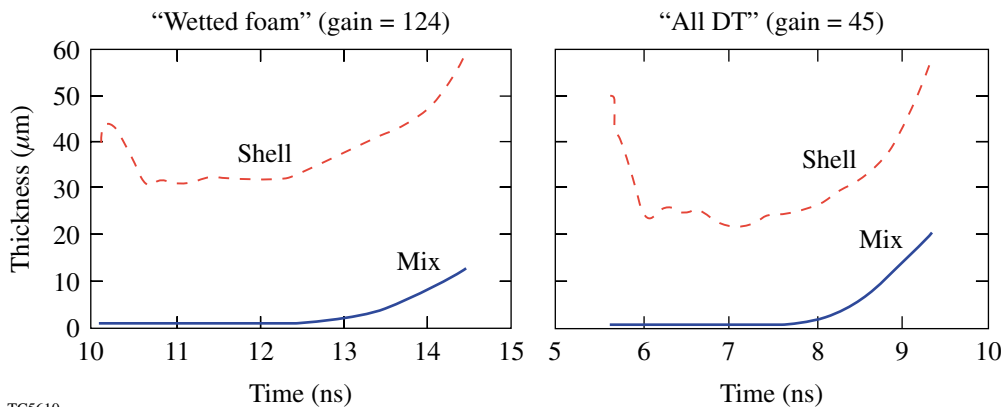
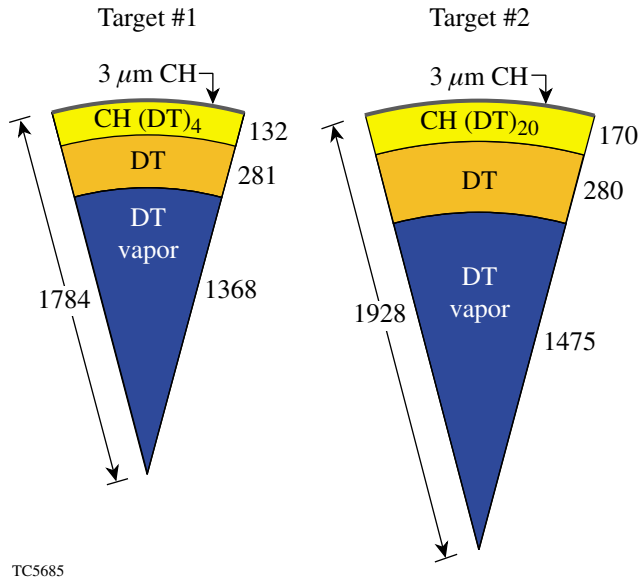


Figure 88.16
Shell thickness and mix thickness as a function of time during the acceleration phase of the implosion for the wetted-foam and all-DT designs shown in Fig. 88.15.

TCS610

the OMEGA laser. The design was tuned to achieve a target gain of 0.3 with the highest-possible adiabat (for maximum stability during acceleration) and the highest-possible implosion velocity (for the maximum stability during deceleration). The target and pulse shape are shown in Fig. 88.18. A target gain in the range of 0.2 to 0.3 would demonstrate the onset of bootstrap heating. Bootstrap heating is the self-heating process whereby alpha particles from the DT reaction deposit their energy back into the fuel and raise the temperature, resulting in a significant increase in the thermonuclear reaction rate. To be

effective, the region of neutron production (hot spot) should be comparable in size to the distance over which alpha particles lose their energy. This corresponds to a ρR of ~ 300 mg/cm². This 35-kJ, wetted-foam design shows a measurable amount of bootstrap heating. The effect of bootstrap heating is seen in Fig. 88.19, which shows the computed neutron yield plotted as a function of variations in the length of the foot of the laser pulse. For the optimal foot length, the neutron yield is highest due to optimal timing of the shocks in the target. To see the effect of bootstrap heating, a second curve in Fig. 88.19 shows

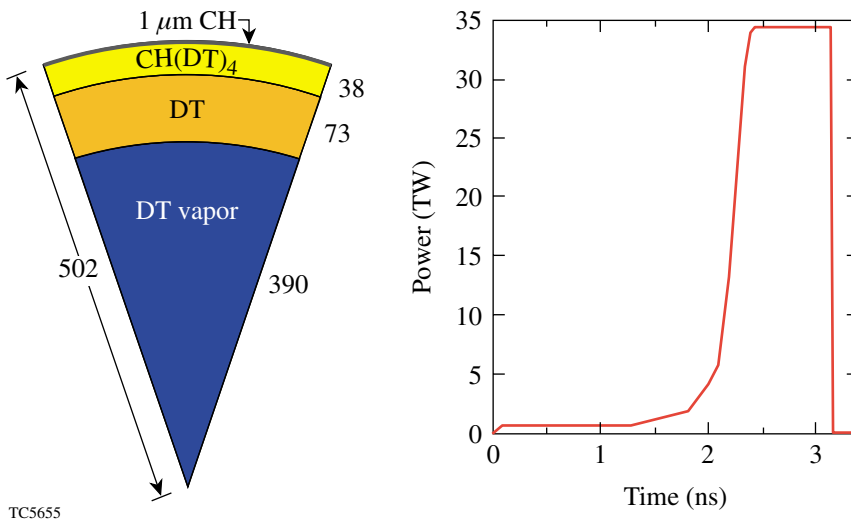


	1.5-MJ Wetted-Foam Designs	
	Target #1	Target #2
Foam (mg/cm ³)	140	30
Gain	81	120
Absorption (%)	90	85
ρR (g/cm ²)	1.4	1.7
Adiabat	2.5	2.0
Margin	48	32
Velocity (cm/s)	4.0×10^7	3.2×10^7

TC5685

Figure 88.17

Comparison between two wetted-foam designs for the NIF. The smaller target has a higher implosion velocity, resulting in greater stability during the deceleration phase of the implosion.



TC5655

Figure 88.18

A 35-kJ wetted-foam design for experiments on the OMEGA laser. This target is a scaled-down version of the smaller target illustrated in Fig. 88.17.

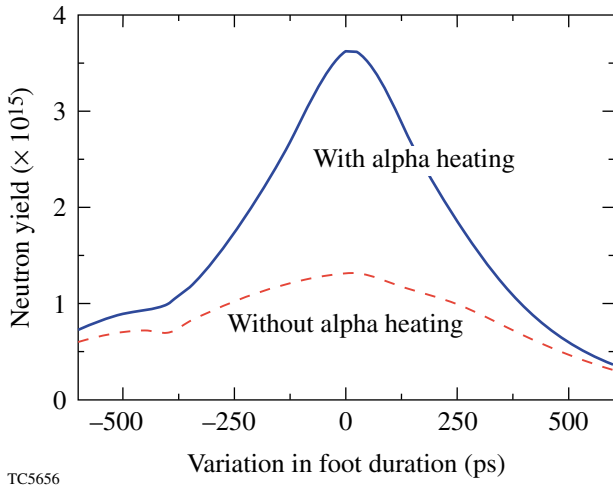


Figure 88.19 The effect of bootstrap heating on neutron yield. Neutron yield is plotted as a function of the length of the foot of the pulse shown in Fig. 88.18. For the optimal pulse length, there is an optimal coalescence of shocks within the fuel, resulting in maximum neutron production. At maximum neutron production there is enough alpha-particle heating of the fuel that the neutron yield is a factor of 3 higher than it would be without this heating.

the neutron yield with alpha-particle heating turned off in the simulation. Under these conditions alpha heating increases the neutron yield by a factor of ~3 at optimal shock timing when the neutron production is largest. Moving away from peak neutron production, the amount of alpha heating becomes too small to significantly increase the temperature. The density and temperature profiles in the fuel at one instant in time during neutron production are shown in Fig. 88.20. The hot region extends close to a ρR of 300 mg/cm^2 , which is the expected condition for bootstrap heating.

To observe these effects on OMEGA, improvements in laser uniformity and target quality are required. The levels of nonuniformity from target-surface roughness and laser nonuniformity would have to be typically a factor of 2 to 4 smaller than required for the NIF because the OMEGA targets are about 3.5 times smaller. An initial stability analysis of this target was performed using a stability postprocessor.⁶ We used a $0.5\text{-}\mu\text{m}$ inner-surface roughness for the DT ice and the laser imprint corresponding to SSD with 1-THz bandwidth and two color cycles and twice the spectral dispersion that is currently used on OMEGA to seed the Rayleigh–Taylor instability from target-surface roughness and laser nonuniformity. These specifications for the laser and target uniformities are beyond

current capabilities on OMEGA, but they should be achievable with extensions of current technology. A plot of shell thickness and mix thickness is shown in Fig. 88.21. At the time of closest approach, the shell is twice as large as the mixed region. This might be adequate but will have to be examined with two-dimensional simulations.

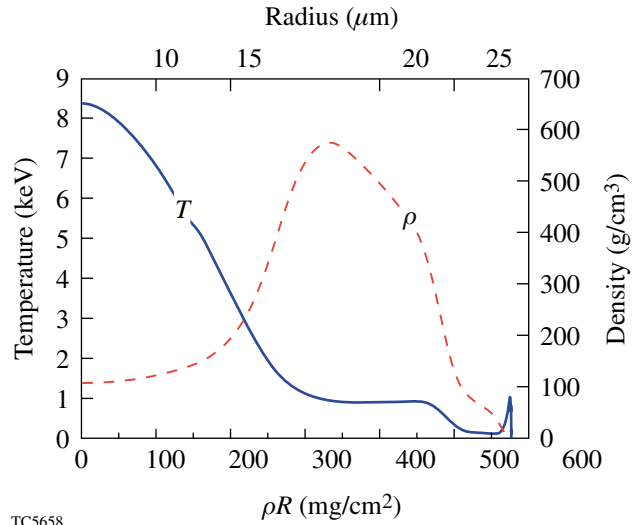


Figure 88.20 Density and temperature profiles at one instant in time during neutron production. The temperature and density profiles of the hot region are characteristic of hot-spot conditions in an igniting target.

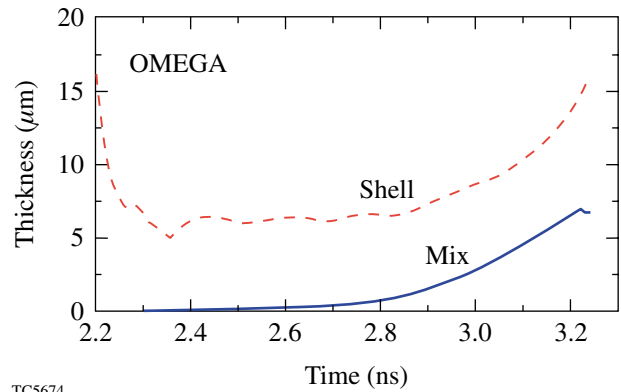


Figure 88.21 Shell thickness and mix thickness as a function of time for the OMEGA wetted-foam design (from Fig. 88.18) during the acceleration phase of the implosion. The laser nonuniformity was a factor of 2 lower than currently achieved on OMEGA, and an inner-surface roughness of $0.5 \mu\text{m}$ was used.

The design presented here will be scaled down to the lower energies (25 to 30 kJ) that can be expected on OMEGA for pulse shapes similar to that shown in Fig. 88.18. While the signal of bootstrap heating will be less dramatic than that shown in Fig. 88.19, the demonstration that this new type of target can be successfully imploded with a greatly increased laser absorption would be an exciting result with significant implications for direct-drive NIF designs. A program for developing the key areas necessary for wetted-foam implosions is being developed. This includes an investigation of the feasibility of fabricating foam shells of the required quality.

ACKNOWLEDGMENT

This work was supported by the U.S. Department of Energy Office of Inertial Confinement Fusion under Cooperative Agreement No. DE-FC03-92SF19460 and the University of Rochester. The support of DOE does not constitute an endorsement by DOE of the views expressed in this article.

REFERENCES

1. J. Nuckolls *et al.*, *Nature* **239**, 139 (1972).
2. M. D. Campbell and W. J. Hogan, *Plasma Phys. Control. Fusion* **41**, B39 (1999).
3. S. E. Bodner, D. G. Colombant, J. H. Gardner, R. H. Lehmborg, S. P. Obenschain, L. Phillips, A. J. Schmitt, J. D. Sethian, R. L. McCrory, W. Seka, C. P. Verdon, J. P. Knauer, B. B. Afeyan, and H. T. Powell, *Phys. Plasmas* **5**, 1901 (1998).
4. P. W. McKenty, V. N. Goncharov, R. P. J. Town, S. Skupsky, R. Betti, and R. L. McCrory, *Phys. Plasmas* **8**, 2315 (2001).
5. R. A. Sacks and D. H. Darling, *Nucl. Fusion* **27**, 447 (1987).
6. V. N. Goncharov, P. McKenty, S. Skupsky, R. Betti, R. L. McCrory, and C. Cherfils-Clérouin, *Phys. Plasmas* **7**, 5118 (2000).
7. V. Lobatchev and R. Betti, *Phys. Rev. Lett.* **85**, 4522 (2000).

Ultrafast Optoelectronic Interface for Digital Superconducting Electronics

Introduction

Ultrafast optoelectronics is an acknowledged field of technological importance for the 21st century, and a very large amount of research has been performed on this topic in recent years.¹ It is estimated that by the year 2006 nearly 13% of developed-world households will be connected to Global Internet via interactive broadband fiber services. This requires very high capacity networks with complex switchboards and routers. Current single-wavelength bit rates for optical fibers are between 2 and 6 Gbit/s, with laboratory demonstrations reaching speeds of up to 40 Gbit/s. Implementation of the optical wave division multiplexing (WDM) technique increases the fiber throughput to well above 1 Tbit/s. Time division multiplexing (TDM) is also an obvious, and in many aspects preferable, multiplexing choice for digital signals to increase the fiber throughput capacity. Implementation of TDM will require ultrahigh-speed transmitters in the electrical domain. Superconducting digital electronics is expected to become the processing medium of choice for these optical telecommunication applications.

The highest-speed digital data processing and manipulation can be achieved using superconducting electronics circuitry based on single-flux-quantum (SFQ) logical devices consisting of a combination of resistively shunted tunnel Josephson junctions (JJ's).² Low-temperature superconducting (LTS) SFQ digital circuits, fabricated in the standard, Nb tri-layer process with 1.5- μm feature size, have demonstrated clock speeds from 20 to 40 GHz. Further reduction of the linewidth to below 0.8 μm would allow JJ circuits to reach speeds of well above 100 GHz, even in complex designs.^{3,4} The road map for the development of SFQ electronics estimates that high-temperature superconducting (HTS) digital circuits should reach 1-THz-range clock rates within the next ten years,⁴ and, indeed, 0.7-ps SFQ pulses generated by intrinsically shunted Y-Ba-Cu-O (YBCO) JJ's have been demonstrated recently.⁵

Integrating SFQ-logic-based processors into ultrafast (e.g., above 30-GHz clock rate), high-performance applications requires, however, a new paradigm for digital input/

output (I/O) communication between the SFQ processor and the outside world. Only optical fiber links can assure multi-GHz bit rates; they are also immune from crosstalk and electromagnetic interference and feature excellent thermal insulation. Together, a SFQ processor and an optical I/O will constitute the new ultrafast optoelectronics, namely superconducting optoelectronics.

This article begins with a general description of a superconducting optoelectronic router followed by, in separate sections, descriptions of progress in the development of optical-to-electrical transducers (OET's) and electrical-to-optical transducers (EOT's), suitable as I/O circuitry for superconducting digital electronics. Finally, a brief summary includes a personal assessment of the current state of the art in the superconducting optoelectronic (I/O) interface.

Superconducting Optoelectronic Router

One of the application areas where superconducting electronics can significantly outperform semiconductor technologies is telecommunication hardware, namely, ultrafast routers and crossbar-type switching structures.⁴ The router is being used in telecommunication systems as the network node that directs the flow of information between different sub-networks. Figure 88.22 shows a schematic of an optoelectronic router.⁶ Information arrives as multiwavelength trains of optical pulses at the router input ports, where, using suitable OET's, it is translated into the electrical domain. Next, information packages are routed to the appropriate output addresses using an ultrafast electronic processing network that provides such packet-switch functions as routing and drop/add, without the need to demultiplex down to lower data rates. Finally, signals are translated again, but this time into the optical domain, using EOT's.

In the superconducting router, the switching circuitry of the electronic information processor is based on the SFQ gates because of their very high switching speed and design simplicity. Present-day SFQ crossbar designs are limited to switching speeds below 10 GHz and utilize copper I/O microwave

transmission lines.⁷ These lines are known to be too dispersive and lossy at frequencies exceeding 30 GHz. They also consume too much cooling power because they constitute a cryogenic-to-room-temperature interface that accounts for up to 75% of the total load. In future-generation, 100-GHz-bandwidth routers, only optical fibers can provide the needed signal transmission bandwidth, as well as excellent thermal insulation. We note that in switching-type systems, contrary to most of the other digital data processing schemes, both the OET's and EOT's have to provide a bandwidth that is at least equal to the operating frequency of the information-processing unit. Thus, the clock rate of the entire router circuit is limited by the digital processor and *not* the I/O circuitry.

In the example in Fig. 88.22, optically coded information has the form of return-to-zero (RZ) pulses. Logical "1's" in subsequent clock cycles are coded as separate pulses, while the absence of a pulse in a given clock cycle is interpreted as logical "0." The RZ coding is optimal for laser pulses and fits naturally to the SFQ logic, which is also coded based on either presence or absence of a pulse in a clock cycle.² Thus, no additional matching circuitry is needed at the I/O ends. Finally, the OET's and EOT's should be optimized for a 1.55- μm -radiation range since this wavelength is the optical communication standard for data transmission.

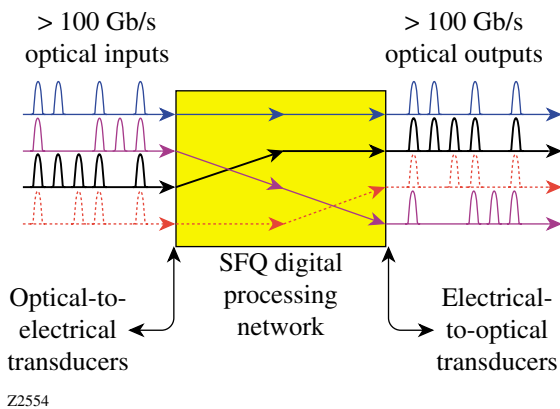


Figure 88.22 Schematic of the superconducting optoelectronics input and output interfaces for an ultrafast SFQ digital information processing network. Each train of optical pulses represents a different optical wavelength due to assumed implementation of the WDM technique.

Superconducting Optical-to-Electrical Transducers

The first superconducting optoelectronic circuit was demonstrated by Dykaar *et al.*^{8,9} As shown in Fig. 88.23(a), a photoconductive metal-semiconductor-metal (MSM) diode (a 50- μm -wide gap in the coplanar line, on the left-hand side of

the junction) was used as the OET, and the generated photoresponse signal was directly applied to switch a tunnel JJ. The structure was fabricated using the Pb-alloy technology¹⁰ on a semi-insulating GaAs substrate, which acted as the active medium for the MSM switch. Since the JJ was not shunted, the circuit operated only with the unbiased junction and when the MSM-generated excitation current pulses (typically ~8 ps wide) exceeded the critical charge (time integral of the pulse) needed to switch a hysteretic JJ into the resistive state.⁹ The circuit was tested using the early version of the cryogenic electro-optic (EO) sampling system,¹¹ with the 50- Ω probe transmission line fabricated on LiTaO₃ and wire-bonded directly to the superconducting coplanar line [Fig. 88.23(a)]. The JJ switching waveform was sampled about 300 μm from the junction [see "sampling point" in Fig. 88.23(a)]. The recorded transient is shown in Fig. 88.23(b).

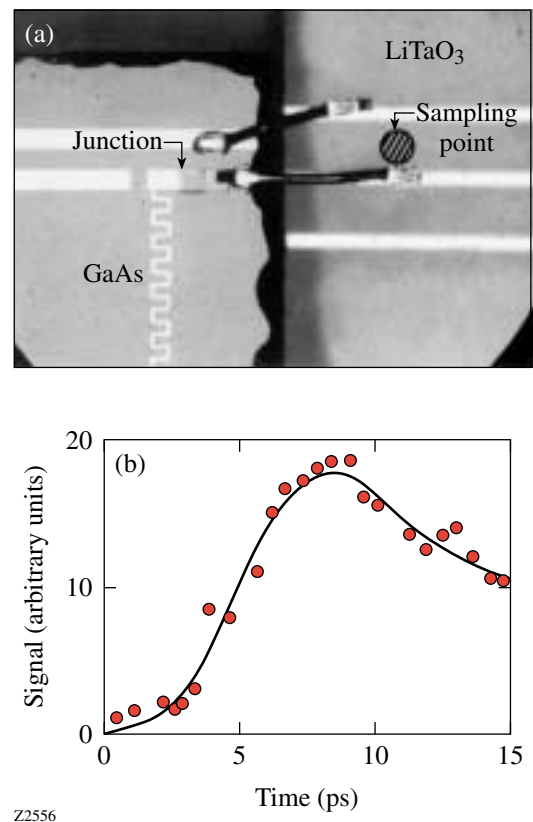


Figure 88.23 (a) Micrograph of an optoelectronic superconducting Pb-alloy circuit consisting of a GaAs photoconductive switch and separately biased Josephson junction (JJ). The circuit is wire-bonded to a transmission line on a LaTiO₃ crystal for EO sampling measurements. (b) Time-resolved switching process of the unbiased JJ shown in (a), driven by an 8-ps-wide electrical transient. The input amplitude was approximately five times the junction critical current. Temperature was 2.1 K.

It exhibits a ~ 3 -ps turn-on delay time, followed by a ~ 5 -ps rise time. The signal fall time is significantly longer, demonstrating that after switching, the junction remained in the transient voltage state, as expected from JSPICE-program numerical simulations.⁹

The usefulness of the structure shown in Fig. 88.23(a) for practical router structures was limited by the use of an unshunted JJ. The hysteretic nature of the junction current–voltage (I – V) characteristics precluded the use of the junction dc bias as an adjustable switching threshold. In addition, the junction exhibited a large resistive-capacitive (RC) time constant, limiting the transducer’s speed of response. Later, Van Zeghbroeck¹² published systematic studies of I – V characteristics of various cryogenic MSM diodes and demonstrated that Nb-Si-Nb devices were compatible with Nb-based JJ circuits.

The next-generation superconducting OET system proposed and implemented by Wang *et al.*¹³ was free of the limitations suffered by its predecessors. The test structures were fabricated at the HYPRES Foundry, using their standard Nb process,¹⁴ and were fully compatible with the current SFQ digital circuit technology. This OET is shown in Fig. 88.24(a) and consists of a Nb-Si-Nb MSM photodiode, integrated with a two-JJ pulse shaper. This arrangement allowed trains of 100-fs-wide optical pulses from an external laser source, incident on the Nb-Si-Nb diode (switching beam), to be transformed into electrical signals and shaped into SFQ pulses by the two-junction Josephson pulse shaper (both JJ’s were externally resistively shunted). The SFQ waveforms were recorded right after the second JJ (sampling beam), using the EO sampling system, and, as shown in Fig. 88.24(b), represented sub-mV, 3.2-ps-wide voltage transients. The integral of the experimental signal was equal to Φ_0 , a quantum of magnetic flux, confirming that indeed the OET output consisted of single SFQ pulses. The measured pulse characteristics were in very good agreement with JSPICE simulations.¹³ The simulations also showed that the width and amplitude of measured SFQ signals were limited by the parameters of the JJ’s used in the pulse shaper and not the Nb-Si-Nb photodiode.

Wide possibilities for superconducting optoelectronic circuits¹⁵ were opened as a result of the successful demonstration that the integrated OET system is indeed able to transform a train of optical pulses into the SFQ-coded input for a superconducting digital electronic circuit at rates of up to 30 Gbit/s for 1.5- μm -feature-size JJ technology (HYPRES standard process¹⁴). Currie, Sobolewski, and Hsiang¹⁶ used Nb-Si-Nb photodiodes to inject approximately 20-ps-wide electrical

pulses into Nb-based superconducting transmission lines to study their propagation properties. They also determined the amount of crosstalk between two Nb microstrips, fabricated at different metallization levels and separated by a dielectric SiO_2 layer (see Fig. 88.25). The time-resolved crosstalk signal was measured using the EO sampler and was >20 dB below the signal propagated in the main transmission line (see “sampling points” in Fig. 88.25). The results were in very good agreement with the simple capacitive model of the signal coupling between the two crossing microstrips. Bulzacchelli *et al.*¹⁷ implemented MSM diodes for an optoelectronic clocking system in which optical pulses were delivered via fiber to a superconducting chip, on which the Nb-Si-Nb OET triggered the SFQ

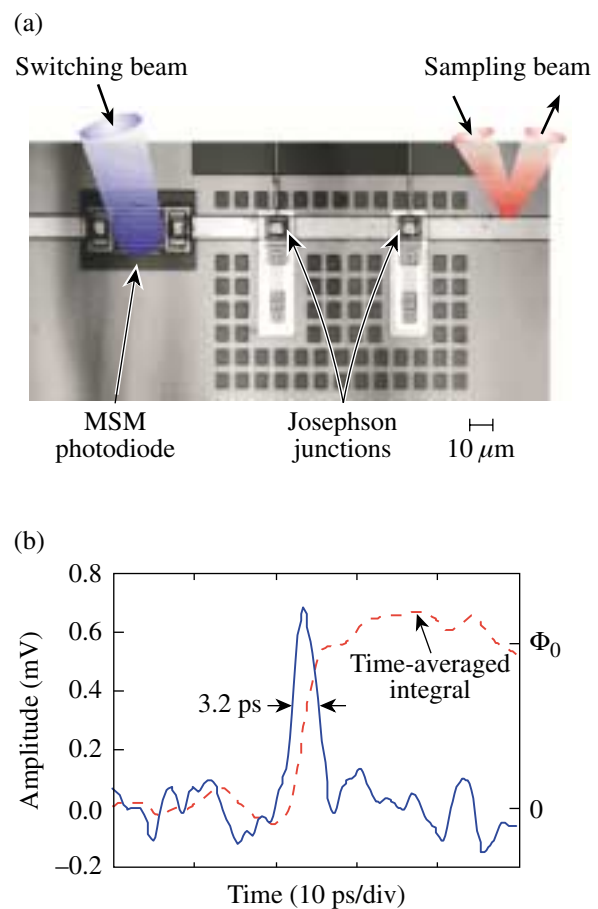


Figure 88.24

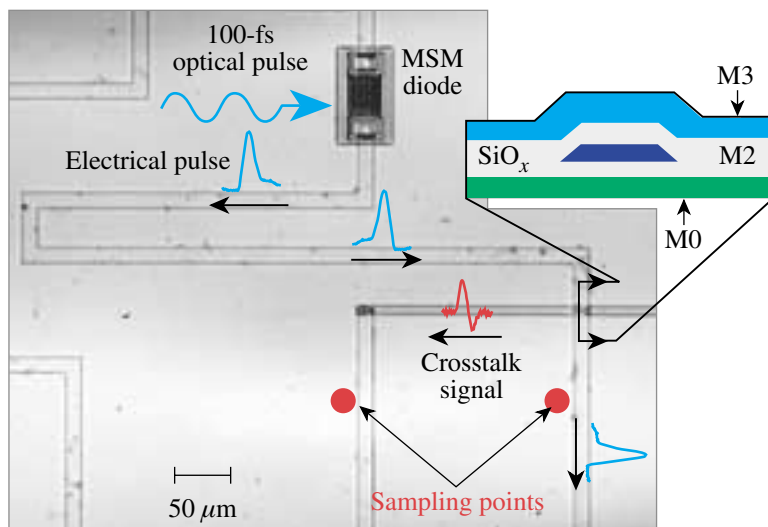
(a) Micrograph of an optoelectronic superconducting Nb circuit consisting of a Nb-Si-Nb MSM photodiode coupled to a microstrip line and followed by a two-junction pulse shaper. The entire circuit was overlaid with a LaTiO_3 crystal for EO sampling measurements (not shown). (b) Time-resolved single SFQ pulse and its time integral. Temperature was 2.1 K.

circuit at frequencies reaching 20.6 GHz. As in the work by Wang *et al.*,¹³ all of these electronic structures were fabricated in the standard, Nb-trilayer HYPRES process.¹⁴

The discovery of HTS materials offered the promise that HTS digital electronics can reach terahertz clock speeds.^{3,4} The characteristic response times of HTS are of the order of single picoseconds¹⁸ and intrinsically shunted YBCO JJ's exhibit a characteristic voltage close to 8 mV,¹⁹ predicting that the corresponding SFQ pulse width, generated during the junction switching event, should be well below 100 fs. To achieve comparable, subpicosecond electrical excitations, Osbahr *et al.*²⁰ used amorphous GaAs, deposited directly on a coplanar YBCO transmission line. The structure acted as a MSM diode, and the authors successfully generated the shortest 0.4-ps-wide electrical input pulses reported to date (~ 2 -THz digital bandwidth). The pulses were used to study propagation properties of YBCO transmission structures. It is interesting that GaAs did not "poison" the YBCO; however, an overlay of Au on the YBCO strips was needed to sustain the highest, THz-frequency components in the propagating pulses. This latter result confirmed the earlier studies²¹ that at above 300 GHz, microwave loss of superconducting YBCO actually exceeds that of normal metals, such as Au or Cu, kept at 77 K.

Independently of semiconducting MSM-type devices, both LTS^{22,23} and HTS¹⁸ microbridges, operated as hot-electron photodetectors, have been proposed as OET's. For LTS photodetectors, NbN was the material of choice since it is character-

ized by a ~ 30 -ps photoresponse time,²⁴ the fastest among conventional superconductors. In the case of HTS structures, the YBCO microbridge was successfully implemented as an optoelectronic interface for switching a grain-boundary YBCO junction.⁵ Figure 88.26(a) presents an integrated YBCO microbridge plus a YBCO–JJ structure. The bridge was independently biased (not shown) and, upon illumination with a femtosecond optical pulse (excitation beam), generated ~ 2 -ps-wide electrical transients, which were then applied to switch the dc-biased JJ. Time-resolved dynamics of the junction were studied with the help of the EO sampling system (sampling beam). The actual test geometry, shown in Fig. 88.26(a), was characterized by a large inductance parallel to the JJ, due to the extended, right-angle-type junction leads. Nevertheless, the authors were able to extract the actual junction switching process and demonstrate [see Fig. 88.26(b)] that the response consisted of a train of 0.65-ps-wide SFQ pulses. The measured signal was in very good agreement with JSPICE simulations performed for a shunted JJ with the characteristic voltage of 2.1 mV. The JJ's estimated power consumption associated with the SFQ pulse generation was $\sim 0.1 \mu\text{W}$, leading to a "switching time" \times "dissipation power" product equal to 0.08 aJ, the lowest reported value for any digital device. Further JSPICE simulations²⁵ predicted that YBCO JJ's with the characteristic voltage above 3.5 mV (well within the reach of the current HTS JJ technology¹⁹) should generate SFQ pulses with a width of < 300 fs, which corresponds to a 3-dB bandwidth of > 1 THz, breaking yet another "barrier" in the development of digital technologies.



Z2312

Figure 88.25

Micrograph of an experimental setup for measuring crosstalk. The circuit uses an MSM diode to generate a picosecond electrical transient, which propagates along the main microstrip line (MSL) and then crosses above the other. At the intersection each line is on a different metallization layer. The signals on the two MSL's are detected at sampling points by the EO system.

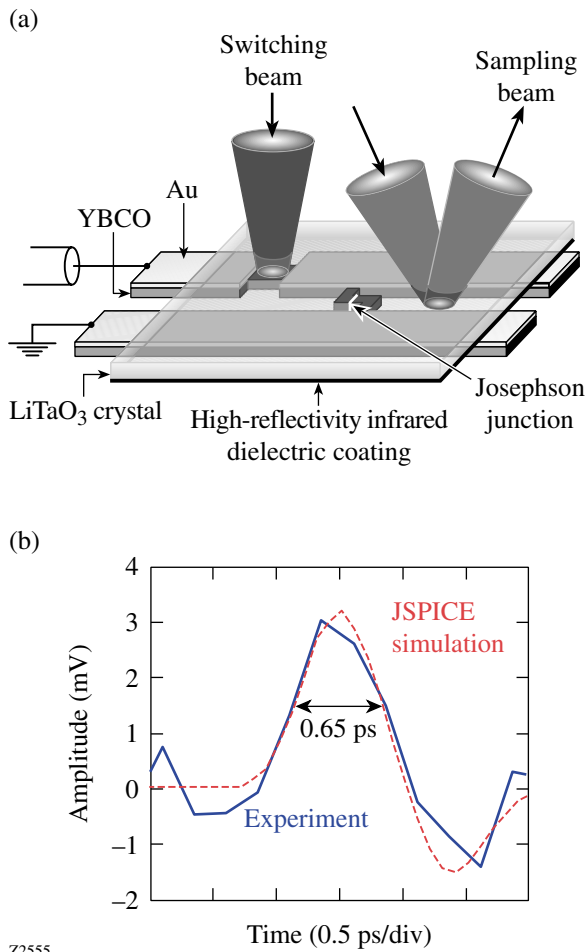


Figure 88.26

(a) Schematic of a coplanar strip transmission line containing a YBCO microbridge and a bicrystal JJ. The entire circuit is overlaid with a LaTiO₃ crystal for EO sampling measurements. (b) Time-resolved, single SFQ pulse and the corresponding numerical JSPICE simulation. Temperature was 20 K.

Superconducting Electrical-to-Optical Transducers

Both the OET and EOT ends of the telecommunication router must, of course, operate at the same speed. In the case of the superconducting crossbar, in the best scenario, the EOT should be able to transform a sequence of “0” and “1” SFQ pulses directly into optically coded information. The design of the SFQ-to-optical output interface is a very challenging problem, mainly due to the extremely low energy being carried by SFQ pulses, and, so far, there are no satisfactory practical solutions. Several new concepts, however, designed specifically for digital superconducting electronics, have recently been proposed.

The first optical output interface for JJ electronics was proposed by Van Zeghbroeck¹² in the form of an actively modulated GaAs/AlGaAs semiconductor laser diode with a sub-mA threshold current. The GaAs/AlGaAs laser diodes were selected because of their low power dissipation and large modulation bandwidth. The first actual implementation of the laser-diode EOT system in a JJ latching integrated circuit was achieved by Nakahara *et al.*²³ The authors used the special high-voltage Josephson circuit to increase the signal level to about 10 mV and then amplified it using a liquid-helium HEMT (high-electron-mobility transistor) semiconducting amplifier. Subsequently, the output was fed into a liquid-He InGaAsP laser. Although only low-frequency tests were performed, the expected maximum speed of the output circuitry was estimated to be approximately 1 GHz.

A laser diode operating at 4.2 K was also used by the HYPRES team^{26,27} to provide a serial output data stream via an optical fiber from a superconducting analog-to-digital converter (ADC) to room-temperature conventional electronics. The output from the ADC was linearized with a parallel-to-serial converter, amplified with an on-chip driver (Josephson amplifier), and used to modulate a laser diode biased at the lasing threshold. The authors also investigated in detail the performance of various laser diodes fabricated for operation at 4.2 K.²⁷ They found that, at low temperatures, the current threshold for lasing reduces significantly, resulting in much lower input power being needed to operate the laser. Unfortunately, the dynamic resistance (dV/dI) also increases significantly near the lasing threshold and the power efficiency (dP_{out}/dI) decreases. To successfully operate a laser as a superconducting EOT, its dynamic resistance should be as small as possible, so that an appreciable current modulation is produced when a small voltage signal is applied. At the same time, dP_{out}/dI should be as large as possible, to get a large modulation of the optical power output. The analysis presented in Ref. 27 indicated that $dV/dI < 10 \Omega$ and $dP_{\text{out}}/dI \geq 0.5 \text{ mW/mA}$ are required for robust operation of a laser-based optical output interface for superconducting electronics. More research on cryogenic laser diodes is needed to achieve these parameters.

Recently, Sobolewski and Park²⁸ proposed a magneto-optic (MO) modulator as an ultrafast EOT. The main advantage of a passive modulation scheme is that it requires only a sensitive medium and optimized coupling between electrical and optical signals to obtain the desired modulation efficiency and speed of response. For cryogenic systems, it is very important that

fiber-coupled modulators represent only a minor thermal load. While the MO effect has been applied to optical modulators²⁹ in current, conventional optoelectronic systems, ultrafast EO modulators are used exclusively as EOT's. Unfortunately, the EO modulators are not practical for superconducting electronics since they require high-voltage driving signals and, thus, are incompatible with SFQ gates.

MO modulators based on the Faraday effect offer a number of advantages for superconducting optoelectronics. Many MO materials, including the most-sensitive europium monochalcogenides, exhibit MO properties only at temperatures below 20 K,³⁰ while the Verdet constant for diluted-magnetic semiconductors, or garnets, increases drastically at low temperatures. In addition, some MO crystals (e.g., EuS and EuSe) are characterized by <2-ps response times, assuring above-150-GHz, 3-dB analog bandwidth.³¹ In garnets, the response is limited by the ferromagnetic resonance frequency (e.g., 82.3 GHz for Bi-YIG³²) with potential for reaching >1 THz.

Figure 88.27 shows the concept of a superconducting MO modulator based on a microwave microstrip line (MSL) with a polarization-sensitive MO active medium and fiber-optic cw

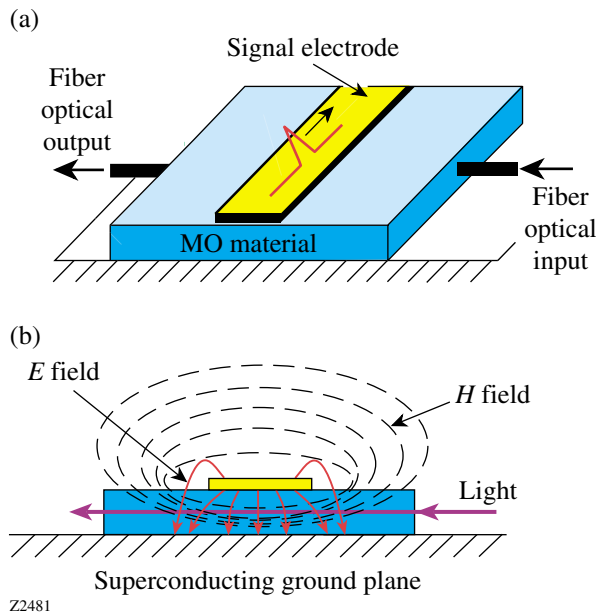


Figure 88.27 Structure of a superconducting MO modulator proposed in Ref. 28. (a) Modulator geometry. (b) Cross section schematically showing spatial distribution of the E and H fields.

light delivery [Fig. 88.27(a)]. The MSL configuration, with the superconducting ground plane, allows for a long interaction distance, and the low characteristic impedance of the line assures that the H -field component of the electromagnetic signal is uniform along the modulator length [Fig. 88.27(b)]. Light modulation direction occurs in parallel to the H field and perpendicular to the signal propagation. Unlike most common EO modulators, this eliminates the need to match the velocities of the electromagnetic signal and light, unless a multipass design is considered. Numerical simulations showed that for the 100- μm -wide, 5- μm -high MSL, filled with the EuSe MO material and assuming that the input current pulse is 1 mA (10-kA/cm² critical current density for a nominal 10- μm^2 Josephson tunnel junction), the H uniformity along the optical pass is >98% and the angle of Faraday rotation for green light reaches $\sim 0.13^\circ$. In a crossed-polarizers modulator geometry, such a polarization rotation angle should give a signal-to-noise ratio of above 10 in the 160-GHz bandwidth of Ref. 33.

Conclusion

Various concepts for ultrafast I/O interfaces for digital superconducting electronics suitable for telecommunication routers have been reviewed. For the input OET, it has been demonstrated experimentally that both the amorphous GaAs photoconductive switch and the YBCO hot-electron photodetector are able to transform the >100-Gbit/s optically coded input information to the electrical domain with sufficient signal-to-noise ratio, speed, and power loading. The Nb-Si-Nb diode is also a desired solution, primarily because of the ease of integration with the standard Nb JJ fabrication process. The Nb MSM's, however, should be patterned with deeply submicron dimensions to reach the single-picosecond response times needed for the ultrafast router applications. From the bias point of view, MSM-type structures have a significant advantage over hot-electron photodetectors since they are highly resistive in the OFF state and do not load the circuit. On the other hand, the responsivity of superconducting photodetectors is significantly higher. Most recently, NbN photodetectors have been demonstrated to respond to single visible and infrared photons,³⁴ making them the leading candidate for future quantum communication and quantum cryptography systems.

Optoelectronic output from the superconducting electronics and, especially, the direct SFQ-to-optical transition is very difficult since SFQ pulses carry very little energy. There is no proven concept that achieves both the needed >100-Gbit/s speed and the required sensitivity. The active laser-diode modulation scheme allows for direct modulation of the optical

output at the processor clock frequency; however, for SFQ electronics, it requires substantial, broadband amplification of SFQ pulses or high-voltage latching Josephson output drivers to drive the laser. In addition, the laser itself, placed inside the dewar, is a significant source of thermal loading. Laser modulation can be a viable option in systems where the output signal has relatively low clock frequency (e.g., in digital decimation filters) since the current EOT designs are limited to speeds of approximately 1 GHz. Extensive research is needed to develop a semiconductor laser diode optimized for ultrafast performance at cryogenic temperatures.

Passive modulation schemes seem to be the approach of choice since, in the modulator case, one needs to achieve only an “imprint” of the SFQ-coded information onto the optical beam to carry it into room temperature and, subsequently, process it using conventional optoelectronics. Passive modulation, based on EO modulators, is the current optoelectronic industry standard. Among optical modulators for superconducting SFQ electronics, MO devices are favored by the author since, at least based on the literature and ultrafast sampling measurements conducted by Freedman,^{31,32} they seem to be fast and sensitive enough, and their performance is actually improved at cryogenic temperatures. The first comprehensive demonstration, however, is yet to be performed.

ACKNOWLEDGMENT

This work was supported by the US Office of Naval Research Grant N00014-00-1-0237.

REFERENCES

1. P. Lagasse *et al.*, *Photonic Technologies in Europe* (Telenor AS, R&D, Norway, 1998), <http://www.infowin.org/ACTS/ANALYSYS/PRODUCTS/THEMATIC/PHOTONIC/>.
2. K. K. Likharev and V. K. Semenov, *IEEE Trans. Appl. Supercond.* **1**, 3 (1991).
3. K. Likharev, *Phys. World* **10**, 39 (1997).
4. P. Bunyk, K. Likharev, and D. Zinoviev, *Int. J. High Speed Electron. Syst.* **11**, 257 (2001).
5. R. Adam, M. Currie, C. Williams, R. Sobolewski, O. Harnack, and M. Darula, *Appl. Phys. Lett.* **76**, 469 (2000).
6. J. X. Przybysz, Northrup Grumman, private communication (1995).
7. Q. Ke *et al.*, *IEEE Trans. Appl. Supercond.* **7**, 2968 (1997).
8. D. R. Dykaar, R. Sobolewski, T. Y. Hsiang, and G. A. Mourou, *IEEE Trans. Magn.* **MAG-23**, 767 (1987).
9. D. R. Dykaar, R. Sobolewski, and T. Y. Hsiang, *IEEE Trans. Magn.* **25**, 1392 (1989).
10. See, e.g., W. Anacker, *IBM J. Res. Dev.* **24**, 107 (1980).
11. D. R. Dykaar, R. Sobolewski, J. M. Chwalek, T. Y. Hsiang, and G. A. Mourou, in *Advances in Cryogenic Engineering*, edited by R. W. Fast (Plenum Press, New York, 1988), Vol. 33, pp. 1097–1104; see also M. Lindgren, M. Currie, C. A. Williams, T. Y. Hsiang, P. M. Fauchet, R. Sobolewski, S. H. Moffat, R. A. Hughes, J. S. Preston, and F. A. Hegmann, *IEEE J. Sel. Top. Quantum Electron.* **2**, 668 (1996).
12. B. Van Zeghbroeck, *IEEE Trans. Appl. Supercond.* **3**, 2881 (1993).
13. C.-C. Wang, M. Currie, D. Jacobs-Perkins, M. J. Feldman, R. Sobolewski, and T. Y. Hsiang, *Appl. Phys. Lett.* **66**, 3325 (1995).
14. *HYPRES Process Design Rules Manual*, HYPRES, Inc., Elmsford, NY 10523.
15. C.-C. Wang, M. Currie, D. Jacobs-Perkins, R. Sobolewski, T. Y. Hsiang, and M. J. Feldman, in *Applied Superconductivity 1995*, edited by D. Dew-Hughes, *Proceedings of EUCAS 1995* (Institute of Physics, Bristol, UK, 1995), Vol. 2, pp. 787–791.
16. M. Currie, R. Sobolewski, and T. Y. Hsiang, *Appl. Phys. Lett.* **73**, 1910 (1998).
17. J. F. Bulzacchelli *et al.*, *IEEE Trans. Appl. Supercond.* **7**, 3301 (1997).
18. M. Lindgren, M. Currie, C. Williams, T. Y. Hsiang, P. M. Fauchet, R. Sobolewski, S. H. Moffat, R. A. Hughes, J. S. Preston, and F. A. Hegmann, *Appl. Phys. Lett.* **74**, 853 (1999).
19. M. A. J. Verhoeven *et al.*, *Appl. Phys. Lett.* **69**, 848 (1996).
20. C. J. Osbahr *et al.*, *Appl. Phys. Lett.* **74**, 1892 (1999).
21. M. C. Nuss *et al.*, *IEEE Electron Device Lett.* **11**, 200 (1990).
22. M. Zorin *et al.*, *IEEE Trans. Appl. Supercond.* **7**, 3734 (1997).
23. K. Nakahara *et al.*, *IEEE Trans. Appl. Supercond.* **4**, 223 (1994).
24. K. S. Il'in, I. I. Milostnaya, A. A. Verevkin, G. N. Gol'tsman, E. M. Gershenzon, and R. Sobolewski, *Appl. Phys. Lett.* **73**, 3938 (1998).
25. R. Adam, R. Sobolewski, and M. Darula, in *Superconducting and Related Oxides: Physics and Nanoengineering IV*, edited by D. Pavuna and I. Bozovic (SPIE, Bellingham, WA, 2000), Vol. 4058, pp. 230–244.

26. L. A. Bunz, R. Robertazzi, and S. Rylov, *IEEE Trans. Appl. Supercond.* **7**, 2972 (1997).
27. D. Gupta, D. V. Gaiarenko, and S. V. Rylov, *IEEE Trans. Appl. Supercond.* **9**, 3030 (1999).
28. R. Sobolewski and J.-R. Park, *IEEE Trans. Appl. Supercond.* **11**, 727 (2001).
29. P. K. Tien and R. J. Martin, *Appl. Phys. Lett.* **21**, 394 (1972).
30. M. P. Mulloy, W. J. Blau, and J. G. Lunney, *J. Appl. Phys.* **73**, 4104 (1993).
31. M. R. Freeman, *J. Appl. Phys.* **75**, 6194 (1994).
32. A. Y. Elezzabi and M. R. Freeman, *Appl. Phys. Lett.* **68**, 3546 (1996).
33. R. Rey-de-Castro and W. Glomb, LLE, private communication (2001).
34. G. N. Gol'tsman, O. Okunev, G. Chulkova, A. Lipatov, A. Semenov, K. Smirnov, B. Voronov, A. Dzardanov, C. Williams, and R. Sobolewski, *Appl. Phys. Lett.* **79**, 705 (2001).

Optimizing the Fabrication of Polyimide Shells

Introduction

Polyimide is being developed as an ablator material for inertial confinement fusion (ICF) targets because of its superior mechanical and thermal properties.¹ A typical target design for the OMEGA laser system consists of a spherical shell, 1 mm in diameter and 1 μm in wall thickness, with a 100- μm -thick layer of solid deuterium and tritium (DT) uniformly deposited on the inner surface. To achieve this, the shells must be both strong and permeable so that they can be filled quickly with DT gas and survive the pressure gradient created in subsequent treatments, including cooling to below 18.9 K and layering by differential heating. Material properties that determine the performance of shells as targets include gas permeability, Young's modulus, tensile strength, and elongation at break.²

Fabrication of spherical polyimide shells has been demonstrated using a vapor deposition polymerization (VDP) method, and preliminary characterization of the shell properties has been conducted.²⁻⁴ In this work, a parametric study was performed on the fabrication process of polyimide shells. The production rate, yield, and reproducibility of the process were optimized. The shells were thoroughly characterized to determine the material properties, microstructures, and surface finish, which were then correlated with the processing parameters. The permeability was also determined at cryogenic temperatures between 130 K and 295 K.

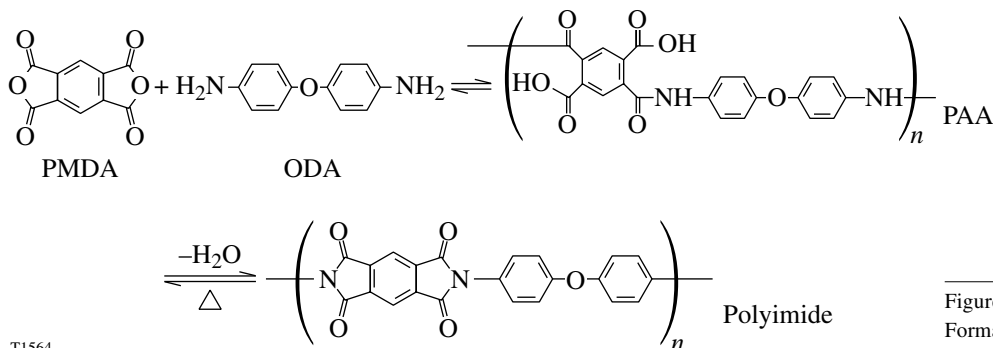
Experimental

1. Fabrication

a. Materials. 1,2,4,5-benzenetetracarboxylic dianhydride (PMDA) (97% purity) and 4,4'-oxydianiline (ODA) (99+% purity; zone refined) were purchased from Aldrich Chemical and used as received. Spherical shells, $\sim 910 \mu\text{m}$ in diameter with a 7- to 17- μm wall thickness and $>99.8\%$ sphericity, made of thermally depolymerizable poly- α -methylstyrene (PAMS) with a molecular weight (MW) of 400,000 were received from General Atomics and used as mandrels without further treatment.

b. Deposition. The fabrication process involved two steps. PMDA and ODA were vapor deposited to form poly(amic acid) (PAA) on either PAMS mandrels or flat substrates. The PAA layer was then converted into polyimide by thermal imidization. In this process, the PAMS mandrels depolymerized and permeated out of the nascent polyimide layer, resulting in freestanding shells. The chemical reaction scheme is shown in Fig. 88.28.

A schematic of the deposition system is shown in Fig. 88.29. The two monomers were separately sublimed from two evaporators directed toward a rotating coating stage.³ The vacuum chamber was maintained at 4.8 to 5.2×10^{-6} Torr throughout deposition. The individual deposition rates of PMDA and ODA



T1564

Figure 88.28

Formation of polyimide from PMDA and ODA.

were measured by depositing each of them separately onto 0.3-cm² PAMS films, which were weighed, before and after deposition, to an accuracy of $\pm 0.05 \mu\text{g}$ using a microbalance (Cahn model 4700). The monomer deposition rates were measured for discrete evaporator temperatures and substrate positions to determine the conditions that yielded equimolar deposition of the monomers. A $3 \times 5\text{-cm}^2$ shutter plate was used to shield the substrate for approximately 30 min until the steady-state deposition rates were reached.

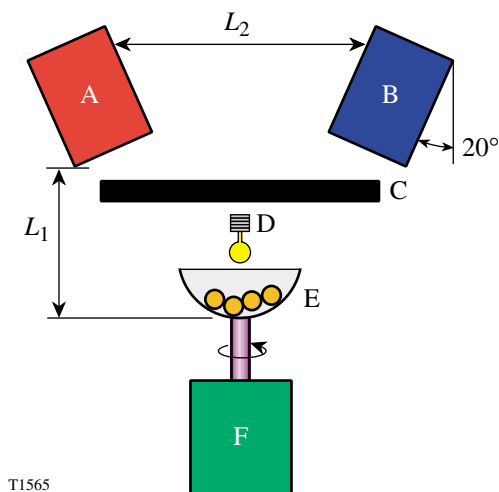


Figure 88.29
Schematic of the deposition system inside the vacuum chamber. A: evaporator for ODA; B: evaporator for PMDA; C: shutter; D: tungsten lamp filament; E: rotating pan with shells; F: motor. Dimensions: $L_1 = 3 \text{ cm}$; $L_2 = 5 \text{ cm}$.

Batches of 20 to 60 PAMS mandrels were over-coated in a 1-cm-diam hemispherical aluminum holder rotating at 60 to 120 rpm.⁵ The static charge created by the motion of the mandrels was neutralized by flooding the entire holder with electrons from a biased tungsten filament (12 V; 20 mA) 0.5 cm above the holder. To examine the effect of a heated substrate, the temperature of the PAMS mandrels was raised from room temperature to 140°C . This was achieved by clamping the shaft of the rotating pan between two copper fingers that were connected to a cartridge heater. The temperature was controlled with an OMEGA CN9001 temperature controller. The pan was preheated at 140°C for 2 to 3 h before deposition began.

Flat films were deposited on either silicon wafers ($1 \times 1 \text{ cm}^2$) or sodium chloride disks (1.3-cm diameter and 0.1-cm thickness; purchased from International Crystal Labora-

tory), which were also rotated at 60 to 120 rpm. The deposition rate was $\sim 7 \mu\text{m/h}$ for flat films and $\sim 3 \mu\text{m/h}$ for shells at room temperature.

c. Imidization. The as-deposited PAA shells were imidized in a NEY Centurion VPM vacuum furnace with programmable temperature (accuracy = $\pm 0.1^\circ\text{C}$). The furnace was purged by a constant $7.5\text{-cm}^3/\text{min}$ flow of nitrogen or air throughout the imidization process. The temperature cycle consisted of a ramp-up (0.1, 0.5, or $1^\circ\text{C}/\text{min}$) from 25 to 300°C , a soak at 300°C for a predetermined duration (1, 3, or 6 h), and cooldown to 25°C at $5^\circ\text{C}/\text{min}$. Images of the shells during imidization were recorded and analyzed to monitor the changes in shell diameter with temperature. Imidized flat films were detached from the substrates by soaking in de-ionized water at 90°C for 24 to 48 h. The films were then dried at 80°C under vacuum for 24 h.

2. Characterization

a. Chemical analysis. Fourier transform infrared (FTIR) spectra were obtained using films approximately $1 \mu\text{m}$ thick deposited on sodium chloride disks. The elemental composition was determined by combustion analysis performed by Oneida Research Services using freestanding films with mass of approximately 10 mg. Solubility was examined by soaking films and shells in concentrated sulfuric acid (97%) at room temperature. The size of the samples was monitored using an optical microscope throughout soaking.

b. X-ray diffraction (XRD). The tested samples included (1) freestanding films ($1 \text{ cm} \times 1 \text{ cm} \times 25 \mu\text{m}$), (2) shells, and (3) flat films made of 10 to 20 flattened shells. A Rigaku D2000 Bragg-Brentano diffractometer⁶ equipped with a copper rotating anode, diffracted beam graphite monochromator, and scintillation detector was used to obtain reflection-mode diffraction patterns from film samples. Data were collected as continuous scans, at a scan rate of $2^\circ 2\theta/\text{min}$. A Bruker AXS microdiffractometer⁷ equipped with a copper rotating anode, Goebel mirrors, a 0.5-mm collimator, and a two-dimensional general area detector diffraction system (GADDS) was used to obtain transmission-mode diffraction patterns for shell and film samples and reflection-mode diffraction patterns for shell samples. Each data set was collected until 10^7 -count total integrated intensity was achieved.

c. Dimensions and surface finish. Shell diameter was measured to an accuracy of $\pm 1 \mu\text{m}$ using a Nikon Optiphot microscope, and the wall thickness was calculated from mass and density. The shell mass was measured to an accuracy of

$\pm 0.05 \mu\text{g}$ using a microbalance, and the density was measured to an accuracy of $\pm 0.001 \text{ g/cm}^3$ using a density column (performed by General Atomics). The wall thickness obtained by this method was confirmed by SEM (scanning electron microscope) micrographs of the wall cross sections obtained on a LEO 982 Field Emission SEM. The thickness of flat films was measured using a Rank Taylor Hobson Talysurf profilometer to an accuracy of $0.1 \mu\text{m}$.

The shell's surface finish was characterized by sphere-mapping (performed by General Atomics) and by using a SEM. Sphere maps were measured for thin-walled ($1.5\text{-}1.8\text{-}\mu\text{m}$) shells that were slightly inflated ($\sim 1\%$) by 4- to 6.5-atm internal pressure of nitrogen. The permeability of nitrogen through the shell wall was sufficiently low to maintain the inflation for ~ 24 h. The same shells were measured again when deflated to compare the surface finish with or without inflation.

d. Property measurements. One hundred to two hundred shells prepared under each imidization condition were measured for gas permeability and mechanical properties. The permeability was determined by measuring the time constant. Young's modulus, tensile strength, and elongation at break were determined by a burst/buckle test. Detailed descriptions of the test procedures can be found elsewhere.^{3,8} Helium permeability at cryogenic temperatures (156 K to 298 K) was determined for Kapton HN and vapor-deposited flat films (dimension = $1 \text{ cm} \times 1 \text{ cm} \times 25 \mu\text{m}$) using a setup reported elsewhere,³ with the addition of a helium leak detector (Edwards Spectron 600D) to measure the helium permeation rates through the films.⁹

Results and Discussion

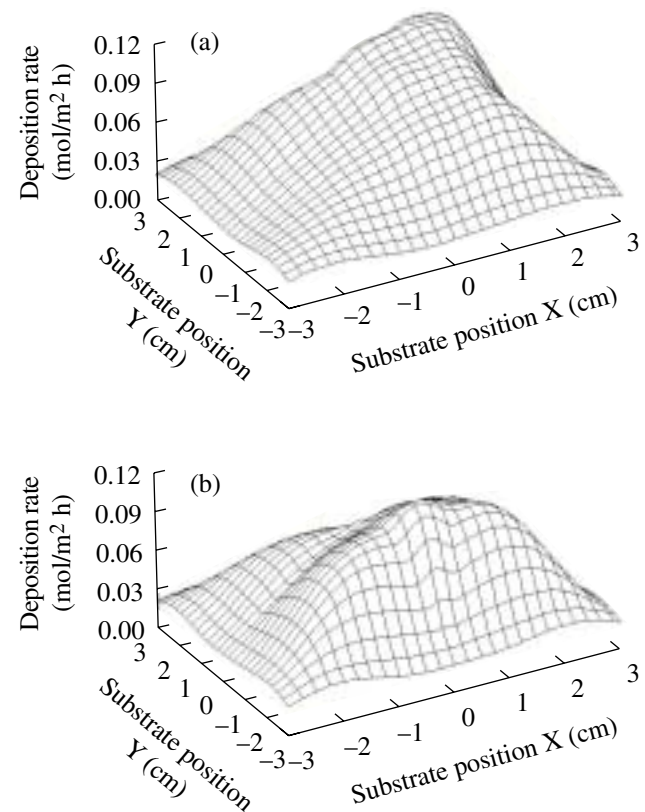
1. Yield and Reproducibility of the Fabrication Process

a. Deposition. Maintaining the stoichiometric ratio (1:1) of monomers when depositing PAA is critical since non-stoichiometric deposition results in greatly deteriorated properties and surface finish.¹⁰⁻¹³ The monomers must also be uniformly deposited over the entire substrate surface. The spatial variation of the monomer deposition rates on the substrate plane is shown in Fig. 88.30 (note that the X-Z plane is the plane of symmetry for the two evaporators). The dependency of the monomer deposition rates on the evaporator temperature is shown in Fig. 88.31. The evaporator temperatures that yielded equimolar monomer deposition were PMDA = 153°C and ODA = 126°C . The substrate located at the center of the chamber floor [(0,0,0) in Fig. 88.30] was minimized in size ($1 \times 1 \text{ cm}^2$ for flat films; $\sim 0.5 \times 0.5 \text{ cm}^2$ for shells) and rotated at 120 rpm to reduce the spatial variability. Figure 88.32

illustrates the smooth surface of a typical shell deposited under the above conditions.

b. Imidization. The key factor that determines the yield of polyimide shells is the stress generated during imidization, which can rupture the shells if not carefully controlled. The main source of stress is the depolymerization of the PAMS mandrels into gaseous products at elevated temperatures. Depending on the depolymerization rate, the products may be unable to permeate out of the polyimide layer at the rate they are produced, creating a pressure differential that inflates the shells.

The changes in shell diameter during imidization under various heating rates and atmospheres are shown in Fig. 88.33. The shells imidized in air inflated more abruptly and at a lower



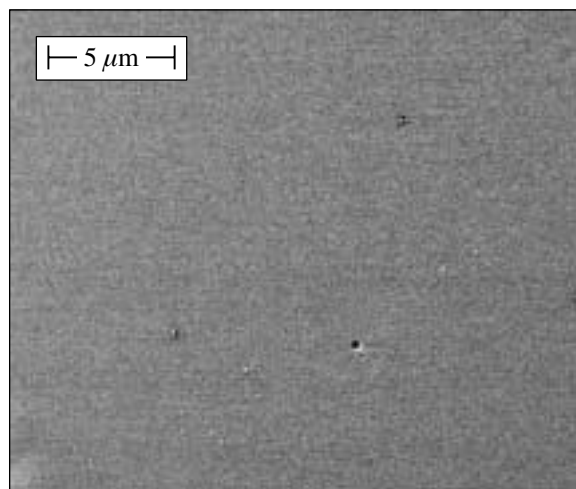
T1570

Figure 88.30

Spatial variation of the monomer deposition rates on the substrate plane: (a) PMDA (153°C), (b) ODA (126°C). Note that the X-Z plane is the plane of symmetry for the two evaporators. The separation between the evaporators is 5 cm, and the vertical distance between the substrate and evaporator planes is 3 cm, as shown in Fig. 88.29.

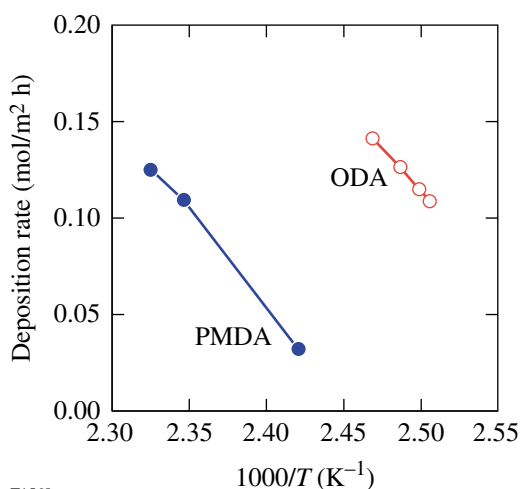
temperature than those imidized in nitrogen. This was attributed to the lower initiation temperature and higher reaction rate of the depolymerization of PAMS in the presence of oxygen. The yield of air-imidized shells was reduced as a result of this drastic inflation, as summarized in Table 88.II. In a nitrogen atmosphere, shells inflated more at higher heating rates due to the more rapid depolymerization of PAMS (Fig. 88.33), and the yield was lowered (Table 88.II). Imidizing at 0.1°C/min in a nitrogen atmosphere minimized the inflation and thus provided the highest yield.

The chemical composition of the polyimide shells and films produced by the optimized process agreed with that of the commercial PMDA-ODA films (Kapton[®]), as shown in the FTIR spectra (Fig. 88.34) and the combustion analysis data (Table 88.III).



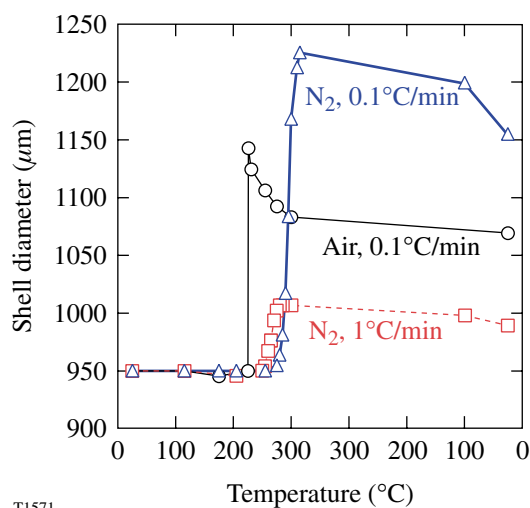
T1569

Figure 88.32
SEM micrograph of the outer surface of a 4- μm -thick polyimide shell.



T1568

Figure 88.31
Dependency of the monomer deposition rates on the evaporator temperature. The deposition rates were measured with $0.3 \times 0.3\text{-cm}^2$ PAMS films located at (0,0,0) of Fig. 88.30.



T1571

Figure 88.33
Changing shell diameter with imidization temperature for three imidization conditions: (a) N_2 , 0.1°C/min, (b) air, 0.1°C/min, and (c) N_2 , 1°C/min. The shells remained spherical throughout imidization.

Table 88.II: Yield of polyimide shells under different imidization conditions.

	Air 0.1°C/min	N_2 0.1°C/min	N_2 0.5°C/min	N_2 1.0°C/min
Yield (%)	60	100	90	60

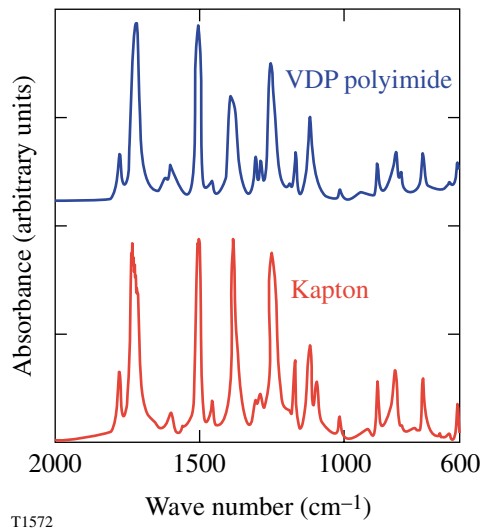


Figure 88.34

FTIR spectra of vapor-deposited polyimide (VDP) and Kapton®. The VDP sample was imidized at 0.1°C/min in N₂ for 6 h. The Kapton spectrum was obtained using a 8-μm-thick Kapton® HN film (DuPont).

Table 88.III: Atomic composition of VDP polyimide (imidized at 0.1°C/min in N₂; 6 h at 300°C) by combustion analysis. The formula of polyimide is C₂₂H₁₀N₂O₅.

	Atomic percent (%)			
	C	H	N	O
VDP (±0.2)	55.3	26.8	5.3	12.7
By formula	56.4	25.7	5.1	12.8

2. Properties of Polyimide Shells

The measured properties of polyimide shells agree with the literature values of commercial Kapton® films,¹⁴ as shown in Table 88.IV. The experimental test matrix employed to obtain these properties used five to ten shells per batch; ten to twenty batches were tested to obtain batch-to-batch reproducibility. The narrow uncertainty intervals listed in Table 88.IV confirm the reproducibility of the process.

3. Effects of Imidization Conditions

Different imidization conditions resulted in different permeability, tensile strength, and flexibility (ultimate strain) but had little effect on the Young's modulus of the shells. The results can be summarized as follows:

a. Imidizing atmosphere (N₂ versus air). The properties of N₂- and air-imidized polyimides are compared in Table 88.V. Imidizing in air instead of nitrogen increased the permeability by ~100% while reducing the strength by ~25%. The elongation at break was also decreased by ~50%. The air-imidized shells possessed lower crystallinity than N₂-imidized shells, as indicated by the x-ray diffraction patterns in Fig. 88.35, where the peak associated with the 002 lattice planes is substantially weaker in the air-imidized samples.

The FTIR spectra in Fig. 88.36 show that the air-imidized samples retained a weak anhydride peak at 1850 cm⁻¹, indicating that a small fraction of the imide groups had been hydrolyzed into anhydride. This may result in a shortened polymer chain length that generally reduces the tensile strength and elongation at break of polymeric materials.¹⁵ Both air- and N₂-imidized shells were cross-linked, as indicated by the fact that they were insoluble in concentrated sulfuric acid.¹⁶ The distinct properties of the air-imidized samples may be attributed to their lower crystallinity and MW.

Table 88.IV: Properties of polyimide shells (imidized at 0.1°C/min in N₂; 6 h at 300°C) and the literature values for Kapton®. E = Young's modulus, σ = tensile strength, and ε = elongation at break.

	Mechanical Properties			Gas Permeability (mol·m/m ² ·Pa·s)			
	E (GPa)	σ (MPa)	ε	He × 10 ¹⁶	H ₂ × 10 ¹⁶	D ₂ × 10 ¹⁶	N ₂ × 10 ¹⁸
VDP shells	3.2±0.1	280±19	0.27±0.02	4.9±0.1	3.6±0.1	3.5±0.1	3.9±0.2
Kapton® ¹³	2.5	231		8.2	4.9	4.4±0.1*	12

*Measured experimentally with 25-μm-thick Kapton® HN films (DuPont).
(Literature value of D₂ permeability through Kapton is unavailable.)

b. Imidizing rate. The properties of polyimide imidized at different heating rates are shown in Table 88.VI. Helium permeability increased with the heating rate, while the tensile strength and flexibility showed an opposite trend. The samples imidized at 1°C/min became soluble, suggesting that the fast heating rate had eliminated cross-linking. The higher permeability and lower tensile properties of the shells imidized at 1°C/min may be attributed to the absence of cross-linking.^{17–19}

The XRD patterns of shells imidized at 1°C/min and 0.1°C/min are compared in Fig. 88.37. The relative intensity of the 002 peak showed that the crystallinity was lower in the 1°C/min sample than in the 0.1°C/min sample. This provides another explanation for the differences in the properties. The

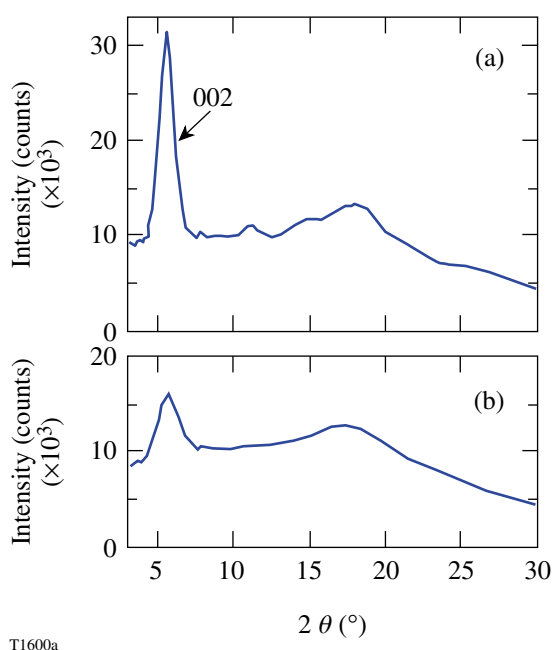


Figure 88.35
1-D x-ray microdiffractometer patterns integrated from 2-D transmission patterns of (a) N₂-imidized and (b) air-imidized samples.

greater strain/stress experienced by the shells imidized at 1°C/min, as shown in Fig. 88.33, is believed to hinder the polyimide molecules from crystallizing.

c. Imidization time at 300°C. As shown in Table 88.VII, the helium permeability, tensile strength, and flexibility increased with the duration for which the samples were cured at 300°C. The samples imidized for 1 h dissolved completely in sulfuric acid, while the samples imidized for more than 3 h were insoluble. As displayed in the FTIR spectra (Fig. 88.38), the intensity of the imide peaks (~1780 and 1380 cm⁻¹) increased with the cure time (no further effect was observed after 6 h at 300°C). The FTIR spectra and solubility results indicate that imidization was incomplete and that cross-linking reactions had not taken place until after 3 h of curing. The low tensile properties and high solubility of the 1-h-cured shells were attributed to the absence of cross-linking and/or lower MW due to incomplete imidization.

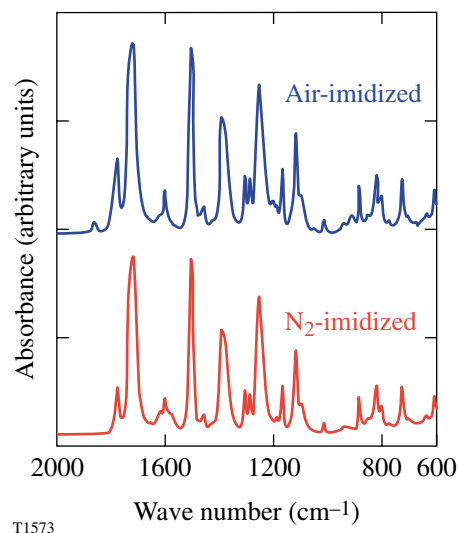


Figure 88.36
FTIR spectra of air- and N₂-imidized VDP polyimide.

Table 88.V: Properties of N₂- and air-imidized VDP polyimide. The permeability and solubility were measured with both film and shell samples, and the other properties were measured with shells only. The imidization conditions (0.1°C/min; 6 h) were the same except for the atmosphere.

Imidizing conditions	Mechanical Properties			Gas Permeability (mol·m/m ² ·Pa·s)			Solubility in H ₂ SO ₄
	<i>E</i> (GPa)	<i>σ</i> (MPa)	<i>ε</i>	He × 10 ¹⁶	D ₂ × 10 ¹⁶	N ₂ × 10 ¹⁸	
N ₂	3.2±0.1	280±19	0.27±0.02	4.9±0.1	3.5±0.1	3.9±0.2	insoluble
Air	3.0±0.2	191±11	0.13±0.03	11.7±0.6	7.6±0.5	8.5±0.2	insoluble

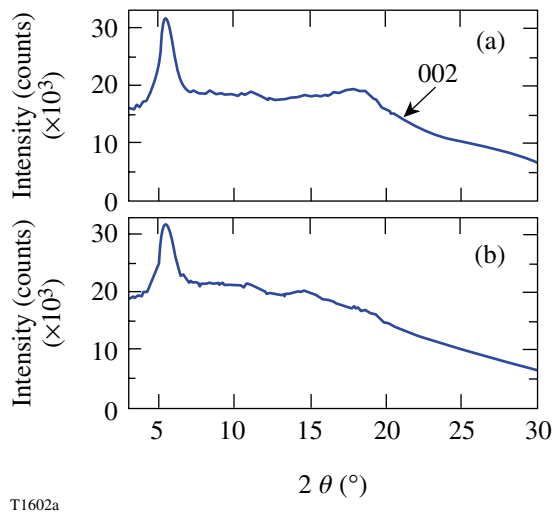


Figure 88.37

1-D x-ray microdiffractometer patterns integrated from 2-D transmission patterns of shells imidized at (a) 0.1°C/min and (b) 1°C/min.

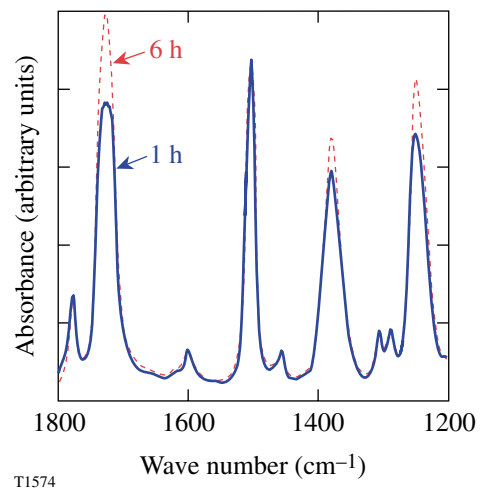


Figure 88.38

FTIR spectra of VDP polyimide imidized for 1 h and 6 h at 300°C.

Table 88.VI: Properties of VDP polyimide imidized at different heating rates. The solubility was tested with both film and shell samples, and the other properties were measured with shells only. The imidization conditions (nitrogen; 6 h) were the same except for the heating rate.

Imidizing conditions	Mechanical Properties			He Permeability $\times 10^{16}$ (mol·m/m ² ·Pa·s)	Solubility in H ₂ SO ₄
	E (GPa)	σ (MPa)	ϵ		
0.1°C/min	3.2±0.1	280±19	0.27±0.02	4.9±0.1	insoluble
0.5°C/min	3.3±0.3	230±26	0.08±0.02	5.3±0.1	insoluble
1.0°C/min	3.3±0.3	136±6	0.03±0.01	5.6±0.2	soluble

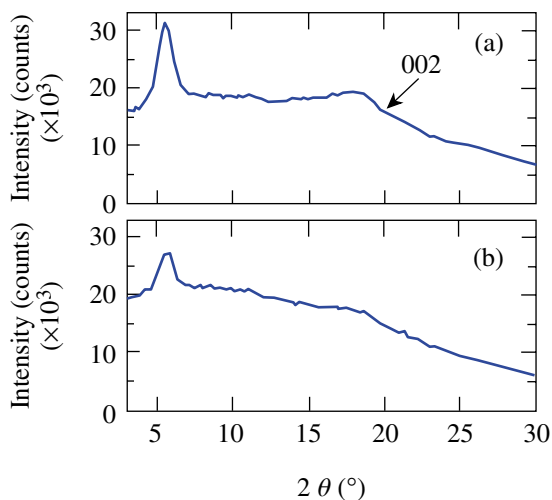
Table 88.VII: Properties of VDP polyimide shells imidized for different durations at 300°C. The solubility was tested with both film and shell samples, and the other properties were measured with shells only. The imidization conditions (nitrogen; 0.1°C/min) were the same except for the duration.

Imidizing conditions	Mechanical Properties			He Permeability $\times 10^{16}$ (mol·m/m ² ·Pa·s)	Solubility in H ₂ SO ₄
	E (GPa)	σ (MPa)	ϵ		
1 h	3.4±0.2	100±10	0.15±0.03	4.1±0.1	soluble
3 h	3.2±0.1			4.6±0.1	insoluble
6 h	3.2±0.1	280±19	0.27±0.02	4.9±0.1	insoluble

4. Biaxial Straining and Permeability

Approximately 150 imidized shells that had been inflated with a biaxial strain of ~ 0.25 were tested for permeability. The results are summarized in Table 88.VIII. The permeability of the shells increased; however, the magnitude of the increase fell into two categories: $\sim 1/3$ of the tested shells became ~ 1000 -fold more permeable, while $\sim 2/3$ showed a moderate increase of $\sim 25\%$. Upon heating to 350°C (within the reported T_g range for polyimide)¹⁴ in nitrogen for 1 h, these shells were recovered to their original dimensions and permeability.

The XRD patterns of the shells before and after straining are shown in Fig. 88.39. Straining the shells decreased their crystallinity as indicated by the reduced intensity of the 002 peak. The lowered crystallinity may account for the moderate permeability increase of the strained shells. It is speculated that the ~ 1000 -fold increase in permeability resulted from crazing/



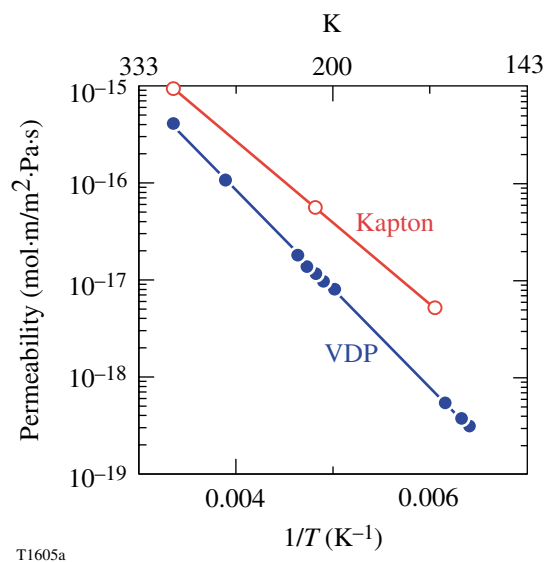
T1604a

Figure 88.39
1-D x-ray microdiffractometer patterns integrated from 2-D transmission patterns of (a) pristine and (b) inflated shells.

shear-banding, which can create microvoids in the shells and thus greatly expedite permeation.²⁰ Importantly, the structural integrity of the inflated shells was not affected since they could be repeatedly flattened and recovered by pressure differential and could contain liquid D_2 at cryogenic temperatures.

5. Cryogenic Permeability

The temperature dependency of the helium permeability through Kapton and VDP films is plotted in Fig. 88.40. The data measured with Kapton agree with those reported by S. A. Letts *et al.*⁹ Both materials followed the Arrhenius relationship over the measured temperature range. The activation energy for permeation calculated from the data was 19.5 and 16.0 KJ/mol for VDP and Kapton, respectively. The good temperature-permeability correlation will allow the permeability to be estimated in an extended temperature range. The higher activation energy of VDP polyimide may be due to its



T1605a

Figure 88.40
Temperature dependency of the helium permeability of VDP and solution-cast polyimide (Kapton) at cryogenic temperatures.

Table 88.VIII: Permeability of polyimide shells before and after straining.

	Permeability ($\text{mol}\cdot\text{m}/\text{m}^2\cdot\text{Pa}\cdot\text{s}$)		
	Before straining (120 shells)	Biaxially strained (~ 0.25)	
		80 shells	40 shells
$\text{He} \times 10^{16}$	4.9 ± 0.1	6.2 ± 0.2	NA*
$\text{N}_2 \times 10^{18}$	3.9 ± 0.2	Not measured	500 \rightarrow 4000

*Permeability too high to measure using current apparatus.

being cross-linked. For polymeric materials, the activation energy is determined by the segmental mobility of the molecules; the segmental mobility is limited when the molecules are cross-linked, resulting in high activation energy.²¹

6. Surface Finish

Figure 88.41 displays the power spectra calculated from the sphere maps of a 1.7- μm -wall shell, inflated and deflated, as described in the **Experimental Section** above. The mode-2 to -20 roughness was reduced when the shell was inflated, suggesting that the low-mode roughness may instead be a “waviness” in the shell wall, which can be eliminated by inflation. Based on this observation, the low-mode roughness of thin-wall cryogenic targets may be significantly reduced since they are kept inflated during application.²²

The SEM micrographs of the surface of as-deposited shells prepared with unheated and heated substrates are shown in Fig. 88.42. Contrary to our expectation that a heated substrate would re-evaporate unreacted monomers and thus eliminate high-mode roughness (coating-induced bumps),⁴ the number density of coating-induced bumps increased with the coating temperature. This may be due to two mechanisms: (1) At higher temperatures the coating rate was slower (50% slower at 140°C than at 25°C), thus the shells experienced more abrasion and collisions, reported to increase surface roughness,⁴ over the longer period required to achieve equivalent thickness. (2) The stoichiometry was offset by disproportional re-evaporation of PMDA and ODA, which have different vapor pressures at 120°C to 140°C.

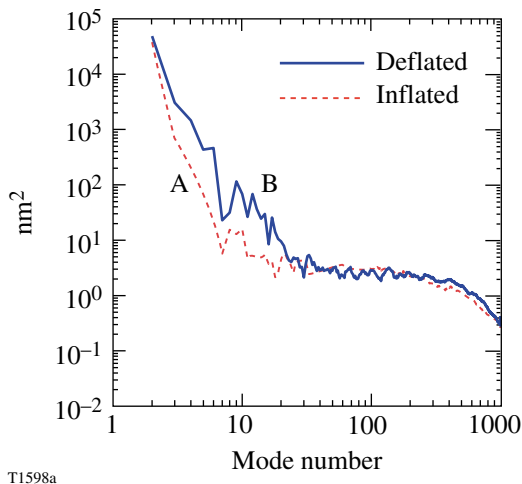


Figure 88.41
Power spectra of a thin-walled (1.8- μm) polyimide shell: A—inflated ($\sim 1\%$) by 6.5 atm N_2 ; B—deflated after the fill gas permeated out.

7. Summary

Vapor-deposited polyimide shells had properties equivalent to commercial polyimide films. The fabrication process was studied parametrically to optimize the shell properties, qualities, and yield, and the results can be summarized in the following:

- Strength and surface smoothness of PAA coating were achieved by maintaining an equimolar deposition of the precursor monomers over the substrate surface. Factors that affected the monomer deposition rates included the evaporating temperature and the geometrical arrangement of the substrate.
- The stress generated during imidization due to depolymerization of PAMS mandrels determined the yield of polyimide shells, which could be controlled by varying the imidization conditions. Imidizing at 0.1°C/min in nitrogen atmosphere minimized the stress and provided the highest yield.
- Shells imidized in air were twice as permeable, $\sim 75\%$ as strong, and $\sim 50\%$ as flexible as their counterparts imidized in nitrogen; the Young's modulus was unaffected; and the crystallinity and MW were lower.

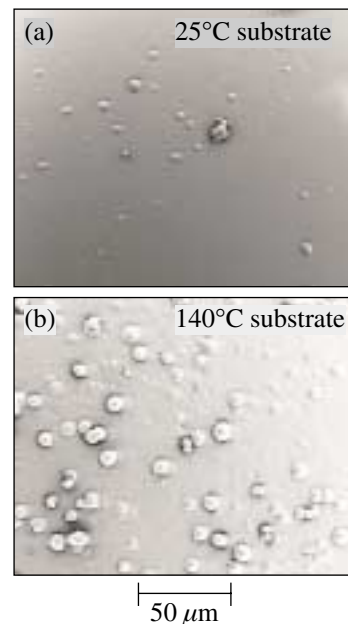


Figure 88.42
SEM micrographs of the surface of as-deposited shells (6- μm coating) prepared at (a) 25°C and (b) 140°C substrate temperatures.

- Increasing the imidization rate increased the permeability (~25%) and solubility and decreased the strength (~50%) and flexibility (~200%), while maintaining the Young's modulus. The samples imidized at the fastest heating rate became soluble with lower crystallinity.
- Imidizing for less than 3 h at 300°C resulted in lower strength, flexibility, and permeability and produced polyimide that was soluble. The imidization was incomplete at 1 h, which may have led to lower MW and the absence of cross-linking.
- Biaxial straining increased the permeability by up to three orders of magnitude but reduced the crystallinity.
- Inflating thin-wall shells reduced the low-mode surface roughness; heating the substrate during coating increased the high-mode roughness.

Conclusion

Polyimide shells can be reproducibly prepared with dimensions required for ICF targets. The properties and quality of shells can be modified and improved via processing parameters. The modifications in the shell properties are attributed to changes in crystallinity, degree of cross-linking, or molecular weight.

ACKNOWLEDGMENT

This work was supported by the U.S. Department of Energy Office of Inertial Confinement Fusion under Cooperative Agreement No. DE-FC03-92SF19460, the University of Rochester, and the New York State Energy Research and Development Authority. The support of DOE does not constitute an endorsement by DOE of the views expressed in this article.

REFERENCES

1. J. J. Sanchez and S. A. Letts, *Fusion Technol.* **31**, 491 (1997).
2. F. Y. Tsai, E. L. Alfonso, S.-H. Chen, and D. R. Harding, *Fusion Technol.* **38**, 83 (2000).
3. E. L. Alfonso, S. H. Chen, R. Q. Gram, and D. R. Harding, *J. Mater. Res.* **13**, 2988 (1998).
4. C. C. Roberts *et al.*, *Fusion Technol.* **35**, 138 (1999).
5. A. Nikroo and D. Woodhouse, *Fusion Technol.* **35**, 202 (1999).
6. R. Jenkins and R. L. Snyder, *Introduction to X-Ray Powder Diffractometry* (Wiley, New York, 1996), Chap. 7, pp. 173–203.
7. B. A. Squires and K. L. Smith, in *Advances in X-Ray Analysis*, edited by P. K. Predecki *et al.* (Plenum Press, New York, 1995), Vol. 38, pp. 511–516.
8. F. Y. Tsai, E. L. Alfonso, S. H. Chen, and D. R. Harding, "Processing Vapor-Deposited Polyimide," to be published in the *Journal of Physics D*.
9. S. Letts *et al.*, presented at the Twelfth Target Fabrication Specialists' Meeting, Jackson Hole, WY, 19–23 April 1998.
10. T. Strunskus and M. Grunze, in *Polyimides: Fundamentals and Applications*, edited by M. K. Ghosh and K. L. Mittal, *Plastics Engineering*, Vol. 36 (Marcel Dekker, New York, 1996), pp. 187–205.
11. E. L. Alfonso, F.-Y. Tsai, S.-H. Chen, R. Q. Gram, and D. R. Harding, *Fusion Technol.* **35**, 131 (1999).
12. R. G. Pethe *et al.*, *J. Mater. Res.* **8**, 3218 (1993).
13. C. C. Roberts *et al.*, *Fusion Technol.* **38**, 94 (2000).
14. Kapton[®] product literature, DuPont[™] High Performance Polymers, Circleville, OH 43113.
15. W. Volksen, P. Cotts, and D. Y. Yoon, *J. Polym. Sci. B, Polym. Phys.* **25**, 2487 (1987).
16. P. M. Cotts and W. Volksen, *ACS Symp. Ser.* **242**, 227 (1984).
17. C. E. Rogers, in *Polymer Permeability*, edited by J. Comyn (Elsevier, London, 1985), Chap. 2, pp. 11–73.
18. G. A. Patfoort, *Polymers: An Introduction to Their Physical, Mechanical and Rheological Behaviour* (Story-Scientia, Gent, Belgium, 1974), pp. 321–323.
19. F. W. Billmeyer, Jr., *Textbook of Polymer Science*, 3rd ed. (Wiley, New York, 1984), Chap. 12, pp. 330–357.
20. E. H. Andrews, in *The Physics of Glassy Polymers*, edited by R. N. Haward (Wiley, New York, 1973), pp. 394–453.
21. A. Singh-Ghosal and W. J. Koros, *Ind. Eng. Chem. Res.* **38**, 3647 (1999).
22. I. Anteby, Ben-Gurion University of the Negev, private communication (1996).

LLE's Summer High School Research Program

During the summer of 2001, 13 students from Rochester-area high schools participated in the Laboratory for Laser Energetics' Summer High School Research Program. The goal of this program is to excite a group of high school students about careers in the areas of science and technology by exposing them to research in a state-of-the-art environment. Too often, students are exposed to "research" only through classroom laboratories, which have prescribed procedures and predictable results. In LLE's summer program, the students experience many of the trials, tribulations, and rewards of scientific research. By participating in research in a real environment, the students often become more excited about careers in science and technology. In addition, LLE gains from the contributions of the many highly talented students who are attracted to the program.

The students spent most of their time working on their individual research projects with members of LLE's technical staff. The projects were related to current research activities at LLE and covered a broad range of areas of interest including optics modeling, laser characterization, cryogenic materials properties, liquid crystal chemistry, laser damage, electro-optic sampling, and the development, modeling, and control of laser fusion diagnostics (see Table 88.IX).

The students attended weekly seminars on technical topics associated with LLE's research. Topics this year included lasers, fusion, holography, the OMEGA Cryogenic Target System, laboratory astrophysics, experimental error analysis, and scientific ethics. The students also received safety training, learned how to give scientific presentations, and were introduced to LLE's resources, especially the computational facilities.

The program culminated on 29 August with the "High School Student Summer Research Symposium," at which the students presented the results of their research to an audience

including parents, teachers, and LLE staff. The students' written reports will be bound into a permanent record of their work that can be cited in scientific publications. These reports are available by contacting LLE.

One hundred and thirty high school students have now participated in the program since it began in 1989. The students this year were selected from approximately 50 applicants.

In 1997, LLE added a new component to its high school outreach activities: an annual award to an Inspirational Science Teacher. This award honors teachers who have inspired High School Program participants in the areas of science, mathematics, and technology and includes a \$1000 cash prize. Teachers are nominated by alumni of the High School Program. Mr. David Dussault, a mathematics and computer science teacher at Livonia High School, was the recipient of LLE's 2001 William D. Ryan Inspirational Teacher Award. Mr. Michael Harvey, a participant in the 1999 Summer Program who nominated Mr. Dussault, writes of his former teacher, "His approach to teaching is unique. He challenges students to work at their own pace and learn on their own. Even more impressive to me than his wisdom in preparing me for college is his love for pure education. Mr. Dussault finds the way to get his message across to every type of student." Mr. Scott Bischooping, principal of Livonia High School, also had many words of praise for Mr. Dussault. He said he has been continually impressed with Mr. Dussault's contributions to both the Math and Computer Science Departments. Two accomplishments that stood out in his mind were the success of a curriculum Mr. Dussault developed, which allows students to earn college math credits, and his dedicated leadership to the school's math team in state and local competitions.

Table 88.IX: High School Students and Projects—Summer 2001.

Name	High School	Supervisor	Brief Project Title
David Bowen	Greece Arcadia	C. Stoeckl	Controlling Scientific Instruments with JAVA
Matthew Fiedler	Brighton	W. Donaldson	Modeling Streak Camera Sweep Speeds
Melisa Gao	Brighton	J. Marozas	Two-Dimensional Phase Unwrapping for the Design of Distributed Phase Plates
Brian Ha	Gates Chili	R. Sobolewski	Optical Characterization of GaAs with MSM Structures
Gabrielle Inglis	Honeoye Falls-Lima	R. Boni	Building and Characterizing 14-GHz InGaAs Fiber-Coupled Photodiodes
Jennifer Jung	Victor	K. Marshall	Guest-Host Dye Systems for Liquid Crystal Electro-Optical Device Application
Joshua Keegan	Aquinas Institute	M. Guardalben	Numerical Modeling of Optical Parametric Chirped Pulse Amplification
Kevin Monajati	Pittsford-Sutherland	K. Marshall	Computational Modeling of Physical Properties in Liquid Crystalline Polymer Systems
Christopher Piro	Honeoye Falls-Lima	R. S. Craxton	Modeling the LCPDI with Refraction and Diffraction
Abigail Rhode	Brockport	J. Taniguchi	Experimental Simulation of Damage in Spatial Filter Lenses
Uyen Tran	Wilson Magnet	S. Regan	Experimental Investigation of the Far Field on OMEGA with an Apertured Near Field
James Wang	McQuaid Jesuit	D. Harding	Cyrogenic Permeability of Polyimide Shells
Jeffrey Wilbur	Victor	J. Lambropoulos	Inclusion Models of Laser Damage

FY01 Laser Facility Report

Improving operational reliability for precision spherical implosions including direct-drive cryogenic targets was the primary priority for FY01 on OMEGA. Laser diagnostics and techniques to characterize and improve power balance performance were extended beyond prior achievements to allow experimentalists to probe fine details of spherical target performance. In particular, plastic-shell implosions with THz SSD (smoothing by spectral dispersion) and polarization smoothing show good reproducibility and performance. All users, including experimentalists fielding indirect-drive (ID) experiments, have benefited from the improved repeatability and reliability that has come from the power balance program. (See Table 88.X for a summary of this year's targets shots.) System improvements were also geared toward specifically improving flexibility for ID experiments. Highlights of these changes and other achievements of FY01 include the following:

- The P510 UV streak camera system was completed to provide streak camera-based pulse shape, pulse timing, and power balance for all beams on every shot. The cameras combine 1000:1 signal to noise at the peak and a bandwidth of 11 GHz. Each cluster of ten beams is captured on a single camera, thus the full complement consists of six ten-beam instruments.
- Power balance of <5% was routinely achieved for 1-ns square pulses by increased execution of periodic laser-tuning shots combined with continuous monitoring and optimization of frequency-conversion-crystal (FCC) tuning.
- Power balance on target was investigated and optimized through careful characterization of x-ray yield from the focal spot of each of the 60 beams. For some implosion shots, the results were used to adjust the power settings of the beams to investigate elimination of residual power balance errors. This technique demonstrated that peak x-ray intensity measurements of 6% rms can be improved to 2% rms.
- Cryogenic target capability was extended through deployment of additional Moving Cryostat Transfer Carts (MCTC's), increased diagnostics, and refined control. Three fully functional MCTC's have been deployed as of the end of FY01, providing flexibility between the filling station, characterization and layering station, and target delivery to OMEGA. While the maximum capacity to shoot up to eight direct-drive cryogenic targets in a week was not realized in FY01, five good cryogenic implosions were accomplished during a two-week ISE (integrated spherical experiments campaign).
- The Wide-Field Target Viewing System (WFTVS) was modified in FY01 to handle images from a mega-pixel-class camera. A 2-k × 2-k array was deployed to provide a four-fold improvement positioning capability over the entire field of view of the viewing system. Indirect-drive targets with point-imaging backlighter targets can now be more precisely positioned in the chamber.
- New elliptical-focal-spot distributed phase plates (DPP's) have been deployed. These optics can be used to create uniform, circular, drive spots on EOS targets and other planar foils when the targets are not normal to the beam. Several designs are available to compensate for the incidence angles of beams from three cones.
- A completely reengineered Path Length Adjustment System (PLAS) was developed and integrated into the system largely to accommodate the flexibility demanded by users from LLNL and LANL. The new hardware and software allow for rapid reconfiguration of beam timing on target. Staggering beam arrival times for backlighting and long drive pulses is frequently requested by the user community.

Table 88.X: The OMEGA target shot summary for FY01.

LLE-ISE	376
LLE-RTI	106
LLE LPI	50
LLE (other)	44
LLE-SSP	113
LLNL	312
LANL	124
NLUF	125
CEA	29
SNL	10
Total	1289

National Laser Users' Facility News

During FY01, 600 OMEGA target shots were taken for external users. This is a 5.1% increase over FY00 and the highest number of target shots ever taken by OMEGA external users in a single year, accounting for ~47% of the total 1289 target shots taken on the system. The external users included eight collaborative teams carrying out work under the National Laser Users' Facility (NLUF) Program as well as collaborations led by scientists from Lawrence Livermore National Laboratory (LLNL), Los Alamos National Laboratory (LANL), Sandia National Laboratory (SNL), the Nuclear Weapons Effects Testing (NWET) Program, and Commissariat à l'Énergie Atomique (CEA) of France.

FY01–FY02 NLUF Experiments

FY01 was the first year that NLUF programs were approved for a two-year period of performance (FY01 and FY02). The eight NLUF experimental campaigns received a total of 125 OMEGA target shots in FY01.

The independent DOE Technical Evaluation Panel for this period, consisting of Dr. David Bradley (LLNL), Dr. David Montgomery (LANL), Dr. Richard Olson (SNL), and Dr. Ned Sauthoff (Princeton Plasma Physics Laboratory), reviewed progress reports submitted in September 2001 by all of the current participants, confirmed that all eight participants made satisfactory progress during FY01, and recommended continued funding and shot allocations for all of the programs through FY02.

In 2Q02 DOE is expected to issue a new solicitation for NLUF programs to be carried out during FY03–FY04. The NLUF shot allocation for FY03 is 12 OMEGA shot days (~120 target shots). The NLUF DOE funding allocation for FY01 and FY02 was \$700,000 to cover the participants' costs for carrying out experiments on OMEGA. It is expected that this funding level may increase in FY03/FY04 to a level more consistent with the high level of interest shown in the use of OMEGA to carry out high-energy-density physics experiments of relevance to the National Nuclear Security Agency (NNSA) Stockpile Stewardship Program (SSP).

The eight NLUF experimental campaigns carried out in FY01 included the following:

Atomic Physics of Hot, Ultradense Plasmas.

Principal Investigators: C. F. Hooper Jr. (University of Florida), D. A. Haynes (Fusion Technology Institute, University of Wisconsin), and collaborators from Los Alamos National Laboratory, the University of Wisconsin, and LLE.

The plasma environment perturbs atomic processes of radiators immersed in hot, dense plasmas. This perturbation is a challenging application of the statistical mechanics of dense plasmas and leads to observable and diagnostically useful variations in the spectrum emitted by the radiators. The focus of this work is to produce hot [electron temperature (T_e) > 1.5 keV], ultradense [electron density (n_e) ~ 5×10^{24} cm⁻³] plasmas using the OMEGA laser in direct-drive mode. In FY01 eleven shots were performed toward this objective. Ar-doped (1% to 2% by atom) CH shells (940- μ m diameter, 20 μ m thick) filled with 15 atm of deuterium were used in these experiments. With 23-kJ-energy, 1-ns square laser pulses, a core $n_e > 2 \times 10^{24}$ cm⁻³ and $T_e \sim 1.15$ keV were observed. Because simulations indicated that ramped pulse shapes can achieve electron densities in the range of 5×10^{24} cm⁻³ to 8×10^{24} cm⁻³, a series of ramped pulse shots were taken later in the year. These data are currently being analyzed.

Determination of Temperature and Density Gradients in Implosion Cores of OMEGA Targets.

Principal Investigators: R. C. Mancini (University of Nevada, Reno), J. A. Koch (LLNL), and collaborators from the University of Wisconsin, LLE, LLNL, and Howard University.

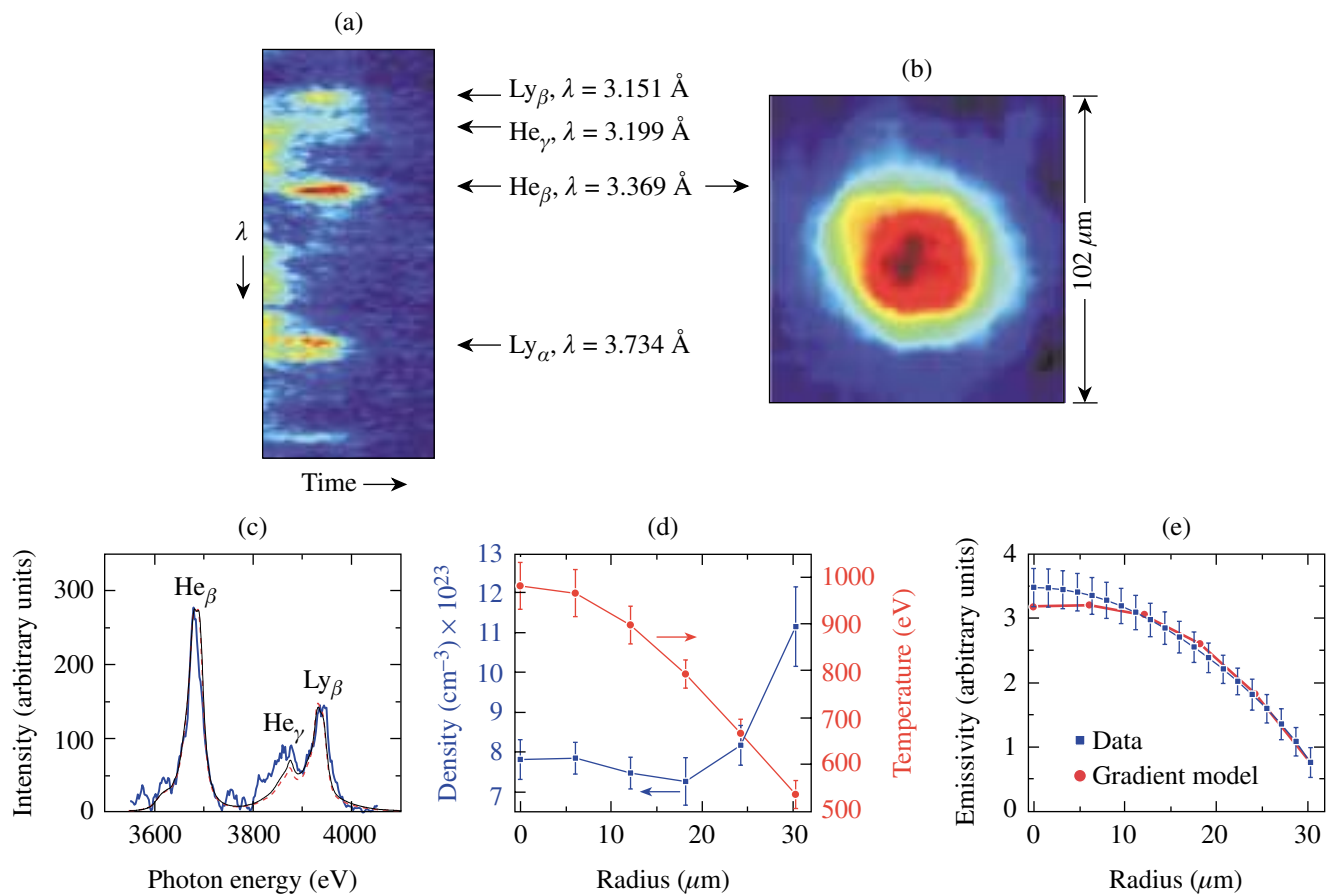
The goal of this project is to determine time-resolved temperature and density gradients in implosion cores on OMEGA indirect-drive implosion experiments using x-ray spectroscopy. The method is based on a novel self-consistent analysis of data from simultaneous, time-resolved x-ray line spectra and x-ray monochromatic images. Argon-doped, deuterium-filled plastic shells placed in gold hohlraums and driven

by 30 UV laser beams of OMEGA were used in these experiments. The aim was to achieve stable, spherically symmetric, and reproducible implosion cores where the proposed spectroscopic gradient determination technique can be tested and established. During FY01, a target design was successfully tested, and argon *K*-shell x-ray line spectra and monochromatic images were recorded on several shots (see Fig. 88.43).

Studies of Fundamental Properties of High-Energy-Density Plasmas.

Principal Investigator: R. Petrasso (MIT Plasma Science and Fusion Center) and collaborators from LLE, LLNL, and SUNY Geneseo.

In FY01, four different types of experiments were carried out under this program. In the first experiment, slowing-down measurements of nascent 14.7-MeV protons generated by D^3He fusion reactions were made in up to eight different directions on the same target shot to characterize the capsule's total ρR variations (see Fig. 88.44). These measurements were carried out using compact wedged range filters (WRF's). In the second class of experiments, DTH-filled CD capsules were imploded with the aim of using knock-on protons to determine the fuel ρR . In the third series of experiments, fuel-shell mix was studied by determining how much shell material is combined with the fuel at burn time. In the final set of experiments, the total ρR 's at the times of shock coalescence and stagnation



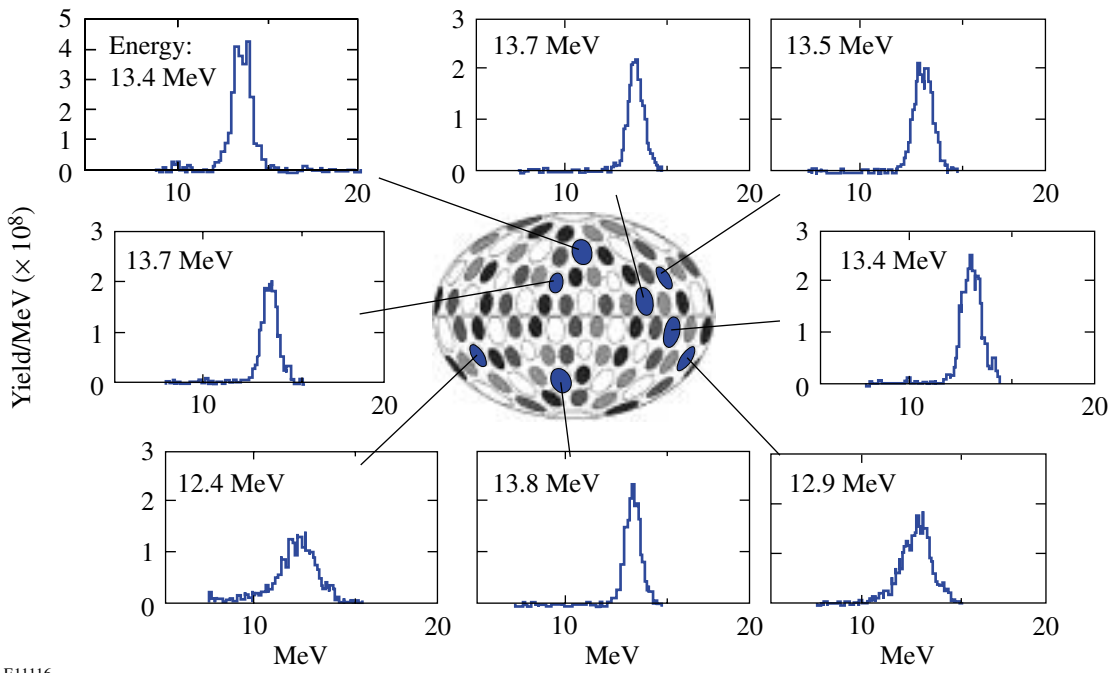
U264

Figure 88.43

(a) Time-resolved argon *K*-shell x-ray spectrum and (b) time-integrated He $_{\beta}$ line monochromatic image from the implosion core of OMEGA shot 23686. (c) Synthetic spectra fits to the x-ray spectrum time-integrated over the emission interval of the He $_{\beta}$ line; the red dashed line is the gradient model, the thin blue line is the uniform model, and the thick blue line is the experimentally measured spectrum. (d) Electron temperature and number density core gradients. (e) Synthetic emissivity fit to the He $_{\beta}$ emissivity profile extracted from the monochromatic image. The emissivity-weighted averages of the gradients, $\langle N_e \rangle_{\epsilon} = 7.8 \times 10^{23} \text{ cm}^{-3}$ and $\langle T_e \rangle_{\epsilon} = 860 \text{ eV}$, show good consistency with the results of the uniform model analysis.

were differentiated. This measurement is based on a comparison of the measured energy spectra of the D^3He primary

protons in implosions of D^3He -filled CH shells to those of CD/CH shells filled with only 3He (see Fig. 88.45).



E11116

Figure 88.44

Data showing 14.7-MeV primary proton slowing down from the implosion of a D^3He -filled capsule. These data are obtained by a combination of seven wedged-range filters (WRF's) and two charged-particle spectrometers (CPS's). Note the variation in mean energy of the protons as a function of angular position. These data imply that there are significant low- ℓ -mode variations in the total areal density of the imploded capsule.

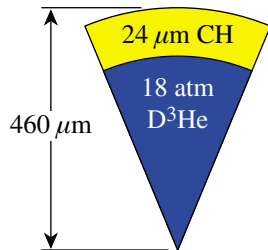
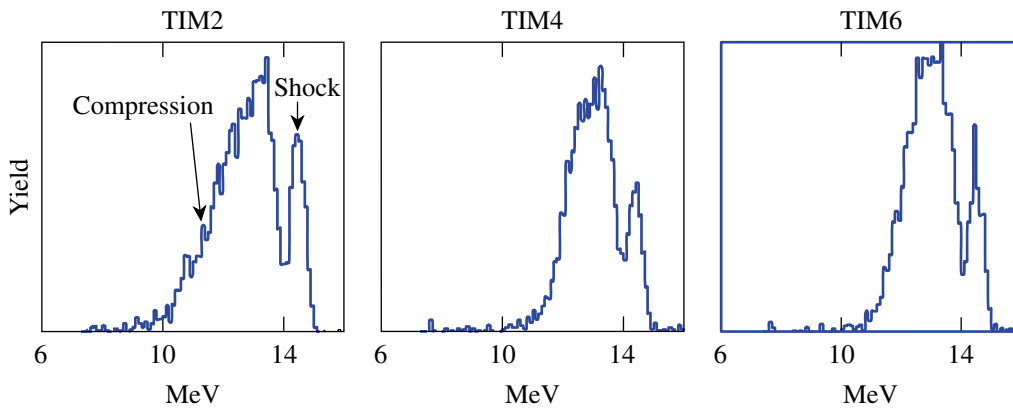


Figure 88.45

WRF data from OMEGA shot 24811 showing primary proton spectra from three different directions. The proton yield at shock time and that produced at peak compression are distinguished by the difference in mean proton energy. The protons generated at the time of the first shock have only a small downshift in energy (~ 0.3 MeV) corresponding to the lower capsule areal density expected at shock time (~ 8 mg/cm²) compared to a downshift of ~ 2.3 MeV at peak compression corresponding to a $\rho R \sim 70$ mg/cm².

E11383

Studies of the Dynamic Properties of Shock-Compressed FCC Crystals by In-Situ Dynamic X-Ray Diffraction.

Principal Investigators: H. Baldis (University of California at Davis), D. H. Kalantar (LLNL), and collaborators from LLNL, LLE, University of California at San Diego, University of Oxford, and LANL.

This experiment uses time-resolved dynamic x-ray diffraction to study the response of a lattice under shock compression as the shock passes through the sample. Recovery of target samples for laboratory examination allowed the residual deformation effects to be examined directly. The shots this year were aimed at developing the capability to record diffraction from multiple lattice planes during passage of a shock through a thin foil of single-crystal copper. Simultaneous recovery of separate shock samples experiments were conducted.

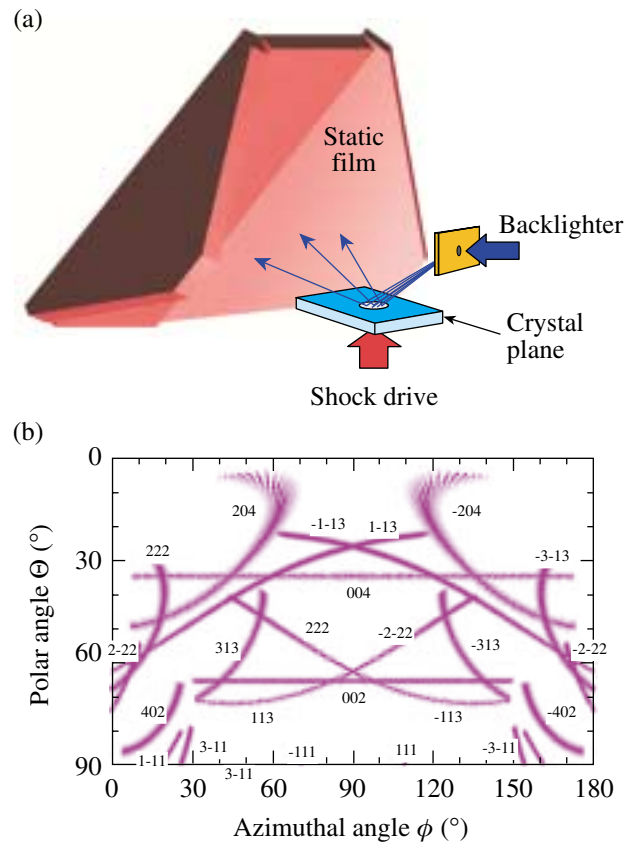
During FY01, the diffraction from the (200) and (020) lattice planes of Cu were recorded using a V x-ray source (2.38 Å). In addition, a modified target was tested using a Cu x-ray source (1.4 Å) to record the (400) lattice planes of Cu. Fielding a large-solid-angle film holder on diffraction experiments taken in August 2001 extended the technique further (see Fig. 88.46).

High-Spatial-Resolution Neutron Imaging of Inertial Fusion Target Plasmas Using Bubble Neutron Detectors.

Principal Investigator: Raymond K. Fisher (General Atomics) and collaborators from LLE, CEA, and LLNL.

Bubble detectors capable of detecting neutrons with a spatial resolution of 5 to 30 μm are one of the most-promising approaches to imaging NIF target plasmas with the desired 5-μm spatial resolution in the target plane. Gel bubble detectors are being tested to record neutron images of ICF implosions in OMEGA experiments. By improving the noise reduction techniques used to analyze the data taken in June 2000, it was possible to image the neutron emission from 6 × 10¹³-yield DT target plasmas with a target plane spatial resolution of ~140 μm, as shown in Fig. 88.47. As expected, the spatial resolution was limited by counting statistics as a result of the low neutron detection efficiency of the easy-to-use gel bubble detectors. The results, which have been submitted for publication, were presented as an invited talk at the October 2001 Meeting of the Division of Plasma Physics of the American Physical Society.

To improve the counting statistics, data taken in May 2001 using a stack of four gel detectors were integrated over a series



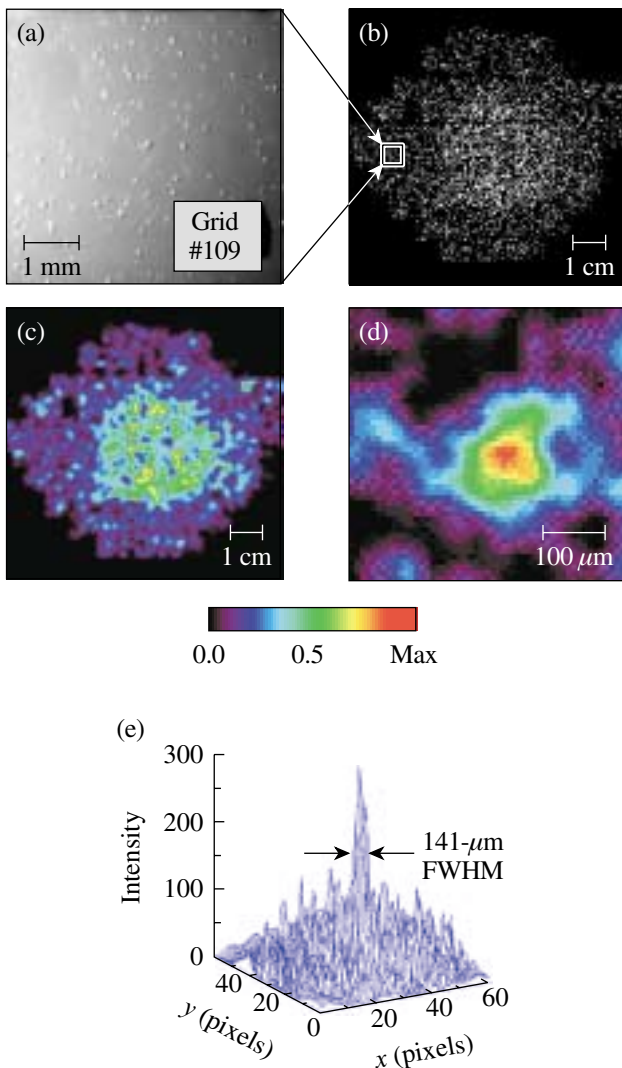
U265

Figure 88.46 (a) Schematic of a static film-based detector that records x rays diffracted from many different lattice planes covering nearly a π-steradian solid angle. (b) Simulated diffraction pattern from multiple lattice planes of Si.

of up to seven high-yield DT shots. Analysis of the 2001 data is still in its early stages. Gel detectors were chosen for these initial tests since the bubbles can be photographed several hours after the neutron exposure. They consist of ~5000 drops (~100 μm in diameter) of bubble detector liquid/cm³ suspended in an inactive support gel that occupies ~99% of the detector volume. Using a liquid bubble chamber detector, along with a light-scattering system to record the bubble locations a few microseconds after the neutron exposure when the bubbles are ~10 μm in diameter, should result in ~1000 times higher neutron detection efficiency and a target plane resolution on OMEGA of ~10 to 50 μm.

Examination of the “Cone-in-Shell” Target Compression Concept for Asymmetric Fast Ignition.

Principal Investigators: Richard B. Stephens (General Atomics) and collaborators from LLNL and the Institute of Laser Engineering (ILE), Osaka University, Osaka, Japan.



U266

Figure 88.47
Bubble detector images from a 6×10^{13} -yield OMEGA shot, including (a) a microscope photograph of 60- μm -diam bubbles in a single grid location, (b) an x - y plot of bubble locations, (c) a coded false color image in the detector plane, and (d) and (e) an unfolded neutron image in the target plane.

Studies of the compression hydrodynamics of targets suitable for the fast-ignition inertial fusion concept have been initiated. The objective is to assemble a dense core of material while maintaining clear access for the ignition pulse through the low-density blowoff. A hollow, high-density cone inserted in the side of the shell and placed inside a cylindrical hohlraum can be used to maintain the ignition pulse access. The cone causes anisotropies in the shell implosion: radiation intensity changes and shear near the cone surface modify the local implosion velocity, and the dense core is assembled from only a partial shell. Modeling (Steve Hatchett, LLNL) suggested

that the consequences of these asymmetries would be relatively minor; it should be feasible to assemble a dense, nearly spherical core with a piece missing. A model system using a hohlraum-driven target was set up to test prediction, and backlit framing camera pictures of the model system were compared to the simulation. The predicted and experimental images look similar (see Fig. 88.48) but there were subtle differences. The collapse time might have changed since the experimental shell density was about half that expected in the interval of the framed images. In addition, the shell seems less separated from the cone, and the cone shape is less defined in the experimental images compared to the simulation. Further analysis will continue in order to understand these changes and to optimize our experimental setup for the next round of experiments.

Supernova Hydrodynamics on the OMEGA Laser.

Principal Investigators: R. Paul Drake (University of Michigan), B. Remington (Center for Laser Astrophysics-ILSA, LLNL), and collaborators from LLNL, CEA Saclay (France), LLE, LANL, University of Arizona, University of Colorado, University of Chicago, SUNY Stony Brook, Naval Research Laboratory, and Eastern Michigan University.

The fundamental motivation of this program is that supernovae are not well understood. Experiments are performed in compressible hydrodynamics and radiation hydrodynamics, relevant to supernovae and supernovae remnants. These experiments produce phenomena in the laboratory that are thought, based on simulations, to be important to astrophysics but that have not been directly observed either in the laboratory or in an astrophysical system. During FY01, this work has focused on the production of an astrophysically relevant, radiative shock and on the three-dimensional, deeply nonlinear evolution of the Rayleigh-Taylor (RT) instability at a decelerating, embedded interface. These experiments required strong compression and decompression, strong shocks (Mach ~ 10 or greater), flexible geometries, and very smooth laser beams, which means that the 60-beam OMEGA laser is the only facility capable of carrying out this program.

Highlights of these Supernova Hydrodynamics experiments include the following:

a. Radiative Precursor Shocks: These experiments involved the initial acceleration of a block of material to high velocity with up to ten OMEGA beams. This block of material then drove a shock wave through low-density foam at a velocity of ~ 100 km/s, which was fast enough to produce a radiative

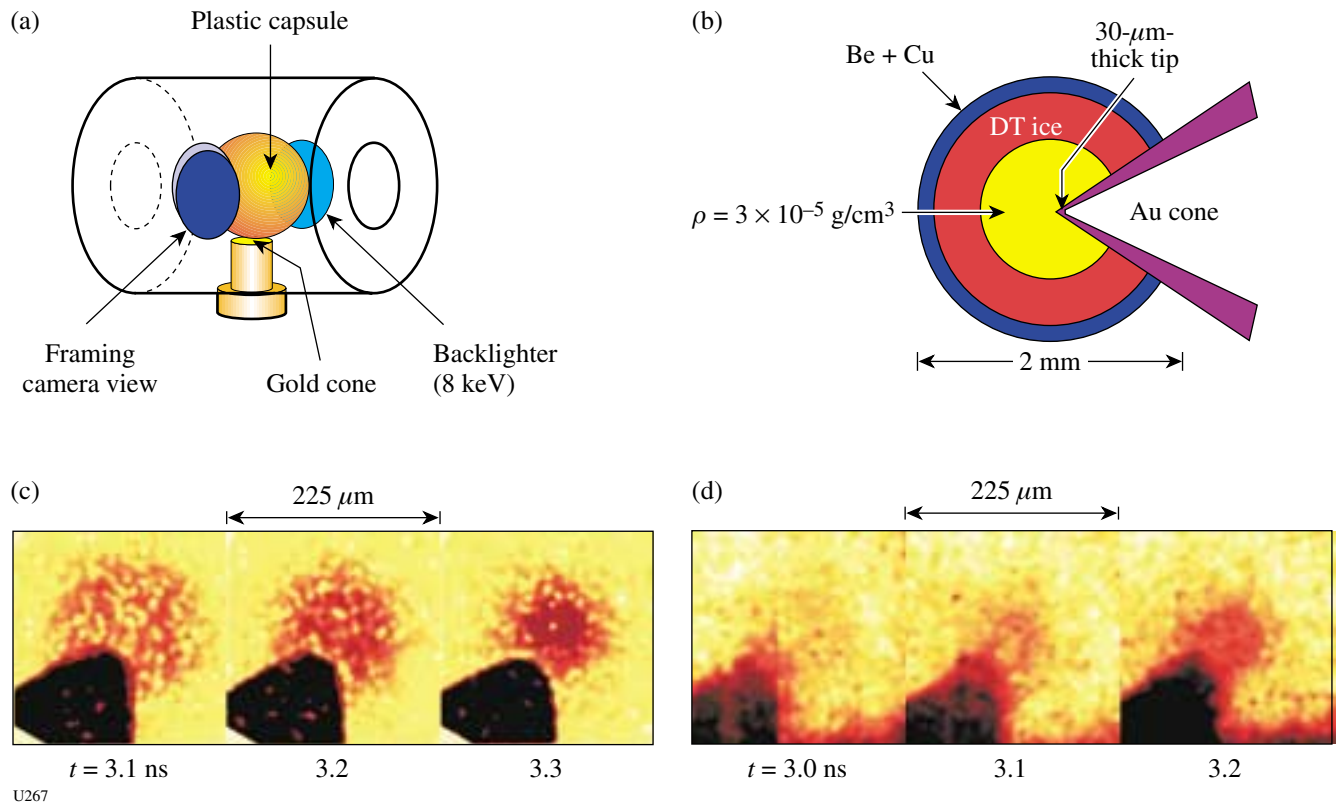


Figure 88.48

(a) Schematic of NIF-scale fast-ignition target; (b) schematic of OMEGA-scale experiment to test the concept; (c) computer simulation of x-ray backlit images of an OMEGA target; and (d) observed backlit images of an OMEGA target experiment just before stagnation.

precursor. The structure of the precursor was diagnosed with absorption spectroscopy using a thulium target. Absorption lines were detected from up to six different ionization states (see Fig. 88.49). The lines from higher ionization states appear at higher temperatures. This allows one, with the help of the OPAL atomic code,¹ to determine the temperature profile in the precursor. It is expected that such experiments will provide quality benchmark cases for astrophysical modeling.

b. 2-D versus 3-D Rayleigh–Taylor: A major issue in the evolution of supernovae is whether three-dimensional effects can resolve the differences between reality and simulations, nearly all of which are carried out in two dimensions. A few 3-D simulations, not yet benchmarked, suggest that 3-D effects are not sufficient to resolve these differences. During FY01, experiments were continued to compare the deep nonlinear

evolution of the RT instability at an embedded interface in both two dimensions and three dimensions (examples from two FY00 shots are shown in Fig. 88.50).

c. Multimode Perturbations and the Onset of Turbulence: During the past year, the study of RT at an embedded interface was extended to begin to examine the growth of multimode perturbations. In addition, the experimental system was analyzed in the context of recent theories regarding the onset of turbulence at shear layers like those between the bubbles and the spikes.

d. Spherically Diverging Experiments: During the past year, a small amount of improved data was obtained on spherically diverging unstable systems. Papers now in progress describe the results obtained on these experiments.

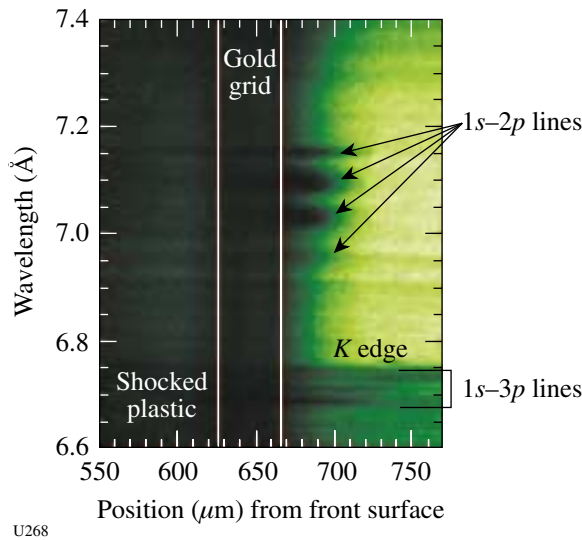


Figure 88.49
An absorption spectrum from the radiative precursor shock experiments at 5.5 ns after the onset of a 1-ns laser pulse. The absorption lines extending to the right of the grid in the image can be analyzed to determine the temperature profile. Initial results show a much shorter precursor than simulations predict.

Optical-Mixing-Controlled Stimulated Scattering Instability Experiments on OMEGA (III) and (IV): Suppressing Backscattering Instabilities by the Externally Controlled Generation of Ion-Acoustic Turbulence.

Principal Investigator: Bedros Afeyan (Polymath Research Inc.) and collaborators from LANL, University of Nevada at Reno, LLNL, and LLE.

The prime objective of this program is to suppress backscattering instabilities by the externally controlled generation of ion-acoustic-wave (IAW) and electron-plasma-wave (EPW) turbulence in different IAW damping regimes. During FY01, the work was directed toward two goals: (1) to generate large-amplitude IAW's at or near the Mach-1 surface of an exploding-foil target (on the pump side of the density peak), and (2) to measure how this reduces the stimulated Raman scattering (SRS) and stimulated Brillouin scattering (SBS) backscattering levels of the pump when the probe/pump energy ratio is high enough.

Planar-foil targets of 5- μm -thick Be were used for the first time this year. According to the hydrodynamic simulations, these Be targets are hydrodynamically similar to the 10- μm -CH targets used in previous years' experiments. A major result of this year's work was the demonstration for the first time in

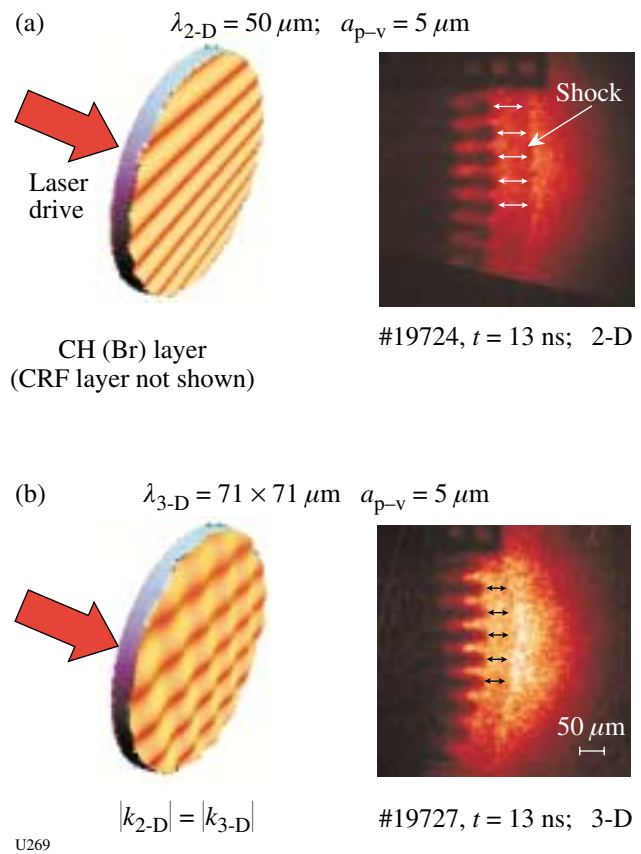
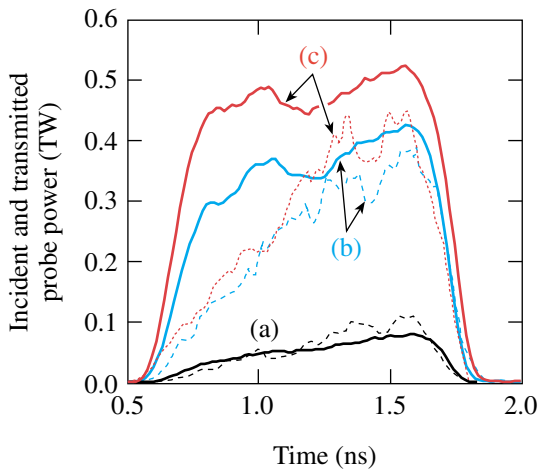


Figure 88.50
Spikes produced by the Rayleigh–Taylor instability during the deceleration of a structured interface. The spikes produced by a 3-D “egg crate” pattern (b) are longer and extend closer to the shock than those produced by a rippled (2-D) interface (a).

equal-frequency crossed beam experiments in flowing plasmas of greater-than-100% transmission of a probe beam intensity due to its interaction with the pump beam and the subsequent energy transfer (see Fig. 88.51). It was also shown that SRS backscattering of the pump beam is suppressed by a factor of 6 or more in the presence of a large IAW driven by the crossing pump and probe beams at or near the Mach-1 surface even in this weak IAW damping limit.

The quality of this year's experiments was improved because it was possible to carry out probe beam intensity scaling experiments using “frequency-conversion-crystal detuning” to adjust the probe beam amplitude. This technique, attempted for the first time during these OMC SSI experiments, allows nearly square, 1-ns laser pulses to be generated over the UV energy range of 30 J to 500 J on target without adjusting the input laser pulse shape of the OMEGA laser.



	Incident probe energy (J)	Energy transfer (%)
a	61	109
b	378	68
c	510	58

Figure 88.51
Optical-mixing-controlled stimulated scattering instability experiments on OMEGA (III) and (IV). Incident (solid curves) and transmitted (dashed or dotted curves) probe beam intensity as a function of time for different probe beam energy levels. At the probe beam energy level of 61 J, the transmitted beam intensity reaches 109% of that incident through the transfer of energy from the pump beam.

U270

FY01 National Laboratory, NWET, and CEA Programs

OMEGA continued a high rate of shot production for external users from the national laboratories (LLNL, LANL, and SNL) as well as from the Nuclear Weapons Effects Testing (NWET) Program, the United Kingdom Atomic Weapons Establishment (AWE), and the Commissariat à l'Énergie Atomique (CEA) of France. A total of 475 target shots were taken for these programs in FY01. The following is a brief summary:

1. LLNL and NWET Campaigns

In FY01 LLNL had 320 shot opportunities at the OMEGA facility, divided as follows: 110 shots for target ignition physics (TIP), 190 shots for high-energy density science (HEDS), and 20 shots for NWET. These opportunities resulted in 312 actual target shots, involving 19 principal investigators (including several shots with collaborators from SNL and LANL). The mini-campaigns are listed in Table 88.XI.

Highlights of LLNL and NWET experiments in FY01 include the following:

Laser-Plasma Interactions: Energy transfer between beams was observed in the forward-scatter geometry and for a range of beam and plasma conditions that are similar to those expected in the NIF. In some cases, the beam energy was enhanced by as much as a factor of 2. This has the potential for creating a symmetry problem for NIF indirect-drive capsules. Substantial energy transfer was observed even at 1/5 the nominal NIF intensity. This indicates that large beams alone may not solve the symmetry problem for indirect-drive capsules. The OMEGA data will motivate an investigation of the

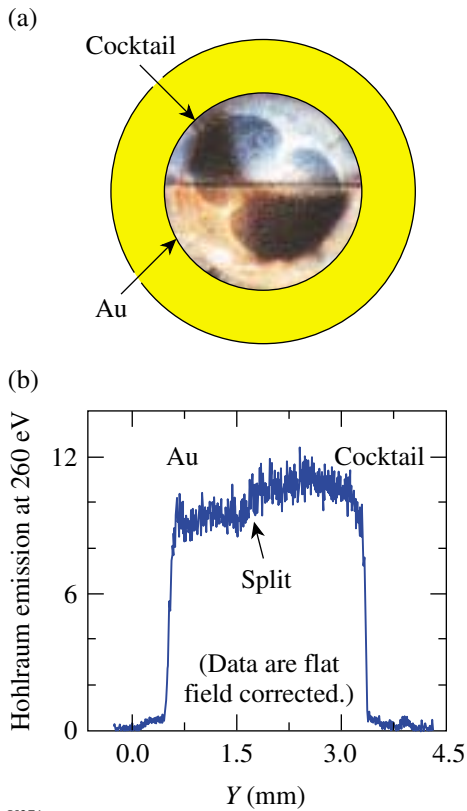
energy transfer issue for a variety of possible NIF target/beam configurations in order to select the optimum configuration.

Cocktail Hohlräume: Experiments to investigate the potential of “cocktail” hohlraum materials to increase soft x-ray emission (and therefore increase the energy coupling to the capsule) in NIF hohlraums were continued. In FY01, Scale 3 hohlraums with a splitback plate (see Fig. 88.52) indicated that the soft x-ray emission of the cocktail material at a photon energy of 260 eV is only 15% enhanced over the case of a conventional hohlraum made only of Au (see Fig. 88.52). In addition, Scale 3/4 and Scale 1 cocktail hohlraums gave the same spectrally integrated drive as gold hohlraums, whereas a 5% increase in T_r was expected. This unexpected observation may be due to lower laser to x-ray conversion efficiency for cocktail hohlraums compared to the standard Au hohlraums. A potential fix to be tested in FY02 is to use Au-lined cocktail hohlraums such that the laser conversion to x rays still occurs in the top Au layer, while the reradiation energetics is dominated by the deeper cocktail layer.

High-Convergence Implosions: The multicone capability of OMEGA continued to be of use in conducting cylindrical-hohlraum capsule implosions with convergence ratios as high as 20. In FY01 HEP5 experiments, the improvement in performance over Nova experiments with similar targets was ascribed to better time-dependent symmetry control and the use of Ar dopant-free fuel (see Fig. 88.53). Experiments with intentionally roughened surfaces demonstrated that the degradation was caused by hydro-instability growth and followed simulation results (see Fig. 88.54).

Table 88.XI: FY01 LLNL and NWET Campaigns.

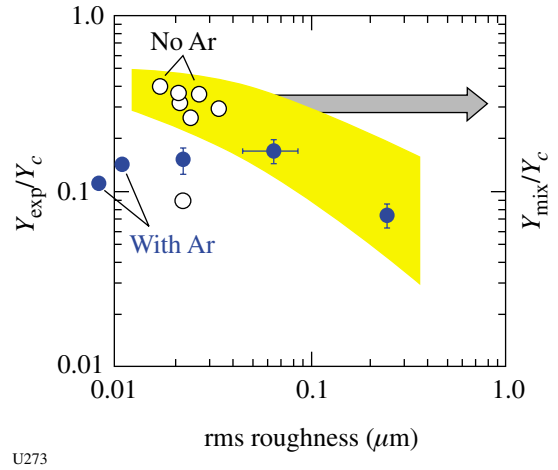
Campaign	Sub-Element	Experiment	Target Shot Allocation	
Target Ignition Physics (TIP)	WBS-1: Energetics	Absolute albedo	5	
		Laser-plasma interactions	10	
		Cocktail holhraum	10	
	WBS 2: Symmetry	NIF foot symmetry	10	
		High-convergence implosions	20	
		WBS 3: Ablator Physics	Shock timing	20
	Ablator burnthrough		5	
	Convergent ablator burnthrough		10	
	Planar RT		10	
	High-Energy-Density Sciences	WBS 4: Diagnostics	X-ray Thomson scattering	5
			Ignition diagnostics	5
		Solid-State Hydro	20	
		Implosion Mix	Pushered shells	10
Hydro I		Richtmyer-Meshkov	20	
Hydro II		Features	15	
Hydro III		Jets	15	
Implosions		NBI	5	
Radiation Transport		RadG	20	
Equation of State (EOS)		Low- and High-Z	35	
NWET	Source Development	X-ray Thomson scattering	5	
		Hot holhraum	10	
		NLTE	5	
		X-ray Thomson scattering	10	
		Backlighter development	5	
		Slit closure	5	
		Dual color	10	
		Gas-filled sources	10	
		Hot-electron sources	5	
		Spheres	5	
		TOTAL	320	



U271

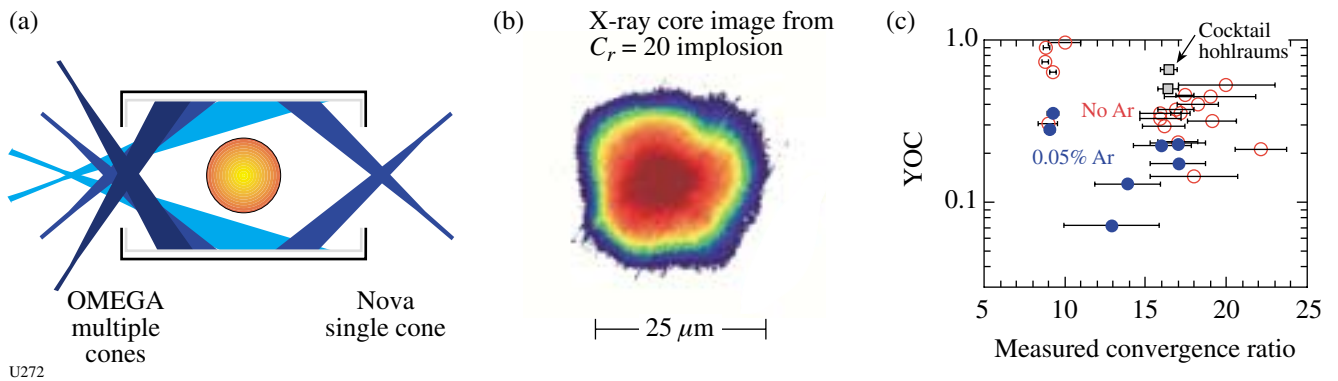
Figure 88.52
 (a) Schematic of the hohlraum configuration used to conduct cocktail material experiments. A split backplate (half cocktail/half Au) is used in a Scale 3 hohlraum. (b) Soft x-ray emission at 260 eV is spatially resolved and shows an ~15% increase in cocktail soft x-ray emission compared to the Au side. This increase is lower than that predicted by *LASNEX* simulations.

NIF-Relevant Hohlraum Symmetry: Investigation of the symmetry of NIF-relevant (WBS 2) hohlraums continued. A configuration for these experiments is shown in Fig. 88.55(a). Thin-shell implosions were imaged with 4.7-keV x rays and yielded symmetry data showing that the asymmetries are small and in agreement with 2-D simulations [see Fig. 88.55(b)].



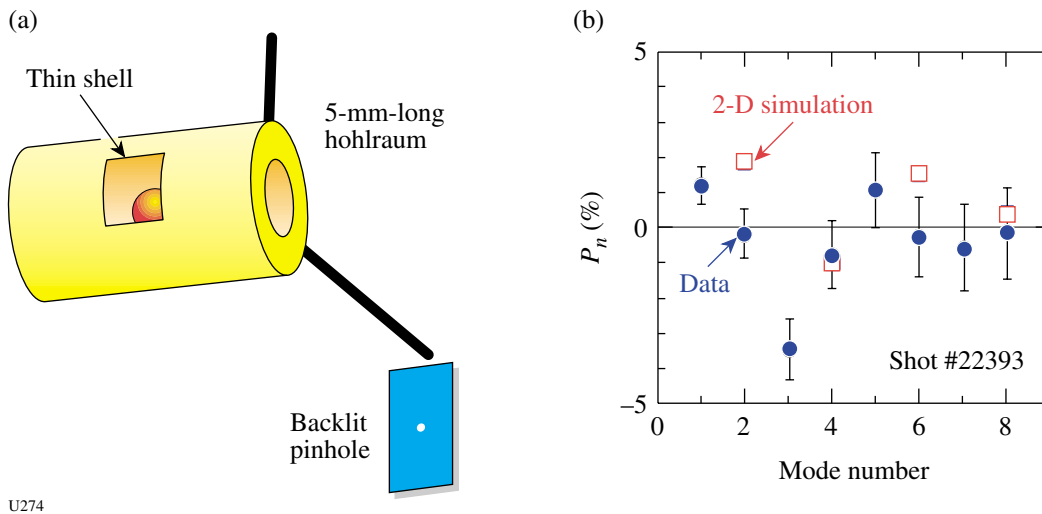
U273

Figure 88.54
 Plot of the ratio of measured neutron yield over that calculated for 1-D clean implosions as a function of measured target roughness. The cases shown are for convergence ratio ~20, indirect-drive implosions carried out on OMEGA. The capsules were intentionally roughened to carry out this experiment. The results are compared to simulations (yellow band) showing the ratio of the neutron yield for an implosion with mix to that of clean 1-D implosions.



U272

Figure 88.53
 (a) Schematic showing the difference between the Nova single-cone hohlraum geometry and that of OMEGA with multiple cones. (b) Typical x-ray image of OMEGA implosion shows symmetric implosion for capsules with convergence ratio ~20. (c) Plot of the ratio of actual neutron yield divided by the calculated 1-D clean yield (YOC) as a function of measured convergence ratio. The improvement in performance of the OMEGA experiments (open circles) over Nova implosions (solid circles) is ascribed to better time-dependent symmetry control and the use of dopant-free fuel.



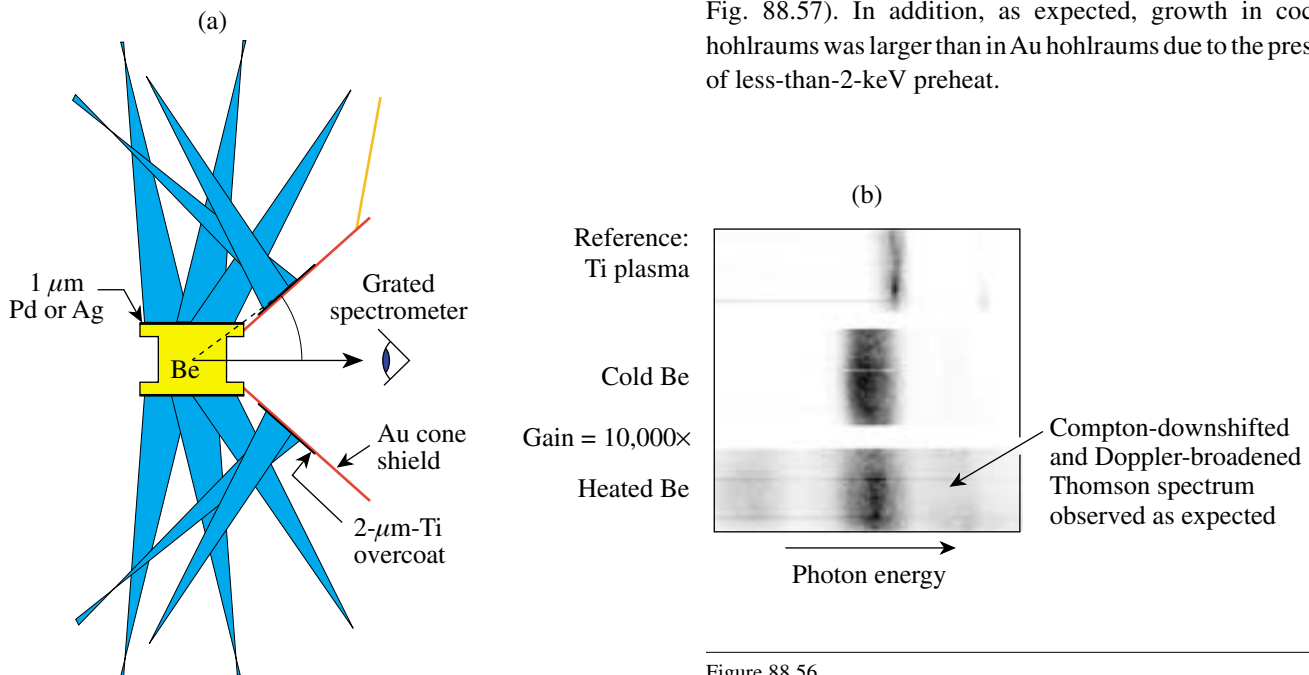
U274

Figure 88.55

Schematic of experimental geometry for OMEGA symmetry experiments. A thin spherical target is imploded inside a 5-mm-long cylindrical hohlraum (a). A point source backlighter provides high-resolution x-ray radiographic images. The resulting data are plotted in (b) showing the inferred asymmetries decomposed in Legendre moments P_n . The open square data points are the results of a 2-D simulation of the asymmetry while the solid circles are the experimental results.

X-Ray Thomson Scattering: The first demonstration of x-ray Thomson scattering as a high-density temperature and density diagnostic was carried out on OMEGA during FY01. The experimental configuration is shown in Fig. 88.56(a). Initial results from these experiments are shown in Fig. 88.56(b).

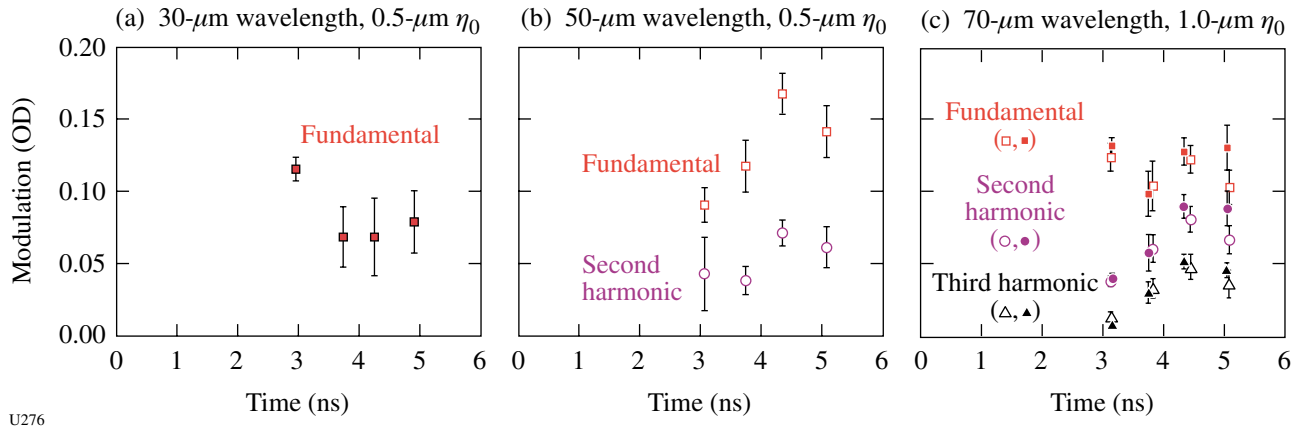
Planar Rayleigh–Taylor Experiments: Polyimide ablator Rayleigh–Taylor (PIRT) experiments continued on radiation-driven targets in FY01. Experiments conducted with 30-, 50-, and 70- μm -wavelength perturbations showed that the RT growth rate with small initial amplitudes was somewhat greater than originally predicted and occurred somewhat earlier (see Fig. 88.57). In addition, as expected, growth in cocktail hohlraums was larger than in Au hohlraums due to the presence of less-than-2-keV preheat.



U275

Figure 88.56

(a) Schematic of x-ray Thomson scattering experiment. (b) Experimental results from x-ray Thomson scattering experiment.



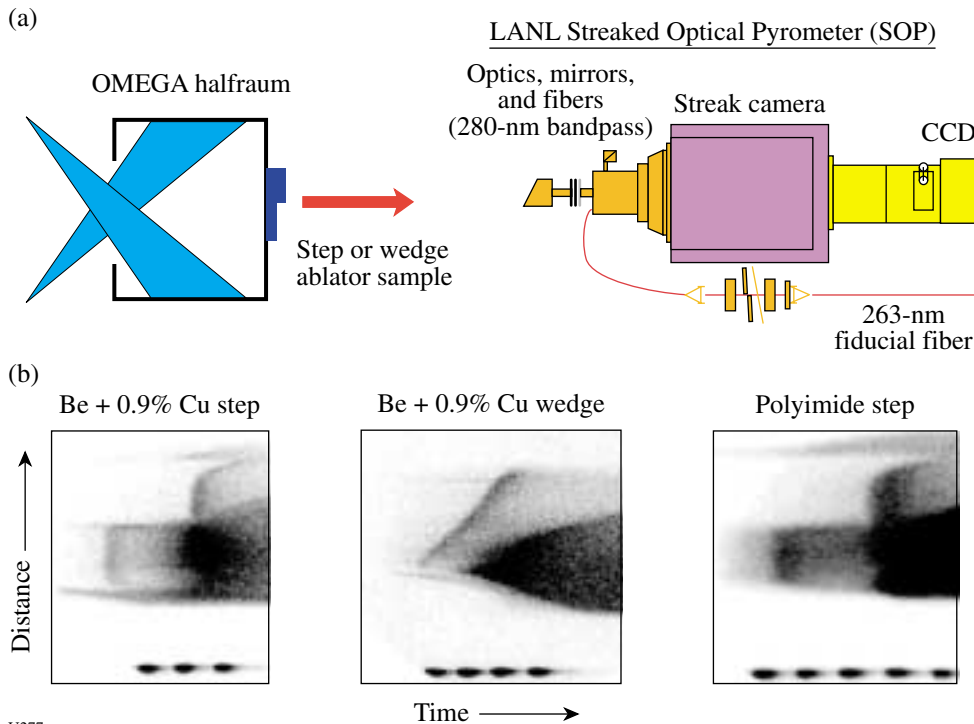
U276

Figure 88.57

Summary of RT growth data from PIRT experiments with Au (open data points) and cocktail (solid points) hohlraums. More growth is evident in cocktail hohlraums than in Au hohlraums. Future shots will attempt to reproduce these results and expand the database.

Shock Timing: A collaboration including scientists from SNL, LANL, and LLNL conducted experiments to investigate shock timing in radiation-driven ablators. A half-hohlraum (halfraum) target was used for these experiments. One configuration featured stepped or wedged ablators attached to a halfraum and interrogated with a LANL streaked optical pyrometer (SOP) as

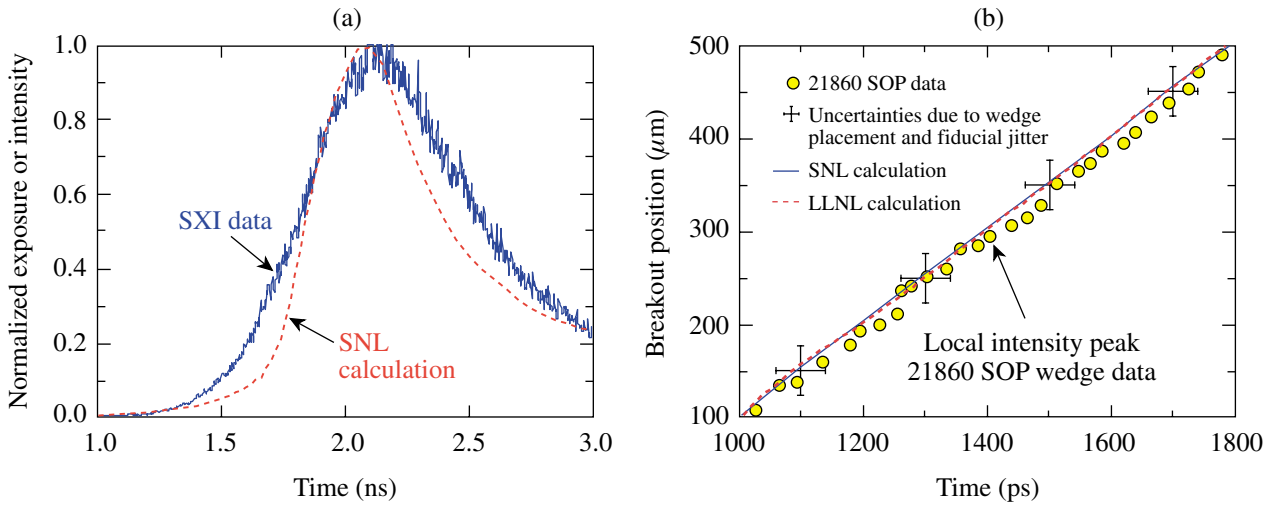
shown in Fig. 88.58. Experiments were also conducted using flat ablator samples and an imaging configuration x-ray streak camera. Initial data with a 160-eV halfraum with Be + 0.9% Cu and polyimide ablators showed that the shock timing could be predicted to within ~ 200 ps (see Fig. 88.59).



U277

Figure 88.58

(a) Schematic of shock-timing experiments and (b) streak camera data from three configurations: Be + 0.9% Cu step; Be + 0.9% Cu wedge; and a polyimide step. The streak photographs have the time axis on the bottom (note temporal fiducial) and the space coordinate on the vertical axis.



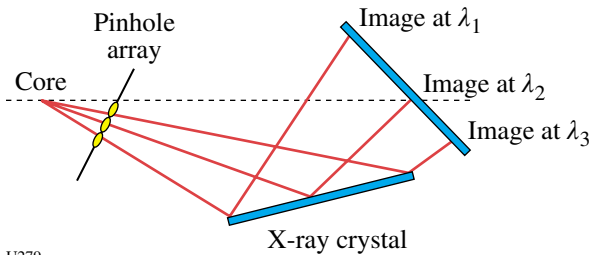
U278

Figure 88.59

Comparison of experimental shock breakout data with SNL and LLNL calculations. (a) Ablation-front burnthrough data and comparison to SNL simulations for planar polyimide sample. (b) Shock-breakout measurements and comparison to SNL (solid line) and LLNL (dashed line) simulations for Be + 0.9% Cu wedge.

Ignition Diagnostics: A new diagnostic for measurement of the ablator areal density (ABRHOR) was tested on OMEGA. ABRHOR is designed to measure spatial variations in shell ρR and/or temperature as an indication of shell breakup and burnthrough. The technique relies on a mid-Z dopant in the ablator. Multiple monochromatic images across an x-ray energy band containing spectral features from the dopant can provide the required data. In FY01, experiments were conducted on OMEGA to test a conceptual design of this instrument based on multiple pinhole imaging off a crystal. [This is

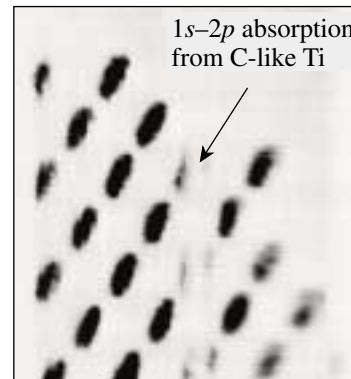
similar to an LLE-developed technique (see Fig. 88.60)]. The OMEGA test was conducted on Ti-doped CH pushers in indirect-drive implosions that were back-illuminated by the core x-ray continuum. Good data were obtained (see Fig. 88.61) from several shots with different drive and capsule parameters. The relatively poor quality of the graphite crystals used in this initial test complicated quantitative analysis. Future experiments will use a multilayer mirror to improve the quality of the data.



U279

Figure 88.60

Schematic of ABRHOR diagnostic. Multiple monochromatic images are obtained across an x-ray energy band containing spectral features from the dopant.



U280

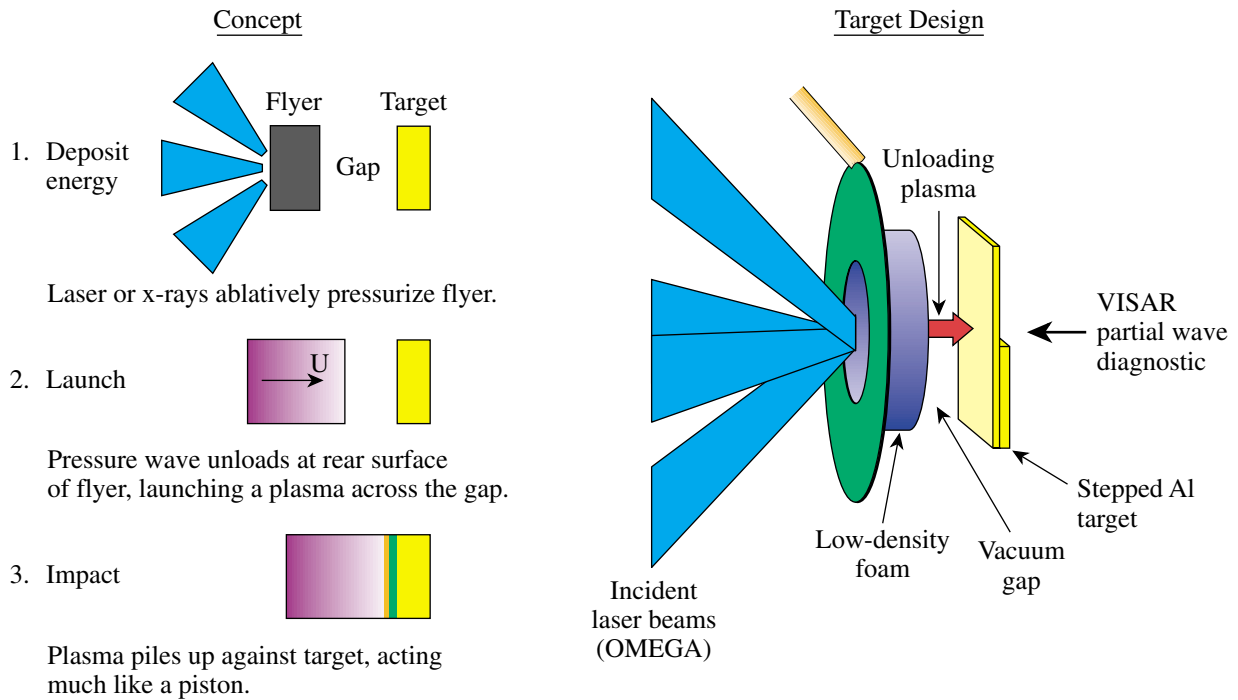
Figure 88.61

Proof-of-principle data from ABRHOR diagnostic. Multiple images of Ti-doped CH pushers are back-illuminated by the self-emission from the core continuum radiation.

IDrive: During FY01, LLNL initiated a series of experiments on OMEGA to test a new laser-driven, high-pressure source (IDrive). The new design (shown in conceptual form in Fig. 88.62) creates a plasma piston that can generate a shockless, continuously loaded high-pressure wave in a flat target. Initial efforts in July 2001 demonstrated that the concept functions as designed. Very low laser energies (less than 30 J/beam) have produced flyer velocities in excess of 12 km/s and shockless

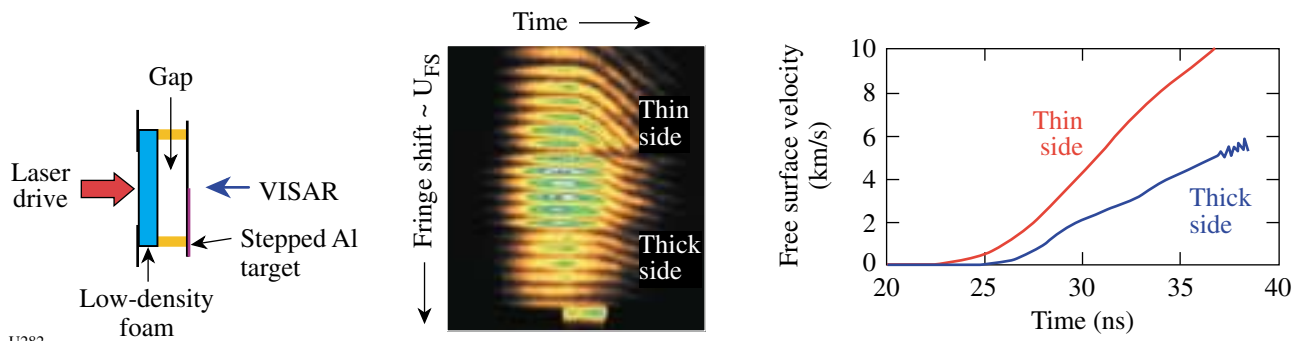
pressure waves up to 0.5 Mbar. Figure 88.63 shows the results from some of the early experiments.

High-Z and Low-Z Equation-of-State (EOS) Experiments: During FY01, significant progress was made on EOS experiments for both high-Z and low-Z matter. Hugoniot data were obtained on diamond and water; the shock metalization thresholds were identified for water, diamond, LiF, and sap-



U281

Figure 88.62 Schematic illustrating the IDrive shockless drive technique and a sketch of the target design for the IDrive experiments.



U282

Figure 88.63 Initial results from the IDrive experiments show the presence of a shockless pressure wave in aluminum.

phire; the shock-melting transition in diamond was accurately identified; accurate double-shock experiments were carried out on water using the transparent anvil technique; and initial experiments were carried out to determine shock-induced melting in metals. In addition, the ASBO diagnostic system (the workhorse of EOS experiments) was upgraded to dual-VISAR capability.

Direct-Drive Richtmeyer–Meshkov (RM) Instability Experiments: In FY01 a series of direct-drive RM experiments were carried out on planar targets with initial perturbation amplitudes of $22\ \mu\text{m}$ and $7\ \mu\text{m}$ and a perturbation wavelength of

$150\ \mu\text{m}$. The experimental data were compared (see Fig. 88.64) with simulations using linear (Meyer–Blewitt) and nonlinear (Sadot) models that do not include shock proximity. In both cases, the models over-predicted the amplitude growth.

Supersonic Jet Experiments: Collaborative experiments among AWE (United Kingdom), LANL, and LLNL continued to investigate the interaction of a supersonic jet with a counter-propagating shock. During FY01, these experiments provided high-quality benchmark data for comparison to the CAL (LLNL), RAGE (LANL), and NYM-PETRA (AWE) hydrocodes (see Fig. 88.65).

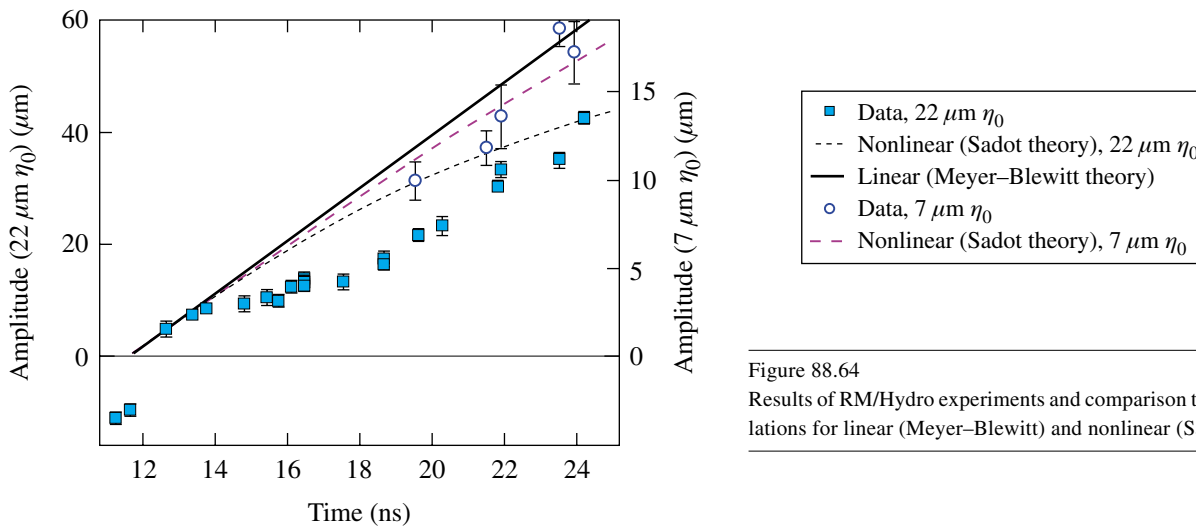
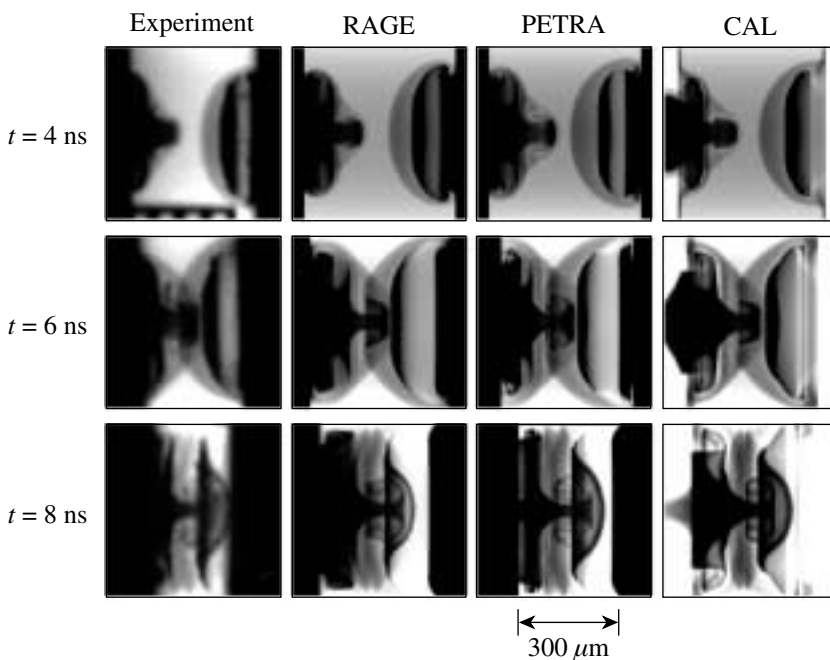


Figure 88.64 Results of RM/Hydro experiments and comparison to theoretical calculations for linear (Meyer–Blewitt) and nonlinear (Sadot) theories.

U283



U284

224

Figure 88.65 Comparison of supersonic jet experiments with various multidimensional computer simulations. The jet and shock are generated in two opposed halfraums. The images are created by x-ray backlighting of the interaction region.

Nonideal Backlit Implosions (NIBI): During FY01, experiments were initiated to investigate the effects of nonuniform illumination on direct-drive capsule implosions. A subset of OMEGA beams was used to implode a capsule while the remaining beams were used to produce x rays from a Fe target to backlight the imploding target. Figure 88.66 shows the results from a near-uniform illumination experiment (shot 23543) and from an implosion with imposed asymmetry in the capsule irradiation (shot 23544).

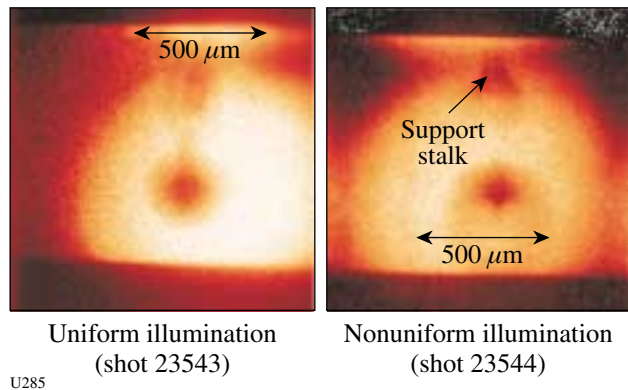


Figure 88.66
X-ray backlit images (Fe backlighter) from near-symmetric (shot 23543) and nonuniform illumination (shot 23544) of low-convergence implosions.

Slit Closure: One of the capability development programs carried out in FY01 involved the investigation of slit and pinhole closure by soft x rays. Figure 88.67 shows the experimental configuration and data obtained on two of these experiments. In this case, a Ti backlighter foil was irradiated by some of the OMEGA beams, and the transmission of the resulting x rays through a slit was measured with a streak camera. The graph compares the x-ray transmission through the slit as a function of time when a Be foil is placed between the Ti foil and the pinhole and when no foil is used. The Be foil is designed to block soft x rays from the Ti from irradiating the pinhole. No difference in transmission between these two cases is observed, implying that soft x rays are not the predominant mechanism for inducing slit or pinhole closure in such configurations. Future shots will investigate the effect of slit tamping on the closure.

Gas-Filled Sources: Experiments continued under the NWET program to develop the efficient x-ray sources to be used as

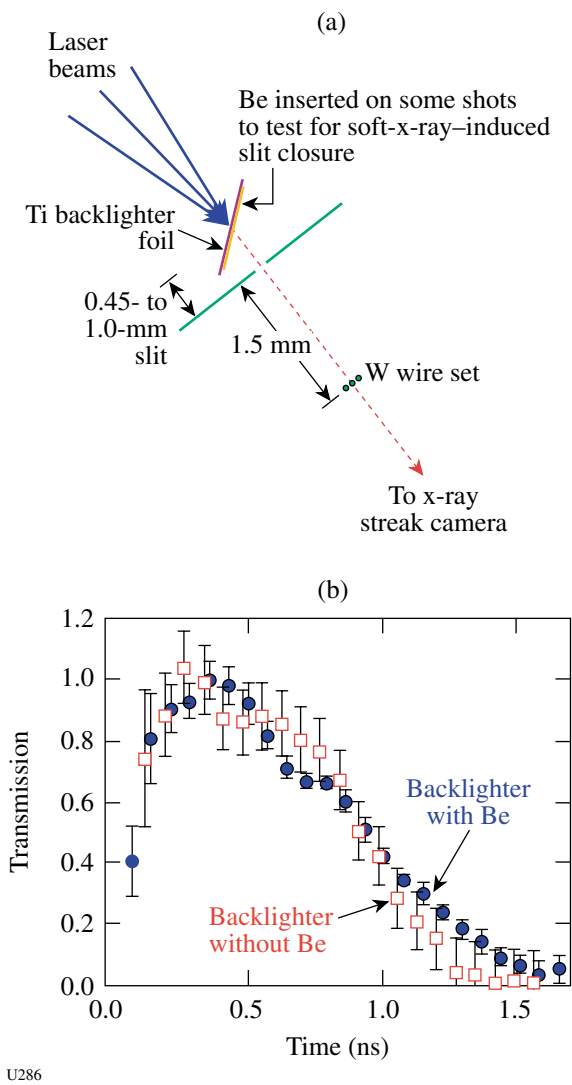
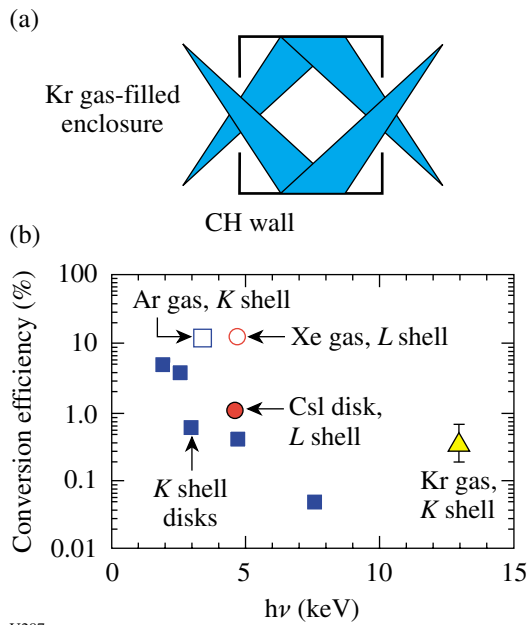


Figure 88.67
(a) Schematic of slit closure experiment and (b) results of transmission measurements.

backlighters for high- ρR and high-Z applications. During FY01, Kr *K*-shell emission was added to the list of efficient underdense multi-keV emitters. The experimental configuration (a Kr-filled CH cylinder) and a summary of the x-ray conversion results for emitters with energy in the range of 2 to 13 keV are shown in Fig. 88.68. The latest Kr gas experiments produced ~0.3% conversion in the ~13-keV Kr *K*-shell emission.



U287

Figure 88.68 (a) Schematic of gas-filled can radiation source experiments. (b) Results of conversion efficiency measurements for a series of gases and disks.

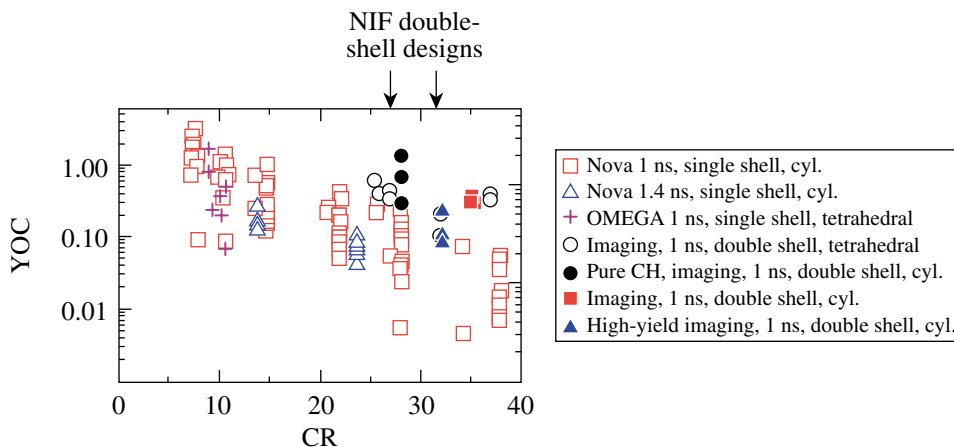
2. Los Alamos National Laboratory Campaigns

In FY01 LANL performed five campaigns on OMEGA. This work has been documented in the form of pre- and postshot reports:

- a. LANL ID01-1: Double shells in cylindrical hohlraums and ACE-A and ACE-B
 - Preshot report LA-UR-00-5574
 - Double-shell postshot report LA-UR-01-0432

- ACE-A postshot report LA-UR-01-1426
- ACE-B postshot report LA-UR-01-5433
- b. DDCYL 01-1: Direct-drive cylinders
 - Preshot report LA-UR-01-0953
 - DDCYL postshot report LA-UR-01-5511
- c. LANL ID01-2: X-ray backlighter development and ACE
 - Preshot report LA-UR-01-1659
 - ACE-A postshot report LA-UR-01-5559
- d. LANL ID01-3: High-yield nuclear diagnostic development and ACE
 - Preshot report LA-UR-01-4381
 - ACE-A postshot report LA-UR-01-5560
 - High-yield postshot report
 - Direct-drive double shells (DDCYL 01-2 cancelled because of the 9/11 events)
 - Preshot report LA-UR-01-5202

Double-Shell Capsules: Work continued on double-shell capsules as an alternative for ignition on the NIF. Previously, good results (high measured neutron yield relative to 1-D clean calculations) had been obtained in spherical hohlraums (a.k.a. “tetrahedral hohlraums,” referring to the locations of the laser entrance holes) with excellent irradiation symmetry. Representative capsules were shot on OMEGA to confirm that similar good results could be obtained with NIF-relevant symmetry in cylindrical hohlraums. Good results were obtained with deuterium-filled capsules, showing that drive symmetry was not the principal issue of performance for these capsules (see Fig. 88.69). Subsequently, larger capsules were shot using direct-drive illumination that would remove any



U288

Figure 88.69 Measured neutron yield divided by 1-D, clean calculated yield (YOC) versus convergence ratio (CR) for all OMEGA imaging and pure-CH imaging shots to date, in tetrahedral and NIF-style cylindrical hohlraums. The data for the NIF-style hohlraums is shown as solid points, while the tetrahedral results are shown as circles or open crosses. In the legend, “cyl” is a cylindrical hohlraum.

M-band asymmetries due to laser spots in the hohlraums. Poor results were obtained in this series. The issues of target fabrication, mix, and direct-drive physics are being investigated to understand the later results.

X-Ray Backlighting Sources: The development of x-ray backlighting sources and the optimization of x-ray conversion efficiency for these sources are important for the design of future NIF experiments. Various mid-Z elements and a variety of spot sizes and intensities of 3ω light have been investigated on OMEGA experiments. Data showing the dependence of conversion efficiency on spot size at similar irradiance have been obtained (Fig. 88.70). The peak x-ray conversion as a function of intensity has been identified for different configurations.

ACE Experiments: The ACE experiments successfully obtained data for the high-energy-density support of the Stockpile Systems Program. Some experiments featured an innovative backlighter system that provides very bright emission and is flat in intensity across the field of view (illustrated in Fig. 88.71).

Direct-Drive Cylindrical Implosions: Direct-drive cylinder work continued in two campaigns. The ablative RT work evaluated target fabrication and image quality to achieve quantitative data for comparison to hydrocode predictions. Figure 88.72 shows imaging x-ray streak camera data from such a cylindrical implosion with a ramp drive pulse. Just before the end of the 2.5-ns linear ramp, the chlorine in the

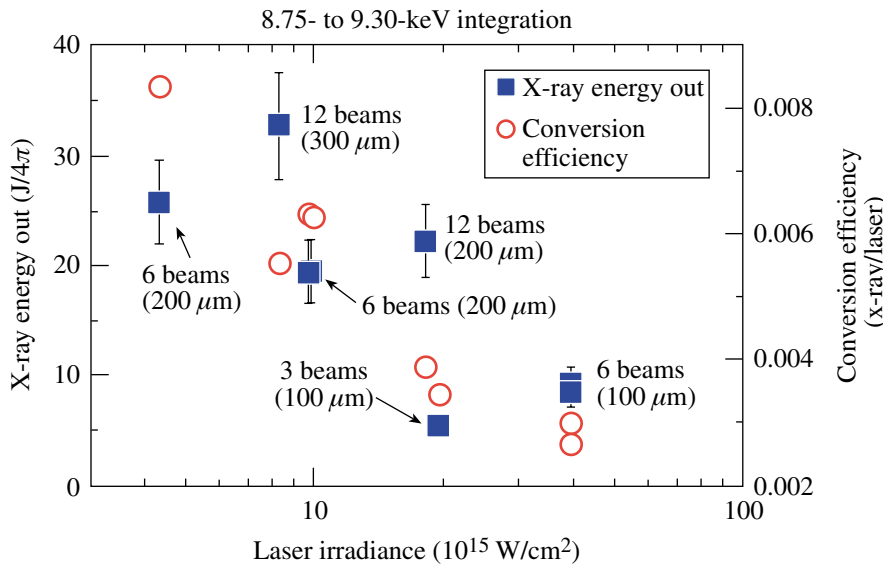


Figure 88.70 Plot of measured x-ray energy in He- α lines of Zn taken using a time-integrated Henway spectrometer versus laser irradiance from overlapped beams with indicated spot size.

U289

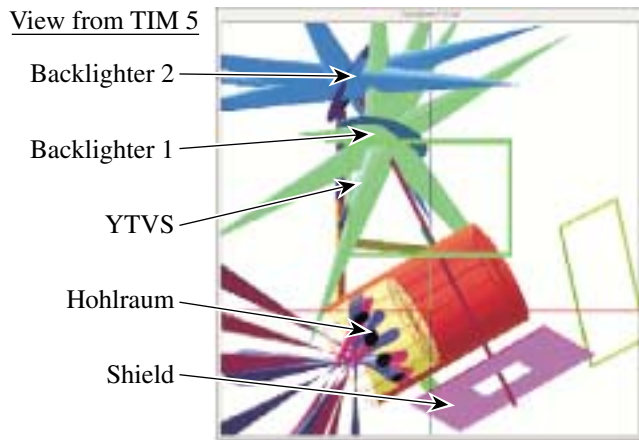


Figure 88.71 The ACE-B geometry with two backlighters irradiated by 17 beams to carry out radiography of a halfraum with 12 drive beams.

U290

marker layer burns through due to the formation of spikes by the action of the RT instability. Unfortunately, it has been decided that, at present, targets with sufficiently small and controlled surface roughness cannot be fabricated to quantitatively address the relevant physics of this experiment so this campaign has been stopped. The direct-drive cylinder mix program has made significant success in demonstrating measurable mix in a convergent, compressible plasma experiment. Thick (60- to 73- μm) ablators separate the direct-drive laser absorption region from the "pure" hydrodynamic marker. Detailed calculations are being made to model this data using a number of codes, including the *RAGE* adaptive mesh refinement code at Los Alamos illustrated in Fig. 88.73. This year mix-width data (Fig. 88.74) were taken at different times during the implosion and compared to the *RAGE* simulations.

NIF Diagnostics: Los Alamos continues to develop Phase 2 fusion product diagnostics for the NIF, including both the Gas Cerenkov gamma-ray burn history diagnostic and pinhole-

aperture neutron imaging. The Gas Cerenkov System obtained definite evidence for the DT fusion gamma on OMEGA. The neutron imaging system, in collaboration with CEA and LLE, obtained images for the first time.

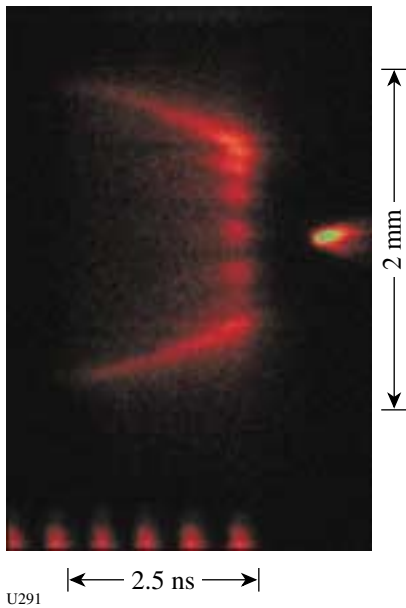


Figure 88.72 Imaging x-ray streak camera (IXRSC) image from shot 22622 showing intensity transversely across the cylinder (up-down) versus time (left-right). The ablation surface implodes, with the spikes of the original $m = 14$ perturbation burning through just before the end of the 2.5-ns linear ramp laser drive. Subsequently, the core of the cylinder implodes and lights up in self-emission.

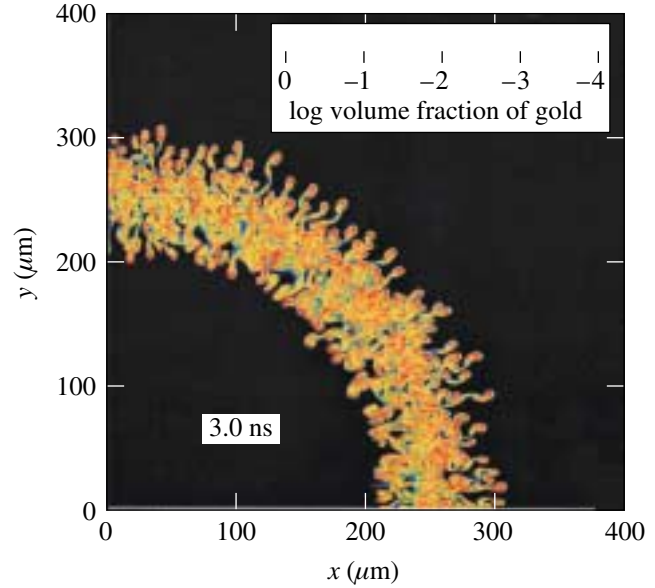


Figure 88.73 *RAGE* simulation of the volume fraction of a gold marker in an r - θ calculation at 3.0 ns into a direct-drive cylindrical mix implosion.

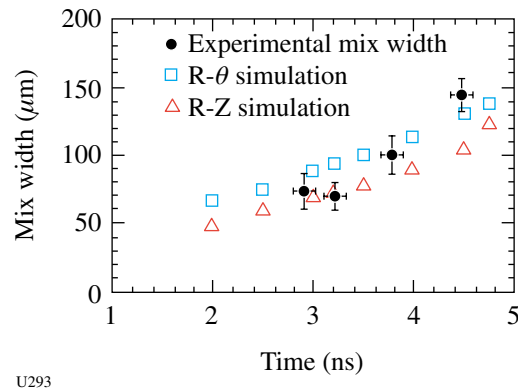


Figure 88.74 Comparison of experimental measurements of rough gold marker mix width in time with *RAGE* simulations.

3. CEA Experiments

CEA scientists participated in several OMEGA experiments during FY01 including neutron imaging development and evaluation and measurement of gamma yields on OMEGA.

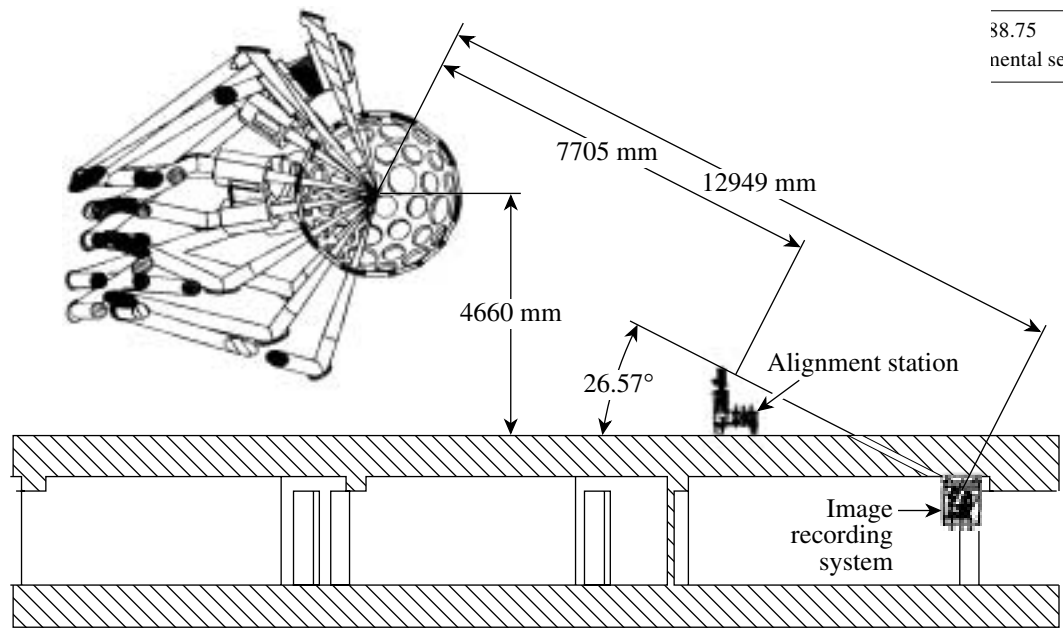
Imaging of the neutrons produced by implosions on the NIF and the LMJ will require spatial resolution as great as $5\ \mu\text{m}$ to distinguish failure mechanisms such as poor implosion symmetry or improper laser pulse shaping. Coded imaging, either by penumbral or annular aperture, will be used to achieve high resolution and good sensitivity.² In FY00, CEA implemented a neutron imaging system (NIS) on OMEGA based on penumbral imaging using a biconical aperture. Using NIS, the neutron burn regions of imploded DT-filled glass microballons with 2.5- and 4.2- μm -thick walls were imaged and produced images with FWHM's of 78 and 62 μm , recorded with a resolution of 60 and 45 μm , respectively.³

This year (FY01), a spatial resolution of 20 μm was attained on implosions of CH and glass targets. The smallest features observed on the implosion of 15-atm-DT-filled CH capsule implosions were $\sim 30\ \mu\text{m}$.

To improve the NIS resolution, LLE drilled a hole in the concrete floor of the Target Bay, allowing a 13-m line of sight and a 1.6-m concrete shield for the NIS CCD detector (Fig. 88.75).

In parallel, a new neutron detector with 250- μm pixels was installed. This detector is made by filling an array of 160,000 capillaries⁴ with a high-optical-index liquid scintillator. The optical-index step between the glass (1.49) and the liquid (1.58) traps the scintillation light produced by the slowing down of the recoil protons scattered by the 14-MeV neutrons. Both the pixel size and the transverse range of the recoil protons limit the neutron detector's spatial resolution to 1.1 mm. With a biconical aperture with a 200- μm field of view placed at 160 mm from target center, the ultimate resolution of NIS is now 17- μm FWHM.

Direct-drive implosions of DT-filled glass targets and CH targets were conducted during the experimental campaign. A typical unfolded neutron image from a CH target implosion (shot 23445) is shown in Fig. 88.76. The target in this case was a 932- μm -diam, 18.9- μm -thick CH shell filled with 15 atm of DT and produced a yield of 2×10^{13} .



38.75
mental setup of the neutron imaging system.

U294

A new neutron detector is now being constructed. The scintillator will be loaded with deuterium to reduce the range of the recoil protons. The expected resolution of the new **detector** will be less than 0.5 mm. In parallel with the construction of the new detector, a thin annular aperture is under development. The first attempt will be made with a 5-cm-thick, 0.66-mm-diam cylinder of tungsten. This effort should lead to high-resolution neutron imaging at a low ($\sim 10^{12}$) level of neutron production.

REFERENCES

1. C. A. Iglesias and S. J. Rose, *Astrophys. J. Lett.* **466**, L115 (1996); F. J. Rogers, B. G. Wilson, and C. A. Iglesias, *Phys. Rev. A, Gen. Phys.* **38**, 5007 (1988).
2. R. A. Lerche *et al.*, *Laser Part. Beams* **9**, 99 (1991).
3. L. Disdier, A. Rouyer, A. Fedotoff, V. Yu. Glebov, C. Stoeckl, and F. J. Marshall, "Neutron Prenumbral Imaging at OMEGA," submitted to *Nuclear Instruments & Methods in Physics Research, Section A; Laboratory for Laser Energetics LLE Review* **86**, 74, NTIS document No. DOE/SF/19460-393 (2001). Copies may be obtained from the National Technical Information Service, Springfield, VA 22161.
4. P. Annis *et al.*, *Nucl. Instrum. Methods Phys. Res. A* **367**, 377 (1995).

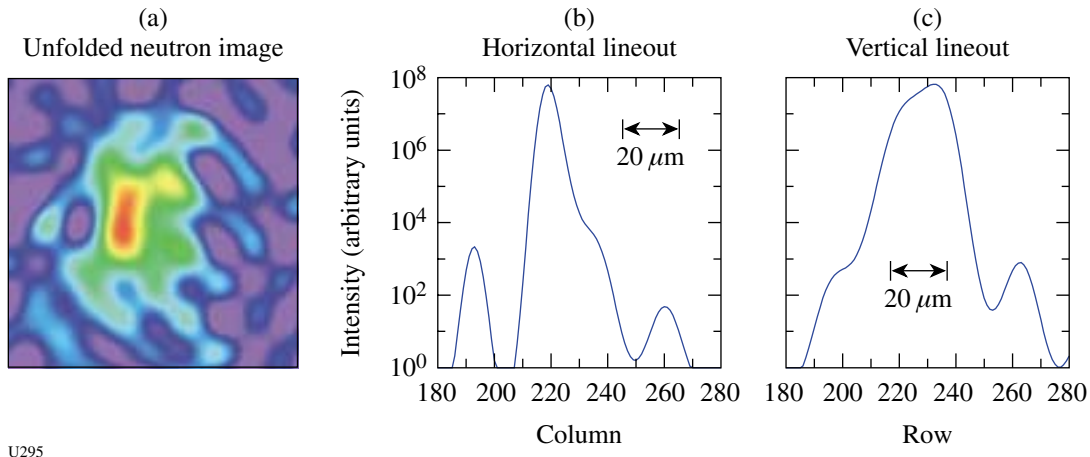


Figure 88.76

(a) Neutron image ($200 \times 200 \mu\text{m}^2$) on shot 23445; (b) horizontal and (c) vertical profiles (43- μm and 75- μm FWHM, respectively). The arrows represent 20 μm in the target plane.

Publications and Conference Presentations

Publications

- R. Adam, R. Sobolewski, and M. Darula, "Subpicosecond Dynamics of the Switching Process in Y-Ba-Cu-O Josephson Junctions," in *Superconducting and Related Oxides: Physics and Nanoengineering IV*, edited by I. Bozovic and D. Pavuna (SPIE, Bellingham, WA, 2000), Vol. 4058, pp. 230–244.
- T. R. Boehly, A. Babushkin, D. K. Bradley, R. S. Craxton, J. A. Delettrez, R. Epstein, T. J. Kessler, J. P. Knauer, R. L. McCrory, P. W. McKenty, D. D. Meyerhofer, S. Regan, W. Seka, S. Skupsky, V. A. Smalyuk, R. P. J. Town, and B. Yaakobi, "Laser-Uniformity and Hydrodynamic-Stability Experiments at the OMEGA Laser Facility," *Laser Part. Beams* **18**, 11 (2000).
- T. R. Boehly, A. Babushkin, D. K. Bradley, R. S. Craxton, J. A. Delettrez, R. Epstein, T. J. Kessler, J. P. Knauer, R. L. McCrory, P. W. McKenty, D. D. Meyerhofer, S. P. Regan, W. Seka, S. Skupsky, V. A. Smalyuk, R. P. J. Town, and B. Yaakobi, "Optical and Plasma Smoothing of Laser Imprinting in Targets Driven by Lasers with SSD Bandwidths Up to 1 THz," *Phys. Plasmas* **8**, 2331 (2001) (invited).
- T. R. Boehly, J. A. Delettrez, J. P. Knauer, D. D. Meyerhofer, B. Yaakobi, R. P. J. Town, and D. Hoarty, "Effect of Shock Heating on the Stability of Laser-Driven Targets," *Phys. Rev. Lett.* **87**, 145003 (2001).
- T. R. Boehly, Y. Fisher, D. D. Meyerhofer, W. Seka, J. M. Soures, and D. K. Bradley, "The Effect of Optical Prepulse on Direct-Drive Inertial Confinement Fusion Target Performance," *Phys. Plasmas* **8**, 231 (2001).
- D. P. Butler, Z. Celik-Butler, and R. Sobolewski, "Y-Ba-Cu-O as an Infrared Radiation Sensing Material," in *Handbook of Advanced Electronic and Photonic Materials and Devices*, edited by H. S. Nawly, Vol. 3: High T_c Superconductors and Organic Conductors (Academic Press, NY, 2001), Chap. 4, pp. 169–195.
- V. Yu. Glebov, D. D. Meyerhofer, C. Stoeckl, and J. D. Zuegel, "Secondary-Neutron-Yield Measurements by Current-Mode Detectors," *Rev. Sci. Instrum.* **72**, 824 (2001).
- W. Göb, W. Liebich, W. Lang, I. Puica, R. Sobolewski, R. Rössler, J. D. Pedarnig, and D. Bäuerle, "Double Sign Reversal of the Vortex Hall Effect in $\text{YBa}_2\text{Cu}_3\text{O}_{7-\delta}$ Thin Films in the Strong Pinning Limit of Low Magnetic Fields," *Phys. Rev. B* **62**, 9780 (2000).
- G. N. Gol'tsman, O. Okunev, G. Chulkova, A. Dzardanov, A. Lipatov, A. Semenov, K. Smirnov, B. Voronov, C. Williams, and R. Sobolewski, "Picosecond Superconducting Single-Photon Optical Detector," *Appl. Phys. Lett.* **79**, 705 (2001).
- V. N. Goncharov, P. McKenty, S. Skupsky, R. Betti, R. L. McCrory, and C. Cherfils-Clérrouin, "Modeling Hydrodynamic Instabilities in Inertial Confinement Fusion Targets," *Phys. Plasmas* **7**, 5118 (2001).
- K. Green and R. Sobolewski, "Extending Scattering-Parameter Approach to Characterization of Linear Time-Varying Microwave Devices," *IEEE Trans. Microw. Theory Tech.* **48**, 1725 (2000).
- P. A. Jaanimagi, R. Boni, and R. L. Keck, "Neutron-Induced Background in Charge-Coupled Device Detectors," *Rev. Sci. Instrum.* **72**, 801 (2001).
- D. Katsis, H. P. Chen, S. H. Chen, L. J. Rothberg, and T. Tsutsui, "Polarized Photoluminescence from Solid Films of Nematic and Chiral-Nematic Poly(*p*-phenylene)s," *Appl. Phys. Lett.* **77**, 2982 (2000).

C. K. Li, D. G. Hicks, F. H. Séguin, J. Frenje, R. D. Petrasso, J. M. Soures, P. B. Radha, V. Yu. Glebov, C. Stoeckl, J. P. Knauer, F. J. Marshall, D. D. Meyerhofer, S. Skupsky, S. Roberts, C. Sorce, T. C. Sangster, T. W. Phillips, and M. D. Cable, "Measuring Fusion Yields, Areal Densities, and Ion Temperatures of Imploded Capsules at OMEGA," *Rev. Sci. Instrum.* **72**, 864 (2001).

A. E. Marino, S. R. Arrasmith, L. L. Gregg, S. D. Jacobs, G. Chen, and Y. Duc, "Durable Phosphate Glasses with Lower Transition Temperatures," *J. Non-Cryst. Solids* **289**, 37 (2001).

F. J. Marshall, T. Ohki, D. McInnis, Z. Ninkov, and J. Carbone, "Imaging of Laser-Plasma X-Ray Emission with Charge-Injection Devices," *Rev. Sci. Instrum.* **72**, 713 (2001).

R. L. McCrory, R. E. Bahr, T. R. Boehly, T. J. B. Collins, R. S. Craxton, J. A. Delettrez, W. R. Donaldson, R. Epstein, V. N. Goncharov, R. Q. Gram, D. R. Harding, P. A. Jaanimagi, R. L. Keck, J. P. Knauer, S. J. Loucks, F. J. Marshall, P. W. McKenty, D. D. Meyerhofer, S. F. B. Morse, O. V. Gotchev, P. B. Radha, S. P. Regan, W. Seka, S. Skupsky, V. A. Smalyuk, J. M. Soures, C. Stoeckl, R. P. J. Town, M. D. Wittman, B. Yaakobi, J. D. Zuegel, R. D. Petrasso, D. G. Hicks, and C. K. Li, "OMEGA Experiments and Preparation for Moderate-Gain Direct-Drive Experiments on NIF," in *C. R. Acad. Sci. Paris*, t.1, Série IV (Elsevier, Amsterdam, 2000), pp. 681–691.

P. W. McKenty, V. N. Goncharov, R. P. J. Town, S. Skupsky, R. Betti, and R. L. McCrory, "Analysis of a Direct-Drive Ignition Capsule Designed for the National Ignition Facility," *Phys. Plasmas* **8**, 2315 (2001) (invited).

D. D. Meyerhofer, J. A. Delettrez, R. Epstein, V. Yu. Glebov, V. N. Goncharov, R. L. Keck, R. L. McCrory, P. W. McKenty, F. J. Marshall, P. B. Radha, S. P. Regan, S. Roberts, W. Seka, S. Skupsky, V. A. Smalyuk, C. Sorce, J. M. Soures, C. Stoeckl, R. P. J. Town, B. Yaakobi, J. D. Zuegel, R. D. Petrasso, S. Padalino, J. A. Frenje, D. G. Hicks, F. H. Séguin, C. K. Li, N. Izumi, R. Lerche, T. C. Sangster, and T. W. Phillips, "Core Performance and Mix in Direct-Drive Spherical Implosions with High Uniformity," *Phys. Plasmas* **8**, 2251 (2001) (invited).

A. V. Okishev, R. Boni, M. Millecchia, P. A. Jaanimagi, W. R. Donaldson, R. L. Keck, W. Seka, K. V. Dukelsky, M. A. Eronyan, V. S. Shevandin, G. M. Ermolaeva, G. E. Nikolaev, and V. B. Shilov, "Unique High-Bandwidth UV Fiber Delivery System for the OMEGA Diagnostics Applications," *IEEE J. Sel. Top. Quantum Electron.* **7**, 471 (2001).

A. V. Okishev, M. D. Skeldon, R. L. Keck, and W. Seka, "A New High-Bandwidth, All-Solid-State Pulse-Shaping System for the OMEGA Laser Facility," in *Laser Optics 2000: Ultrafast Optics and Superstrong Laser Fields*, edited by A. A. Andreev and V. E. Yashin (SPIE, Bellingham, WA, 2001), pp. 69–73.

S. P. Regan, J. A. Marozas, J. H. Kelly, T. R. Boehly, W. R. Donaldson, P. A. Jaanimagi, R. L. Keck, T. J. Kessler, D. D. Meyerhofer, W. Seka, S. Skupsky, and V. A. Smalyuk, "Experimental Investigation of Smoothing by Spectral Dispersion," *J. Opt. Soc. Am. B* **17**, 1483 (2000).

A. B. Shorey, S. D. Jacobs, W. I. Kordonski, and R. F. Gans, "Experiments and Observations Regarding the Mechanisms of Glass Removal in Magnetorheological Finishing," *Appl. Opt.* **40**, 20 (2001).

A. B. Shorey, K. M. Kwong, K. M. Johnson, and S. D. Jacobs, "Nanoindentation Hardness of Particles Used in Magnetorheological Finishing (MRF)," *App. Opt.* **39**, 5194 (2000).

V. A. Smalyuk, T. R. Boehly, L. S. Iwan, T. J. Kessler, J. P. Knauer, F. J. Marshall, D. D. Meyerhofer, C. Stoeckl, B. Yaakobi, and D. K. Bradley, "Fourier-Space Image Processing for Spherical Experiments on OMEGA," *Rev. Sci. Instrum.* **72**, 635 (2001) (invited).

V. A. Smalyuk, V. N. Goncharov, B. Yaakobi, J. A. Delettrez, F. J. Marshall, D. D. Meyerhofer, and S. P. Regan, "Evolution of Shell Nonuniformities Near Peak Compression of a Spherical Implosion," *Phys. Rev. Lett.* **87**, 155002 (2001).

V. A. Smalyuk, B. Yaakobi, J. A. Delettrez, F. J. Marshall, and D. D. Meyerhofer, "Compressed-Shell Integrity Measurements in Spherical Implosions Experiments," *Phys. Plasmas* **8**, 2872 (2001).

V. A. Smalyuk, B. Yaakobi, F. J. Marshall, and D. D. Meyerhofer, "X-Ray Spectroscopic Measurements of Areal Density and Modulations in Areal Density of Compressed Shells in Implosion Experiments on OMEGA," in *Atomic Processes in Plasmas: Twelfth Topical Conf.*, edited by R. C. Mancini and R. A. Phaneuf (American Institute of Physics, New York, 2000), pp. 15–24.

R. Sobolewski, D. P. Butler, and Z. Celik-Butler, "Cooled and Uncooled Infrared Detectors Based on Yttrium Barium Copper Oxide," in *Smart Optical Inorganic Structures and Devices*, edited by S. P. Asmontas and J. Gradauskas (SPIE, Bellingham, WA, 2001), Vol. 4318, pp. 204–214 (invited).

C. Stoeckl, V. Yu. Glebov, D. D. Meyerhofer, W. Seka, B. Yaakobi, R. P. J. Town, and J. D. Zuegel, "Hard X-Ray Detectors for OMEGA and NIF," *Rev. Sci. Instrum.* **72**, 1197 (2001).

OMEGA External User Publications

P. Amendt, A. I. Shestakov, O. L. Landen, D. K. Bradley, S. M. Pollaine, L. J. Suter, and R. E. Turner, "Thin-Shell Symmetry Surrogates for the National Ignition Facility: A Rocket Equation Analysis," *Phys. Plasmas* **8**, 2908 (2001).

J. L. Bourgade, B. Villette, J. L. Bocher, J. Y. Boutin, S. Chiche, N. Dague, D. Gontier, J. P. Jadaud, B. Savale, R. Wrobel, and R. E. Turner, "DMX: An Absolutely Calibrated Time-Resolved Broadband Soft X-Ray Spectrometer Designated for MJ-Class-Laser-Produced Plasmas," *Rev. Sci. Instrum.* **72**, 1173 (2001).

A. B. Bullock, O. L. Landen, and D. K. Bradley, "Relative X-Ray Backlighter Intensity Comparison of Ti and Ti/Sc Combination Foils Driven in Double-Sided and Single-Sided Laser Configurations," *Rev. Sci. Instrum.* **72**, 686 (2001).

A. B. Bullock, O. L. Landen, and D. K. Bradley, "10- and 5- μm -Pinhole-Assisted Point-Projection Backlit Imaging for the National Ignition Facility," *Rev. Sci. Instrum.* **72**, 690 (2001).

E. Dattolo, L. Suter, M.-C. Monteil, J.-P. Jadaud, N. Dague, S. Glenzer, R. Turner, D. Juraszek, B. Lasinski, C. Decker, O. Landen, and B. MacGowan, "Status of Our Understanding and Modeling of X-Ray Coupling Efficiency in Laser-Heated Hohlräume," *Phys. Plasmas* **8**, 260 (2001).

S. C. Evans, T. N. Archuleta, J. A. Oertel, and P. J. Walsh, "Quantitative X-Ray Imager," *Rev. Sci. Instrum.* **72**, 705 (2001).

J. A. Frenje, K. M. Green, D. G. Hicks, C. K. Li, F. H. Séguin, R. D. Petrasso, T. C. Sangster, T. W. Phillips, V. Yu. Glebov, D. D. Meyerhofer, S. Roberts, J. M. Soures, C. Stoeckl, K. Fletcher, S. Padalino, and R. J. Leeper, "A Neutron Spectrometer for Precise Measurements of DT Neutrons from 10 to 18 MeV at OMEGA and the National Ignition Facility," *Rev. Sci. Instrum.* **72**, 854 (2001).

D. G. Hicks, C. K. Li, F. H. Séguin, J. A. Frenje, R. D. Petrasso, and T. C. Sangster, "Optimal Foil Shape for Neutron Time-of-Flight Measurements Using Elastic Recoils," *Rev. Sci. Instrum.* **72**, 859 (2001).

D. G. Hicks, C. K. Li, F. H. Séguin, J. D. Schnittman, A. K. Ram, J. A. Frenje, R. D. Petrasso, J. M. Soures, D. D. Meyerhofer, S. Roberts, C. Sorce, C. Stoeckl, T. C. Sangster, and T. W. Phillips, "Observations of Fast Protons Above 1 MeV Produced in Direct-Drive Laser Fusion Experiments," *Phys. Plasmas* **8**, 606 (2001).

J. O. Kane, H. F. Robey, B. A. Remington, R. P. Drake, J. Knauer, D. D. Ryutov, H. Louis, R. Teyssier, O. Hurricane, D. Arnett, R. Rosner, and A. Calder, "Interface Imprinting by a Rippled Shock Using an Intense Laser," *Phys. Rev. E* **63**, 055401/1 (2001).

J. R. Kimbrough, P. M. Bell, G. B. Christianson, F. D. Lee, D. H. Kalantar, T. S. Perry, N. R. Sewall, and A. J. Wootton, "National Ignition Facility Core X-Ray Streak Camera," *Rev. Sci. Instrum.* **72**, 748 (2001).

O. L. Landen, D. R. Farley, S. G. Glendinning, L. M. Logory, P. M. Bell, J. A. Koch, F. D. Lee, D. K. Bradley, D. H. Kalantar, C. A. Back, and R. E. Turner, "X-ray Backlighting for the National Ignition Facility," *Rev. Sci. Instrum.* **72**, 627 (2001).

A. Loveridge-Smith, A. Allen, J. Belak, T. R. Boehly, A. Hauer, B. Holian, D. Kalantar, G. Kyrala, R. W. Lee, P. Lomdahl, M. A. Meyers, D. Paisley, S. Pollaine, B. Remington, D. C. Swift, S. Weber, and J. S. Wark, "Anomalous Elastic Response of Silicon to Uniaxial Shock Compression on Nanosecond Time Scales," *Phys. Rev. Lett.* **86**, 2349 (2001).

G. L. Morgan, R. R. Berggren, P. A. Bradley, F. H. Cverna, J. R. Faulkner, P. L. Gobby, J. A. Oertel, F. J. Swenson, J. A. Tegtmeier, R. B. Walton, M. D. Wilke, and D. C. Wilson, "Development of a Neutron Imaging Diagnostic for Inertial Confinement Fusion Experiments," *Rev. Sci. Instrum.* **72**, 865 (2001).

T. J. Murphy, C. W. Barnes, R. R. Berggren, P. Bradley, S. E. Caldwell, R. E. Chrien, J. R. Faulkner, P. L. Gobby, N. Hoffman, J. L. Limerson, K. A. Klare, C. L. Lee, J. M. Mack, G. L. Morgan, J. A. Oertel, J. Swenson, P. J. Walsh, R. B. Walton, R. G. Watt, M. D. Wilke, D. C. Wilson, C. S. Young, S. W. Haan, R. A. Lerche, M. J. Moran, T. W. Phillips,

T. C. Sangster, R. J. Leeper, C. L. Ruiz, G. W. Cooper, L. Disdier, A. Rouyer, A. Fedotoff, V. Yu. Glebov, D. D. Meyerhofer, J. M. Soures, C. Stoeckl, J. A. Frenje, D. G. Hicks, C. K. Li, R. D. Petrasso, F. H. Séguin, K. Fletcher, S. Padalino, and R. K. Fisher, "Nuclear Diagnostics for the National Ignition Facility," *Rev. Sci. Instrum.* **72**, 773 (2001) (invited).

T. J. Murphy, J. L. Jimerson, R. R. Berggren, J. R. Faulkner, J. A. Oertel, and P. J. Walsh, "Neutron Time-of-Flight and Emission Time Diagnostics for the National Ignition Facility," *Rev. Sci. Instrum.* **72**, 850 (2001).

J. A. Oertel, T. N. Archuleta, and L. S. Schrank, "The Large-Format X-Ray Imager," *Rev. Sci. Instrum.* **72**, 701 (2001).

S. M. Pollaine, D. K. Bradley, O. L. Landen, R. J. Wallace, O. S. Jones, P. A. Amendt, L. J. Suter, and R. E. Turner, "National Ignition Facility–Scale Hohlraum Asymmetry Studies by Thin Shell Radiography," *Phys. Plasmas* **8**, 2357 (2001).

H. F. Robey, J. O. Kane, B. A. Remington, R. P. Drake, O. A. Hurricane, H. Louis, R. J. Wallace, J. Knauer, P. Keiter, D. Arnett, and D. D. Ryutov, "An Experimental Test Bed for the Study of Hydrodynamic Issues in Supernovae," *Phys. Plasmas* **8**, 2446 (2001).

J. Seely, C. Back, R. Deslattes, L. Hudson, G. Holland, P. Bell, and M. Miller, "Hard X-Ray Spectrometers for the National Ignition Facility," *Rev. Sci. Instrum.* **72**, 2562 (2001).

Conference Presentations

S. D. Jacobs and S. R. Arrasmith “Magnetorheological Finishing of Optics,” ASME International Joint Tribology Conference, Seattle, WA, 1–4 October 2000.

R. L. McCrory, R. E. Bahr, R. Betti, T. R. Boehly, T. J. B. Collins, R. S. Craxton, J. A. Delettrez, W. R. Donaldson, R. Epstein, J. Frenje, V. Yu. Glebov, V. N. Goncharov, O. V. Gotchev, R. Q. Gram, D. R. Harding, D. G. Hicks, P. A. Jaanimagi, R. L. Keck, J. Kelly, J. P. Knauer, C. K. Li, S. J. Loucks, L. D. Lund, F. J. Marshall, P. W. McKenty, D. D. Meyerhofer, S. F. B. Morse, R. D. Petrasso, P. B. Radha, S. P. Regan, S. Roberts, F. Séguin, W. Seka, S. Skupsky, V. A. Smalyuk, C. Sorce, J. M. Soures, C. Stoeckl, R. P. J. Town, M. D. Wittman, B. Yaakobi, and J. D. Zuegel, “OMEGA ICF Experiments and Preparation for Direct-Drive Ignition on NIF,” 18th IAEA Fusion Energy Conference, Sorrento, Italy, 4–10 October 2000.

The following presentations were made at the 16th Interdisciplinary Laser Science Conference (ILS-XVI), Providence, RI, 22–26 October 2000:

M. J. Guardalben, L. Ning, N. Jain, and D. J. Battaglia, “Investigation of Error Sources in the Liquid Crystal Point Diffraction Interferometer (LCPDI).”

J. H. Kelly, A. Babushkin, R. Boni, W. R. Donaldson, P. A. Jaanimagi, R. L. Keck, R. L. McCrory, S. F. B. Morse, A. V. Okishev, R. G. Peck, R. G. Roides, W. Seka, M. D. Skeldon, and K. A. Thorp, “Safely Operating a Large-Scale Laser Facility for Fusion Research.”

T. Z. Kosc, K. L. Marshall, and S. D. Jacobs, “Polymer Liquid Crystal Flakes for Switchable Optical Devices.”

K. L. Marshall, M. J. Guardalben, S. M. Corsello, M. S. Moore, I. A. Lippa, and R. P. Brecker, “Device Applications of Highly Soluble Near-Infrared Transition Metal Dyes in Liquid Crystal Hosts.”

The following presentations were made at the 42nd Annual Meeting of the APS Division of Plasma Physics, Quebec City, Canada, 23–27 October 2000:

R. Betti, M. Umansky, and V. Lobatchev, “Theory of the Deceleration-Phase Rayleigh–Taylor Instability.”

T. R. Boehly, “Optical and Plasma Smoothing of Laser Imprinting in Targets Driven by Lasers with SSD Bandwidths up to 1 THz” (invited).

T. R. Boehly, B. Yaakobi, J. P. Knauer, D. D. Meyerhofer, R. P. J. Town, D. Hoarty, and O. Willi, “Measurements of Shock Heating Al Absorption Spectroscopy in Planar Targets.”

T. J. B. Collins and S. Skupsky, “Imprint Reduction with Shaped Pulses.”

R. S. Craxton, J. A. Marozas, and S. Skupsky, “Two-Dimensional Hydrodynamic Simulations of SSD Laser Imprint.”

J. A. Delettrez, S. P. Regan, P. B. Radha, and R. P. J. Town, “A New Model for the Analysis of Burnthrough Experiments on OMEGA.”

R. Epstein, J. A. Delettrez, P. B. Radha, T. R. Boehly, S. P. Regan, B. Yaakobi, and J. J. MacFarlane, “Two-Dimensional Simulations of X-Ray Absorption Spectra from Nonuniformly Driven Planar Targets.”

J. A. Frenje, K. M. Green, D. G. Hicks, C. K. Li, F. H. Séguin, R. D. Petrasso, T. C. Sangster, T. W. Phillips, V. Yu. Glebov, D. D. Meyerhofer, S. Roberts, J. M. Soures, C. Stoeckl, K. Fletcher, and S. Padalino, “A Neutron Spectrometer for Precise Measurements of DT Neutrons from 10 to 18 MeV at OMEGA and the National Ignition Facility.”

V. Yu. Glebov, D. D. Meyerhofer, and C. Stoeckl, “Measurement of Secondary Neutron Yield by Copper Activation.”

O. V. Gotchev, P. A. Jaanimagi, J. P. Knauer, F. J. Marshall, and D. D. Meyerhofer, “A High-Throughput, High-Resolution, Streaked Kirkpatrick-Baez Microscope for Planar Direct-Drive Experiments on OMEGA.”

D. G. Hicks, C. K. Li, F. H. Séguin, A. K. Ram, J. A. Frenje, R. D. Petrasso, J. M. Soures, V. Yu. Glebov, D. D. Meyerhofer, S. Roberts, C. Sorce, C. Stoeckl, T. C. Sangster, and T. W. Phillips, “Charged-Particle Acceleration and Energy Loss Measurements on OMEGA.”

A. V. Kanaev and C. J. McKinstrie, “Numerical Simulations of the SSD- and DPP-Smoothed Laser Beam Filamentation and Forward Stimulated Brillouin Scattering in Plasmas.”

R. L. Keck, W. R. Donaldson, P. A. Jaanimagi, W. Seka, and R. Boni, “Beam Power Matching on the OMEGA Laser.”

D. Keller, T. J. B. Collins, J. A. Delettrez, R. Epstein, P. W. McKenty, P. B. Radha, R. P. J. Town, G. A. Moses, P. P. H. Wilson, and J. J. MacFarlane, “Modeling Planar Burnthrough and Adiabatic Experiments Using *DRACO*.”

J. P. Knauer, R. Betti, T. R. Boehly, T. J. B. Collins, D. D. Meyerhofer, R. P. J. Town, and V. A. Smalyuk, “Measured Reduction of RT Growth at the Ablation Interface by Modification of the Isentrope.”

M. V. Kozlov and C. J. McKinstrie, “Nonlinear Sound Waves in Two-Ion Plasmas.”

C. K. Li, D. G. Hicks, F. H. Séguin, J. A. Frenje, K. M. Green, R. D. Petrasso, J. M. Soures, D. D. Meyerhofer, V. Yu. Glebov, C. Stoeckl, S. Roberts, T. C. Sangster, and T. W. Phillips, “Measurements of Areal Densities and Temperatures from DT Capsule Implosions on OMEGA.”

V. Lobatchev, M. Umansky, and R. Betti, “Growth Rates of the Deceleration-Phase Rayleigh–Taylor Instability.”

J. A. Marozas and J. D. Zuegel, “The Smoothing Performance of Various Picket-Fence Schemes on NIF.”

F. J. Marshall, J. A. Delettrez, D. D. Meyerhofer, T. A. Ohki, S. P. Regan, V. A. Smalyuk, B. Yaakobi, and J. A. Oertel, “Monochromatic Imaging of Direct-Drive Implosions on OMEGA.”

P. W. McKenty, V. N. Goncharov, R. P. J. Town, S. Skupsky, R. Betti, and R. L. McCrory, “Analysis of a Direct-Drive Ignition Capsule Designed for the NIF.”

C. J. McKinstrie and M. V. Kozlov, “SBS from Fast and Slow Waves in Two-Ion Plasmas.”

D. D. Meyerhofer, J. A. Delettrez, R. Epstein, V. Yu. Glebov, V. N. Goncharov, R. L. Keck, R. L. McCrory, P. W. McKenty, F. J. Marshall, P. B. Radha, S. P. Regan, S. Roberts, W. Seka, S. Skupsky, V. A. Smalyuk, J. M. Soures, C. Stoeckl, C. Sorce, R. P. J. Town, B. Yaakobi, J. D. Zuegel, R. D. Petrasso, S. Padalino, J. A. Frenje, D. G. Hicks, F. H. Séguin, C. K. Li,

N. Izumi, R. Lerche, T. C. Sangster, and T. W. Phillips, “Core Performance and Mix in Direct-Drive Spherical Implosions with High Uniformity” (invited).

P. B. Radha, V. Yu. Glebov, F. J. Marshall, D. D. Meyerhofer, R. D. Petrasso, S. P. Regan, W. Seka, S. Skupsky, V. A. Smalyuk, J. M. Soures, C. Stoeckl, and B. Yaakobi, “A Measurement-Based Picture of Core Conditions in OMEGA Implosions.”

S. P. Regan, J. A. Delettrez, B. Yaakobi, R. Epstein, D. D. Meyerhofer, W. Seka, P. B. Radha, and R. P. J. Town, “Laser-Driven Burnthrough Experiments on OMEGA with 1-THz SSD.”

F. H. Séguin, J. A. Frenje, C. K. Li, D. G. Hicks, K. M. Green, R. D. Petrasso, V. Yu. Glebov, C. Stoeckl, P. B. Radha, J. M. Soures, D. D. Meyerhofer, S. Roberts, C. Sorce, T. C. Sangster, M. D. Cable, S. Padalino, and K. Fletcher, “Secondary-Proton Spectra from D_2 -Filled OMEGA Targets.”

W. Seka, D. D. Meyerhofer, R. S. Craxton, S. P. Regan, R. E. Bahr, R. W. Short, B. Yaakobi, J. Fuchs, D. Montgomery, and B. Afeyan, “Stimulated Brillouin Scattering in Very Long Velocity Scale-Length NIF Plasmas.”

R. W. Short, “The Effects of Beam-Intensity Structure on Two-Plasmon Decay in Direct-Drive Laser Fusion Targets.”

R. W. Short and A. Simon, “Propagation of Plasma Waves in Weakly Collisional Plasmas.”

A. Simon, R. W. Short, R. Betti, and V. N. Goncharov, “The Effect of Weak Collisions on Plasma Oscillations.”

V. A. Smalyuk, J. A. Delettrez, F. J. Marshall, D. D. Meyerhofer, S. P. Regan, R. P. J. Town, and B. Yaakobi, “Time-Resolved Measurements of Compressed Shell Temperature and Areal Density with Titanium-Doped Targets on OMEGA.”

C. Stoeckl, J. A. Delettrez, V. Yu. Glebov, P. W. McKenty, and D. D. Meyerhofer, “Comparison of Neutron Burn History Measurements with One- and Two-Dimensional Hydrodynamic Simulations.”

R. P. J. Town, J. A. Delettrez, V. N. Goncharov, D. R. Harding, P. W. McKenty, and R. L. McCrory, “The Effect of Elevated Internal Gas Pressure on Direct-Drive Cryogenic Target Performance.”

M. Umansky, J. P. Freidberg, and R. Betti, "Stability of the Resistive Wall Mode in the Presence of Moving Walls."

The following presentations were made at the Annual Symposium on Optical Materials for High Power Lasers, Boulder, CO, 16–18 October 2000:

S. Papernov, A. W. Schmid, R. Krishnan, and L. Tsybeskov, "Using Colloidal Gold Nanoparticles for Studies of Laser Interaction with Defects in Thin Films."

A. L. Rigatti, D. J. Smith, G. L. Mitchell, J. Dirmeyer, A. W. Schmid, and S. Papernov, "Moisture Barrier Coatings to Prevent Environmental Degradation of KDP Crystals."

D. J. Smith, J. B. Oliver, J. Howe, C. Stolz, and A. Rigatti, "The Use of Hafnia/Silica Multilayer Coatings on Large Mirrors and Polarizers for the National Ignition Facility."

J. Taniguchi, N. LeBarron, J. Howe, D. Smith, C. Stolz, C. Weinzapfel, and J. Kimmons, "Functional Damage Thresholds of Hafnia/Silica Coating Designs for the NIF Laser."

A. V. Okishev, "High-Energy Solid-State Lasers for ICF Applications" International Congress on "Optics-XXI Century," St. Petersburg, Russia, 16–18 October 2000.

S. P. Regan, J. A. Delettrez, B. Yaakobi, V. A. Smalyuk, F. J. Marshall, D. D. Meyerhofer, W. Seka, D. A. Haynes, Jr., and C. F. Hooper, Jr., "Characterization of Direct-Drive-Implosion Core Conditions on OMEGA with Time-Resolved Ar *K*-Shell Spectroscopy Radiative Properties of Hot Dense Matter," Santa Barbara, CA, 30 October–3 November 2000.

L. Waxer and J. Kelly, "Spectral Sculpting for NIF Demonstration Project," Third Annual Joint US-JAPAN Workshop on Laser-Driven Inertial Fusion Energy (IFE), Livermore, CA, 25–27 January 2001.

W. Seka, S. P. Regan, D. D. Meyerhofer, B. Yaakobi, C. Stoeckl, R. S. Craxton, R. W. Short, H. A. Baldis, and J. Fuchs, "Multibeam Interaction Experiments Under Direct-Drive NIF Conditions," 4th International Workshop on Laser-Plasma Interaction Physics, Banff, Alberta, Canada, 21–24 February 2001.

The following presentations were made at OPTO Northeast and Imaging 2001, Rochester, NY, 10–11 April 2001:

J. E. DeGroot, S. D. Jacobs, L. L. Gregg, and A. E. Marino, "Exploring Optical Polishing Pitch."

L. L. Gregg and S. D. Jacobs, "The Optics Suitcase—A Tool for Learning."

M. J. Guardalben, L. Ning, N. Jain, D. J. Battaglia, and K. L. Marshall, "Comparison of a Liquid Crystal Point Diffraction Interferometer (LCPDI) and a Commercial Phase-Shifting Interferometer."

S. D. Jacobs, S. R. Arrasmith, I. A. Kozhinova, L. L. Gregg, H. J. Romanofsky, and A. B. Shorey, "Magnetorheological Finishing: MRF of Optical Glasses and Crystals."

A. E. Marino, S. R. Arrasmith, L. L. Gregg, S. D. Jacobs, G. Chen, and Y. Duc, "Developing a Durable Phosphate Glass with a Low Glass Transition Temperature."

J.-R. Park, W. R. Donaldson, R. Boni, and R. Sobolewski, "Optical Properties of a Dual Diffusing Sphere Fiber Optic Detector."

The following presentations were made at the Conference on Lasers and Electro-Optics, Baltimore, MD, 6–11 May 2001:

W. R. Donaldson, J. H. Kelly, R. L. Keck, and R. Boni, "Predicting and Measuring Optical Pulse Shapes on the OMEGA Laser System."

M. J. Guardalben, A. Babushkin, R. S. Craxton, R. L. Keck, W. R. Donaldson, and K. A. Thorp, "Obtaining UV Energy Balance with 1-THz Spectral Bandwidth on the 60-Beam OMEGA Laser."

J. Li, T. Y. Hsiang, and W. R. Donaldson, "High-Speed Bragg Modulator on AlGaAs Waveguides."

T. Z. Kosc, K. L. Marshall, S. D. Jacobs, and B. Klehn, "Polymer Cholesteric Liquid Crystal Flakes for Display and Other Electro-Optic Applications," Novel Optical Materials and Applications, NOMA Cetraro, Italy, 20–27 May 2001.

The following presentations were made at the 31st Anomalous Absorption Conference, Sedona, AZ, 3–8 June 2001:

R. S. Craxton, D. D. Meyerhofer, W. Seka, R. W. Short, and R. P. J. Town, "Design of Long-Scale-Length Plasmas for Interaction Physics Experiments on OMEGA."

J. A. Delettrez, C. Stoeckl, S. P. Regan, P. W. McKenty, D. D. Meyerhofer, and J. P. Knauer, "Precision One-Dimensional LILAC Simulations of CH-Shell Implosions on the OMEGA Laser."

R. Epstein, J. A. Delettrez, V. Yu. Glebov, V. N. Goncharov, P. W. McKenty, P. B. Radha, S. Skupsky, V. A. Smalyuk, and C. Stoeckl, "One-Dimensional Simulation of the Effects of Unstable Mix on Neutron and Charged-Particle Yield from Laser-Driven Implosions Experiments."

V. Yu. Glebov, D. D. Meyerhofer, P. B. Radha, W. Seka, S. Skupsky, J. M. Soures, C. Stoeckl, S. Padalino, L. Baumgart, R. Colburn, J. Fuschino, and T. C. Sangster, "Current Status of Tertiary Neutron Diagnostic by Carbon Activation."

Y. A. Kholodov, "A Comparison of Monotone Schemes of High-Order Accuracy for Hyperbolic Problems."

V. N. Goncharov, S. Skupsky, R. Betti, J. A. Marozas, P. W. McKenty, and R. P. J. Town, "Hydrodynamic Stability of Moderate- to High-Gain Direct-Drive Target Designs for the NIF."

S. P. Regan, J. A. Delettrez, V. A. Smalyuk, B. Yaakobi, F. J. Marshall, R. Epstein, V. Yu. Glebov, P. A. Jaanimagi, D. D. Meyerhofer, P. B. Radha, W. Seka, S. Skupsky, J. M. Soures, C. Stoeckl, R. P. J. Town, D. A. Haynes, Jr., C. F. Hooper, Jr., C. K. Li, R. D. Petrasso, and F. H. Séguin, "Core-Mix Measurements of Direct-Drive Implosions on OMEGA."

W. Seka, S. P. Regan, D. D. Meyerhofer, B. Yaakobi, C. Stoeckl, R. S. Craxton, R. W. Short, H. Baldis, and J. Fuchs, "Multibeam SBS Interaction Experiments in OMEGA Long-Scale-Length Plasmas."

R. W. Short, R. S. Craxton, W. Seka, and D. D. Meyerhofer, "Theoretical Interpretation of SBS Observations in OMEGA Long-Scale-Length Plasma Experiments."

A. Simon and R. W. Short, "Damping and Spatial Propagation of Oscillations in Weakly Collisional Plasma."

C. Stoeckl, R. E. Bahr, V. Yu. Glebov, D. D. Meyerhofer, W. Seka, R. W. Short, and B. Yaakobi, "Measurements on the Two-Plasmon-Decay Instability on OMEGA."

A. Sunahara, J. A. Delettrez, R. W. Short, and S. Skupsky, "Electron Thermal Conduction in Inertial Confinement Fusion."

R. L. McCrory, J. A. Delettrez, R. Epstein, V. Yu. Glebov, R. L. Keck, P. W. McKenty, F. J. Marshall, D. D. Meyerhofer, P. B. Radha, S. P. Regan, S. Roberts, W. Seka, S. Skupsky, V. A. Smalyuk, C. Sorce, C. Stoeckl, J. M. Soures, R. P. J. Town, B. Yaakobi, J. D. Zuegel, J. A. Frenje, C. K. Li, R. D. Petrasso, F. H. Séguin, K. Fletcher, S. Padalino, C. Freeman, N. Izumi, R. Lerche, T. W. Phillips, and T. C. Sangster, "Core Performance in Direct-Drive Spherical Implosions on OMEGA," Pulsed Power Plasma Science 2001, Las Vegas, NV, 17–22 June 2001.

D. D. Meyerhofer, R. Betti, T. R. Boehly, J. A. Delettrez, R. Epstein, V. Yu. Glebov, V. N. Goncharov, D. R. Harding, R. L. Keck, R. L. McCrory, P. W. McKenty, F. J. Marshall, P. B. Radha, S. P. Regan, S. Roberts, W. Seka, S. Skupsky, V. A. Smalyuk, C. Sorce, C. Stoeckl, J. M. Soures, R. P. J. Town, B. Yaakobi, J. A. Frenje, C. K. Li, R. D. Petrasso, F. H. Séguin, K. Fletcher, S. Padalino, C. Freeman, N. Izumi, R. Lerche, T. W. Phillips, and T. C. Sangster, "Interferences of Mix in Direct-Drive Spherical Implosions with High Uniformity," 28th EPS Conference on Controlled Fusion and Plasma Physics, Madeira, Portugal, 18–22 June 2001.

D. D. Meyerhofer, J. H. Kelly, R. P. J. Town, L. J. Waxer, S. J. Loucks, R. L. McCrory, W. Seka, and S. Skupsky, "An Integrated Fast Ignitor Experiment for OMEGA," 5th Workshop on Fast Ignitor of Fusion Targets, Madeira, Portugal, 18–22 June 2001.

T. R. Boehly, B. Yaakobi, J. P. Knauer, D. D. Meyerhofer, and R. P. J. Town, "Measurements of Shock Heating in Laser-Driven Targets," 12th Biennial International Conference of the APS Topical Group on Shock Compression of Condensed Matter, Atlanta, GA, 24–29 June 2001.

G. Chen, Y. Du, A. Marino, L. L. Gregg, S. R. Arrasmith, and S. D. Jacobs, "Effect of SnO on Chemical Durability of Phosphate Glasses," The International Congress on Glass ICG 2001, Edinburgh, Scotland, 2–6 July 2001.

The following presentations were made at the 14th Target Fabrication Meeting, West Point, NY, 15–19 July 2001:

E. L. Alfonso, R. Q. Gram, and D. R. Harding, "CFD Modeling of Temperature/Pressure Gradients While Cooling Thin-Walled Direct-Drive Capsules."

R. Q. Gram and D. R. Harding, "Filling and Cooling Thin-Walled Cryogenic Targets."

L. D. Lund, D. R. Harding, D. J. Lonobile, D. Jacobs-Perkins, and T. Hinterman, "Alignment, Vibration, and Shroud Retraction: Initial Performance of the OMEGA Cryogenic Target Handling System."

P. W. McKenty, C. Stoeckl, V. N. Goncharov, M. J. Bonino, V. Yu. Glebov, D. R. Harding, D. D. Meyerhofer, and R. L. McCrory, "The Role of Improved Target Surface Roughness in Recent OMEGA Gas-Filled Implosion Experiments."

D. D. Meyerhofer, C. Chiritescu, T. J. B. Collins, J. A. Delettrez, R. Epstein, V. Yu. Glebov, D. R. Harding, R. L. Keck, S. J. Loucks, L. D. Lund, R. L. McCrory, P. W. McKenty, F. J. Marshall, S. F. B. Morse, S. P. Regan, P. B. Radha, S. Roberts, W. Seka, S. Skupsky, V. A. Smalyuk, C. Sorce, C. Stoeckl, J. M. Soures, R. P. J. Town, J. A. Frenje, C. K. Li, R. D. Petrasso, F. H. Séguin, K. Fletcher, C. Padalino, C. Freeman, N. Izumi, R. Lerche, T. W. Phillips, and T. C. Sangster, "Cryogenic-Target Experiments on OMEGA."

S. G. Noyes, M. J. Bonino, D. Turner, J. Tidu, and D. R. Harding, "Target Fabrication Techniques at LLE."

S. Skupsky, R. Betti, V. N. Goncharov, R. L. McCrory, P. W. McKenty, R. P. J. Town, D. D. Meyerhofer, and D. R. Harding, "Wetted-Foam Target Designs for the NIF and OMEGA."

F.-Y. Tsai, E. L. Alfonso, S. H. Chen, D. R. Harding, and T. N. Blanton, "Effects of Processing Conditions on the Quality and Properties of Vapor-Deposited Polyimide Shells."

M. D. Wittman, D. R. Harding, P. W. McKenty, H. Huang, L. S. Iwan, T. J. Kessler, L. Elasky, and J. Sailer, "Layering and Characterization of Solid Deuterium Fuel Layers in Permeation-Filled Cryogenic Targets for OMEGA."

A. V. Tikhonravov, M. K. Trubetskov, I. V. Kockikov, J. B. Oliver, and D. J. Smith, "Real-Time Characterization and Optimization of *E*-Beam Evaporated Optical Coatings," Optical Interference Coatings, Topical Meeting and Tabletop Exhibit, Banff, Alberta, Canada, 15–20 July 2001.

S. D. Jacobs, S. R. Arrasmith, I. A. Kozhinova, S. R. Gorodkin, L. L. Gregg, H. J. Romanofsky, and T. D. Bishop II, "Effects of Changes in Fluid Composition on Magnetorheological Finishing of Glasses and Crystals," 10th International Conference on Precision Engineering (ICPE), Yokohama, Japan, 18–20 July 2001.

The following presentations were made at SPIE's 46th Annual Meeting, The International Symposium on Optical Science and Technology, San Diego, CA, 29 July–3 August 2001:

S. R. Arrasmith, S. D. Jacobs, J. Lambropoulos, A. Maltsev, W. Kordonski, D. Golini, and E. Cleaveland, "The Use of Magnetorheological Finishing (MRF) to Relieve Residual Stress and Subsurface Damage on Lapped Semiconductor Silicon Wafers."

J. E. DeGroot, S. D. Jacobs, L. L. Gregg, and A. E. Marino, "Quantitative Characterization of Optical Polishing Pitch."

I. A. Kozhinova, S. R. Arrasmith, J. C. Lambropoulos, S. D. Jacobs, and H. J. Romanofsky, "Anisotropy in MRF Removal Rate for a Sapphire Single Crystal."

The following presentations were made at the EuroConference on Advanced Diagnostics for Magnetic and Inertial Fusion, Varenna, Italy, 3–7 September 2001:

R. L. Keck, W. R. Donaldson, V. Yu. Glebov, P. A. Jaanimagi, F. J. Marshall, P. W. McKenty, D. D. Meyerhofer, S. P. Regan, W. Seka, C. Stoeckl, and R. Boni, "Laser and X-Ray Irradiation Diagnostics That Have Paved the Path Toward Significantly Improved ICF Target Performance."

W. Seka, R. S. Craxton, R. L. Keck, J. P. Knauer, D. D. Meyerhofer, S. P. Regan, C. Stoeckl, B. Yaakobi, R. E. Bahr, D. Montgomery, B. Baldis, and R. Kirkwood, "Laser-Plasma Interaction Diagnostics for ICF Fusion Research."

C. Stoeckl, J. A. Delettrez, R. Epstein, V. Yu. Glebov, R. L. Keck, R. L. McCrory, P. W. McKenty, F. J. Marshall, D. D. Meyerhofer, P. B. Radha, S. P. Regan, S. Roberts, W. Seka, S. Skupsky, V. A. Smalyuk, C. Sorce, J. M. Soures, R. P. J. Town, B. Yaakobi, J. A. Frenje, C. K. Li, R. D. Petrasso, F. H. Séguin, K. Fletcher, S. Padalino, C. Freeman, N. Izumi, R. Lerche, T. W. Phillips, and T. C. Sangster, "Measuring Core Performance and Mix in Direct-Drive Spherical Implosions on OMEGA."

The following presentations were made at the Second International Conference on Inertial Fusion Sciences and Applications, Kyoto, Japan, 9–14 September 2001:

C. K. Li, F. H. Séguin, J. A. Frenje, S. Kurebayashi, R. D. Petrasso, J. M. Soures, D. D. Meyerhofer, V. Yu. Glebov, P. B. Radha, S. Roberts, W. Seka, C. Stoeckl, and T. C. Sangster, "Charged-Particle Spectroscopy on OMEGA and Recent Results of Capsule Implosion Studies."

D. D. Meyerhofer, J. H. Kelly, R. P. J. Town, L. J. Waxer, S. J. Loucks, R. L. McCrory, W. Seka, and S. Skupsky, "An Integrated Fast Ignitor Experiment for OMEGA."

P. B. Radha, J. A. Delettrez, R. Epstein, V. Yu. Glebov, V. N. Goncharov, R. L. Keck, R. L. McCrory, P. W. McKenty, F. J. Marshall, D. D. Meyerhofer, S. P. Regan, S. Roberts, W. Seka, S. Skupsky, V. A. Smalyuk, C. Sorce, C. Stoeckl, J. M. Soures, R. P. J. Town, B. Yaakobi, J. D. Zuegel, J. A. Frenje, C. K. Li, C. K. Petrasso, F. H. Séguin, K. Fletcher, S. Padalino, C. Freeman, N. Izumi, R. Lerche, T. W. Phillips, and T. C. Sangster, "Compressed Core Conditions in Direct-Drive Spherical Implosions on OMEGA."

S. P. Regan, B. Yaakobi, J. A. Delettrez, V. A. Smalyuk, F. J. Marshall, R. Epstein, V. Yu. Glebov, P. A. Jaanimagi, D. D. Meyerhofer, P. B. Radha, W. Seka, S. Skupsky, J. M. Soures, C. Stoeckl, R. P. J. Town, D. A. Haynes, Jr., C. F. Hooper, C. K. Li, R. D. Petrasso, and F. H. Séguin, "High-Density, Direct-Drive Implosions on OMEGA."

S. Skupsky, R. Betti, T. J. B. Collins, V. N. Goncharov, D. R. Harding, R. L. McCrory, P. W. McKenty, D. D. Meyerhofer, and R. P. J. Town, "High-Gain, Direct-Drive Target Designs for the National Ignition Facility."

R. P. J. Town, V. N. Goncharov, P. W. McKenty, J. A. Delettrez, R. Epstein, R. L. McCrory, P. B. Radha, S. Skupsky, V. Yu. Glebov, D. R. Harding, D. D. Meyerhofer, F. J. Marshall, S. P. Regan, W. Seka, V. A. Smalyuk, C. Stoeckl, J. M. Soures, B. Yaakobi, and J. D. Zuegel, "OMEGA Direct-Drive Cryogenic Target Physics."

UNIVERSITY OF
ROCHESTER